

Dissertation zur Erlangung des Doktorgrades
der Fakultät für Chemie und Pharmazie
der Ludwig-Maximilians-Universität München

**Solid electrolytes and sulfide-based cathodes for
next-generation solid-state-batteries: Synthesis,
transport properties and nanostructure engineering**

Anna-Katharina Sophia Lia Hatz

aus

München

2021

Erklärung

Diese Dissertation wurde im Sinne von §7 der Promotionsordnung vom 28. November 2011 von Frau Dr. Bettina V. Lotsch betreut.

Eidesstattliche Versicherung

Diese Dissertation wurde eigenständig und ohne erlaubte Hilfe erarbeitet.

München, 28.11.2021

Anna-Katharina Hatz

Dissertation eingereicht am: 09.08.2021

1. Gutachterin: Dr. Bettina V. Lotsch

2. Gutachterin: Dr. Wolfgang Schnick

Mündliche Prüfung am 18.10.2021

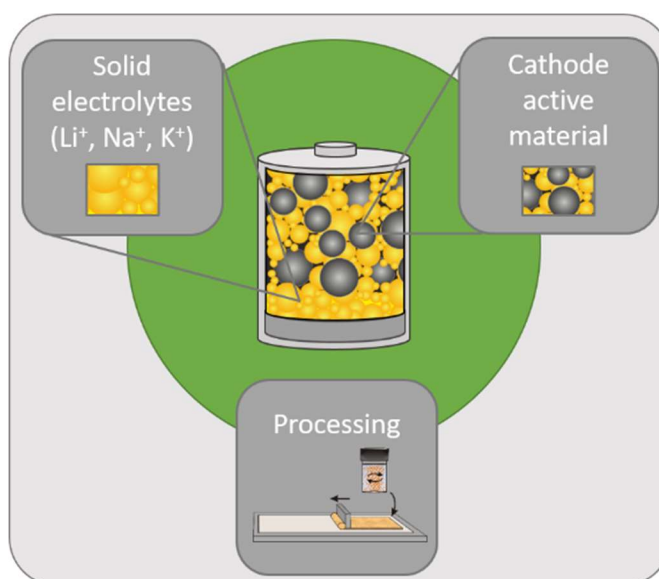
„Wer immer tut, was er schon kann, bleibt immer das, was er schon ist.“

Henry Ford

Abstract

Thriving for a green future, ambitious goals are set for the next generation of rechargeable batteries: They should deliver a high capacity and power and enable fast charging. Solid-state-batteries are considered one of the most promising technologies to achieve that jump in battery performance while guaranteeing high safety. The development of inorganic solid electrolytes is seen as key to progress, and the substitution of lithium by sodium or potassium and the development of Cobalt- and Nickel-free cathodes offer a reduction in cost and increased sustainability. This work contributes to the latter by

rationalizing the poor battery performance of the ordered, rock-salt-type cathode materials Li_3NbS_4 and Li_3TaS_4 based on their inherently poor electronic and ionic conduction properties. It investigates several solid electrolytes showing fast lithium, sodium and potassium ion conductivity. For the first time, the ionic conductivity and diffusivity of Li_2SiP_2 and LiSi_2P_3 are reported and for a series of supertetrahedral sodium phosphidosilicates (from $\text{Na}_{23}\text{Si}_{19}\text{P}_{33}$ (T3T3) to $\text{HT-NaSi}_2\text{P}_3$ (T5T5)) an increase in ionic conductivity with increasing supertetrahedra size is found. The latter insight is then applied to discover KSi_2P_3 , the first fast, non-oxide-based potassium ion conductor. Moreover, light is shed on the trend in ionic conductivity in the Na_5AlSi_4 - Na_4Si_4 solid solution series. Here, the interplay of charge carrier concentration and low site symmetry of sodium ions leads to orders of magnitude increased conductivity. To tackle the question of how to process solid electrolytes on an industrial scale, the processability of the fast solid electrolyte Li_7SiPS_8 in aprotic solvents with a low donor number is demonstrated and the decomposition mechanism of thiophosphates in alcohols is revealed. Last but not least, this thesis presents fast water-assisted lithium ion conduction in restacked lithium tin sulfide nanosheets demonstrating that restacking and the presence of humidity in the environment can enhance lithium ion conductivity. All of these projects contribute to a solid future of lithium ion batteries and beyond by developing and disclosing the properties of new and already known solid electrolytes and cathode materials.



Danksagung

Danke Bettina, dass du mir die Möglichkeit gegeben hast meine Doktorarbeit im spannenden Feld der Festelektrolyte unter deiner Betreuung als Teil deiner Arbeitsgruppe am Max-Planck-Institut für Festkörperforschung und in München an der Ludwig-Maximilians-Universität durchzuführen. Ich danke dir für deine jahrelange Unterstützung, die vielen wissenschaftlichen Diskussionen, dem guten menschlichen Miteinander und dass du mir immer die Möglichkeit und das Vertrauen gegeben hast eigenen Ideen nachzugehen. Außerdem möchte ich mich bei dir Nella für deine wissenschaftliche Unterstützung und tatkräftigen Begleitung meiner Projekte herzlich bedanken.

Des Weiteren möchte ich mich bei euch, meinen beiden wunderbaren Co-Autoren Arthur und Sascha bedanken. Über die Jahre haben wir es gemeinsam geschafft, diese strukturell, synthetisch und elektrochemisch anspruchsvollen Systeme neu zu erschaffen und zu charakterisieren. Es war mir eine Freude mit euch zusammen zu arbeiten und mit euch durch die Täler und Gipfel der Forschung zu wandern. Ohne euch wäre diese Arbeiten nicht möglich gewesen. Mein Dank gebührt auch all meinen anderen Co-Autoren und Korrektoren, die mir zur Seite standen (Danke Tanja, Igor, Robert, Doug, Markus, Sebastian, Maxwell, Marco) und Studenten und Praktikanten (Danke Ausra, Ye, Nadine, Rik, Fiona, Julian, Lucas) die meine Projekte durch ihre Arbeit unterstützt haben und damit maßgeblich zum Erfolg beigetragen haben.

Hier möchte ich mich auch noch explizit bei Ihnen Prof. Johrendt, Prof. Karaghiosoff und Prof. Dinnebier bedanken, dass wir gemeinsam an diesen spannenden Projekten gearbeitet haben sowie bei Prof. Schnick, Prof. Bein und Prof. Janek, dass Sie Teil meiner Prüfungskommission sind.

Besonderer Dank gebührt meiner gesamten Arbeitsgruppe, den Stuttgartern und Münchnern, die meine Doktorarbeitszeit zu einer ganz besonderen Zeit gemacht haben an die ich in Zukunft immer gerne zurückdenken werde. Hier habe ich nicht nur Kollegen, sondern auch Freunde gefunden. Insbesondere möchte ich auch noch euch, meinen FestBatt Kollegen (Christian, Max, Hien) besonderen Dank aussprechen! Wir waren ein Spitzenteam und sind zusammen wirkliche Meeting-Profis geworden (das gilt auch für die anderen FestBatt Kollegen aus ganz Deutschland: AG Janek, AG Zeier, AG Kwade, AG Albe, AG Latz, AG Wall, AG Granwehr).

Ansonsten möchte ich noch den Mitgliedern von NIM (besonders dem Studentboard: Magnus, Sana, Tobias, Lukas) für die gute Zeit als Teil des Graduierten Programms danken sowie meinen Laborkollegen vom AK Schnick (Fabi, Jonny, Timo, Irina) und der wissenschaftlichen Unterstützung aus dem Maier Department des MPI, insbesondere Igor Moudrakovski für die vielen NMR Messungen, und Rotraut Merkle und Rob Usiskin für die internen Review Verfahren und aufmunternden Worte.

Zu guter Letzt, danke ich euch, meiner Familie, Partner und Freunden. Ihr habt mich während meiner Doktorarbeit begleitet und unterstützt, getröstet und motiviert, wenn nötig mit Essen und Ablenkung versorgt, und meine Erfolge mit mir gefeiert.

Danke.

Table of contents

Erklärung.....	2
Abstract.....	4
Danksagung.....	5
Table of contents	6
1 Introduction	8
2 Theoretical background	10
2.1 Rechargeable batteries	10
2.1.1 Working principle of a lithium ion battery.....	11
2.1.2 Key performance indicators of a battery.....	12
2.1.3 Processes and phenomena limiting battery performance	14
2.2 Concepts for improving batteries (next generation batteries).....	16
2.2.1 Improvement of the electrodes.....	16
2.2.2 Improvement of electrolyte.....	19
2.2.3 Battery systems beyond lithium	19
2.3 Solid–state–batteries.....	21
2.3.1 Solid electrolytes.....	22
2.3.2 Processing of solid electrolytes for SSBs.....	27
3 Theoretical Background of Analytical Methods.....	29
3.1 Ionic Conduction in solids	29
3.2 Measurement of the specific conductivity	34
3.2.1 Impedance spectroscopy of solid ionic conductors.....	35
3.2.2 Potentiostatic and galvanostatic polarization measurements for determining partial electronic conductivity and transference numbers	44
3.3 Measurement of ion diffusivities <i>via</i> pulsed field gradient NMR.....	46
4 Experimental, Results and Discussion.....	49
4.1 Taking a closer look: (Micro)Structure and electronic properties of rock–salt–type Li_3NbS_4 and Li_3TaS_4	49
4.1.1 Supporting Information	69
4.2 Lithium ion transport dynamics in Li_2SiP_2 and LiSi_2P_3	91
4.2.1 Supporting Information	101
4.3 Fast Sodium Ion Conductivity in Supertetrahedral Phosphidosilicates	103
4.3.1 Supporting Information	114
4.4 Polymorphism and fast Potassium-Ion Conduction in the T5 Supertetrahedral Phosphidosilicate KSi_2P_3	161
4.4.1 Supporting Information	173

4.5	Finding the right blend: Interplay between structure and sodium ion conductivity in the system $\text{Na}_5\text{AlS}_4\text{-Na}_4\text{SiS}_4$	204
4.5.1	Supporting Information	220
4.6	Chemical stability and ionic conductivity of LGPS-type solid electrolyte tetra- Li_7SiPS_8 after solvent treatment	247
4.6.1	Supporting Information	265
4.7	Fast water-assisted lithium ion conduction in restacked lithium tin sulfide nanosheets	281
4.7.1	Supporting Information	303
5	Summary, Conclusion and Outlook	342
6	References	345
7	Appendix.....	350
7.1	List of Publications.....	350
7.1.1	First-authored.....	350
7.1.2	Second-authored	350
7.2	Contributions to Conferences	351
7.2.1	Oral presentations	351
7.2.2	Poster presentations	351
7.3	Curriculum Vitae	352

1 Introduction

Rechargeable batteries are one of the key technologies enabling Europe's transition from fossil fuels and nuclear power to renewable energy. They are central for applications ranging from stationary energy storage, stabilizing the power grid, over electric vehicles (EV), enabling CO₂-emission free mobility to many more aspects of modern life. However, a few years ago, almost no batteries were manufactured in Europe causing a dependency on foreign suppliers. Thus, based on the European Green Deal¹, the Circular Economy Action Plan² and the European Industrial Strategy³, the European Battery Alliance⁴ consisting of EU countries, industrial participants and the scientific community is building up battery technology and production capacity in the EU. A match of production and demand is anticipated by 2025 and from that onwards a battery market of up to 250 billion € is predicted.⁴ However, to ensure sustainability of European batteries, they should not only show a competitive, high performance, but also a closed life cycle loop.¹⁻⁴ At the beginning of a battery life, a local and responsible sourcing of the raw materials is needed. Then the raw materials should be processed in an environmentally friendly fashion into a cell using mostly renewable energy. Then, the cell serves its primary use as e.g. in an EV, possibly followed by a secondary use as e.g. a stationary energy storage device. Towards the end of a battery life, the cell is recycled and the recovered materials are returned to the battery production. In total, the requirements for the next generation batteries are high. They should not only be affordable, reliable and safe but also sustainable.

In order to replace the state of the art lithium ion battery (LIB), the concept of the solid-state-battery (SSB), in which the liquid electrolyte of a LIB is substituted by a solid electrolyte, is worldwide regarded as particularly attractive.⁵⁻¹¹ The SSB promises a higher safety in terms of flammability and potentially enables a jump in energy density as well as fast rate capability. The search of the latter is mainly driven by the demand of the automotive sector.¹² The central component in a SSB is the solid electrolyte that should have a high ionic conductivity, and a large potential stability window among others. Ideally, the solid electrolyte only contains earth-abundant elements that are low-cost, and it should be easy to process and resistant to a large number of environmental influences. Consequently, the search for the "ideal" solid electrolyte of the future does not only take the optimization of lithium-ion based systems into consideration, but also the elimination of critical elements such as lithium, cobalt and nickel.^{7,13} The substitution of these elements can be realized by the use of e.g. sodium or potassium ion based materials or alternative cathodes for LIBs. These measures promise drastically reduced costs and less dependence on raw materials from outside the EU. However, since meeting all criteria with one material is very challenging, battery materials are also optimized for specific applications where one criterion dominates the other such as weight vs. life time.

This work contributes to the development of cobalt and nickel-free lithium ion cathode materials as well as lithium, sodium and potassium ion solid electrolytes in a variety of projects. First in chapter 4.1 the ordered rock-salt-type crystal structures and the real microstructures of Li₃NbS₄ and Li₃TaS₄ are described and the poor battery performance of these cathode materials is rationalized by the inherent poor electronic properties originating from their structure. Second, in the structural family of supertetrahedral phosphidosilicates several new compounds showing high ionic conductivities are introduced. In chapter 4.2, the ionic conductivity and diffusivity of Li₂SiP₂ and LiSi₂P₃ is investigated for the first time exposing grain boundaries as limiting factor for performance. In chapter 4.3, the structure-property-relationship of a series of six new supertetrahedral sodium phosphidosilicates showing an increase in ionic conductivity with increasing supertetrahedra size up to $4 \times 10^{-4} \text{ S cm}^{-1}$ in HT-NaSi₂P₃ is revealed.¹⁴ In chapter 4.4, the rationale of large supertetrahedral entities leading to high ionic conductivity is transferred to a potassium based system, leading to the discovery of the first, fast non-oxide based potassium ion conductor KSi₂P₃.¹⁵ Moreover, in the newly introduced sulfide based material series Na₅AlS₄-

Na_4SiS_4 in chapter 4.5, the enhancement of ionic conductivity by several orders of magnitude by the interplay of charge carrier concentration and low site symmetry of sodium ions is brought to light.¹⁶ To move the solid electrolyte research beyond the introduction of new compounds, the known fast solid electrolyte Li_7SiPS_8 ¹⁷ is treated with solvents simulating processing during battery cell manufacturing. The evaluation of chemical stability and ionic conductivity of Li_7SiPS_8 in chapter 4.6 finds that aprotic solvents with a donor number $< 15 \text{ kcal mol}^{-1}$ are suitable for industrial slurry fabrication and proposes a reaction mechanism for the decomposition in alcohols into oxygen-substituted thioethers. In chapter 4.7, restacked lithium tin sulfide (Li-TS) is investigated, to better understand the influence of suspension based exfoliation and restacking of an ion conducting material and of environmental conditions such as humidity on its lithium ion conduction properties. Despite the complicated structure of Li-TS, which is dominated by severe disorder and a variable lithium ion content, Li-TS is capable of a fast water-assisted lithium ion conduction at high humidities exceeding that of parental $\text{Li}_{0.8}\text{Sn}_{0.8}\text{S}_2$.

Summarizing, this work further develops new and already known solid electrolytes and sulfide based cathode materials. By bringing structure and properties into context, this work contributes to a solid future of lithium ion batteries and beyond playing a vital role in reaching the ambitious goals for a greener and stronger battery production in Europe and elsewhere.

2 Theoretical background

2.1 Rechargeable batteries

There are several different ways to store electrical energy ranging from mechanical, over electrical, thermal, chemical to electrochemical storage. The selection of storage depends on the amount of energy that should be stored and requirements originating from the targeted application such as the desired mobility, size, life time and many more. For mobile devices and medium scale energy storage, the battery has emerged as the storage medium of choice and is implemented in various devices such as pacemakers, mobile phones, electric vehicles (EVs) or serves as stationary energy storage.

In Figure 1 the most important parameters of a battery are summarized in the spider diagrams as deduced in this thesis. An “ideal” battery (Figure 1a) shows a high energy density (how much energy can be stored), high power (how much energy can be extracted in a given time interval), high charge/discharge rates (how fast can the energy be extracted) and a long life time (high cycling stability).¹⁸⁻²¹ Besides, it is low cost, safe, easy to process and recycle, environmentally friendly and operates in a broad temperature window without a temperature managing system and the application of a high pressure. Under storage conditions, it shows only a low self-discharge. To meet all these requirements is a multifaceted, highly challenging task. Depending on the application, not all requirements must be fully fulfilled. For the application in electrical vehicles for instance, the requirements are still quite high as visualized in Figure 1b, but the cost can be in a medium range, as EVs, at least at the moment, are premium class vehicles.¹² According to a recent benchmarking analysis, a gravimetric energy density of 400 Wh kg^{-1} , an volumetric energy density of 1000 Wh L^{-1} and a cycle life of at least 200 cycles with a capacity retention of 80 % are targeted for current research projects.²² In contrast, for stationary systems (Figure 1c), the weight of a storage unit does not matter so much, thus, the gravimetric energy density is not so important.¹³

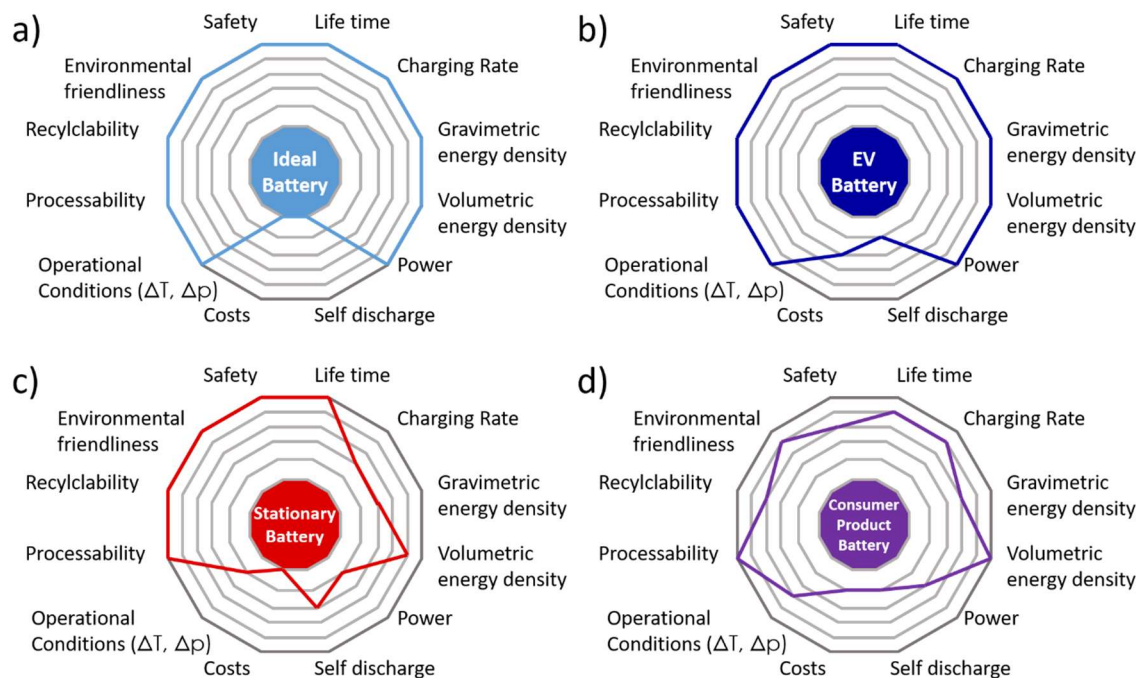


Figure 1 Estimated requirements for batteries based on the targeted application: a) an ideal battery b) a battery for the application in electric vehicles (EVs) c) a stationary battery for grid storage d) a battery for portable consumer products such as a mobile phone. The given values are a qualitative estimates based on the references in this thesis [5-3, 18-22, ff.]

However, as large amounts of material are required, low costs are of much higher importance. Safety is a key requirement for both applications (EVs and stationary storage), since the life of humans can be directly endangered by e.g. large burning battery packs.²³ For a battery in a portable consumer product such as a mobile phone (Figure 1d), the size is of utmost importance, thus the volumetric energy density needs to be high, but other factors are not so important, due to the reduced size. However, before going into details on how to improve the current state of art lithium ion technology, a concise introduction to rechargeable batteries based on Petrovic *et al.*²¹ and Julien *et al.*²⁰ is given in the following chapters 1.1.1-1.2.2, additional references are given at the relevant position.

2.1.1 Working principle of a lithium ion battery

A battery allows converting chemical energy to electrical energy (electrochemical energy storage). In a primary cell, the transformation of chemical to electrical energy is irreversible. The most commonly used representative of primary cells is the alkaline (Zn–MnO₂) battery. In a secondary battery (accumulator) the conversion reaction is reversible, thus, after a first discharge, the chemical reactions can be reversed by the supply of electrical energy (charging). During discharge, the current is created from the reaction between two materials (electrodes). An electron blocking, but ion permeable material (electrolyte) separates these two electrodes. Thus, for the reaction to proceed, the electrons move from the one electrode (anode, negative pole) through an outer circuit to the other electrode (cathode, positive pole) providing electrical energy. The respective ions move through the electrolyte to the cathode to recombine there with electrons and be stored in the cathode material.

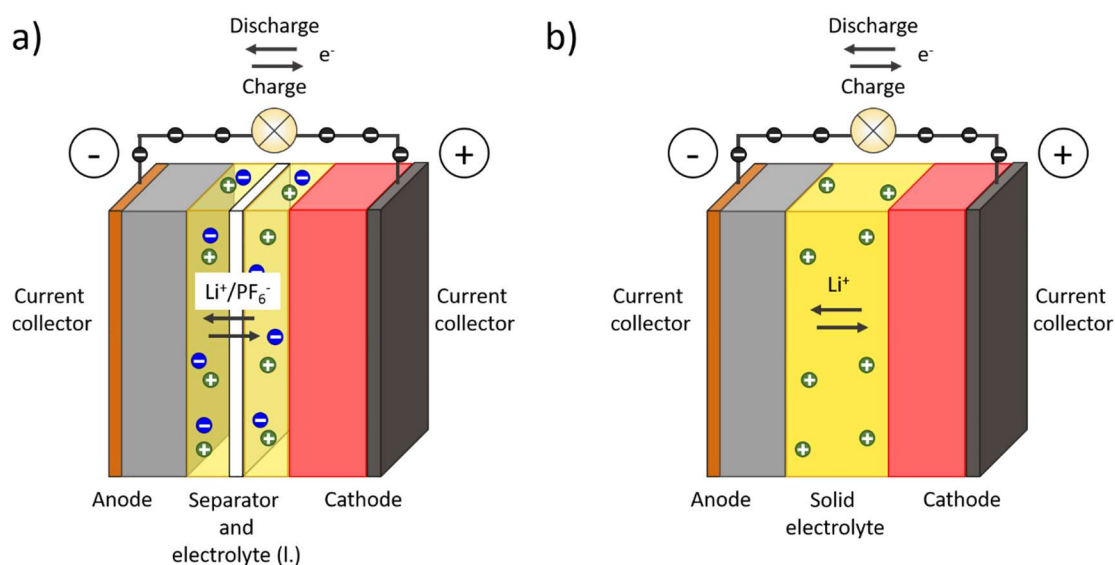


Figure 2 Schemes of a) a state-of-the-art lithium ion battery with a liquid electrolyte and a separator and b) a solid-state-battery with a solid electrolyte replacing the liquid electrolyte and separator.

The most commonly used secondary battery is the lithium ion battery (LIB) introduced by Sony²⁴ in the 1990s and schematically drawn in Figure 2a. As negative electrode (anode), typically graphite-type carbon that intercalates lithium between carbon layers is used. During discharge, the material is oxidized and lithium ions and electrons are created according to (1).



The electrons move through the outer circuit and the ions through a separator soaked with a typical electrolyte mixture consisting of an aprotic organic solvent such as dimethyl carbonate and other alkyl carbonate solvents containing lithium hexafluorophosphate salt (LiPF₆). If a solid

electrolyte replaces the liquid electrolyte and separator, a solid–state–battery (SSB), which is in focus of this work, is created (cf. Figure 2b).

At the positive electrode (cathode) a lithium metal oxide, in the easiest case LiCoO_2 with a deficiency of lithium (x) incorporates the incoming lithium ions and electrons according to (2) reducing Co^{4+} to Co^{3+} .



LiCoO_2 is a layered material with the redox active transition metal $\text{Co}^{3+}/\text{Co}^{4+}$. It is a so–called intercalation cathode that allows the de/insertion of lithium without severe structural changes ($0 < x < 1$) enabling repeated cycling (charge/discharging). The total reaction in a LIB is:



Upon charging, the direction of the reactions switches by applying a current. Nominally, during charging, the negative electrode (anode) is LiCoO_2 , but in favor of convention and simplification, the following text will refer to the materials as cathode and anode from the perspective of the discharge process.

2.1.2 Key performance indicators of a battery

As visible from reaction (3), the driving force of the cell reaction is the difference in chemical potential of lithium in the anode (C) μ_A^i and cathode material (LiCoO_2) μ_C^i . The difference in chemical potential sets the basis of the maximal potential V_{OCV} (open circuit potential) a cell can give according to equation (4) with n being the number of electronic charges involved in the reaction and F the Faraday constant.

$$V_{OCV} = \frac{1}{nF} (\mu_A^i - \mu_C^i) \quad (4)$$

The Nernst–equation (5) allows calculating the potential of the cell reaction under non–standard conditions taking the effect of concentrations in solution or effective pressure, and temperature into account. In a generalized reaction, μ_B^i and μ_D^i are the chemical potentials of a species in the products of the anodic oxidation and cathodic reduction, respectively, and R is the gas constant and T the absolute temperature.

$$E = E^0 - \frac{RT}{nF} \ln \frac{\mu_B^i \mu_D^i}{\mu_A^i \mu_C^i} \quad (5)$$

The standard electrode potential E^0 of a cell can be calculated as difference of the standard reduction potential E_{red}^0 of the cathode and anode, respectively. These E_{red}^0 values are measured against the standard hydrogen electrode (SHE) and listed in the standard electrode potential series.

$$E^0 = E_{red}^0(\text{cathode}) - E_{red}^0(\text{anode}) \quad (6)$$

Since lithium has the lowest standard redox potential of -3.04 V against the SHE, the dominance of lithium based batteries enabling a high cell voltage is self–explanatory. However, in reality the cell voltage is limited by the stable potential window of the liquid electrolyte in a LIB, which is typically 4.2 V (depending on the electrolyte and cathode). Another advantage of lithium is its low molecular weight (6.9 g mol^{-1}) enabling high specific capacities as the theoretical capacity Q_{th} [Ah kg^{-1}] or [mAh g^{-1}] of a material can be calculated *via* (7) taking the molecular weight M_w and

number of involved charges n into account. Pure lithium metal has a high specific capacity of 3860 mAh g⁻¹.

$$Q_{th} = \frac{nF}{3600 \times M_w} \times 1000 = \frac{26.8}{M_w} \times n \times 1000 \quad (7)$$

The specific capacity determines the specific energy of a cell. The theoretical specific energy E_{theo} (gravimetric energy density) [Wh kg⁻¹] of a battery is the product of the standard cell potential E^0 and the theoretically stored charge, i.e. the theoretical capacity as given in (8).

$$E_{theo} = E^0 Q_{th} \quad (8)$$

For a complete cell, the capacity of the anode and cathode have to be taken into consideration according to (9).

$$Q_{th,cell} = \left(\frac{1}{Q_{cathode}} - \frac{1}{Q_{anode}} \right)^{-1} \quad (9)$$

In practice, the specific energy E_{pr} is calculated by (10) as product of the operating potential V_{oc} and the measured discharge capacity Q_{dis} at an appropriate discharge rate.

$$E_{pr} = V_{oc} Q_{dis} \quad (10)$$

The energy in respect to the volume of a battery is described by the volumetric energy density [Wh L⁻¹]. But in a device, the actual energy density of a whole battery pack/system is further reduced by additional components such as additives to the active electrode materials, the current collectors, the electrolyte, the separator and casing, which all add to the weight and volume of a battery but not the energy stored. After considering this addition to weight and volume and the imperfect nature of electrochemical reactions, the actual battery energy is typically 25–35% of the theoretical energy of the active materials.

The rate of the discharge/charge of a battery is the C-rate. The C-rate measures the time relative to the maximum capacity of a cell. A discharge at nC rate means a full discharge in $1/n$ hours. For instance, a rate of $C/2$ means a full discharge within 2 h. For many applications, in particular the charging of electric vehicles, a fast charging rate with high current densities is desired to minimize the time users have to wait to recharge their vehicle.

Another important key parameter for the performance of a battery is the power P_{out} [W], given as product of the discharge current I_{dis} and the discharge voltage V_{dis} .

$$P_{out} = I_{dis} V_{dis} \quad (11)$$

After normalizing to the specific weight the power density (specific power) [W kg⁻¹] can be derived.

The performance of a battery over time, i.e. the cycling stability, is represented by the coulombic efficiency (CE) which is given as ratio of capacity of discharge and following charging cycle in (12). Ideally, the battery capacity should stay above 98 % of the first cycle for several hundred cycles.

$$CE(\%) = \frac{Q_{dis}}{Q_{ch}} \times 100\% \quad (12)$$

2.1.3 Processes and phenomena limiting battery performance

Since batteries are multicomponent systems, the interaction between the different materials and their properties lead to a complex behavior and there are many possibilities that limit the performance of a battery making it non-ideal as summarized in the following.

The choice of electrode materials determines the possible voltage window and theoretically achievable capacity. As the electrode material (in particular the cathode) makes up the major part of a cell in volume and weight, the prices of raw materials and processing dictates a large portion of the costs.¹³ The selection of elements in the electrode materials also determines the sustainability of a battery (where and how are the raw materials mined, is recycling possible, among others). The partial electronic and ionic conductivity of the electrode materials influences the rates of charging and power density. Here, the microstructure and (particle and electrode composite) morphology of the electrodes come into play influencing the ionic and electronic percolation paths (tortuosity) in the electrodes. The latter limit the accessible amount of active material especially during charging at higher rates.^{11, 25} The influence of the surface area of the electrodes is ambivalent. On the one side, a large surface area allows for high rates due to short diffusion paths and high currents, on the other side, a lot of active material gets consumed by the formation of a solid-electrolyte-interface (SEI) with the liquid electrolyte in a typical LIB, enlarging the irreversible capacity loss. The reaction at the electrodes severely influences the cell performance in general. For example, the repeated volumetric expansion and contraction (breathing) of typical NMC cathode materials during de/intercalation of lithium in the host structure, leads to crack formation and mechanical failure of the active material, eventually leading to severe capacity loss over time.

Besides the electrodes, the electrolyte is a key component of a battery. Its ionic conductivity, determines the rate and power and thus should be as high as possible. Whereas, to avoid the transport of electrons through the cell, the electronic conductivity should be as low as possible. In the state of the art LIB a liquid electrolyte on the basis of organic carbonate solvents with lithium salts is employed. The ionic conductivity of the liquid electrolyte is limited to about 10 mS cm^{-1} with a transference number lower than one, posing a limiting factor for high charging rates and the application of high currents. Moreover, the redox stability of the organic liquid is limited to a potential window of about 4.2 V restricting the effective maximum voltage a battery with a liquid electrolyte can have. An advantage of a liquid is the good wetting of the (partially porous) electrodes. But, at the interface to the electrolyte is consumed by a reaction with the electrodes forming a SEI, contributing to the loss of active material.

Upon subsequent cycling, the SEI acts either as a passivating layer kinetically stabilizing the cell (after e.g. a formation cycle) or, when the electronic conductivity is too high, grows with cycling of the battery leading to continuous capacity fading (limited cycle life). The growth of the SEI increases the internal resistances (leading to slower kinetics and heat losses). When a battery heats up, either due to high ambient temperature or poor thermal management (cell design) the SEI can break down enabling an unhindered, exothermic reaction of the electrolyte with the electrodes in turn leading to a further increase in temperature. At elevated temperatures $>100 \text{ }^\circ\text{C}$, the organic solvent decomposes releasing flammable gases, such as ethane and methane building up a high pressure in a cell. Then the cell can blow up and when the gases come in contact with oxygen from air they can catch fire.²³ Such a fatal increase in temperature, can also be caused by the fast release of energy during a short-circuit, which is often caused by lithium metal dendrites that grow through the internal of a cell. Mechanical damaging of a cell pack, e.g. in a car accident can lead to the same hazardous outcome. Moreover, if a cell is overcharged the state of the art oxide base cathode materials evolve oxygen gas also increasing the risk of a thermal runaway.²³

Besides the choice of material, microstructuring and assembly, the way of cycling and temperature management is of utter importance for the performance. As mentioned earlier, often a formation

cycle is needed to enable kinetic stabilization of the cell. However, overcharging can lead to a decomposition of the electrodes, e.g. cathodes releasing gaseous oxygen, or a decomposition of the electrolyte.²⁶ A too large discharge can lead to irreversible capacity loss. The temperature should be kept in an optimum range avoiding too low temperatures that slows down the transfer kinetics or even freezes out the liquid electrolyte and too high temperatures posing a safety risk.

2.2 Concepts for improving batteries (next generation batteries)

There are many concepts proposed to improve standard LIBs as well as to change to completely alternative battery system for example based on other alkali metals rather than lithium as summarized in Figure 3. In the following, a few approaches classified by battery component are introduced.

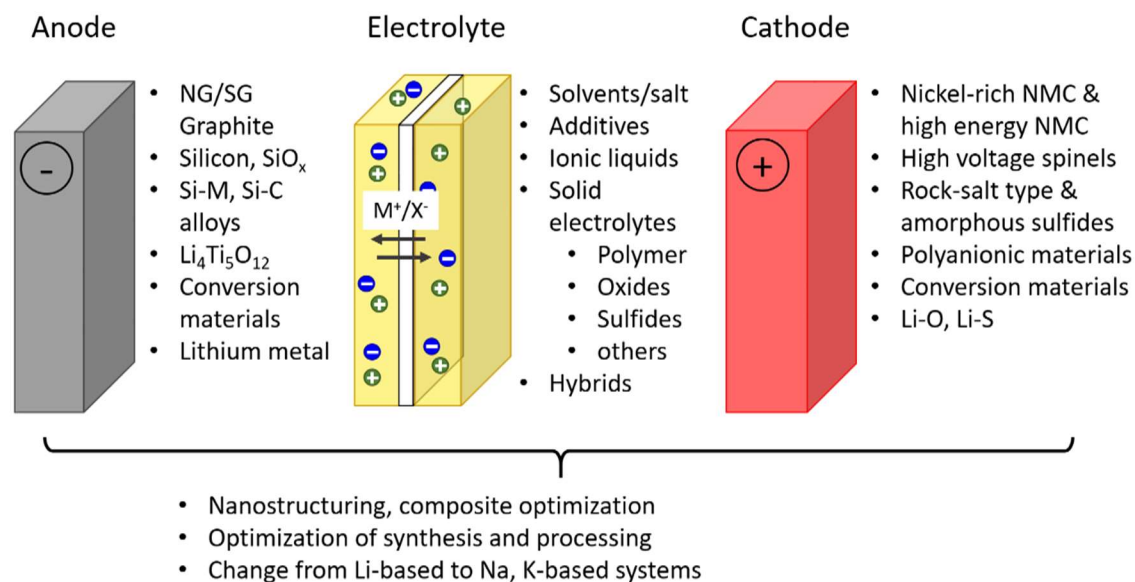


Figure 3 Overview over next generation materials and additional improvement strategies for rechargeable batteries.

2.2.1 Improvement of the electrodes

2.2.1.1 Anode

The state of the art anode material in a LIB is graphite (mostly natural graphite (NG)).²⁷ As introduced in chapter 1.1.1, graphite reversibly intercalates lithium between the layers and forms LiC_6 in the charged state. It ensures relatively stable cycling and easy processing, since graphite itself is not hazardous and stable under ambient conditions.

Nevertheless, some challenges remain: on the one side, the rate capability, especially for charging (lithiation) of graphite is limited to a maximum of 1 C and associated with lithium dendrite formation (lithium plating) at the electrode surface. The limited rate is a problem for desired fast charging of in particular EVs and appears to be the complex interplay of phase transitions, domain size, particle size and morphology, electrode architecture, the SEI, the desolvation of Li^+ prior to entering the SEI layer, and the ambient temperature.²⁷ At the moment, synthetic graphite (SG) instead of the prevailing NG is already employed for fast charging applications, due to superior de-/lithiation kinetics, which is attributed to the rather isotropic orientation of the crystalline domains in SG and a large proportion of edge-planes at the particle surface. However, due to extensive research, the energy density of graphite anodes has essentially reached its maximum. To further enhance the energy density, the addition of silicon, under-stoichiometric silicon oxide or silicon-metal, and silicon-carbon alloys into graphite composite electrodes is a promising approach that is already pursued in industrial research.²⁷⁻³⁰ The main challenge of using pure Si, which offers the high theoretical capacity of 3578 mAh g^{-1} alloying with lithium forming $\text{Li}_{15}\text{Si}_4$, is the large volume expansion up 300 % during lithiation resulting in severe cracking and eventually capacity loss and poor cyclability. Large efforts were made to stabilize Si by nanostructuring, amorphization, and making composites and alloys. Recently, for instance the Evonik AG introduced their Si-C based material Siridion Black[®] that can lead to a total increase of 15 % in energy density of a LIB with excellent cycling stability.^{31, 32} The authors claim the superior

properties being the result of the formation of an amorphous Si-C alloy nanoparticle with a gradient of C from a C-rich surface to a Si-rich center of the particle, obtained by a gas phase synthesis.

In academic research there are many proposed alternatives to graphite such as $\text{Li}_4\text{Ti}_5\text{O}_{12}$, lithium-metal alloys, sulphides, oxides (e.g. Sn, SnO_2 , SnS_2 ...), but that could never compete with graphite in terms of performance, cost, sustainability.^{33, 34}

Another strongly pursued approach is the use of the pure lithium metal anode (LMA) that in principle enables the highest possible energy density and is decisive for the realization of Li-S and Li-O post-LIB concepts.^{35, 36} Attempts to combine a LMA with state of the art liquid electrolytes repeatedly showed poor cycling efficiency and lead to short-circuit due to lithium dendrite growth.^{37, 38} However, the combination of a LMA with solid electrolytes forming a SSB (cf. chapter 1.3) has led to promising results: the use of polymer electrolytes enabled high energy densities (but low charge/discharge rates) and the use of inorganic solid electrolytes such as $\text{L}_{10}\text{GeP}_2\text{S}_{12}$ -type thiophosphates provided high energy and power densities.³⁹ Recently, even the cycling of a SSB with a thiophosphate electrolyte without the presence of an initial lithium metal reservoir was demonstrated, further pointing into the direction of optimized energy and power density.⁴⁰ There are still drawback and open question regarding the use of LMAs. In particular the growth and dissolution of dendrites at the interface to the solid electrolyte need to be understood and controlled efficiently to ensure a high safety and reliable performance of the cell.³⁵

2.2.1.2 Cathode

Several cathode materials have been commercialized in LIBs such as LiFePO_4 (LFP), the layered oxides $\text{Li}[\text{Ni}_x\text{Mn}_y\text{Co}_z]\text{O}_2$ ($x+y+z = 1$) (e.g. $\text{Li}_{1.1}[\text{Ni}_{1/3}\text{Mn}_{1/3}\text{Co}_{1/3}]_{0.9}\text{O}_2$ (NMC-111)) and $\text{LiNi}_{0.8}\text{Co}_{0.15}\text{Al}_{0.05}\text{O}_2$ (NCA) derived from LiCoO_2 (in the α - NaFeO_2 -type) and LiMn_2O_4 (LMO) in the spinel structure. With these materials the demanding goals of e.g. the application of batteries in EVs cannot be met (cf. Figure 1b) and the next generation of cathode materials is sought after. Potential candidates are further developed oxide based materials, but also alternative materials with alternative structures such as polyanionic materials (e.g. borates, silicates and phosphates among others) and conversion materials (e.g. halogenides, sulphides, nitrides, phosphides and many more) also allowing multi-electron-transfer.¹² From a cost and sustainability perspective, especially, the substitution of critical elements such as cobalt and possibly also nickel is desired.⁴¹⁻⁴⁴ The use of low cost and abundant oxygen from air or elemental sulphur as cathode has been explored in the last decades in the so-called lithium-air and lithium-sulfide batteries.³⁶ In theory, these cathodes in combination with a LMA enable the highest possible energy densities. However, despite intensive effort, both systems have not been fully realized and still face severe challenges, such as the use of unfiltered air for the Li-O system and the capacity fading due to polysulfide shuttles in Li-S batteries.^{36, 45-47}

It must be noted, that the full potential of improved cathode materials can only be realized in combination with an anode providing a higher energy density and rate capability and an electrolyte providing a higher stability window or showing other properties such as the suppression of dendrite or polysulfide formation which is anticipated for solid electrolytes.^{12, 35, 36} In the following chapters, we want to focus on the developments of oxide and sulfide based cathode active materials (CAM).

2.2.1.2.1 Oxide based cathode active materials

The family of oxide based materials possess the highest technological maturity and in principle there are three groups of material: nickel-rich NCM ($\text{Li}[\text{Ni}_{1-x}\text{Co}_y\text{Mn}_z]\text{O}_2$ ($x \leq 0.4$)), high energy NCM ($x\text{Li}_2\text{MnO}_3(1-x)\text{LiMO}_2$ ($M = \text{Ni}, \text{Co}, \text{Mn}$) and high voltage spinels (nickel substituted LiMn_2O_4 (LNM)).⁴⁸⁻⁵⁰ By increasing the nickel content in NCM (to e.g. NCM622, NCM811) the reversible capacity and rate capability increases due to higher electronic and ionic conductivities and the

need for expensive and critical cobalt decreases. However, the high nickel content reduces the thermal stability.²⁶ By integrating the Li_2MnO_3 into layered LiMO_2 ($\text{M}=\text{Ni}, \text{Co}, \text{Mn}$), the structure is stabilized and allows for a larger degree of lithiation and can be cycled to higher voltages and materials such as NCM523 are currently under investigation.^{51, 52} However, so far the cycling stability is limited. The substitution of nickel in the LiMn_2O_4 spinel, high voltages can be achieved and the material is inexpensive and has high electronic and ionic conductivities, but similar to high energy NCM, capacity fading is severe in these systems. Very recently, in academia, the substitution of LiNiO_2 with elements such as Mn and Al emerged showing promising results for $\text{LiNi}_{1-x-y}\text{Mn}_x\text{Al}_y\text{O}_2$ for this entirely cobalt free compound.⁴¹ Besides the overall stoichiometry, elemental gradients forming core shell cathode particles can have beneficial influence on the performance.⁵³ Nevertheless, additional open questions for the next generation of oxide cathode materials remain: the powder morphology and particle size distribution can have a large impact on the performance and needs to be understood and controlled and a synthesis scale up route, especially in a continuous process, is still lacking.

2.2.1.2.2 Sulfide based cathode active materials

A completely cobalt- and nickel-free alternative to the introduced oxide cathodes are lithium metal sulfides ($\text{Li}_x\text{M}_y\text{S}_z$, $\text{M}=\text{Cu}^{2+}, \text{Fe}^{2+}, \text{Ti}^{4+}, \text{Nb}^{5+}, \text{Ta}^{5+}$). Although they offer only a limited voltage range, they promise high energy densities and a better compatibility with sulfide based solid electrolytes supporting the development of high performance solid-state-batteries (cf. chapter 1.3). Lithium metal sulfides are easily oxidized and reduced, i.e. showing anionic redox chemistry. This reversible multi-electron process allows the incorporation of large amounts of lithium leading to high capacities.^{12, 44, 54-64} Cells built from metal sulfides such as Li_2TiS_3 or ball-milled Li_3NbS_4 as cathode with standard liquid electrolytes show capacities between 339–425 mAh g^{-1} with a potential ranging between 2.2–2.5 V vs Li^+/Li resulting in a theoretical gravimetric specific energy of 780–850 Wh kg^{-1} exceeding that of NCM-622 (590 Wh kg^{-1}).^{44, 56}

In principle, different advantages result from the use of sulfide based cathodes in combination with sulfide based solid electrolytes and first attempts were demonstrated.^{56, 58, 59, 64} These advantages are the following: i) Simple cold pressing of thiophosphate based solid electrolytes such as crystalline Li_3PS_4 , $\text{Li}_2\text{S}\cdot\text{P}_2\text{S}_5$ (LPS) glasses, $\text{Li}_6\text{PS}_5\text{X}$ ($\text{X} = \text{Cl}, \text{Br}, \text{I}$), $\text{Li}_{10}\text{Ge}_2\text{PS}_{12}$ -type materials etc. should enable an intimate contact between these mechanically soft materials. 2) Since the oxidation potential of typical oxide based cathode materials exceeds the thermodynamic stability of typical thiophosphate-based solid electrolytes,^{65, 66} they are oxidized at the interface to CAM particles, leading to an overall decline in cell performance.⁶⁵ Whereas, an oxidation at the interface with a sulfide based CAM is not expected. 3) Sulfide-based CAMs possess an inherently higher electronic conductivity of with respect to isostructural lithium metal oxides. This could enable a cathode composite formulation without the need to add electronically conducting additives such as carbon, increasing the overall energy density and preventing side reactions with the solid electrolyte.⁶⁷

A SSB of a lithium metal anode, $\beta\text{-Li}_3\text{PS}_4$ as solid electrolyte and layered $\text{Li}_{1.13}\text{Ti}_{0.57}\text{Fe}_{0.3}\text{S}_2$ ⁵⁹ as CAM showed good cyclability with no initial irreversible capacity. Furthermore, the aforementioned ball-milled rock-salt-type materials Li_2TiS_3 and Li_3NbS_4 were combined with glassy LPS in an SSB.^{56, 64} Both SSBs demonstrated high capacities of 300–400 mAh g^{-1} and a high capacity retention >90 % after 50 and 200 cycles, respectively. Since ball-milled Li_3NbS_4 is a promising candidate for the application as CAM in a SSE, but the structural and electronical characterisation was poor so far due to its poor crystallinity, we set out in this work (cf. chapter 4.1) to synthesized, crystalline, phase pure Li_3NbS_4 and its heavier homologue Li_3TaS_4 to deepen the understanding of structure-property relationship in these type of materials.

2.2.2 Improvement of electrolyte

Since the state of the art electrolyte in a LIB is mixture of aprotic organic solvents with lithium ion containing salts, there are several ways to tune its most important properties. These are the ionic conductivity (cf. equation (18(22(23)), the transference number (cf. equation (40)), the formed SEI going hand in hand with the coulombic efficiency, the viscosity and the thermal stability.^{37, 38, 68}

Different aprotic organic solvents ranging from carbonates, over phosphonates to nitriles and many more can be mixed in different ratios to meet the diverse physical and chemical requirements of a battery application. The solvent should dissolve the lithium salts, thus it needs a high dielectric constant but be still fluid enough (low viscosity) to allow for a fast lithium ion transport. The solvent should only show a low reactivity towards the electrodes, remain liquid in a wide temperature range (high boiling point, low melting point) and be safe in terms of flammability, toxicity and environment. Mostly the mixing of different organic esters and ethers (dimethyl carbonate (DMC), ethyl carbonate (EC), propylene carbonate (PC), etc.) has been explored.

Different lithium salts that can be combined with different solvents to tune the properties. Common salt are LiPF_6 , LiClO_4 , LiBF_4 , LiAsF_6 , lithium bis(trifluoromethanesulfonyl)imide (LiTFSI), lithium trifluoromethanesulfonate (LiCF_3SO_3), and others.

Besides, the use of a broad variety of additives such as crown ether, aza-ethers, borates, and many other organic compounds in low concentrations has been explored enabling the present high performance of LIBs in the first place.⁶⁹ These additives modify targeted properties, especially on the electrode surface, without changing the main components.

As further improvement of the electrolyte, especially in regard to its kinetics and compatibility with a LMA, is demanded by the market (cf. Figure 1), and liquid electrolytes fail to meet these criteria, alternative electrolyte concepts came on the stage.^{37, 38} Ionic liquids are one attractive also liquid alternative to solvent based electrolytes.⁷⁰ They still ensure a good wetting of the electrode active materials and enable the use of high voltage cathodes (up to 5 or 6 V vs. Li). But it is still difficult to achieve stable passivation layers and the anions of the ionic liquids show co-intercalation into the electrode. In the last decade, solid electrolytes reemerged as another attractive electrolyte, enabling high performance SSBs. The concept and advantages of an SSB and requirements for a good solid electrolyte are introduced in chapter 1.3 in more depth. Solid electrolytes in primary batteries are known since many decades and successfully implemented in e.g. pace marker devices.^{71, 72} However, due to limited ionic conductivity of alkali metal ions (Li^+ , Na^+ , K^+) in easy to process 3D conductors for rechargeable batteries, SBBs were not of large scale, industrial relevance for a long time. With the implementation of polymers into batteries for the application in the blue car of Bolloré in 2012, solid electrolytes were successfully applied in EVs for the first time.⁷³ Now, they give great hope for higher safety due to the absence of flammable liquids, for enabling the use of the LMA (cf chapter 1.2.1.1) by an increased mechanical stability and for high charging rates due to the high ionic conductivity of modern solid electrolytes. Additionally, by the combination with solvent-based liquid electrolytes or ionic liquids forming so-called hybrid systems, solid electrolytes enable the exploration of a larger parameter space for finding the optimal electrolyte.⁷⁴

2.2.3 Battery systems beyond lithium

In terms of cost, sustainability, geopolitical reasons and performance, the exclusive use of lithium ion based systems for rechargeable batteries is currently under debate.^{13, 24, 75, 76} In particular, the sheer mass of lithium containing materials needed for millions (if not billions) of electrical vehicles and other material demanding applications such as stationary storage systems, sparks the search for alternatives.⁷⁷ In the last years, rechargeable batteries based on other monovalent alkali metals ions (Na^+ , K^+), but also based on multivalent ions such as Mg^{2+} and Zn^{2+} , Al^{3+} , and Si^{4+} were

introduced.⁷⁷ Although showing promising results, only a few of those systems reached technologic maturity. Inherently, all systems based on alternative ions have the disadvantage of a higher atomic mass and lower possible potential windows in comparison to lithium ions. That lowers the accessible power and energy densities. For highly demanding technologies such as EVs, lithium ion based systems probably will prevail. However, due to enabling completely different cell chemistries (and potentially avoiding the use of “critical” elements such as Co and Ni) and due to e.g. lower costs and the higher mobility of sodium ions (and others), alternative ions are attractive choices for less demanding applications lowering the overall demand for lithium in batteries.

Here, a brief introduction of sodium ion and potassium ion batteries follows, since two new sodium ion conducting material series (cf. Na_5AlSi_4 – Na_4Si_4 series in chapter 4.5 and sodium phosphidosilicates in chapter 4.3) and one potassium ion conducting solid electrolyte (KSi_2P_3 in chapter 4.4) are presented in this work.

2.2.3.1 Sodium ion batteries

The substitution of lithium ions by sodium ions creating sodium ion batteries (NIBs) has several advantages. The cost of the typically used raw material Na_2CO_3 is much lower than of Li_2CO_3 (150 \$/t < 13000 \$/t in 2019).^[2] The regional accessibility of Na_2CO_3 is much more beneficial for western countries such as the USA and the possibility for harvesting sodium by desalination of sea water is a valuable alternative mining source for the European Union. Besides, a broad variety of nickel and cobalt free cathodes, also dramatically reducing the cost of a NIB in comparison to a LIB, are available and show promising performance with competitive volumetric energy densities.^{13, 78} For the installation of stationary storage in urban environments the volumetric energy density is the key performance indicator, since the battery has not to be moved and the mass does not matter so much.¹³

NIBs work in the same fundamental way as LIBs and until now a broad range of materials applicable in a NIB have been developed.^{77, 79} Typical cathode materials are layered oxide cathodes (e.g. $\text{Na}_{2/3}\text{Fe}_{1/2}\text{Mn}_{1/2}\text{O}_2$), prussian blue analogues (PBA) and polyanion cathodes. As anode, hard carbon (partially disordered carbon), non-carbon intercalation compounds such as $\text{Na}_2\text{Ti}_3\text{O}_7$ and conversion anodes (alloying reaction anodes such as Sn, Sb, P) can be utilized. The use of graphite is not possible, since Na^+ does not intercalate into graphite. The employed positive current collectors, as well as electrolytes and separators, are usually similar to LIBs, except for the use of sodium salts in the electrolyte.⁷⁹ Since these electrolytes pose the same safety hazards as for LIBs, the utilization of solid electrolytes to build Na–SSBs is currently under investigation. Very recently, a Na–SSB based on a halide–SE coated NaCrO_2 cathode, a sulfide based electrolyte and a Na–Sn anode, showed the anticipated performance with stable cycling for 1000 cycles.⁷⁸ However, similar to LIBs, although there already a variety of good sodium ion conducting solid electrolytes available, still new improved materials for the optimal material combination are looked for (cf. chapter 1.3.1). Going to the solid state, could additionally enable the use of the sodium metal anode (or other high capacity anodes) further increasing the energy density.¹³ In comparison to lithium, sodium does not electrochemically alloy with aluminium at room temperature. Consequently, a replacement of expensive copper by cheaper aluminium is possible at the anode.

2.2.3.2 Potassium ion batteries

Potassium ion batteries (KIBs), are another alternative to LIBs. Similar to NIBs, they promise lower costs due to significantly lower K_2CO_3 prices (790 \$/t) and alternative Co and Ni free cathodes.⁷⁷ ⁸⁰ In contrast to sodium ions, potassium ions enable the utilization of a conventional graphite anode.⁷⁷ Besides, although potassium ions are heavier than sodium ions, the gravimetric difference of a full cell is not necessarily larger than 10 %, since the mass of potassium ions only accounts for a small percentage of the system.^{81, 82} Moreover, upon solvation in organic solvents,

potassium ions have the smallest radius, increasing mobility and making KIBs attractive for applications that require high charging rates.^{81–83}

At the horizon, post-KIBs including aqueous KIBs, potassium-sulfur (K-S), potassium-selenium (K-Se), and K-SSBs, along with their respective advantages are emerging.⁸⁴ And although the variety of fast solid potassium ion conductor at room temperature is limited so far (see chapter 1.3.1.3 and 3.4), a K-SSBs was already assembled with a potassium metal anode, $K_2Fe_4O_7$ as solid electrolyte and prussian blue analogue cathode demonstrating high charge/discharge rates.⁸⁵ In this work, the first fast, non-oxide based solid potassium conductor KSi_2P_3 , which does not contain any transition metal ions (which are prone to redox reactions), is introduced in chapter 4.4, enlarging the family of potassium ion conductors for the development of high performance K-SSBs.

2.3 Solid-state-batteries

Batteries built with a solid electrolyte are so-called solid-state-batteries (SSBs, Figure 2b). SBBs can be realized with a broad range of materials based on Li-ion, Na-ion, technology and others.^{6–9, 11, 86, 87} They can be built with different classes of electrolytes coming in different forms ranging from thin films (e.g. LiPON⁸⁸, polymers⁸⁹) to particles (e.g. oxide, sulfide ceramics)⁶. Figure 4, depicts the microstructure of a SSB with a particulate solid electrolyte, a cathode composite and a lithium metal anode and highlights the different interfaces present in such a cell.

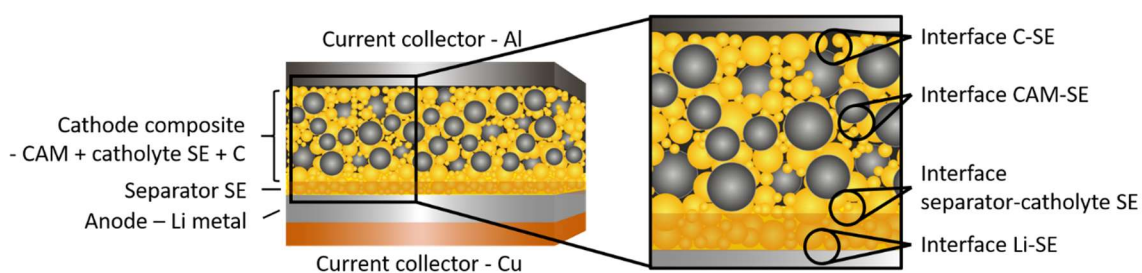


Figure 4 Scheme showing the microstructure of a solid-state battery consisting of a lithium metal anode, a ceramic particulate solid electrolyte (separator SE) and a cathode composite containing a SE (catholyte), cathode active material (CAM) and electronically conducting carbon additive (C). Different important interfaces representing the redox stability of the solid electrolyte against the anode-, cathode-material and the carbon additive are highlighted.

Recently, Li-SSBs reemerged worldwide as attractive cell concept, since in the last years solid electrolytes showing sufficiently high ionic conductivities of up to 25 mS cm^{-1} at 25°C ($\text{Li}_{9.54}\text{Si}_{1.74}\text{P}_{1.44}\text{S}_{11.7}\text{Cl}_{0.3}$)³⁹, being significantly better conductors than common liquid electrolytes, and forming stable SEIs in contact to lithium metal (lithium thiophosphates (LPS), $\text{Li}_7\text{La}_3\text{Zr}_2\text{O}_{12}$ (LLZO), etc.) were developed. For the next generation of Li-SSBs, the development targets are a specific energy of 400 Wh kg^{-1} , an energy density of 1000 Wh L^{-1} and a cycle life of at least 200 cycles with a capacity retention of 80%.²² For the next generation of SSBs on Na-ion bases, the development targets are a specific energy of 250 Wh kg^{-1} , an energy density of 700 Wh L^{-1} and a high cycle life.¹³ In general, several advantages for SSBs over LIBs are anticipated: 1) The substitution of the solvent based liquid electrolyte with a solid electrolyte leads to a higher thermal stability and reduces the risk gas evolution and fire. 2) Due to increased thermal stability, the need for thermal managing is reduced. The use of batteries at lower temperatures is enabled, because there is no liquid-transition (freezing) accompanied by a dramatic reduction of ionic conductivity as for liquid electrolytes. 3) Implementing a solid electrolyte gets rid of the need for casings containing the liquid electrolyte and enables bipolar stacking. 4) The extremely high ionic conductivity and transference number of 1 (in inorganic solid electrolytes) enables high charging rates and reduces polarization effects in a cell. 5) The high mechanical stability and altered SEI formation potentially enables the use of a LMA (chapter 1.2.1.1). Ideally, the LMA is cycled without providing a lithium metal reservoir (lithium foil) in the discharged state (as demonstrated by Lee

*et al.*⁴⁰). Lithium metal free anodes are potentially easier to produce and cheaper. 6) The use of a solid electrolyte avoids the use of fluorine–containing conducting salts and binders. 7) The absence of a liquid electrolyte simplifies recycling.

Naturally there are drawbacks and challenges to overcome, before high performance SSBs can be commercialized.⁷⁷ Each promising combination of anode, cathode and electrolyte has to be optimized and critical problems solved. One problem of solid electrolytes is the poor contacting (vs. good wetting with liquid electrolytes) of the active materials. That is mostly overcome by the application of high pressures (up to 500 MPa) in laboratory set–ups. For large scale applications however, systems showing excellent performance without the application of external pressure must be developed (e.g. by the use of binders, modifications, microstructure engineering).

Moreover, for most of the solid electrolytes the redox stability is limited, i.e. they are either reduced by the anode (halides), oxidized by the cathode (LLZO) or even both (thiophosphates).^{77, 90} Thus, the usage of at least two different electrolytes implemented as a solid electrolyte separator and a catholyte is envisioned, as indicated in Figure 4, exploiting the beneficial properties of different SEs. The ionic conductivity of the solid electrolyte in a thin separator can be significantly lower than in the case of the catholyte. Thus, e.g. the combination of polymer or oxide based separators (low conductivity, but high reduction stability) and thiophosphates as catholyte (high ionic conductivity) are possible. Design and processing of the separator in sufficiently thin (< 50 μm) and mechanically stable layers, which are ideally stable against dendrite growth if a LMA is used, are currently under development. The nature of the formed SEI (by reduction by the anode) is of high importance. It is favorable, if it is ionically conducting and electronically blocking as for LPS, but unfavorable if both charge carriers are conducted through the SEI leading to a continuous decline in cell performance (e.g. mixed ionic electronic conducting SEI of LGPS). The ionic conductivity in the catholyte should be as high as possible (at least > 10 mS cm^{-1}) to ensure fast enough transport to the CAM and avoid polarization.⁹¹ Ideally, the catholyte is stable against oxidation by the CAM (formation of e.g. oxo-(thio)phosphates) and present carbon additives⁹² that no aging phenomena occur either during storage or operation. Alternatively, a reaction of the catholyte at the interface to CAM can be avoided by using a protective layer or additive design.^{93, 94} Coatings based on lithium niobate, zirconate, etc are currently under investigation. An alternative to that is the application of CAMs with lower potentials such as lithium metal sulfide based materials (chapter 1.2.1.2.2).

2.3.1 Solid electrolytes

In this work the structure, properties and processing of several new solid electrolytes from different material families for the potential application in Li–, Na– and K–SSBs is investigated. In general, the properties of a solid electrolyte dictate the overall cell performance. For decades, solid electrolytes based on different material classes ranging from polymers to inorganic glasses and crystalline ceramics have been explored for the application in a rechargeable battery, but there is still need for new electrolytes with optimized properties.^{5, 86, 87, 95-97}

Ideally, a solid electrolyte for the application in a rechargeable battery has a high ionic conductivity, a low electronic conductivity, a high ion selectivity, a large potential window, beneficial mechanical properties (soft), is easy to process, low–cost and safe in a large window of operational conditions as summarized in Figure 5. In the last years, inorganic, non–oxide materials, demonstrated their superior properties in comparison to oxide and polymer based solid electrolytes. In general, they have an ion selectivity close to 1, i.e. they only conduct lithium ions, have very high ionic conductivities without large contributions of grain boundaries and are relatively soft, enabling the preparation of cells only by cold pressing. An introduction to the mechanism and influencing factors on ion conduction in crystalline inorganic solids (structure–property relationship) and in particular, the materials presented in this thesis, is given in chapter 2.

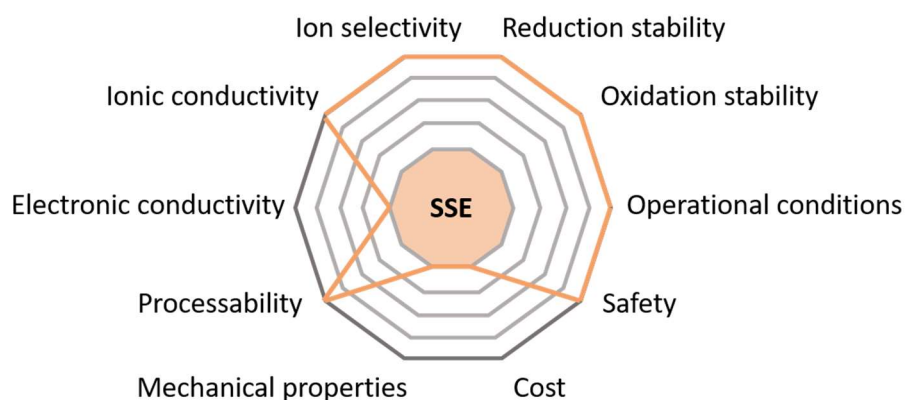


Figure 5 Qualitative summary of properties of an ideal solid electrolyte for the application in a rechargeable battery deduced in this work.

2.3.1.1 Ortho-thiophosphates

One of the most promising materials class for the application as solid electrolyte in SSBs are the thiophosphates. Sparked by the discovery of liquid like ionic conduction in $\text{Li}_{10}\text{GeP}_2\text{S}_{12}$ ⁹⁸ in 2011, a search for more representatives of this structure-type lead to a whole family of LGPS-type materials.⁹⁹ In the LGPS-family, S can be partially replaced by O, Ge can be replaced by Sn (LSnPS) and partially by Si and Al, and a related Na analogue of the Sn-substituted variant is accessible. Since Ge is expensive, especially the substitution with the lightweight and easily accessible Si is pursued, but the synthesis of the material with a P:Si ratio of 2 has not been successful. However, $\text{Li}_{11}\text{Si}_2\text{PS}_{12}$ ¹⁰⁰ was obtained under high-pressure conditions (but only in small quantities) and exhibited a promising large lithium ion diffusivity clearly exceeding that of LGPS and LSnPS. The authors found a correlation between the diffusivity and the unit cell volume of the cation substituted LGPS-type electrolytes: the smaller the unit cell volume the higher the diffusivity. The enhanced diffusivities are in agreement with theoretical predictions cation substituted LGPS-type electrolytes.⁹⁰ By the addition of LiCl to the synthesis, $\text{Li}_{9.54}\text{Si}_{1.74}\text{P}_{1.44}\text{S}_{11.7}\text{Cl}_{0.3}$ ³⁹ one of the fastest lithium ion conductor to-date with an ionic conductivity of 25 mS cm^{-1} was obtained. The exact origin of the boost in ionic conductivity is still under debate, but the material showed extremely high charging rate capabilities in a SSB. In 2019, the glassy ceramic tetra-Li₇SiPS₈¹⁷ (LiSiPS) was introduced and the inhibiting influence of the amorphous side phase on the ionic conductivity was deduced. Like the other LGPS-type materials, LiSiPS is a solid solution of lithium ortho-thiophosphate and an ortho-thiosilicate and crystallizes isotypically to tetragonal Li_7GePS_8 .¹⁰¹ The PS_4/SiS_4 tetrahedra partially order with an underlying pseudocubic face-centered unit cell as depicted in Figure 6. The lithium ions sit either tetrahedrally or octahedrally coordinated in the anionic framework, forming chains along the *c*-axis (cf. Figure 6a). With a room temperature ionic conductivity of 2 mS cm^{-1} , LiSiPS holds great promise for the application in SSBs and is used as model system for the study in chapter 4.6. As representative of the LGPS-type family, LiSiPS is treated with a broad range of solvents, evaluating potential solvent candidates for processing on industrial scale (cf. chapter 1.3.2 and 3.6).

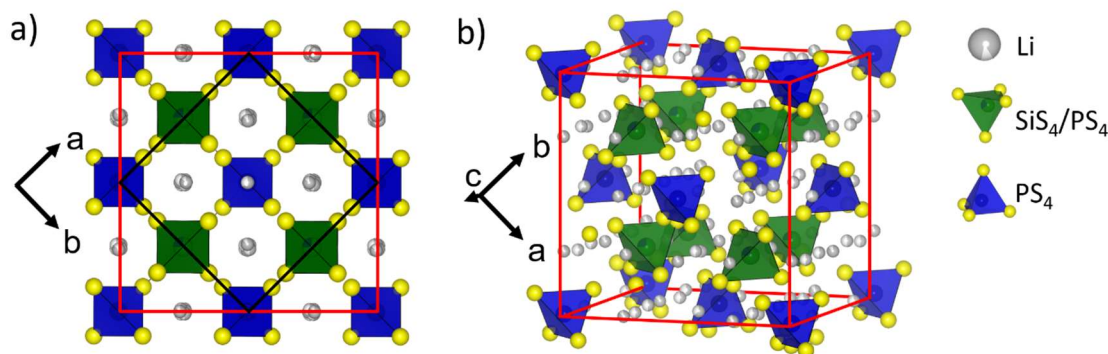


Figure 6 Crystal structure of tetra- Li_7SiPS_8 a) viewed along the c -axis and b) rotated depiction. The black lines mark the tetragonal primitive unit cell and the red lines the underlying pseudocubic face-centered unit cell.

Another highly interesting class of thiophosphates are the halogen substituted argyrodites ($\text{Li}_6\text{PS}_5\text{X}$, $\text{X} = \text{Cl}, \text{Br}, \text{I}$). In $\text{Li}_6\text{PS}_5\text{X}$, the X^- form a cubic close packing with PS_4 tetrahedra occupying the octahedral sites as depicted in Figure 7. Free S^{2-} sit in half of the tetrahedral voids. In $\text{Li}_6\text{PS}_5\text{I}$, the I^- and S^{2-} anions are ordered on the different crystallographic sites, but for the Br^- and Cl^- -containing compounds the anions are significantly disordered (site disorder) leading to higher conductivities and lower activation energies.¹⁰²⁻¹⁰⁴ Since the $\text{Li}_6\text{PS}_5\text{X}$ ($\text{X} = \text{Cl}, \text{Br}, \text{I}$) compounds lack a tetrel element ($\text{T} = \text{Ge}, \text{Si}, \text{Sn}$), they show a higher reduction stability compared to the LGPS-type materials.¹⁰⁵ The tetrel element is typically reduced to LiT-alloys when LGPS-type materials are brought into contact with a LMA showing significant electronic conduction (mixed ionic–electronic conducting interface) leading to a subsequent destruction of the electrolyte and fade in battery performance. The argyrodites only decompose into electronically insulating products such as Li_3P , Li_2S and LiX leading to a stable SEI formation. In a round robin study, that material class was used to investigate the quality of measurements of ionic conductivity and activation energy by electrochemical impedance spectroscopy of thiophosphate based solid electrolytes in different laboratories across the world.¹⁰⁶ The ionic conductivity showed a relative standard deviation 35–50 % and the activation energy a relative standard deviation 5–15 % across all samples pointing to the necessity of a more rigorous methodology for the evaluation of samples, in particular the need to report ionic conductivities as a function of the external pressure applied.

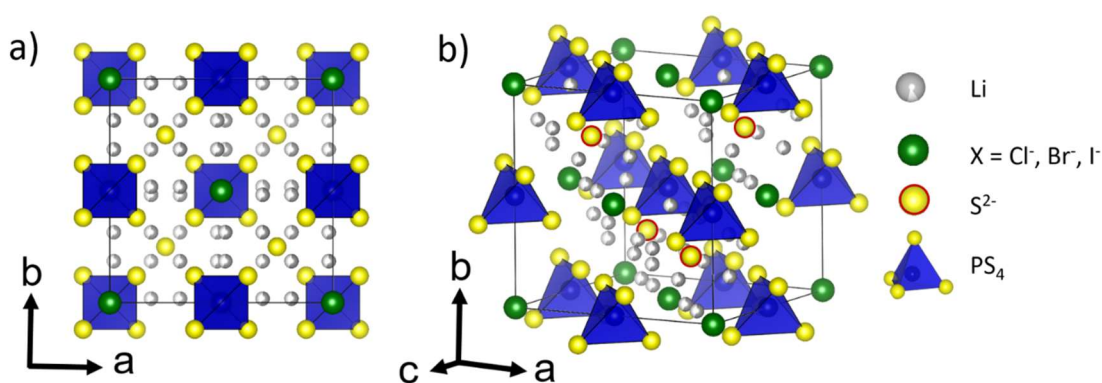


Figure 7 Crystal structures of $\text{Li}_6\text{PS}_5\text{X}$ with $\text{X} = \text{Cl}, \text{Br}, \text{I}$. In a) viewed along the c -axis and b) in a rotated perspective highlighting the cubic closed packing of the X^- anions. The black lines mark the unit cell.

2.3.1.2 Ortho-thiotetrelates and -trielates and other sulfides

Ternary ortho-thiophosphates are characterized by the presence of isolated PS_4^{3-} tetrahedra building the anionic framework of the ionic conductors. Replacing the P atom with other elements

such as the tetrels Si, Sn and even the triels Al, thiosilicates^{16, 107, 108}, thiostannates¹⁰⁹ and thioaluminats¹⁶ containing SiS_4^{4-} , SnS_4^{4-} and AlS_4^{5-} anions can be formed. Together with sulfides showing other patterns of M_xS_y connectivities such as rocksalt-type Li_2SnS_3 ^{110, 111} and layered $\text{Li}_{0.8}\text{Sn}_{0.8}\text{S}_2$ ¹¹² containing octahedrally coordinated Sn^{4+} , these thiotetrelates and –trielates show relatively fast ion conduction either for lithium or sodium ions, especially, when iso- or aliovalent doping is applied. Usually, doping increases the defect concentration and raises the ionic conductivity dramatically (cf. chapter 2.1).

One example is the sodium thiostannat Na_4SnS_4 .¹⁰⁹ By silicon doping, the conductivity of Na_4SnS_4 improves by two orders of magnitude. In this work in chapter 4.5, the materials space of sodium thio-ortho-tetrelates and –trielates is enlarged by aliovalent substitution of Al into Na_4SiS_4 .¹⁶ That leads to the discovery of the three new ion conducting materials Na_5AlS_4 , Na_4SiS_4 , and $\text{Na}_9(\text{AlS}_4)(\text{SiS}_4)$ crystallizing in different structures. The enhancement of ionic conductivity of $\text{Na}_{8.5}(\text{AlS}_4)_{0.5}(\text{SiS}_4)_{1.5}$ in comparison to the border phases can be rationalized by an increase in charge carrier concentration accompanied by a low site symmetry of sodium ions in that structure.

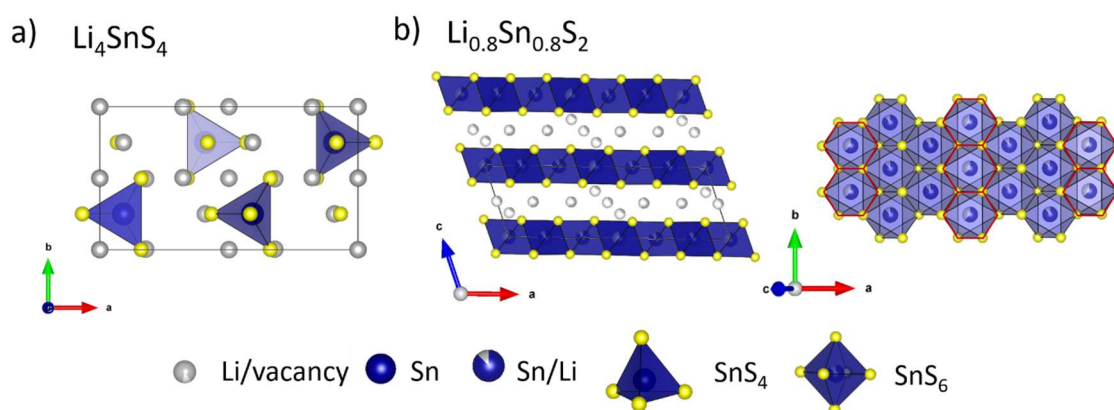


Figure 8 a): Crystal structure Li_4SnS_4 and b) of $\text{Li}_{0.8}\text{Sn}_{0.8}\text{S}_2$ with partially substituted tin positions. A top-view of the layers illustrates the different Sn/Li positions (highlighted in red). The black lines represent the unit cells.

Another example is the lithium thiostannat Li_4SnS_4 .¹¹³ It crystallizes isostructural to the thio-LISICON Li_4GeS_4 in the orthorhombic space group $Pnma$ (no. 62) as shown in Figure 8a. Li_4SnS_4 has an ionic conductivity of $7 \times 10^{-5} \text{ S cm}^{-1}$ at 20°C that after doping with As^{5+} increases to 1 mS cm^{-1} .¹¹⁴ The doping with As^{5+} additionally enhances the stability of the compound towards humidity in air. In combination with LiI , Li_4SnS_4 forms a glass that is coat-able from a methanol solution retaining a moderate ionic conductivity of 0.4 mS cm^{-1} , potentially opening ways for solvent based electrode processing.¹¹⁵ Li_2SnS_3 is one example of an ion conducting thiostannat with a higher coordination number. It features octahedrally coordinated Li^+ and Sn^{4+} and shows an ionic conductivity of $< 2 \times 10^{-5} \text{ S cm}^{-1}$ at room temperature, but is stable under ambient atmosphere.¹¹¹ The structure can be deduced as an ordered variation of a rock-salt-type structure forming $[\text{SnS}_3]_2$ -layers of honeycomb nets with lithium ions occupying the space between the ABAB stacked layers. The observed enhanced stability towards humidity in air is in accordance with the exfoliation behavior of Li_2SnS_3 , observed by Kuhn *et al.* with Li_2SnS_3 (with $x = 0.33$) being part for the solid-solution series $\text{Li}_{4x}\text{Sn}_{1-x}\text{S}_2$ with $0.11 \leq x \leq 0.33$.¹¹⁰ The members of the solid solution series do not decompose upon contact with water but rather exfoliate into nanosheets comprised of a defective anionic Sn-S network. $\text{Li}_{0.8}\text{Sn}_{0.8}\text{S}_2$ a member of the solid solution series, which is a lithium depleted version of Li_2SnS_3 , also possess significant ionic conductivity at room temperature ($1 \times 10^{-5} \text{ S cm}^{-1}$) and exfoliates into single layer nanosheets.^{110, 112, 116} $\text{Li}_{0.8}\text{Sn}_{0.8}\text{S}_2$ crystallizes in the monoclinic space group $C2/m$ (no. 12). Octahedrally and tetrahedrally coordinated lithium is arranged between layers of edge-sharing tin sulfide octahedra as shown in Figure 8b. Within the layers, Sn is partially substituted by Li and the preferential occupancy of two different Sn positions (highlighted in Figure 8b in red) leads to the monoclinic supercell. The ionic conductivity of

$\text{Li}_{0.8}\text{Sn}_{0.8}\text{S}_2$ increases from 0.01 up to 10 mS cm^{-1} upon the hydration with water forming $\text{Li}_{0.8}\text{Sn}_{0.8}\text{S}_2 \cdot x \text{ H}_2\text{O}$ ($x = 0$ and 0.8) hydrates.^{116, 117} That conductivity is very high for a solid electrolyte. Since for the development of solid-state batteries, the exploration of lithium ion conducting solid electrolytes that are on the one hand robust against environmental conditions (such as humidity) and can be fashioned into thin films and other device geometries by solvent based processing are desired,⁸⁶ the conduction properties of exfoliated and restacked Li-TS are investigated in chapter 4.7. Li-TS is capable of a fast water-assisted lithium ion conduction at high humidities exceeding that of parental $\text{Li}_{0.8}\text{Sn}_{0.8}\text{S}_2$. Thus, we find that nano-sizing, solution processing and restacking can even boost the performance in a humid environment.

2.3.1.3 Phosphidosilicates

Phosphidosilicates are an emerging class of fast conducting solid electrolytes that contain only earth-abundant elements. In phosphidosilicates, SiP_4^{8-} anions with varying degree of connectivity are the main building units. The structure of a supertetrahedral phosphidosilicate, as investigated in this thesis, schematically shown in Figure 9a. The representative supertetrahedron in Figure 9a is built from three SiP_4 units forming a so-called T3 supertetrahedron. Three T3 supertetrahedra are connected *via* corners or share a SiP_4 unit forming interpenetrating rings. The topology of the supertetrahedra can be described as interpenetrating sphalerite- or diamond-like networks.

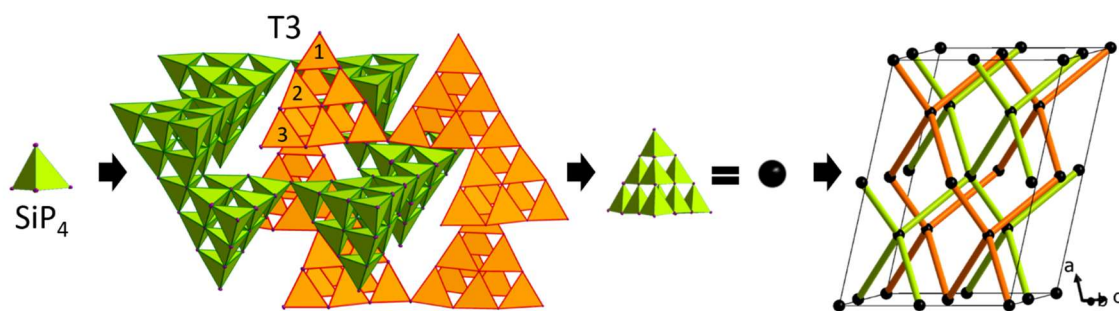


Figure 9 Example of the building units of supertetrahedral phosphidosilicates. Here, the T3 supertetrahedra are built from three SiP_4 tetrahedra. The supertetrahedra form interpenetrating networks of six-membered rings. The topology of T3 supertetrahedra can be described by two interpenetrating diamond-like networks. The nodes represent the centers of gravity of the T3 supertetrahedra.

In the last years, two lithium ion containing representatives of that class were introduced. Li_2SiP_2 ^{118, 119} (T2) and LiSi_2P_3 ¹¹⁸ (T4 and T5) consist of interpenetrating 3D networks of corner-sharing SiP_4 supertetrahedra with lithium ions located in channels between the supertetrahedra (cf. chapter 4.2). Li_2SiP_2 shows reasonably fast ionic conductivity at room temperature, but so far conductivity data on LiSi_2P_3 has been missing. A complementation of the data on ion conduction and diffusion of Li_2SiP_2 and LiSi_2P_3 is given in this thesis in chapter 4.2.

The promising ion conduction properties of the lithium phosphidosilicates initiated the search for its sodium and potassium ion counterparts. In chapter 4.3, a series of supertetrahedral sodium phosphidosilicates is explored. By increasing the supertetrahedra size from T3 to T5, respectively, by the formal addition of neutral " Si_3P_4 ", the ionic conductivity increases several orders of magnitude up to $4 \times 10^{-4} \text{ S cm}^{-1}$ in $\text{HT-NaSi}_2\text{P}_3$ making this material competitive to state-of-the-art sodium ion conductors.^{5, 7, 14} In chapter 4.4, the connection of large supertetrahedral entities leading to high ionic conductivities is transferred to a potassium based system, leading to the discovery of the first, fast non-oxide based potassium ion conductor KSi_2P_3 .¹⁵ As potassium ion batteries are the at most immature technology in comparison with NIBs and LIBs, there are only a few well characterized, high performance solid electrolytes. Until now, all solid electrolytes have been based on oxides with $\text{K}_2\text{Fe}_4\text{O}_7$ ⁸⁵ being the fastest with 50 mS cm^{-1} at room temperature. Chapter 4.4 gives a summary over all oxide based potassium ion electrolytes and so far transition-metal-free compounds that are not prone to redox reactions have been missing. KSi_2P_3 shows a

room temperature total ionic conductivity which is comparable to that of the sodium analogue NaSi_2P_3 , and higher than that of the lithium compound LiSi_2P_3 .

2.3.2 Processing of solid electrolytes for SSBs

Processing inorganic solid electrolytes into electrode composites or separator electrolytes, is key to the realization of high-performance next generation SSBs especially in regard to upscaling in an industrial production.^{40, 120-123} However, most solid electrolytes are characterized after a regular high-temperature solid state synthesis and the influence of processing on these relatively new materials, their properties and the interaction/interface to other components of a full cell is not fully understood yet. Typically, batteries are built into coin, pouch or cylindrical cells.²¹ For that the electrode materials have to be brought into intimate contact with the sheet-type current collectors and shaped into the needed forms. To produce free standing electrolyte separators or cathode composites including solid electrolytes, primarily solvent based processes are applied as visualized in Figure 10. For some sulfide based electrolytes the procedures have been established on the basis of typical battery production processes.^{40, 120-124} The solid electrolyte is obtained by a synthesis in a first step. Then a dispersion of the solid electrolyte in an organic solvent with optimized properties like viscosity, particle size distribution and drying speed is prepared and often a polymeric binder (typically a polymer such as isobutyl isobutyrate, polyvinylidene fluoride (PVDF) or nitrile-butadiene rubber (NBR)) is added to the dispersion. For the cathode composite, the CAM, and usually a carbon-based additive (such as Vapor grown carbon nanofibers (VGCF)) are added to ensure electronic percolation and structural integrity of the thick composite, respectively. Then the mixture is coated onto a substrate *via* doctor blading/tape casting. Alternatively, the CAM is coated onto the current collector foil in a first step and the electrolyte suspension is added in a second step, infiltrating the pre-dried CAM.¹²⁵ In general, a cathode composite should be as dense and pore-free as possible. Besides, the volume fraction of CAM should be as high as possible without reducing the effective ionic conductivity of the solid electrolyte too much and preserving also a high electronic percolation.²⁵ For obtaining free standing separator electrolytes a transfer method was introduced.⁴⁰ Subsequently, the sheets are dried and sometimes densified *via* warm pressing.⁴⁰ In the future, the as prepared cathode should be combined with the separator and anode in a roll-to-roll process enabling a fast cell production on industrial scale.

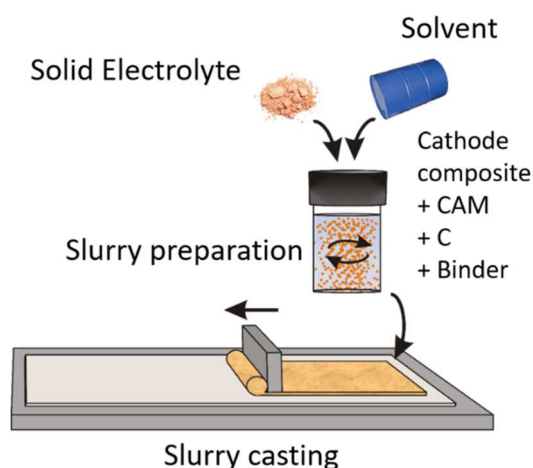


Figure 10 Scheme of slurry preparation and casting process for the preparation of thin solid electrolyte films, electrode films or electrode infiltration.

In general, the choice of solvent in these processes is often subject to screening or to the intuition of the operator (and literature comparisons), but data on chemical reactions, changes in structure and composition, changes in microstructure key parameters such the ionic conductivity are only

rarely published. In this work in chapter 4.6, we set out to gather an in-depth understanding of the interplay between a broad variety of solvents and the fast ionic conductor LiSiPS during processing. Chapter 4.6 gives a review on the existing literature of solvent processing of thiophosphates and takes a closer look on the chemical stability and the ionic conductivity of LiSiPS. We clarify that residual water in solvents up to 800 ppm has only a minor influence on the properties and propose a general decomposition mechanism of thiophosphates in alcohols.

3 Theoretical Background of Analytical Methods

3.1 Ionic Conduction in solids

For a wide range of applications, in particular in the fields of energy storage and conversion and sensing (environmental monitoring), solid state electrolytes and mixed ionic–electronic materials are key components. These materials are essential parts of devices such as batteries, fuel cells and sensors. Controlling and optimizing the properties of solid electrolytes and mixed ionic–electronic materials is indispensable for improving the device. A basic understanding of the underlying ionic diffusion process and ionic conduction under the influence of an electric field, is mandatory to find suitable strategies for optimization.¹²⁶

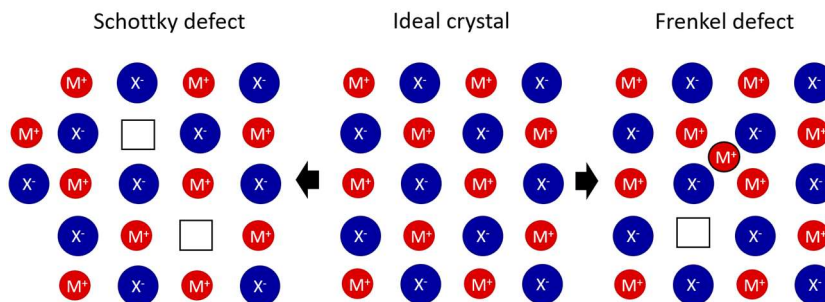


Figure 11 Schematic depiction of Schottky and Frenkel defects in respect to an ideal crystal without intrinsic defects.

A solid in the fully ordered ideal state is invariant. Ionic movement originates from the behavior of so-called intrinsic defects that are created in structures above 0 K by an increase in configurational entropy as driving force. In e.g. an ionic crystal in Figure 11, these intrinsic point defects can be either caused by the movement of a cation and anion to the surface of the material leaving behind vacant lattice sites (Schottky defects) or by the movement of an ion to an interstitial lattice site leaving behind a vacancy in the lattice (Frenkel defect).¹²⁷ The latter is relevant in crystal structures that possess unoccupied positions that are suitable for occupation with the respective ion. Since the number of intrinsic defects in many structures is rather low, the introduction of extrinsic defects by an excess or deficiency of an ion is very important to increase ionic conductivity to application-relevant levels. The excess or deficiency of an ion can be caused by non-stoichiometry or the introduction of aliovalent ions without changing the overall structure.¹²⁸ Exceptions from this are several solid fast ionic conductors, that in contrast to the idealized picture of crystal structures, possess a sublattice of sites that is only partially occupied.¹²⁶ This sublattice of mobile charge carriers supports a random distribution of carriers over an excess number of sites with a similar potential resembling the disordered nature of ions in a liquid. Nevertheless, the transport of ions in fast ionic conductors still occurs *via* jumps between crystallographic sites rather than a liquid-like motion as in aqueous or molten salt electrolytes.

As there is a wide range of factors influencing ion motion in solids and the outcome of tuning one parameter is not easily predictable, here a brief description of the classical model treating ion transport in solids as uncorrelated ion hopping followed by a compilation of influencing factors loosely adapted from Gao *et al.*¹²⁹ and Tuller *et al.*¹²⁶ is given.

Uncorrelated ion hops, depending on point defects such as vacancies or interstitials, can be described with a random walk model.¹³⁰ In equation (13) with a random diffusion coefficient D_r , the jump length a between two neighboring sites and the jump frequency of successful jumps ν is used to describe ion motion in solids. Depending on the dimensionality of diffusion the geometric factor b takes the value of 2 (1D), 4 (2D) or 6 (3D). The schematic drawing in Figure 12 shows an ion hopping between two octahedral coordinated sites *via* a tetrahedral empty interstitial position with the corresponding energy landscape.

$$D_r = \frac{a^2 \nu}{b} \quad (13)$$

The random diffusion coefficient D_r is a microscopic quantity and is typically measured by microscopic techniques such as NMR relaxometry, variable temperature NMR and quasi elastic neutron scattering (QENS) among others.

By linking the jump frequency ν to thermally activated Brownian motion, ν can be described with expression (14) with ν_0 being the attempt frequency (or the number of successful and unsuccessful jumps), ΔG the Gibbs free energy of activation, k_b the Boltzmann constant and T the temperature. This expression can be broken down by describing the Gibbs free energy by the activation entropy ΔS (entropy of migration) and the activation enthalpy ΔH .

$$\nu = \nu_0 e^{\frac{-\Delta G}{k_b T}} = \nu_0 e^{\frac{\Delta S}{k_b}} e^{\frac{-\Delta H}{k_b T}} \quad (14)$$

The activation enthalpy ΔH is often referred to as activation energy or activation barrier and denoted as E_a , particular in the context of temperature dependent measurements. For intrinsic defects that are thermally activated, the activation energy is the sum of the defect formation energy and the migration energy. For extrinsic defects (which often have a much higher concentration than intrinsic defects), the activation energy represents the migration energy. However, if there are strong interactions between defects or mobile ions, the situation is more complex and a defect trapping energy has to be considered.

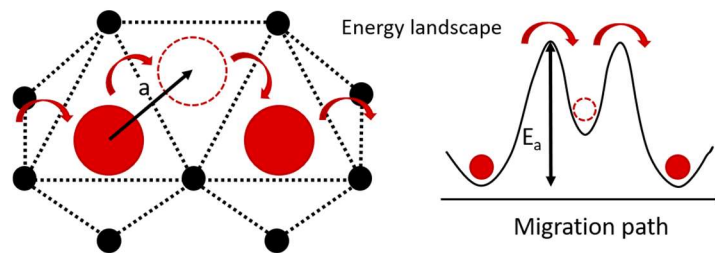


Figure 12 Scheme of ion hopping via interstitial tetrahedral site with corresponding energy landscape.

To link the random diffusion coefficient D_r to the macroscopically observed ionic diffusion, described by the diffusion coefficient D , it is modified by the Haven ratio H and the correlation factor f as given in (15).

$$D = \frac{D_r \cdot f}{H} \quad (15)$$

Here, f takes single-ion and H multi-ion correlations into account. The correlation factor f is defined as the ratio of the tracer diffusion coefficient D^{tr} and the random diffusion coefficient (cf. (16)), whereas the Haven ratio is the ratio between the tracer diffusion coefficient D^{tr} and the long-range diffusion coefficient D .¹³¹ In a random, uncorrelated system f and H are both 1.

$$f = \frac{D^{tr}}{D_r} ; H = \frac{D^{tr}}{D} \quad (16)$$

D^{tr} and D are both macroscopic quantities describing the ion transport on a relatively large length scale. D^{tr} can be quantified by methods such as tracer diffusion detection or pulsed field gradient

NMR (cf. p. 42). The long-range diffusion coefficient D , which is linked to the long-range conduction σ , can be deduced by the Nernst–Einstein equation (17). Here, n is the charge carrier concentration, z the charge of the ion and e the elementary charge. (The ionic conductivity σ is typically assessed in terms of electrochemical impedance spectroscopy (cf. p. 33)).

$$\sigma = \frac{Dnz^2e^2}{k_bT} \quad (17)$$

By combining equation (13)–(17) the isotropic 3D ionic conductivity can be expressed in the following way:

$$\sigma = \frac{1}{6H} \frac{f}{k_bT} \frac{nz^2e^2}{k_bT} a^2v_0 e^{\frac{\Delta S}{k_bT}} e^{-\frac{\Delta H}{k_bT}} \quad (18)$$

To evaluate the activation energy of ionic conduction, the conductivity is measured as a function of temperature. The formula (18) is typically simplified to equation (19) with the pre-exponential factor σ_0 given in (20).

$$\sigma = \frac{\sigma_0}{T} e^{-\frac{E_a}{k_bT}} \quad (19)$$

$$\sigma_0 = \frac{1}{6Hk_b} \frac{f}{k_bT} \frac{nz^2e^2}{k_bT} a^2v_0 e^{\frac{\Delta S}{k_bT}} \quad (20)$$

By forming the natural logarithm, the formula (19) can be linearized and equation (21) is obtained. By plotting $\ln(\sigma T)$ vs. $1/T$ the activation energy E_a can be obtained from the slope of the linear regression line and the pre-exponential factor σ_0 as intercept with the Y-axis.

$$\ln(\sigma T) = \ln \sigma_0 - \frac{E_a}{k_bT} \quad (21)$$

Therefore, for a high ionic conductivity a material should possess a high pre-exponential factor and a low activation energy.

Since the electrical conductivity is the proportionality constant between the current density J and the electrical field E , it can be alternatively described as the total sum of the product of the charge carrier concentration n_i , the mobility μ_i and the charge ($z_i \cdot e$) of all charge carriers in a system (i) as given in (22). The charge carrier concentration influences the thermodynamics of a system and the mobility of a charge the kinetics. Since solid electrolytes are typically single ion conductors with a rigid anionic network (anions do not move), only the conduction of electronic charge carriers (electrons or holes) and not on anions has to be taken into consideration. Normally, the concentration and conductivity of these electronic charge carriers is several magnitudes lower than that of the ionic ones (this is a prerequisite for a good SE) and can be often neglected.

$$\frac{J}{E} = \sigma = \sum_i n_i \mu_i z_i e \quad (22)$$

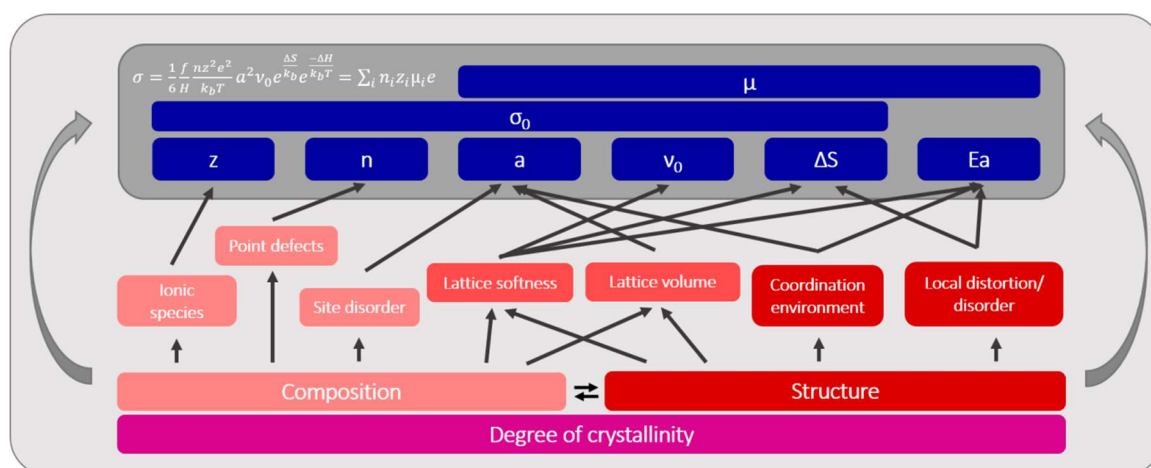


Figure 13 Summary of influences on the pre-exponential factor, activation energy and mobility regarding ionic conductivity.

Now, let's take a look on what influences the ionic conductivity and tackle the question on how to change a material to increase its ionic conductivity. In the following, we focus on fast solid ionic conductors. In Figure 13, a variety of influences are assigned to the parameters influencing the conductivity (in the models above). Obviously, the overall composition of a system strongly influences its structure and properties. Regarding the structure, fast ionic conduction was found in both, crystalline and amorphous solids. For crystalline solids a highly ordered, immobile sublattice (i.e., e.g. a rigid anionic framework) providing continuous open channels for ion transport and a sublattice that minimizes the activation (migration) energy while providing high charge carrier concentrations within the mobile carrier sublattice were determined to be beneficial for ion transport.¹²⁶

In this work, we applied these structural design principles on a series of sodium phosphidosilicates¹⁴ (chapter 4.3). We went from $\text{Na}_{23}\text{Si}_{19}\text{P}_{33}$ (T3T3), only possessing fully occupied sodium positions and relatively small channels between the rigid phosphidosilicate anionic framework to $\text{HT-NaSi}_2\text{P}_3$ ($\text{Na}_{23}\text{Si}_{46}\text{P}_{69}$, T5T5) by formally adding charge neutral "Si₃P₄" increasing the supertetrahedra size from T3 to T5. This addition led to a structure with larger channels and only partially occupied sodium positions. These changes boosted the ionic conductivity from initially 2×10^{-9} to 4×10^{-4} S cm⁻¹ at 25 °C and lowered the activation energy from 0.47 eV to 0.25 eV in $\text{HT-NaSi}_2\text{P}_3$. Consequently, these structural guidelines allowed us to develop the first non-oxide based fast potassium ion conductor KSi_2P_3 , which is isostructural to its sodium cousin and exhibits a low E_a of 0.20 eV and an ionic conductivity of 3×10^{-4} S cm⁻¹ at 25 °C.¹⁵

A change in lattice volume, with in principle a larger lattice volume (more space for an ion to move) leading to a reduced activation barrier and an increased jump distance a can increase ionic conductivity. The lattice volume can be changed by either mechanical strain or strain introduced by a change in chemical composition. However, as a change in chemical compositions also alters parameters such as coordination environment, energy landscape and site disordering, the outcome on ionic conductivity is not easily predictable. Besides, structural bottle necks for ion migration can tighten although the lattice volume increases. As Krauskopf *et al.*¹³² demonstrated, the substitution of Ge⁴⁺ with Sn⁴⁺ in $\text{Li}_{10}\text{Ge}_{1-x}\text{Sn}_x\text{P}_2\text{S}_{12}$ leads to an initially unexpected lower conductivity. The origin of this behavior was deduced to an increase in the lattice softness and the strengthening of the local ionic bond between Li⁺ and S²⁻ increasing the activation barrier.

The lattice properties can be tuned *via* substitution of atoms (usually isovalent substitution). One prominent example is the increase in lattice softness by the exchange of e.g. oxygen by sulfur that is generally regarded as beneficial for ion transport increasing the ion mobility μ and was known to decrease the activation energy.^{126, 129, 133} The covalency of atomic bonds (e.g. Li–S vs. Li–O) directly influence the softness or elastic stiffness of a lattice which is correlated to the lattice vibrations (phonons). The anion polarizability (e.g. Γ^- better polarizable than Cl^- ; lattice with Γ^- softer than with Cl^-) influences the oscillator strength of a lattice and thus the attempt frequency ν_0 of an ion hopping. The attempt frequency is related to the activation energy (migration enthalpy) carrying the ion across the saddle point of a transition state during ion hopping (as depicted in Figure 12). However, as recently shown by Kraft *et al.*¹⁰² and being in accordance with the Meyer–Nedel–rule (compensation effect), the lattice vibrations and correlated attempt frequencies do not only influence the activation energy but also the pre-exponential factor σ_0 (cf. equation (18)). A lattice softening leads to a decrease in activation energy and pre-exponential factor *via* a change of the attempt frequency and by a change in the entropy of migration.^{134, 135} The E_a and σ_0 tend to compensate each other not necessarily leading to a higher ionic conductivity with increased lattice softness. In cases where the Meyer–Nedel–rule applies, improving the conductivity *via* engineering of the lattice softness is inherently limited. A way to lower the energy barrier and to increase the pre-exponential factor simultaneously was demonstrated recently by Di Stefano *et al.*¹³⁶ They showed for $\text{LiTi}_2(\text{PS}_4)_3$ that the highly distorted coordination polyhedra of lithium ions lead to a frustrated energy landscape manifesting itself by lowering the energy barrier, but increasing the pre-exponential-factor by a raise in entropy and average jump distance for lithium ions. In this work, we suspect a similar influence in the $\text{Na}_5\text{AlSi}_4\text{--Na}_4\text{Si}_4$ substitution series¹⁶ (chapter 4.5), rationalizing the superior properties of $\text{Na}_{8.5}(\text{AlSi}_4)_{0.5}(\text{SiSi}_4)_{1.5}$ in respect to the border phases by a flattening of the energy landscape by the presence of highly distorted sodium coordination polyhedra. Further studies are necessary on the complex interplay between structural factors and the energetics of ion transport in these systems.

Staying within a certain structure type, excess or deficiency of charge carriers (e.g. Li^+) caused by or without aliovalent substitution of atoms (i.e. introduction of point defects) leads to a change in defect and/or charge carrier concentration. Since extrinsic defects often dominate the ionic conduction process, this type of modification greatly enhances ionic conductivity. A change in composition, and/or in the synthesis method can severely influence the defect concentration. As elucidated for ball-milled seemingly cubic Na_3PS_4 by Krauskopf *et al.*¹³⁷, the high ionic conductivity does not depend on the crystal structure but rather depends on differences in the defect concentration induced by the harsh ball-milling conditions. Synthesis *via* ball-milling or rapid quenching does not only influence the defect concentration, but also the site disorder of cation and anions as recently shown for rare earth halides Li_3MCl_6 ($\text{M} = \text{Er}, \text{Y}$)¹³⁸ and halide containing lithium argyrodites $\text{Li}_6\text{PS}_5\text{X}$ ($\text{X} = \text{Cl}, \text{Br}, \text{and I}$)^{103, 104}. In ball-milled Li_3MCl_6 ($\text{M} = \text{Er}, \text{Y}$), where Er/Y are disordered to a new position, a cation defect emerges that improves the ionic conductivity and decreases the activation barrier. In $\text{Li}_6\text{PS}_5\text{X}$ ($\text{X} = \text{Cl}, \text{Br}, \text{and I}$), the site-disorder between S^{2-} and X^- can be engineered *via* rapid quenching from high temperatures. The site-disorder, present at high temperature is kinetically trapped by the fast cooling and leads to a decrease in the jump distance between clustered lithium ions (cages) that are present in the lithium ion substructure. These cages expand with anion site disorder, leading to better connected pathways for ion migration enhancing the overall ionic conductivity.

Long-range cation-disorder plays a huge role facilitating lithium ion diffusion in lithium-excess cation-disordered rock-salt-type lithium metal oxide cathode (DRX) materials.^{139, 140} Usually, high-energy density cathodes are well-ordered, layered materials with lithium ions and other cations occupying distinct sites. In disordered $\text{Li}_{1.211}\text{Mo}_{0.467}\text{Cr}_{0.3}\text{O}_2$, Lee *et al.*¹³⁹ observed an unexpectedly facile lithium diffusion. From calculations, they deduced the percolation of a certain type of active diffusion channel in disordered Li-excess materials to be responsible for the enhanced diffusion. However, local distortion and short-range order (SRO) in seemingly cation-

disordered materials should not be underestimated as already shown DRX cathode materials by Ji *et al.*¹⁴⁰ and can inhibit fast lithium diffusion worsening the overall battery performance. They explain the hindered lithium ion transport in $\text{Li}_{1.2}\text{Mn}_{0.4}\text{Zr}_{0.4}\text{O}_2$ compared to the isostructural $\text{Li}_{1.2}\text{Mn}_{0.4}\text{Ti}_{0.4}\text{O}_2$ by a difference in SRO, which is only detectable by local methods such as transmission electron microscopy. In this work, our study on Li_3NbS_4 and Li_3TaS_4 (chapter 4.1) touches upon this topic and highlights the importance of thorough microstructure analysis, as SRO can be decisive for the electrical properties.

Another phenomenon that influences the ionic conductivity is the controversial “paddle wheel” effect (or “revolving door”) that is used to describe a coupled cation–anion transport.^{129, 141, 142} As described by the paddlewheel effect, polyanions such as SO_4^{2-} , closo-borates, PS_4^{3-} and others do not show translational motion, but show a certain freedom for rotation facilitating the ion migration. The revolving door mechanism says that ion migration leads to rotation of the anion. Currently, the exact mechanism is still unclear.

Fast ionic conduction is not only present in crystalline solids, but also in amorphous material such as inorganic glasses.^{126, 143} Therefore, the existence of a highly ordered lattice with suitable ion channels can be helpful, but is not necessary to allow for fast ion conduction. The absence of long–range order (equivalent to liquids) characterizes amorphous materials. However, they retain a certain short–range order. The ionic conductivity of a material e.g. lithium thiophosphates in the amorphous state can be superior compared to its crystalline counterpart,¹⁴⁴ however, it can also be the other way round. For instance, even only the presence of a minor amorphous side phase in a crystalline solid electrolyte can have a severe detrimental influence on the performance as demonstrated for the glassy ceramic Li_7SiPS_8 by Harm *et al.*¹⁷

A rather special case, touched upon in this thesis, is the water–assisted lithium ion conduction in restacked lithium tin sulfide nanosheets (chapter 4.7).¹⁴⁵ Here and in crystalline $\text{Li}_2\text{Sn}_2\text{S}_5$ –hydrates,¹¹⁶ the systems represent the borderline case between ionic conduction in a solid vs. a liquid (i.e. aqueous solution). In the $\text{Li}_2\text{Sn}_2\text{S}_5$ hydrates and restacked Li–TS, upon hydration with gaseous water lithium ions are coordinated with water molecules between the tin sulfide anionic layers due to the large hydration energy of lithium (leading to a swelling of the material). During conduction, the anions stay rigid, but the lithium ions can move much faster than in the parental water–free $\text{Li}_2\text{Sn}_2\text{S}_5$ anhydrate as the intercalated water screens the interaction of the lithium ions with the ionic framework.

3.2 Measurement of the specific conductivity

The following introduction on the measurement of the specific conductivity of solid electrolytes by terms of impedance spectroscopy is compiled from textbooks from Orazem¹⁴⁶, Laszla¹⁴⁷, MacDonalds¹⁴⁸ and a review from Huggins¹⁴⁹. Other sources are marked where they were used.

The specific conductivity σ [S cm^{-1}] ($\text{S} = \text{Siemens} = \Omega^{-1}$), which is a key property of many materials and can arise either from the movement of electrons, holes or ions and is calculated *via* equation (23) by dividing the thickness d by the area A times the resistance R of the sample.

$$\sigma = \frac{d}{A \cdot R} \quad (23)$$

The resistance R of a conductor can be measured by applying a direct current (DC) and measuring the resulting voltage following Ohm’s law (24).

$$R = \frac{U}{I} \quad (24)$$

However, this technique can be only applied if suitable non-blocking electrodes for the respective charge carrier are available leading to a rectangular response curve upon the DC application as shown in Figure 14a. For electrons and holes a simple metal is suitable, but for an ionic conductor an appropriate material that conducts both the same ionic species and electrons is needed otherwise one of the charge carriers is blocked at the interface of the electrode leading an increase of the voltage over time similar to Figure 14b.¹²⁸

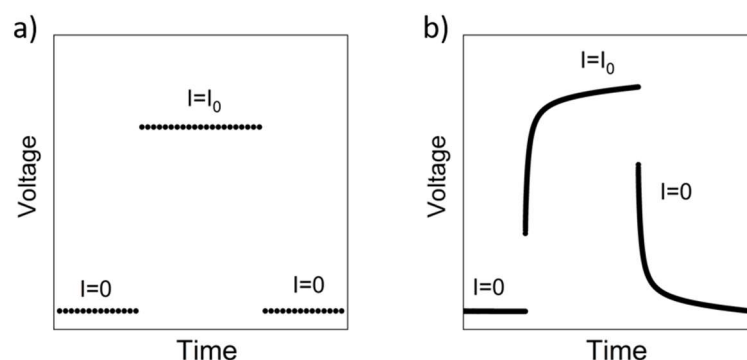


Figure 14 a) rectangular shape of voltage response to a current I_0 according to Ohm's law (24) if non-blocking electrodes are applied b) polarization curve if ion-blocking electrodes are used.

For e.g. a lithium ion conductor, the use of lithium metal or lithium metal alloys is possible, but often leads to practical limitations. Due to the high negative potential, these material reduce the material that is characterized and dramatically altering its properties. Therefore, the destruction-free method of choice is to apply ion-blocking electrodes (a non-alloying metal) and use impedance spectroscopy to determine the ionic resistance. The partial electronic conductivity is measured *via* galvanostatic or potentiostatic polarization with ion-blocking electrodes (cf. chapter 2.2.2).¹⁵⁰

3.2.1 Impedance spectroscopy of solid ionic conductors

Impedance spectroscopy is a standard technique to probe electrochemical properties and was developed for a broad variety of applications. It allows probing interfacial processes such as redox reactions and adsorption to investigate for example the corrosion of materials and electrocatalytic reactions. It can help to elucidate geometric effects (e.g. linear, spherical or cylindrical mass transfer) or to simply determine the resistance of a solution. It is applied in many fields such as ionic conductors, batteries, fuel cells, sensors and membranes besides others.

But what is actually impedance? A simple definition is as follows: the complex impedance Z of an electrical circuit is the response of an (electrochemical) system (in the steady state), as response to an alternating current (AC). In a measurement, the current response I and phase shift ϕ upon the application of a small perturbation voltage U is measured. From this the impedance is calculated, following Ohm's law (24) on first sight. The unit of the impedance is $[\Omega]$. The impedance of a resistor Z_R follows Ohm's law (25), because if a current is applied to a resistor the voltage follows immediately without a time delay.

$$Z_R = R = \frac{U}{I} \quad (25)$$

If the impedance of more complex electrical circuit element such as an inductor (**I**) or a capacitor (**C**) is investigated, a dependence of the impedance on the time (i.e. on the frequency) is found.

The impedance Z_L of an inductor, a simple metal coil with the inductance L , depends on the angular frequency ω as described in (26).

$$Z_L = i\omega L \quad (26)$$

The impedance of a capacitor Z_c is proportional to the reciprocal angular frequency times the capacitance C .

$$Z_c = \frac{1}{i\omega C} \quad (27)$$

Since an alternating current is typically described as a sinus function, the impedance Z can be calculated *via* (28) by dividing the voltage function $U(t)$ by the current function $I(t)$. The voltage function $U(t)$ consists of the amplitude of the voltage U_0 times $\sin(\omega t)$ and current function $I(t)$ includes a phase shift ϕ caused by the time delayed response of a system possessing inductive or capacitive properties.

$$Z = \frac{U(t)}{I(t)} = \frac{U_0 \sin(\omega t)}{I_0 \sin(\omega t + \phi)} = Z_0 \frac{\sin(\omega t)}{\sin(\omega t + \phi)} \quad (28)$$

In Figure 15, the current response of the basic electrical circuit elements a) resistor, b) inductor and c) capacitor with standard values ($R = 50 \Omega$, $L = 10 \mu\text{H}$ and $C = 1 \mu\text{F}$) is schematically shown. On the right, the current and voltage as a function of time is given. On the left, the so-called Nyquist plot that divides the impedance in a complex plane with a real (Z_{Re}) and an imaginary (Z_{Im}) part. This is possible by describing the AC current as a linear combination of a cosine and a sinus function and switching to polar coordinates by applying the Euler expression given in (29). By applying the Euler expression (29) in equation (28), the impedance is expressed as equation (30).

$$e^{i\phi} = \cos(\omega t) + i\sin(\omega t + \phi) \quad (29)$$

$$Z = \frac{U(t)}{I(t)} = \frac{U_0 \cdot e^{i\omega t}}{I_0 \cdot e^{i(\omega t - \phi)}} = \frac{U_0}{I_0} \cdot e^{i\phi} \quad (30)$$

Expression (30) can be split into the real and imaginary part as shown in (31). By convention, in the Nyquist plot, the positive Y-axis is the negative imaginary part. It equals all capacitive properties in the measurement. The frequency is only given implicitly with being large close to 0 ($\omega \rightarrow \infty$, $Z_{Re/Im} \rightarrow 0$) and small at maximum distance from 0 ($\omega \rightarrow 0$, $Z_{Re/Im} \rightarrow \infty$).

$$Z = \frac{U_0}{I_0} \cdot e^{i\phi} = |Z|e^{i\phi} = Z_{Re} + iZ_{Im} \quad (31)$$

In the middle of Figure 15, the so-called Bode plot shows the magnitude of impedance vector $|Z|$ and the phase shift ϕ as function of frequency. The magnitude is calculated *via* (32) and the phase angle is defined as (33).

$$|Z| = \sqrt{Z_{Re}^2 + Z_{Im}^2} \quad (32)$$

$$\phi = \tan^{-1}\left(\frac{Z_{Im}}{Z_{Re}}\right) \quad (33)$$

A simple resistor gives only one value in the Nyquist plot and straight line with no phase shift in the Bode-Plot, because it shows no dependence on the frequency. The impedance of a capacitor increases to infinity ($-Z_{im} \rightarrow \infty$) with decreasing frequency ($\omega \rightarrow 0$) and shows a phase shift of -90° . The inductor shows the same behavior but with opposite sign ($Z_{im} \rightarrow \infty$; $\phi = 90^\circ$).

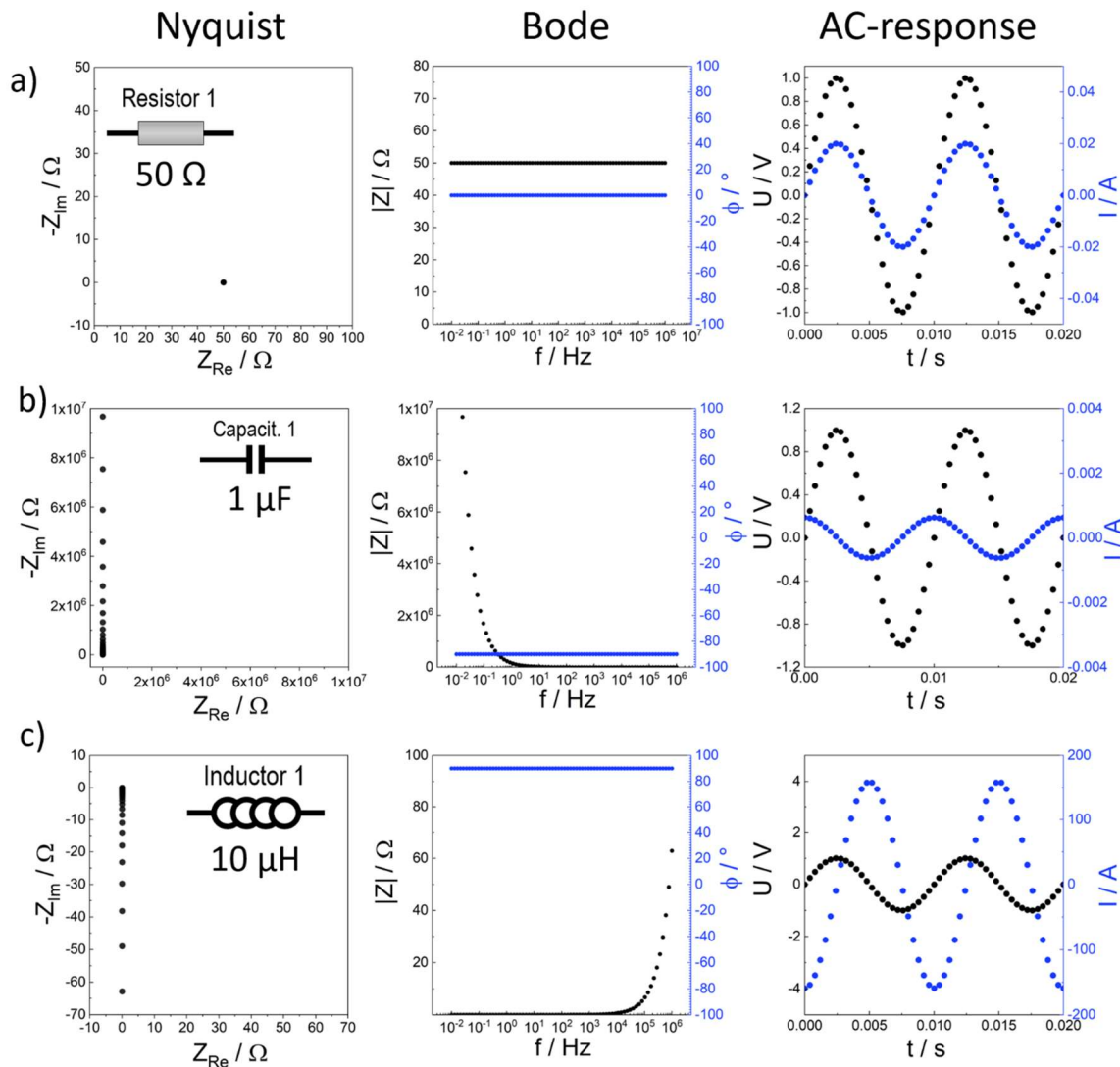


Figure 15 Impedance response of the simple circuit elements a) resistor, b) a capacitor and c) an inductor given in a Nyquist plot (left), a Bode plot (middle), and the U/I curves as function of time.

Circuit elements re combined by Kirchoff's law for a combination in series (34) or in parallel (35). Impedance spectra of typical combinations of circuit elements are given in Figure 16.

$$\begin{array}{c} \text{---} \square \text{---} \text{---} \text{---} \text{---} \text{---} \text{---} \end{array} \quad Z = Z_1 + Z_2 = R + \frac{1}{i\omega C} \quad (34)$$

$$\begin{array}{c} \text{---} \square \text{---} \\ \text{---} \text{---} \text{---} \end{array} \quad \frac{1}{Z} = \frac{1}{Z_1} + \frac{1}{Z_2} = \frac{1}{R} + i\omega C; Z = \frac{R}{1 + i\omega C} \quad (35)$$

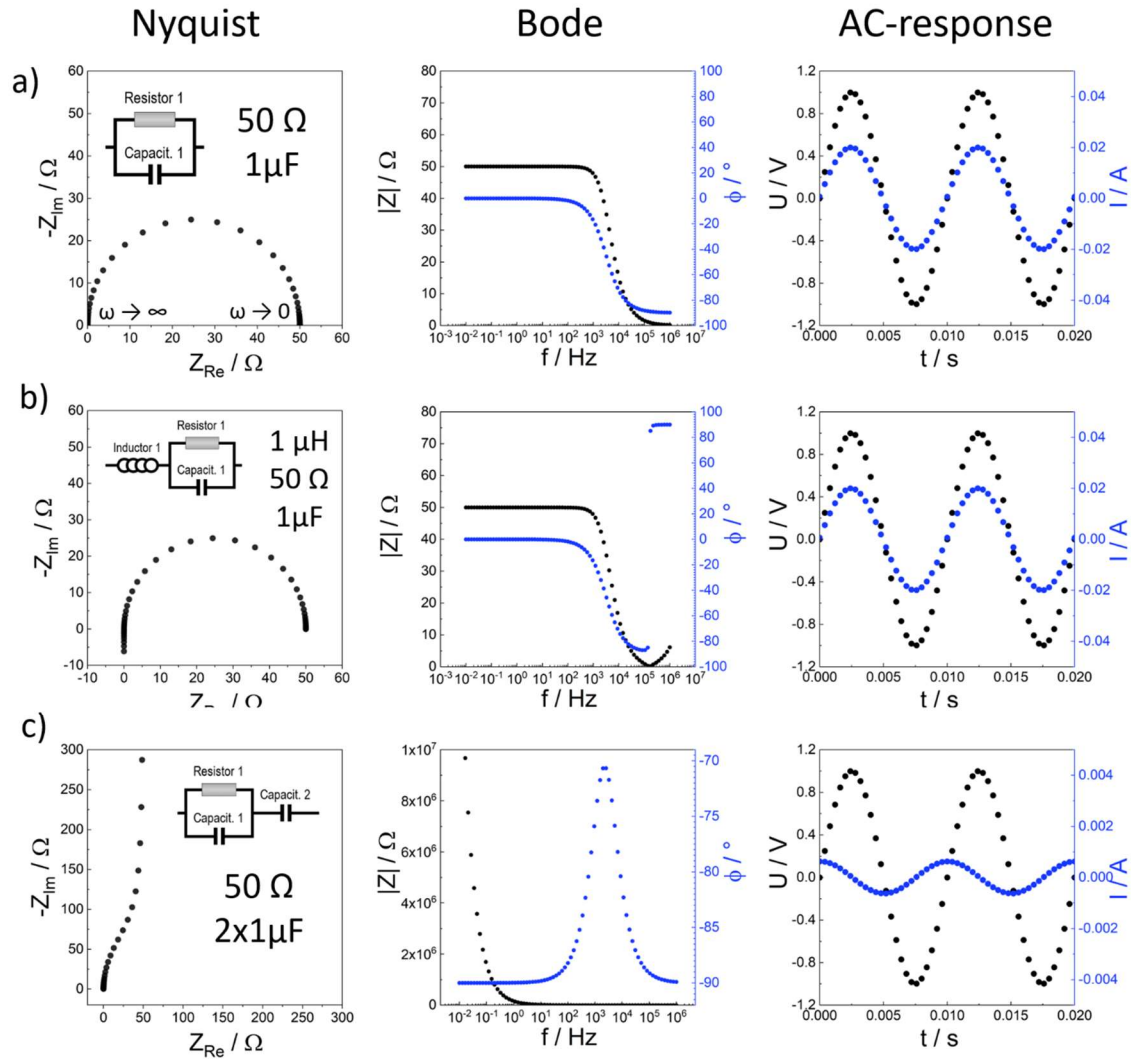


Figure 16 Impedance response of typical combination of circuit elements a) resistor and capacitor in parallel, b) inductor in series with a resistor and a capacitor in parallel c) a resistor and a capacitor in parallel with a second a capacitor in series. The spectra are given as Nyquist plot (left), as Bode plot (middle) and the U/I curves as function of time.

A solid ionic conductor possesses a unique electrochemical behavior that is modelled by at least an equivalent circuit with a resistance and capacitor in parallel resulting in a semicircle in the Nyquist-plot (cf. Figure 16a, more details see 2.2.1.1). The resistance represents the ion conducting properties and the capacitor the dielectric behavior of the material. Depending on the frequency, the current can either pass through the resistance or the capacitor. At high frequencies ($\omega \rightarrow \infty$) the impedance of the capacitor is very low (lower than the impedance of the resistor Z_R), thus the current passes unhindered and the total impedance is low (Figure 17a). When the frequency increases, Z_C increases and the current starts to pass through the resistor (Figure 17b). When Z_C exceeds Z_R , the total current passes through the resistor and the semicircle in the Nyquist-plots intersects with the X-axis (no imaginary component of vector Z , no phase-shift $\phi=0$, Figure 17c). The Z_{Re} value obtained at this point gives the resistance R that is used to calculate the specific conductivity σ in (23).

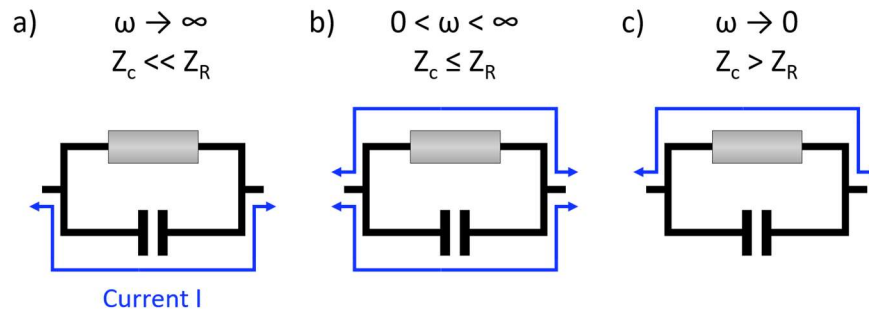


Figure 17 Current flow as function of angular frequency.

A capacitance C can be obtained by fitting the semicircle with an equivalent circuit model. By comparing C with literature data, often the origin of the capacitance can be assigned being either the bulk, grain boundaries or something else (see Table 1). If the capacitance is small $\sim 10^{-12}$ F and corresponds to the bulk properties of a material, the relative permittivity (dielectric constant) ϵ_r of the material can be calculated *via* equation (36) using the relative permittivity of the vacuum ϵ_0 , the thickness of sample d and the area A .

$$\epsilon_r = \frac{Cd}{\epsilon_0 A} \quad (36)$$

Since a typical dielectric constant of a non-polar solid is in the range of 1–100 (vs. ferroelectric materials that have much higher dielectric constants), a value above this threshold hints to other processes rather than the bulk response.

Table 1 Possible interpretation of capacitance values adapted from ref.¹⁵¹

Capacitance / F	Possible origin
10^{-12}	bulk
10^{-11}	Minor, second phase
10^{-11} – 10^{-8}	Grain boundary, current constrictions ¹⁵²
10^{-10} – 10^{-9}	Bulk ferroelectric
10^{-9} – 10^{-7}	Surface layer
10^{-7} – 10^{-5}	Sample–electrode interface
10^{-4}	Electrochemical reaction

In Figure 16b an inductor influences the impedance at high frequencies ($\omega \rightarrow \infty$) and leads to positive Z_{im} values. Such a behavior is regularly observed, if long cables (that behave as a simple inductor) and frequencies > 1 MHz are used. A typical value of inductance of 1 m of cable is about $1 \mu\text{H}$.¹⁵³

In a typical experiment, the solid ionic conductor is placed between two blocking metal electrodes. Therefore, the ions are blocked at the interface to the electrode and accumulate (they cannot penetrate into the metal). Thus, a polarization at the electrode takes place equaling the behavior of another capacitor placed in series to the material (cf. Figure 16c). If this capacitor shows an ideal behavior, the polarization leads to a straight line ($-Z_{im} \rightarrow \infty$, $\phi = -90^\circ$) going upwards in the Nyquist plot.

If the semicircle or the spike representing the ion polarization is depressed or deviates from -90° , respectively, the empirically developed constant phase element (CPE) can substitute the ideal capacitor in an equivalent circuit model. This can happen if a distribution of relaxation times is

present, which is observed frequently for polycrystalline samples with e.g. a certain surface roughness, heterogeneity and inhomogeneity in the material. For liquid electrolytes the polarization often shows a ϕ of 45° , which is modelled with a Warburg element and represents a diffusion limited regime for the polarization of ions. As to our knowledge, for ion conducting solids this context has not been shown to apply, thus we refrain from using the Warburg element for modelling such a non-ideal capacitor and restrict ourselves to the use of a CPE for modelling.

The impedance Z_{CPE} of this empirical parameter is given (38) where Q is the effective CPE coefficient and α is the CPE's exponential factor.

$$Z_{CPE} = \frac{1}{Q(i\omega)^\alpha} \quad (37)$$

If the CPE is placed in parallel to a resistor, an effective capacitance C_{eff} can be calculated by the Brug-equation¹⁵⁴ (38) with Q being the effective CPE coefficient, R the resistance in parallel to the CPE, α a fitting parameter between $0 < \alpha < 1$ (if $\alpha = 1$ the CPE is an ideal capacitor).

$$C_{eff} = \left(\frac{Q}{R^{\alpha-1}} \right)^{1/\alpha} \quad (38)$$

In Figure 18a typical impedance spectrum of a solid electrolyte with contributions stemming from the bulk properties, grain boundaries and an imperfect polarization of ions at the electrodes is simulated with the respective values. Since a fitting of such a spectrum with an equivalent circuit model is not unambiguous and always demands the application of a reasonable model for interpretation, complementing analytical techniques should be applied. Such techniques could be analysis of the surface morphology, structure, microstructure, composition, and dc electrochemical characterization and many more. In general, studies may begin with simple and well understood sample followed by a subsequent increase in complexity e.g. a substitution series.

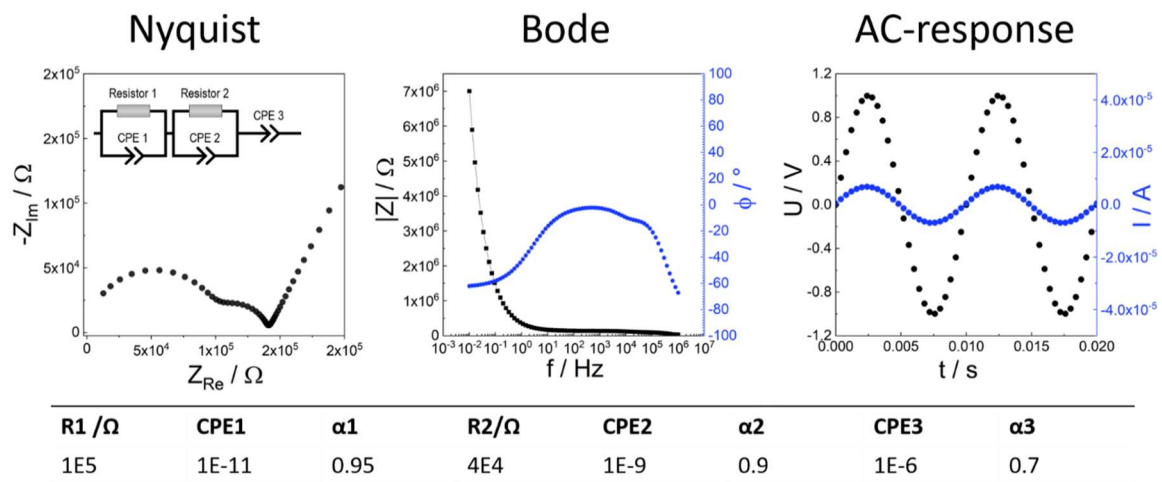


Figure 18 typical response of a real solid electrolyte sample showing several contributions to the impedance.

3.2.1.1 Microstructural models for polycrystalline solids

To probe the bulk ionic conductivity of a material directly, impedance spectroscopy can be applied on single crystals. However, since this is sample- and instrumental-wise very demanding and often even impossible (either large single crystals are necessary, or single grains of an electron beam stable sample are evaluated using microcontacts)^{155, 156}, in practice the ionic conductivity of polycrystalline powder samples is measured most often. As the presence of secondary phases

including impurity phases, grain boundaries and even the atmosphere from the environment (i.e. porosity of a sample) and (imperfect) interfaces such as the sample–electrode–interface influence the impedance response of a sample, one can think of such a system in terms of different simple layer models as depicted in Figure 19.¹⁵⁷ If enough information on the system under investigation is available (e.g. thickness of the grain boundary), these models can help to deduce the microscopic properties such as the resistivity of the grain boundary phase. Otherwise, the measured properties such as the resistivity of a sample (after correction for length/area) are only macroscopic properties meaning that the microscopic conductivity of e.g. the grain boundary can deviate from the macroscopic conductivity.¹⁴⁸

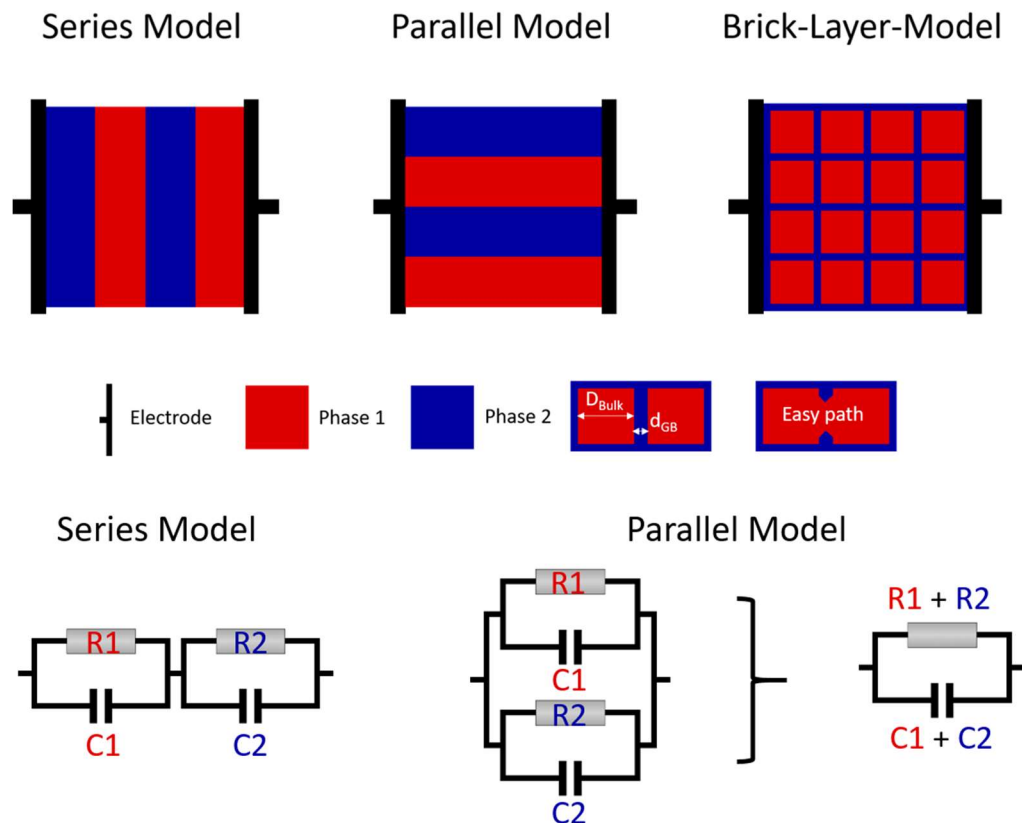


Figure 19 Series, parallel and Brick-Layer-Model for a two phase system of a polycrystalline ionic conductor with respective equivalent circuit models.

The simple arrangement of two phases between a pair of electrodes is either in parallel or in series in respect to the electrode as drawn in Figure 19. In the series model¹⁵⁸, a (R)(C)–element is assigned to each phase representing the ion conducting and capacitive properties of the solid as described above (cf. chapter 33). These two phases are in series to each other resulting in a linear mixing of their resistivities. This is represented by the serial arrangement of the two (R)(C) – elements. In the impedance spectrum two semicircles are present and well resolved if the capacities differ enough. In the parallel model, the phases are stacked across the electrodes and parallel to each other. This leads to linear mixing of the conductivities that is represented by a parallel arrangement of the two (R)(C)–elements. However, this arrangement is equivalent to a single (R)(C)–element which shows only one relaxation (semicircle). The contributions of the two phases cannot be distinguished. For a real polycrystalline sample, these two models are over simplified and especially the layer model cannot describe the behavior of grain boundaries in solid electrolytes. A more realistic picture is drawn by the Brick–Layer–Model^{159, 160} (cf. Figure 19), where the microstructure is treated as an array of cubic grains covered by thin a layer of grain boundary (normally in 3D, but in Figure 19 simplified to 2D). The thickness of the grains (bulk) is

much larger than the thickness of the grain boundaries $D_{bulk} \gg d_{GB}$. In this system, the current can flow depending on the respective conductivities σ_{bulk} and σ_{GB} either through the grain and across a grain boundary (case 1) or within the grain boundaries (case 2). If the conductivity of the grain boundaries is high ($\sigma_{GB} \gg \sigma_{bulk}$), the current flows within the grain boundary (case 2) and the impedance spectrum does not contain information about the grain properties (consistent with parallel model). If the conductivity of the grain boundaries is low ($\sigma_{bulk} \gg \sigma_{GB}$), the current flows through the grains and across the grain boundary (case 1). This is consistent with a situation in the series model leading to two contributions in the impedance spectrum. To obtain information about the nature of the “grain boundary” material, complementary methods such as electron microscopy or temperature dependent measurements assessing the activation energy of the present processes give information. If the activation energy of the “grain boundary” differs largely from the activation energy of the bulk (i.e. higher), the presence of a real second phase (= grain boundary) or a space-charge region¹⁶¹ seems plausible. Space-charge regions form near interfaces to compensate for defects and impurities segregated to surfaces, grain and phase boundaries introducing a resistive layer into the system.^{126, 161} If the activation energy of the “grain boundary” is very similar to the bulk, this second phase could just be the inclusion of atmosphere into a porous sample leading to current constriction equaling the situation of the presence of a resistive second phase.^{152, 162} This can be the case if a sample is not 100 % dense or e.g. imperfect grain-to-grain contacts are present. Both cases are rather the rule than the exception. Or in other words, there are regions of good contact between grains where ions can pass through easily (“easy paths”) and regions where ion conduction is hindered.¹⁶³ Since, in the second phase there is no fundamentally different activation barrier for ion hopping, the activation energy of the resistance stemming from current constriction equals the activation energy of the bulk.

Calculations, based on finite-elements, taking a non-ideal microstructure into account that substantially influences the “grain boundary” semicircle in an impedance spectrum of a polycrystalline material where developed by Fleig *et al.*^{162, 152, 164, 165} These show the limit of the Brick-Layer-Model: an irregular shape and size of grains, as well as non-ideal and different fractions of contact area, and many more factors influence the size and shape (depression) of the low frequency semicircle (“grain-boundary” semicircle). The Brick-Layer-Model sets the basis to understand ion conduction in polycrystalline solids, but the exact impedance response is influenced by a large variety of factors and a deconvolution solely based on impedance spectroscopy is rather impossible.

In reality, especially for soft materials such as fast sulfide based solid electrolytes (e.g. LGPS-type materials) a deconvolution of the bulk and grain boundary contributions is inherently difficult.¹⁶⁶ The bulk ionic conductivity is often extremely high, and its impedance response is only measurable under extreme conditions such as low temperatures (–140 °C) or at high frequencies > 10 MHz. The grain boundaries are not highly resistive and show a very similar activation barrier as the bulk. The microstructure of these materials can be very complicated and since these materials are not stable in the electron beam, only limited information about the microstructure of fast sulfide based solid electrolytes is available so far.

3.2.1.2 Remarks on bias errors, artifacts and convolution of processes

Since in impedance spectroscopy only the resulting net current and phase shift of a sample and measurement setup as function of frequency are measured, the existence of many bias errors, convolution of processes, and other influences has to be kept in mind. An extensive discussion of bias errors can be found by Orazem¹⁴⁶ and MacDonalds¹⁴⁸. From a user perspective, the following influences are particularly important:

- 1) Bias errors can arise from the instrument set up. Parts of the measured system are not the investigated sample, but electrical components such as wires and connectors, also giving rise to

impedance in particular at high frequencies. These have to be identified in terms of model identification and minimized by optimizing the setup.

2) The system under investigation can show non-stationary behavior during a measurement (in particular at low frequencies). A non-stationary behavior is caused for example by a change in temperature, change in concentration and growth of interface among others. To identify such a deviation from the stationary behavior, the Kramers–Kronig–relation is applied. Under the conditions of causality, linearity and stability of a system, it allows to calculate of the real part of the impedance from the frequency and the imaginary part, or vice versa. If the system does not behave accordingly, a deviation between the measured data and the calculated data *via* the Kramers–Kronig–relation occurs. In this work, the test was applied through the software Relaxis3 from RHD INSTRUMENTS. This program is based on a modelling of the data by a long series of (R)(C)-elements and a subsequent linearization of the problem.

3) The choice of measurement parameters, especially the amplitude of the excitation voltage is very important. The excitation voltage should be as small as possible, to keep the investigated system in the linear (ohmic) regime where a current responds linearly to an applied voltage ($R = U/I$). Typically, the root mean square of the excitation voltage has a value of 0.01–0.1 V for solid electrolytes. By checking the impedance response to differing voltages, the linearity of a new sample in the region of choice can be confirmed. Alternatively, the Kramers–Kronig–relation can be applied.

4) The preparation of the sample is of crucial importance. If a new material is characterized, it should be as phase pure as possible. Especially the presence of highly conducting side phases (electronically or ionically) is undesired, because these could dominate the overall impedance of the system. The surrounding atmosphere and temperature also influences the system and its conductivity. Often even trace amounts of water can adsorb onto the surface of a material leading to conduction on the surface, or changing the degree of doping etc. To assess the bulk properties, a polycrystalline material should be compacted into a pellet as dense as possible. If helpful, a sample pellet can be directly synthesized and/or sintered after pelletizing and/or hot-pressed into a pellet. Deconvolution of bulk and other influences on the conductivity is in principle possible by e.g. temperature, pressure, bias and thickness dependent measurements. Alternatively, the microstructure such as particle size and shape can be varied.

5) To ensure a good contact of the sample with the electrodes, the surface should be as smooth as possible. This avoids additional sample–electrode resistances and poor shape of the impedance spectrum by a convergence of the capacitance values or the different processes.¹⁴⁹ Therefore, samples can be polished (if possible) or the electrode itself can be applied *via* techniques such as sputtering leading to a low surface roughness and thus to a maximal contact with a rigid electrode (e.g. common stainless steel electrode). Moreover, a suitable electrode material avoiding reaction with the material under investigation (be aware of non-blocking electrodes) or even alloying with charge carrier needs to be selected. Therefore, e.g. for lithium ion conductors, ruthenium metal that does not allow with lithium is suitable. Using other materials such as gold, platinum, indium or graphite should always be critically checked in the applied parameter range. Electrodes made from materials such as indium metal and graphite foil are mechanically soft and can improve the electrode contact if other techniques are not available.

6) To obtain good data, a sufficiently high signal to noise ratio should be ensured by e.g. averaging over several measurements per frequency. For temperature dependent measurements at least a heating and cooling cycle should be analyzed.

3.2.2 Potentiostatic and galvanostatic polarization measurements for determining partial electronic conductivity and transference numbers

To determine the partial electronic conductivity and the ionic transference number of a mainly ionic conducting sample (solid electrolyte) or a mixed ionic–electronic conducting sample (electrode material), direct current (DC) galvanostatic or potentiostatic polarization measurements with ion–blocking electrodes can be applied. From the presence or absence of a polarization in the EIS measurements, the majority charge carrier in the system can be identified either as electronic (no polarization) or ionic (polarization), respectively. According to Maier *et al.*^{167, 168}, the processes in a mixed conducting sample can be described with the equivalent circuit model in Figure 20 as a parallel arrangement of electrical R_{eon} and ionic resistance R_{ion} with the bulk capacitor C_{bulk} and the ion blocking capacitor C_{block} .

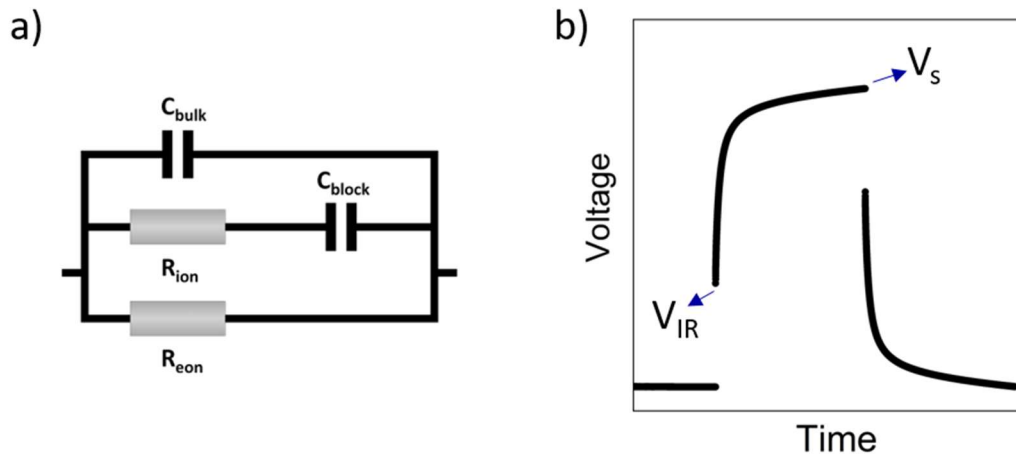


Figure 20 a) equivalent circuit model of a mixed ionic–electronic conducting sample between blocking electrodes and b) a exemplary voltage curve with an IR drop V_{IR} and a saturation voltage V_s .

For the DC polarization measurement, typically, a small current or moderate voltage is applied until a steady state of the corresponding voltage or current, respectively, is reached. The observed initial sharp IR-drop after turning on the current (or voltage) represents the total resistance of the sample in the time interval of the measurement ($V_{IR} = IR_{tot}$, typically measured in 0.1 s). The total resistance R_{tot} includes the ionic and electronic contributions R_{ion} and R_{eon} in parallel:

$$\frac{1}{R_{tot}} = \frac{1}{R_{eon}} + \frac{1}{R_{ion}} \quad (39)$$

At the steady state, the saturation voltage V_s representing the electronic resistance ($V_s = IR_{eon}$), is obtained. From this the partial electronic conductivity can be calculated *via* equation (23). If a sample does not reach a steady state, the estimated partial electronic conductivity represents an upper limit.

Subsequently, the determination of the partial conductivities *via* EIS (σ_{ion}) and DC polarization (σ_{eon}) allows the calculation of the ionic transference numbers t_i :

$$t_i = \frac{\sigma_{ion}}{\sigma_{ion} + \sigma_{eon}} \quad (40)$$

For a mainly ionic conductor, the transference number is ideally close to 1.0 to avoid a reduction of the material and a shorting of e.g. a battery cell. If the transference number is much greater

than zero, but much smaller than one, a material is considered being a mixed conductor.¹⁶⁹ For an electrode material (mixed conductor) both partial conductivities should be large.

3.3 Measurement of ion diffusivities *via* pulsed field gradient NMR

Pulsed field gradient NMR (PFG NMR) allows probing the tracer diffusion coefficient D^{tr} giving information about the long-range diffusion in a material that is linked to the ionic conductivity by the Nernst–Einstein–equation (cf. equation (16) and (17)).¹²⁹ This is an invasion and contact free alternative to the application of impedance spectroscopy to obtain information about the ion transport kinetics in a material. PFG NMR can be applied on different nuclei such as ^1H , ^7Li , ^{19}F , ^{23}Na and ^{31}P in liquids and solids. The only prerequisite for a successful measurement is that the diffusion coefficient is high enough in the temperature range accessible with the respective NMR spectrometer.

As depicted in Figure 21, the motion of molecules or ions is determined in relation to the locally varied magnetic field by measuring an attenuation of the NMR signal in a spin–echo–experiment.¹⁷⁰ A gradient coil (Maxwell–coil) generates the local varied magnetic field and applying a gradient causes a frequency variation of nuclei as a function of position along the direction of the gradient. The first gradient pulse leads to a dephasing of the nuclei spins, thus the magnetization vectors rotate differently at different positions in the tube cancelling out the total signal. Within the diffusion time Δ , the nuclei diffuse changing their position accordingly. The second gradient pulse leads to a refocusing of the nuclei spins, thus the total signal reappears. The physical movement of the nuclei reduces the effectiveness of the refocusing pulse reducing the resulting signal strength (I). The field gradient strength g and duration of the magnetic field gradient pulse δ determine the distance that a nucleus can diffuse and still yield a signal.¹⁷¹

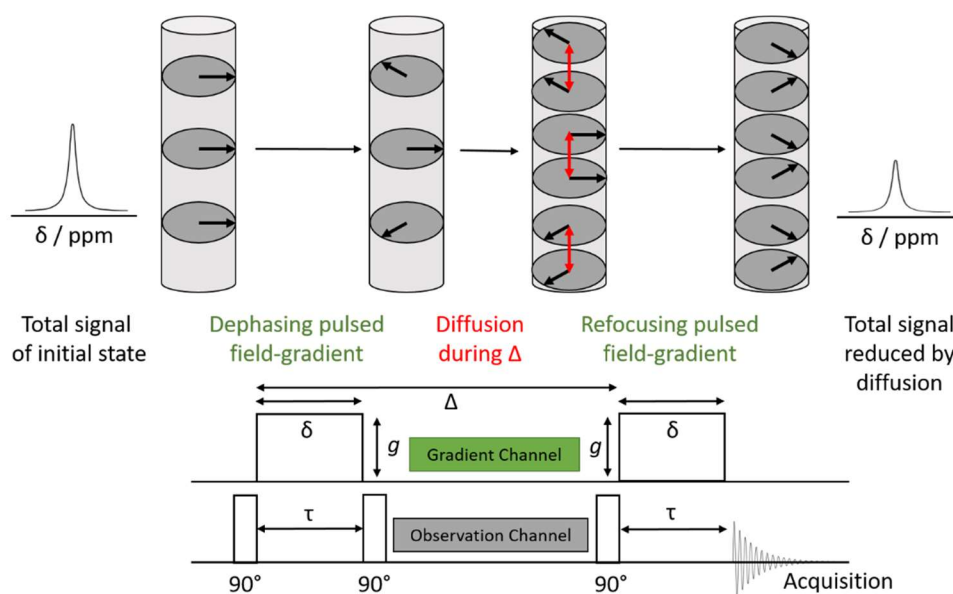


Figure 21 Working principle of PFG NMR measurement: the by ionic motion attenuated signal is observed with a stimulated spin echo experiment (PFG-SSE in the observation channel).

By increasing the gradient strength g (the variable in the measurement), the intensity being the observable of the measurement (either integration over the area of the static NMR spectrum or intensity of the signal) decreases accordingly as schematically drawn in Figure 22. Subsequently, the data is evaluated by processing the measured echo attenuation curve $I(g, \delta, \Delta)$ using the Stejskal–Tanner equation (41).¹⁷² With γ being the gyromagnetic ratio of the nucleus under investigation, g the strength and δ the duration of the pulse field gradient, D^{tr} is the tracer diffusion coefficient, and Δ the time interval between the field gradients.

$$I(g, \delta, \Delta) = I_0 e^{(-\gamma^2 \delta^2 g^2) D^{tr} (\Delta - \frac{\delta}{3})} \quad (41)$$

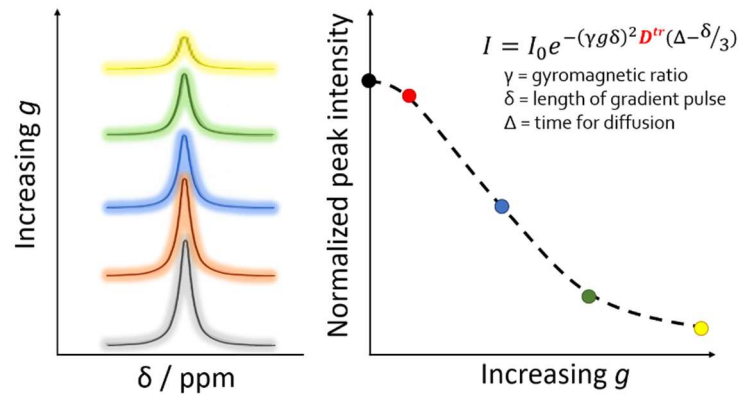


Figure 22 Attenuation of signal intensity by increasing the gradient strength as observed in a PFG NMR measurement to extract the tracer diffusion coefficient by fitting with the Stejskal–Tanner equation.

Tuning g and Δ allows investigating processes occurring at different time and length scales. In general, PFG NMR probes the motion of ions on the time scale of 10^{-2} to 1 s with a length scale of about $10 \mu\text{m}$. Equation (42) estimates the isotropic diffusion radius of the observed nucleus.¹⁷³

$$r_{rms} = \sqrt{2D_{NMR}\Delta} \quad (42)$$

The diffusion coefficient obeys an Arrhenius-type law in a temperature dependent measurement.

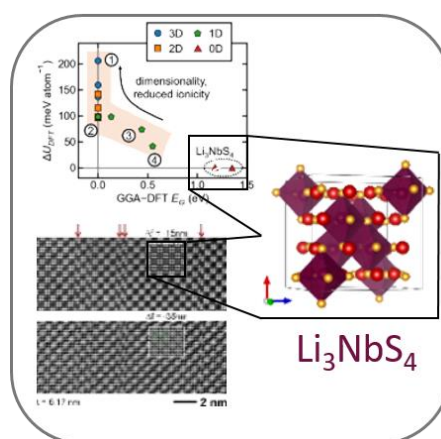
4. Experimental, Results and Discussion

4.1 Taking a closer look: (Micro)Structure and electronic properties of rock-salt type Li_3NbS_4 and Li_3TaS_4

A.-K. Hatz, S. Harm, V. Duppel, R. Hooijer, P. Minnman, L. Balzat, J. Blahusch, D. H. Fabini, B. V. Lotsch

Abstract

One approach to improve lithium ion batteries is the implementation of novel cathode materials based on lithium metal sulfides. These materials are cobalt- and nickel-free alternatives to state-of-the-art oxide cathodes and they promise a better compatibility with sulfide-based solid electrolytes supporting the development of high performance all-solid-state-batteries (ASSB). One of these materials is ball-milled Li_3NbS_4 that has been only rudimentarily characterized to date due to its low crystallinity. Here, we have synthesized phase pure and highly crystalline Li_3NbS_4 and its heavier homologue Li_3TaS_4 *via* high temperature synthesis and analyzed their structure and electronic properties.



Both compounds crystallize in a low-temperature polymorph which is isostructural to the cubic cation-ordered rock-salt-type Li_3NbO_4 ($\bar{I}43m$, Nr. 217) corroborating the proposed rock-salt-type structure of ball-milled Li_3NbS_4 . Crystallization from the melt yields a high temperature tetragonal polymorph with a new structure type exhibiting an alternative cation-order ($P4_12_12$, Nr. 92). By a combination of computational methods, we show that the observed ordering reflects a competition between electrostatic considerations, covalency, and a tendency to avoid extended connectivity that is *not* observed in the corresponding oxides. Anomalies in the powder X-ray diffractogram of cubic Li_3NbS_4 are explained by a defect-rich microstructure elucidated by high-resolution transmission electron microscopy reflecting the tendency to preserve isolated $[\text{M}_4\text{S}_{16}]^{12-}$ -clusters ($\text{M} = \text{Nb}, \text{Ta}$). Consistent with the local cluster motif, both materials possess pronounced bandgaps and are poor, predominately electronic conductors ($< 10^{-8} \text{ S cm}^{-1}$), while cubic Li_3NbS_4 fails as cathode active material in an ASSB. These findings are in direct contrast to the reports on superior battery performance of ball-milled Li_3NbS_4 , hinting to a large influence of amorphous phases or the absence of short-range order induced by ball-milling opening up new starting points for the evaluation of ball-milled sulfide-based cathode materials.

Introduction

Lithium ion batteries (LIBs) are the state of the art energy source for a variety of devices ranging from portable consumer electronics to electric vehicles and beyond. For further improving the performance in terms of high energy density, long cycle life and fast charge/discharge kinetics, different strategies are currently being pursued. All-solid-state-batteries (ASSBs), for instance, promise high charging rates by incorporating fast ion conducting solid electrolytes, as well as an increase in energy density by enabling the use of a lithium metal anode.¹⁻⁴ Recently, high

performance systems without providing a lithium metal reservoir (lithium foil) in the discharged state were introduced, optimizing the energy density even further.^{5,6} Another way to increase the capacity is the implementation of high voltage cathodes or high-capacity cathode materials that allow a reversible multi-electron process to incorporate more lithium.^{7,8} Lately, materials based on sulfides that show anion redox chemistry, have emerged.⁹⁻¹⁹ They not only promise high energy densities, but also cobalt- and nickel-free alternatives to state-of-the-art high-capacity cathode materials for LIBs.

In cells employing standard liquid electrolytes and metal sulfides such as Li_2TiS_3 or Li_3NbS_4 as the cathode, capacities between 339 mAh g^{-1} for layered Li_2TiS_3 ¹¹, 386 mAh g^{-1} for rock-salt-type Li_3NbS_4 ¹⁰ and 425 mAh g^{-1} for rock-salt-type Li_2TiS_3 ¹⁰ have been reported. The potential ranges between ~ 2.2 – 2.5 V vs Li+/Li and 2.5–3.5 electrons are transferred (multi-electron process). Their theoretical gravimetric specific energy is between 780–850 Wh kg^{-1} exceeding that of standard NCM-622 (lithium-nickel-cobalt-manganese-oxide) of 590 Wh kg^{-1} .

The exact mechanism of the anion redox chemistry remained unclear until recently: after reports on $\text{Li}_{1.33-2x/3}\text{Ti}_{0.67-x/3}\text{S}_{2.28}$ ¹⁶ that mentioned sulfide oxidation upon delithiation (charging), Flamarly-Mespoulie *et al.*¹¹ confirmed the formation of S_2^{2-} species via X-ray photoemission spectroscopy (XPS) in the layered sulfide LiTiS_2 - Li_2TiS_3 series. Almost at the same time, Hansen *et al.*¹² reported on lithium-rich layered iron sulfide Li_2FeS_2 showing that delithiation results from oxidation of Fe^{2+} to Fe^{3+} followed by reversible formation of polysulfides (S-S bonds; S_2^{2-}). Thus, Li_2FeS_2 can reversibly store ≥ 1.5 electrons per formula unit and supports extended cycling.

High reversibility of the anion redox in some cathode materials seems to be supported by amorphization during charging (delithiation) with a return to the pristine crystal structure during discharging (lithiation). Disordered cubic rock-salt-type Li_2TiS_3 ^{9,10} and disordered antifluorite-type Li_3CuS_2 ¹³ show such a behaviour that enables the reversible formation of polysulfide bonds, without irreversible structural degradation. Hints to a similar behaviour were found for the solid solution series $x\text{Li}_2\text{S}\cdot\text{NbS}_2\cdot(2-x)\text{S}$ ($x=0.5$ – 2 ; LiNbS_4 - Li_4NbS_4).^{18,19} Additionally, amorphous species play a vital role during cycling of mechanochemically prepared amorphous NbS_x ($x=3$ – 5).²⁰

To enhance the performance of LIBs, first attempts to combine ASSBs and lithium metal sulfide cathodes were made.^{10,13,14,19} In theory, several advantages can be deduced for such a system. 1) The combination of lithium metal sulfide with thiophosphate based solid electrolytes such as crystalline Li_3PS_4 , $\text{Li}_2\text{S}\cdot\text{P}_2\text{S}_5$ (LPS) glasses, $\text{Li}_6\text{PS}_5\text{X}$ ($\text{X}=\text{Cl}, \text{Br}, \text{I}$), $\text{Li}_{10}\text{Ge}_2\text{PS}_{12}$ -type materials etc. seems promising since both material classes are mechanically soft and intimate contact between these materials can be realized by simple cold pressing. 2) The redox potential of regular metal oxides exceeds the thermodynamic stability of thiophosphate-based electrolytes,^{21,22} i.e. the thiophosphates are oxidized at the interface to the metal oxide cathode particles, leading to an overall decline in cell performance.²¹ However, to first approximation, oxidation at the interface with metal sulfide cathodes is not expected, potentially leading to a much more stable cell performance. 3) The inherently higher electronic conductivity of lithium metal sulfides with respect to isostructural lithium metal oxides should enable a cell fabrication without electronically conducting additives such as carbon, increasing the overall capacity and preventing side reactions with the solid electrolyte.²³

An ASSB of layered $\text{Li}_{1.13}\text{Ti}_{0.57}\text{Fe}_{0.3}\text{S}_2$ ¹⁴ with β - Li_3PS_4 as solid electrolyte and a lithium anode exhibited good cyclability, small polarization, and no initial irreversible capacity. In the latter work, the layered metal sulfide was also proposed as a novel coating material for regular metal oxide

cathodes. First proof-of-principle experiments demonstrated superior cell performance. Besides, the aforementioned rock-salt type materials Li_2TiS_3 and Li_3NbS_4 were successfully combined with glassy LPS in an ASSB.^{10, 19} Both cells showed high capacities of about 300–400 mAh g^{-1} and a high capacity retention >90 % after 50 and 200 cycles, respectively. The cell working with Li_3NbS_4 showed a good performance at higher currents as compared to its titanium counterpart (0.5 mA cm^{-1} vs. 0.1 mA cm^{-1}).

The X-ray powder diffraction pattern of Li_3NbS_4 synthesized *via* mechanochemical ball-milling (hereafter denoted as bm- Li_3NbS_4) showed only a few very broad reflections, indicating the presence of an amorphous side phase.^{10, 17, 19} A rock-salt-type structure was assumed in accordance with bm- Li_3NbS_4 crystallizing isostructural to cation-disordered Li_3NbO_4 (after nickel doping).²⁴ However, the reported high electronic conductivity of $>10^{-2}$ S cm^{-1} is unexpected for an un-doped rock-salt-type material with bonding character between ionic and covalent and a band gap of 1.4 eV (i.e. being a semiconductor according to simulations on cubic Li_3NbS_4 on the materials project platform (MP-769032)).^{25, 26} In cation-disordered nickel doped Li_3NbO_4 ²⁴ the ionic contributions (conduction of lithium ions) dominate its electrical properties.

We therefore set out to synthesize phase pure, highly crystalline Li_3NbS_4 to take a closer look at its structure and properties, unbiased by the presence of an amorphous side phase. As is well-known from solid electrolytes, the presence of an amorphous side phase can strongly influence electronic and ionic transport.²⁷ Such characterisation of structure and properties is necessary to understand why bm- Li_3NbS_4 is superior to the intercalation of lithium in metallic NbS_2 .²⁸ For comparison, we synthesized the heavier homologue Li_3TaS_4 . We find that at low temperatures both compounds crystallize in the non-centrosymmetric, cation-ordered rock-salt-derived Li_3NbO_4 -type^{29, 30} structure with space group $\bar{1}43m$ (Nr. 217). At high temperatures, both adopt a new cation-ordered, rock-salt-derived structure type, characterized by enantiomorphic symmetry in the tetragonal space group $P4_12_12$ (Nr. 92). For phase pure cubic Li_3NbS_4 (cub- Li_3NbS_4), which can only be obtained upon quenching from moderate temperature, we find *via* high-resolution transmission electron microscopy (HRTEM) an intriguing microstructure of small, cation-ordered domains joined by planar defects, explaining anomalies in the powder X-ray diffractogram (PXRDs) that could be mistaken for cation disorder at first sight. We find that both materials are predominately electronic conductors with a low electronic and ionic conductivity of $<1.5 \times 10^{-8}$ S cm^{-1} and that cubic Li_3NbS_4 fails as cathode active material in an ASSB. These results are rationalized by the computational investigation of the thermodynamics of cation ordering of rock-salt type structures with a stoichiometry of Li_3MS_4 ($M = \text{Nb}^{5+}, \text{Ta}^{5+}$) by Madelung energies, a determination of the dimensionality of M^{V+} -S connectivity, and the analysis of space group symmetry as well as an examination of the phase stability and electronic structure by DFT calculations. The observed ordering reflects a competition between electrostatic considerations, covalency, and a tendency to avoid extended connectivity that is *not* observed in the corresponding oxides, in accordance with the observed poor electronic and ionic conductivity in the here prepared Li_3MS_4 ($M = \text{Nb}^{5+}, \text{Ta}^{5+}$) compounds.

Experimental

Synthesis of single crystals

Li_3TaS_4 and Li_3NbS_4 single crystals were obtained from a stoichiometric mixture of Li_2S (99.9 % ALFA AESAR), Ta or Nb (powders, 99.9 % SIGMA ALDRICH) and S (sublimed *in vacuo*, GRÜSSING). The mixture was placed in a glassy carbon crucible and sealed in a quartz tube under vacuum (10^{-3} mbar). The

mixture was heated at 950 °C for tetra- Li_3TaS_4 and at 750 °C for cub- Li_3NbS_4 for 30 h (110 °C/h) each. Subsequently, the products were cooled down with 30 °C/h to room temperature (RT) and red single crystals could be separated from a heterogeneous mixture containing LiNbS_2 side phase. To obtain phase pure cub- Li_3NbS_4 , the same initial reagent mixture was heated at 600 °C for 90 h (100 °C/h) and then rapidly quenched in a water bath to RT. A fine dark red powder was obtained. To obtain cub- Li_3TaS_4 and tetra- Li_3NbS_4 , the same reaction mixtures were heated at 600 °C and 850 °C for 90 h (100 °C/h), respectively. Subsequently, the products were cooled down with 25 °C/h to RT.

Energy dispersive X-ray spectroscopy

Energy dispersive X-ray spectroscopy (EDX) was performed on a Jeol JSM-6500 and an electron field emission source with an EDX-detector from OXFORD Instruments.

Transmission electron microscopy

Bulk samples of cub- Li_3NbS_4 and tetra- Li_3TaS_4 were ground and distributed onto a holey carbon/copper grid. TEM was performed with a PHILIPS CM 30 ST microscope (300 kV, LaB_6 cathode) equipped with a spinning star device enabling the use of precession electron diffraction (PED)³¹. Simulations of the diffraction patterns and the high-resolution micrographs (multi-slice formalism) were obtained with the JEMS software package.³² Images were taken with a TVIPS TemCam-F216 CMOS Camera.

Single crystal X-ray diffraction

Single crystal X-ray diffraction measurements were performed on a BRUKER D8 Quest diffractometer with fixed- κ -geometry, an $1\mu\text{S}$ microfocus-source with $\text{Mo-K}_{\alpha 1}$ radiation ($\lambda = 70.93$ pm), a graphite(001) monochromator, OXFORD CRYOSYSTEMS cooling and a PHOTON 100 CCD-detector with Peltier-cooling. Crystal samples were prepared in 0.1 mm glass capillary tips in paraffin oil dried over metallic potassium. The structure solution and refinement were performed with the programs SHELXS97, SHELXL97, and PLATON.³³

Powder X-ray diffraction

PXRD was measured on a STADI P diffractometer working in Debye-Scherrer geometry with $\text{Cu-K}_{\alpha 1}$ ($\lambda = 154.0562$ pm) or $\text{Mo-K}_{\alpha 1}$ radiation ($\lambda = 70.93$ pm) and a Ge(111) monochromator. The powder was filled in a glass capillary under Ar atmosphere and sealed. Rietveld refinement was performed with TOPAS Academic v.5.³⁴

Inductively coupled plasma optical emission spectroscopy (ICP-OES)

For a quantitative assessment of the Li and Ta/Nb ratio in the samples, ICP-OES was performed with a VARIAN Vista-Pro and a VARIAN Vista RL spectrometer. The characteristic wavelengths are separated with an Echelle-Polychromator (VARIAN) and detected with a photomultiplier. The materials were digested in a microwave (Discover-SP-D von CEM) in concentrated HNO_3 (65 %) and HF (40 %) in ratio of 1:2 at 155 °C for 25 min.

Differential scanning calorimetry

For differential scanning calorimetry (DSC) measurement, about 50 mg of samples was sealed in small quartz ampoules with ~5 mm outer diameter and ~15 mm length under Ar. For improved heat-flow, the quartz ampoules were placed in Pt-crucibles. The measurements were carried out using a NETSCH STA 449 F5 Jupiter with an Ar flow of 20 mL/minute in a temperature range between room temperature and 1020 °C for Li_3TaS_4 and 850 °C Li_3NbS_4 and heating/cooling rates of 5 and 15 K/min. The data was analyzed with the NETSCH Proteus software package.

Electrochemical measurements

Cylindrical pellets of Li_3TaS_4 and Li_3NbS_4 were prepared by uniaxial cold pressing (10 kN) with a thickness of 0.5–1.0 mm and a diameter of 5 mm. The pellets were sputtered with ruthenium metal as ion-blocking electrodes on both sides. Impedance spectra (1 MHz–1 Hz, rms AC voltage of 100 mV) and DC potentiostatic polarization were measured with an Ivium compactstat.h (24 bit instrument) in a two-electrode setup after 1 h of equilibration time inside a glovebox under argon. For temperature control, RHD INSTRUMENTS TSC Battery cells were loaded onto a RHD INSTRUMENTS Microcell HC cell stand with an integrated Peltier heater. The analysis of the spectra was performed with RelaxIS3 from RHD INSTRUMENTS.

Computational methods

Calculations of phase stability and electronic structure were performed using the Kohn–Sham formulation of density functional theory with a plane-wave basis set and the projector-augmented wave formalism³⁵ as implemented in VASP.^{36–38} Exchange and correlation were treated by the revised Perdew–Burke–Ernzerhof generalized gradient approximation functional for solids (PBEsol).³⁹ Plane wave cutoff was 600 eV due to the anticipated steep gradients around small, electropositive Li^+ . Structures were relaxed to a force tolerance on the ions of $1 \text{ meV } \text{Å}^{-1}$. Several tools implemented in pymatgen⁴⁰ were utilized in the examination of the thermodynamics of cation ordering: Ewald summation of Madelung energies,⁴¹ determination of the dimensionality of M^V –S connectivity,⁴² and analysis of space group symmetry via the interface to spglib⁴³. Random cation orderings were generated with custom python code. Crystal structures were visualized with VESTA.⁴⁴

Results and discussion

Structural characterization

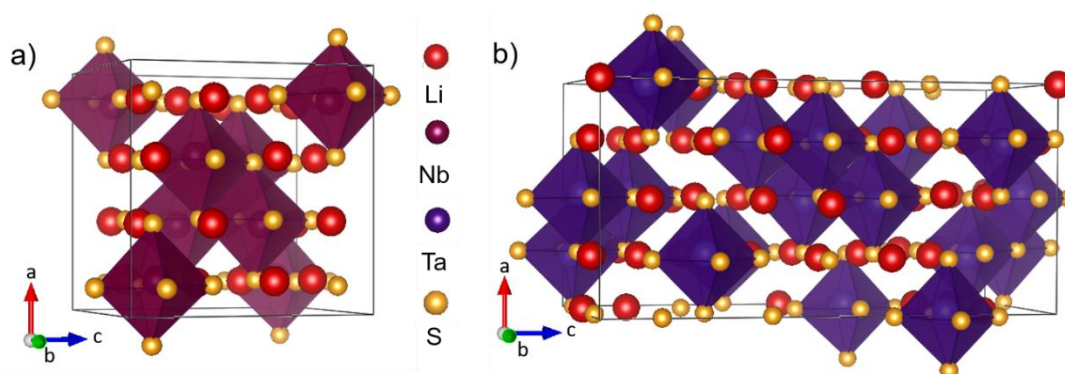


Figure 1 Depiction of a) cub-Li₃NbS₄ ($\bar{I}43m$ (Nr. 217)) being isostructural to Li₃NbO₄. The cation order gives rise to [Nb₄S₁₆]-clusters surrounded by lithium ions. b) tetra-Li₃TaS₄ ($P4_12_12$ (Nr. 92)) has [Ta₄S₁₆]-clusters that are connected via edges in a plane rather than in a tetrahedron as in cub-Li₃NbS₄.

By slowly cooling from temperatures below the melting point of Li₃NbS₄ and above that of Li₃TaS₄ (cf. DSC measurements in Figure S2), red single crystals of Li₃NbS₄ and Li₃TaS₄ were obtained and used for structure determination (the crystallographic data and refinement parameters are summarized in Table 1). The stoichiometry was confirmed by EDX and ICP-OES measurements (cf. Table S11 and Table S12). Li₃NbS₄ is isotypic to cation-ordered rock-salt type Li₃NbO₄^{29, 30} in the cubic space group $\bar{I}43m$ (Nr. 217) and is hereafter denoted as cub-Li₃NbS₄ (crystallographic data given in Table 1, Table S1-Table S5). The structure can be viewed as decorated rock-salt structure⁴⁵ (cations are octahedrally coordinated by anions and vice versa building a three-dimensional network of edge-sharing octahedra) in which the nature of the cation order gives rise to isolated clusters of four edge-sharing NbS₆ octahedra building Nb₄S₁₆-tetramers as shown in Figure 1a. These clusters can be viewed as 0D polyanions (no connection between polyanions) that are surrounded by lithium ions occupying octahedral positions. On the contrary, Li₃TaS₄ (hereafter denoted as tetra-Li₃TaS₄) crystallizes in the tetragonal space group ($P4_12_12$, Nr. 92, enantiomorphous with $P4_32_12$, Nr. 96) showing a different cation ordering (crystallographic data given in Table 1, Table S6-Table S10). The crystal structure of tetra-Li₃TaS₄ consists of [Ta₄S₁₆]-clusters that are connected *via* edges in a plane rather than in a tetrahedron as in cub-Li₃NbS₄. Notably, Li₃TaS₄ is not isotypic to monoclinic Li₃TaO₄, which occurs in three different monoclinic polymorphs. As such, tetra-Li₃TaS₄ represents a new structure type.⁴⁶⁻⁴⁸

Table 1 Crystallographic information and data for the structure solution and refinement of cub-Li₃NbS₄ and tetra-Li₃TaS₄ on the basis of single crystal data. Standard deviations are given in parentheses.

Formula	Li ₃ NbS ₄	Li ₃ TaS ₄
space group	$\bar{I}43m$ (Nr. 217)	$P4_12_12$ (Nr. 92)
$a / \text{\AA}$	10.2865(5)	10.2878(3)
$b / \text{\AA}$	-	20.6069(6)
$V_{\text{cell}} / \text{\AA}^3$	1088.44(9)	2181.01(11)
Z	8	16
$\rho_{\text{X-ray}} / \text{g}\cdot\text{cm}^{-3}$	2.953	4.020

μ / mm^{-1}	3.567	21.520
θ -range / °	4.85–39.99	2.21–40.00
reflections measured	15394	61396
independent reflections	663	6753
parameters	21	148
R_σ	0.0133	0.0210
R_{int}	0.0399	0,0468
$R_1 (F^2 > 2\sigma(F^2)) / \text{all}$	0.0202/0.0206	0.0189/0.0213
$wR_2 (F^2 > 2\sigma(F^2)) / \text{all}$	0.0513/0.0513	0.0582/0.0692
Goof	1.333	1.323
$\Delta\rho_{\text{max/min}} / \text{e}\cdot\text{\AA}^{-3}$	1.514/−1.234	2.339/−2361

When Li_3NbS_4 is cooled from the melt (cf. DSC in Figure S2b) the high temperature polymorph can be obtained. It crystallizes in the tetragonal structure with layered $\text{Li}_{0.5}\text{NbS}_2$ and Li_2S as side phases (cf. Figure S1b and c) and lattice parameters of $a = 10.30$ and $b = 20.61$ Å according to Rietveld refinement. As both polymorphs have different unit cell sizes, the high temperature phase (tetra) having a lower symmetry than the low temperature phase is rather unusual, but not without precedence. The low temperature polymorph of Li_3TaS_4 in the cubic structure (cf. Figure S1b and d) with $a = 10.30$ Å is accessible, when the reaction mixture is moderately cooled from 600 °C after a protracted solid state reaction. After applying the DSC program on cub- Li_3TaS_4 (first melting and then recrystallizing), tetra- Li_3TaS_4 is obtained. Notably, there is no group–subgroup relationship between the two polymorphs (cubic and tetra), and the phase transition is reconstructive as there is a substantial energy barrier between them (see below). The change in the $[\text{M}_4\text{S}_{16}]$ -clusters (M=Nb, Ta) of the reconstructive phase transition is depicted in Figure 2.

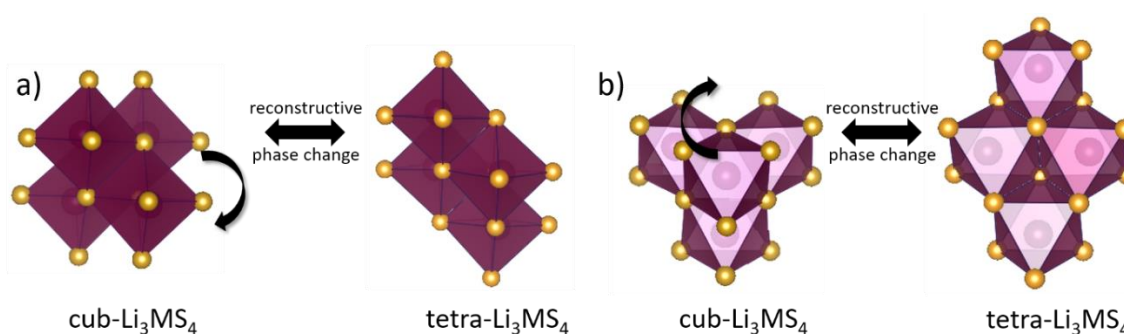


Figure 2 Depiction of change of position of MS_6 octahedron (M=Nb, Ta) in $[\text{M}_4\text{S}_{16}]$ -clusters between cubic and tetragonal Li_3MS_4 from perspective a) and b).

Microstructure of cub- Li_3NbS_4

Phase pure cub- Li_3NbS_4 ($a = 10.30$ Å) is obtained by quenching the reaction mixture from 600 °C. However, the reflections in the powder diffractogram in Figure 3a are unusual, showing a mismatch of intensity and reflection profile, similar to diffractograms of the nominally cation-disordered Li-excess rock-salt $\text{Li}_{1.25}\text{Nb}_{0.25}\text{Mn}_{0.5}\text{O}_2$ ⁴⁹ (solid solutions of rock-salt type Li_3NbO_4 and LiMnO_2 , Li-excess vs. LiMnO_2) and cannot be fitted adequately *via* Rietveld refinement with the cubic structure. In general, the reflections of such a cation-ordered rock-salt type structure can be

categorized into reflections stemming from the rock-salt aristo-type structure (backed with grey in Figure 3a, scheme Figure 4a) and from the cation-ordered hetto-type structure resulting in additional super-structure reflections (all other reflections in Figure 3a; scheme Figure 4b). A compound containing more than one type of cation (e.g. NaCl vs. $\text{Na}_{1-x}\text{K}_x\text{Cl}$) only showing the rock-salt aristo-type reflections would be regarded as fully cation-disordered (cf. Figure 4a). Here, for phase pure cub- Li_3NbS_4 , the intensities and profiles of the reflections stemming from the rock-salt aristo-type do not match the super-structure reflections: The intensity of the aristo-type reflections is higher than expected and the profiles are very narrow and sharp. On the other hand, the super-structure reflections show a lower than expected intensity and significant broadening. These profiles normally hint to small crystalline domains and the presence of planar defects.

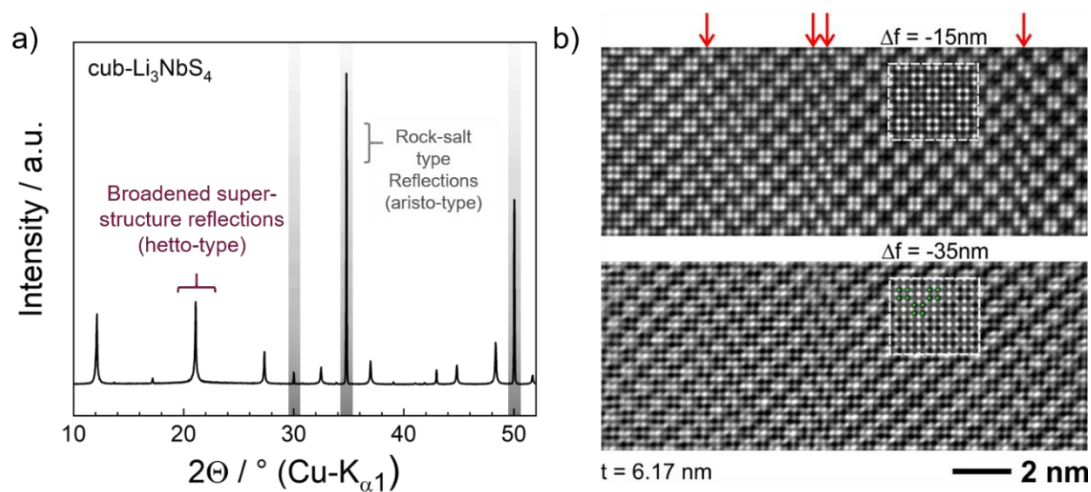


Figure 3 a) powder diffractogram of phase pure cub- Li_3NbS_4 shows unusual reflections: the reflection profile and intensities of the reflections stemming from the aristo-type do not fit the ones stemming from the hetto-type. b) HRTEM images show defect rich cub- Li_3NbS_4 , zone axis [001]. Simulations are inserted (exemplary Nb atoms are marked as green dots) and show a good agreement.

Considering the previous reports of fully cation-disordered bm- Li_3NbS_4 ^{10, 19}, a microstructure as sketched in Figure 4c with small cation-ordered domains next to large cation-disordered Li_3NbS_4 regions seemed a plausible explanation for the observed deviations in the diffractogram. However, HRTEM, which is a local method, shows a different picture: small domains of fully ordered cub- Li_3NbS_4 (< 9 nm) are connected to each other via planar defects in [001] and [101] as visible in Figure 3b, Figure S and Figure S4. There are no fully cation-disordered domains present. At the domain boundary, the Nb^{5+} are still clustered in isolated polyanions. We conclude from this, that the abnormalities in the PXRD do not result from cation-disorder, but from the defect rich microstructure in cub- Li_3NbS_4 .

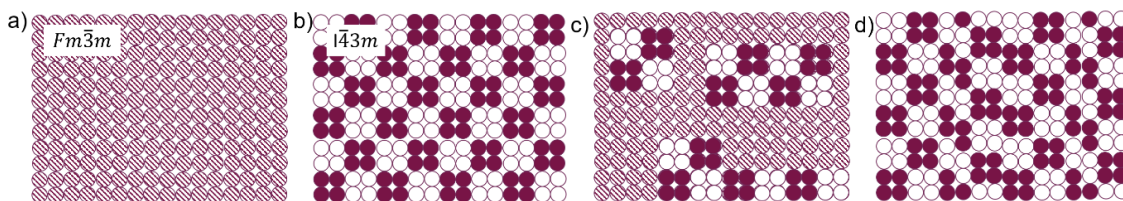


Figure 4 Schematic depiction of possible cation-ordering and microstructure. a) Hypothetical cation-disordered rock-salt structure in Li_3NbS_4 (Li^+ in white and Nb^{5+} in purple). b) Fully ordered cub- Li_3NbS_4 ; c) Domains of cation-ordered cub- Li_3NbS_4 next to cation-disordered domains. d) Domains of cation-ordered cub- Li_3NbS_4 connected via {100} planar defects.

Microstructure of tetra- Li_3TaS_4

The microstructure of tetra- Li_3TaS_4 shows larger domains than in cub- Li_3NbS_4 and only minor amounts of defects as visible in Figure S5. The simulations fit excellently to the precession electron diffraction (PED) images.

Electronic properties

Besides a high theoretical voltage and capacity, a high performance cathode material should possess beneficial electrical properties, i.e. a high electronic and ionic conductivity, for beneficial kinetics and low charge transfer resistance within a cell. The state-of-the-art oxide-based cation-ordered rock-salt type materials are ionic materials with a large band gap. Thus, they are mainly electrically insulating. The ionic conductivity is also very low, due to a high potential barrier for lithium ions to move between edge-sharing octahedral positions in these rock-salt type structures (high activation energy) and the low number of intrinsic vacancies (if fully occupied, without substitution with lower valence transition metals). Pure cation-ordered cub- Li_3NbO_4 shows a poor lithium ion conductivity of about $4 \times 10^{-7} \text{ S cm}^{-1}$ at $300 \text{ }^\circ\text{C}$ with an activation energy of 0.78 eV .²⁴ Upon the increase in vacancies by substitution of lithium with nickel and the associated stabilization of a cation-disordered phase, the ionic conductivity increases to $5 \times 10^{-4} \text{ S cm}^{-1}$ at $300 \text{ }^\circ\text{C}$. By the substitution of both lithium and niobium by nickel, manganese or iron, an increase in partial electronic conductivity was assumed by Yabuuchi *et al.*⁵⁰ The appearance of the powder turned from white (Li_3NbO_4) to black ($\text{Li}_{1.3}\text{Nb}_{0.3}\text{Mn}_{0.4}\text{O}_2$) indicating a decrease in band gap, but no explicit data on the electronic conductivity was reported and carbon additives were still needed to improve the performance. Besides, Yabuuchi *et al.* derived that their observed excellent electrode performance is partially due to fast lithium migration in this cation-disordered compound. This reasoning is based on reports of Lee *et al.*⁵¹ that demonstrated a facile lithium diffusion in $\text{Li}_{1.211}\text{Mo}_{0.467}\text{Cr}_{0.3}\text{O}_2$ and traced the origins of this unexpected behaviour back to percolation of a certain type of active diffusion channels enabled by the Li-excess (vs. LiMO_2) inside the cation-disordered structure. For the sulfide analogue bm- Li_3NbS_4 , a high electronic conductivity of $0.2\text{--}1 \times 10^{-2} \text{ S cm}^{-1}$ was reported but no data for ionic conductivity were given.^{17, 19} Besides, very little is known about tantalum containing compounds: the ionic conductivity of the rock-salt structured β - Li_3TaO_4 solid solution series $\text{Li}_{3+5x}\text{Ta}_{1-x}\text{O}_4$ ($0 \leq x \leq 0.059$) was in the range of 10^{-6} to $10^{-3} \text{ S cm}^{-1}$ (at $200 \text{ }^\circ\text{C}$ to $850 \text{ }^\circ\text{C}$) with activation energies ranging from $0.63\text{--}0.68 \text{ eV}$. The ionic conductivity decreased with increasing Li content presumably by limited available empty Li sites.⁴⁸ Regarding sulfides, only the battery performance of TaS_2 as lithium intercalation compound was investigated so far.⁵²

In Figure 5, the impedance spectra and corresponding potentiostatic polarization measurements of phase pure cub- Li_3NbS_4 (a) and tetra- Li_3TaS_4 (b) reveal a predominate electronic conductivity of $1.5 \times 10^{-8} \text{ S cm}^{-1}$ (at $25 \text{ }^\circ\text{C}$) and $7.2 \times 10^{-10} \text{ S cm}^{-1}$ (at $95 \text{ }^\circ\text{C}$), respectively. For tetra- Li_3TaS_4 , only at elevated temperature the data was reliable. For both samples a depressed semicircle is present in the impedance spectra and the phase angle approaches zero at low frequencies demonstrating that the conducting species (electronic charge carriers) is not blocked at the ruthenium metal electrode (ion-blocking electrode). These data can be fitted with an equivalent circuit model of a resistance R in parallel with a constant phase element (CPE), representing the contribution of conduction and capacity in the material. From the CPE, effective capacitances (C_{eff}) of $10^{-12}\text{--}10^{-11} \text{ F}$ can be derived via the Brug-equation⁵³ $C_{\text{eff}} = (Q/(R^{\alpha-1}))^{1/\alpha}$ indicating that the measured response probably rises from the bulk of the materials.⁵⁴ Since under these conditions the electronic

conductivity predominates, a possible ionic conductivity must be below $1.5 \times 10^{-8} \text{ S cm}^{-1}$ (at 25 °C) for cub- Li_3NbS_4 and below $7.2 \times 10^{-10} \text{ S cm}^{-1}$ (at 95 °C) for tetra- Li_3TaS_4 . Concluding, the Li_3MS_4 (M=Nb, Ta) compounds show a higher electronic conductivity than the oxides, but similarly low ionic conductivities. However, the electronic conductivity cub- Li_3NbS_4 is far below the conductivity observed for bm- Li_3NbS_4 .

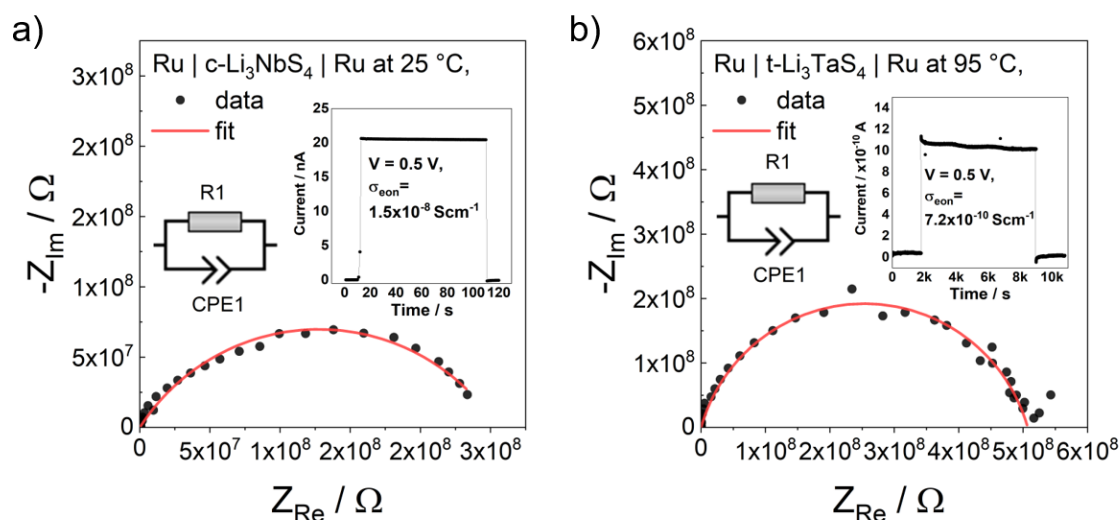


Figure 5 Impedance spectra and potentiostatic polarization measurements at 0.5 V of a) cub- Li_3NbS_4 at 25 °C showing a predominantly electronic conductivity of roughly $1.5 \times 10^{-8} \text{ S cm}^{-1}$ and b) tetra- Li_3TaS_4 at 95 °C showing a predominantly electronic conductivity of $7.2 \times 10^{-10} \text{ S cm}^{-1}$.

Nevertheless, we built an ASSB with cub- Li_3NbS_4 as cathode active material, halogen substituted argyrodite as ionic conductor, vapor grown carbon fibers as electronic conducting additive and InLi alloy as anode as shown in Figure S6b to test the ability of the material as cathode. However, cycling of the material in a potential window of 0.9–2.5 V, even at a very low C-rate (0.033 C, cf. Figure S6a) shows a poor discharge capacity and limited cyclability. Taking also the measured low currents during potential sweeps of the ASSB (Figure S6b) into consideration, the results of the ASSB testing suggest severe kinetic limitations for lithium de/insertion into cub- Li_3NbS_4 , as already foreshadowed by the low electronic and ionic conductivity measured for the pure compound.

Electronic structure and thermodynamics of cation order/disorder

To rationalize the electronic conductivity of these possible cathode materials, as well as to reconcile the ordered polymorphs we observe with the reports of cation disorder despite the large mismatch in charge and bonding tendencies between Nb^{5+} and Li^+ , we turned to computational examination of the electronic structures and the thermodynamics of cation order.

The computed electronic densities of states (DOS) for both polymorphs of both compounds are given in Figure 6. These calculations use the generalized gradient approximation (the tetragonal polymorph has 128 atoms in the primitive cell, making hybrid functionals prohibitively expensive) which is known to poorly reproduce experimental bandgaps, and we focus here on the qualitative trends in bandgaps and orbital contributions. The bandgaps of the Nb compounds are somewhat narrower than those of the Ta compounds, consistent with the darker color observed in experiment (dark red/black for cub- Li_3NbS_4 , red for tetra- Li_3TaS_4). The inclusion of spin-orbit coupling for heavy Ta has a negligible effect (Figure S7). As expected for the isolated $[\text{M}^{\text{V}}_4\text{S}_{16}]^{12-}$ tetramers, the bands (not shown) are quite flat, and the orbital contributions reflect the closed-

shell configuration: $S p$ orbitals dominate the valence bands, while the transition metal t_{2g} orbitals make up the lowest conduction bands.

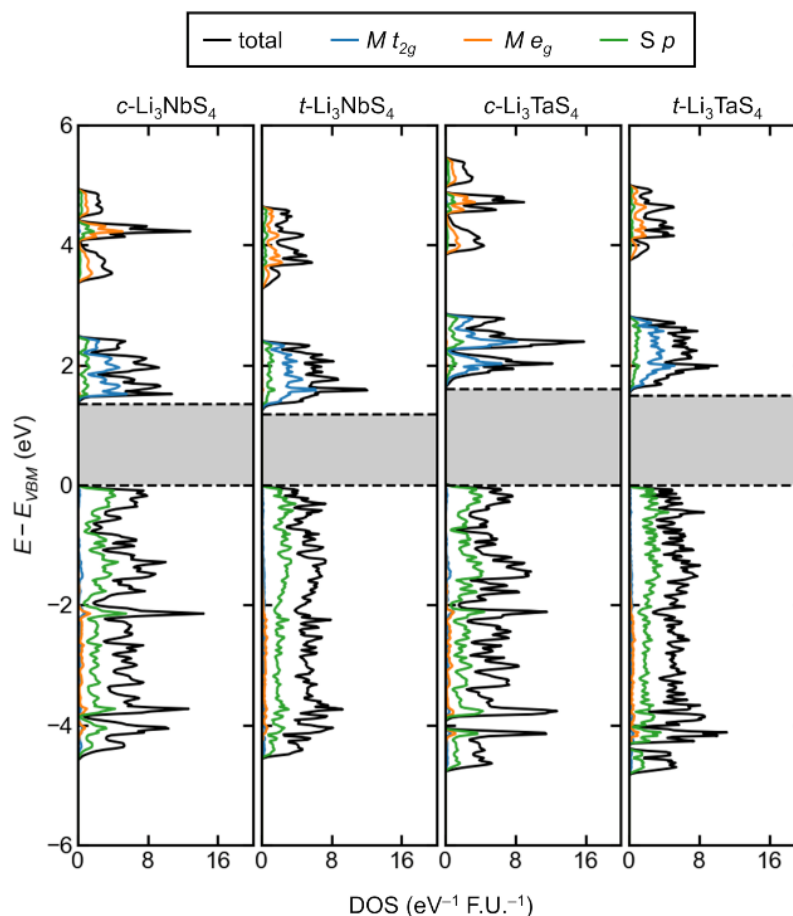


Figure 6 Computed densities of states (DOS, „F.U.“ = formula unit) of both polymorphs of Li_3NbS_4 and Li_3TaS_4 (GGA–PBEsol). As expected, the valence bands are derived primarily from $S p$, and the conduction bands from transition metal t_{2g} orbitals. The narrower bandgap (gray shading) for Li_3NbS_4 is consistent with the experimentally observed colors. Band widths (not shown) are modest, as expected for the isolated $[\text{Nb}_4\text{S}_{16}]^{12-}$ tetramers.

Over the last century, various empirical rules have been devised for predicting and rationalizing the structures of ionic crystals, notably including those by Pauling. While these have demonstrated immense utility, they also come with notable limitations. The ability to explicitly compute energies, charge densities, and associated properties by quantum chemical calculations has overcome some of these limitations, while sometimes introducing new challenges in terms of interpretability. In reviewing cation-ordered rock-salt oxides, Mather and co-workers⁴⁵ noted that $A_3M^V\text{O}_4$ phases appear to be more complex and unpredictable in their structures than several other stoichiometries in this class, possibly related to the fact that Pauling’s 2nd rule (of local electrostatic valence) cannot be satisfied. This is exemplified by the distinct structure types adopted by $\alpha\text{-Li}_3\text{TaO}_4$, $\beta\text{-Li}_3\text{TaO}_4$, and Li_3SbO_4 , despite their similar ionic radii and $M^V\text{-O}$ bond lengths.⁴⁵ With this background in mind, in the following section, we address the observed polymorphism of Li_3NbS_4 and Li_3TaS_4 , our finding of a new structure type, and the possibility of cation disorder in these systems.

Though these sulfides exhibit greater M^V -S covalency than the corresponding oxides, electrostatics should still play an important role in the energetics of cation ordering. We generated random 3:1 Li/ M^V orderings in rock-salt supercells and computed their Madelung energies, and the results are shown as histograms in Figure 7a. While the smallest supercells can be studied exhaustively, the number of possible configurations grows intractably large with supercell size ($\sim 10^7$ configurations for a 2x2x2 supercell with respect to the rock-salt conventional cell, $\sim 10^{14}$ for 4x2x2) and we generate only 1000 random samples at each size. Several features of these distributions are of note. First, the tetra-Li₃NbS₄ polymorph is slightly favored (Madelung energy $\sim 1.4\%$ more negative) compared to the cub-Li₃NbS₄ polymorph. Second, there are several orderings, particularly at small supercell sizes, that are more favorable from a purely electrostatic perspective than the experimentally observed polymorphs. Lastly, the energy distributions shift upward with supercell size. That is, as they approach a state of no long-range order, they became more unfavorable – the (electrostatic) energy of mixing is positive. Electrostatic considerations, then, favor relatively simple, high symmetry arrangements of the two cations.

Next, using density functional theory (DFT) calculations, we optimize the low Madelung energy orderings of Li₃NbS₄ up to a 2x1x1 supercell size (those in the shaded area in Figure 7a) and evaluate their total energies as well as their electronic structures. The energy differences with respect to cub-Li₃NbS₄ are plotted against their band gaps in Figure 7b. Importantly, these possible alternative orderings which appeared favorable from an electrostatic perspective are without exception actually substantially higher in energy (42–207 meV atom⁻¹) than the observed structures. Barely visible on this energy scale, the tetra-Li₃NbS₄ polymorph is just 0.65 meV atom⁻¹ above cub-Li₃NbS₄ in energy (a similar difference of 0.16 meV atom⁻¹ is found for the respective polymorphs of Li₃TaS₄). This is consistent with the finding that the tetragonal polymorphs are the high temperature phases, which result from cooling the melt, while the cubic polymorphs are the low temperature phases, accessed by prolonged solid state reaction well below melting. Recall that there is no group–subgroup relationship between the two polymorphs, and they have different unit cell sizes, so this finding is not in any obvious sense in conflict with the notion that matter adopts higher symmetry arrangements at high temperature, and lower symmetries at low temperature. There is a substantial energy barrier between them (as the phase transition is reconstructive) which combines with the small difference in free energy at the relevant temperatures to explain why the tetragonal phase is obtained on cooling from the melt even at the relatively modest rate of 25–30 °C/h: A much slower rate would be required for significant conversion to the cubic polymorph.

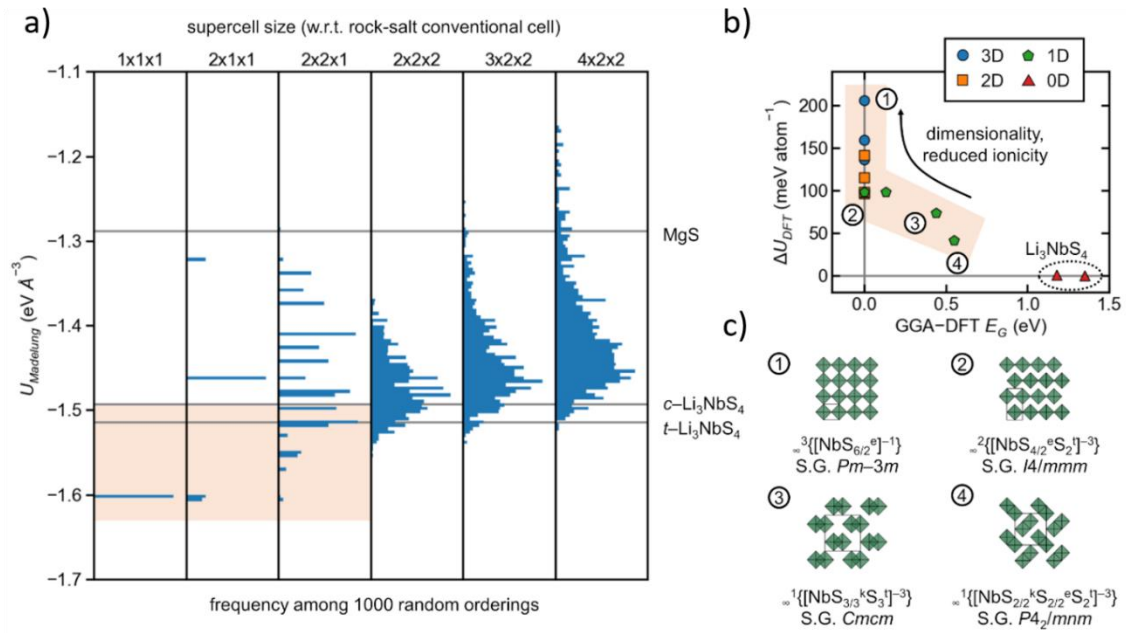


Figure 7 Energetics of cation ordering in Li_3NbS_4 . (a) Madelung energies, U_{Madelung} , of 1000 random $\text{Li}^+/\text{M}^{5+}$ cation orderings (rock-salt, $a = 5 \text{ \AA}$) for various supercell sizes. The Madelung energies of the cub- Li_3NbS_4 (c- Li_3NbS_4) and tetra- Li_3NbS_4 (t- Li_3NbS_4) structures (with idealized atomic positions) are overlaid, as is the energy for $\text{Mg}^{2+}\text{S}^{2-}$ at the same lattice parameter. Orderings without extended Nb–S connectivity are extremely rare (see text). (b) DFT-computed energies relative to the cub- Li_3NbS_4 , ΔU_{DFT} , of the small-supercell orderings from (a) which are competitive in Madelung energy with the observed polymorphs (shaded region), as well as those of the observed polymorphs, as a function of computed bandgap. The dimensionality of the Nb–S anions is indicated. Extended connectivity tends to produce configurations which are metallic or nearly so, reducing the ionic part of the lattice energy (see text). (c) Crystal structures of several low Madelung energy orderings from (b). Nb–S polyanions are depicted as green octahedra, and Li cations are omitted for clarity. The Niggli formulae of the anions and the space group symmetries are indicated. See the text for a discussion of the importance of the second-order Jahn–Teller (SOJT) distortion for $d^0 \text{Nb}^{5+}$.

To understand why alternative cation orderings (in respect to the observed cub- Li_3NbS_4 and tetra- Li_3TaS_4), which seem favorable from an electrostatic perspective, are in fact energetically quite unfavorable, consider the clear bandgap-dependence in Figure 7b. All of these alternative orderings with small supercells are metals or narrow gap semiconductors, and the bandgap is inversely related to the total energy. We hypothesize that a metallic or nearly metallic charge distribution is suppressing the „ionic“ part of the total energy, reducing the electrostatic stabilization that one would expect for these orderings. Recall that the Madelung energy is computed as the energy of a periodic lattice of point charges in vacuum interacting only via Coulomb forces. The charge distribution (and dielectric screening of the Coulomb interaction) in the real crystal is not taken into account, and would be much less energetically favorable in a metal or narrow gap semiconductor approaching metallicity.

We can further relate the bandgaps to the crystal structures by examining the dimensionality of extended M^V –S connectivity (annotated by the markers in Figure 7b). All the 3D and 2D phases are metallic, 1D phases are metallic or have narrow bandgaps, and only the 0D experimentally observed phases have substantial gaps. The structures (and Niggli formulae of the extended anions) of several of these phases are shown in Figure 7c. Examining the band structures (not shown) of several of these orderings, extended connectivity is associated with broadening of the conduction band due to stronger interaction of $M^V t_{2g}$ and S $3p$, to the point that they fully overlap

the valence band in the metallic case. This marks an important departure from the case of the oxides – Li₃TaO₄, Na₃BiO₄, and Li₃SbO₄ all exhibit extended M^V -O connectivity but they maintain substantial bandgaps due to the much deeper $2p$ orbitals of O. We note that at this stoichiometry, OD structures (with isolated M^V -S polyanions) are not possible up to a supercell size of $2 \times 2 \times 1$ as there will be, at minimum, extended connectivity in the direction of the short lattice vector. However, they remain extremely rare at the larger supercell sizes – only five, zero, and zero among 1000 random samples for $2 \times 2 \times 2$, $3 \times 2 \times 2$, and $4 \times 2 \times 2$, respectively. Notably, all five observed random $2 \times 2 \times 2$ orderings with OD connectivity are very low symmetry (space group $P1$) and electrostatically disfavored relative to the observed cubic polymorph.

The remaining important factor which we have not yet discussed is covalency. While it is generally hard to predict *a priori* whether a particular M^V -S polyanion structure will be favored over another without resorting to quantum chemical calculations, one consideration that is more easily spotted is the second-order Jahn–Teller (SOJT) effect. In short, ions like Nb⁵⁺ and Ta⁵⁺ with the d^0 electron configuration are more stable in an acentric environment than in perfect octahedral coordination, as this allows for a stabilizing interaction between the t_{2g} orbitals of the ligand p orbitals which is symmetry-forbidden in the undistorted state. Thus, cation orderings which reduce the site symmetry for M^V to one without inversion are favored. In practice, this criterion is met for all but the most high-symmetry configurations (e.g. those labeled #1 and #2 in Figure 7b,c).

Combining these findings, the cubic polymorph appears to be the smallest, highest symmetry (electrostatically-favorable) cation ordering which allows for fully isolated M^V -S polyanions which maintain a large bandgap. The structure of this polyanion also allows for SOJT distortions of the d^0 metal environment. The tetragonal polymorph maintains the isolated polyanions (though with a slightly different polyanion structure and packing thereof) as well as the SOJT distortions, and presumably allows for a slightly larger vibrational entropy (*vide infra*). Notably, even the abundant planar defects observed in *c*-Li₃NbS₄ maintain the isolated nature of the polyanions. Thus, the ordering observed in these sulfides reflects a competition between electrostatic considerations (generally favoring high overall symmetry), covalency (favoring acentric M^V site symmetry), and a tendency to avoid extended connectivity, the latter of which is *not* observed in the corresponding oxides. Disordered configurations which maintain isolated polyanions appear to be electrostatically unfavorable, while those with extended connectivity are even more so for the same reasons as the metallic or narrow gap ordered configurations above.

Having shown above that other cation orderings (or disordered configurations) appear to be energetically unfavorable compared to the two observed polymorphs, we turn to the question of whether they may be stabilized at finite temperature. The Gibbs free energy, which is minimized for the thermodynamically favored phase in the isothermal–isobaric ensemble, is given by $G = U + pV - TS$. We can then define equation (1)

$$\Delta G = \Delta U + p\Delta V - T(\Delta S_{elec} + \Delta S_{mix} + \Delta S_{vib}) \quad (1)$$

as the difference in Gibbs free energy (ΔG) with respect to the low temperature cubic polymorph, and separate the entropic term into electronic (ΔS_{elec}), cation mixing (ΔS_{mix}), and vibrational (ΔS_{vib}) contributions. The $p\Delta V$ term is negligible for solid–solid transitions at ambient pressure (of order ~ 10 – 4 meV atom⁻¹ even for a large ΔV of 10 %).

From the DFT calculations on low Madelung energy orderings above, we estimate a lower bound on the energy term of roughly 50 meV atom⁻¹. Note that the experimentally observed tetragonal

polymorph is an exception, at $< 1 \text{ meV atom}^{-1}$ above the observed cubic polymorph, explaining why a typically small difference in vibrational entropy can stabilize this phase before melting. We cannot guarantee that other rare low energy orderings do not exist, though they have not been observed experimentally. With respect to the possibility of cation disorder, this is a rather conservative lower bound on the energy of mixing, as lower symmetry, larger supercell orderings (approximating disorder) appear to be much higher in energy even than 50 meV atom^{-1} .

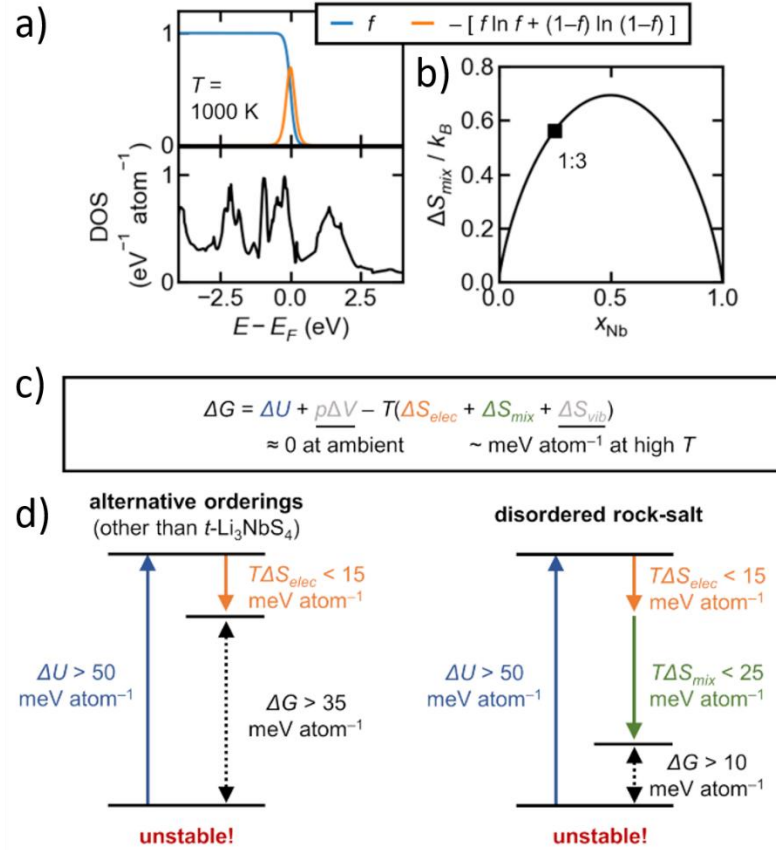


Figure 8 Thermodynamics of cation order/disorder in Li_3NbS_4 . (a) Quantities used in computing an upper bound for the contribution of electronic entropy at 1000 K. The density of states (DOS) for the metallic ordering from Figure 7 with the highest DOS at the Fermi energy (E_F) is shown, as well as the Fermi–Dirac distribution (f) and the occupational factor in the configurational entropy integral (see text). (b) Ideal solution mixing entropy, ΔS_{mix} , representing an upper bound for the real mixing entropy, with the 1:3 cation ratio indicated. k_B is the Boltzmann constant. (c) Energetic, volumetric, and entropic contributions to the Gibbs free energy with respect to the observed low temperature cubic polymorph (ΔG , see text). (d) Schematic diagrams of (isothermal–isobaric) thermodynamics based on an estimated lower bound for energy differences from Figure 7 and the upper bounds for entropy differences at $T = 1000 \text{ K}$ from (a) and (b). Both alternative orderings and disordered configurations are disfavored (see text for discussion of the high temperature tetragonal polymorph).

The electronic entropy S_{elec} (configurational entropy associated with the different ways to occupy the states near E_F at finite temperature) is given by equation (2)

$$S_{\text{elec}} = -k_B \int n(E)[f \ln f + (1-f) \ln(1-f)]dE \quad (2)$$

where $f(E, T)$ is the Fermi–Dirac distribution. $f(E, T)$ and the occupational factor in the electronic entropy integral are shown in Figure 8a at 1000 K (approximating the temperature of the reactions described here), alongside the DOS for the most metallic ordering from Figure 7b. The densities of states at the Fermi level, $N(E_F)$, for the various electrostatically favored orderings in Figure 7b (0–0.65 eV⁻¹ atom⁻¹) give rise to electronic entropy contributions at 1000 K of TS_{elec} =0–14 meV atom⁻¹. Therefore, we define $T\Delta S_{elec}$ = 15 meV atom⁻¹ as an upper bound for this term. Again, this is a conservative choice, as the metallic ordering which gives this large entropy contribution is actually much higher in energy than the configurations with energies closer to the lower bound for ΔU selected above.

Turning to the cation mixing term, the upper bound for ΔS_{mix} is quite simply the ideal entropy of mixing in a two-component mixture at 1:3 stoichiometry (Figure 8b), which works out to ~25 meV atom⁻¹ at 1000 K (there is a factor of ½ here because there is no mixing on the sulfur sublattice). While not particularly small, this mixing entropy is much lower than that of multinary mixtures with more components and equimolar compositions, as for entropy-stabilized rock salt oxides with five distinct metals.⁵⁵

The last term, the vibrational entropy contribution, is costly to compute explicitly, but is typically of the order of ~ meV atom⁻¹ (it can be somewhat higher for certain structure types like perovskites with large differences in the vibrational DOS for different polymorphs, or substantially higher in plastic crystals with rotating molecular ions, neither of which are applicable here). Note that this is corroborated by the small energy differences (< 1 meV atom⁻¹) computed between the experimentally observed low temperature and high temperature Li₃(Nb,Ta)S₄ polymorphs, where the other entropy difference terms are zero. This term is thus small relative to the others discussed above.

Taken together, these estimates of the various energetic and entropic contributions to the Gibbs free energy (shown schematically in Figure 8d) suggest that cation-disordered Li₃NbS₄ and Li₃TaS₄ are likely quite thermodynamically unfavorable, and other cation orderings are only accessible if, like the tetra-Li₃TaS₄ structure, they exhibit very competitive energies. As noted in the discussion above, such low energy orderings appear to be extremely rare, and are a manifestation of the competition between electrostatics (favoring high symmetry Li⁺/*M*⁵⁺ motifs), SOJT distortions of the *M*⁵⁺ environment (favoring somewhat low site symmetry for the *d*⁰ cation), and the need for electronically insulating configurations with isolated *M*^V–S polyanions so as not to suppress the electrostatic contribution to the total energy.

Discussion

Now the question arises, whether the [Nb₄S₁₆]-clusters are still preserved in bm-Li₃NbS₄ or if a real cation disorder is present, which is a interesting future avenue of research. Overall, the preservation of this structural motif seems plausible to us, since similar to the quenching from high temperatures as applied here, high energy ball milling should lead to a large number of structural defects and small domains sizes, but not necessarily to a loss of short-range order.

What do our findings on microstructure and electronic properties imply about cation-disordered rock-salt-type bm-Li₃NbS₄? First, as deduced for cub-Li₃NbS₄, a material may show an apparent cation-disorder, but in reality only contains large amounts of planar defects. Thus, as high energy ball milling leads to a large number of structural defects and small domain sizes, similar to quenching from high temperatures (as applied here), a local cation-order in bm-Li₃NbS₄ is plausible

and also corroborated by our computations of the thermodynamics of cation ordering, which highly favours low connectivity inside the structure. The short-range order (SRO) in ball-milled materials should be investigated in the future by local methods such as HRTEM or pair-distribution function analysis. In general, the importance of SRO in seemingly cation-disordered rock-salt-type structures should not be underestimated as already shown for long-range disordered rock-salt-type (DRX) lithium metal oxide cathode materials by Ji *et al.*⁵⁶. They explain the significantly different Li transport by subtle structural differences between DRX $\text{Li}_{1.2}\text{Mn}_{0.4}\text{Ti}_{0.4}\text{O}_2$ (LMTO) and $\text{Li}_{1.2}\text{Mn}_{0.4}\text{Zr}_{0.4}\text{O}_2$ (LMZO). By electron diffraction they observe diffuse scattering patterns that are completely different for the two materials, indicating significant difference in SRO. In LMTO they find characteristics of octahedral cation clusters similar to $[\text{Li}_3\text{Fe}_3]$ in cubic- LiFeO_2 ⁵⁷, whereas the SRO in LMZO is possibly associated with tetrahedral clusters⁵⁸. The authors then deduce the clustering being influenced by the charge and size of the present transition metal cations with respect to the lithium ions.

Second, by comparing the obtained conductivities of cub- Li_3NbS_4 and tetra- Li_3TaS_4 with literature values in Table 2 it becomes evident that the ionic and electronic conductivity in cation-ordered rock-salt materials at room temperature (RT) are much lower than in bm- Li_3NbS_4 . To elucidate if the high electronic conductivity of bm- Li_3NbS_4 is caused by the cation-disorder or by amorphous side phases (amorphous NbS_x < 20 nm were reported)²⁰ the material needs to be explored in more depth. Notably, full cation-disorder opens the possibility of long range -(Nb,Ta)-S- percolation networks, whereas the ordered materials (and the local structure we observe) has only isolated tetramers and very ionic interaction with the surrounding lithium ions. However, a cation-disorder is normally only beneficial in Li-excess materials⁵¹ and only increases the ionic rather than the electronic conductivity. Therefore, our findings make the presence of amorphous species, which are possibly very similar to the precursor NbS_2 ⁵⁹ with properties ranging from semiconducting to metallic, or NbS_3 ⁶⁰ that possess Nb-Nb bonds and a high electronic conductivity, highly plausible.

Table 2 Summary and comparison of electronic properties of cub- Li_3NbS_4 and tetra- Li_3TaS_4 . *values are upper limits estimated from the electronic conductivities.

Material	$\sigma_{\text{eon}} / \text{S cm}^{-1}$	$\sigma_{\text{ion}} / \text{S cm}^{-1}$	Temperature / °C	Literature
bm- Li_2TiS_3	8×10^{-6}	n.a.	RT	10
bm- Li_3NbS_4	$0.2\text{--}1 \times 10^{-2}$	n.a.	RT	10, 17, 19
$\text{Li}_{2.8}\text{Ni}_{0.1}\text{NbO}_4$	n.a.	5×10^{-4}	300	24
cub- Li_3NbS_4	1.5×10^{-8}	$< 1.5 \times 10^{-8*}$	25	<i>This work</i>
Tetra- Li_3TaS_4	7.2×10^{-10}	$< 7.2 \times 10^{-10*}$	95	<i>This work</i>

Conclusion

Concluding, taking a closer look at the seemingly ordinary ternary sulfides cub- Li_3NbS_4 and tetra- Li_3TaS_4 lead to the discovery of 1) unexpected cation-order in rock-salt-type tetra- Li_3MS_4 (M = Nb, Ta) and 2) of an intriguing microstructure found by HRTEM that explains the unusual profiles and intensities of sub- and superstructure reflections in the PXRD, contradicting simple cation-disorder. The poor electronic properties match naïve assumptions on these types of materials and are corroborated by our computational description, but disagree with findings reported earlier on bm-

Li₃NbS₄. However, they set the basis to re-investigate the structure and properties of this promising anion-redox active cathode material. Similar to Li₃NbO₄^{24, 50} a substitution with other transition metals such as Ni, Mn and Fe could be explored to further improve the ionic conduction properties. On the one hand, this might increase the number of ionic charge carriers and on the other hand, it might increase the mobility of charge carriers as demonstrated for oxide based lithium-excess DRX materials. Here, ball-milling seems to be the synthesis method of choice introducing electronically conducting species. Another approach for improvement could be a substitution of sulfide with selenide anions, which in the solid solution series Li₂FeS_{2-y}Se_y lead to a controllable shift in the high voltage oxidation plateau.¹⁵ Besides, these sulfide based cathode materials could be applied in a sulfide electrolyte based ASSB as a blend with common oxide cathode materials. Here, the sulfides could function as a protection layer for the solid electrolyte enabling better cycling stability. All in all, our findings open up a playground for material optimization in metal sulfide electrode materials combined with a thorough understanding of their complex structures across multiple length scales.

Acknowledgement

We thank Jarka Obel and Marie-Luise Schreiber for measuring ICP, and Dr. Peter Mayer for measuring SXRD. Besides, we thank Lorenz Kienle and Lucien Eisenburger for fruitful discussions about HRTEM images. Financial support was granted by the German Federal Ministry of Research and Education (BMBF), project O3XP0177B (FestBatt) and the Center for NanoScience (CeNS). D.H.F. gratefully acknowledges financial support from the Alexander von Humboldt Foundation.

Author Contributions

AKH conceived and designed this study; AKH; RH, LB conducted the synthesis; RH and SH were responsible for measuring SCXRD and SH performed structure determination; VD measured HRTEM; JB measured TGA; DHF performed the calculation and interpretation DFT and Madelung energies; AKH analyzed and measured EIS and polarization data; PM built and measured SSBs; AKH and DHF wrote sections of the manuscript; BVL commented on the manuscript.

References

- [1] Y. Kato, S. Hori, T. Saito, K. Suzuki, M. Hirayama, A. Mitsui, M. Yonemura, H. Iba and R. Kanno, *Nat. Energy*, 2016, **1**, 16030.
- [2] J. Janek and W. G. Zeier, *Nat. Energy*, 2016, **1**, 16141.
- [3] Z. Zhang, Y. Shao, B. Lotsch, Y.-S. Hu, H. Li, J. Janek, L. F. Nazar, C.-W. Nan, J. Maier, M. Armand and L. Chen, *Energy Environ. Sci.*, 2018, **11**, 1945-1976.
- [4] B. V. Lotsch and J. Maier, *J. Electroceramics*, 2017, **38**, 128-141.
- [5] M. J. Wang, E. Carmona, A. Gupta, P. Albertus and J. Sakamoto, *Nat. Commun.*, 2020, **11**, 5201.
- [6] Y.-G. Lee, S. Fujiki, C. Jung, N. Suzuki, N. Yashiro, R. Omoda, D.-S. Ko, T. Shiratsuchi, T. Sugimoto, S. Ryu, J. H. Ku, T. Watanabe, Y. Park, Y. Aihara, D. Im and I. T. Han, *Nat. Energy*, 2020, **5**, 299-308.
- [7] D. Andre, S.-J. Kim, P. Lamp, S. F. Lux, F. Maglia, O. Paschos and B. Stiaszny, *J. Mater. Chem. A*, 2015, **3**, 6709-6732.
- [8] R. J. Clément, Z. Lun and G. Ceder, *Energy Environ. Sci.*, 2020, **13**, 345-373.

- [9] A. Sakuda, K. Ohara, T. Kawaguchi, K. Fukuda, K. Nakanishi, H. Arai, Y. Uchimoto, T. Ohta, E. Matsubara, Z. Ogumi, K. Kuratani, H. Kobayashi, M. Shikano, T. Takeuchi and H. Sakaebe, *Sci. Rep.*, 2018, **8**, 15086.
- [10] A. Sakuda, T. Takeuchi, K. Okamura, H. Kobayashi, H. Sakaebe, K. Tatsumi and Z. Ogumi, *Sci. Rep.*, 2014, **4**, 4883.
- [11] F. Flamarý-Mespoulie, A. Boulineau, H. Martinez, M. R. Suichomel, C. Delmas, B. Pecquenard and F. Le Cras, *Energy Storage Mater.*, 2020, **26**, 213-222.
- [12] C. J. Hansen, J. J. Zak, A. J. Martinolich, J. S. Ko, N. H. Bashian, F. Kaboudvand, A. Van der Ven, B. C. Melot, J. Nelson Weker and K. A. See, *J. Am. Chem. Soc.*, 2020, **142**, 6737-6749.
- [13] Y. Kawasaki, H. Tsukasaki, T. Ayama, S. Mori, M. Deguchi, M. Tatsumisago, A. Sakuda and A. Hayashi, *ACS Appl. Energy Mater.*, 2021, **4**, 20-24.
- [14] F. Marchini, S. Saha, D. Alves Dalla Corte and J. M. Tarascon, *ACS Appl. Mater. Interfaces*, 2020, **12**, 15145-15154.
- [15] A. J. Martinolich, J. J. Zak, D. N. Agyeman-Budu, S. S. Kim, N. H. Bashian, A. Irshad, S. R. Narayan, B. C. Melot, J. Nelson Weker and K. A. See, *Chem. Mater.*, 2021, **33**, 378-391.
- [16] S. Saha, G. Assat, M. T. Sougrati, D. Foix, H. Li, J. Vergnet, S. Turi, Y. Ha, W. Yang, J. Cabana, G. Rousse, A. M. Abakumov and J.-M. Tarascon, *Nat. Energy*, 2019, **4**, 977-987.
- [17] A. Sakuda, K. Kuratani, T. Takeuchi, H. Kiuchi, T. Kawaguchi, M. Shikano, H. Sakaebe and H. Kobayashi, *Electrochem.*, 2017, **85**, 580-584.
- [18] A. Sakuda, T. Takeuchi, H. Kobayashi, H. Sakaebe, K. Tatsumi and Z. Ogumi, *Electrochem.*, 2014, **82**, 880-883.
- [19] A. Sakuda, T. Takeuchi, M. Shikano, H. Sakaebe and H. Kobayashi, *Front. Energy*, 2016, **4**.
- [20] A. Sakuda, N. Taguchi, T. Takeuchi, H. Kobayashi, H. Sakaebe, K. Tatsumi and Z. Ogumi, *ECS Electrochem. Lett.*, 2014, **3**, A79-A81.
- [21] R. Koerver, F. Walther, I. Aygün, J. Sann, C. Dietrich, W. G. Zeier and J. Janek, *J. Mater. Chem. A*, 2017, **5**, 22750-22760.
- [22] W. D. Richards, L. J. Miara, Y. Wang, J. C. Kim and G. Ceder, *Chem. Mater.*, 2016, **28**, 266-273.
- [23] W. Zhang, T. Leichtweiß, S. P. Culver, R. Koerver, D. Das, D. A. Weber, W. G. Zeier and J. Janek, *ACS Appl. Mater. Interfaces*, 2017, **9**, 35888-35896.
- [24] V. L. McLaren, C. A. Kirk, M. Poisot, M. Castellanos and A. R. West, *Dalton Trans.*, 2004, DOI: 10.1039/B316396M, 3042-3047.
- [25] K. Persson, *Journal*, 2016, DOI: 10.17188/1298621.
- [26] A. Jain, S. P. Ong, G. Hautier, W. Chen, W. D. Richards, S. Dacek, S. Cholia, D. Gunter, D. Skinner, G. Ceder and K. a. Persson, *APL Mater.*, 2013, **1**, 011002.
- [27] S. Harm, A.-K. Hatz, I. Moudrakovski, R. Eger, A. Kuhn, C. Hoch and B. V. Lotsch, *Chem. Mater.*, 2019, **31**, 1280-1288.
- [28] Y. Liao, K.-S. Park, P. Singh, W. Li and J. B. Goodenough, *J. Power Sources*, 2014, **245**, 27-32.
- [29] K. Ukei, H. Suzuki, T. Shishido and T. Fukuda, *Acta Crystallogr. Sect. C*, 1994, **50**, 655-656.
- [30] G. Blasse, *Z. Anorg. Allg. Chemie*, 1963, **326**, 44-46.
- [31] R. Vincent and P. A. Midgley, *Ultramicroscopy*, 1994, **53**, 271-282.
- [32] P. A. Stadelmann, *Ultramicroscopy*, 1987, **21**, 131-145.
- [33] G. Sheldrick, *Acta Crystallogr. A* 2008, **64**, 112-122.
- [34] A. A. Coelho, *J. Appl. Crystallogr.*, 2018, **51**, 210-218.
- [35] P. E. Blöchl, *Phys. Rev. B*, 1994, **50**, 17953-17979.
- [36] G. Kresse and J. Hafner, *Phys. Rev. B*, 1993, **47**, 558-561.
- [37] G. Kresse and J. Hafner, *Phys. Rev. B*, 1994, **49**, 14251-14269.
- [38] G. Kresse and J. Furthmüller, *Comput. Mater. Sci*, 1996, **6**, 15-50.
- [39] J. P. Perdew, A. Ruzsinszky, G. I. Csonka, O. A. Vydrov, G. E. Scuseria, L. A. Constantin, X. Zhou and K. Burke, *Phys. Rev. Lett.*, 2008, **100**, 136406.
- [40] S. P. Ong, W. D. Richards, A. Jain, G. Hautier, M. Kocher, S. Cholia, D. Gunter, V. L. Chevrier, K. A. Persson and G. Ceder, *Comput. Mater. Sci*, 2013, **68**, 314-319.

- [41] A. Y. Toukmaji and J. A. Board, *Compt. Phys. Commun.*, 1996, **95**, 73-92.
- [42] P. M. Larsen, M. Pandey, M. Strange and K. W. Jacobsen, *Phys. Rev. Mater.*, 2019, **3**, 034003.
- [43] A. Togo and I. Tanaka, *arXiv*, 2018, 1808.01590.
- [44] K. Momma and F. Izumi, *J. Appl. Crystallogr.*, 2011, **44**, 1272-1276.
- [45] G. C. Mather, C. Dussarrat, J. Etourneau and A. R. West, *J. Mater. Chem.*, 2000, **10**, 2219-2230.
- [46] G. Blasse, *Z. Anorg. Allg. Chemie*, 1964, **331**, 44-50.
- [47] M. Zocchi, M. Gatti, A. Santoro and R. S. Roth, *J. Solid State Chem.*, 1983, **48**, 420-430.
- [48] S. Shari, K. B. Tan, C. C. Khaw, Z. Zainal, O. J. Lee and S. K. Chen, *Mater. Sci-Poland*, 2020, **38**, 465-474.
- [49] M. A. Jones, P. J. Reeves, I. D. Seymour, M. J. Cliffe, S. E. Dutton and C. P. Grey, *Chem. Commun.*, 2019, **55**, 9027-9030.
- [50] N. Yabuuchi, M. Takeuchi, M. Nakayama, H. Shiiba, M. Ogawa, K. Nakayama, T. Ohta, D. Endo, T. Ozaki, T. Inamasu, K. Sato and S. Komaba, *Proc. Natl. Acad. Sci USA*, 2015, **112**, 7650-7655.
- [51] J. Lee, A. Urban, X. Li, D. Su, G. Hautier and G. Ceder, *Science*, 2014, **343**, 519-522.
- [52] M. S. Whittingham, *Prog. Solid State Chem.*, 1978, **12**, 41-99.
- [53] G. J. Brug, A. L. G. van den Eeden, M. Sluyters-Rehbach and J. H. Sluyters, *J. Electroanal. Chem. Interf. Electrochem.*, 1984, **176**, 275-295.
- [54] J. T. S. Irvine, D. C. Sinclair and A. R. West, *Adv. Mater.*, 1990, **2**, 132-138.
- [55] C. M. Rost, E. Sachet, T. Borman, A. Moballegh, E. C. Dickey, D. Hou, J. L. Jones, S. Curtarolo and J. P. Maria, *Nat. Commun.*, 2015, **6**, 8485.
- [56] H. Ji, A. Urban, D. A. Kitchaev, D.-H. Kwon, N. Artrith, C. Ophus, W. Huang, Z. Cai, T. Shi, J. C. Kim, H. Kim and G. Ceder, *Nat. Commun.*, 2019, **10**, 592.
- [57] M. Mitome, S. Kohiki, Y. Murakawa, K. Hori, K. Kurashima and Y. Bando, *Acta Crystallogr. B*, 2004, **60**, 698-704.
- [58] J. Hauck, *Acta Crystallogr., Sect. A*, 1980, **36**, 228-237.
- [59] Y. H. Huang, C. C. Peng, R. S. Chen, Y. S. Huang and C. H. Ho, *Appl. Phys. Lett*, 2014, **105**, 093106.
- [60] M. A. Bloodgood, P. Wei, E. Aytan, K. N. Bozhilov, A. A. Balandin and T. T. Salguero, *APL Materials*, 2018, **6**.
- [61] J. E. Gareh, M. G. Barker and M. J. Begley, *Mater. Res. Bull.*, 1995, **30**, 57-63.

4.1.1 Supporting information for Taking a closer look: (Micro)Structure and electronic properties of rock-salt type Li₃NbS₄ and Li₃TaS₄Table S1 Crystallographic data and structural solution and refinement data of cub-Li₃NbS₄. All standard deviations are given in units of the last digit in parentheses.

cub-Li ₃ NbS ₄	
Crystal class	kubisch
Space group	$\bar{1}43m$, (Nr. 217)
Lattice parameter	$a = 10.2865(5)$ Å
V [Å ³]	1088.44(9)
Z	1
Density [gcm ⁻³]	2.953
Diffractometer	Bruker D8 Venture (Rotary anode), MoK α -radiation, Göbel mirror
Temperature [K]	295
Absorption coefficient [mm ⁻¹]	3.576
ϑ -range [°]	4.85–39.99
Index-range	$-18 \leq h \leq$ $18, -18 \leq k$ $\leq 18,$ $-18 \leq l \leq 18$
reflections measured	15394
independent reflections	663
independent reflections with ($I \geq 2\sigma(I)$)	657
R_{int}	0.0399
R_{σ}	0.0133
$F(000)$	912

corrections	Lorentz-, polarisation-, absorption effects
Absorption correction	numerical
Structure solution	Direct methods, SHELXS97
Structure refinement	Least-Squares on F ² , SHELXL97
Number of free parameter	21
Goof	1.333
R-values (for reflections with $I \geq 2\sigma(I)$)	R1 = 0.0202, wR2 = 0.0513
R-values (all data)	R1 = 0.0206, wR2 = 0.0513
Residual electron density [e ⁻ /Å ⁻³]	1.514/-1.234
Extinction coefficient	0.0011(5)

Table S2 Interatomic distances of the compound cub-Li₃NbS₄. All standard deviations are given in units of the last digit in parentheses.

Atom1	Atom2	Distance [Å]	Atom1	Atom2	Distance [Å]
Li	S1	2.519(4) ⁱ	Li		2.631(4) ^{vii}
	S1	2.519(4) ⁱⁱ	Li		2.699(5) ^{viii}
	S1	2.631(4) ⁱⁱⁱ	S2	Nb	2.6411(5) ⁱⁱⁱ
	S1	2.631(4) ^{iv}		Nb	2.6411(5) ^{viii}
	S2	2.697(5)		Nb	2.6411(5) ^{iv}
	S1	2.699(5) ^v		Li	2.697(5) ⁱ
	Nb	3.279(5)		Li	2.697(5) ⁱⁱ
	Li	3.487(8) ⁱ	Nb	S1	2.3201(5) ⁱ
	Li	3.487(8) ⁱⁱ		S1	2.3201(5) ⁱⁱ
S1	Nb	2.3201(5)		S2	2.6411(5) ^{vii}
	Li	2.519(4) ⁱ		S2	2.6411(5) ^v

Li	2.519(4) ⁱⁱ	S2	2.6411(5) ^{vi}
Li	2.631(4) ^{vi}	Li	3.279(5) ⁱ
		Li	3.279(5) ⁱⁱ

i	x, z, y	ii	z, x, y	iii	-y+
$\frac{1}{2}, x-\frac{1}{2}, -z+\frac{1}{2}$	$\frac{1}{2}, y-\frac{1}{2}, -x+\frac{1}{2}$	iv	$y-\frac{1}{2}, -x+\frac{1}{2}, -z+\frac{1}{2}$	v	$-x+\frac{1}{2}, -y+\frac{1}{2}, z+\frac{1}{2}$
$\frac{1}{2}, -x+\frac{1}{2}, -y+\frac{1}{2}$	$\frac{1}{2}, z+\frac{1}{2}, y+\frac{1}{2}$	vi	$y+\frac{1}{2}, -x+\frac{1}{2}, -z+\frac{1}{2}$	vii	$-y+\frac{1}{2}, x+\frac{1}{2}, -z+\frac{1}{2}$
$\frac{1}{2}, x+\frac{1}{2}, -y+\frac{1}{2}$	$\frac{1}{2}, z-\frac{1}{2}$	viii	$-x+\frac{1}{2}, -y+\frac{1}{2}, z-\frac{1}{2}$		

Table S3 Coefficients of the anisotropic deflection parameters [\AA^2] for cub-Li₃NbS₄. U_{ij} is defined as: $U_{ij} = \exp(-2\pi^2[U_{11}(ha^*)^2 + \dots + 2U_{21}hka^*b^*])$. All standard deviations are given in units of the last digit in parentheses.

Atom	U_{11}	U_{22}	U_{33}	U_{23}	U_{13}	U_{12}
Li	0.0186(11)	= U_{11}	0.0205(19)	0.0034(11)	= U_{23}	-0.002(2)
S1	0.01336(13)	= U_{11}	0.0103(2)	0.00087(9)	= U_{23}	-0.00018(16)
S2	0.00879(13)	= U_{11}	= U_{11}	0.00018(12)	= U_{23}	= U_{23}
Nb	0.01101(8)	= U_{11}	= U_{11}	-0.00142(6)	= U_{23}	= U_{23}

Table S4 Bond angle of cub-Li₃NbS₄. All standard deviations are given in units of the last digit in parentheses

Atoms	Angle [°]	Atoms	Angle [°]	Atoms	Angle [°]
S1-L ⁱ -S1 ⁱⁱ	89.36(17)	Nb-Li-Li ⁱⁱ	57.87(7)	S1-Nb ⁱⁱ -S1	99.52(2)
S1-L ⁱ -S1 ⁱⁱⁱ	93.546(18)	Li-L ⁱ -L ⁱⁱ	60.0	S1-Nb ⁱ -S2 ^{vii}	164.61(2)
S1-L ⁱⁱⁱ -S1 ⁱⁱⁱ	176.90(18)	Nb-S1-L ⁱ	85.20(8)	S1-Nb ⁱⁱ -S2 ^{vii}	90.36(2)
S1-L ⁱ -S1 ^{iv}	176.90(18)	Nb-S1-L ⁱⁱ	85.20(8)	S1-Nb-S2 ^{vii}	90.36(2)
S1-L ⁱⁱ -S1 ^{iv}	93.546(18)	Li-S1 ⁱ -L ⁱⁱ	87.6(2)	S1-Nb ⁱ -S2 ^v	90.36(2)
S1-L ⁱⁱⁱ -S1 ^{iv}	83.53(15)	Nb-S1-L ^{vi}	97.05(11)	S1-Nb ⁱⁱ -S2 ^v	90.36(2)
S1-L ⁱ -S2	95.77(13)	Li-S1 ⁱ -L ^{vi}	174.88(5)	S1-Nb-S2 ^v	164.61(2)
S1-L ⁱⁱ -S2	95.77(13)	Li-S1 ⁱⁱ -L ^{vi}	87.99(14)	S2-Nb ^{vii} -S2 ^v	77.72(3)
S1-L ⁱⁱⁱ -S2	82.87(14)	Nb-S1-L ^{vii}	97.05(11)	S1-Nb ⁱ -S2 ^{vi}	90.36(2)
S1-L ^{iv} -S2	82.87(14)	Li-S1 ⁱ -L ^{vii}	87.99(14)	S1-Nb ⁱⁱ -S2 ^{vi}	164.61(2)

S1-Li ⁱ -S1 ^v	91.93(15)	Li-S1 ⁱⁱ -Li ^{vii}	174.88(5)	S1-Nb-S2 ^{vi}	90.36(2)
S1-Li ⁱⁱ -S1 ^v	91.93(15)	Li-S1 ^{vi} -Li ^{vii}	96.28(15)	S2-Nb ^{vii} -S2 ^{vi}	77.72(3)
S1-Li ⁱⁱⁱ -S1 ^v	89.06(12)	Nb-S1-Li ^{viii}	168.51(12)	S2-Nb ^v -S2 ^{vi}	77.72(3)
S1-Li ^{iv} -S1 ^v	89.06(12)	Li-S1 ⁱ -Li ^{viii}	86.519(15)	S1-Nb ⁱ -Li ⁱ	99.70(9)
S2-Li-S1 ^v	169.2(2)	Li-S1 ⁱⁱ -Li ^{viii}	86.519(16)	S1-Nb ⁱⁱ -Li ⁱ	49.957(14)
S1-Li ⁱ -Nb	44.84(8)	Li-S1 ^{vi} -Li ^{viii}	90.60(11)	S1-Nb-Li ⁱ	49.957(14)
S1-Li ⁱⁱ -Nb	44.84(8)	Li-S1 ^{vii} -Li ^{viii}	90.60(11)	S2-Nb ^{vii} -Li ⁱ	95.69(9)
S1-Li ⁱⁱⁱ -Nb	137.91(7)	Nb-S2 ⁱⁱⁱ -Nb ^{viii}	101.06(3)	S2-Nb ^v -Li ⁱ	140.04(2)
S1-Li ^{iv} -Nb	137.91(7)	Nb-S2 ⁱⁱⁱ -Nb ^{iv}	101.06(3)	S2-Nb ^{vi} -Li ⁱ	140.04(2)
S2-Li-Nb	93.83(13)	Nb-S2 ^{viii} -Nb ^{iv}	101.06(3)	S1-Nb ⁱ -Li	49.957(14)
S1-Li ^v -Nb	97.02(16)	Nb-S2 ⁱⁱⁱ -Li	88.22(7)	S1-Nb ⁱⁱ -Li	49.957(14)
S1-Li ⁱ -Li ⁱ	90.63(9)	Nb-S2 ^{viii} -Li	165.25(12)	S1-Nb-Li	99.70(9)
S1-Li ⁱⁱ -Li ⁱ	46.20(11)	Nb-S2 ^{iv} -Li	88.22(7)	S2-Nb ^{vii} -Li	140.04(2)
S1-Li ⁱⁱⁱ -Li ⁱ	132.58(11)	Nb-S2 ⁱⁱⁱ -Li ⁱ	165.25(12)	S2-Nb ^v -Li	95.69(9)
S1-Li ^{iv} -Li ⁱ	90.60(8)	Nb-S2 ^{viii} -Li	88.22(7)	S2-Nb ^{vi} -Li	140.04(2)
S2-Li-Li ⁱ	49.72(8)	Nb-S2 ^{iv} -Li ⁱ	88.22(7)	Li-Nb ⁱ -Li	64.25(14)
S1-Li ^v -Li ⁱ	138.02(7)	Li-S2-Li ⁱ	80.56(17)	S1-Nb ⁱ -Li ⁱⁱ	49.957(14)
Nb-Li-Li ⁱ	57.87(7)	Nb-S2 ⁱⁱⁱ -Li ⁱⁱ	88.22(7)	S1-Nb ⁱⁱ -Li ⁱⁱ	99.70(9)
S1-Li ⁱ -Li ⁱⁱ	46.20(11)	Nb-S2 ^{viii} -Li ⁱⁱ	88.22(7)	S1-Nb-Li ⁱⁱ	49.957(14)
S1-Li ⁱⁱ -Li ⁱⁱ	90.63(9)	Nb-S2 ^{iv} -Li ⁱⁱ	165.25(12)	S2-Nb ^{vii} -Li ⁱⁱ	140.04(2)
S1-Li ⁱⁱⁱ -Li ⁱⁱ	90.60(8)	Li-S2-Li ⁱⁱ	80.56(17)	S2-Nb ^v -Li ⁱⁱ	140.04(2)
S1-Li ^{iv} -Li ⁱⁱ	132.58(11)	Li-S2 ⁱ -Li ⁱⁱ	80.56(17)	S2-Nb ^{vi} -Li ⁱⁱ	95.69(9)
S2-Li-Li ⁱⁱ	49.72(8)	S1-Nb ⁱ -S1 ⁱⁱ	99.52(2)	Li-Nb ⁱ -Li ⁱⁱ	64.25(14)
S1-Li ^v -Li ⁱⁱ	138.02(7)	S1-Nb ⁱ -S1	99.52(2)	Li-Nb-Li ⁱⁱ	64.25(14)

i x, z, y ii z, x, y

iii $-\gamma + \frac{1}{2}, x - \frac{1}{2}, -z + \frac{1}{2}$ iv $\gamma - \frac{1}{2}, -x + \frac{1}{2}, -z + \frac{1}{2}$ v $-x + \frac{1}{2}, -\gamma + \frac{1}{2}, z + \frac{1}{2}$ vi $\gamma + \frac{1}{2}, -x + \frac{1}{2}, -z + \frac{1}{2}$

$$\begin{array}{l} \frac{1}{2}, -z+\frac{1}{2}\text{vii} -y+\frac{1}{2}, x+\frac{1}{2}, -z+\frac{1}{2}\text{viii} \\ -x+\frac{1}{2}, -y+\frac{1}{2}, z-\frac{1}{2} \end{array}$$

Table S5 Standardized fractional atomic coordinates and equivalent isotropic deflection parameter [\AA^2] for cub-Li₃NbS₄. The equivalent isotropic deflection parameter is defined as one third of the trace of the anisotropic deflection parameter. All standard deviations are given in units of the last digit in parentheses.

Atom	occupation	Wyckoff- position	x	y	z	U_{equi}
Li	1	-	0.1347(4)	= x	0.3744(5)	0.0192(8)
S1	1	-	0.37952(4)	= x	0.13603(5)	0.01233(9)
S2	1	-	0.11391(6)	= x	= x	0.00879(13)
Nb	1	-	0.359854(17)	= x	= x	0.01101(8)

Table S6 Crystallographic data and structural solution and refinement data of tetra-Li₃TaS₄. All standard deviations are given in units of the last digit in parentheses.

tetra-Li ₃ TaS ₄	
Crystal system	tetragonal
Space group	$P4_12_12$, (Nr. 92)
Lattice parameter	$a = 10.2878(3) \text{ \AA}$ $c = 20.6069(6) \text{ \AA}$
V [\AA^3]	2181.01(11)
Z	8
Density [g cm^{-3}]	4.020
Diffractometer	Bruker D8 Venture (Drehanode), MoK $_{\alpha}$ -Strahlung, Göbelspiegel
Temperature [K]	295
Absorption coefficient [mm^{-1}]	21.520

ϑ -range [°]	2.21–40.00
Index-range	$-18 \leq h \leq 18, -$ $18 \leq k \leq 18,$ $-37 \leq l \leq 37$
reflections measured	61306
independent reflections	6753
independent reflections with ($I \geq 2\sigma(I)$)	6476
R_{int}	0.0468
R_{σ}	0.0210
$F(000)$	2336
corrections	Lorentz-, polarisations-, absorption effects
Absorption correction	numerical
Structure solution	Direct methods, SHELXS97
Structure refinement	Least-Squares on F^2 , SHELXL97
Number of free parameter	148
Goof	1.323
R -values (for reflections with $I \geq 2\sigma(I)$)	$R1 = 0.0189, wR2 = 0.0582$
R -values (all data)	$R1 = 0.0213, wR2 = 0.0692$
Residual electron density [$e^{-}/\text{\AA}^{-3}$]	2.339/–2.361
Extinction coefficient	?

Table S7 Interatomic distances of the compound tetra-Li₃TaS₄. All standard deviations are given in units of the last digit in parentheses.

Atom1	Atom2	Distance [Å]	Atom1	Atom2	Distance [Å]
S1	Ta1	2.3185(9)	Li5	S6	2.508(11)
	Li2	2.578(9)		S4	2.661(11) ^{viii}

	Li3	2.587(12)		S5	2.711(10)
	Li2	2.589(9) ⁱ		S7	2.729(10) ⁱ
	Li1	2.61(2) ⁱ	S4	Ta3	2.3005(11) ^{xi}
	Li4	2.703(12) ⁱⁱ		Li5	2.661(11) ⁱⁱⁱ
Li1	S8	2.54(2) ⁱⁱⁱ		Li2	2.696(11) ^{xii}
	S5	2.569(12) ^{iv}		Li1	2.700(15) ^{vi}
	S5	2.594(12)	S5	Ta3	2.4459(9) ^{xi}
	S1	2.61(2) ^v		Li1	2.569(12) ^{xii}
	S7	2.635(15) ⁱ		Ta1	2.6322(10) ^v
	S4	2.700(15) ^{vi}	S6	Li6	1.88(5) ^v
	Li2	3.44(2)		Ta1	2.3258(9) ^v
Ta1	S2	2.3124(11)		Li7	2.642(12) ^v
	S6	2.3258(9) ⁱ	S7	Li2	2.578(11) ^v
	S7	2.5916(8) ⁱ		Ta1	2.5916(8) ^v
	S8	2.6254(9) ^{vii}		Ta3	2.6333(8) ^{xi}
	S5	2.6322(10) ⁱ		Li1	2.635(15) ^v
	Li6	3.17(6)		Ta2	2.6391(10) ^{xi}
	Li2	3.306(9) ⁱ		Li5	2.729(10) ^v
	Li3	3.431(9)	S8	Ta2	2.4497(9)
	Li7	3.432(8)		Li1	2.54(2) ^{viii}
Li2	S6	2.464(11)		Ta1	2.6254(9) ^x
	S7	2.578(11) ⁱ		Li4	2.687(11) ^{viii}
	S1	2.589(9) ^v		Li6	2.96(8) ^v
	S4	2.696(11) ^{iv}	Li6	S6	1.88(5) ⁱ
	S3	2.835(11) ⁱⁱ		S6	1.88(5) ^{vii}
	Ta1	3.306(9) ^v		Li7	2.4(2)

	Li5	3.431(15)		S8	2.96(8) ⁱ
S2	Li3	2.522(9) ^{vii}		S8	2.96(8) ^{vii}
	Li5	2.553(10)		Ta1	3.17(6) ^{xiii}
	Li3	2.628(9)		Li3	3.25(4) ^{vii}
	Li7	2.6309(11)		Li3	3.25(4) ⁱ
	Li4	2.717(11) ^{viii}	Li7	S3	2.614(12) ^{viii}
S3	Ta2	2.3005(11) ⁱⁱⁱ		S3	2.614(12) ^x
	Li5	2.545(11)		S2	2.6309(11) ^{xiii}
	Li4	2.562(13)		S6	2.642(12) ^{vii}
	Li3	2.602(12) ^{vii}		S6	2.642(12) ⁱ
	Li7	2.614(12) ⁱⁱⁱ		Ta2	3.396(17)
	Li2	2.835(11) ^{ix}		Ta1	3.432(8) ^{xiii}
Li3	S2	2.522(9) ^x	Ta2	S3	2.3005(11) ^x
	S8	2.575(12)		S3	2.3005(11) ^{viii}
	S3	2.602(12) ^x		S8	2.4497(9) ^{xiii}
	S6	2.819(12)		S7	2.6391(10) ^{xiv}
	Li6	3.25(4) ^v		S7	2.6391(10) ^{xv}
	Ta2	3.446(12)		Li3	3.446(12) ^{xiii}
Li4	S4	2.446(13)	Ta3	S4	2.3005(11) ^{xiv}
	S5	2.662(11)		S4	2.3005(11) ^{xv}
	S8	2.687(11) ⁱⁱⁱ		S5	2.4459(9) ^{xv}
	S1	2.703(11) ^{ix}		S5	2.4459(9) ^{xiv}
	S2	2.717(11) ⁱⁱⁱ		S7	2.6333(8) ^{xv}
				S7	2.6333(9) ^{xiv}

ⁱ $y-\frac{1}{2}, -x+\frac{1}{2}, z+\frac{1}{4}$
ⁱⁱⁱ $-y+\frac{1}{2}, x-\frac{1}{2}, z+\frac{1}{4}$
^{iv} $x-\frac{1}{2}, -y+\frac{1}{2}, -z+\frac{3}{4}$
^v $-y+\frac{1}{2}, x+\frac{1}{2}, z+\frac{1}{4}$

- vi $y, x, -z+1$ vii $-x+\frac{1}{2}, y-\frac{1}{2}, -z+\frac{1}{4}$
- viii $y+\frac{1}{2}, -x+\frac{1}{2}, z+\frac{1}{4}$ ix $-y+1, -x, -z+\frac{1}{2}$
- x $-x+\frac{1}{2}, y+\frac{1}{2}, -z+\frac{1}{4}$
- xi $-x+1, -y+1, z+\frac{1}{2}$ xii $x+\frac{1}{2}, -y+\frac{1}{2}, -z+\frac{3}{4}$ xiii $y, x, -z$ xiv $-y+1, -x+1, -z+\frac{1}{2}$ xv $-x+1, -y+1, z-\frac{1}{2}$

Table S8 Coefficients of the anisotropic deflection parameters [\AA^2] for tetra-Li₃TaS₄. U_{ij} is defined as: $U_{ij} = \exp(-2\pi^2[U_{11}(ha^*)^2 + \dots + 2U_{21}hka^*b^*])$. All standard deviations are given in units of the last digit in parentheses.

Atom	U_{11}	U_{22}	U_{33}	U_{23}	U_{13}	U_{12}
S1	0.0117(3)	0.0082(3)	= U_{11}	0.0002(3)	-0.0006(3)	-0.0004(3)
Li1	0.023(6)	0.065(8)	0.047(8)	-0.025(6)	-0.018(5)	0.010(5)
Ta1	0.00884(5)	0.00843(5)	0.00688(5)	0.00098(4)	0.00104(4)	-0.00087(4)
Li2	0.022(4)	0.020(4)	0.026(4)	-0.003(3)	-0.008(4)	0.011(3)
S2	0.0090(3)	0.0117(4)	0.0110(3)	0.0005(3)	-0.0006(3)	0.0010(3)
S3	0.0079(3)	0.0132(4)	0.0115(3)	-0.0002(3)	-0.0011(3)	0.0000(3)
Li3	0.023(4)	0.012(4)	0.042(6)	-0.022(4)	-0.001(4)	-0.007(3)
Li4	0.033(5)	0.024(5)	0.038(6)	0.003(4)	-0.004(5)	-0.024(4)
Li5	0.021(5)	0.035(6)	0.017(4)	-0.007(4)	-0.005(3)	0.001(4)
S4	0.0133(4)	0.0079(3)	0.0115(3)	-0.0008(3)	0.0000(3)	0.0009(2)
S5	0.0106(3)	0.0090(3)	0.0061(3)	-0.0001(3)	0.0005(3)	-0.0002(2)
S6	0.0125(4)	= U_{11}	0.0075(3)	-0.0010(3)	-0.0004(3)	-0.0002(3)
S7	0.0075(3)	0.0077(3)	0.0063(3)	-0.0002(2)	= U_{23}	-0.0013(2)
S8	0.0111(3)	0.0078(3)	0.0060(3)	-0.0003(3)	-0.0009(3)	0.0001(2)
Li6	1.1(3)	= U_{11}	0.013(12)	0.008(8)	-0.008(8)	= U_{11}
Li7	0.046(7)	= U_{11}	0.006(4)	0.012(4)	-0.012(4)	-0.023(9)
Ta2	0.00803(5)	= U_{11}	0.00878(7)	-0.00105(4)	0.00105(4)	-0.00159(6)
Ta3	0.00787(5)	= U_{11}	0.00841(7)	-0.00091(4)	0.00091(4)	-0.00139(6)

Table S9 Bond angle of cub-Li₃TaS₄. All standard deviations are given in units of the last digit in parentheses

Atoms	Angle [°]	Atoms	Angle [°]	Atoms	Angle [°]
Ta1-S1-Li2	93.6(2)	Li4-S3-Li7 ⁱⁱⁱ	92.6(3)	Ta2-S8-Li4 ^{viii}	88.1(3)
Ta1-S1-Li3	88.60(19)	Li3-S3 ^{vii} -Li7 ⁱⁱⁱ	87.42(19)	Li1-S8 ^{viii} -Li4 ^{viii}	85.3(3)

Li2-S1-Li3	88.7(4)	Ta2-S3 ⁱⁱⁱ -Li2 ^{ix}	168.8(2)	Li3-S8-Li4 ^{viii}	88.0(3)
Ta1-S1-Li2 ⁱ	84.5(2)	Li5-S3-Li2 ^{ix}	91.1(3)	Ta1-S8 ^x -Li4 ^{viii}	169.2(3)
Li2-S1-Li2 ⁱ	178.1(3)	Li4-S3-Li2 ^{ix}	90.9(3)	Ta2-S8-Li6 ^v	156(3)
Li3-S1-Li2 ⁱ	91.2(4)	Li3-S3 ^{vii} -Li2 ^{ix}	85.6(3)	Li1-S8 ^{viii} -Li6 ^v	106(3)
Ta1-S1-Li1 ⁱ	95.0(3)	Li7-S3 ⁱⁱⁱ -Li2 ^{ix}	82.8(3)	Li3-S8-Li6 ^v	71(2)
Li2-S1-Li1 ⁱ	97.3(4)	S2-Li3 ^x -S8	86.3(3)	Ta1-S8 ^x -Li6 ^v	69(3)
Li3-S1-Li1 ⁱ	172.8(4)	S2-Li3 ^x -S1	94.1(4)	Li4-S8 ^{viii} -Li6 ^v	101(3)
Li2-S1 ⁱ -Li1 ⁱ	83.0(4)	S8-Li3-S1	179.1(6)	S6-Li6 ⁱ -S6 ^{vii}	150(10)
Ta1-S1-Li4 ⁱⁱ	172.3(3)	S2-Li3 ^x -S3 ^x	89.2(4)	S6-Li6 ⁱ -Li7	75(6)
Li2-S1-Li4 ⁱⁱ	93.6(4)	S8-Li3-S3 ^x	86.6(4)	S6-Li6 ^{vii} -Li7	75(6)
Li3-S1-Li4 ⁱⁱ	88.7(3)	S1-Li3-S3 ^x	94.3(4)	S6-Li6 ⁱ -S8 ⁱ	102.6(14)
Li2-S1 ⁱ -Li4 ⁱⁱ	88.3(4)	S2-Li3 ^x -S2	177.3(5)	S6-Li6 ^{vii} -S8 ⁱ	89.1(14)
Li1-S1 ⁱ -Li4 ⁱⁱ	87.0(4)	S8-Li3-S2	95.1(4)	Li7-Li6-S8 ⁱ	113(4)
S8-Li1 ⁱⁱⁱ -S5 ^{iv}	82.9(5)	S1-Li3-S2	84.5(3)	S6-Li6 ⁱ -S8 ^{vii}	89.1(14)
S8-Li1 ⁱⁱⁱ -S5	97.5(6)	S3-Li3 ^x -S2	93.2(3)	S6-Li6 ^{vii} -S8 ^{vii}	102.6(14)
S5-Li1 ^{iv} -S5	177.7(7)	S2-Li3 ^x -S6	91.3(3)	Li7-Li6-S8 ^{vii}	113(4)
S8-Li1 ⁱⁱⁱ -S1 ^v	177.2(6)	S8-Li3-S6	90.7(4)	S8-Li6 ⁱ -S8 ^{vii}	134(7)
S5-Li1 ^{iv} -S1 ^v	94.3(5)	S1-Li3-S6	88.4(4)	S6-Li6 ⁱ -Ta1	46.8(12)
S5-Li1-S1 ^v	85.2(5)	S3-Li3 ^x -S6	177.2(5)	S6-Li6 ^{vii} -Ta1	123(5)
S8-Li1 ⁱⁱⁱ -S7 ⁱ	84.4(5)	S2-Li3-S6	86.3(4)	Li7-Li6-Ta1	75(4)
S5-Li1 ^{iv} -S7 ⁱ	83.8(4)	S2-Li3 ^x -Li6 ^v	74(3)	S8-Li6 ⁱ -Ta1	147.2(16)
S5-Li1-S7 ⁱ	98.5(5)	S8-Li3-Li6 ^v	60(3)	S8-Li6 ^{vii} -Ta1	50.59(5)
S1-Li1 ^v -S7 ⁱ	96.0(7)	S1-Li3-Li6 ^v	119(2)	S6-Li6 ⁱ -Ta1 ^{xiii}	123(5)
S8-Li1 ⁱⁱⁱ -S4 ^{vi}	94.6(6)	S3-Li3 ^x -Li6 ^v	142.7(10)	S6-Li6 ^{vii} -Ta1 ^{xiii}	46.8(12)
S5-Li1 ^{iv} -S4 ^{vi}	93.8(5)	S2-Li3-Li6 ^v	105(3)	Li7-Li6-Ta1 ^{xiii}	75(4)
S5-Li1-S4 ^{vi}	83.9(4)	S6-Li3-Li6 ^v	35.2(7)	S8-Li6 ⁱ -Ta1 ^{xiii}	50.59(5)

S1-Li1 ^v -S4 ^{vi}	84.9(5)	S2-Li3 ^x -Ta1	136.5(4)	S8-Li6 ^{vii} -Ta1 ^{xiii}	147.2(16)
S7-Li1 ⁱ -S4 ^{vi}	177.4(6)	S8-Li3-Ta1	137.1(3)	Ta1-Li6-Ta1 ^{xiii}	149(7)
S8-Li1 ⁱⁱⁱ -Li2	132.4(5)	S1-Li3-Ta1	42.49(14)	S6-Li6 ⁱ -Li3 ^{vii}	114(3)
S5-Li1 ^{iv} -Li2	92.5(5)	S3-Li3 ^x -Ta1	90.8(3)	S6-Li6 ^{vii} -Li3 ^{vii}	59.8(11)
S5-Li1-Li2	88.8(5)	S2-Li3-Ta1	42.33(14)	Li7-Li6-Li3 ^{vii}	80(4)
S1-Li1 ^v -Li2	48.3(4)	S6-Li3-Ta1	90.7(3)	S8-Li6 ⁱ -Li3 ^{vii}	143(2)
S7-Li1 ⁱ -Li2	48.0(4)	Li6-Li3 ^v -Ta1	124.5(6)	S8-Li6 ^{vii} -Li3 ^{vii}	48.7(3)
S4-Li1 ^{vi} -Li2	133.1(7)	S2-Li3 ^x -Ta2	92.0(3)	Ta1-Li6-Li3 ^{vii}	68.2(11)
S2-Ta1-S1	98.40(3)	S8-Li3-Ta2	45.20(19)	Ta1-Li6 ^{xiii} -Li3 ^{vii}	106(2)
S2-Ta1-S6 ⁱ	99.79(4)	S1-Li3-Ta2	135.6(4)	S6-Li6 ⁱ -Li3 ⁱ	59.8(11)
S1-Ta1-S6 ⁱ	99.25(4)	S3-Li3 ^x -Ta2	41.87(18)	S6-Li6 ^{vii} -Li3 ⁱ	114(3)
S2-Ta1-S7 ⁱ	91.78(3)	S2-Li3-Ta2	90.6(3)	Li7-Li6-Li3 ⁱ	80(4)
S1-Ta1-S7 ⁱ	91.20(3)	S6-Li3-Ta2	135.4(4)	S8-Li6 ⁱ -Li3 ⁱ	48.7(3)
S6-Ta1 ⁱ -S7 ⁱ	163.04(3)	Li6-Li3 ^v -Ta2	105(2)	S8-Li6 ^{vii} -Li3 ⁱ	143(2)
S2-Ta1-S8 ^{vii}	89.58(3)	Ta1-Li3-Ta2	115.9(2)	Ta1-Li6-Li3 ⁱ	106(2)
S1-Ta1-S8 ^{vii}	167.13(3)	S4-Li4-S3	178.4(6)	Ta1-Li6 ^{xiii} -Li3 ⁱ	68.2(11)
S6-Ta1 ⁱ -S8 ^{vii}	89.25(3)	S4-Li4-S5	85.6(4)	Li3-Li6 ^{vii} -Li3 ⁱ	159(7)
S7-Ta1 ⁱ -S8 ^{vii}	78.40(3)	S3-Li4-S5	93.0(4)	Li6-Li7-S3 ^{viii}	137.4(3)
S2-Ta1-S5 ⁱ	166.95(3)	S4-Li4-S8 ⁱⁱⁱ	96.3(4)	Li6-Li7-S3 ^x	137.4(3)
S1-Ta1-S5 ⁱ	90.41(3)	S3-Li4-S8 ⁱⁱⁱ	83.0(4)	S3-Li7 ^{viii} -S3 ^x	85.2(5)
S6-Ta1 ⁱ -S5 ⁱ	88.18(3)	S5-Li4-S8 ⁱⁱⁱ	92.4(4)	Li6-Li7-S2 ^{xiii}	88.3(4)
S7-Ta1 ⁱ -S5 ⁱ	78.36(3)	S4-Li4-S1 ^{ix}	91.5(4)	S3-Li7 ^{viii} -S2 ^{xiii}	92.8(3)
S8-Ta1 ^{vii} -S5 ⁱ	80.15(3)	S3-Li4-S1 ^{ix}	89.3(4)	S3-Li7 ^x -S2 ^{xiii}	89.6(3)
S2-Ta1-Li6	78(3)	S5-Li4-S1 ^{ix}	90.0(3)	Li6-Li7-S2	88.3(4)
S1-Ta1-Li6	131(2)	S8-Li4 ⁱⁱⁱ -S1 ^{ix}	172.0(5)	S3-Li7 ^{viii} -S2	89.6(3)
S6-Ta1 ⁱ -Li6	36.1(4)	S4-Li4-S2 ⁱⁱⁱ	92.6(4)	S3-Li7 ^x -S2	92.8(3)

S7-Ta1 ⁱ -Li6	137.6(19)	S3-Li4-S2 ⁱⁱⁱ	88.9(4)	S2-Li7 ^{xiii} -S2	176.6(7)
S8-Ta1 ^{vii} -Li6	61(3)	S5-Li4-S2 ⁱⁱⁱ	176.7(5)	Li6-Li7-S6 ^{vii}	43.4(3)
S5-Ta1 ⁱ -Li6	103(3)	S8-Li4 ⁱⁱⁱ -S2 ⁱⁱⁱ	90.5(3)	S3-Li7 ^{viii} -S6 ^{vii}	94.28(3)
S2-Ta1-Li2 ⁱ	101.87(19)	S1-Li4 ^{ix} -S2 ⁱⁱⁱ	87.3(4)	S3-Li7 ^x -S6 ^{vii}	174.14(8)
S1-Ta1-Li2 ⁱ	51.22(18)	S6-Li5-S3	174.4(5)	S2-Li7 ^{xiii} -S6 ^{vii}	84.6(3)
S6-Ta1 ⁱ -Li2 ⁱ	48.11(18)	S6-Li5-S2	94.9(4)	S2-Li7-S6 ^{vii}	93.0(3)
S7-Ta1 ⁱ -Li2 ⁱ	141.2(2)	S3-Li5-S2	89.8(3)	Li6-Li7-S6 ⁱ	43.4(3)
S8-Ta1 ^{vii} -Li2 ⁱ	136.94(17)	S6-Li5-S4 ^{viii}	90.9(3)	S3-Li7 ^{viii} -S6 ⁱ	174.14(8)
S5-Ta1 ⁱ -Li2 ⁱ	91.15(19)	S3-Li5-S4 ^{viii}	91.9(4)	S3-Li7 ^x -S6 ⁱ	94.28(3)
Li6-Ta1-Li2 ⁱ	81.0(17)	S2-Li5-S4 ^{viii}	91.5(3)	S2-Li7 ^{xiii} -S6 ⁱ	93.0(3)
S2-Ta1-Li3	49.93(19)	S6-Li5-S5	82.9(3)	S2-Li7-S6 ⁱ	84.6(3)
S1-Ta1-Li3	48.91(19)	S3-Li5-S5	92.3(4)	S6-Li7 ^{vii} -S6 ⁱ	86.9(5)
S6-Ta1 ⁱ -Li3	99.2(2)	S2-Li5-S5	176.3(5)	Li6-Li7-Ta2	180(5)
S7-Ta1 ⁱ -Li3	97.7(2)	S4-Li5 ^{viii} -S5	91.5(3)	S3-Li7 ^{viii} -Ta2	42.6(3)
S8-Ta1 ^{vii} -Li3	139.4(2)	S6-Li5-S7 ⁱ	93.7(4)	S3-Li7 ^x -Ta2	42.6(3)
S5-Ta1 ⁱ -Li3	139.26(18)	S3-Li5-S7 ⁱ	83.9(3)	S2-Li7 ^{xiii} -Ta2	91.7(4)
Li6-Ta1-Li3	106(4)	S2-Li5-S7 ⁱ	83.7(3)	S2-Li7-Ta2	91.7(4)
Li2-Ta1 ⁱ -Li3	66.5(3)	S4-Li5 ^{viii} -S7 ⁱ	173.6(4)	S6-Li7 ^{vii} -Ta2	136.6(3)
S2-Ta1-Li7	49.99(13)	S5-Li5-S7 ⁱ	93.5(3)	S6-Li7 ⁱ -Ta2	136.6(3)
S1-Ta1-Li7	98.2(2)	S6-Li5-Li2	45.8(3)	Li6-Li7-Ta1 ^{xiii}	62.8(3)
S6-Ta1 ⁱ -Li7	50.26(16)	S3-Li5-Li2	131.5(4)	S3-Li7 ^{viii} -Ta1 ^{xiii}	90.56(5)
S7-Ta1 ⁱ -Li7	141.48(10)	S2-Li5-Li2	89.2(4)	S3-Li7 ^x -Ta1 ^{xiii}	131.55(18)
S8-Ta1 ^{vii} -Li7	94.6(2)	S4-Li5 ^{viii} -Li2	136.5(5)	S2-Li7 ^{xiii} -Ta1 ^{xiii}	42.31(11)
S5-Ta1 ⁱ -Li7	138.34(18)	S5-Li5-Li2	87.2(3)	S2-Li7-Ta1 ^{xiii}	135.5(4)
Li6-Ta1-Li7	43(4)	S7-Li5-Li2	47.8(3)	S6-Li7 ^{vii} -Ta1 ^{xiii}	42.60(12)
Li2-Ta1 ⁱ -Li7	64.7(2)	Ta3-S4 ^{xi} -Li4	93.9(3)	S6-Li7 ⁱ -Ta1 ^{xiii}	94.1(4)

Li3-Ta1-Li7	63.4(3)	Ta3-S4 ^{xi} -Li5 ⁱⁱⁱ	172.0(2)	Ta2-Li7-Ta1 ^{xiii}	117.2(3)
S6-Li2-S1	96.9(4)	Li4-S4-Li5 ⁱⁱⁱ	89.6(4)	Li6-Li7-Ta1	62.8(3)
S6-Li2-S7 ⁱ	98.6(3)	Ta3-S4 ^{xi} -Li2 ^{xii}	95.3(2)	S3-Li7 ^{viii} -Ta1	131.55(18)
S1-Li2-S7 ⁱ	85.9(3)	Li4-S4-Li2 ^{xii}	91.5(3)	S3-Li7 ^x -Ta1	90.56(5)
S6-Li2-S1 ^v	88.9(3)	Li5-S4 ⁱⁱⁱ -Li2 ^{xii}	91.8(4)	S2-Li7 ^{xiii} -Ta1	135.5(4)
S1-Li2-S1 ^v	172.6(4)	Ta3-S4 ^{xi} -Li1 ^{vi}	89.4(3)	S2-Li7-Ta1	42.31(11)
S7-Li2 ⁱ -S1 ^v	97.9(4)	Li4-S4-Li1 ^{vi}	174.6(4)	S6-Li7 ^{vii} -Ta1	94.1(4)
S6-Li2-S4 ^{iv}	176.9(4)	Li5-S4 ⁱⁱⁱ -Li1 ^{vi}	86.5(3)	S6-Li7 ⁱ -Ta1	42.60(12)
S1-Li2-S4 ^{iv}	85.5(3)	Li2-S4 ^{xii} -Li1 ^{vi}	92.3(5)	Ta2-Li7-Ta1	117.2(3)
S7-Li2 ⁱ -S4 ^{iv}	83.5(4)	Ta3-S5 ^{xi} -Li1 ^{xii}	97.3(4)	Ta1-Li7 ^{xiii} -Ta1	125.6(5)
S1-Li2 ^v -S4 ^{iv}	88.6(3)	Ta3-S5 ^{xi} -Li1	88.8(4)	S3-Ta2 ^x -S3 ^{viii}	100.52(5)
S6-Li2-S3 ⁱⁱ	93.1(4)	Li1-S5 ^{xii} -Li1	170.63(4)	S3-Ta2 ^x -S8	96.69(3)
S1-Li2-S3 ⁱⁱ	86.1(3)	Ta3-S5 ^{xi} -Ta1 ^v	101.18(3)	S3-Ta2 ^{viii} -S8	94.08(3)
S7-Li2 ⁱ -S3 ⁱⁱ	166.6(4)	Li1-S5 ^{xii} -Ta1 ^v	97.5(5)	S3-Ta2 ^x -S8 ^{xiii}	94.08(3)
S1-Li2 ^v -S3 ⁱⁱ	88.9(3)	Li1-S5-Ta1 ^v	88.2(5)	S3-Ta2 ^{viii} -S8 ^{xiii}	96.69(3)
S4-Li2 ^{iv} -S3 ⁱⁱ	85.2(2)	Ta3-S5 ^{xi} -Li4	85.5(3)	S8-Ta2-S8 ^{xiii}	163.12(5)
S6-Li2-Ta1 ^v	44.65(16)	Li1-S5 ^{xii} -Li4	88.6(5)	S3-Ta2 ^x -S7 ^{xiv}	90.92(3)
S1-Li2-Ta1 ^v	141.0(4)	Li1-S5-Li4	84.8(5)	S3-Ta2 ^{viii} -S7 ^{xiv}	167.93(3)
S7-Li2 ⁱ -Ta1 ^v	103.5(3)	Ta1-S5 ^v -Li4	170.2(3)	S8-Ta2-S7 ^{xiv}	80.68(3)
S1-Li2 ^v -Ta1 ^v	44.28(14)	Ta3-S5 ^{xi} -Li5	168.5(2)	S8-Ta2 ^{xiii} -S7 ^{xiv}	86.20(3)
S4-Li2 ^{iv} -Ta1 ^v	132.7(3)	Li1-S5 ^{xii} -Li5	88.2(4)	S3-Ta2 ^x -S7 ^{xv}	167.93(3)
S3-Li2 ⁱⁱ -Ta1 ^v	89.5(3)	Li1-S5-Li5	84.6(4)	S3-Ta2 ^{viii} -S7 ^{xv}	90.92(3)
S6-Li2-Li5	46.9(2)	Ta1-S5 ^v -Li5	88.0(2)	S8-Ta2-S7 ^{xv}	86.20(3)
S1-Li2-Li5	92.5(3)	Li4-S5-Li5	84.6(4)	S8-Ta2 ^{xiii} -S7 ^{xv}	80.68(3)
S7-Li2 ⁱ -Li5	51.7(2)	Li6-S6 ^v -Ta1 ^v	97.1(8)	S7-Ta2 ^{xiv} -S7 ^{xv}	77.95(4)
S1-Li2 ^v -Li5	94.9(3)	Li6-S6 ^v -Li2	151(6)	S3-Ta2 ^x -Li7	50.26(2)

S4-Li ^{iv} -Li5	135.1(5)	Ta1-S6 ^v -Li2	87.2(2)	S3-Ta2 ^{viii} -Li7	50.26(2)
S3-Li2 ⁱⁱ -Li5	139.5(5)	Li6-S6 ^v -Li5	120(6)	S8-Ta2-Li7	98.44(2)
Ta1-Li2 ^v -Li5	66.9(2)	Ta1-S6 ^v -Li5	100.3(2)	S8-Ta2 ^{xiii} -Li7	98.44(2)
S6-Li2-Li1	91.5(3)	Li2-S6-Li5	87.3(3)	S7-Ta2 ^{xiv} -Li7	141.023(19)
S1-Li2-Li1	135.3(5)	Li6-S6 ^v -Li7 ^v	62(6)	S7-Ta2 ^{xv} -Li7	141.023(19)
S7-Li2 ⁱ -Li1	49.4(3)	Ta1-S6 ^v -Li7 ^v	87.15(5)	S3-Ta2 ^x -Li3 ^{xiii}	94.99(15)
S1-Li2 ^v -Li1	48.7(3)	Li2-S6-Li7 ^v	89.8(4)	S3-Ta2 ^{viii} -Li3 ^{xiii}	49.0(2)
S4-Li2 ^{iv} -Li1	88.1(4)	Li5-S6-Li7 ^v	171.9(2)	S8-Ta2-Li3 ^{xiii}	142.8(2)
S3-Li2 ⁱⁱ -Li1	137.3(4)	Li6-S6 ^v -Li3	85.0(4)	S8-Ta2 ^{xiii} -Li3 ^{xiii}	48.2(2)
Ta1-Li2 ^v -Li1	65.2(3)	Ta1-S6 ^v -Li3	169.3(2)	S7-Ta2 ^{xiv} -Li3 ^{xiii}	134.30(19)
Li5-Li2-Li1	62.6(4)	Li2-S6-Li3	85.9(3)	S7-Ta2 ^{xv} -Li3 ^{xiii}	89.62(14)
Ta1-S2-Li3 ^{vii}	96.1(3)	Li5-S6-Li3	87.7(3)	Li7-Ta2-Li3 ^{xiii}	63.58(13)
Ta1-S2-Li5	97.0(2)	Li7-S6 ^v -Li3	84.55(18)	S3-Ta2 ^x -Li3	49.0(2)
Li3-S2 ^{vii} -Li5	91.1(4)	Li2-S7 ^v -Ta1 ^v	87.4(2)	S3-Ta2 ^{viii} -Li3	94.99(15)
Ta1-S2-Li3	87.7(3)	Li2-S7 ^v -Ta3 ^{xi}	90.6(2)	S8-Ta2-Li3	48.2(2)
Li3-S2 ^{vii} -Li3	175.39(5)	Ta1-S7 ^v -Ta3 ^{xi}	97.40(3)	S8-Ta2 ^{xiii} -Li3	142.8(2)
Li5-S2-Li3	91.0(4)	Li2-S7 ^v -Li1 ^v	82.6(5)	S7-Ta2 ^{xiv} -Li3	89.62(14)
Ta1-S2-Li7	87.7(2)	Ta1-S7 ^v -Li1 ^v	166.9(4)	S7-Ta2 ^{xv} -Li3	134.30(19)
Li3-S2 ^{vii} -Li7	91.0(4)	Ta3-S7 ^{xi} -Li1 ^v	91.2(3)	Li7-Ta2-Li3	63.58(13)
Li5-S2-Li7	174.6(4)	Li2-S7 ^v -Ta2 ^{xi}	165.8(2)	Li3-Ta2 ^{xiii} -Li3	127.2(3)
Li3-S2-Li7	86.5(4)	Ta1-S7 ^v -Ta2 ^{xi}	97.40(3)	S4-Ta3 ^{xiv} -S4 ^{xv}	101.07(5)
Ta1-S2-Li4 ^{viii}	173.3(3)	Ta3-S7 ^{xi} -Ta2 ^{xi}	101.94(3)	S4-Ta3 ^{xiv} -S5 ^{xv}	96.43(4)
Li3-S2 ^{vii} -Li4 ^{viii}	89.7(4)	Li1-S7 ^v -Ta2 ^{xi}	90.4(5)	S4-Ta3 ^{xv} -S5 ^{xv}	94.06(3)
Li5-S2-Li4 ^{viii}	86.2(4)	Li2-S7 ^v -Li5 ^v	80.5(3)	S4-Ta3 ^{xiv} -S5 ^{xiv}	94.06(3)
Li3-S2-Li4 ^{viii}	86.3(4)	Ta1-S7 ^v -Li5 ^v	86.6(2)	S4-Ta3 ^{xv} -S5 ^{xiv}	96.43(4)
Li7-S2-Li4 ^{viii}	88.8(4)	Ta3-S7 ^{xi} -Li5 ^v	170.1(2)	S5-Ta3 ^{xv} -S5 ^{xiv}	163.48(4)

Li5-S3-Li4	90.1(4)	Ta2-S8-Li1 ^{viii}	97.1(4)	S5-Ta3 ^{xv} -S7 ^{xv}	80.95(3)
Ta2-S3 ⁱⁱⁱ -Li3 ^{vii}	89.1(3)	Ta2-S8-Li3	86.6(3)	S5-Ta3 ^{xiv} -S7 ^{xv}	86.22(3)
Li5-S3-Li3 ^{vii}	89.5(3)	Li1-S8 ^{viii} -Li3	172.3(4)	S4-Ta3 ^{xiv} -S7 ^{xiv}	167.86(3)
Li4-S3-Li3 ^{vii}	176.4(4)	Ta2-S8-Ta1 ^x	101.42(3)	S4-Ta3 ^{xv} -S7 ^{xiv}	90.53(4)
Ta2-S3 ⁱⁱⁱ -Li7 ⁱⁱⁱ	87.2(3)	Li1-S8 ^{viii} -Ta1 ^x	98.4(3)	S5-Ta3 ^{xv} -S7 ^{xiv}	86.22(3)
Li5-S3-Li7 ⁱⁱⁱ	173.4(3)	Li3-S8-Ta1 ^x	87.53(19)	S5-Ta3 ^{xiv} -S7 ^{xiv}	80.95(3)
				S7-Ta3 ^{xv} -S7 ^{xiv}	78.16(4)
Ta2-S3 ⁱⁱⁱ -Li5	98.7(2)	Li1-S7 ^v -Li5 ^v	83.4(4)	S4-Ta3 ^{xiv} -S7 ^{xv}	90.53(4)
Ta2-S3 ⁱⁱⁱ -Li4	94.5(2)	Ta2-S7 ^{xi} -Li5 ^v	86.5(2)	S4-Ta3 ^{xv} -S7 ^{xv}	167.86(3)

$$i \quad y-\frac{1}{2}, -x+\frac{1}{2}, z+\frac{1}{4} \quad iii \quad -y, -x+1, -z+\frac{1}{2} \quad iii \quad -y+\frac{1}{2}, x-\frac{1}{2}, z+\frac{1}{4} \quad iv \quad x-\frac{1}{2}, -y+\frac{1}{2}, -z+\frac{3}{4}$$

$$v \quad -y+\frac{1}{2}, x+\frac{1}{2}, z+\frac{1}{4} \quad vi \quad y, x, -z+1 \quad vii \quad -x+\frac{1}{2}, y-\frac{1}{2}, -z+\frac{1}{4} \quad viii \quad y+\frac{1}{2}, -x+\frac{1}{2}, z+\frac{1}{4} \quad ix$$

$$-y+1, -x, -z+\frac{1}{2} \quad x-\frac{1}{2}, y+\frac{1}{2}, -z+\frac{1}{4} \quad xi \quad -x+1, -y+1, z+\frac{1}{2} \quad x+\frac{1}{2}, -y+\frac{1}{2}, -z+\frac{3}{4} \quad xiii$$

$$y, x, -z \quad xiv \quad -y+1, -x+1, -z+\frac{1}{2} \quad xv \quad -x+1, -y+1, z-\frac{1}{2}$$

Table S10 Standardized fractional atomic coordinates and equivalent isotropic deflection parameter [\AA^2] for tetra-Li₃TaS₄. The equivalent isotropic deflection parameter is defined as one third of the trace of the anisotropic deflection parameter. All standard deviations are given in units of the last digit in parentheses.

Atom	occupation	Wyckoff- position	x	y	z	U _{equiv}
S1	1	-	0.00217(10)	0.48557(8)	0.12897(4)	0.01055(13)
Li1	1	-	0.0090(12)	0.249(2)	0.3725(7)	0.045(4)
Ta1	1	-	0.017729(15)	0.261362(14)	0.120615(7)	0.00805(3)
Li2	1	-	0.0212(11)	0.4840(11)	0.2537(4)	0.0227(19)
S2	1	-	0.24129(10)	0.24283(9)	0.12761(5)	0.01058(15)
S3	1	-	0.24177(10)	0.00115(9)	0.25391(5)	0.01089(14)
Li3	1	-	0.2530(12)	0.4978(8)	0.1223(6)	0.026(2)

Li4	1	-	0.2522(11)	0.0053(11)	0.3781(6)	0.032(2)
Li5	1	-	0.2568(10)	0.2480(11)	0.2513(5)	0.024(2)
S4	1	-	0.25919(10)	0.01524(10)	0.49664(5)	0.01087(15)
S5	1	-	0.25988(9)	0.26387(9)	0.38255(4)	0.00855(13)
S6	1	-	0.26033(11)	0.49129(10)	0.25905(4)	0.01084(13)
S7	1	-	0.26433(10)	0.49210(8)	0.49507(4)	0.00716(12)
S8	1	-	0.50286(10)	0.50810(9)	0.11758(4)	0.00831(12)
Li6	1	-	0.082(14)	= x	0	0.74(17)
Li7	1	-	0.2474(12)	= x	0	0.033(4)
Ta2	1	-	0.480768(14)	= x	0	0.00828(4)
Ta3	1	-	0.762282(15)	= x	0	0.00805(4)

Table S11 EDX measurements of cub- Li_3NbS_4 and tetra- Li_3TaS_4 .

Element	a%	a%	a%	Element	a%	a%	a%
S	75.2	80	73	S	79.9	79.4	79.9
Ta	19.3	20	18	Nb	20.1	20.7	20.1
Ratio S:Ta	3.9	4.0	4.1		4.0	3.8	4.0

Table S12 ICP measurements of cub- Li_3NbS_4 and tetra- Li_3TaS_4 .

Element	wt%	wt%	Element	wt%	wt%
Li	6.6	6.6	Li	8.6	8.4
Ta	54.9	54.7	Nb	38.3	38.5
Ratio Li:Ta	3.1	3.1		3.0	2.9

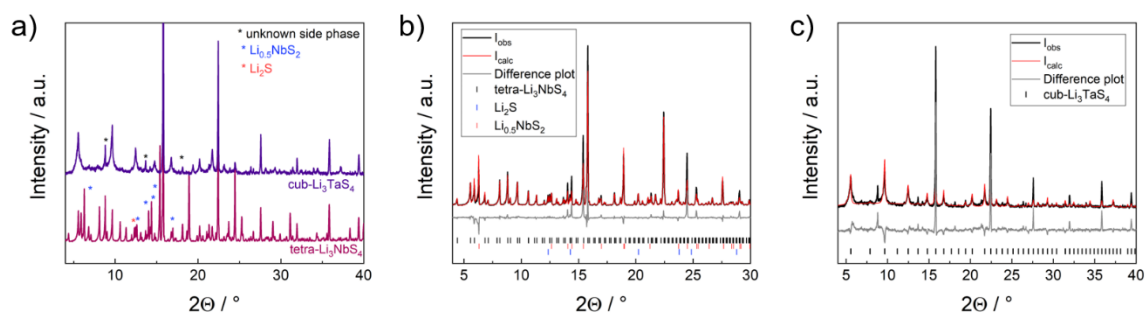


Figure S1 a) comparison of PXRDs of tetra- Li_3NbS_4 and cub- Li_3TaS_4 with a Li_2S and $\text{Li}_{0.5}\text{NbS}_2$ ⁶¹ side phase. Rietveld refinement of b) tetra- Li_3NbS_4 and c) cub- Li_3TaS_4 . All diffractograms were measured with $\text{Mo-K}\alpha_1$ radiation. Notably, the PXRD of cub- Li_3TaS_4 shows the same peculiarity as for cub- Li_3NbS_4 .

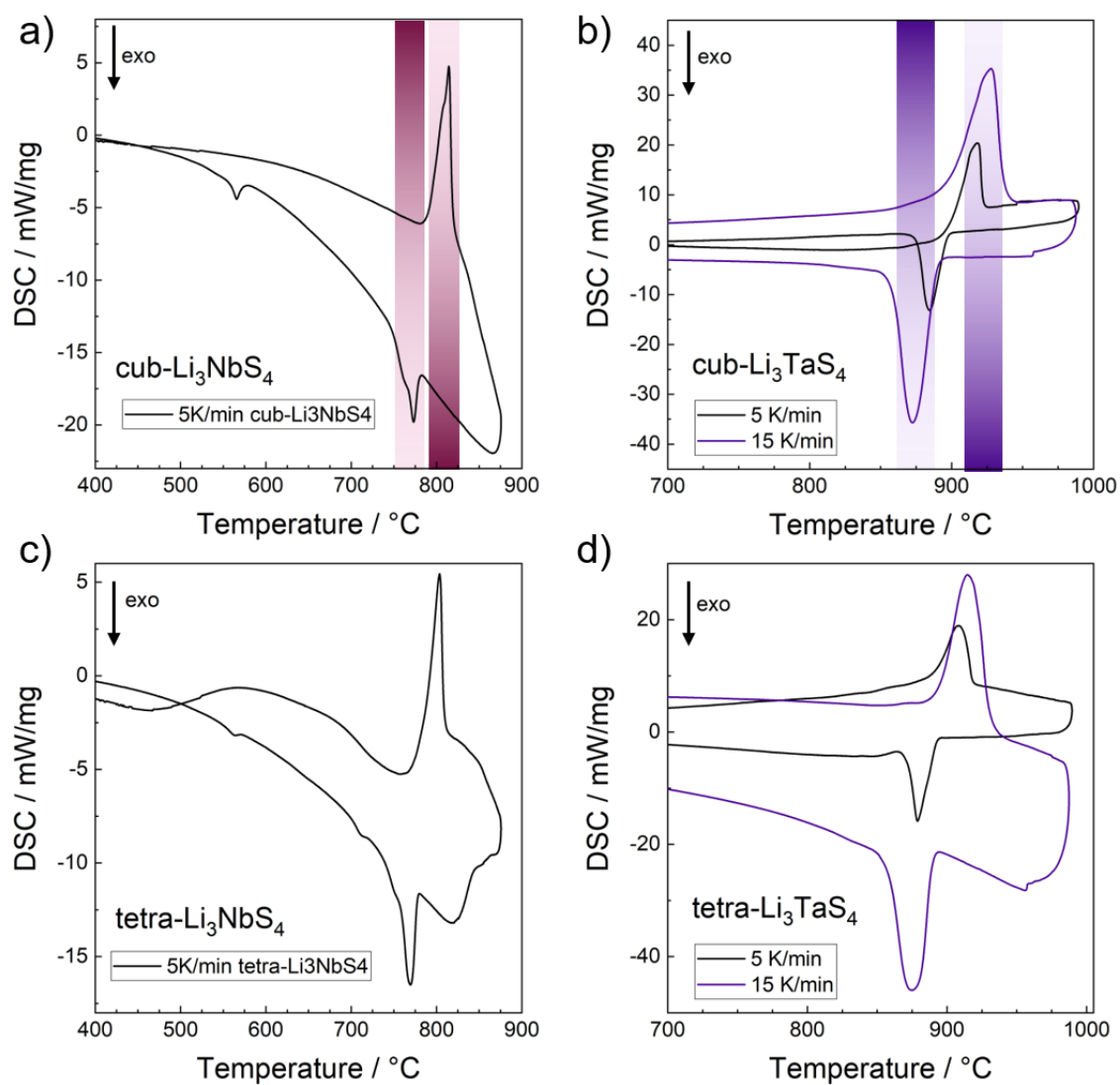


Figure S2 DSC measurements of cubic and tetragonal Li_3NbS_4 and Li_3TaS_4 .

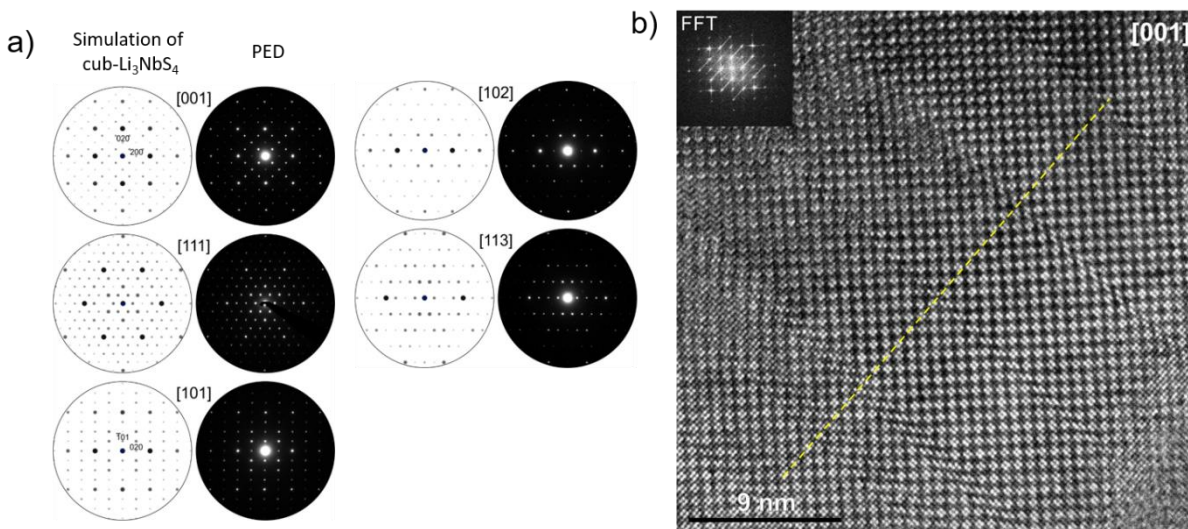


Figure S3 a) Precession electron diffraction (PED) images match simulated patterns of cub- Li_3NbS_4 very well. b) Fourier transformed (FFT) of HRTEM image in [001] show diffusive streaks indicating the presence of a large number of defects. The ordered domains smaller than $< 9\text{ nm}$ are attached to each other via dislocations.

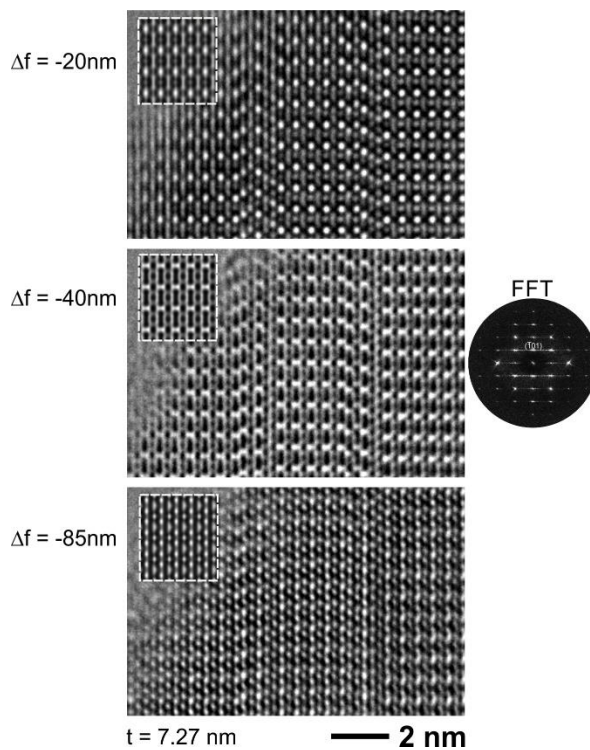


Figure S4 HRTEM image of defects in cub- Li_3NbS_4 , zone axis [101]. Diffuse lines along (-101) are also visible in the FFT.

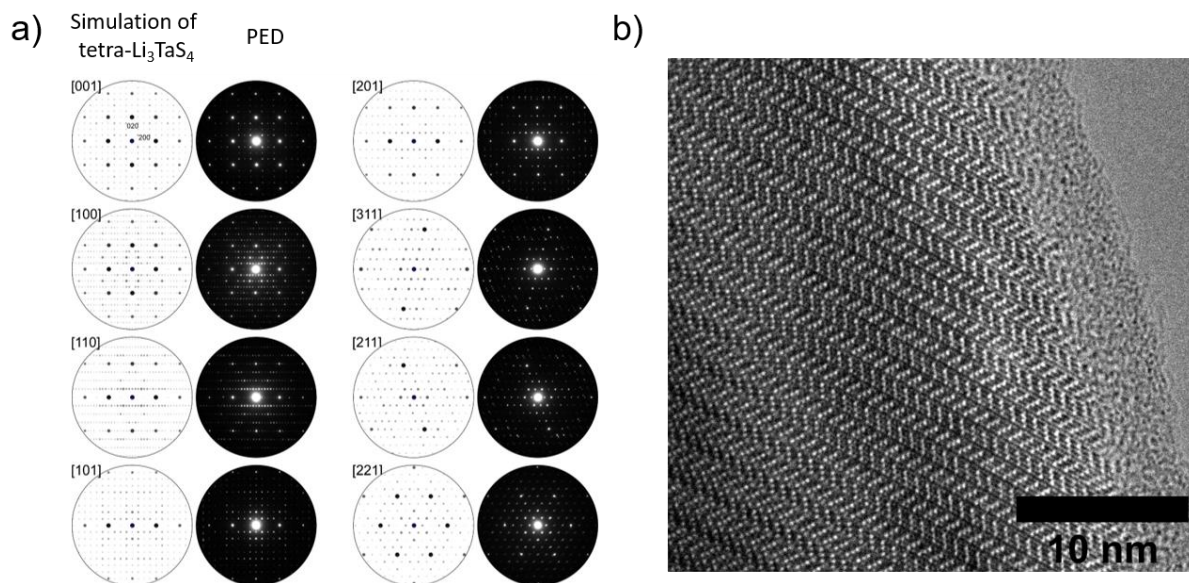


Figure S5 a) PED images match simulated patterns of tetra- Li_3TaS_4 very well. b) In the representative HRTEM image of tetra- Li_3TaS_4 (zone axis $[110]$), a large ordered domain is visible.

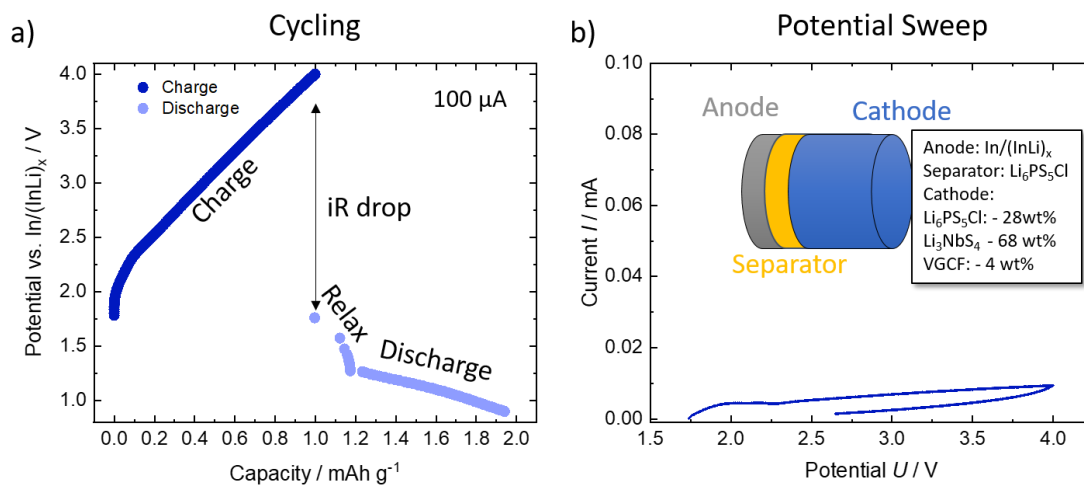


Figure S6 Applying cub- Li_3NbS_4 as cathode material in an ASSB. a) charge/discharge curve with 0.033C showing only limited discharge of the material suggesting severe limitations for lithium incorporation b) the low currents during the potential sweep show high kinetic limitations for lithium de/insertion.

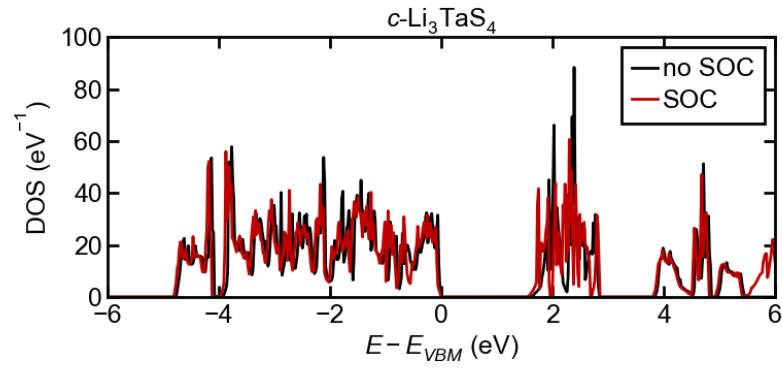


Figure S7 Negligible effect of spin-orbit coupling (SOC). Because of its effect on the Ta 5d states, inclusion of SOC narrows the computed bandgap of $c\text{-Li}_3\text{TaS}_4$ by 70 meV. But this correction remains small relative to the change upon Nb substitution (~ 250 meV) and should not affect the conclusions drawn here.

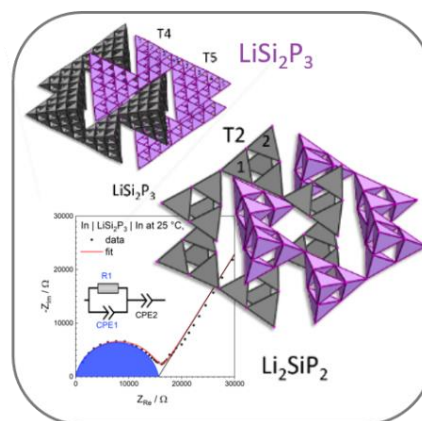
4.2 Lithium ion transport dynamics in Li_2SiP_2 and LiSi_2P_3

A.-K. Hatz*, A. Haffner*, I. Moudrakovski, B. V. Lotsch

*These authors contributed equally to this work

Abstract

Phosphidosilicates are an emerging class of solid ion conducting materials for lithium, sodium and even potassium ion based systems. They show a large structural variety with anions ranging from isolated $[\text{SiP}_4]^{8-}$ tetrahedra in Li_8SiP_4 to large supertetrahedral entities built from connected SiP_4 tetrahedra in LiSi_2P_3 . In addition, they possess high ionic conductivities $> 1\text{mS cm}^{-1}$ as in lithium-rich $\text{Li}_{14}\text{SiP}_6$. To extend the available data on Li_2SiP_2 and LiSi_2P_3 , we report on their lithium diffusivities measured by pulse field gradient nuclear magnetic resonance spectroscopy and on the electrical conduction properties of LiSi_2P_3 measured by electrochemical impedance spectroscopy and galvanostatic polarization. The diffusion coefficient of LiSi_2P_3 of $4.8 \times 10^{-13}\text{ m}^2\text{ s}^{-1}$ (at $25\text{ }^\circ\text{C}$) is much higher than that of Li_2SiP_2 ($6.8 \times 10^{-15}\text{ m}^2\text{ s}^{-1}$). As derived from the Nernst-Einstein equation, the diffusivity of LiSi_2P_3 formally corresponds to an ionic conductivity of $2.5 \times 10^{-4}\text{ S cm}^{-1}$. However, we observe that the measured ionic conductivity of polycrystalline LiSi_2P_3 of up to $3.1 \times 10^{-5}\text{ S cm}^{-1}$ with an activation energy of $0.38 \pm 0.02\text{ eV}$ is limited presumably by grain boundaries.



Introduction

For all kinds of devices, ranging from portable consumer electronics to electric vehicles and beyond, lithium ion batteries (LIBs) are the state of the art energy source. For the application in electric vehicles, the safety and performance requirements for LIBs are high: they should have a high gravimetric and volumetric energy density, a long cycle life and fast charge/discharge kinetics as well as low flammability. All-solid-state-batteries (ASSBs) that incorporate fast ion conducting solid electrolytes with negligible electronic conductivity give hope to several improvements. On the one hand, by the use of a lithium metal anode they enable high charging rates and an increase in energy density.¹⁻⁴ On the other hand, they promise a higher safety by replacing the temperature sensitive, flammable liquid electrolyte by a durable solid, especially when inorganic solids are employed. The most important key performance indicator for the solid electrolyte (SE) is the ionic conductivity that should be at least as high as 10 mS cm^{-1} to ensure an optimal performance of an ASSB.⁵ In the last years, several fast ionic conductors were developed and the performance of thiophosphate based systems stands out.^{3, 4, 6} One of the fastest known ion conductors is $\text{Li}_{9.54}\text{Si}_{1.74}\text{P}_{1.44}\text{S}_{11.7}\text{Cl}_{0.3}$, which is part of the large family of $\text{Li}_{10}\text{Ge}_2\text{PS}_{12}$ (LGPS)-type ionic conductors, with an ionic conductivity of 25 mS cm^{-1} at room-temperature.^{1, 7-11} However, since batteries are complicated systems and the most suitable electrolyte is hard to predict, alternatives are constantly sought after. In the last years, the family of phosphidosilicates that exhibit a large structural variety was introduced as lithium, sodium and potassium ion conductors.¹²⁻¹⁷ There are several known lithium containing phosphidosilicates showing differing structures and ionic conductivities: Li_5SiP_3 ,¹⁸ Li_8SiP_4 ,¹⁷ $\text{Li}_{14}\text{SiP}_6$,¹⁶ $\text{Li}_{10}\text{Si}_2\text{P}_6$,¹⁹ $\text{Li}_3\text{Si}_3\text{P}_7$,¹⁹ Li_2SiP_2 ,^{12, 17} and LiSi_2P_3 .¹² The lithium phosphidosilicate with the simplest structure is Li_8SiP_4 . It is comprised of isolated $[\text{SiP}_4]^{8-}$

tetrahedra that are surrounded by Li atoms and shows an ionic conductivity of $6 \times 10^{-6} \text{ S cm}^{-1}$ at 25°C and an activation energy E_a^{EIS} of 0.53 eV determined by electrochemical impedance spectroscopy (EIS) (vs. $E_a^{\text{T1NMR}}=0.38 \text{ eV}$ determined by T_1 -relaxometry nuclear magnetic resonance spectroscopy (NMR)). By a formal addition of Li_3P , the lithium-rich $\text{Li}_{14}\text{SiP}_6$ is formed. Its structure is closely related to the anti-fluorite type and is based on a cubic close packing of P atoms. All tetrahedral voids are fully occupied by Li and Si atoms in a mixed occupancy and all octahedral voids are occupied by Li atoms with a probability of 50%. As a consequence of the occupational disorder of Li and Si, the structure can be understood as a mixture of $[\text{SiP}_4]^{8-}$ tetrahedra and P^{3-} ions in a ratio of 1:2 similar to the simultaneous appearance of $[\text{PS}_4]^{3-}$ and S^{2-} in lithium argyrodites²⁰⁻²². The ionic conductivity of $\text{Li}_{14}\text{SiP}_6$ of $1 \times 10^{-3} \text{ S cm}^{-1}$ is the highest among all phosphidosilicates to date and shows a medium activation energy of 0.33 eV.

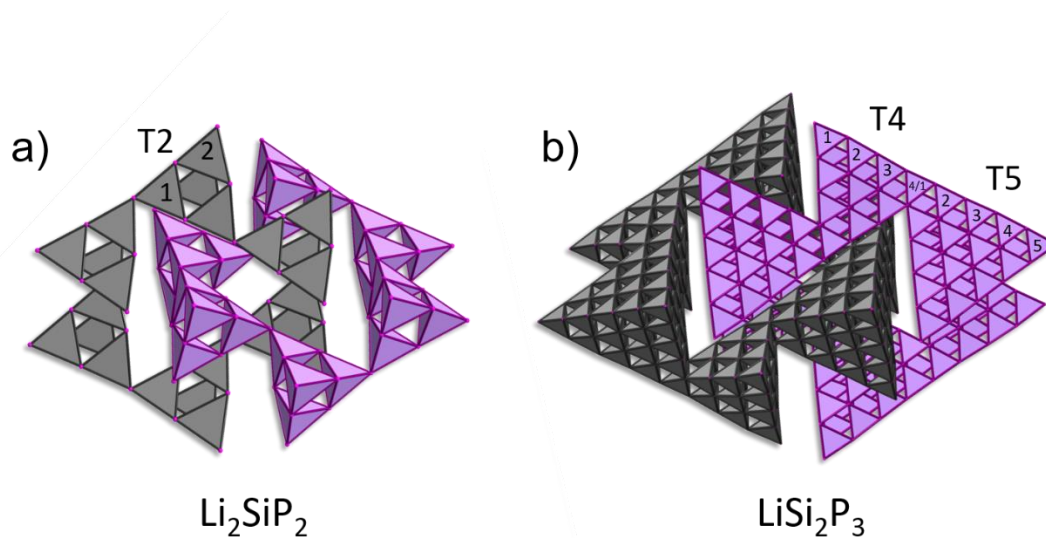


Figure 1 visualization of a) interpenetrating rings of T2 supertetrahedra that are connected via common vertices in Li_2SiP_2 and b) interpenetrating rings of connected T4 and T5 supertetrahedra sharing common SiP_4 entities in LiSi_2P_3 .

In contrast to that, Li_2SiP_2 ^{12, 17} shows a completely different structure as shown in Figure 1a. It contains two interpenetrating diamond-like tetrahedral networks consisting of corner-sharing T2 supertetrahedra. These supertetrahedra are built from SiP_4 tetrahedra that are in general connected either by common vertices (in Li_2SiP_2) or by sharing a SiP_4 entity (in LiSi_2P_3 shown in Figure 1b). Li_2SiP_2 has only a low ionic conductivity of $3 \times 10^{-7} \text{ S cm}^{-1}$ at 25°C and a high activation energy of E_a^{EIS} of 0.56 eV ($E_a^{\text{T1NMR}}=0.49 \text{ eV}$; cf. Table 1).¹⁷ For Li_5SiP_3 , $\text{Li}_{10}\text{Si}_2\text{P}_6$, $\text{Li}_3\text{Si}_3\text{P}_7$, and LiSi_2P_3 only the crystal structures were reported so far. The from powder X-ray diffraction assigned antifluorite-type structure of Li_5SiP_3 strongly resembles Li_8SiP_4 , and the material could not be reproduced by the authors of the latter compound (Eickhoff *et al.*¹⁹). In contrast, $\text{Li}_{10}\text{Si}_2\text{P}_6$ is a monoclinic form of Li_5SiP_3 containing covalently bound $[\text{Si}_2\text{P}_6]^{10-}$ units. In $\text{Li}_3\text{Si}_3\text{P}_7$, SiP_4 tetrahedra are linked via common vertices and connected by polyphosphide chains to form unique $\infty^2[\text{Si}_3\text{P}_7]^{3-}$ double layers. LiSi_2P_3 , the main subject of this work, consists of T4 and T5 supertetrahedra that form sphalerite-like interpenetrating networks as visualized in Figure 1b. The lithium ions are located in the open spaces between the supertetrahedra similar to the $LT\text{-NaSi}_2\text{P}_3$ ¹⁴ polymorph. Since $LT\text{-NaSi}_2\text{P}_3$ was identified as fast sodium ion conductor with $\sigma(\text{Na}^+) = 1.2 \times 10^{-5} \text{ S cm}^{-1}$ and an E_a^{EIS} of 0.23 eV ($E_a^{\text{T1NMR}} = 0.14 \text{ eV}$), we decided to revisit LiSi_2P_3 to assess its diffusion and ion conducting properties. The former report on a Li^+ activation energy of 0.10 eV measured by T1-

relaxometry indicated a facile ion transport in LiSi_2P_3 .¹² Here, we show that the diffusivity D_{NMR} measured by pulsed field gradient (PFG) NMR of $4.8 \times 10^{-13} \text{ m}^2 \text{ s}^{-1}$ (at 20 °C) is much higher than the diffusivity D_{NMR} of $6.1 \times 10^{-14} \text{ m}^2 \text{ s}^{-1}$ (at 100 °C) of Li_2SiP_2 . Using the Nernst-Einstein equation, the diffusivity of LiSi_2P_3 corresponds to an ionic conductivity of $2.5 \times 10^{-4} \text{ S cm}^{-1}$. However, an ionic conductivity of polycrystalline LiSi_2P_3 of up to $3.1 \times 10^{-5} \text{ S cm}^{-1}$ with an activation energy of $0.38 \pm 0.02 \text{ eV}$ was measured by EIS and thus appears to be limited presumably by grain boundaries.

Experimental

Synthesis and pellet preparation of Li_2SiP_2 and LiSi_2P_3

Li_2SiP_2 and LiSi_2P_3 were prepared according to Haffner *et al.*¹² and the respective powder X-ray diffractograms are given in Figure S 1. Subsequently, the fine ground powder was pressed into pellets with a diameter of 5 mm and thicknesses between 0.5–1 mm by uniaxial cold-pressing (1 GPa, 2 tons). The pellets were placed in a glassy carbon crucible and sealed under argon in a quartz ampule. They were annealed at 800 °C for 10–50 h and slowly cooled to room temperature.

Measurement of conduction properties

The as-prepared pellets were contacted with Indium metal on both sides as ion-blocking electrodes. Temperature dependent impedance spectra (1 MHz–0.1 Hz, rms AC voltage of 50 mV) and potentiostatic polarization were measured with an Ivium compactstat.h (24 bit instrument) in a two-electrode setup with custom made Swagelok cells inside a glovebox under argon atmosphere. At each temperature step the sample was equilibrated for 1 h. Fitting of the spectra by an equivalent circuit model was performed with RelaxIS3 from RHD INSTRUMENTS.

Pulsed field gradient NMR

^7Li NMR spectra and Pulse Field Gradient (PFG) NMR measurements were executed on a Bruker Avance-III 400 MHz instrument (magnetic field of 9.4 T, and ^7Li Larmor frequency of 155.56 MHz), equipped with a diff60 single gradient diffusion probe. The probe allows for pulse field gradients g of up to 30 T/m and variable temperature measurements up to +150 °C. The diffusion measurements were performed using a stimulated echo pulse sequence.²³ Diffusion times of 100 and 200 ms were used, with an effective gradient duration of 1 ms. Repetition times were in a range of 3 times longer than the spin-lattice relaxation time, T_1 , allowing for a good magnetization recovery. The echo attenuation curves $S(g, \delta, \Delta)$ were processed using the Stejskal-Tanner equation given in equation (2).²⁴ The results of the PFG measurements were analyzed using relaxation module of BRUKER TOPSPIN3.6 processing software.

Results

As demonstrated before by Haffner *et al.*, only a single narrow resonance indicating a rapid exchange of lithium ions at RT is observed in the ^7Li NMR of Li_2SiP_2 and LiSi_2P_3 , respectively. To obtain more detailed information on the ^7Li mobility, we measured the temperature-dependent spin-lattice-relaxation times (T_1) and self-diffusion coefficients.

The ^7Li -NMR spin-lattice relaxation times (T_1) at different temperatures were obtained by the saturation recovery technique.²⁵ The integrated intensities are fitted by a mono-exponential

function. The obtained relaxations rates ($1/T_1$) follow an Arrhenius-type law that can be described in the so-called low-temperature regime ($\omega_0\tau_c \gg 1$) by equation (1), with the Lamor frequency ω_0 , the jump rate $1/\tau_0$, the interaction strength $G(0)$, the activation energy E_a , Boltzmann constant k_b and the temperature T .^{25, 26}

$$\frac{1}{T_1} = \frac{4}{3} G(0) \frac{1}{\omega_0^2 \tau_0} e^{\frac{-E_a}{k_b T}} \quad (1)$$

The logarithmic plot of the inverse relaxation time ($1/T_1$) as a function of the inverse temperature shows a good linear correlation (Figure 1a), down to -23 °C (250 K) for both compounds. Below that temperature a flattening occurs for Li₂SiP₂. However, since the very low temperature regime is not of interest for the ion conduction properties at room temperature, we excluded this regime from fitting. From the slopes of the linear fits, an activation energy E_a^{T1NMR} of 0.23 eV and 0.17 eV for Li₂SiP₂ and LiSi₂P₃, respectively, is derived. These values are larger than the activation energies determined by T₁-relaxometry earlier (0.1 eV for Li₂SiP₂ and 0.07 eV for LiSi₂P₃).¹² This discrepancy is unclear to us, but as the new values are much more typical for a solid electrolyte and match the results obtained by PFG NMR (*vide infra*) as well as bulk activation energies of the structurally very similar compounds HT-NaSi₂P₃¹⁴ and KSi₂P₃-mC928¹⁵, we consider them to be more reliable. Besides, analysis of the temperature dependent evolution of the static ⁷Li line width was also evaluated to deduce another activation energy (E_a^{static}) for Li₂SiP₂.¹⁷ Here, the activation energy E_a^{static} of 0.49 eV (ref 17) is larger than the ones observed by us (vs. $E_a^{\text{T1NMR}} = 0.23$ eV (this work), $E_a^{\text{PFGNMR}} = 0.30$ eV (this work)) and matches the activation energy obtained from EIS much better (*vide infra*). Thus, the question arises as to what kind of activation energy is probed by which method. The comparison of the activation energies in this particular case suggests that the line broadening might estimate the activation energy of the total conductivity (including the grain boundaries) while T₁-relaxometry and PFG-NMR might probe intra grain process (bulk conductivity).

For evaluation of the PFG NMR data, the measured echo attenuation curves $S(g, \delta, \Delta)$ were processed using the Stejskal–Tanner equation (2),²⁴ with $\gamma=1.398 \times 10^8$ Hz/T being the ⁷Li gyromagnetic ratio, g is the strength and δ the duration of the pulse field gradient, D_{NMR} is the effective self-diffusion coefficient, and Δ is the time interval between the field gradients that defines the diffusion time scale.

$$S(g, \delta, \Delta) = e^{(-\gamma^2 \delta^2 g^2) D_{\text{NMR}} (\Delta - \frac{\delta}{3})} \quad (2)$$

For LiSi₂P₃ a diffusion coefficient D_{NMR} of 4.8×10^{-13} m²s⁻¹ (at 25 °C) was obtained, which is much higher than the D_{NMR} of 6.1×10^{-14} m²s⁻¹ (at 100 °C) of Li₂SiP₂. The D_{NMR} of Li₂SiP₂ below 90 °C was too low to be measured by PFG NMR, indicating a much lower ion mobility in Li₂SiP₂ than in LiSi₂P₃. The temperature dependent diffusion coefficients, since they stem from an ion hopping process, also obey an Arrhenius-type law. As shown in Figure 1b, an E_a^{PFGNMR} of 0.30 eV and 0.18 eV are obtained for Li₂SiP₂ and LiSi₂P₃, respectively. These activation energies are comparatively low. LiSi₂P₃, which possesses a higher lithium ion diffusivity, also shows the lower activation barrier. The E_a^{PFGNMR} are consistent with the values obtained from T₁ relaxometry, indicating that the same process, most likely the lithium ion diffusion, is observed for both methods in this case. By equation (3) the isotropic diffusion radius can be estimated.²⁷

$$r_{\text{rms}} = \sqrt{2D_{\text{NMR}}\Delta} \quad (3)$$

For LiSi_2P_3 ($\Delta = 100$ ms) the r_{rms} is $0.3 \mu\text{m}$ (at 25°C) and for Li_2SiP_2 $0.1 \mu\text{m}$. These diffusion radii are much smaller than the average grain size of several μm indicating that the ion diffusion in the bulk of the material is probed via PFG NMR, rather than grain boundary processes.

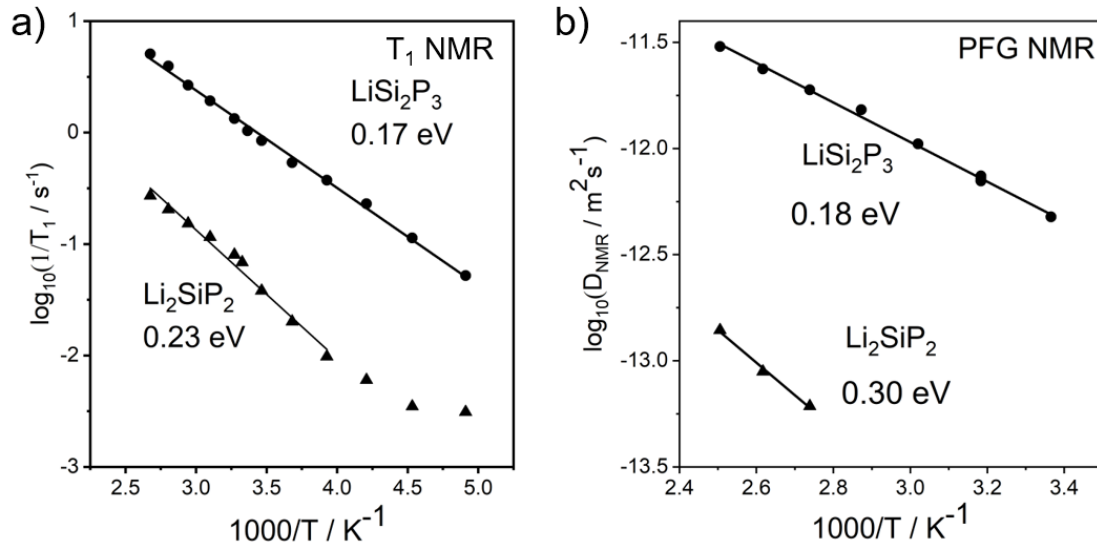


Figure 2 a) T_1 relaxation data and b) diffusion coefficients from temperature dependent PFG NMR measurements of Li_2SiP_2 and LiSi_2P_3 .

Since the ionic conductivity of Li_2SiP_2 was already evaluated elsewhere,¹⁷ we focused on LiSi_2P_3 in our impedance spectroscopy study. In Figure 2a, a representative impedance spectrum at 25°C is presented, showing one semicircle at high frequencies stemming from the ionic and capacitive properties of the sample with a low frequency spike originating from the polarization of lithium ions at the interface to the blocking electrodes. The spectrum can be fitted by an equivalent circuit model consisting of a resistance (R_1) in parallel to a constant phase element (CPE1) with another CPE element in series accounting for the ion polarization at the blocking electrodes. The CPE models a depressed semicircle that originates from deviations from the behaviour of an ideal capacitor. This is the case if a distribution of relaxation times is present, which is observed frequently for polycrystalline samples. From the CPE, an effective capacitance (C_{eff}) can be calculated by the Brug-equation²⁸ (4) with Q being the effective CPE coefficient, R the resistance in parallel to the CPE, and α a fitting parameter between $0 < \alpha < 1$ (if $\alpha=1$ the CPE is an ideal capacitor).

$$C_{\text{eff}} = \left(\frac{Q}{R^{\alpha-1}} \right)^{1/\alpha} \quad (4)$$

For the data in Figure 2a a C_{eff} of $6.3 \times 10^{-11} \text{ F}$ ($\alpha = 0.87$) can be calculated, indicating that the measured response is dominated by grain boundary contributions.²⁹ This large C_{eff} would correspond to a theoretical dielectric constant ϵ_r of 326, which can be calculated via (5) with the relative permittivity of the vacuum ϵ_0 , the thickness of the sample d , and the area A :

$$\epsilon_r = \frac{C_{\text{eff}} d}{\epsilon_0 A} \quad (5)$$

Since a typical dielectric constant of a non-ferroelectric solid is in the range of 1–100, a value of 326 is clearly too large and does not represent the bulk response. The C_{eff} of all samples are given in Table S 1. A further deconvolution of the spectra was not possible. In the future, low temperature measurements should be conducted to extract the bulk response of the material.

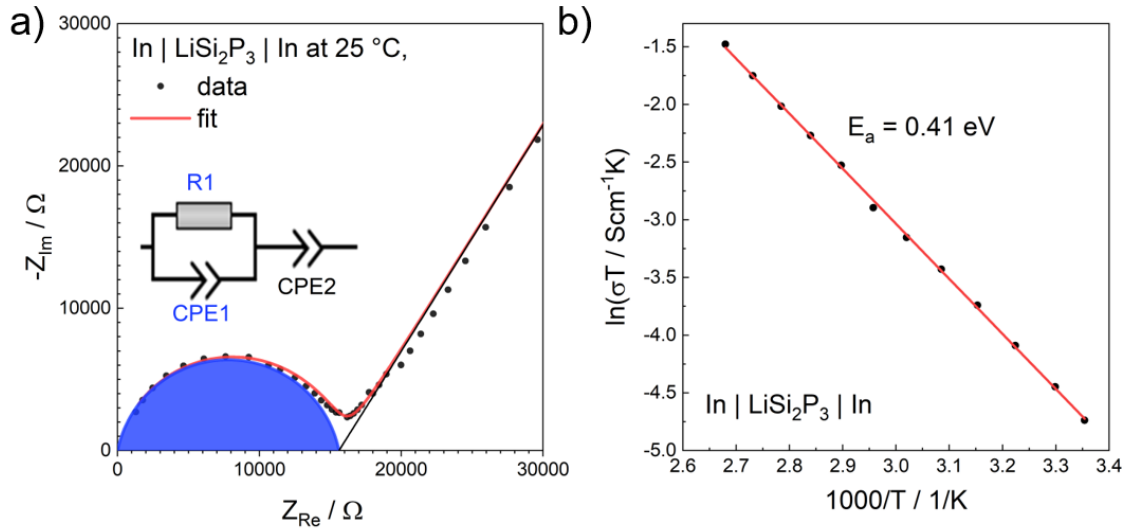


Figure 3 a) Impedance spectrum at 25 °C fitted with the respective equivalent circuit given in the inset. b) Representative plot of the temperature dependent ionic conductivity of LiSi_2P_3 .

To evaluate the activation energy, LiSi_2P_3 was heated to 100 °C. At higher temperatures, a second very broad semicircle at lower frequencies is present as visible in Figure S 1a showing a large C_{eff} of about 10^{-7} F, thus probably stemming from the electrode interface.²⁹ From the high frequency semicircle, representing the total ionic conductivity, an activation energy E_a^{EIS} of 0.38 ± 0.02 eV is obtained (average of six samples given in Table S 1). A representative plot is shown in Figure 2b. Since E_a^{EIS} of LiSi_2P_3 is significantly larger than the activation energies obtained by NMR ($E_a^{\text{T1NMR}} = 0.17$ eV, $E_a^{\text{PFGNMR}} = 0.18$ eV), this points to the presence of resistive grain boundaries inhibiting ion transport between different grains.

In Table S 1 the ionic conductivity and activation energy of six samples from one LiSi_2P_3 batch is given. The arithmetic mean, i.e. average ionic conductivity of all samples, is $1.7 \pm 0.96 \times 10^{-5}$ S cm^{-1} with a maximum value of 3.1×10^{-5} S cm^{-1} . By comparing three samples that were densified with a pressure of 1 GPa to three samples densified with 2 GPa before sintering at 800 °C, it becomes evident that the higher pressure leads to a higher ionic conductivity by roughly a factor of 2 (cf. Table S 1: 1×10^{-5} (1 GPa) vs. 2×10^{-5} (2 GPa)). This increase in ionic conductivity upon the application of a higher densification pressure corroborates the dominance of grain boundaries and current constrictions on the ion transport properties resulting from a sub optimal densification.

To further evaluate whether the NMR diffusion experiments of LiSi_2P_3 and Li_2SiP_2 probe the same process as the EIS measurements, the NMR conductivity (σ_{NMR}) was calculated based on the Nernst-Einstein equation (6) with n being the charge carrier concentration, e the elementary charge, k_B the Boltzmann constant, and T the temperature using the diffusion coefficient D_{NMR} obtained by PFG NMR.

$$\sigma_{NMR} = \frac{D_{NMR} n z^2 e^2}{k_B T} \quad (6)$$

In (6), uncorrelated lithium motion is implicitly assumed with a Haven ratio of 1. Subsequently, the calculated values can be considered a lower limit for the conductivity of the crystalline phase since many fast lithium ion conductors such as the LGPS-type materials show a strongly correlated jump process of the cation sublattice and therefore Haven ratios smaller than 1.³⁰

The charge carrier concentration of a crystalline solid can be calculated by (7) with $x(Li)$ the numbers of lithium ions per sum formula, Z number of sum formulas per unit cell, and the volume of the unit cell V_Z .

$$n = \frac{x(Li) \cdot Z}{V_Z} \quad (7)$$

Using this formula, a n of $2.338 \times 10^{28} \text{ m}^{-3}$ for Li₂SiP₂ ($x(Li) = 2$, $Z = 32$, $V_Z = 2736.6 \text{ \AA}^{-3}$) and $8.357 \times 10^{27} \text{ m}^{-3}$ for LiSi₂P₃ ($x(Li) = 1$, $Z = 100$, $V_Z = 11966.0 \text{ \AA}^{-3}$) is obtained. Therefore, a σ_{NMR} of $7.1 \times 10^{-5} \text{ S cm}^{-1}$ at 100 °C, which is larger by a factor of 4 than the σ_{EIS} of $1.8 \times 10^{-5} \text{ S cm}^{-1}$ at 100 °C extrapolated from the EIS data obtained by Toffoletti *et al.*¹⁷ is derived for Li₂SiP₂ (extrapolation to 25 °C: $D_{NMR} = 6.8 \times 10^{-15} \text{ m}^2 \text{ s}^{-1}$; $\sigma_{EIS} = 9.9 \times 10^{-6} \text{ S cm}^{-1}$). By taking the larger E_a^{EIS} of 0.56 eV (ref 17) and the lower ionic conductivity measured by EIS (ref 17) into consideration, then it is reasonable to assume that the conductivity is also limited for Li₂SiP₂ by grain boundaries. For LiSi₂P₃ a σ_{NMR} of $2.5 \times 10^{-4} \text{ S cm}^{-1}$ at 25 °C ($9.8 \times 10^{-4} \text{ S cm}^{-1}$ at 100 °C) is calculated, clearly exceeding the measured maximum σ_{EIS} of $3.1 \times 10^{-5} \text{ S cm}^{-1}$ by one order of magnitude.

Although impedance spectroscopy and NMR already show that lithium ion conduction is the dominant charge transport process in LiSi₂P₃, we measured the partial electronic conductivity σ_{eon} via galvanostatic polarization. A representative potential curve is shown in Figure S 1b and the respective values are given in Table S 1. LiSi₂P₃ shows an average σ_{eon} of $5.1 \pm 2.6 \times 10^{-9} \text{ S cm}^{-1}$ resulting in a transference number calculated by (8) of 0.998 ± 0.001 , thus corroborating the dominantly ion conducting nature of LiSi₂P₃.

$$t_i = \frac{\sigma_{ion}}{\sigma_{ion} + \sigma_{eon}} \quad (87)$$

Discussion

In Table 1, all of the above measured and calculated values of Li₂SiP₂ and LiSi₂P₃ are collected and compared to the other known lithium phosphidosilicates. The performance of LiSi₂P₃ can be ranked as mediocre (cf. Table 1). Nevertheless, the relatively high possible bulk conductivity of $2.5 \times 10^{-4} \text{ S cm}^{-1}$ estimated by PFG NMR gives hope to a further improvement of the performance if the microstructure (sample preparation) can be improved. Since for a realistic implementation into a solid battery device the development of either thin solid electrolyte films or an optimal infiltration of the cathode material is indispensable, we are optimistic that the handling of the material can be improved similar to known oxide based ion conductors.

Table 1 List of all measured and calculated conductivities, diffusivities at 25 °C and activation energies of Li_2SiP_2 , LiSi_2P_3 , Li_8SiP_4 , $\text{Li}_{14}\text{SiP}_6$.

	$\sigma_{\text{EIS}} /$ S cm^{-1}	$\sigma_{\text{NMR}} /$ S cm^{-1}	$D_{\text{NMR}} /$ m^2s^{-1}	$E_a^{\text{EIS}} / \text{eV}$	$E_a^{\text{T1NMR}} / \text{eV}$	$E_a^{\text{static}} /$ eV	$E_a^{\text{PFGNMR}} / \text{eV}$
Li_2SiP_2	$3.0 \times 10^{-7*}$	$9.9 \times 10^{-6\dagger}$	6.8×10^{-15}	0.56*	0.23	0.49*	0.30
LiSi_2P_3	3.1×10^{-5}	$2.5 \times 10^{-4\dagger}$	4.8×10^{-13}	0.38	0.17	-	0.18
Li_8SiP_4	$6 \times 10^{-6*}$	-	-	0.53*	-	0.38*	-
$\text{Li}_{14}\text{SiP}_6$	$1 \times 10^{-3\#}$	-	-	0.33 [#]	-	-	-

Value adapted from *ref.¹⁷ and #ref.¹⁶ and †calculated from Nernst-Einstein-equation

Moreover, it becomes evident that the achievable maximum ionic conductivity of LiSi_2P_3 is higher than that of Li_2SiP_2 by a factor of 50. This indicates that the lithium ion mobility in the structure comprised of large T4 and T5 supertetrahedral entities is more facile than in the structure made up of T2 supertetrahedra. A similar trend was already observed for supertetrahedral Si-P networks containing sodium ions instead of lithium ions.¹⁴ Here, the ionic conductivity increased with increasing supertetrahedra size and a maximum ionic conductivity of $4 \times 10^{-4} \text{ S cm}^{-1}$ for *HT-NaSi}_2\text{P}_3* solely comprised of T5T5 supertetrahedral entities was achieved. The homeotypic potassium ion containing KSi_2P_3 -*mC928*, which is the first solid non-oxide based potassium ion conductor to date, also possess a high bulk ionic conductivity of roughly $3 \times 10^{-4} \text{ S cm}^{-1}$.¹⁵ However, despite of a large effort to synthesize a T5T5 modification of LiSi_2P_3 , we have not been successful so far. Presumably, the smaller size of the lithium ions inhibit the formation of solely T5 supertetrahedra. Lithium ions are regarded harder than sodium and potassium ions in terms of the Hard-Soft-Acid-Base (HSAB) concept, and are less prone to form stable compounds with the large T5 supertetrahedral anions. Besides, since the activation energy of LiSi_2P_3 obtained by EIS (0.38 eV) is much larger than the ones obtained by NMR (0.18 eV, cf. Table 1), the presence of resistive grain boundaries is obvious. In general, materials with the T4T5 structure (for both lithium and sodium phosphidosilicates) show as a more severe influence of grain boundaries and current constrictions in contrast to materials with the T5T5 structure. We associate that trend with less beneficial mechanical properties of the T4T5 structure. These materials are rather hard and grain boundaries and current constriction phenomena lower the overall ionic conductivity. For the T5T5 structure, the more beneficial mechanical properties promoting an intimate grain to grain contact allow an assessment of their bulk properties via EIS. In general, we want to point out the importance of the assessment of mechanical properties and microstructure effects when characterizing new solid electrolytes. Consequently, we propose to use local methods such as high-resolution transmission electron microscopy and low temperature and/or high frequency impedance spectroscopy to gather further information about grain boundaries in phosphidosilicates.

Conclusion

We characterized the Li ion mobility of Li_2SiP_2 and LiSi_2P_3 via NMR and EIS complementing the already available literature data. Our results suggest that the ionic conductivity of these compounds is severely limited by grain boundaries. To optimize the mechanical and ionic properties a tuning of the lattice softness by substitution of for instance silicon with softer aluminum might be a viable option. Besides, this would increase the amount of lithium ions in the structure potentially leading to an increase in ionic conductivity similar to lithium-rich $\text{Li}_{14}\text{SiP}_6$ ¹⁶. Another way to optimize and maybe even to access the T5T5 LiSi_2P_3 modification could be mechanochemical synthesis. For example, recently, the superionic conductor Li_9AlP_4 was synthesized from the elements via ball-milling and subsequent annealing at moderate temperatures.³¹ Before, via classical high temperature routes, this material was inaccessible.

Acknowledgement

Financial support was provided by the German Federal Ministry of Research and Education (BMBF), project 03XP0177B (FestBatt) and the Center for NanoScience (CeNS).

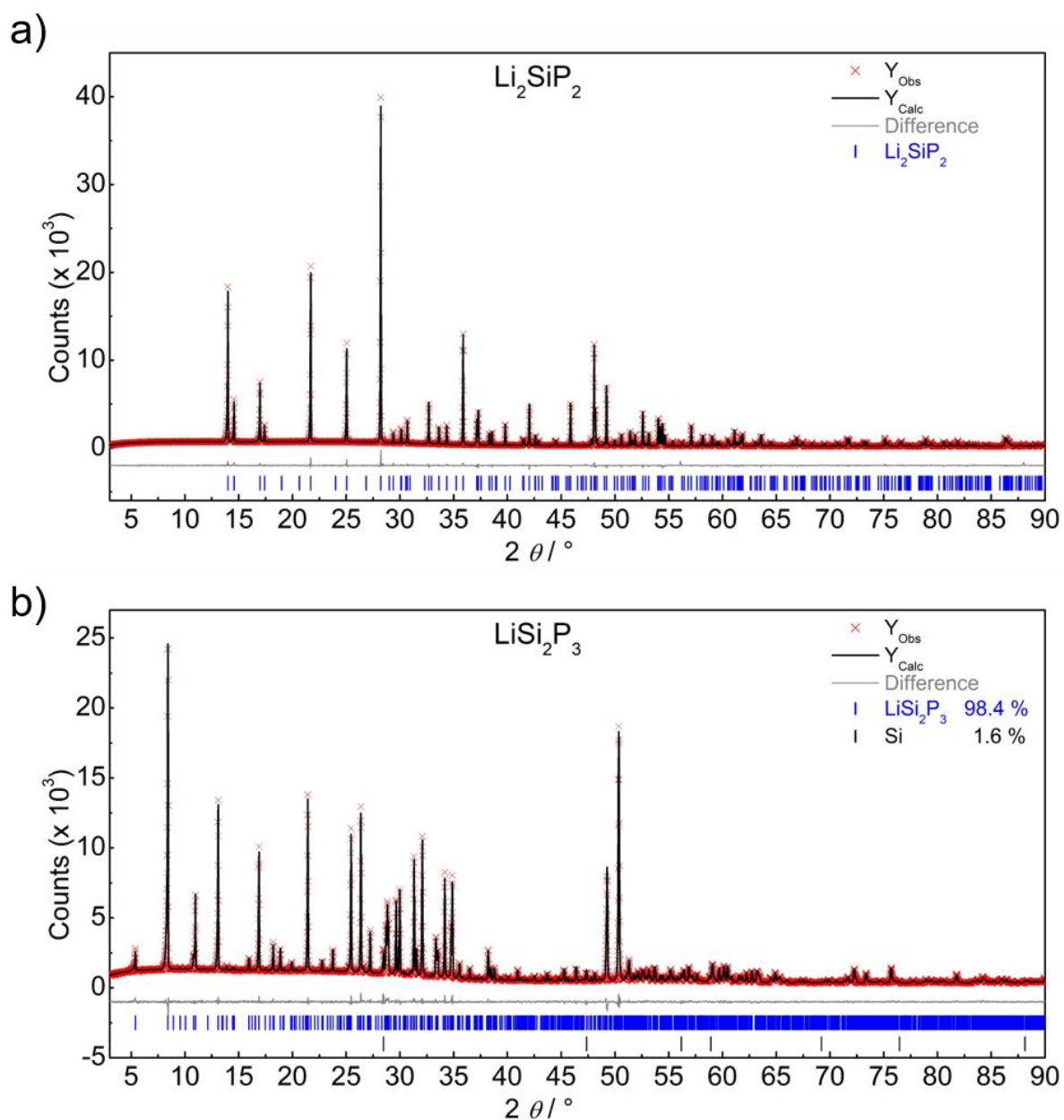
Author Contributions

AH, AKH conceived and designed this study; AH conducted the synthesis and was responsible for measuring PXRD; AKH measured EIS and potentiostatic polarization; IM measured NMR; AKH analysed EIS, potentiostatic polarization and NMR data; AH and AKH interpreted the interplay of structure and conductivity; All authors wrote and commented on the manuscript.

References

- [1] Y. Kato, S. Hori, T. Saito, K. Suzuki, M. Hirayama, A. Mitsui, M. Yonemura, H. Iba and R. Kanno, *Nat. Energy*, 2016, **1**, 16030.
- [2] J. Janek and W. G. Zeier, *Nat. Energy*, 2016, **1**, 16141.
- [3] Z. Zhang, Y. Shao, B. Lotsch, Y.-S. Hu, H. Li, J. Janek, L. F. Nazar, C.-W. Nan, J. Maier, M. Armand and L. Chen, *Energy Environ. Sci.*, 2018, **11**, 1945-1976.
- [4] B. V. Lotsch and J. Maier, *J. Electroceramics*, 2017, **38**, 128-141.
- [5] A. Bielefeld, D. A. Weber and J. Janek, *ACS Appl. Mater. Interfaces*, 2020, **12**, 12821-12833.
- [6] F. Zheng, M. Kotobuki, S. Song, M. O. Lai and L. Lu, *J. Power Sources*, 2018, **389**, 198-213.
- [7] S. Harm, A.-K. Hatz, I. Moudrakovski, R. Eger, A. Kuhn, C. Hoch and B. V. Lotsch, *Chem. Mater.*, 2019, **31**, 1280-1288.
- [8] Y. Kato, S. Hori and R. Kanno, *Adv. Energy Mater.*, 2020, **10**, 2002153.
- [9] S. Hori, K. Suzuki, M. Hirayama, Y. Kato, T. Saito, M. Yonemura and R. Kanno, *Faraday Discuss.*, 2014, **176**, 83-94.
- [10] P. Bron, S. Johansson, K. Zick, J. Schmedt auf der Günne, S. Dehnen and B. Roling, *J. Am. Chem. Soc.*, 2013, **135**, 15694-15697.
- [11] A. Kuhn, O. Gerbig, C. Zhu, F. Falkenberg, J. Maier and B. V. Lotsch, *Phys. Chem. Chem. Phys.*, 2014, **16**, 14669-14674.
- [12] A. Haffner, T. Bräuniger and D. Johrendt, *Angew. Chem. Int. Ed. Engl.*, 2016, **55**, 13585-13588.

-
- [13] A. Haffner, A.-K. Hatz, C. Hoch, B. V. Lotsch and D. Johrendt, *Eur. J. Inorg. Chem.*, 2020, DOI: 10.1002/ejic.201901083, 617-621.
- [14] A. Haffner, A.-K. Hatz, I. Moudrakovski, B. V. Lotsch and D. Johrendt, *Angew. Chem. Int. Ed. Engl.*, 2018, **57**, 6155-6160.
- [15] A. Haffner, A.-K. Hatz, O. E. O. Zeman, C. Hoch, B. V. Lotsch and D. Johrendt, *Angew. Chem. Int. Ed. Engl.*, 2021, **60**, 13641-13646.
- [16] S. Strangmuller, H. Eickhoff, D. Muller, W. Klein, G. Raudaschl-Sieber, H. Kirchhain, C. Sedlmeier, V. Baran, A. Senyshyn, V. L. Deringer, L. van Wullen, H. A. Gasteiger and T. F. Fassler, *J. Am. Chem. Soc.*, 2019, **141**, 14200-14209.
- [17] L. Toffoletti, H. Kirchhain, J. Landesfeind, W. Klein, L. vanWüllen, H. A. Gasteiger and T. F. Fässler, *Chem. Eur. J.*, 2016, **22**, 17635-17645.
- [18] R. Juza and W. Schulz, *Z. Anorg. Allg. Chemie*, 1954, **275**, 65-78.
- [19] H. Eickhoff, L. Toffoletti, W. Klein, G. Raudaschl-Sieber and T. F. Fässler, *Inorg. Chem.*, 2017, **56**, 6688-6694.
- [20] S. T. Kong, Ö. Gün, B. Koch, H. J. Deiseroth, H. Eckert and C. Reiner, *Chem. Eur. J.*, 2010, **16**, 5138-5147.
- [21] H.-J. Deiseroth, J. Maier, K. Weichert, V. Nickel, S.-T. Kong and C. Reiner, *Z. Anorg. Allg. Chemie*, 2011, **637**, 1287-1294.
- [22] H.-J. Deiseroth, S.-T. Kong, H. Eckert, J. Vannahme, C. Reiner, T. Zaiß and M. Schlosser, *Angew. Chem. Int. Ed. Engl.*, 2008, **47**, 755-758.
- [23] J. E. Tanner, *Int. J. Chem. Phys.*, 1970, **52**, 2523-2526.
- [24] E. O. Stejskal and J. E. Tanner, *Int. J. Chem. Phys.*, 1965, **42**, 288-292.
- [25] A. Kuhn, M. Kunze, P. Sreeraj, H. D. Wiemhöfer, V. Thangadurai, M. Wilkening and P. Heitjans, *Solid State Nucl. Magn. Reson.*, 2012, **42**, 2-8.
- [26] R. Böhmer, K. R. Jeffrey and M. Vogel, *Prog. Nucl. Magn. Reson. Spectrosc.*, 2007, **50**, 87-174.
- [27] A. Einstein, *Ann. Phys.*, 1905, 549.
- [28] G. J. Brug, A. L. G. van den Eeden, M. Sluyters-Rehbach and J. H. Sluyters, *J. Electroanal. Chem. Interf. Electrochem.*, 1984, **176**, 275-295.
- [29] J. T. S. Irvine, D. C. Sinclair and A. R. West, *Adv. Mater.*, 1990, **2**, 132-138.
- [30] A. Marcolongo and N. Marzari, *Phys. Rev. Mater.*, 2017, **1**.
- [31] T. M. F. Restle, C. Sedlmeier, H. Kirchhain, W. Klein, G. Raudaschl-Sieber, V. L. Deringer, L. van Wullen, H. A. Gasteiger and T. F. Fassler, *Angew. Chem. Int. Ed. Engl.*, 2020, **59**, 5665-5674.

4.2.1 Supporting Information for “Lithium ion transport dynamics in Li_2SiP_2 and LiSi_2P_3 ”Figure S 1 Powder X-ray diffractograms and Rietveld refinement of a) Li_2SiP_2 and b) LiSi_2P_3 .Table S 1 Partial conductivities, pressing pressure, activation energy and capacitances of several LiSi_2P_3 samples.

Sample	Pressing pressure / GPa	$\sigma_{\text{ion}} / \text{S cm}^{-1}$	E_a / eV	$C_{\text{eff}} / \text{F}$	$\sigma_{\text{eon}} / \text{S cm}^{-1}$	Transference number
a	1	7.4E-06	0.39	6.4E-11	1.65E-9	0.998
b	1	1.0E-05	0.38	9.5E-11	5.16E-9	0.996
c	1	1.3E-05	0.36	1.1E-10	2.83E-9	0.998
d	2	3.0E-05	n.a.	6.9E-11	n.a.	n.a.
e	2	3.1E-05	0.41	6.3E-11	8.65E-9	0.9997
f	2	1.1E-05	0.37	4.2E-11	7.21E-9	0.9993
Average		1.7E-05	0.38	7.4E-11	5.10E-09	0.998

 St. dev. 9.6E-06 0.02 2.3E-11 2.61E-09 0.001

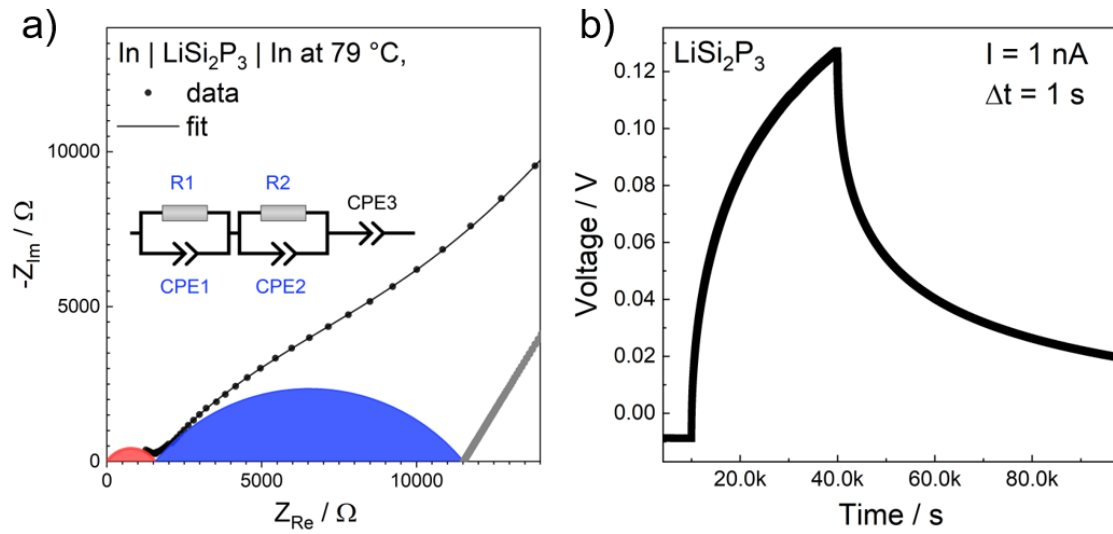


Figure S 2 a) impedance spectrum of LiSi_2P_3 at elevated temperatures showing a second semicircle at lower frequencies. The model in the inset was used for fitting. b) Representative galvanostatic polarization measurement with a current of 1 nA clearly showing a strong polarization. Even after 40 ks no plateau was reached, thus the electronic conductivity represents an upper limit.

4.3 Fast Sodium Ion Conductivity in Supertetrahedral Phosphidosilicates

A. Haffner*, A.-K. Hatz*, I. Moudrakovski, B. V. Lotsch, D. Johrendt

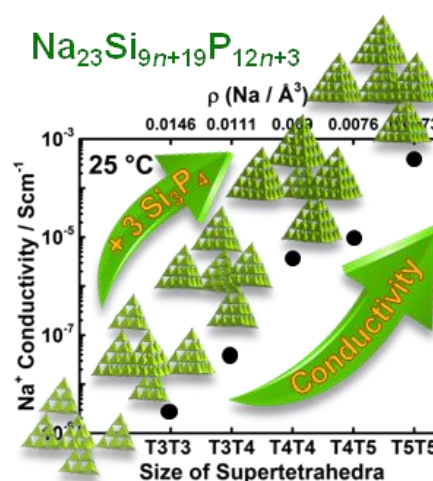
*These authors contributed equally to this work

Published in *Angew. Chem. Int. Ed. Engl* **2018**, 57 (21), 6155-6160.

DOI: doi:10.1002/anie.201801405

Abstract

Fast sodium ion conductors are key components of sodium-based all-solid-state batteries, which hold promise as safe systems for large-scale storage of electrical power. Here, we report the synthesis, crystal structure determination and Na⁺-ion conductivities of six new sodium ion conductors, the phosphidosilicates Na₁₉Si₁₃P₂₅, Na₂₃Si₁₉P₃₃, Na₂₃Si₂₈P₄₅, Na₂₃Si₃₇P₅₇, *LT*-NaSi₂P₃ and *HT*-NaSi₂P₃, which are entirely based on earth-abundant elements. The new structures exhibit SiP₄ tetrahedra assembling interpenetrating networks of T3 to T5 supertetrahedral clusters, which can be hierarchically assigned to sphalerite- or diamond-type structures. ²³Na solid-state NMR spectra and geometrical pathway analysis indicate Na⁺-ion mobility between the supertetrahedral cluster networks. Electrochemical impedance spectroscopy revealed Na⁺-ion conductivities up to $\sigma(\text{Na}^+) = 4 \cdot 10^{-4} \text{ Scm}^{-1}$ with an activation energy of $E_a = 0.25 \text{ eV}$ in *HT*-NaSi₂P₃ at 25 °C. The conductivities increase with the size of the supertetrahedral clusters due to the dilution of Na⁺-ions as the charge density of the anionic supertetrahedral networks decreases.



Introduction

A supertetrahedron or supertetrahedral cluster is a segment of the sphalerite-type structure. The number of constituting tetrahedra in a T_n supertetrahedron is $t_n = n(n+1)(n+2)/6$ where n is the number of tetrahedra along the cluster edges.^[1] Crystal structures with supertetrahedra T_n up to T5 have been found for example in indium-based chalcogenides like Cd₄In₁₆S₃₅¹⁴⁻, Cd₄In₁₆S₃₃¹⁰⁻ and Cu₇In₂₈S₅₃¹⁵⁻ and were discussed as pathways to new open framework structures.^[1-5] On the other hand, supertetrahedra are often connected via vertices and form rather dense interpenetrating networks. Examples are ZnI₂,^[6] Li₂SiN₂ (T2),^[7] Na₆B₁₀S₁₈ (T3),^[8] and Ca_{18.75}Li_{10.5}[Al₃₉N₅₅]:Eu²⁺ (T5).^[9] These interpenetrating supertetrahedral networks do not exhibit big pores, but their topology enforces an inhomogeneous distribution of the cations by confining them into the spaces between the large clusters. This introduces limitations to the coordination of the cations, which may be weaker bonded in more irregular surroundings by the anions of the cluster surfaces. Thus, supertetrahedral

anionic networks potentially favor the mobility of the cations and are therefore candidates for fast ion conductivity. The recently reported Li^+ -ion mobility in the phosphidosilicates Li_2SiP_2 ^[10] and LiSi_2P_3 ^[11] with supertetrahedral networks based on SiP_4 entities supports this concept.

Because of the versatile structural chemistry of phosphidosilicates^[12-17] and the immense interest in new, earth-abundant solid-state ionic conductors, we have now addressed sodium phosphidosilicates. Though sodium based batteries^[18,19] and solid state Na^+ electrolytes are intensively investigated,^[20-25] Na_5SiP_3 ^[13] is the only hitherto known SiP based compound. In the system Na-Si-P we came across the six new compounds $\text{Na}_{19}\text{Si}_{13}\text{P}_{25}$, $\text{Na}_{23}\text{Si}_{19}\text{P}_{33}$, $\text{Na}_{23}\text{Si}_{28}\text{P}_{45}$, $\text{Na}_{23}\text{Si}_{37}\text{P}_{57}$ and *LT-/HT-NaSi₂P₃* whose crystal structures are reported herein. ²³Na solid state MAS NMR spectra, T_1 -relaxometry and impedance spectroscopy were used to quantify the Na^+ -ion conductivity, which increases with the supertetrahedral cluster size.

Structural characterization by X-ray diffraction

Table 1 summarizes the results of the X-ray crystal structure determinations. All compounds exhibit SiP_4 based supertetrahedral clusters. $\text{Na}_{19}\text{Si}_{13}\text{P}_{25}$ has two different motives (Fig. 1a): the first is a T3 supertetrahedron. The second contains two edge sharing SiP_4 tetrahedra bridged by another vertex sharing SiP_4 tetrahedron with an additional P–P single bond (217.6 pm). Each T3 supertetrahedron shares three vertices with the Si_3P_8 unit. The fourth vertex of the T3 tetrahedron is connected via a single P–P bond (221.4 pm) to the Si_3P_8 unit, leading to a P_3 -chain (Figure 1a). The charge neutral formula is $(\text{Na}^{+1})_{19}(\text{Si}^{+4})_{13}(\text{P}^{-1})(\text{P}^{-2})_2(\text{P}^{-3})_{22}$. Condensation of the two motives forms a three-dimensional sphalerite-like network. The voids are interpenetrated with a second crystallographically independent but symmetrically equivalent network. Figure 1b shows the connectivity of the Si_3P_8 and T3 entities and emphasizes the interpenetration of the six-membered rings.

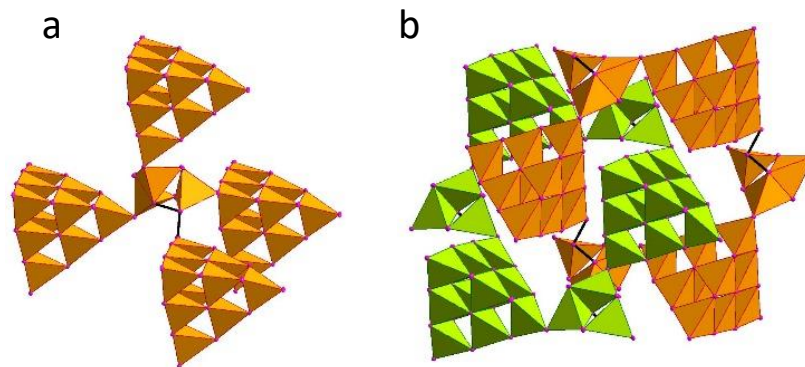


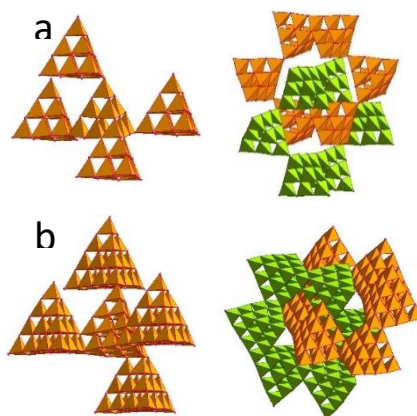
Figure 1. Crystal structure of $\text{Na}_{19}\text{Si}_{13}\text{P}_{25}$. (a) Connectivity of T3 and Si_3P_8 entities with two single P–P bonds (221.4 and 217.6 pm) leading to a P_3 -chain. (b) Interpenetrating six-membered rings of alternating building units.

$\text{Na}_{23}\text{Si}_{19}\text{P}_{33}$ contains solely T3 tetrahedra whereas in $\text{Na}_{23}\text{Si}_{37}\text{P}_{57}$ only T4 tetrahedra occur (Figure 2a, 2b). Every T3 tetrahedron is connected to three T3 by common vertices and to a fourth T3 by sharing one SiP_4 tetrahedron. This anionic structure is isotopic to $\text{Li}_9\text{B}_{19}\text{S}_{33}$.^[26] $\text{Na}_{23}\text{Si}_{37}\text{P}_{57}$ has this motif the other way round with T4 units: only one vertex linkage but three fusions occur, which means that two supertetrahedra share one common SiP_4 unit (Figure 2b).

Table 1. Crystallographic data of $\text{Na}_{19}\text{Si}_{13}\text{P}_{25}$, $\text{Na}_{23}\text{Si}_{19}\text{P}_{33}$, $\text{Na}_{23}\text{Si}_{28}\text{P}_{45}$, $\text{Na}_{23}\text{Si}_{37}\text{P}_{57}$, $\text{LT-NaSi}_2\text{P}_3$ and $\text{HT-NaSi}_2\text{P}_3$.

Formula	$\text{Na}_{19}\text{Si}_{13}\text{P}_{25}$	$\text{Na}_{23}\text{Si}_{19}\text{P}_{33}$	$\text{Na}_{23}\text{Si}_{28}\text{P}_{45}$	$\text{Na}_{23}\text{Si}_{37}\text{P}_{57}$	$\text{LT-NaSi}_2\text{P}_3$	$\text{HT-NaSi}_2\text{P}_3$
space group	$P\bar{1}$ (2)	$C2/c$ (15)	$P2_1/c$ (14)	$C2/c$ (15)	$I4_1/a$ (88)	$I4_1/acd$ (142)
$a / \text{\AA}$	13.3550 (5)	28.4985 (10)	19.1630 (8)	34.1017 (18)	19.5431 (6)	20.8976 (13)
$b / \text{\AA}$	15.3909 (5)	16.3175 (6)	23.4038 (11)	16.5140 (9)	19.5431 (6)	20.8976 (13)
$c / \text{\AA}$	15.4609 (6)	13.8732 (5)	19.0220 (8)	19.5764 (11)	34.5317 (11)	40.081 (2)
$\alpha / ^\circ$	118.0540 (10)	90	90	90	90	90
$\beta / ^\circ$	111.7050 (10)	102.3510 (10)	104.3020 (10)	111.528 (2)	90	90
$\gamma / ^\circ$	93.0540 (10)	90	90	90	90	90
$V_{\text{cell}} / \text{\AA}^3$	2503.64 (16)	6302.1 (4)	8266.7 (6)	10255.5 (10)	13188.8 (9)	17504 (2)
Z	2	4	4	4	100	128
$\rho_{\text{X-ray}} / \text{g cm}^{-3}$	2.091	2.197	2.177	2.159	2.167	2.090
μ / mm^{-1}	1.317	1.402	1.442	1.463	1.491	1.438
Θ -range / $^\circ$	2.543–27.5	2.496–30.508	2.203–25.681	2.214–30.507	2.359–30.508	2.198–30.557
refl. measured	81805	100893	186348	120166	158298	257162
independent refl.	11484	9634	15704	15633	10080	6714
Parameters	517	343	880	557	378	251
R_{o}	0.0228	0.0154	0.0616	0.0364	0.0273	0.0164
R_{int}	0.0362	0.0313	0.1119	0.0562	0.0610	0.0618
R_1 ($F^2 > 2\sigma(F^2)$) / all	0.0361 / 0.0455	0.0284 / 0.0349	0.0641 / 0.1188	0.0457 / 0.0762	0.0334 / 0.0586	0.0443 / 0.0618
wR_2 ($F^2 > 2\sigma(F^2)$) / all	0.0907 / 0.0943	0.0705 / 0.0741	0.1157 / 0.1345	0.1122 / 0.1279	0.0632 / 0.0708	0.1244 / 0.1387
GooF	1.042	1.063	1.022	1.035	1.013	1.171
$\Delta\rho_{\text{max/min}} / \text{e \AA}^{-3}$	+1.755/-1.474	+1.816/-0.929	+2.826/-1.086	+2.105/-1.004	+0.953/-0.788	+1.597/-1.290

$\text{Na}_{23}\text{Si}_{28}\text{P}_{45}$ contains T3 and T4 tetrahedra, whereby every T3 shares vertices to two other T3, one T4 and is fused with another T4 tetrahedra (Figure 3a). Every T4 cluster is fused with two other T4, one T3 and vertex shared with one T3 entity (Figure 3b). Four different six-membered supertetrahedral ring motives occur (Figure S10), leading to six interpenetration modes (Figure 3c, for details see SI).

**Figure 2.** Crystal structures of $\text{Na}_{23}\text{Si}_{19}\text{P}_{33}$ (a) and $\text{Na}_{23}\text{Si}_{37}\text{P}_{57}$ (b). The connected T3 or T4 entities (left) form interpenetrating networks of six-membered rings (right).

In contrast to the complex patterns of $\text{Na}_{23}\text{Si}_{28}\text{P}_{45}$ the crystal structures of $\text{LT-NaSi}_2\text{P}_3$ and $\text{HT-NaSi}_2\text{P}_3$ are relatively simple. In $\text{LT-NaSi}_2\text{P}_3$ every T4 cluster is coordinated tetrahedrally by four T5 tetrahedra

and vice versa by sharing one SiP_4 unit (Figure 4a). *HT-NaSi₂P₃* contains solely T5 units tetrahedrally connected by four other T5 entities as depicted in Figure 4b. The resulting tetrahedral networks are interpenetrated by a second network (Figure 4 right).

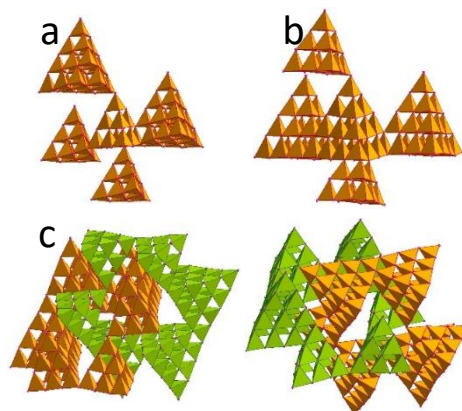


Figure 3. Crystal structure of $\text{Na}_{23}\text{Si}_{28}\text{P}_{45}$. (a), and (b) Connectivities of the T3 and T4 clusters. (c) Two out of six modes of interpenetrating six-membered rings of T3 and T4 supertetrahedra.

The T5 supertetrahedra in *LT-NaSi₂P₃* and *HT-NaSi₂P₃* lack one Si atom in their centers. This was already observed in other T5 compounds, namely $[\text{In}_{34}\text{S}_{54}]^{6-}$ [27] LiSi_2P_3 [11] and *HP-B₂S₃*. [28] The infinite connection of SiP_4 supertetrahedra formally gives SiP with sphalerite-type structure. Assuming Si^{4+} and P^{3-} ions, SiP is not electroneutral and Si vacancies are required, leading to Si_3P_4 , which is unknown. However, Si_3P_4 was investigated theoretically by DFT methods yielding a pseudo-cubic structure with similar lattice parameters ($a = 502.7$ pm and $c = 499.8$ pm) [29] as those derived from a T5 supertetrahedron ($a = 494$ to 534 pm). Therefore, the reason for the absence of one Si in the center of the T5 entities is the tendency to attain charge neutrality in the interior of the cluster.

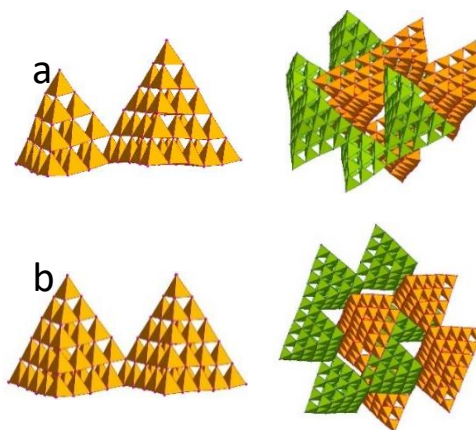


Figure 4. Crystal structures of *LT-NaSi₂P₃* (a) and *HT-NaSi₂P₃* (b). The connected T4/T5 or T5/T5 entities form interpenetrating networks of six-membered rings (right).

The sodium ions are located between the supertetrahedral networks as exemplarily shown in Fig. 5 and exhibit irregular NaP_x polyhedra. The Na–P distances measure between 271.1 pm up to extremely elongated 398.0 pm. Octahedral and trigonal prismatic coordination predominates, while trigonal bipyramids and trigonal and quadratic pyramids also occur. Additionally, *HT*- NaSi_2P_3 contains higher coordinated Na^+ -ions such as twofold capped trigonal prisms. Moreover, many Na^+ -ions reveal large anisotropic thermal displacement ellipsoids (Fig. 5) and relatively high residual electron densities in their vicinities. While all Na^+ sites are fully occupied in $\text{Na}_{19}\text{Si}_{13}\text{P}_{25}$ and $\text{Na}_{23}\text{Si}_{19}\text{P}_{33}$, some are partially occupied in the other compounds (Fig. 5, Table 2 and S1-6). This deficiency is ascribed to the incorporation of Na^+ -ions into the increasing voids between the supertetrahedral anionic networks with constant charges (except $\text{Na}_{19}\text{Si}_{13}\text{P}_{25}$). These findings are typical for compounds that exhibit a high mobility of Na^+ -ions and thus suggest a possible (high) sodium ion conductivity.^[30]

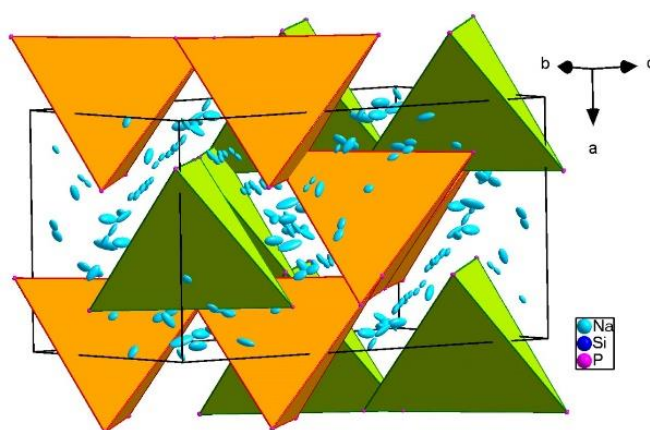


Figure 5. Unit cell of *HT*- NaSi_2P_3 . Supertetrahedral entities are depicted as enlarged single tetrahedra. Na^+ -ions are located between the tetrahedral networks with increased anisotropic displacement ellipsoids.

Table 2. Average occupancies and sodium densities in $\text{Na}_{19}\text{Si}_{13}\text{P}_{25}$ (T3), $\text{Na}_{23}\text{Si}_{19}\text{P}_{33}$ (T3T3), $\text{Na}_{23}\text{Si}_{28}\text{P}_{45}$ (T3T4), $\text{Na}_{23}\text{Si}_{37}\text{P}_{57}$ (T4T4), *LT*- NaSi_2P_3 (T4T5) and *HT*- NaSi_2P_3 (T5T5).

Compound	T3	T3T3	T3T4	T4T4	T4T5	T5T5
\emptyset -occ (Na)	1	1	0.958	0.821	0.625	0.571
ρ (Na/ \AA^3)	0.0152	0.0146	0.0111	0.0090	0.0076	0.0073

Structural characterization by NMR

Na^+ -ion mobility is supported by solid-state NMR measurements both under static and MAS conditions. In spite of a variety of distinct crystallographic Na sites with diverse coordination, ^{23}Na MAS NMR spectra of virtually every compound demonstrate a single and relatively sharp resonance (Figure 5).

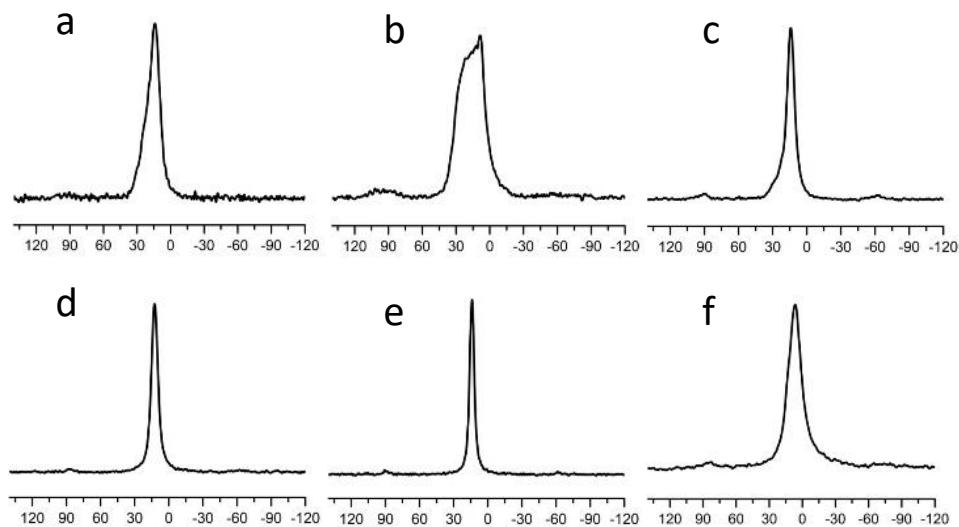


Figure 6. ^{23}Na MAS NMR spectra ($\nu_{\text{rot}} = 10$ kHz) at room temperature of $\text{Na}_{19}\text{Si}_{13}\text{P}_{25}$ (a), $\text{Na}_{23}\text{Si}_{19}\text{P}_{33}$ (b), $\text{Na}_{23}\text{Si}_{28}\text{P}_{45}$ (c), $\text{Na}_{23}\text{Si}_{37}\text{P}_{57}$ (d), $\text{LT-NaSi}_2\text{P}_3$ (e) and $\text{HT-NaSi}_2\text{P}_3$ (f). δ (^{23}Na) = 14.04, 8.63, 14.19, 12.61, 13.98, 6.6 ppm and FWHM (^{23}Na) = 12.89, 27.50, 8.01, 6.82, 4.81 and 14.53 ppm.

The broader signal of $\text{Na}_{23}\text{Si}_{19}\text{P}_{33}$ is likely a result of both second-order quadrupolar broadening and overlap of several signals (cf. Figure 6b). Less effective motional averaging of the different chemical environments experienced by the Na^+ -ions results in a broader linewidth indicating lower Na^+ -ion mobility. The relatively sharp signals of the other compounds mean enhanced averaging. The overall signal's width roughly decreases with increasing size of the tetrahedral building units. The sharpest signal belongs to $\text{LT-NaSi}_2\text{P}_3$, which consists of T4 and T5 tetrahedra and indicates enhanced Na^+ -ion mobility.

Sodium ion conduction

Possible Na^+ -ion migration pathways were extracted from geometrical analysis with Topos^[31] using covalent radii for silicon and phosphorus.^[32] The calculations resulted in a rather isotropic distribution of pathways. Four big channels occur in all compounds (Fig. S43-S48). With increasing supertetrahedral building units, the width of these channels increases. Shorter pathways connect the channels along every supertetrahedral face, leading to almost three-dimensional sodium migration pathways (Figures S43-S48). Such isotropic trajectories are desirable for fast ion conduction, since blocking effects have less impact on 3D compared to lower dimensional ion diffusion.

Na^+ -ion conductivities were determined by impedance spectroscopy. DC galvanostatic polarization measurements (Figure S50) revealed negligible contributions of electronic conductivity to the overall conductivity, which is desired in the context of solid electrolytes for battery applications. The ionic conductivities of all compounds (T3-T5T5) at 25 °C are plotted in Figure 7 as a function of size of their supertetrahedral entities. In addition, the sodium density in the compounds is given in the upper x-axis. For a detailed description of the data analysis see S51-S55 in the SI. All samples were sintered below their synthesis temperature to avoid decomposition (T3-T4T4 at 400 °C; T4T5 and T5T5

additionally at 800 °C, marked #). σ_{total} (black) refers to the total ionic conductivity including all grain boundary contributions of at least four samples of each compound. The conductivities of samples with optimized morphologies with only one semicircle in the EIS are plotted in orange (σ_{best}). The total ionic conductivity clearly increases with supertetrahedra size from $1.76 \cdot 10^{-9} \text{ Scm}^{-1}$ to $4.0 \cdot 10^{-4} \text{ Scm}^{-1}$. This trend is also valid if only the grain boundary process at higher frequencies (cf. Figure S57) is evaluated and if the “best” samples with only one grain boundary contribution are compared (orange). Fig. S58 shows a plot including the data of T4T5 and T5T5 samples sintered at 400 °C.

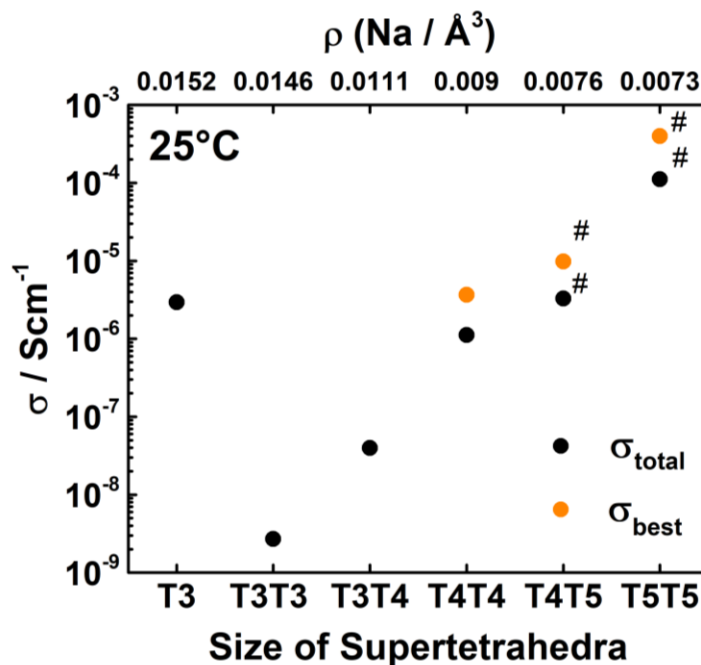


Figure 7. Ionic conductivity at 25 °C increases with the size of the supertetrahedral entities in the Na-Si-P structures and with a decrease in sodium density $\rho(\text{Na}/\text{\AA}^3)$. For details see text.

Discussion

The increase in conductivity is rationalized by the increasing space between the supertetrahedra as observed in the pathway analysis. By enlarging the supertetrahedra all channels and shorter connecting pathways become broader. Moreover, the relation between the phases T3T3 to T5T5 can be rationalized by adding $3 \times \text{Si}_3\text{P}_4$ to the formulae: $\text{Na}_{23}\text{Si}_{19}\text{P}_{33}$ (T3T3) + $3 \times \text{Si}_3\text{P}_4 \rightarrow \text{Na}_{23}\text{Si}_{28}\text{P}_{45}$ (T3T4) + $3 \times \text{Si}_3\text{P}_4 \rightarrow \text{Na}_{23}\text{Si}_{37}\text{P}_{57}$ (T4T4) + $3 \times \text{Si}_3\text{P}_4 \rightarrow \text{Na}_{23}\text{Si}_{46}\text{P}_{69}$ (T4T5 or T5T5). The general formula is $\text{Na}_{23}\text{Si}_{9n+19}\text{P}_{12n+33}$ ($n = 0 - 3$). Adding charge neutral " Si_3P_4 " to the anionic framework reduces the charge density, thus reduces the effective charge acting on the Na^+ -ions. Besides, the Na^+ -ions are "diluted", i.e. the Na density decreases and the number of partially occupied Na sites increases, which in turn increases the conductivity (cf. Tables 2, S1-S6 and Figure 7). In Figure 8a, the activation energies (E_a) obtained from the grain boundary process at higher frequencies and from the measurements showing only one semicircle (cf. SI Equation 5) confirm the facilitation of the Na^+ -ion movement in the larger structures. In general, a lower E_a is associated with a more facile movement of the ions.^[33] Here, the activation energies decrease dramatically along the series T3T3 to T5T5 with increasing

supertetrahedra size and Na⁺-ion conductivity from 0.47 eV to 0.23 eV. The E_a of the two fastest materials LT -NaSi₂P₃ (T4T5, 0.23 eV) and HT -NaSi₂P₃ (T5T5, 0.25 eV) are even lower compared to existing fast Na⁺-ion conductors like Na₃PS₄ (0.29 eV)^[22], Na₃SbS₄ (0.25 eV)^[23], Na₃P_{0.5}As_{0.5}S₄ (0.27 eV)^[34] and Na₃Zr₂(SiO₄)₂(PO₄) (0.26 eV)^[24].

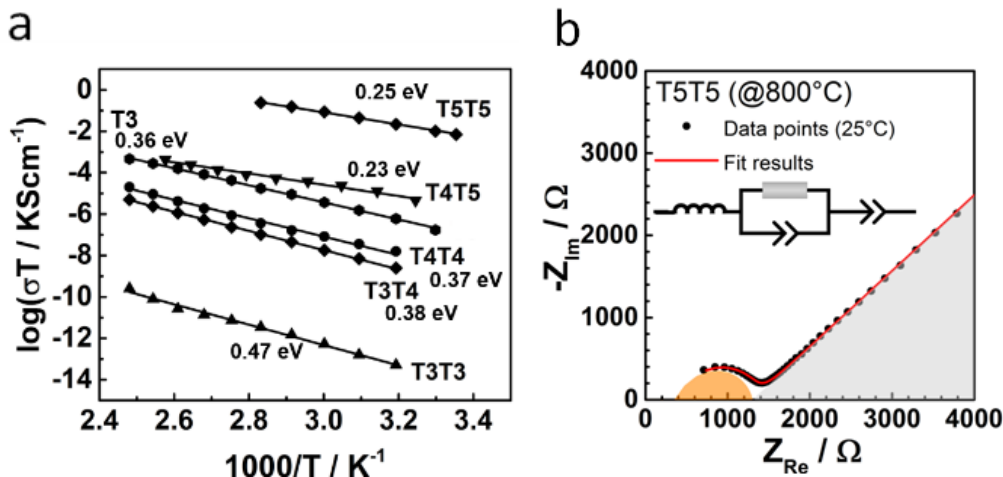


Figure 8. (a) Comparison of the activation energies of all compounds. (b) Complex impedance plot of T5T5 sintered at 800 °C.

Na₁₉Si₁₃P₂₅ (T3) does not follow the described trend. Its total conductivity of $2.9 \cdot 10^{-6} \text{ Scm}^{-1}$ is close to that of Na₂₃Si₃₇P₅₇ (T4T4, $3.7 \cdot 10^{-6} \text{ Scm}^{-1}$) and its E_a of 0.36 eV is very close to that of the T4T4 sample. The relatively high conductivity may be connected to the low density of 2.091 g cm^{-3} . Apparently, the replacement of a T3 supertetrahedron by a Si₃P₈ unit in Na₁₉Si₁₃P₂₅ creates extra space for the movement of Na⁺-ions. HT -NaSi₂P₃ (T5T5) exhibits the highest total ionic conductivity of $4 \cdot 10^{-4} \text{ Scm}^{-1}$ at 25 °C. (cf. Figure 8b). Thus, HT -NaSi₂P₃ is *en par* with very fast Na⁺-ion conductors such as Na₃PS₄^[22] ($2 \cdot 10^{-4} \text{ Scm}^{-1}$) and NASICON-type Na_{3.4}Sc₂(SiO₄)_{0.4}(PO₄)_{2.6}^[35,36] ($7 \cdot 10^{-4} \text{ Scm}^{-1}$), but slightly slower than materials such as NASICON produced by Ceramtec^[37], β -Alumina^[38], Na_{3.1}Zr_{1.95}Mg_{0.5}Si₂PO₁₂^[39], Na₃SbS₄^[23], Na₁₁Sn₂PS₁₂^[40, 41], NaCB₉H₁₀^[25] and Na(C₉H₁₀)(CB₁₁H₁₂)^[42] with conductivities of 10^{-3} - 10^{-2} Scm^{-1} .

For a deeper understanding of the origin and bulk vs. grain boundary contributions to the conductivity, the capacitance of the semicircle in the EIS has to be considered: assuming a realistic relative permittivity ϵ between 1-100 for a non-ferroelectric solid like HT -NaSi₂P₃, the bulk capacitance calculated by $C = \epsilon_0 \epsilon A / d$ with ϵ_0 being the vacuum permittivity should be in the low pF range.^[43] Here, in Figure 8b and in a measurement of T5T5 at -60 °C (Figure S56), the capacitance is in the range of 20-100 pF and thus much larger than the expected bulk value. Consequently, we attribute the semicircle to a grain boundary process where ion transport is limited by geometrical current constriction effects.^[44-46] The bulk properties of T5T5 are concealed by the grain boundary contributions and could not be deconvoluted. The bulk conductivity of this material thus potentially exceeds $4 \cdot 10^{-4} \text{ Scm}^{-1}$ at ambient conditions. This assumption is corroborated by ²³Na-T₁-relaxometry data showing a low E_a of 0.11 eV for T5T5 (Figure 9b). This suggests fast ion dynamics in the bulk, similar to β -Alumina. The grain boundary E_a of polycrystalline β -Alumina is 0.26 eV ($\sigma_{\text{GB}} = 1 \cdot 10^{-3} \text{ Scm}^{-1}$), while the bulk E_a amounts to only 0.15 eV ($\sigma_{\text{bulk}} = 8 \cdot 10^{-3} \text{ Scm}^{-1}$).^[38] For T4T5 similar results were obtained.

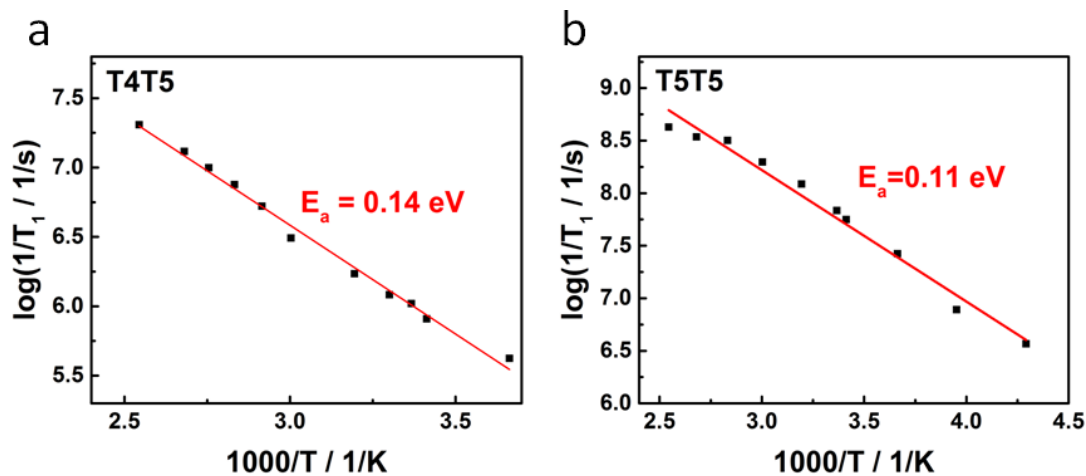


Figure 9. Temperature dependence of the ^{23}Na - T_1 -relaxation time in the samples T4T5 (a) and T5T5 (b).

Conclusion

In summary, the herein reported phosphidosilicates are fast Na^+ -ion conductors and our systematic study shows that the conductivity increases with the size of the supertetrahedra. It is demonstrated that the enhanced conductivity is due to the dilution of the Na^+ -ions since the anionic charge of the supertetrahedral networks keeps constant (except $\text{Na}_{19}\text{Si}_{13}\text{P}_{25}$). *HT*- NaSi_2P_3 with the largest supertetrahedral entities (T5) exhibits the highest total conductivity of up to $4 \cdot 10^{-4} \text{ Scm}^{-1}$ at 25°C which is competitive to known fast ionic conductors.^[22,35,36] Impedance and NMR data indicate the existence of an even more facile and fast bulk conductivity, motivating additional research on the family of sodium phosphidosilicates for Na^+ -ion conduction.

Experimental Section

All experiments and measurements were performed in an argon filled glovebox. The compounds were synthesized by solid state reactions of the elements in alumina crucibles at 750 to 1100 $^\circ\text{C}$. Further details on elemental analysis, NMR, electrochemical spectroscopy are in the SI. Details of the crystal structure determinations are may be obtained from the CCDC database (www.ccdc.cam.ac.uk) on quoting the deposition numbers 1816420-1816425.

Acknowledgements

A. Haffner and A.-K. Hatz contributed equally to this work. The authors thank C. Minke for MAS-NMR measurements and Rotraut Merkle for advises. Financial support granted by the Max Planck Society, the University of Munich (LMU), the Center for NanoScience (CeNS), and the Deutsche Forschungsgemeinschaft (DFG) through research grants and the Cluster of Excellence Nanosystems Initiative Munich (NIM) are gratefully acknowledged.

Author Contributions

AH, AKH conceived and designed this study; AH conducted the synthesis and was responsible for measuring SCXRD, PXRD, NMR, EDX; AKH measured EIS; AH performed structure determination;

IM measured ^{23}Na relaxometry and temperature dependent NMR; AH performed the calculation of TOPOS data and analysed MAS NMR; AKH analysed EIS and ^{23}Na relaxometry and temperature dependent NMR data; AH and AKH interpreted the interplay of structure and conductivity; AH and AKH wrote sections of the manuscript; All authors wrote and commented on the manuscript.

References

- [1] H. Li, J. Kim, T. L. Groy, M. O'Keeffe, O. M. Yaghi, *J. Am. Chem. Soc.* **2001**, *123*, 4867.
- [2] C. Wang, Y. Li, X. Bu, N. Zheng, O. Zivkovic, C.-S. Yang, P. Feng, *J. Am. Chem. Soc.* **2001**, *123*, 11506.
- [3] L. Wang, T. Wu, F. Zuo, X. Zhao, X. Bu, J. Wu, P. Feng, *J. Am. Chem. Soc.* **2010**, *132*, 3283.
- [4] H. Li, A. Laine, M. O'Keeffe, O. M. Yaghi, *Science* **1999**, *283*, 1145.
- [5] G. Férey, *Angew. Chem. Int. Ed.* **2003**, *42*, 2576.
- [6] P. H. Fourcroy, D. Carre, J. Rivet, *Acta Crystallogr. B* **1978**, *34*, 3160.
- [7] S. Pagano, M. Zeuner, S. Hug, W. Schnick, *Eur. J. Inorg. Chem.* **2009**, 1579.
- [8] A. Hammerschmidt, P. z. Hebel, F. Hiltmann, B. Krebs, *Z. Anorg. Allg. Chem.* **1996**, *622*, 76.
- [9] P. Wagatha, P. Pust, V. Weiler, A. S. Wochnik, P. J. Schmidt, C. Scheu, W. Schnick, *Chem. Mater.* **2016**, *28*, 1220.
- [10] L. Toffoletti, H. Kirhhain, J. Landesfeind, W. Klein, L. v. Wüllen, H. A. Gasteiger, T. F. Fässler, *Chem. Eur. J.* **2016**, *22*, 17635.
- [11] A. Haffner, T. Bräuniger, D. Johrendt, *Angew. Chem. Int. Ed.* **2016**, *55*, 13585.
- [12] B. Eisenmann, H. Jordan, H. Schäfer, *Mater. Res. Bull.* **1982**, *17*, 95.
- [13] B. Eisenmann, M. Somer, *Z. Naturforsch. B* **1985**, *40*, 886.
- [14] B. Eisenmann, M. Somer, *Z. Naturforsch. B* **1984**, *39*, 736.
- [15] B. Eisenmann, J. Klein, *J. Less-Common Met.* **1991**, *175*, 109.
- [16] K. Feng, L. Kang, W. Yin, W. Hao, Z. Lin, J. Yao, Y. Wu, *J. Solid State Chem.* **2013**, *205*, 129.
- [17] A. J. Springthorpe, J. G. Harrison, *Nature* **1969**, *222*, 977.
- [18] D. Kundu, E. Talaie, V. Duffort, L. F. Nazar, *Angew. Chem. Int. Ed.* **2015**, *54*, 3431-3448; *Angew. Chem.* **2015**, *127*, 3495-3513.
- [19] N. Yabuuchi, K. Kubota, M. Dahbi, S. Komaba, *Chemical Reviews* **2014**, *114*, 11636-11682.
- [20] J. W. Fergus, *Solid State Ion.* **2012**, *227*, 102.
- [21] Zhang, L.; Yang, K.; Mi, J.; Lu, L.; Zhao, L.; Wang, L.; Li, Y.; Zeng, H., *Adv. Energy Mater.* **2015**, *5*, 1501294.
- [22] A. Hayashi, K. Noi, A. Sakuda, M. Tatsumisago, *Nat. Commun.* **2012**, *3*, 856.
- [23] L. Zhang, D. Zhang, K. Yang, X. Yan, L. Wang, J. Mi, B. Xu, Y. Li, *Adv. Sci.* **2016**, *3*, 1600089.
- [24] Q. Ma, M. Guin, S. Naqash, C.-L. Tsai, F. Tietz, O. Guillon, *Chem. Mater.* **2016**, *28*, 4821.
- [25] W. S. Tang, M. Matsuo, H. Wu, V. Stavila, W. Zhou, A. A. Talin, A. V. Soloninin, R. V. Skoryunov, O. A. Babanova, A. V. Skripov, A. Unemoto, S.-I. Orimo, T. J. Udovic, *Adv. Energy Mater.* **2016**, *6*, 1502237.
- [26] F. Hiltmann, P. z. Hebel, A. Hammerschmidt, B. Krebs, *Z. Anorg. Allg. Chem.* **1993**, *619*, 293.
- [27] C. Wang, X. Bu, N. Zheng, P. Feng, *J. Am. Chem. Soc.* **2002**, *124*, 10268.
- [28] T. Sasaki, H. Takizawa, K. Uheda, T. Yamashita, T. Endo, *J. Solid State Chem.* **2002**, *166*, 164.
- [29] M. Huang, Y. P. Feng, A. T. L. Lim, J. C. Zheng, *Phys. Rev. B* **2004**, *69*, 054112.
- [30] Lasia, A. In *Modern Aspects of Electrochemistry*; Conway, B. E., Bockris, J. O. M., White, R. E., Eds.; Springer US: Boston, MA, 2002, p 143.
- [31] V. A. Balatov, A. P. Shevchenko, *Topos Professional*, 4.0, Samara State University: Samara, 2010.
- [32] A. Haffner, D. Johrendt, *Z. Anorg. Allg. Chem.* **2017**, *643*, 1717.
- [33] J. C. Bachman, S. Muy, A. Grimaud, H.-H. Chang, N. Pour, S. F. Lux, O. Paschos, F. Maglia, S. Lupart, P. Lamp, L. Giordano, Y. Shao-Horn, *Chem. Rev.* **2016**, *116*, 140.
- [34] Z. Yu, S.-L. Shang, J.-H. Seo, D. Wang, X. Luo, Q. Huang, S. Chen, J. Lu, X. Li, Z.-K. Liu, D. Wang, *Adv. Mater.* **2017**, *29*, 1605561.
- [35] M. Kaus, M. Guin, M. Yavuz, M. Knapp, F. Tietz, O. Guillon, H. Ehrenberg, S. Indris, *J. Phys. Chem. C* **2017**, *121*, 1449.
- [36] M. Guin, F. Tietz, O. Guillon, *Solid State Ion.* **2016**, *293*, 18.

-
- [37] W. G. Coors, J. H. Gordon, S. G. Menzer, US 2010/0297537 A1, 2010.
- [38] A. Hooper, *J. Phys. D: Appl. Phys.* **1977**, *10*, 1487.
- [39] S. Song, H. M. Duong, A. M. Korsunsky, N. Hu, L. Lu, *Sci. Rep.* **2016**, *6*, 32330.
- [40] Duchardt, M.; Ruschewitz, U.; Adams, S.; Dehnen, S.; Roling, B., *Angew. Chem. Int. Ed.* **2018**, *57*, 1351-1355.
- [41] Zhang, Z.; Ramos, E.; Lalere, F.; Assoud, A.; Kaup, K.; Hartman, P.; Nazar, L. F., *Energy Environ. Sci.* **2018**, *11*, 87-93.
- [42] W. S. Tang, K. Yoshida, A. V. Soloninin, R. V. Skoryunov, O. A. Babanova, A. V. Skripov, M. Dimitrievska, V. Stavila, S.-I. Orimo, T. J. Udovic, *ACS Energy Lett.* **2016**, *1*, 659.
- [43] J. R. Macdonald, W. B. Johnson, In *Impedance Spectroscopy*; John Wiley & Sons, Inc.: 2005, p 1.
- [44] J. Fleig, J. Maier, *J. Am. Ceram. Soc.* **1999**, *82*, 3485.
- [45] A. Kuhn, V. Duppel, B. V. Lotsch, *Energy Environ. Sci.* **2013**, *6*, 3548.
- [46] P. Bron, S. Johansson, K. Zick, J. Schmedt auf der Günne, S. Dehnen, B. Roling, *J. Am. Chem. Soc.* **2013**, *135*, 1569

4.3.1 Supporting Information for: Fast Sodium Ion Conductivity in Supertetrahedral Phosphidosilicates

Table of Contents

- **Experimental Section** containing synthesis, single crystal X-ray diffraction, X-ray powder diffraction, EDX and NMR spectroscopy and electrical conductivity measurements
- **Additional crystallographic data** for $\text{Na}_{19}\text{Si}_{13}\text{P}_{25}$ (Table S1), for $\text{Na}_{23}\text{Si}_{19}\text{P}_{33}$ (Table S2), for $\text{Na}_{23}\text{Si}_{28}\text{P}_{45}$ (Table S3), for $\text{Na}_{23}\text{Si}_{37}\text{P}_{57}$ (Table S4), for $\text{LT-NaSi}_2\text{P}_3$ (Table S5) and for $\text{HT-NaSi}_2\text{P}_3$ (Table S6)
- **Crystal structures** of $\text{Na}_{19}\text{Si}_{13}\text{P}_{25}$ (Figure S1 – Figure S4), $\text{Na}_{23}\text{Si}_{19}\text{P}_{33}$ (Figure S5 – Figure S8), $\text{Na}_{23}\text{Si}_{28}\text{P}_{45}$ (Figure S9 – Figure S12), $\text{Na}_{23}\text{Si}_{37}\text{P}_{57}$ (Figure S13 – Figure S16), $\text{LT-NaSi}_2\text{P}_3$ (Figure S17 – Figure S19), $\text{HT-NaSi}_2\text{P}_3$ (Figure S20 – Figure S22).
- **Rietveld refinement** of $\text{Na}_{19}\text{Si}_{13}\text{P}_{25}$ (Figure S23), of $\text{Na}_{23}\text{Si}_{19}\text{P}_{33}$ (Figure S24), of $\text{Na}_{23}\text{Si}_{28}\text{P}_{45}$ (Figure S25), of $\text{Na}_{23}\text{Si}_{37}\text{P}_{57}$ (Figure S26), of $\text{LT-NaSi}_2\text{P}_3$ (Figure S27) and of $\text{HT-NaSi}_2\text{P}_3$ (Figure S28).
- **^{29}Si and ^{31}P solid state MAS NMR** of $\text{Na}_{19}\text{Si}_{13}\text{P}_{25}$ (Figure S29), of $\text{Na}_{23}\text{Si}_{19}\text{P}_{33}$ (Figure S30), of $\text{Na}_{23}\text{Si}_{28}\text{P}_{45}$ (Figure S31), of $\text{Na}_{23}\text{Si}_{37}\text{P}_{57}$ (Figure S32), of $\text{LT-NaSi}_2\text{P}_3$ (Figure S33), of $\text{HT-NaSi}_2\text{P}_3$ (Figure S34) and ^{23}Na NMR spectra of $\text{LT-NaSi}_2\text{P}_3$ (Figure S35) and $\text{HT-NaSi}_2\text{P}_3$ (Figure S36) at various temperatures
- **Elemental analysis by EDX** and scanning electron microscopy of $\text{Na}_{19}\text{Si}_{13}\text{P}_{25}$ (Figure S37, Table S7), of $\text{Na}_{23}\text{Si}_{19}\text{P}_{33}$ (Figure S38, Table S8), of $\text{Na}_{23}\text{Si}_{28}\text{P}_{45}$ (Figure S39, Table S9), of $\text{Na}_{23}\text{Si}_{37}\text{P}_{57}$ (Figure S40, Table S10), of $\text{LT-NaSi}_2\text{P}_3$ (Figure S41, Table S11) and of $\text{HT-NaSi}_2\text{P}_3$ (Figure S42, Table S12).
- **Structural analysis of possible Na^+ migration pathways** of $\text{Na}_{19}\text{Si}_{13}\text{P}_{25}$ (Figure S43), of $\text{Na}_{23}\text{Si}_{19}\text{P}_{33}$ (Figure S44), of $\text{Na}_{23}\text{Si}_{28}\text{P}_{45}$ (Figure S45), of $\text{Na}_{23}\text{Si}_{37}\text{P}_{57}$ (Figure S46), of $\text{LT-NaSi}_2\text{P}_3$ (Figure S47) and of $\text{HT-NaSi}_2\text{P}_3$ (Figure S48).
- **Electrochemical analysis:** Determination of electronic conductivity via DC polarization experiments (Figure S49, Figure S50, Table S13), EIS spectra of all samples with equivalent circuit analysis (Figure S51 – Figure S55), low Temperature EIS of sample T5T5 (Figure S56), comparison of conductivities with samples of T4T5 and T5T5 sintered at 400 °C (Figure S57-S58).

Synthesis

Due to the sensitivity of the educts and products to air moisture all experiments and measurements were performed in an argon filled glovebox (Unilab, MBraun, $O_2 < 0.1$ ppm, $H_2O < 0.1$ ppm). All reactions were carried out in alumina crucibles welded under purified argon atmosphere in silica tubes which were placed in tube furnaces.

$Na_{23}Si_{19}P_{33}$ was synthesized by heating stoichiometric amounts of metallic Na (Alfa Aesar, 99.8 %), Si powder (Smart Elements, 99.8 %) and red phosphorus (Chempur, > 99 %) as multi-phase product. A phase-pure sample could only be prepared by using *in situ* formed 7.5 equivalents of Na_2S in addition as crystallization agent. Therefore, 41.9 mg of sodium were heated with 25.6 mg of Si, 49.0 mg P and 11.5 mg of sulfur (Merck, 99.0 %) to 100 °C (20 °C/h) before the temperature was increased to 850 °C with a 100 °C/h rate. This temperature was maintained for 40 h, slowly cooled down (10 °C/h) to 450 °C and finally quenched to room temperature. To eliminate Na_2S the sample was washed several times with dry methanol. Sorbed methanol was removed in high vacuum. ICP and elemental analysis revealed absence of sulfur, carbon, oxygen and hydrogen in the product.

$Na_{23}Si_{28}P_{45}$ was prepared by heating 19.5 mg of elemental Na with 29.0 mg Si and 51.4 mg of red phosphorus with the same temperature program to 900 °C for 60 h before the reaction was slowly cooled down to 450 °C and quenched to room temperature.

In the same way $Na_{23}Si_{37}P_{57}$ was synthesized with 31.7 mg Na, 62.4 mg Si and 105.9 mg P. The reaction time was decreased to 40 h.

$LT-NaSi_2P_3$ was obtained by reaction of stoichiometric amounts of the elements. Therefore, 26.7 mg Na, 65.3 mg Si and 108.0 mg P were reacted with the same heating protocol to 1000 °C. The reaction time was set to 40 h and the sample was cooled down with a 5 °C/h rate to 450 °C before the sample was quenched to room temperature. The multi-phased sample was ground and reheated leading to a phase-pure product.

$HT-NaSi_2P_3$ was synthesized from $LT-NaSi_2P_3$ as starting material. Therefore, $LT-NaSi_2P_3$ was ground thoroughly and filled in alumina crucibles. These were placed and welded in thick-walled silica tubes (2 mm) to withstand the high phosphorus pressure during reaction. These ampoules were welded a second time in tight-fitting silica tubes for further enhancing stability. These setups were welded a third time in larger silica tubes for sustaining an inert argon atmosphere in case of cracking of the first two tubes. This 3-layered set-up was heated to 1100 °C for 50 h before the temperature was decreased to 450 °C with 20 °C/h. In case of non-phase-pure samples this procedure was repeated.

$Na_{19}Si_{13}P_{25}$ was synthesized by reaction of 27.7 mg Na, 23.2 mg Si and 49.1 mg P not above 750 °C for 40 h. After homogenization this procedure was repeated twice.

Single-Crystal X-ray Diffraction

Suited crystals were selected under paraffin oil to prevent hydrolysis and sealed in oil filled Hilgenberg glass capillaries. Diffraction data were collected on a Bruker D8 Quest diffractometer equipped with a Photon-I detector at ambient temperatures using Mo-K α radiation ($\lambda = 0.71073$ Å). The structures were solved and refined using SHELX97.

X-ray Powder Diffraction

Polycrystalline samples were ground and sealed in Hilgenberg glass capillaries under argon atmosphere. Measurements were carried out on a Stoe Stadi-P powder diffractometer with a Stoe Mythen-1k detector and a Ge monochromator in Debye-Scherrer geometry at room temperature using Mo-K α radiation. For Rietveld refinement the Topas package was used.

EDX Measurements

Samples for energy dispersive X-ray spectroscopy were prepared by placing single crystals on conductive and adhesive carbon pads. These were inserted quickly in an EVO-Ma 10 scanning electron microscope (Zeiss) equipped with a field emission gun at an acceleration voltage not above 15 kV. For elemental analysis a Bruker X-Flash 410-M detector was used and received data were analyzed with the QUANTAX 200 software package. Signals of oxygen were not taken into account due to partial hydrolysis of the samples by short contact with air during sample insertion.

Nuclear Magnetic Resonance

^{23}Na , ^{29}Si and ^{31}P spectra of powdered samples were measured on a Bruker Avance III 500 (magnetic field of 11.74 T) under MAS conditions at Larmor frequencies of ν_0 (^{23}Na) = 132.33 MHz, ν_0 (^{29}Si) = 99.38 MHz and ν_0 (^{31}P) = 202.49 MHz and on a Bruker Avance III 400 spectrometer (magnetic field 9.4 T) at Larmor frequencies of ν_0 (^{23}Na) = 105.79 MHz, and ν_0 (^{31}P) = 161.9 MHz. For ^{23}Na and ^{29}Si spectra a zirconia rotor with 4 mm diameter with a rotation frequency of 10 kHz was used while ^{31}P spectra were recorded at a rotation frequency of 50 kHz in a 1.3 mm or at 16 kHz in a 4 mm rotor. Variable temperature ^{23}Na -T₁-relaxation time measurements were performed on stationary samples at 9.4 T in order to determine the activation energies for Na⁺-ion mobility. The temperature in the experiments was controlled using a Bruker BVT3000 temperature controller.

Electrical Conductivity Measurements

Electrochemical impedance spectroscopy and galvanostatic polarization measurements were performed with an Ivium compactstat.h (24 bit instrument) in a two-electrode setup using a home-built impedance cell which was kept under argon atmosphere during all measurements. Before measuring, the samples were ground thoroughly and compacted to a pellet of about 1 mm thickness and 5 mm in diameter by uniaxial cold pressing (500 MPa). All pellets were subsequently annealed at 400 °C for 10 h in glassy carbon crucibles under purified argon atmosphere. Additionally, pellets of *LT*- and *HT*-NaSi₂P₃ were annealed at 800 °C. After annealing, the pellets were sandwiched between indium foil (Alfa Aesar, 0.127 mm of thickness, 99.99% (metals basis)) to enhance the contact with the measuring cells. No reactions between In and the samples were observed. The applied root mean square AC voltage was between 10-100 mV with a higher voltage for the less conducting samples. The analysis of the impedance spectra was carried out by means of the RelaxIS software from rhid instruments.

Table S1: Fractional atomic coordinates and equivalent thermal displacement parameters for Na₁₉Si₁₃P₂₅.

Atom	Wyckoff Symbol	x	y	z	$U_{eq} / \text{\AA}^2$
P1	2i	0.01458 (6)	0.40324 (5)	0.08750 (6)	0.00944 (13)
P2	2i	0.01898 (6)	0.40738 (5)	0.33334 (6)	0.00977 (14)
P3	2i	0.06603 (6)	0.39863 (5)	0.72214 (6)	0.01108 (14)
P4	2i	0.09190 (6)	0.19480 (6)	0.90106 (6)	0.01401 (15)
P5	2i	0.09273 (6)	0.84754 (5)	0.44804 (6)	0.01190 (14)
P6	2i	0.09714 (6)	0.20479 (6)	0.38150 (6)	0.01707 (16)
P7	2i	0.09879 (6)	0.19435 (5)	0.13958 (6)	0.01121 (14)
P8	2i	0.16207 (6)	0.86078 (5)	0.09007 (6)	0.01244 (14)
P9	2i	0.20224 (6)	0.66644 (5)	0.27243 (6)	0.01208 (14)
P10	2i	0.21058 (6)	0.66610 (5)	0.51667 (6)	0.01350 (15)
P11	2i	0.24343 (6)	0.10719 (6)	0.65492 (6)	0.01319 (15)
P12	2i	0.27725 (6)	0.47032 (5)	0.08499 (6)	0.01219 (14)
P13	2i	0.28883 (6)	0.46665 (5)	0.32396 (6)	0.00999 (14)
P14	2i	0.28999 (6)	0.47568 (6)	0.56498 (6)	0.01341 (15)
P15	2i	0.29307 (7)	0.03026 (6)	0.45126 (7)	0.02120 (17)
P16	2i	0.32741 (6)	0.12727 (6)	0.81610 (6)	0.01409 (15)
P17	2i	0.36479 (6)	0.25813 (6)	0.13539 (6)	0.01587 (15)
P18	2i	0.36825 (7)	0.26292 (6)	0.37097 (6)	0.01765 (16)
P19	2i	0.39249 (7)	0.31518 (6)	0.63087 (6)	0.01975 (17)
P20	2i	0.40919 (6)	0.92806 (6)	0.07004 (6)	0.01578 (15)
P21	2i	0.54715 (6)	0.18329 (6)	0.74298 (7)	0.01851 (16)
P22	2i	0.60352 (7)	0.07942 (6)	0.35375 (7)	0.02150 (18)
P23	2i	0.63984 (6)	0.70444 (6)	0.08421 (6)	0.01508 (15)
P24	2i	0.75099 (6)	0.34971 (5)	0.09819 (6)	0.01165 (14)
P25	2i	0.83748 (6)	0.14530 (6)	0.15687 (6)	0.01396 (15)
Si1	2i	0.01372 (6)	0.23632 (6)	0.01382 (6)	0.00987 (15)
Si2	2i	0.01582 (6)	0.24037 (6)	0.25335 (6)	0.01051 (15)
Si3	2i	0.06867 (6)	0.56140 (6)	0.80125 (6)	0.00906 (14)
Si4	2i	0.11596 (6)	0.68960 (6)	0.37850 (6)	0.00949 (14)
Si5	2i	0.19563 (6)	0.50146 (6)	0.19387 (6)	0.00951 (14)

Si6	2i	0.20057 (6)	0.50221 (6)	0.43162 (6)	0.00963 (15)
Si7	2i	0.26786 (6)	0.30258 (6)	0.01348 (6)	0.01106 (15)
Si8	2i	0.27666 (6)	0.30601 (6)	0.47594 (6)	0.01229 (15)
Si9	2i	0.27760 (6)	0.29624 (6)	0.24260 (6)	0.01096 (15)
Si10	2i	0.37785 (7)	0.16812 (6)	0.62228 (6)	0.01348 (16)
Si11	2i	0.47959 (6)	0.08361 (6)	0.78751 (6)	0.01181 (15)
Si12	2i	0.73841 (6)	0.04345 (6)	0.46084 (6)	0.01272 (16)
Si13	2i	0.76065 (6)	0.18502 (6)	0.02698 (6)	0.01027 (15)
Na1	2i	0.0267 (2)	0.01173 (14)	0.1628 (2)	0.0705 (7)
Na2	2i	0.04089 (12)	0.38378 (11)	0.52204 (11)	0.0301 (3)
Na3	2i	0.04727 (11)	0.40635 (10)	0.90900 (10)	0.0223 (3)
Na4	2i	0.06619 (13)	0.07026 (14)	0.45236 (14)	0.0401 (4)
Na5	2i	0.12204 (11)	0.23224 (11)	0.74648 (11)	0.0260 (3)
Na6	2i	0.14254 (12)	0.84154 (10)	0.26631 (11)	0.0280 (3)
Na7	2i	0.2225 (2)	0.04768 (18)	0.0657 (3)	0.0923 (9)
Na8	2i	0.22733 (11)	0.67618 (11)	0.09566 (11)	0.0250 (3)
Na9	2i	0.28106 (17)	0.4316 (2)	0.7492 (2)	0.0942 (10)
Na10	2i	0.35285 (16)	0.03557 (15)	0.29066 (15)	0.0560 (5)
Na11	2i	0.3716 (2)	0.0228 (2)	0.9399 (2)	0.0957 (10)
Na12	2i	0.45184 (16)	0.61703 (13)	0.10586 (18)	0.0565 (6)
Na13	2i	0.47376 (11)	0.48149 (10)	0.26437 (11)	0.0255 (3)
Na14	2i	0.53550 (11)	0.26049 (12)	0.05804 (12)	0.0308 (3)
Na15	2i	0.55155 (14)	0.24492 (17)	0.31718 (17)	0.0543 (5)
Na16	2i	0.57862 (16)	0.27835 (19)	0.55815 (16)	0.0723 (7)
Na17	2i	0.79415 (11)	0.35190 (11)	0.30292 (11)	0.0260 (3)
Na18	2i	0.82125 (16)	0.13804 (13)	0.33876 (13)	0.0410 (4)
Na19	1h	0.5000	0.5000	0.5000	0.0416 (6)
Na20	1f	0.5000	0.0000	0.5000	0.1154 (17)

Table S2: Fractional atomic coordinates and equivalent thermal displacement parameters for Na₂₃Si₁₉P₃₃.

Atom	Wyckoff Symbol	x	y	z	U _{eq} / Å ²
------	----------------	---	---	---	----------------------------------

P1	<i>8f</i>	0.03955 (2)	0.15532 (3)	0.37825 (3)	0.00793 (8)
P2	<i>8f</i>	0.05030 (2)	0.01206 (3)	0.70661 (3)	0.01035 (8)
P3	<i>8f</i>	0.05506 (2)	0.31232 (3)	0.18660 (3)	0.00952 (8)
P4	<i>8f</i>	0.06946 (2)	0.12786 (3)	0.02366 (3)	0.00879 (8)
P5	<i>8f</i>	0.13005 (2)	0.32656 (3)	0.43414 (3)	0.01223 (9)
P6	<i>8f</i>	0.14407 (2)	0.14300 (3)	0.28316 (3)	0.00896 (8)
P7	<i>8f</i>	0.15488 (2)	0.46589 (3)	0.22467 (3)	0.01142 (8)
P8	<i>8f</i>	0.15907 (2)	0.03346 (3)	0.62597 (3)	0.01082 (8)
P9	<i>8f</i>	0.16619 (2)	0.28639 (3)	0.08012 (3)	0.00906 (8)
P10	<i>8f</i>	0.23986 (2)	0.29527 (3)	0.32908 (3)	0.01212 (8)
P11	<i>8f</i>	0.25401 (2)	0.12992 (3)	0.18687 (3)	0.01066 (8)
P12	<i>8f</i>	0.26971 (2)	0.03255 (3)	0.52006 (3)	0.01014 (8)
P13	<i>8f</i>	0.31871 (2)	0.38843 (3)	0.06780 (3)	0.01039 (8)
P14	<i>8f</i>	0.40578 (2)	0.23744 (3)	0.17508 (3)	0.01102 (8)
P15	<i>8f</i>	0.42349 (2)	0.05755 (3)	0.01435 (3)	0.01212 (8)
P16	<i>8f</i>	0.51752 (2)	0.21912 (3)	0.06869 (3)	0.01310 (9)
P17	<i>4e</i>	0.0000	0.57416 (4)	0.2500	0.01032 (11)
Si1	<i>8f</i>	0.02039 (2)	0.22291 (3)	0.06892 (3)	0.00842 (8)
Si2	<i>8f</i>	0.09293 (2)	0.23920 (3)	0.31918 (3)	0.00841 (8)
Si3	<i>8f</i>	0.10758 (2)	0.05954 (3)	0.15971 (3)	0.00830 (8)
Si4	<i>8f</i>	0.11343 (2)	0.37471 (3)	0.12073 (3)	0.00864 (8)
Si5	<i>8f</i>	0.18720 (2)	0.38782 (3)	0.35964 (3)	0.00918 (8)
Si6	<i>8f</i>	0.19828 (2)	0.21351 (3)	0.21704 (3)	0.00829 (8)
Si7	<i>8f</i>	0.21425 (2)	0.04378 (3)	0.07195 (3)	0.00824 (8)
Si8	<i>8f</i>	0.37337 (2)	0.30197 (3)	0.03399 (3)	0.00830 (8)
Si9	<i>8f</i>	0.45934 (2)	0.15359 (3)	0.12455 (3)	0.00915 (9)
Si10	<i>4e</i>	0.0000	0.07676 (4)	0.2500	0.00788 (11)
Na1	<i>8f</i>	0.00984 (4)	0.42050 (7)	0.43871 (9)	0.0469 (3)
Na2	<i>8f</i>	0.07756 (3)	0.45655 (6)	0.31513 (7)	0.0306 (2)
Na3	<i>8f</i>	0.08375 (4)	0.15390 (6)	0.61137 (10)	0.0423 (3)
Na4	<i>8f</i>	0.10975 (3)	0.00853 (5)	0.40551 (6)	0.02455 (18)
Na5	<i>8f</i>	0.20040 (3)	0.17476 (6)	0.48032 (7)	0.0325 (2)

Na6	8f	0.25706 (4)	0.46335 (7)	0.19478 (8)	0.0387 (2)
Na7	8f	0.30261 (5)	0.12549 (9)	0.38452 (7)	0.0545 (4)
Na8	8f	0.31528 (4)	0.29047 (7)	0.22881 (8)	0.0399 (3)
Na9	8f	0.33663 (3)	0.09645 (5)	0.09127 (7)	0.02456 (18)
Na10	8f	0.41582 (4)	0.09643 (8)	0.34842 (11)	0.0549 (3)
Na11	4e	0.0000	0.83159 (8)	0.2500	0.0347 (3)
Na12	4c	0.2500	0.2500	0.0000	0.0253 (3)
Na13	4a	0.0000	0.0000	0.0000	0.0299 (3)

Table S3: Fractional atomic coordinates, equivalent thermal displacement parameters and occupation factors for Na₂₃Si₂₈P₄₅.

Atom	Wyckoff Symbol	x	y	z	U_{eq} / Å²	Occ.
P1	4e	0.04883 (10)	0.35598 (8)	0.09089 (10)	0.0084 (4)	1
P2	4e	0.05016 (10)	0.22378 (8)	0.42543 (10)	0.0093 (4)	1
P3	4e	0.05031 (10)	0.28771 (8)	0.25308 (9)	0.0085 (4)	1
P4	4e	0.05978 (10)	0.19749 (8)	0.08731 (10)	0.0097 (4)	1
P5	4e	0.06276 (10)	0.06004 (8)	0.44000 (10)	0.0105 (4)	1
P6	4e	0.06865 (10)	0.13087 (8)	0.26911 (10)	0.0116 (4)	1
P7	4e	0.07594 (10)	0.46296 (8)	0.37115 (10)	0.0119 (4)	1
P8	4e	0.07846 (10)	0.52716 (8)	0.78782 (10)	0.0098 (4)	1
P9	4e	0.08117 (10)	0.04650 (8)	0.11113 (10)	0.0105 (4)	1
P10	4e	0.08404 (10)	0.60512 (8)	0.62225 (10)	0.0106 (4)	1
P11	4e	0.08853 (10)	0.54334 (8)	0.21086 (10)	0.0104 (4)	1
P12	4e	0.08913 (10)	0.61637 (8)	0.38891 (10)	0.0105 (4)	1
P13	4e	0.10081 (10)	0.70438 (8)	0.22576 (10)	0.0098 (4)	1
P14	4e	0.10573 (10)	0.63855 (9)	0.05724 (10)	0.0156 (4)	1
P15	4e	0.10728 (10)	0.77224 (8)	0.40038 (10)	0.0115 (4)	1
P16	4e	0.21091 (10)	0.29997 (8)	0.40604 (10)	0.0111 (4)	1
P17	4e	0.21337 (10)	0.36117 (8)	0.23933 (9)	0.0100 (4)	1
P18	4e	0.21774 (10)	0.43154 (8)	0.08746 (10)	0.0119 (4)	1
P19	4e	0.21979 (10)	0.27630 (8)	0.07612 (9)	0.0088 (4)	1
P20	4e	0.22641 (10)	0.21109 (8)	0.24893 (10)	0.0105 (4)	1

P21	4e	0.22744 (10)	0.14589 (8)	0.42384 (10)	0.0093 (4)	1
P22	4e	0.23206 (10)	0.82144 (8)	0.11358 (10)	0.0113 (4)	1
P23	4e	0.23235 (11)	0.12647 (8)	0.08648 (10)	0.0141 (4)	1
P24	4e	0.24023 (10)	0.52865 (8)	0.37062 (10)	0.0120 (4)	1
P25	4e	0.24607 (10)	0.05954 (8)	0.27299 (10)	0.0101 (4)	1
P26	4e	0.25028 (10)	0.52317 (8)	0.61460 (9)	0.0089 (4)	1
P27	4e	0.25173 (10)	0.61303 (9)	0.20326 (10)	0.0130 (4)	1
P28	4e	0.42123 (11)	0.45642 (8)	0.38215 (10)	0.0135 (4)	1
P29	4e	0.42443 (10)	0.05096 (8)	0.13224 (10)	0.0129 (4)	1
P30	4e	0.44436 (10)	0.37275 (8)	0.23081 (10)	0.0094 (4)	1
P31	4e	0.44894 (11)	0.31107 (8)	0.41121 (11)	0.0152 (4)	1
P32	4e	0.45026 (13)	0.43602 (9)	0.05848 (11)	0.0234 (5)	1
P33	4e	0.45901 (11)	0.15397 (8)	0.41492 (10)	0.0124 (4)	1
P34	4e	0.46174 (10)	0.27614 (8)	0.08455 (10)	0.0123 (4)	1
P35	4e	0.46362 (10)	0.21997 (8)	0.25527 (10)	0.0118 (4)	1
P36	4e	0.57883 (10)	0.02647 (8)	0.29780 (10)	0.0128 (4)	1
P37	4e	0.59681 (10)	0.10951 (8)	0.13809 (10)	0.0128 (4)	1
P38	4e	0.59978 (10)	0.46783 (8)	0.21074 (11)	0.0133 (4)	1
P39	4e	0.60104 (10)	0.39557 (8)	0.39182 (10)	0.0098 (4)	1
P40	4e	0.62070 (10)	0.30455 (8)	0.23249 (10)	0.0101 (4)	1
P41	4e	0.62233 (12)	0.36706 (10)	0.06104 (11)	0.0234 (5)	1
P42	4e	0.62357 (10)	0.23825 (8)	0.40919 (10)	0.0137 (4)	1
P43	4e	0.74562 (10)	0.18943 (8)	0.12546 (10)	0.0112 (4)	1
P44	4e	0.76399 (10)	0.48823 (8)	0.05891 (10)	0.0117 (4)	1
P45	4e	0.76724 (10)	0.39730 (8)	0.21428 (10)	0.0085 (4)	1
Si1	4e	0.01117 (10)	0.27316 (8)	0.13186 (10)	0.0088 (4)	1
Si2	4e	0.01202 (10)	0.14220 (9)	0.46790 (10)	0.0100 (4)	1
Si3	4e	0.01827 (10)	0.20960 (9)	0.30542 (10)	0.0101 (4)	1
Si4	4e	0.03003 (11)	0.05308 (9)	0.31959 (10)	0.0104 (4)	1
Si5	4e	0.03012 (10)	0.12333 (8)	0.14691 (11)	0.0101 (4)	1
Si6	4e	0.04200 (10)	0.52868 (8)	0.66480 (10)	0.0096 (4)	1
Si7	4e	0.12365 (10)	0.53941 (8)	0.33356 (10)	0.0093 (4)	1

Si8	4e	0.13538 (10)	0.62460 (9)	0.17537 (10)	0.0098 (4)	1
Si9	4e	0.13635 (10)	0.69416 (8)	0.34740 (10)	0.0091 (4)	1
Si10	4e	0.17152 (10)	0.35304 (8)	0.12048 (10)	0.0082 (4)	1
Si11	4e	0.17179 (10)	0.22445 (8)	0.45367 (10)	0.0089 (4)	1
Si12	4e	0.17239 (10)	0.28665 (8)	0.28746 (10)	0.0084 (4)	1
Si13	4e	0.18126 (11)	0.19865 (8)	0.12714 (10)	0.0096 (4)	1
Si14	4e	0.18490 (10)	0.06703 (8)	0.46854 (10)	0.0092 (4)	1
Si15	4e	0.19017 (11)	0.13606 (8)	0.30291 (10)	0.0100 (4)	1
Si16	4e	0.20287 (10)	0.05641 (8)	0.15101 (10)	0.0089 (4)	1
Si17	4e	0.20364 (10)	0.59919 (8)	0.66226 (10)	0.0091 (4)	1
Si18	4e	0.28263 (10)	0.60654 (8)	0.32513 (10)	0.0097 (4)	1
Si19	4e	0.47969 (10)	0.45022 (8)	0.17799 (10)	0.0105 (4)	1
Si20	4e	0.47986 (10)	0.38363 (8)	0.35190 (10)	0.0091 (4)	1
Si21	4e	0.49953 (10)	0.29424 (8)	0.20154 (10)	0.0088 (4)	1
Si22	4e	0.50095 (11)	0.35295 (9)	0.03556 (10)	0.0115 (4)	1
Si23	4e	0.50282 (10)	0.23432 (9)	0.37560 (10)	0.0104 (4)	1
Si24	4e	0.54501 (10)	0.03195 (8)	0.17517 (10)	0.0103 (4)	1
Si25	4e	0.62693 (10)	0.47416 (9)	0.33374 (11)	0.0117 (4)	1
Si26	4e	0.64515 (10)	0.38579 (9)	0.17841 (11)	0.0118 (4)	1
Si27	4e	0.64830 (10)	0.31588 (8)	0.35388 (10)	0.0099 (4)	1
Si28	4e	0.79975 (10)	0.48338 (8)	0.17803 (10)	0.0091 (4)	1
Na1	4e	0.07943 (18)	0.41807 (14)	0.23327 (18)	0.0280 (8)	1
Na2	4e	0.0949 (2)	0.36334 (16)	0.4564 (2)	0.0437 (10)	1
Na3	4e	0.0961 (2)	0.77335 (17)	0.0458 (2)	0.0413 (10)	1
Na4	4e	0.0969 (4)	0.5110 (3)	0.0654 (3)	0.086 (3)	0.800 (13)
Na5	4e	0.0980 (2)	0.53262 (15)	0.50053 (18)	0.0463 (11)	1
Na6	4e	0.10046 (19)	0.83248 (16)	0.2586 (2)	0.0408 (10)	1
Na7	4e	0.25194 (17)	0.73749 (14)	0.23042 (18)	0.0310 (8)	1
Na8	4e	0.2840 (3)	0.4096 (2)	0.4035 (4)	0.100 (2)	1
Na9	4e	0.2852 (3)	0.5481 (3)	0.0910 (3)	0.056 (2)	0.793 (12)
Na10	4e	0.2957 (2)	0.47480 (17)	0.2446 (2)	0.0429 (10)	1
Na11	4e	0.34425 (16)	0.36148 (14)	0.08820 (17)	0.0252 (7)	1

Na12	4e	0.34683 (16)	0.29341 (14)	0.27121 (19)	0.0289 (8)	1
Na13	4e	0.35073 (16)	0.23080 (14)	0.44277 (18)	0.0261 (7)	1
Na14	4e	0.3680 (3)	0.0408 (3)	0.4160 (2)	0.103 (2)	1
Na15	4e	0.3718 (3)	0.1792 (2)	0.1274 (3)	0.088 (3)	0.953 (14)
Na16	4e	0.4355 (2)	0.09648 (16)	0.27678 (19)	0.0462 (11)	1
Na17	4e	0.4749 (3)	0.1137 (4)	0.0232 (4)	0.133 (4)	0.905 (14)
Na18	4e	0.5516 (3)	0.0560 (2)	0.4467 (3)	0.0531 (19)	0.868 (12)
Na19	4e	0.5908 (2)	0.2239 (2)	0.0539 (2)	0.0579 (13)	1
Na20	4e	0.5947 (5)	0.0273 (3)	0.0052 (3)	0.160 (4)	1
Na21	4e	0.59964 (19)	0.16202 (17)	0.2787 (2)	0.0406 (10)	1
Na22	4e	0.7366 (2)	0.2933 (2)	0.0295 (3)	0.0667 (14)	1
Na23	4e	0.74298 (19)	0.11380 (15)	0.00752 (16)	0.0316 (8)	1
Na24	4e	0.8864 (4)	0.4058 (4)	0.0773 (4)	0.092 (4)	0.680 (13)

Table S4: Fractional atomic coordinates, equivalent thermal displacement parameters and occupation factors for Na₂₃Si₃₇P₅₇.

Atom	Wyckoff Symbol	x	y	z	U_{eq} / Å²	Occ.
P1	8f	0.01693 (3)	0.15717 (5)	0.11897 (5)	0.01517 (17)	1
P2	8f	0.04189 (3)	0.42413 (5)	0.22558 (5)	0.01250 (16)	1
P3	8f	0.05413 (3)	0.12541 (5)	0.57707 (5)	0.01111 (16)	1
P4	8f	0.06201 (3)	0.30447 (5)	0.45991 (5)	0.01124 (16)	1
P5	8f	0.07898 (3)	0.16570 (5)	0.32672 (5)	0.01306 (17)	1
P6	8f	0.12913 (3)	0.40501 (5)	0.17870 (5)	0.01371 (17)	1
P7	8f	0.13552 (3)	0.03067 (5)	0.12583 (5)	0.01409 (17)	1
P8	8f	0.13989 (3)	0.54150 (5)	0.04112 (5)	0.01090 (15)	1
P9	8f	0.14781 (3)	0.14320 (5)	0.51777 (5)	0.01174 (16)	1
P10	8f	0.15507 (3)	0.31414 (5)	0.40911 (5)	0.01427 (17)	1
P11	8f	0.19849 (3)	0.04481 (5)	0.31944 (5)	0.00961 (15)	1
P12	8f	0.20089 (3)	0.21504 (5)	0.20782 (5)	0.01607 (18)	1
P13	8f	0.21270 (3)	0.38816 (5)	0.10741 (5)	0.00995 (15)	1
P14	8f	0.26952 (3)	0.03842 (5)	0.51590 (5)	0.01371 (17)	1
P15	8f	0.27351 (3)	0.20265 (5)	0.39862 (5)	0.01146 (16)	1

P16	<i>8f</i>	0.28048 (3)	0.37781 (5)	0.29646 (5)	0.01063 (15)	1
P17	<i>8f</i>	0.28532 (3)	0.05426 (5)	0.25675 (5)	0.01168 (16)	1
P18	<i>8f</i>	0.29100 (3)	0.22954 (5)	0.15188 (5)	0.01225 (16)	1
P19	<i>8f</i>	0.30316 (3)	0.39313 (5)	0.04463 (5)	0.01337 (17)	1
P20	<i>8f</i>	0.36481 (3)	0.21687 (5)	0.34297 (5)	0.01444 (17)	1
P21	<i>8f</i>	0.37467 (3)	0.07657 (5)	0.20201 (5)	0.01214 (16)	1
P22	<i>8f</i>	0.37472 (3)	0.39257 (5)	0.23414 (5)	0.01053 (15)	1
P23	<i>8f</i>	0.38392 (3)	0.25129 (5)	0.09558 (5)	0.01484 (17)	1
P24	<i>8f</i>	0.43493 (3)	0.49417 (5)	0.06067 (5)	0.01295 (16)	1
P25	<i>8f</i>	0.45776 (3)	0.24491 (5)	0.28523 (5)	0.01070 (16)	1
P26	<i>8f</i>	0.46157 (2)	0.08715 (5)	0.15020 (5)	0.00935 (15)	1
P27	<i>8f</i>	0.47103 (3)	0.22644 (6)	0.02029 (5)	0.01629 (18)	1
P28	<i>8f</i>	0.55020 (3)	0.06558 (5)	0.09656 (5)	0.01077 (15)	1
P29	<i>4e</i>	0.0000	0.00960 (7)	0.2500	0.0117 (2)	1
Si1	<i>8f</i>	0.01909 (3)	0.21413 (5)	0.48636 (5)	0.01033 (17)	1
Si2	<i>8f</i>	0.03180 (3)	0.08765 (5)	0.35114 (5)	0.01087 (17)	1
Si3	<i>8f</i>	0.08869 (3)	0.49821 (5)	0.20108 (5)	0.00987 (16)	1
Si4	<i>8f</i>	0.10159 (3)	0.06058 (5)	0.54088 (5)	0.01053 (17)	1
Si5	<i>8f</i>	0.10984 (3)	0.23162 (5)	0.43004 (5)	0.01066 (17)	1
Si6	<i>8f</i>	0.17461 (3)	0.47570 (5)	0.14800 (5)	0.01056 (17)	1
Si7	<i>8f</i>	0.24204 (3)	0.13244 (5)	0.29262 (5)	0.01021 (17)	1
Si8	<i>8f</i>	0.24838 (3)	0.29941 (5)	0.19697 (5)	0.01021 (17)	1
Si9	<i>8f</i>	0.26161 (3)	0.46607 (5)	0.08426 (5)	0.00984 (16)	1
Si10	<i>8f</i>	0.31321 (3)	0.11788 (5)	0.48831 (5)	0.01067 (17)	1
Si11	<i>8f</i>	0.31922 (3)	0.28811 (5)	0.37891 (5)	0.01162 (17)	1
Si12	<i>8f</i>	0.32953 (3)	0.45776 (5)	0.27655 (5)	0.00987 (16)	1
Si13	<i>8f</i>	0.32976 (3)	0.14542 (6)	0.24110 (6)	0.01592 (19)	1
Si14	<i>8f</i>	0.33913 (3)	0.31402 (5)	0.13598 (5)	0.01091 (17)	1
Si15	<i>8f</i>	0.40218 (3)	0.13296 (5)	0.43502 (5)	0.01084 (17)	1
Si16	<i>8f</i>	0.41004 (3)	0.30473 (5)	0.32247 (5)	0.01046 (17)	1
Si17	<i>8f</i>	0.41922 (3)	0.16965 (5)	0.18642 (5)	0.01036 (17)	1
Si18	<i>8f</i>	0.50871 (3)	0.16094 (5)	0.12029 (5)	0.00958 (16)	1

Si19	4e	0.0000	0.51187 (7)	0.2500	0.0090 (2)	1
Na1	8f	0.01769 (9)	0.40109 (14)	0.06994 (12)	0.0668 (8)	1
Na2	8f	0.07005 (6)	0.03221 (12)	0.19818 (12)	0.0431 (5)	1
Na3	8f	0.09140 (6)	0.43808 (11)	0.37815 (10)	0.0370 (4)	1
Na4	8f	0.10071 (18)	0.1613 (3)	0.0268 (2)	0.0661 (19)	0.512 (6)
Na5	8f	0.10649 (19)	0.2521 (2)	0.2278 (2)	0.159 (2)	1
Na6	8f	0.11016 (16)	0.3703 (3)	0.0134 (3)	0.0234 (15)	0.311 (5)
Na7	8f	0.13314 (6)	0.01924 (11)	0.39139 (10)	0.0325 (4)	1
Na8	8f	0.19901 (7)	0.3849 (2)	0.32441 (13)	0.0879 (11)	1
Na9	8f	0.21036 (8)	0.17317 (14)	0.45686 (16)	0.0338 (9)	0.681 (6)
Na10	8f	0.21516 (7)	0.0676 (2)	0.10465 (12)	0.0798 (10)	1
Na11	8f	0.2289 (2)	0.2790 (3)	0.0011 (3)	0.0491 (19)	0.373 (5)
Na12	8f	0.31971 (17)	0.1162 (3)	0.0490 (2)	0.0825 (19)	0.627 (5)
Na13	8f	0.46411 (7)	0.35697 (12)	0.15271 (14)	0.0580 (7)	1
Na14	4e	0.0000	0.26391 (16)	0.2500	0.0526 (9)	1
Na15	4a	0.0000	0.0000	0.0000	0.0602 (10)	1

Table S5: Fractional atomic coordinates, equivalent thermal displacement parameters and occupation factors for LT-NaSi₂P₃.

Atom	Wyckoff Symbol	x	y	z	$U_{eq} / \text{\AA}^2$	Occ.
P1	16f	0.00325 (3)	0.01532 (3)	0.37758 (2)	0.01224 (11)	1
P2	16f	0.00358 (3)	0.38033 (3)	0.54724 (2)	0.00993 (10)	1
P3	16f	0.00721 (3)	0.03856 (3)	0.23647 (2)	0.00943 (10)	1
P4	16f	0.01871 (3)	0.04359 (3)	0.08615 (2)	0.00902 (10)	1
P5	16f	0.03762 (3)	0.16844 (3)	0.31112 (2)	0.01389 (11)	1
P6	16f	0.04085 (3)	0.17886 (3)	0.15817 (2)	0.00933 (10)	1
P7	16f	0.05092 (3)	0.16632 (3)	0.01303 (2)	0.00940 (10)	1
P8	16f	0.13319 (3)	0.12702 (3)	0.47610 (2)	0.00870 (10)	1
P9	16f	0.13438 (3)	0.11468 (3)	0.62674 (2)	0.00955 (10)	1
P10	16f	0.13934 (3)	0.25710 (3)	0.54859 (2)	0.00930 (10)	1
P11	16f	0.14063 (3)	0.01387 (3)	0.30778 (2)	0.00861 (10)	1
P12	16f	0.14527 (3)	0.01024 (3)	0.15893 (2)	0.01001 (10)	1

P13	16f	0.17502 (3)	0.14498 (3)	0.23887 (2)	0.01132 (11)	1
P14	16f	0.17546 (3)	0.13397 (3)	0.08557 (2)	0.00946 (10)	1
P15	16f	0.25992 (3)	0.52668 (3)	0.01774 (2)	0.01302 (11)	1
P16	16f	0.30116 (3)	0.11249 (3)	0.16167 (2)	0.01190 (11)	1
P17	16f	0.33771 (3)	0.23282 (3)	0.09083 (2)	0.01218 (11)	1
P18	16f	0.38099 (3)	0.01062 (3)	0.04924 (2)	0.01225 (11)	1
P19	8e	0.0000	0.2500	0.47272 (2)	0.01457 (16)	1
P20	4b	0.0000	0.2500	0.6250	0.0099 (2)	1
Si1	16f	0.06067 (3)	0.05602 (3)	0.58814 (2)	0.00907 (11)	1
Si2	16f	0.06513 (3)	0.19330 (3)	0.51356 (2)	0.00877 (11)	1
Si3	16f	0.06841 (3)	0.31626 (3)	0.58676 (2)	0.00822 (10)	1
Si4	16f	0.08716 (3)	0.09475 (3)	0.27131 (2)	0.00936 (11)	1
Si5	16f	0.09351 (3)	0.09493 (3)	0.12600 (2)	0.00871 (11)	1
Si6	16f	0.12232 (3)	0.21737 (3)	0.19787 (2)	0.00885 (11)	1
Si7	16f	0.12669 (3)	0.21960 (3)	0.05214 (2)	0.00849 (11)	1
Si8	16f	0.19079 (3)	0.05443 (3)	0.51645 (2)	0.00890 (11)	1
Si9	16f	0.19761 (3)	0.18680 (3)	0.58965 (2)	0.00892 (11)	1
Si10	16f	0.22072 (3)	0.06613 (3)	0.19805 (2)	0.01003 (11)	1
Si11	16f	0.25150 (3)	0.18830 (3)	0.12403 (2)	0.00894 (11)	1
Si12	16f	0.28548 (3)	0.30974 (3)	0.05497 (2)	0.00886 (11)	1
Si13	8e	0.0000	0.2500	0.27198 (2)	0.00908 (15)	1
Na1	16f	0.0250 (4)	0.0138 (3)	0.4822 (2)	0.102 (4)	0.242 (3)
Na2	16f	0.0430 (7)	0.1622 (3)	0.39636 (12)	0.075 (5)	0.422 (17)
Na3	16f	0.0957 (10)	0.1333 (7)	0.3854 (3)	0.089 (7)	0.272 (13)
Na4	16f	0.1384 (2)	0.0420 (2)	0.02678 (14)	0.0406 (18)	0.254 (4)
Na5	16f	0.15773 (7)	0.25349 (7)	0.30840 (5)	0.0626 (5)	1
Na6	16f	0.26924 (6)	0.01225 (6)	0.10398 (4)	0.0406 (3)	1
Na7	16f	0.35642 (13)	0.14604 (7)	0.02307 (4)	0.1003 (8)	1
Na8	16f	0.38552 (13)	0.50341 (10)	0.06227 (8)	0.1031 (13)	0.758 (3)
Na9	16f	0.41983 (6)	0.05155 (8)	0.19151 (4)	0.0545 (4)	1
Na10	16f	0.4789 (9)	0.1597 (6)	0.1019 (3)	0.130 (6)	0.300 (11)

Table S6: Fractional atomic coordinates, equivalent thermal displacement parameters and occupation factors for HT-NaSi₂P₃.

Atom	Wyckoff Symbol	x	y	z	$U_{eq} / \text{\AA}^2$	Occ.
P1	32g	0.03874 (4)	0.06180 (4)	0.15553 (2)	0.0178 (2)	1
P2	32g	0.03979 (4)	0.05999 (4)	0.27855 (2)	0.01323 (19)	1
P3	32g	0.05032 (4)	0.19243 (4)	0.34671 (2)	0.01272 (18)	1
P4	32g	0.06298 (4)	0.19718 (4)	0.03587 (2)	0.0180 (2)	1
P5	32g	0.06831 (4)	0.31159 (4)	0.27854 (2)	0.01276 (18)	1
P6	32g	0.17881 (4)	0.18301 (4)	0.27740 (2)	0.01355 (18)	1
P7	32g	0.18592 (4)	0.08157 (4)	0.03437 (2)	0.01254 (18)	1
P8	32g	0.19673 (4)	0.32806 (4)	0.15752 (2)	0.01589 (19)	1
P9	32g	0.29607 (4)	0.05675 (4)	0.28044 (2)	0.01653 (19)	1
P10	32g	0.30377 (4)	0.07723 (4)	0.09519 (2)	0.01317 (18)	1
P11	32g	0.31183 (4)	0.19693 (4)	0.15923 (2)	0.01251 (18)	1
P12	32g	0.42365 (4)	0.06857 (4)	0.15775 (2)	0.01241 (18)	1
Si1	32g	0.11182 (4)	0.12280 (4)	0.37412 (2)	0.01161 (19)	1
Si2	32g	0.11842 (4)	0.24176 (4)	0.31211 (2)	0.01186 (19)	1
Si3	32g	0.12577 (4)	0.14470 (4)	0.00126 (2)	0.01303 (19)	1
Si4	32g	0.25008 (4)	0.14925 (4)	0.06338 (2)	0.01259 (19)	1
Si5	32g	0.25633 (4)	0.26490 (4)	0.12595 (2)	0.01227 (19)	1
Si6	32g	0.36738 (4)	0.01595 (4)	0.06165 (2)	0.01337 (19)	1
Si7	32g	0.37964 (4)	0.25719 (4)	0.06314 (2)	0.01160 (19)	1
Si8	16e	0.22772 (6)	0.0000	0.2500	0.0145 (3)	1
Si9	16d	0.0000	0.2500	0.00172 (3)	0.0127 (2)	1
Na1	32g	0.0206 (6)	0.0618 (3)	0.0435 (3)	0.093 (4)	0.532 (15)
Na2	32g	0.1568 (5)	0.0699 (5)	0.1127 (2)	0.093 (5)	0.323 (7)
Na3	32g	0.1634 (2)	0.30810 (16)	0.04093 (11)	0.1387 (19)	1
Na4	32g	0.1716 (4)	0.2749 (6)	0.2217 (2)	0.076 (4)	0.456 (15)
Na5	32g	0.3155 (2)	0.0374 (2)	0.36036 (12)	0.0614 (13)	0.5
Na6	32g	0.31554 (16)	0.08682 (16)	0.20814 (9)	0.0586 (12)	0.688 (7)
Na7	16f	0.0467 (6)	0.2967 (6)	0.1250	0.190 (11)	0.423 (14)
Na8	16f	0.4384 (4)	0.6884 (4)	0.1250	0.229 (10)	0.577 (14)

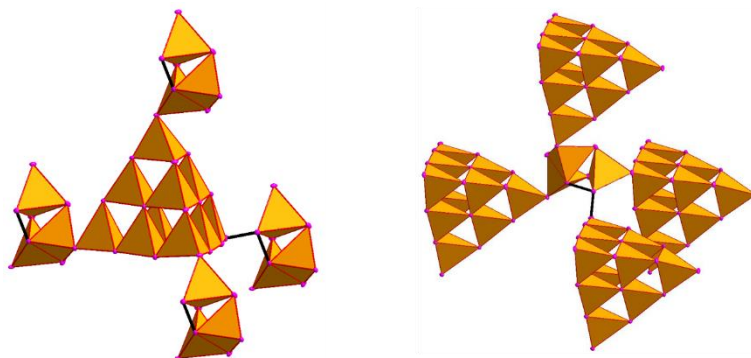


Figure S1: Building units of $\text{Na}_{19}\text{Si}_{13}\text{P}_{25}$ consisting of T3 supertetrahedral clusters and Si_3P_8 entities. Three Si_3P_8 units are connected with a T3 tetrahedron by common vertices. The fourth supertetrahedral vertex is linked to another Si_3P_8 entity by one P–P single bond (left). The connection of four T3 tetrahedra to one Si_3P_8 unit is similar (right).

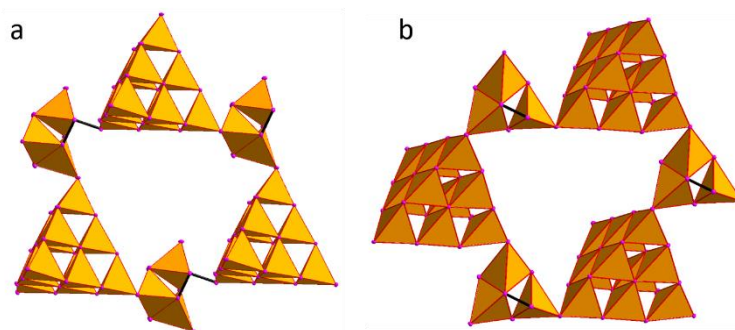


Figure S2: Two different ring motives formed of alternating building units in $\text{Na}_{19}\text{Si}_{13}\text{P}_{25}$. (a) Six-membered ring with four vertex and two homonuclear P–P single bond condensations. (b) All vertex shared six-membered ring.

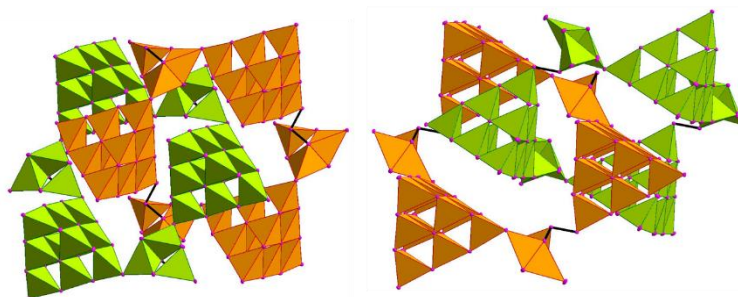


Figure S3: Two different interpenetration modes of crystallographic independent but symmetrically equivalent networks in $\text{Na}_{19}\text{Si}_{13}\text{P}_{25}$. Ring a (Fig. S2) is interpenetrated by ring b (Fig. S2) (left) and a homo-interpenetration of ring a (Fig. S2) can be observed (right).

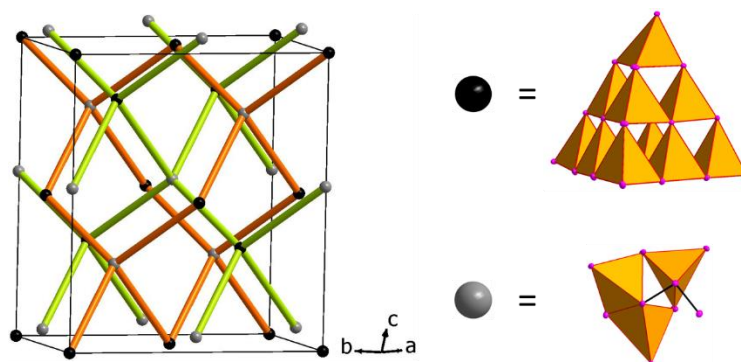


Figure S4: Topology of the two interpenetrating sphalerite-like networks. Nodes represent the centers of gravity of respective building units.

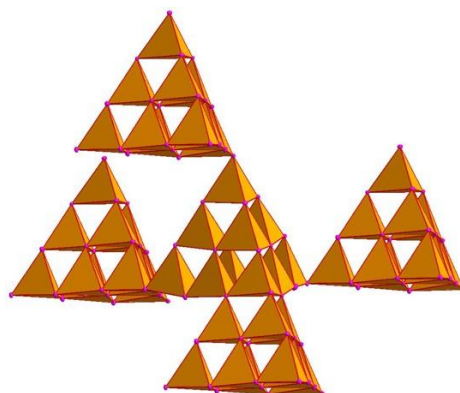


Figure S5: Supertetrahedral building unit of $\text{Na}_{23}\text{Si}_{19}\text{P}_{33}$. A T3 cluster is vertex shared with three other T3 entities and fused with another T3 supertetrahedron by one common SiP_4 unit.

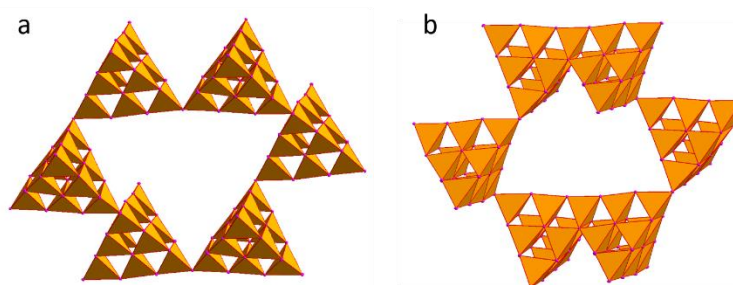


Figure S6: Two different ring motives formed by T3 clusters in $\text{Na}_{23}\text{Si}_{19}\text{P}_{33}$. (a) All vertex shared six-membered ring. (b) Six-membered ring consisting of T3 entities with four common vertices and two fusions.

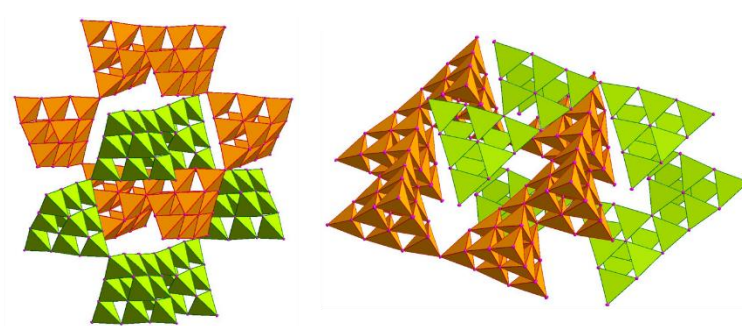


Figure S7: Two different interpenetration modes of crystallographic independent but symmetrically equivalent networks in $\text{Na}_{23}\text{Si}_{19}\text{P}_{33}$. Ring a (Fig. S6) is interpenetrated by ring b (Fig. S6) (left) and a homo-interpenetration of ring b (Fig. S6) can be observed (right).

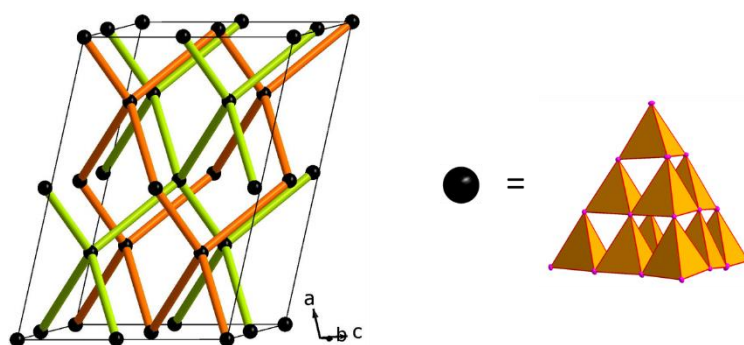


Figure S8: Topology of the two interpenetrating diamond-like networks. Nodes represent the centers of gravity of the T3 supertetrahedra.

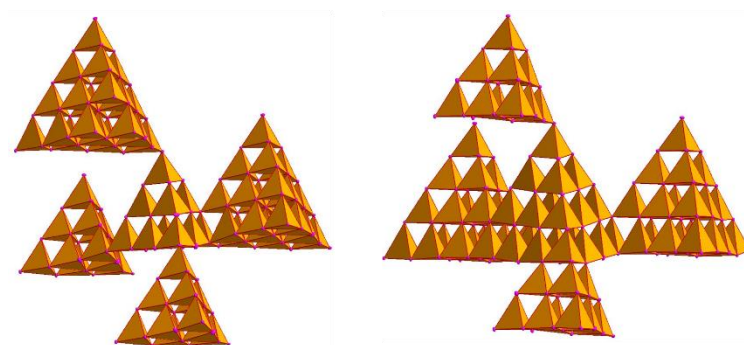


Figure S9: Basic building units of $\text{Na}_{23}\text{Si}_{28}\text{P}_{45}$ consisting of T3 and T4 clusters. Every T3 entity is connected to one T4 and two T3 entities by common vertices and fused with one T4 tetrahedron (left). Every T4 cluster is fused with two other T4 and one T3 entity and vertex shared with one T3 cluster (right).

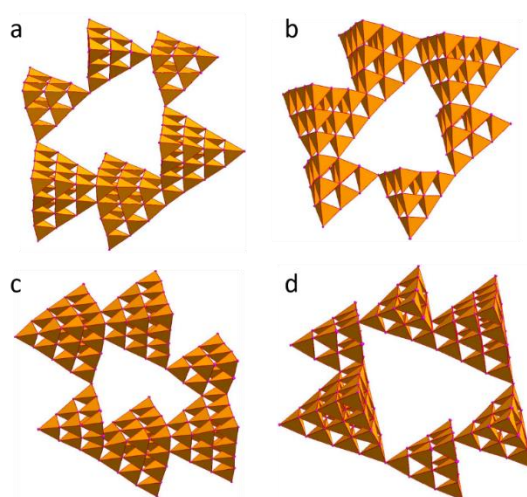


Figure S10: Four different six-membered ring motives are formed by T3 and T4 clusters in $\text{Na}_{23}\text{Si}_{28}\text{P}_{45}$. (a) Three sequent T3 entities are vertex shared and three T4 clusters are fused likewise. T3 and T4 entities are condensed by common vertices. (b) Ring derived from ring a by replacing vertex condensation between T3 and T4 supertetrahedra by fusion. (c) Two double units of fused T4 clusters which are turned by two T3 tetrahedra by two common vertices and two fusions into a ring motive. (d) Ring consisting of two double units of vertex shared T3 entities, which are twice fused and twice vertex shared with two T4 clusters.

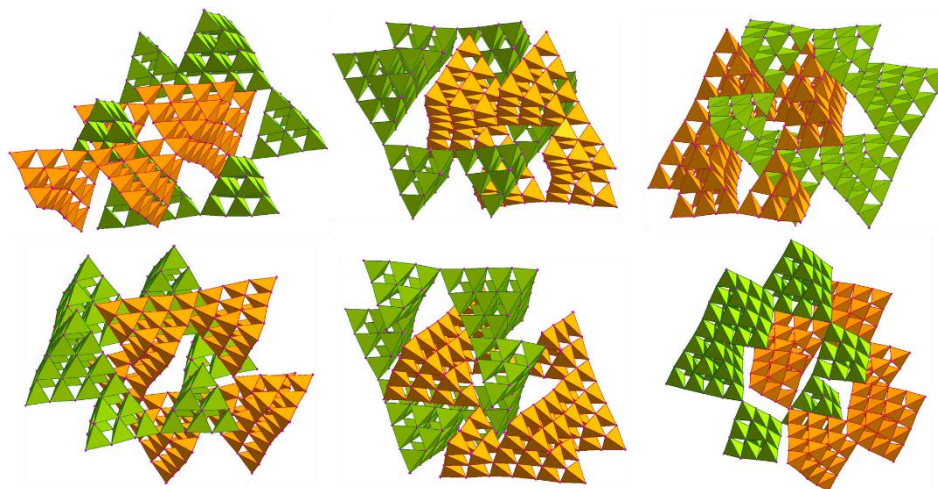


Figure S11: Six different interpenetration modes of crystallographic independent but symmetrically equivalent networks in $\text{Na}_{23}\text{Si}_{28}\text{P}_{45}$. Entanglement of rings a and d (top, left), rings b and d (top, middle), rings a and b (top, right), rings c and b (bottom, left), rings c and d (bottom middle) and a and c (bottom, right). No homo-interpenetration of one ring can be observed.

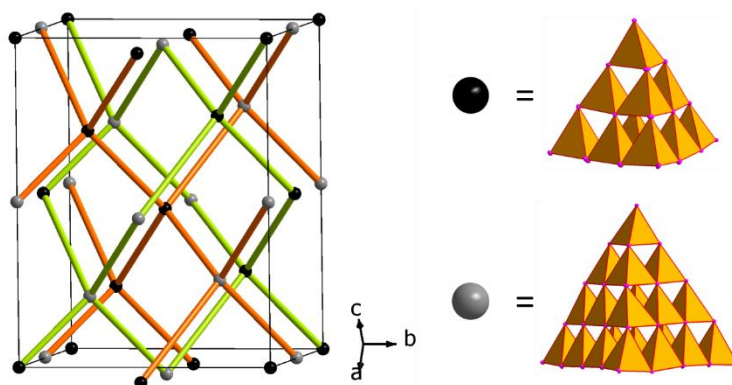


Figure S12: Topology of the two interpenetrating symmetrically equivalent but crystallographic independent networks, which are a hierarchically combination of the diamond- and the sphalerite-type structure. Nodes represent the centers of gravity of the T3 and T4 supertetrahedra.

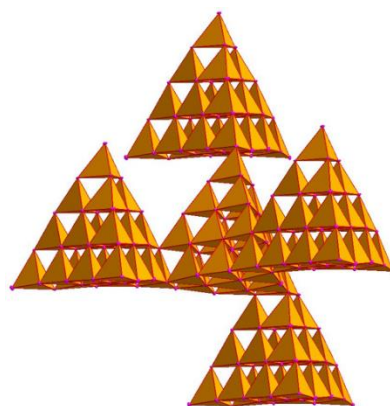


Figure S13: Supertetrahedral building unit of $\text{Na}_{23}\text{Si}_{37}\text{P}_{57}$. A T4 cluster is fused with three other T4 entities by one common SiP_4 unit and vertex shared with another T4 supertetrahedron.

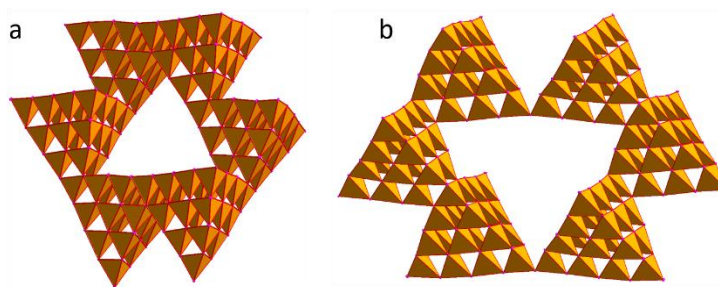


Figure S14: Two different ring motives formed by T4 clusters in $\text{Na}_{23}\text{Si}_{37}\text{P}_{57}$. (a) All fused six-membered ring. (b) Six-membered ring consisting of T4 entities with two common vertices and four fusions.

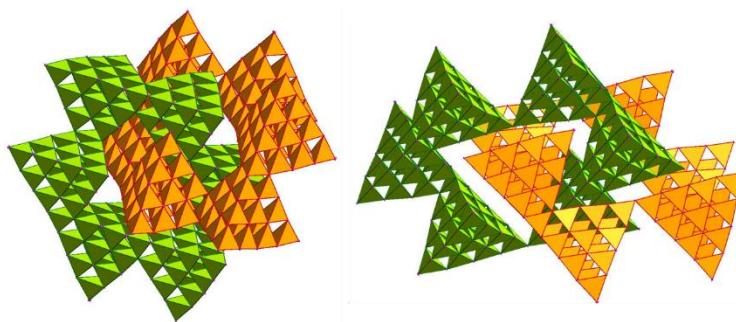


Figure S15: Two different interpenetration modes of crystallographic independent but symmetrically equivalent networks in $\text{Na}_{23}\text{Si}_{37}\text{P}_{57}$. Ring a is interpenetrated by ring b (left) and a homo-interpenetration of ring b can be observed (right).

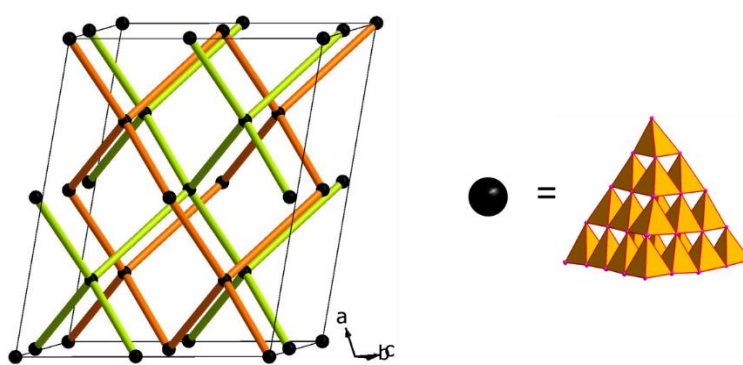


Figure S16: Topology of the two interpenetrating diamond-like networks of $\text{Na}_{23}\text{Si}_{37}\text{P}_{57}$. Nodes represent the centers of gravity of the T4 supertetrahedra.

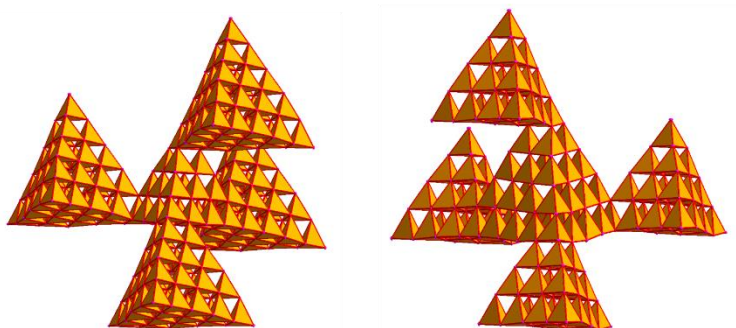


Figure S17: Building units of $\text{LT-NaSi}_2\text{P}_3$ consisting of T4 and T5 supertetrahedral clusters. Every T4 supertetrahedron is fused with four T5 entities by one common SiP_4 tetrahedron (left) and vice versa (right).

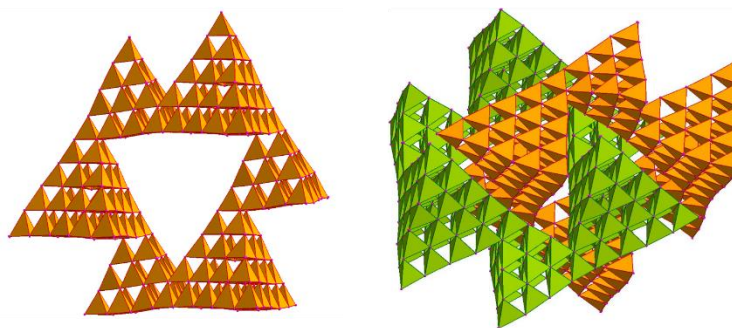


Figure S18: Six-membered ring motive of alternating T4 and T5 clusters connected by fusion the whole structure can be described with in $LT-NaSi_2P_3$ (left). Only one single interpenetration mode is existent (right).

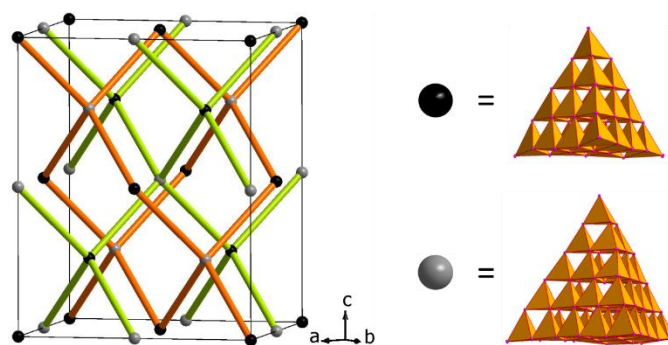


Figure S19: Topology of the two interpenetrating sphalerite-like networks of $LT-NaSi_2P_3$. Nodes represent the centers of gravity of the T4 and T5 supertetrahedra.

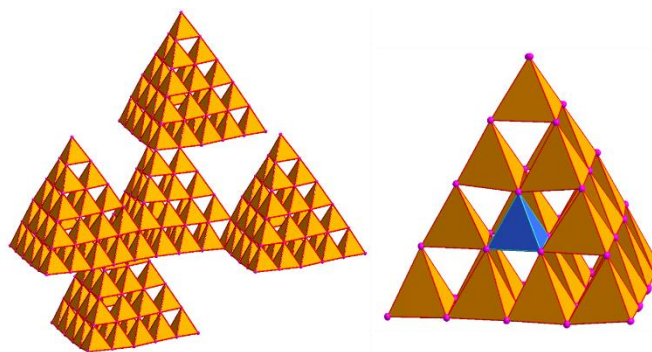


Figure S20: Building unit of $HT-NaSi_2P_3$ consisting of solely T5 supertetrahedral clusters. Every T5 supertetrahedron is fused with four other T5 entities by one common SiP_4 tetrahedron (left). T5 cluster with one missing silicon core, depicted as blue tetrahedron (right, top layer is not displayed due to a better view).



Figure S21: Six-membered ring motive of all-fused T5 supertetrahedra the whole structure can be described with in HT- NaSi_2P_3 (left). Only one single interpenetration mode is existent (right).

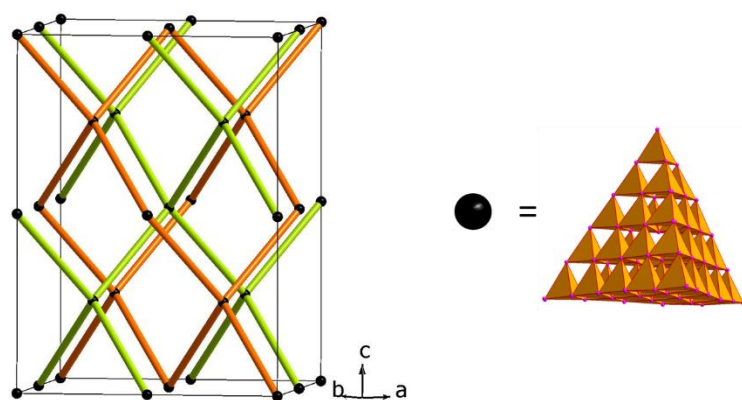


Figure S22: Topology of the two interpenetrating diamond-like networks of HT- NaSi_2P_3 . Nodes represent the centers of gravity of the T5 supertetrahedra.

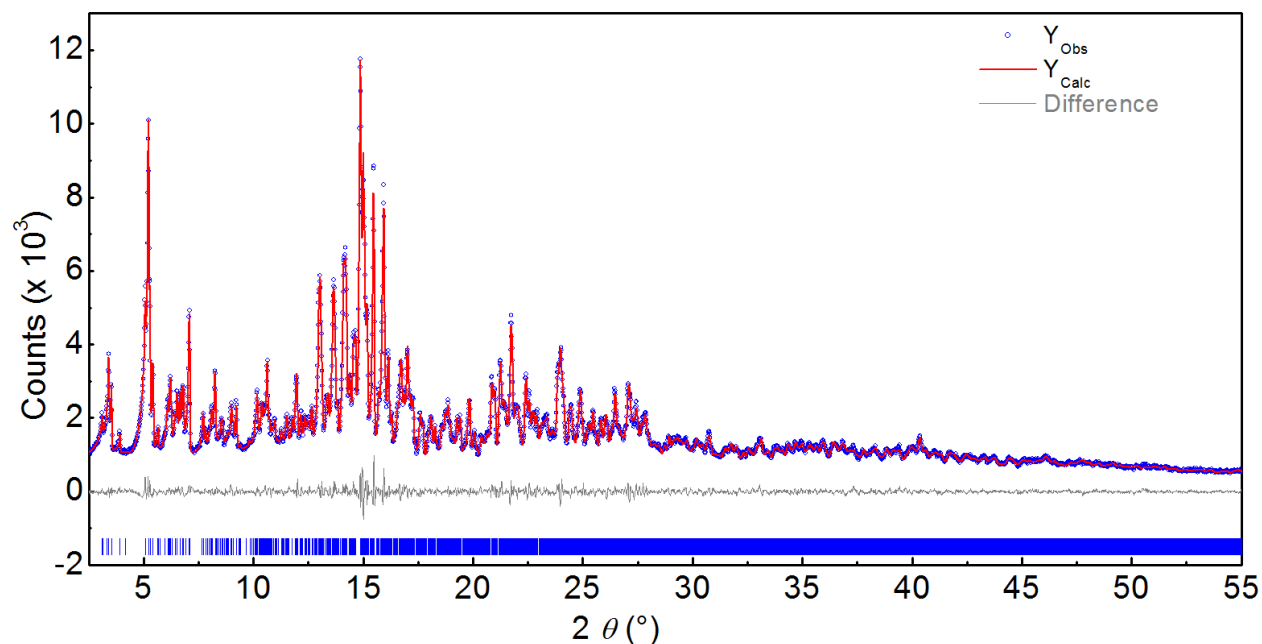


Figure S23. Observed (blue circles) and calculated (red line) powder diffraction pattern as well as difference plot (grey) of the Rietveld refinement of $\text{Na}_{19}\text{Si}_{13}\text{P}_{25}$.

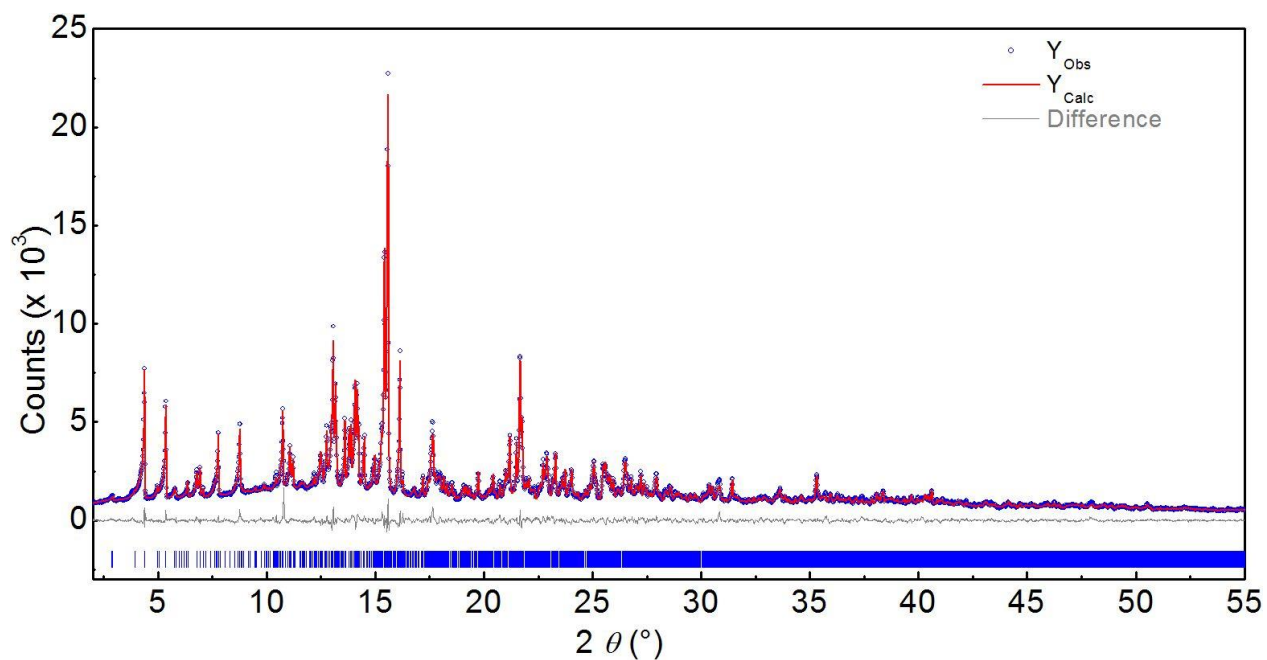


Figure S24. Observed (blue circles) and calculated (red line) powder diffraction pattern as well as difference plot (grey) of the Rietveld refinement of $\text{Na}_{23}\text{Si}_{19}\text{P}_{33}$. Peak positions are illustrated by vertical blue bars.

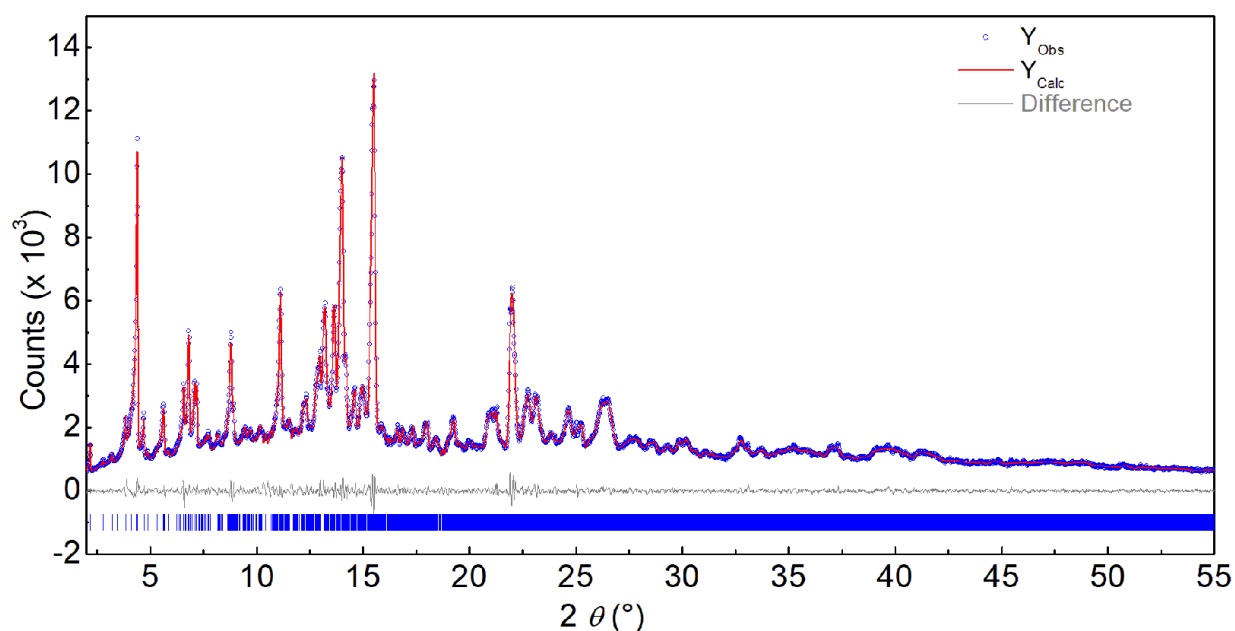


Figure S25. Observed (blue circles) and calculated (red line) powder diffraction pattern as well as difference plot (grey) of the Rietveld refinement of $\text{Na}_{23}\text{Si}_{28}\text{P}_{45}$. Peak positions are illustrated by vertical blue bars.

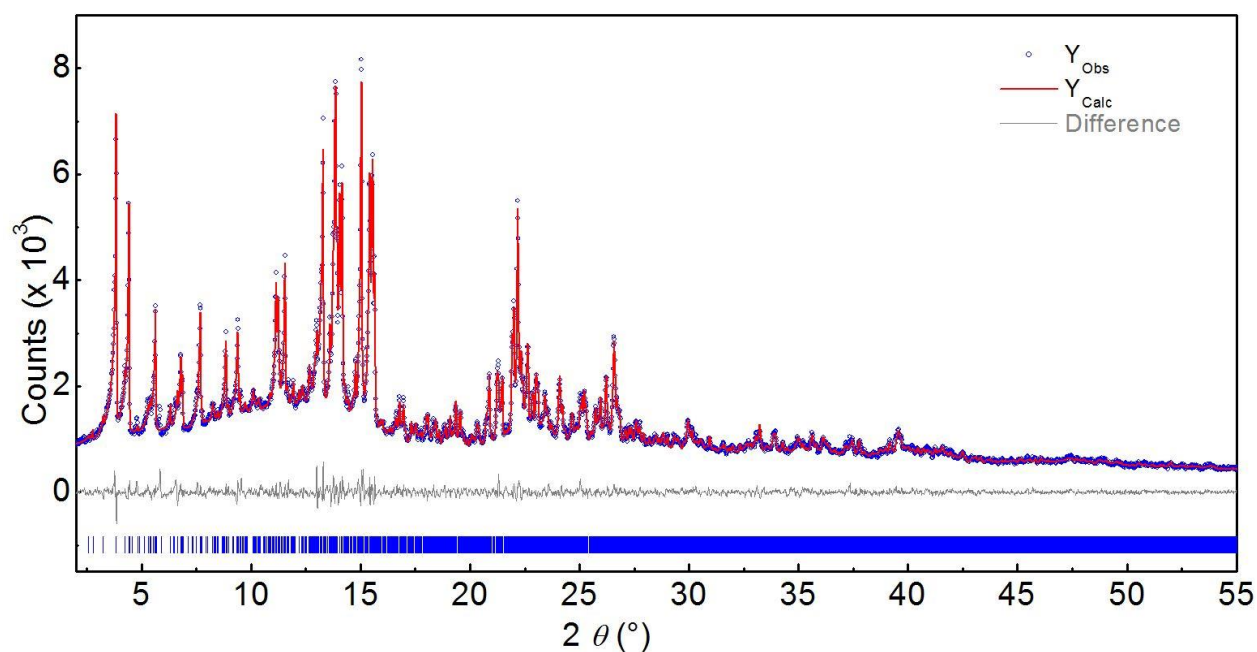


Figure S26. Observed (blue circles) and calculated (red line) powder diffraction pattern as well as difference plot (grey) of the Rietveld refinement of $\text{Na}_{23}\text{Si}_{37}\text{P}_{57}$. Peak positions are illustrated by vertical blue bars.

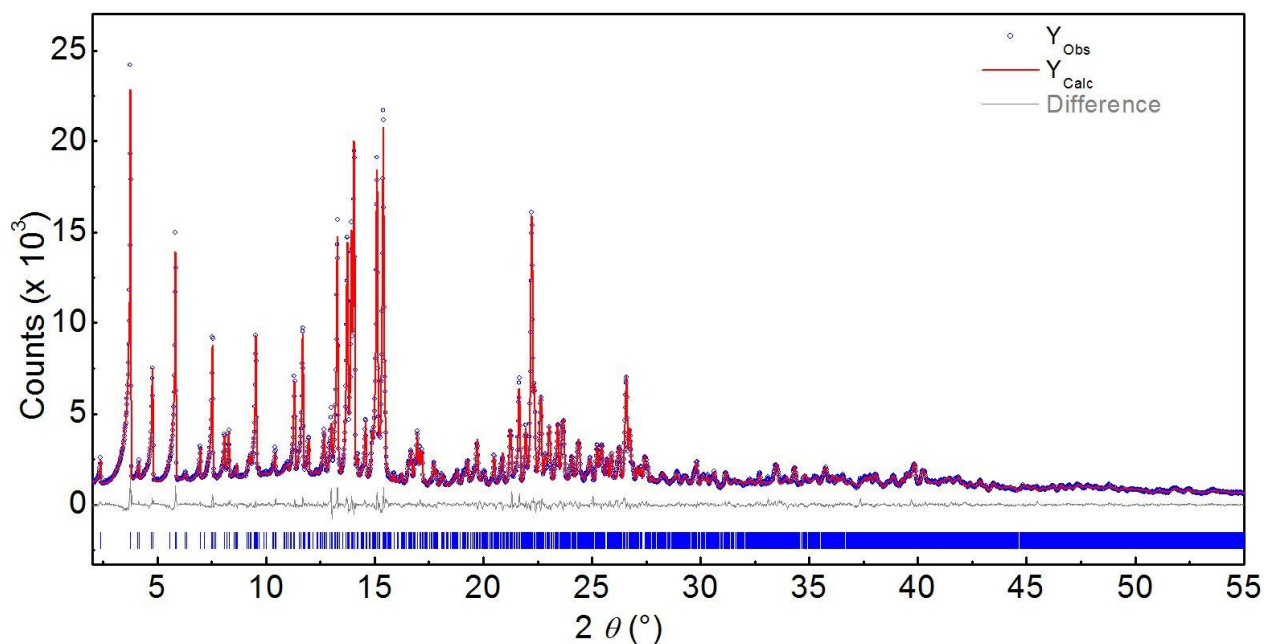


Figure S27. Observed (blue circles) and calculated (red line) powder diffraction pattern as well as difference plot (grey) of the Rietveld refinement of LT-NaSi₂P₃. Peak positions are illustrated by vertical blue bars.

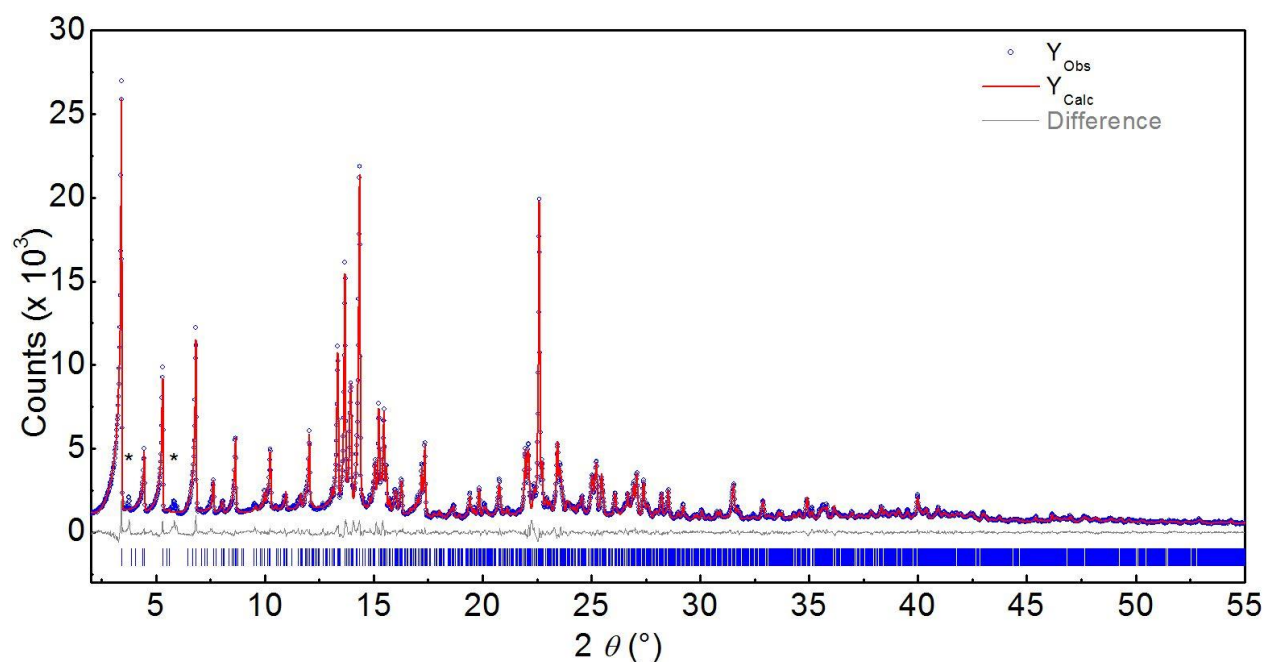


Figure S28. Observed (blue circles) and calculated (red line) powder diffraction pattern as well as difference plot (grey) of the Rietveld refinement of HT-NaSi₂P₃. Peak positions are illustrated by vertical blue bars. Asterisked peaks represent LT-NaSi₂P₃ as side phase (4.38 wt%).

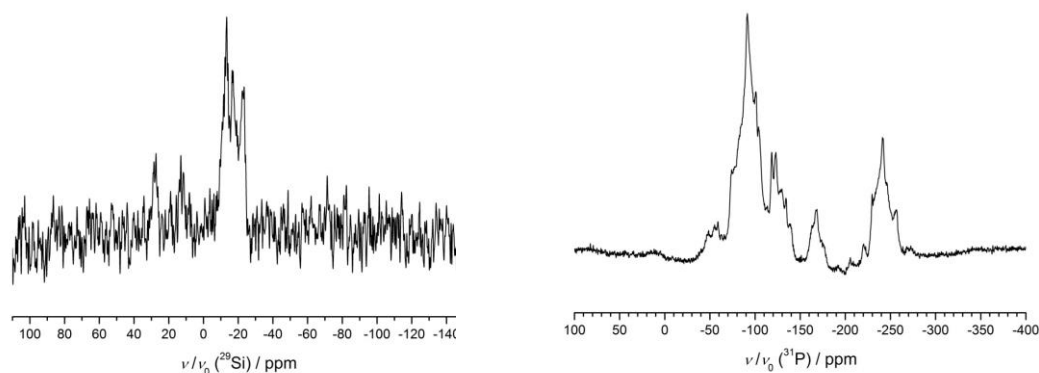


Figure S29. (left) ^{29}Si MAS NMR spectrum of $\text{Na}_{19}\text{Si}_{13}\text{P}_{25}$ with broad resonance between $\delta = -23.39$ and -13.34 ppm ($\nu_0 = 10$ kHz). (right) ^{31}P MAS NMR spectrum of $\text{Na}_{19}\text{Si}_{13}\text{P}_{25}$ with broad resonances between $\delta = -263.69$ and -229.74 ppm, -175.16 and -163.05 ppm and -139.12 and -48.58 ppm ($\nu_0 = 50$ kHz). If the signal between $\delta = -175.16$ and -163.05 is assigned to one phosphorus site then the integration of all signals yields 24 crystallographic P sites (25 cryst. distinct sites for P).

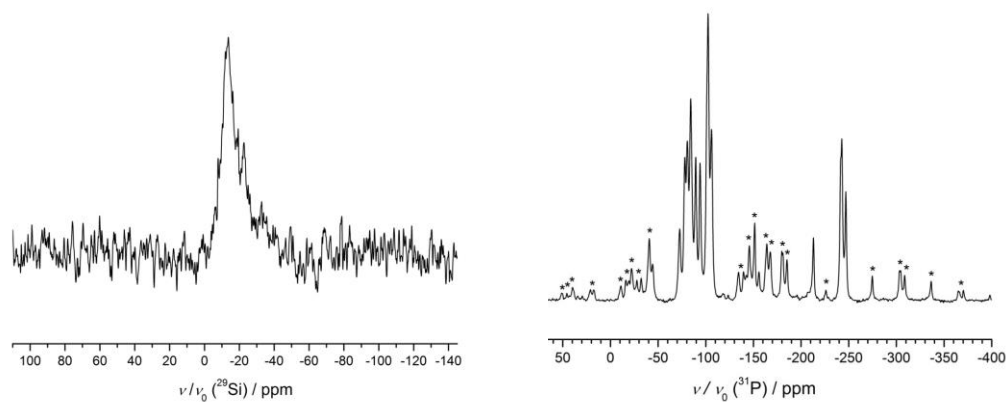


Figure S30. (left) ^{29}Si MAS NMR spectrum of $\text{Na}_{23}\text{Si}_{19}\text{P}_{33}$ with a broad resonance at $\delta = -13.68$ ppm ($\nu_0 = 10$ kHz). (right) ^{31}P MAS NMR spectrum of $\text{Na}_{23}\text{Si}_{19}\text{P}_{33}$ with resonances at $\delta = -247.00$, -242.77 , -213.04 , -106.03 , -102.43 , -94.01 , -89.47 , -84.21 , -80.66 , -78.07 , -72.67 ppm ($\nu_0 = 12.5$ kHz). If the signal at $\delta = -247.00$ ppm is assigned to one phosphorus site then the integration of all signals yields 17.5 crystallographic P sites (16.5 cryst. different sites for P). Rotational sidebands are marked with asterisks.

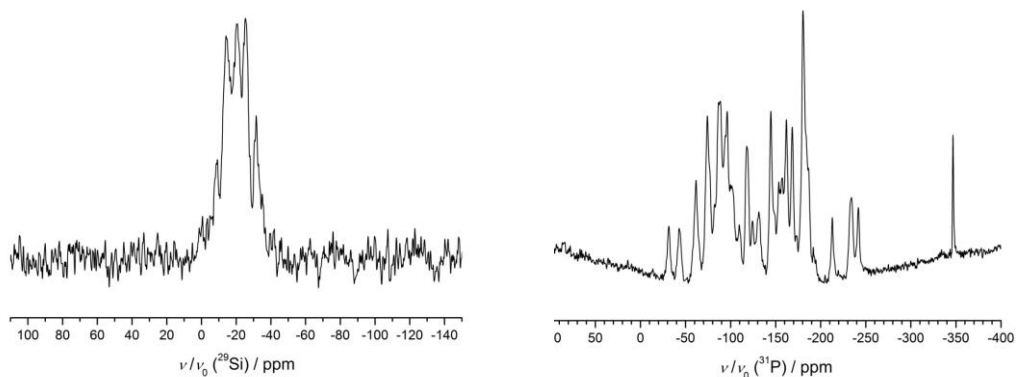


Figure S31. (left) ^{29}Si MAS NMR spectrum of $\text{Na}_{23}\text{Si}_{28}\text{P}_{45}$ with broad resonances at $\delta = -31.58, -25.39, -20.69, -14.14$ and -9.14 ppm ($\nu_0 = 10$ kHz). (right) ^{31}P MAS NMR spectrum of $\text{Na}_{23}\text{Si}_{28}\text{P}_{45}$ with resonances at $\delta = -346.71, -241.78, -234.08, -212.86, -180.34, -168.41, -161.90, -157.25, -144.63, -131.30, -117.86, -96.13, -88.53, -74.22, -61.65, -42.84$ and -31.43 ppm ($\nu_0 = 50$ kHz). If the signal at $\delta = -31.43$ ppm is assigned to one phosphorus site then the integration of all signals yields in 48 crystallographic P sites (45 cryst. different sites for P).

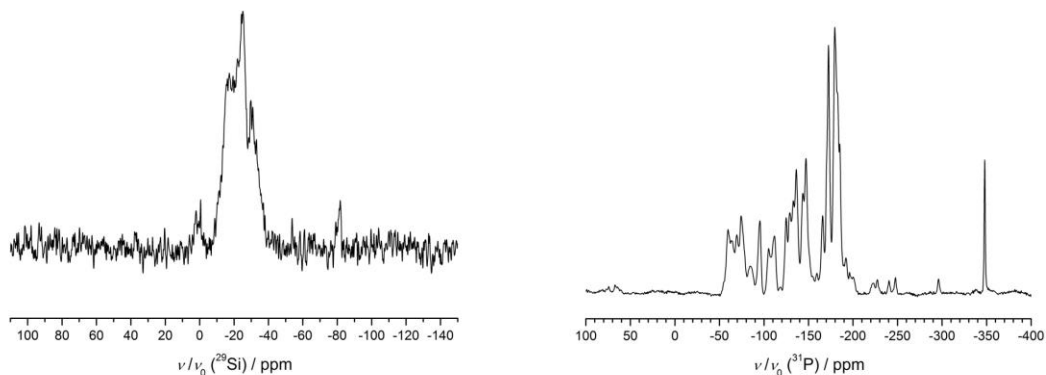


Figure S32. (left) ^{29}Si MAS NMR spectrum of $\text{Na}_{23}\text{Si}_{37}\text{P}_{57}$ with a broad resonance between $\delta = -38.49$ and -9.49 ppm ($\nu_0 = 10$ kHz). Additional small resonances at $\delta = -81.74$ and -0.52 ppm are assigned to small amounts of impurities. (right) ^{31}P MAS NMR spectrum of $\text{Na}_{23}\text{Si}_{37}\text{P}_{57}$ with resonances at $\delta = -347.91, -179.58, -172.53, -165.94, -147.11, -136.25, -124.89, -111.70, -105.23, -95.45, -74.33, -69.51$ and -59.66 ppm ($\nu_0 = 50$ kHz). If the signal at $\delta = -347.91$ ppm is assigned to one phosphorus site then the integration of all signals yields in 30.5 crystallographic P sites (desired value 28.5 sites for P). Resonances at $\delta = -296.03, -247.70, -240.51$ and -227.45 ppm are assigned to small amounts of impurities.

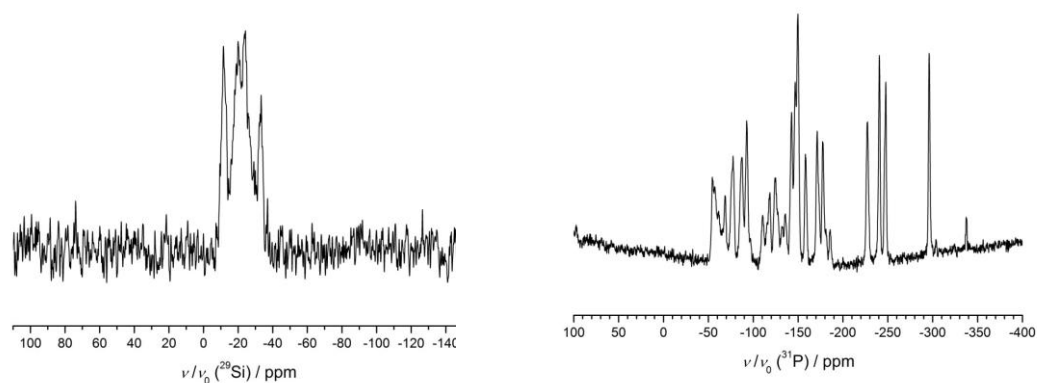


Figure S33. (left) ^{29}Si MAS NMR spectrum of $\text{LT-NaSi}_2\text{P}_3$ with broad resonances at $\delta = -33.34, -24.17, -19.95$ and -11.47 ppm ($\nu_0 = 10$ kHz). (right) ^{31}P MAS NMR spectrum of $\text{LT-NaSi}_2\text{P}_3$ with resonances at $\delta = -296.09, -247.76, -240.60, -227.41, -177.38, -171.35, -158.12, -149.77, -146.68, -142.71, -135.85, -124.97, -118.57, -110.42, -92.69, -87.18, -77.51, -68.64$ and -54.39 ppm ($\nu_0 = 50$ kHz). If the signal at $\delta = -296.09$ ppm is assigned to one phosphorus site then the integration of all signals yields in 19 crystallographic P sites (18.75 cryst. different sites for P). The resonance at $\delta = -337.34$ ppm is assigned to a small amount of impurity.

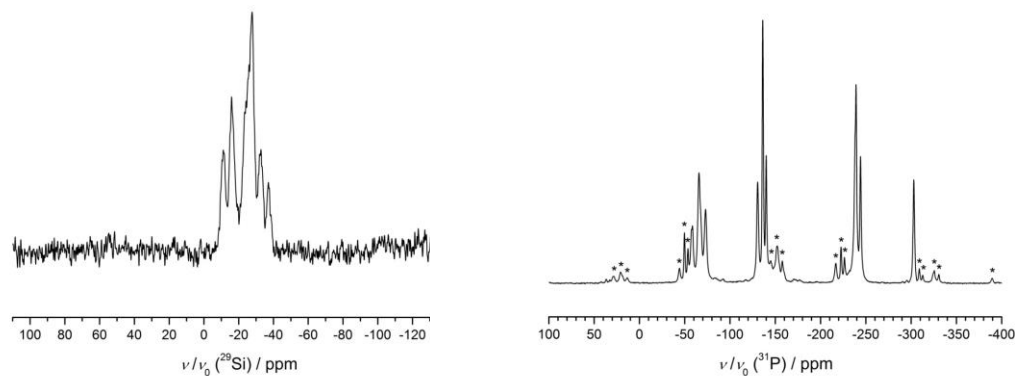


Figure S34. (left) ^{29}Si MAS NMR spectrum of $\text{HT-NaSi}_2\text{P}_3$ with broad resonances at $\delta = -37.09, -32.82, -27.71, -15.87$ and -11.10 ppm ($\nu_0 = 10$ kHz). (right) ^{31}P MAS NMR spectrum of $\text{HT-NaSi}_2\text{P}_3$ with resonances at $\delta = -302.12, -233.12, -239.38, -140.06, -135.98, -130.59, -73.33, -65.68, -58.52$ ppm ($\nu_0 = 14$ kHz). If the signal at $\delta = -302.12$ ppm is assigned to one phosphorus site then the integration of all signals yields in 12 crystallographic P sites (12 cryst. different sites for P). Rotational sidebands are marked with asterisks.

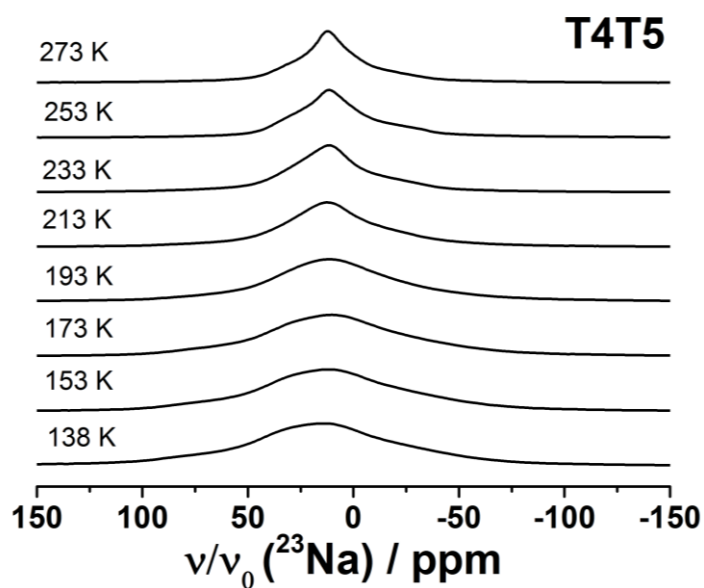


Figure S35. ²³Na-NMR spectra at the indicated temperatures of LT-NaSi₂P₃.

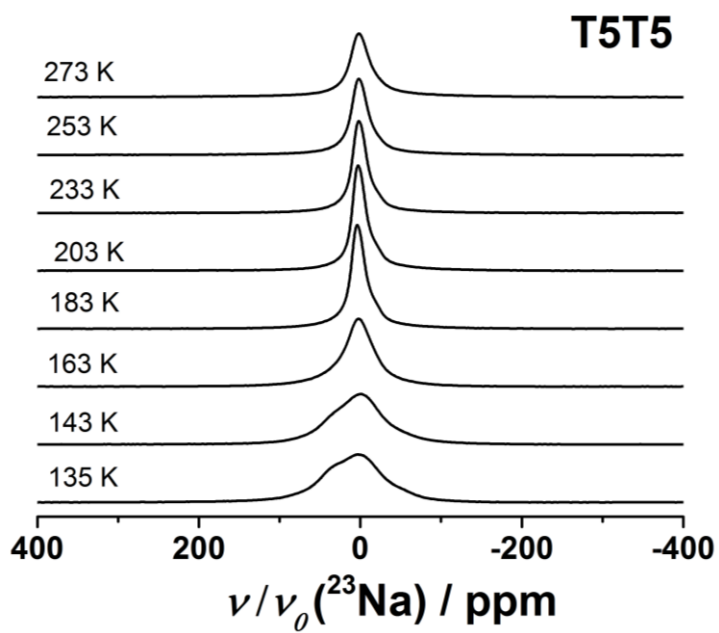


Figure S36. ²³Na-NMR spectra at the indicated temperatures of HT-NaSi₂P₃.

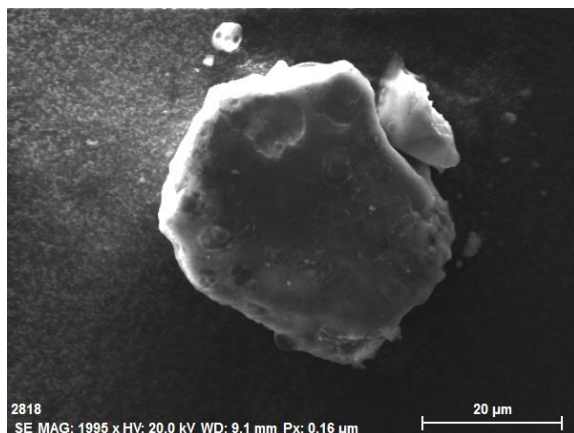


Figure S37: Scanning electron micrograph of $\text{Na}_{19}\text{Si}_{13}\text{P}_{25}$.

Table S7: EDX elemental analysis of $\text{Na}_{19}\text{Si}_{13}\text{P}_{25}$. Average of eight measuring points of a polycrystalline sample. Signals of oxygen were not taken into account due to hydrolysis by contact with air.

	Na	Si	P
EDX point 1 [atom%]	31.98	24.16	43.86
EDX point 2 [atom%]	33.05	21.13	45.82
EDX point 3 [atom%]	33.10	22.03	44.88
EDX point 4 [atom%]	33.36	21.33	45.30
EDX point 5 [atom%]	33.04	23.51	43.44
EDX point 6 [atom%]	33.45	25.19	41.36
EDX point 7 [atom%]	34.64	23.94	41.42
EDX point 8 [atom%]	33.18	22.24	44.58
Average [atom%]	33.23	22.94	43.83
Calculated [atom%]	33.33	22.81	43.86

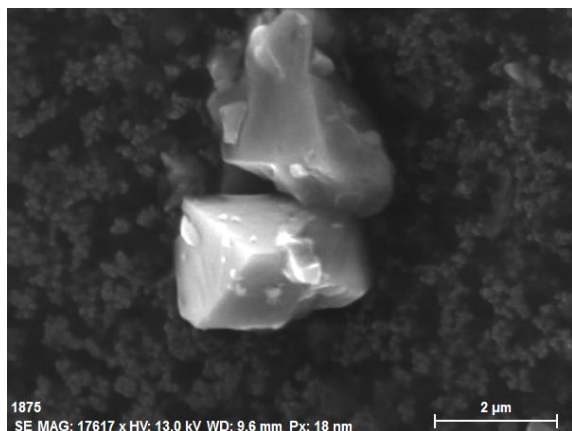


Figure S38: Scanning electron micrograph of $\text{Na}_{23}\text{Si}_{19}\text{P}_{33}$.

Table S8: EDX elemental analysis of $\text{Na}_{23}\text{Si}_{19}\text{P}_{33}$. Average of eight measuring points of a polycrystalline sample. Signals of oxygen were not taken into account due to hydrolysis by contact with air.

	Na	Si	P
EDX point 1 [atom%]	30.74	23.77	45.49
EDX point 2 [atom%]	30.68	23.65	45.67
EDX point 3 [atom%]	29.01	26.13	44.86
EDX point 4 [atom%]	30.33	25.10	44.57
EDX point 5 [atom%]	29.27	25.81	44.92
EDX point 6 [atom%]	29.90	26.83	43.27
EDX point 7 [atom%]	30.71	26.42	42.87
EDX point 8 [atom%]	29.58	25.52	44.89
Average [atom%]	30.03	25.40	44.57
Calculated [atom%]	30.66	25.33	44.00

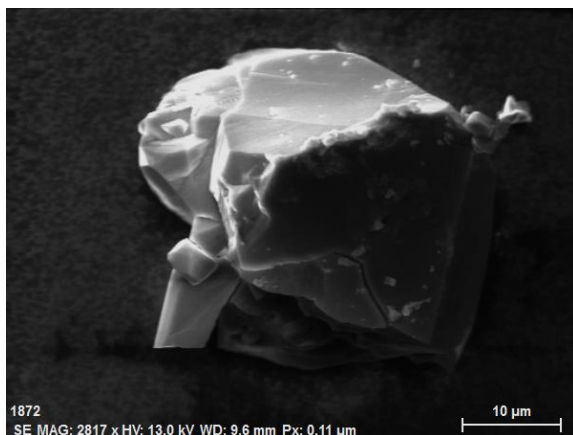


Figure S39: Scanning electron micrograph of $\text{Na}_{23}\text{Si}_{28}\text{P}_{45}$.

Table S9: EDX elemental analysis of $\text{Na}_{23}\text{Si}_{28}\text{P}_{45}$. Average of eight measuring points of a polycrystalline sample. Signals of oxygen were not taken into account due to hydrolysis by contact with air.

	Na	Si	P
EDX point 1 [atom%]	24.47	28.11	47.42
EDX point 2 [atom%]	22.89	30.50	46.62
EDX point 3 [atom%]	25.23	28.69	46.08
EDX point 4 [atom%]	24.88	27.80	47.32
EDX point 5 [atom%]	21.46	30.51	48.04
EDX point 6 [atom%]	25.05	28.64	46.31
EDX point 7 [atom%]	23.03	30.34	46.63
EDX point 8 [atom%]	22.46	30.72	46.82
Average [atom%]	23.68	29.41	46.91
Calculated [atom%]	23.96	29.17	46.88

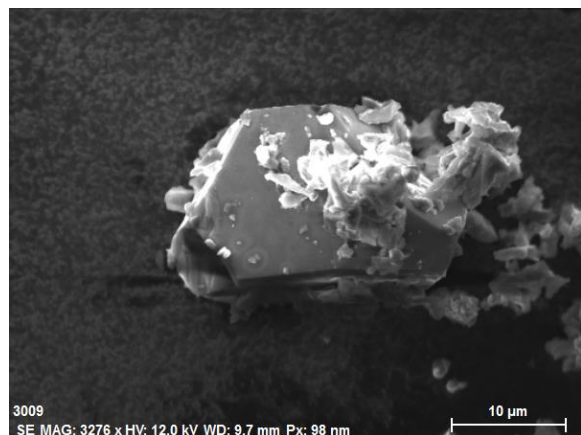


Figure S40: Scanning electron micrograph of $\text{Na}_{23}\text{Si}_{37}\text{P}_{57}$.

Table S10: EDX elemental analysis of $\text{Na}_{23}\text{Si}_{37}\text{P}_{57}$. Average of eight measuring points of a polycrystalline sample. Signals of oxygen were not taken into account due to hydrolysis by contact with air.

	Na	Si	P
EDX point 1 [atom%]	17.68	33.63	48.69
EDX point 2 [atom%]	19.55	32.22	48.22
EDX point 3 [atom%]	19.60	31.94	48.47
EDX point 4 [atom%]	20.18	31.59	48.23
EDX point 5 [atom%]	20.67	31.19	48.14
EDX point 6 [atom%]	19.78	31.77	48.46
EDX point 7 [atom%]	18.99	31.67	49.35
EDX point 8 [atom%]	19.29	31.15	49.56
Average [atom%]	19.47	31.89	48.64
Calculated [atom%]	19.66	31.62	48.72

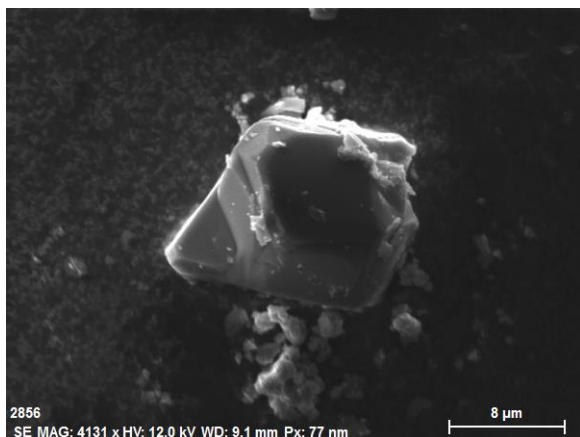


Figure S41: Scanning electron micrograph of LT- NaSi_2P_3 .

Table S11: EDX elemental analysis of LT- NaSi_2P_3 . Average of eight measuring points of a polycrystalline sample. Signals of oxygen were not taken into account due to hydrolysis by contact with air.

	Na	Si	P
EDX point 1 [atom%]	16.65	35.90	47.46
EDX point 2 [atom%]	17.31	33.11	49.57
EDX point 3 [atom%]	17.21	32.86	49.92
EDX point 4 [atom%]	15.67	34.87	49.46
EDX point 5 [atom%]	17.46	32.85	49.69
EDX point 6 [atom%]	17.01	33.06	49.94
EDX point 7 [atom%]	18.09	33.29	48.62
EDX point 8 [atom%]	16.71	34.35	48.94
Average [atom%]	17.01	33.79	49.20
Calculated [atom%]	16.67	33.33	50.00

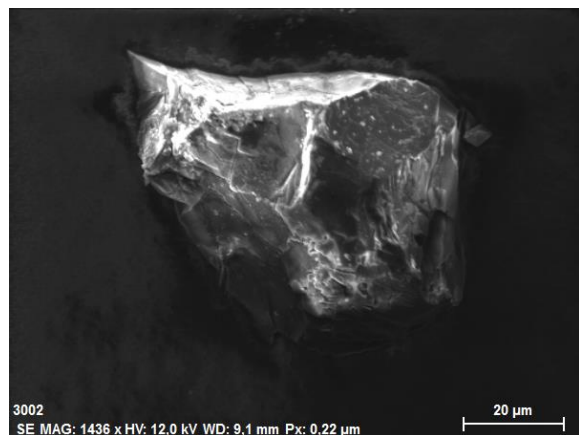


Figure S42: Scanning electron micrograph of HT- NaSi_2P_3 .

Table S12: EDX elemental analysis of HT- NaSi_2P_3 . Average of eight measuring points of a polycrystalline sample. Signals of oxygen were not taken into account due to hydrolysis by contact with air.

	Na	Si	P
EDX point 1 [atom%]	14.79	34.34	50.87
EDX point 2 [atom%]	15.38	34.47	50.14
EDX point 3 [atom%]	15.18	34.37	50.45
EDX point 4 [atom%]	15.97	33.77	50.26
EDX point 5 [atom%]	15.12	34.02	50.86
EDX point 6 [atom%]	15.08	33.79	51.13
EDX point 7 [atom%]	14.66	34.46	50.88
EDX point 8 [atom%]	16.16	33.99	49.86
Average [atom%]	15.29	34.15	50.56
Calculated [atom%]	16.67	33.33	50.00

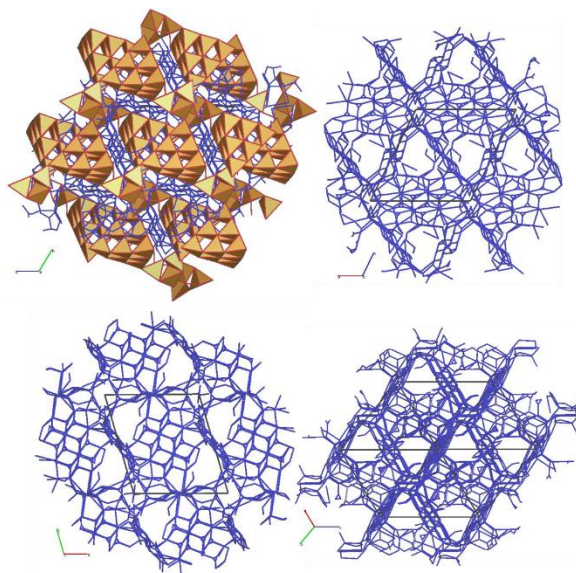


Figure S43: Calculated possible sodium ion pathways according to the voids in the structure of $\text{Na}_{19}\text{Si}_{13}\text{P}_{25}$. View along $[100]$ (top, left), $[010]$ (top, right), $[001]$ (bottom, left) and $[111]$ (bottom, right).

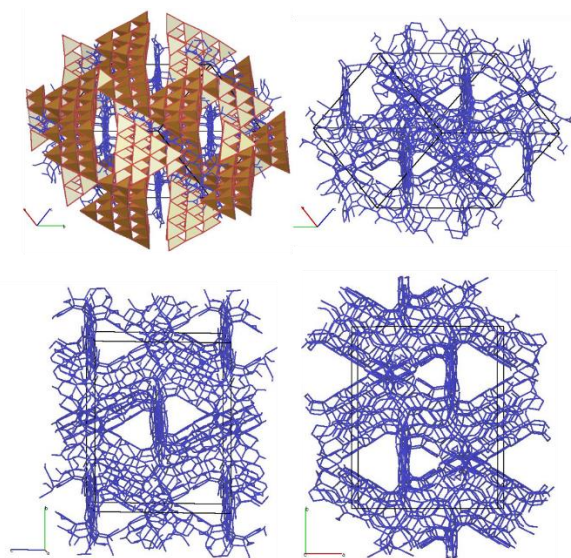


Figure S45: Calculated possible sodium ion pathways according to the voids in the structure of $\text{Na}_{23}\text{Si}_{28}\text{P}_{45}$. View along $[11-1]$ (top, left), $[-111]$ (top, right), $[100]$ (bottom, left) and $[001]$ (bottom, right).

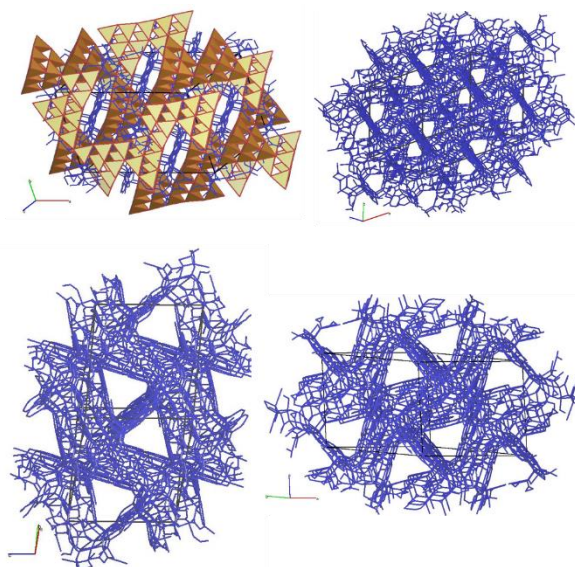


Figure S44: Calculated possible sodium ion pathways according to the voids in the structure of $\text{Na}_{23}\text{Si}_{19}\text{P}_{33}$. View along $[112]$ (top, left), $[1-12]$ (top, right), $[1-10]$ (bottom, left) and $[110]$ (bottom, right).

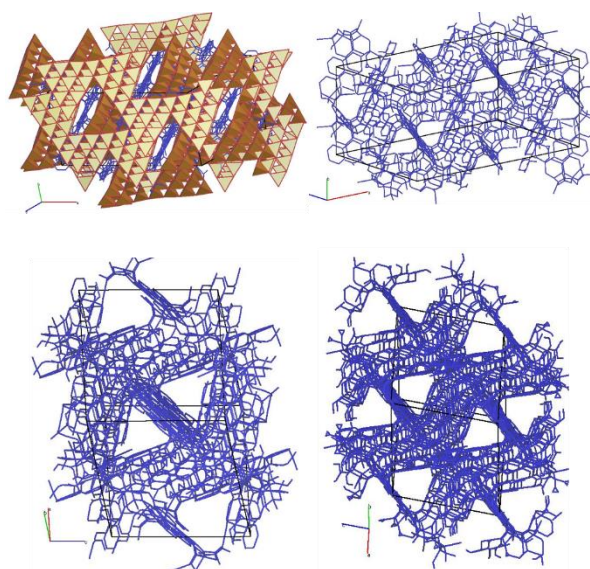


Figure S46: Calculated possible sodium ion pathways according to the voids in the structure of $\text{Na}_{23}\text{Si}_{37}\text{P}_{57}$. View along $[112]$ (top, left), $[1-12]$ (top, right), $[1-10]$ (bottom, left) and $[110]$ (bottom, right).

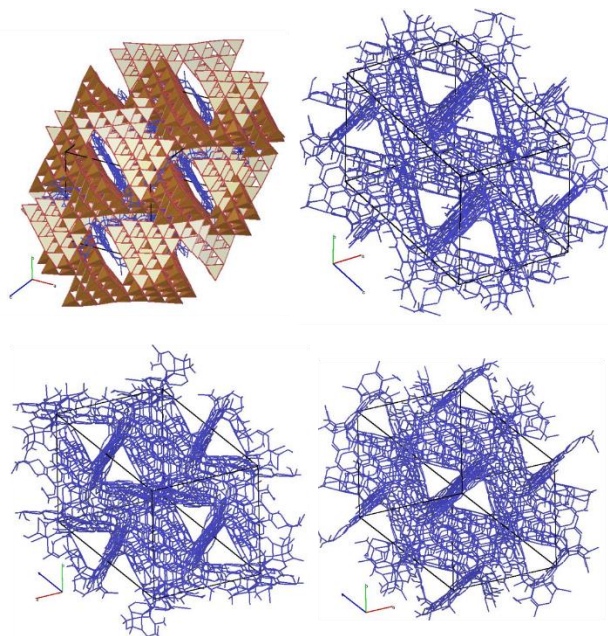


Figure S47: Calculated possible sodium ion pathways according to the voids in the structure of $LT\text{-NaSi}_2\text{P}_3$. View along $[111]$ (top, left), $[-111]$ (top, right), $[11-1]$ (bottom, left) and $[1-11]$ (bottom, right).

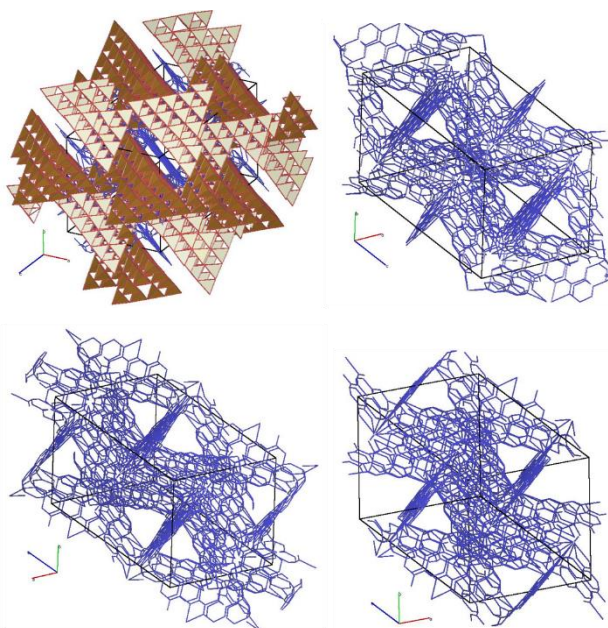


Figure S48: Calculated possible sodium ion pathways according to the voids in the structure of $HT\text{-NaSi}_2\text{P}_3$. View along $[111]$ (top, left), $[-111]$ (top, right), $[11-1]$ (bottom, left) and $[1-11]$ (bottom, right).

Determination of electronic conductivity

To determine the electronic conductivities and ionic transference numbers, DC galvanostatic polarization measurements with ion-blocking electrodes (Indium metal) were conducted on all samples. No reactions between In and the samples were observed under these conditions. A current of 10 nA was always turned on between 1000-1500 s (each data point was collected in an interval of 0.1 s). Therefore, the samples except the T3T4 sample did not reach a steady state and the estimation of the electronic conductivity represents an upper limit. From the polarization in the EIS measurements it is clear that ions are the majority charge carrier in these systems. According to Maier,^[1-2] the processes in an ionically and electronically conducting sample between two ion blocking electrodes can be described with the simplified equivalent circuit model in Figure S47 as parallel arrangement of electrical R_{eon} and ionic resistance R_{ion} with the bulk capacitor C_{bulk} and the ion blocking capacitor C_{block} .

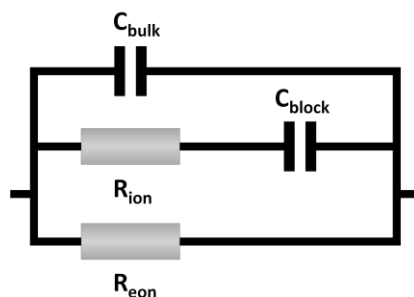


Figure S49: Equivalent circuit model of an ionic and electronic conducting sample between two ion blocking electrodes.

The initial sharp IR-drop in the DC polarization experiment after turning on the current contains the total resistance of the sample ($V_{IR}=IR_{tot}$). The total resistance R_{tot} includes R_{ion} and R_{eon} in parallel:

$$\frac{1}{R_{tot}} = \frac{1}{R_{eon}} + \frac{1}{R_{ion}} \quad (1)$$

After a long time of current flow the saturation voltage V_s , which can be assigned to the electronic resistance ($V_s=IR_{eon}$), is obtained. With the value for R_{eon} the ionic resistance R_{ion} can be calculated from R_{tot} . But this method exhibits some problems for materials with high ionic conductivity, because the resistance of the IR-drop measured after an interval time of 0.1 s is equivalent with the impedance at a frequency of 10 Hz and thus includes grain boundary contributions and polarization effects. For the fast ionic conductors (T3, T4T4, T4T5, T5T5), the ionic conductivity was approximated by the value obtained by EIS at room temperature.

This allows the determination of the ionic transference numbers t_i , which depends on the ionic (σ_{ion}) and electronic (σ_{eon}) conductivity of all samples according to the following equation:

$$t_i = \frac{\sigma_{\text{ion}}}{\sigma_{\text{ion}} + \sigma_{\text{eon}}} \quad (2)$$

For a good ionic conductor, the transference number is ideally as close as possible to 1.0. If t_i is much greater than zero, but much smaller than one, a material is considered to be a mixed conductor.^[3]

The DC measurements of all samples are shown in Figure S48 and the electronic conductivity and ionic transference number for each compound is listed in Table S13. All samples except T3T3 ($t_i=0.6507$), show a transference number that is close to 1. The sample T3T3 shows the behavior of a mixed ionic-electronic conductor because of its relatively low ionic conductivity.

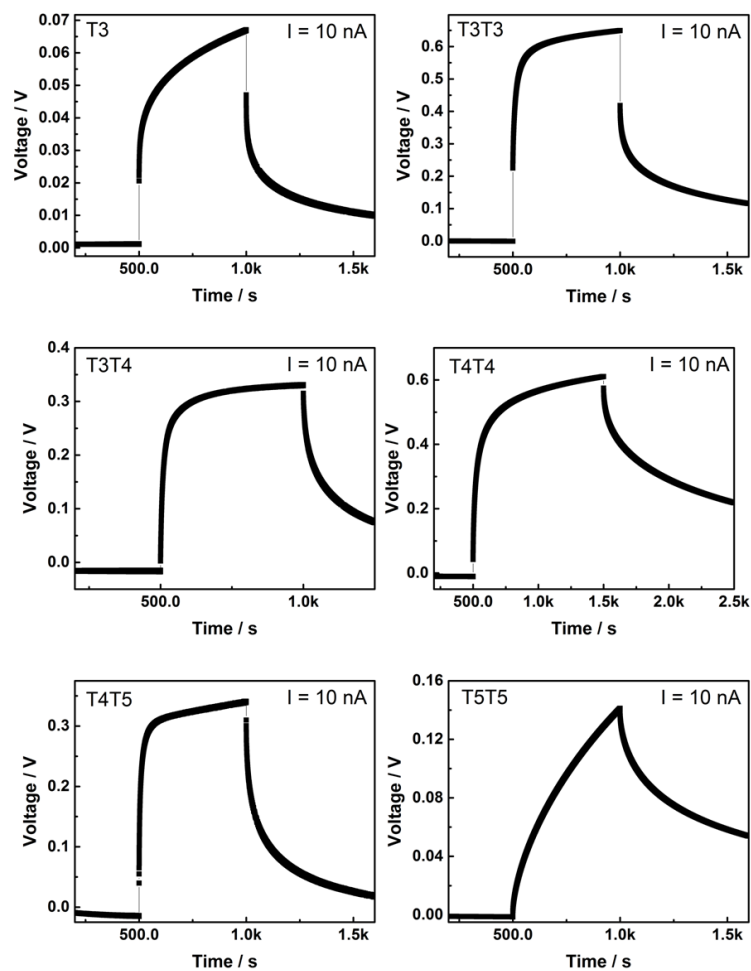


Figure S50: Plots of DC galvanostatic polarization measurements at RT with a current of 10 nA turned on between 1000-1500 s. The DC measurements were conducted with the same samples right after the EIS measurements.

Table S13: Results of DC galvanostatic polarization measurements including ionic transference number and upper limit of electronic conductivity.

Sample	$\sigma_{eon} / \text{Scm}^{-1}$	t_i
T3	$1.5 \cdot 10^{-7}$	0.9851
T3T3	$1.4 \cdot 10^{-8}$	0.6507
T3T4	$2.7 \cdot 10^{-8}$	0.9868
T4T4	$8.2 \cdot 10^{-9}$	0.9967
T4T5	$1.3 \cdot 10^{-8}$	0.9746
T5T5	$3.2 \cdot 10^{-8}$	0.9993

Temperature dependent EIS and equivalent circuit modelling of T3, T3T3, T3T4, T4T4, T4T5, T5T5

The representative impedance spectra of the samples $\text{Na}_{19}\text{Si}_{13}\text{P}_{25}$ (T3), $\text{Na}_{23}\text{Si}_{19}\text{P}_{33}$ (T3T3), $\text{Na}_{23}\text{Si}_{28}\text{P}_{45}$ (T3T4), $\text{Na}_{23}\text{Si}_{37}\text{P}_{57}$ (T4T4) *LT*- NaSi_2P_3 (T4T5) and *HT*- NaSi_2P_3 (T5T5) in Figure S49-S53 contain one to two semicircles at high frequencies and a spike at low frequencies. In general, the semicircles can be attributed to bulk or to grain boundary conductivity. In the simplest case, the impedance of one semicircle can be described with an equivalent circuit model containing a parallel arrangement of a resistor R and a capacitor C resembling the capacitive and conductive behavior of a solid electrolyte.^[4-5] If the semicircles are depressed, the capacitor can be replaced by a constant phase element (CPE). This element takes a dispersion of relaxation times ($\tau=1/RC$) caused for instance by surface roughness of the sample or electrodes or non-uniform current distribution into consideration.^[6] If the CPE is placed in parallel to a resistance, an effective capacitance C_{eff} can be calculated from the fitted values of Q , R and the factor α by:^[7]

$$C_{eff} = \frac{(RQ)^{1/\alpha}}{R} \quad (3)$$

At low frequencies the spectra show a capacitive spike in the μF range due to the accumulation of Na^+ -ions at the interface between pellet and metal electrode. This polarization is a typical characteristic of a solid ionic conductor and can be modeled by a capacitor or CPE in series to the RC-element.^[4-5] By estimating the intersection of the semicircle with the real part of the impedance (Z_{Re}) in a Nyquist plot, the resistance (R) of the conduction process is obtained. The ionic conductivity (σ) is the inverse of R depending on the thickness (l) of the sample and the surface area of the electrodes (A):^[3, 7]

$$\sigma = \frac{l}{AR} \quad (4)$$

By measuring the conductivity as function of temperature information about the activation energy E_a of the ion hopping through the structure of the solid (activated jump process) can be obtained in an Arrhenius-type function with R being the ideal gas constant, σ_0 an pre-exponential factor and T the temperature:^[7-10]

$$\sigma = \frac{\sigma_0}{T} \cdot e^{\frac{-E_a}{RT}} \quad (5)$$

In Figure S49-53 the spectra were fitted with an equivalent circuit containing a capacitor parallel to the serial connection of RC elements. This accounts for cable and stray capacitance of the measurement setup and was kept constant at 20 pF during the fitting routine.^[11]

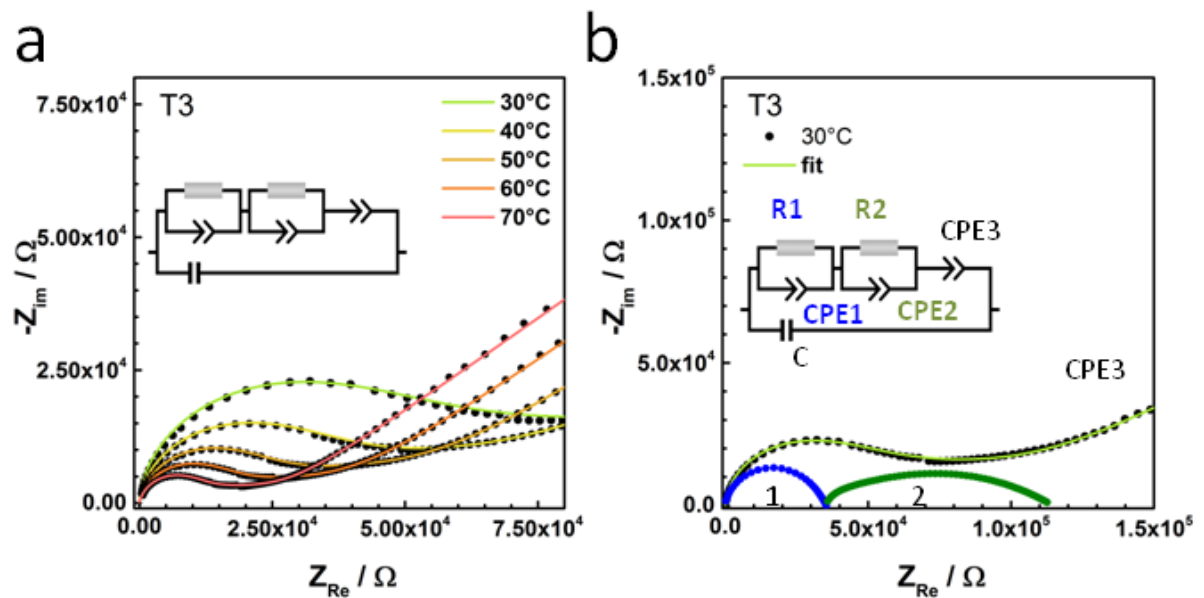


Figure S51: Representative EIS measurements of the sample T3 sintered at 400 °C (a) measurements and fits at different temperatures (b) fit of data measured at 30 °C with visualization of contributions to the fit with the shown model.

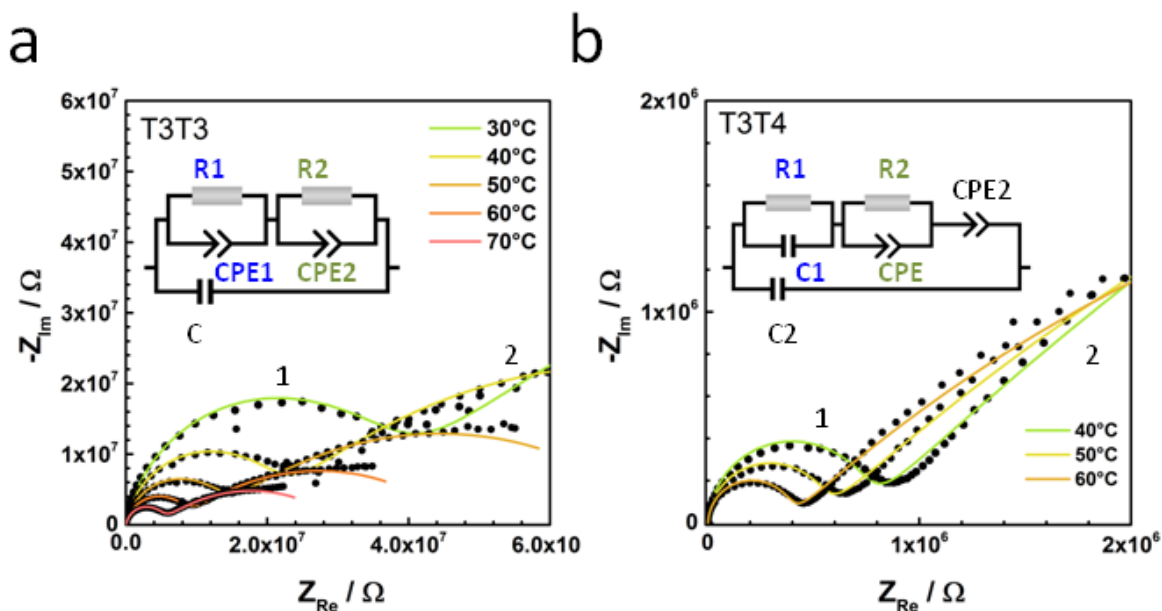


Figure S52: Representative EIS measurements with fits and applied model of the samples (a) T3T3, (b) T3T4 sintered at 400 °C. The contributions to the fit are indicated with the numbers 1 and 2 corresponding to the R1-CPE1 and R2-CPE2 elements.

For the capacitance of all contributions in the samples T3, T3T3 and T3T4 only values in the range of 10 nF to 0.1 nF were obtained. The R-CPE elements at higher frequencies (R1-CPE1 in S49-50) showed capacitances of about 10-100nF and at lower frequencies at least one order of magnitude larger. Thus, only conductivities limited by grain boundary properties were measured.^[4] The activation energies for the observed processes shown in the main text were different for each Na-Si-P compound. For sample $\text{Na}_{19}\text{Si}_{13}\text{P}_{25}$ (T3) the activation energy for the sum of both processes inside the extremely broad semicircle (cf. Figure S49a and b) was 0.36 eV. A clear deconvolution of the processes in the broad semicircle in T3 was difficult. Therefore, only the total conductivity was considered. For sample T3T3 the activation energies for both semicircles were very similar with 0.47 eV and 0.44 eV. Interestingly, no polarization spike was observed for T3T3 (cf. S50a). This corroborates the assumption that T3T3 is a mixed ionic-electronic conductor due to its comparable low ionic conductivity. For sample T3T4 the semicircle at lower frequencies (Figure S50b R2-CPE2) showed a much higher E_a and higher resistance than the one at high frequencies (0.69 eV for R2-CPE2 vs. 0.38 eV for R1-CPE1). This can indicate highly resistive layers at grain-to-grain contacts.^[12-13]

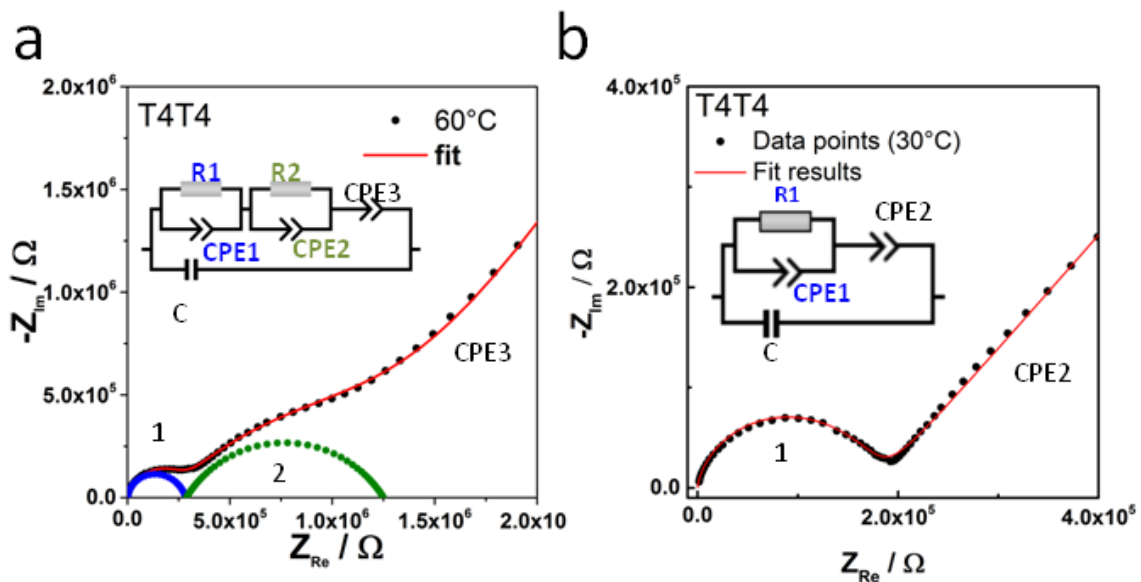


Figure S53: Representative EIS measurements of the sample T4T4 sintered at 400 °C (a) average sample showing two semicircles in the EIS, (b) best sample of T4T4 showing only one semicircle.

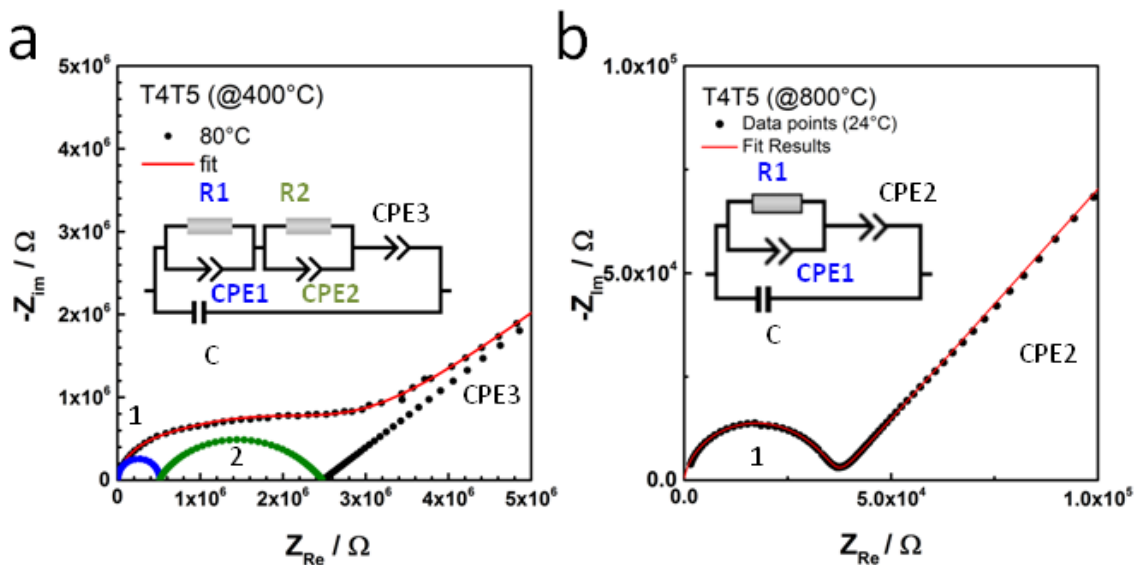


Figure S54: Representative EIS measurements of the sample T4T5 sintered at (a) 400 °C, (b) 800 °C.

The samples T4T4, T4T5 and T5T5 sintered at 400 °C show similar properties as T3T4 but have higher conductivities and lower E_a (cf. Figure S51a and S52a). For the presented best samples of T4T4 and T4T5 (and T5T5 as mentioned in the main text) in Figure S51b and S52b only one semicircle is visible, probably because this sample received the optimal sintering and pressing treatment. The capacitance of the R1-CPE1 element of the best samples of T4T4 and T4T5 was 20 pF, thus still higher as expected for bulk properties.

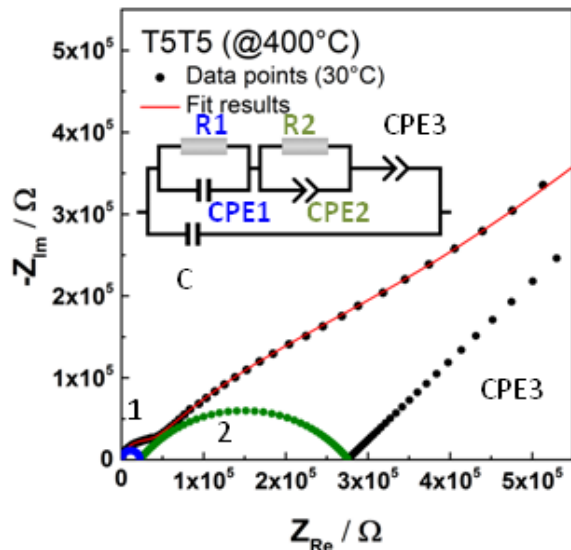


Figure S55: Representative EIS impedance measurement of the samples T5T5 sintered at 400 °C showing two semicircles.

Especially, for samples T4T5 (Figure S64a) and T5T5 (Figure S65) a non ideal microstructure of the pellets was noticed. Subsequently, for improving the microstructure the pellets were sintered at 800 °C (cf. Figure S68). For the other compounds (T3, T3T3, T3T4, T4T4) phase transitions occurred at such high sintering temperatures leading to a mixture of compounds in the pellet. Hence, they were sintered at 400 °C only.

Low temperature EIS of T5T5

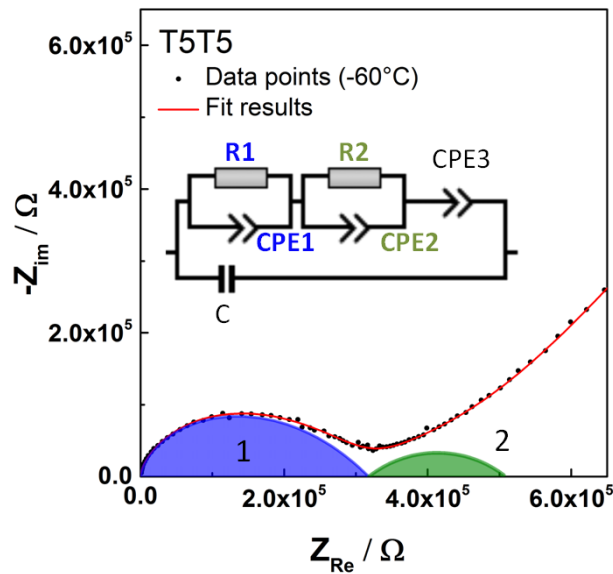


Figure S56: The electrochemical impedance of the T5T5 samples was measured at $-60\text{ }^{\circ}\text{C}$ showing a capacitance of about 20 pF ($C_{\text{eff}1}$ calculated from $R1$ and $CPE1$). The extraction of the capacitance from the measurement at $25\text{ }^{\circ}\text{C}$ was difficult due to the small resistance and the influence of cable induction on the spectrum.

Comparison of ionic conductivities of samples sintered at different temperatures

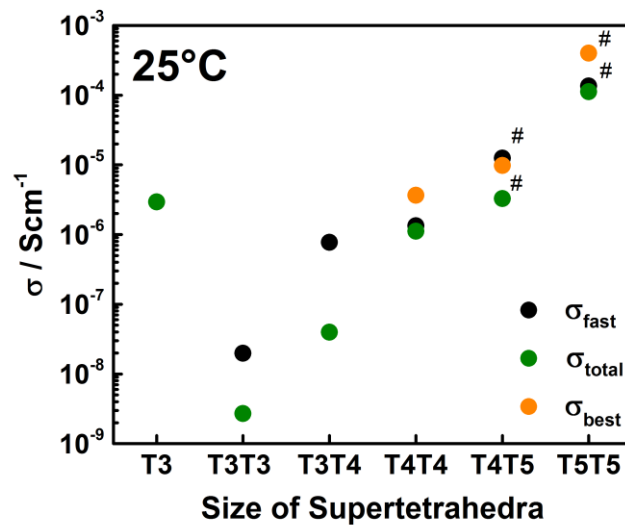


Figure S57: Ionic conductivities at $25\text{ }^{\circ}\text{C}$ increases with the size of the supertetrahedral entities in the Na-Si-P structures. The samples T3-T4T4 were sintered at $400\text{ }^{\circ}\text{C}$. T4T5 and T5T5 were sintered at $800\text{ }^{\circ}\text{C}$ (marked with a hash). σ_{fast} (black) refers to the average conductivity of at least four samples calculated from the resistance of the high frequency arc (cf. R1-CPE1 in Figure S49-53). σ_{total} (green) refers to the corresponding total conductivity (sum of the resistances of both semicircles; R1+R2). Additionally, the conductivities of the samples showing only one semicircle in the EIS are plotted in orange (σ_{best}).

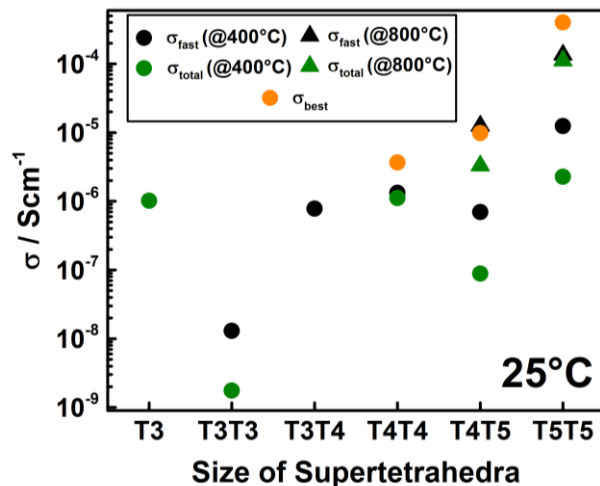


Figure S58: Comparison of the ionic conductivity of all samples at 25 °C. The conductivity increases with the size of the supertetrahedral entities in the Na-Si-P structures. The samples T3-T4T4 were sintered at 400 °C (points). This Figure also includes the conductivity values of T4T5 and T5T5 sintered at 400 °C (points) and at 800 °C (triangles). Especially for the sample T4T5 it is obvious that the microstructure is not optimal for impedance measurements and the performance is reduced in comparison to the samples sintered at 800 °C.

References

- [1] J. Maier, *Physical Chemistry of Ionic Materials*, John Wiley & Sons, Chichester, **2004**, pp. 419-462.
- [2] A. Senocrate, I. Moudrakovski, G. Y. Kim, T.-Y. Yang, G. Gregori, M. Grätzel, J. Maier, *Angew. Chem. Int. Ed.* **2017**, *56*, 7755-7759.
- [3] Wei Gao, N. M. Sammes, *An Introduction to Electronic and Ionic Materials*, World Scientific Publishing Co. Pte. Ltd, Singapore, **1999**, pp. 306-330.
- [4] J. T. S. Irvine, D. C. Sinclair, A. R. West, *Adv. Mater.* **1990**, *2*, 132-138.
- [5] A. Lasia, in *Modern Aspects of Electrochemistry* (Eds.: B. E. Conway, J. O. M. Bockris, R. E. White), Springer US, Boston, **2002**, pp. 143-248.
- [6] J. R. Macdonald, W. B. Johnson, in *Impedance Spectroscopy*, John Wiley & Sons, Inc., Hoboken, **2005**, pp. 1-26.
- [7] V. F. Lvovich, in *Impedance Spectroscopy: Applications to Electrochemical and Dielectric Phenomena*, John Wiley & Sons Inc., Hoboken, **2012**, pp. 38-47.
- [8] P. Bron, S. Dehnen, B. Roling, *J. Power Sources* **2016**, *329*, 530-535.
- [9] S. Deabate, F. Henn, S. Devautour, J. C. Giuntini, *J. Electrochem. Soc.* **2003**, *150*, J23.
- [10] J. Maier, in *Physical Chemistry of Ionic Materials*, John Wiley & Sons, Chichester, **2004**, pp. 283-292.
- [11] A. Kuhn, V. Duppel, B. V. Lotsch, *Energy Environ. Sci.* **2013**, *6*, 3548-3552.
- [12] J. Fleig, J. Maier, *J. Am. Ceram. Soc.* **1999**, *82*, 3485-3493.
- [13] P. Bron, S. Johansson, K. Zick, J. Schmedt auf der Günne, S. Dehnen, B. Roling, *J. Am. Chem. Soc.* **2013**, *135*, 15694-15697.

4.4 Polymorphism and fast Potassium-Ion Conduction in the T5 Supertetrahedral Phosphidosilicate KSi_2P_3

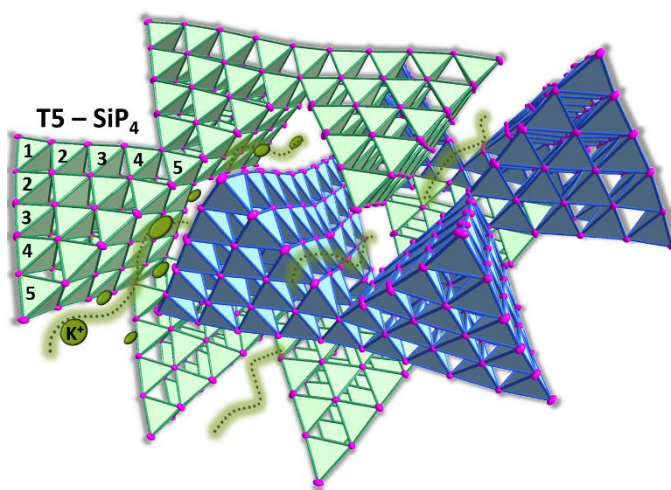
A. Haffner*, A.-K. Hatz*, O. E. O. Zeman, C. Hoch, B. V. Lotsch, D. Johrendt

*These authors contributed equally to this work

Published in *Angew. Chem. Int. Ed. Engl.* **2021**, 60 (24), 13641-13646.
DOI: 10.1002/anie.202101187

Abstract

The all-solid-state battery (ASSB) is a promising candidate for electrochemical energy storage. In view of the limited availability of lithium, however, alternative systems based on earth-abundant and inexpensive elements are urgently sought. Besides the well-studied sodium-based systems, potassium-based systems offer the advantage of low cost and a large electrochemical window but are hardly explored. Here we report on the synthesis and crystal structure of K-ion conducting T5 KSi_2P_3 , which was inspired by recent discoveries of fast ion conductors in the family of alkali phosphidosilicates. KSi_2P_3 is composed of SiP_4 tetrahedra forming interpenetrating networks of large T5 supertetrahedra. The compound passes through a reconstructive phase transition from the known T3 to the new tetragonal T5 polymorph at 1020 °C with enantiotropic displacive phase transitions upon cooling at about 155 °C and 80 °C. The potassium ions are located in large channels between the T5 supertetrahedral networks and show facile movement through the structure. The bulk ionic conductivity can be as high as $2.6 \cdot 10^{-4}$ S/cm at 25 °C with an average activation energy of 0.20 eV. This is remarkable high for a potassium ion conductor at room temperature, and marks KSi_2P_3 as the first non-oxide solid potassium ion conductor.



Introduction

All-solid-state batteries (ASSB) with solid instead of liquid electrolytes are traded as the next generation energy storage devices because they provide higher energy densities and faster charging rates than conventional systems.^[1-6] For the development of ASSBs, the solid electrolyte is a critical component and its ionic conductivity a key performance indicator. Up to now, several lithium ion conducting materials are well investigated. Lithium conducting garnets such as doped $\text{Li}_7\text{La}_3\text{Zr}_2\text{O}_{12}$ and $\text{Li}_{1.4}\text{Al}_{0.4}\text{Ti}_{1.6}(\text{PO}_4)_3$ exhibit bulk ionic conductivities up to 10^{-3} S/cm at room temperature. Similar and even higher lithium ion conductivities in the range of $1.6 \cdot 10^{-4}$ to $2.5 \cdot 10^{0/2}$ S/cm were found in ternary lithium thiophosphates,^[7] halide argyrodites,^[8-9] $\text{Li}_{10}\text{GeP}_2\text{S}_{12}$ -type

materials^[10] and rare-earth halides.^[11-13] Recently phosphidosilicates turned out to be candidates for solid electrolytes. These compound contain SiP_4 tetrahedra, which are isolated in Li_8SiP_4 ,^[14] while in $\text{Li}_{10}\text{Si}_2\text{P}_6$ or $\text{Li}_3\text{Si}_3\text{P}_7$ ^[15] the tetrahedra are condensed via edges or vertices to reduce the charge, reminiscent of related nitridosilicates. The SiP_4 tetrahedra in Li_2SiP_2 ^[14] form interpenetrating networks of T2 supertetrahedra, while in LiSi_2P_3 ^[16] fused T4 and T5 entities are present. The lithium ion conductivities range between $4 \cdot 10^{-7}$ S/cm (Li_2SiP_2)^[14] and $1 \cdot 10^{-3}$ S/cm ($\text{Li}_{14}\text{SiP}_6$)^[17] with activation energies of 0.49 to 0.30 eV, respectively. NMR data of LiSi_2P_3 reveal an activation energy of about 0.1 eV indicating an even more facile ion transport in this compound. However, batteries based on lithium are restricted especially for large scale applications by the limited availability of lithium and its uncertain costs.^[18-22] Therefore, systems with earth abundant low cost alternatives such as sodium or potassium are requested. Several solid sodium electrolytes like Na_3PS_4 ^[23] or NaSICON-type $\text{Na}_{3.4}\text{Sc}_2(\text{SiO}_4)_{0.4}(\text{PO}_4)_{2.6}$ ^[24-25] have conductivities on the order of $2 \cdot 10^{-4}$ S/cm and $7 \cdot 10^{-4}$ S/cm, respectively. β -Alumina,^[26] Na_3SbS_4 ^[27-28] or $\text{Na}_{11}\text{Sn}_2\text{PS}_{12}$ ^[29-30] exceed these conductivities by about one order of magnitude. The phosphidosilicates $\text{Na}_{23}\text{Si}_{9n+19}\text{P}_{12n+33}$ based on interpenetrating networks of fused T3 to T5 supertetrahedra turned out to be competitive.^[31] *HT*- NaSi_2P_3 exhibits solely T5 entities and shows a total sodium ion conductivity of $4 \cdot 10^{-4}$ S/cm with a low activation energy (E_a) of 0.25 eV. NMR data reveal an even lower activation energy of 0.11 eV, suggesting a facile Na hopping process. While sodium is much more abundant than lithium, it has a less negative electrode potential (-2.71 V) compared to lithium (-3.04 V). In contrast, potassium has a lower potential than Na (-2.93 V) enabling an improved cell output voltage.

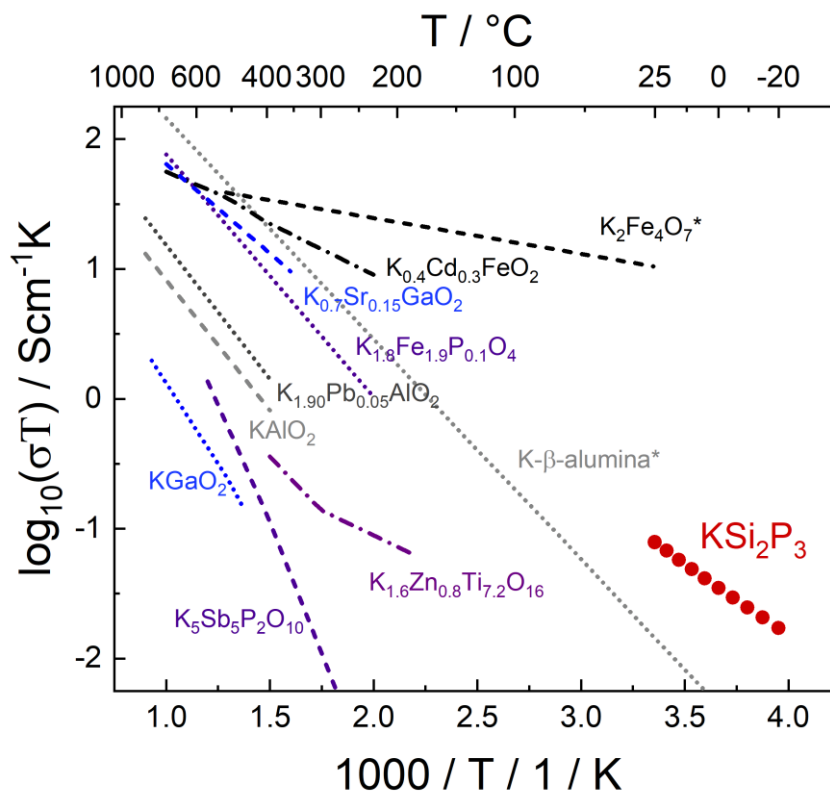


Figure 1. Ionic conductivity of potassium ion conductors and conductivity data of KSi_2P_3 -mC928 (sample 2c in Table S9). Asterisks indicate single-crystal data. References and activation energies are listed in Table S8.

Since the availability of potassium is comparable with sodium and it is also low in cost, the exploration of potassium ion batteries (KIBs) appears promising. So far, studies on KIBs employing potassium metal anodes, solid electrolytes and cathodes such as Prussian blue with remarkable capacities and cycling stabilities were reported.^[32-35] Surprisingly, only a few solid potassium ion electrolytes are known as shown in Figure 1 (values and references are given in Table S8). These materials are oxides, mainly discovered by Burmakin *et al.*, and show conductivities in a reasonable range for applications (10^{-4} - 10^{-2} S/cm) only at high temperatures of 300-400 °C. The only exception is hydrothermally synthesized polycrystalline $\text{K}_2\text{Fe}_4\text{O}_7$ showing an excellent performance with a conductivity of $5 \cdot 10^{-2}$ S/cm at room temperature. However, single crystal impedance spectroscopy^[34] shows that the potassium ion migration with an activation energy of 0.08 eV is strongly two-dimensional in this compound.

In this work, we targeted the family of potassium phosphidosilicates to discover new solid electrolytes. Currently only the compounds K_2SiP_2 ^[36] and the layered T3 KSi_2P_3 ^[37] are known in this system. Both are not promising as ion conductors because of the lack of partial occupied potassium sites. Here we report three new polymorphs of KSi_2P_3 with T5 supertetrahedral structures related to the sodium conductor NaSi_2P_3 .^[31] These new polymorphs are characterized by powder X-ray diffraction data based on the single-crystal structure refinement of the high temperature polymorph. ^{29}Si and ^{31}P MAS NMR spectra and the electronic properties of the monoclinic modification were determined, showing a remarkably high $\sigma_{\text{bulk}}(\text{K}^+)$ of up to $2.6 \cdot 10^{14}$ S/cm at 25 °C and an average low activation energy of 0.20 eV. This material hence qualifies as the first non-oxide fast solid potassium ion conductor.

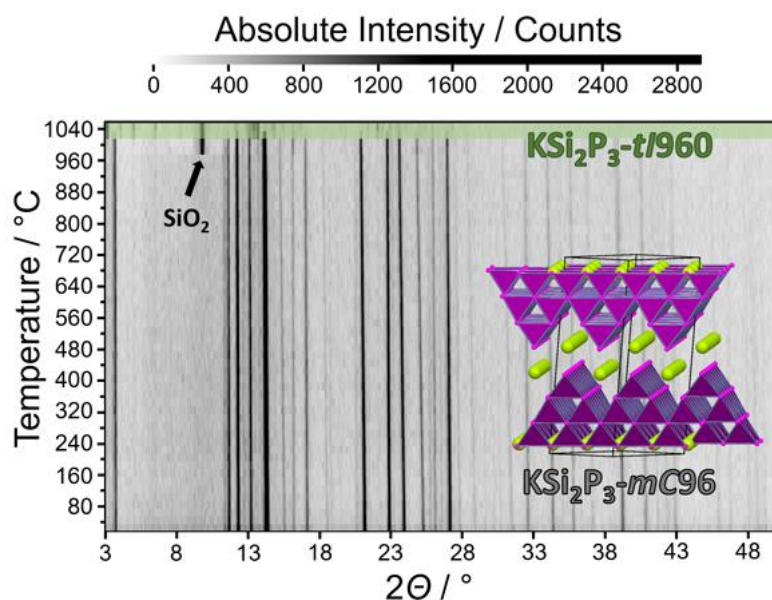


Figure 2. High temperature $\text{Mo-K}\alpha_1$ X-ray powder diffraction measurements of a KSi_2P_3 -mC96 sample with a phase transition to KSi_2P_3 -t/960 at about 1020 °C (highlighted in green). Inset shows the crystal structure of the known KSi_2P_3 -mC96 compound.

Structural characterization by X-ray diffraction

KSi_2P_3 (space group $C2/c$) was first described by Feng *et al.*^[37] and is denominated as $\text{KSi}_2\text{P}_3\text{-}mC96$ in the following. It contains SiP_4 tetrahedra which form T3 supertetrahedra according to the nomenclature proposed by Yaghi.^[38] These T3 entities are fused by one common SiP_4 tetrahedron resulting in a layered structure with the K^+ ions located on two fully occupied general Wyckoff sites between T3 supertetrahedral layers (see inset of Figure 2). This structure is stable upon heating to 1000 °C.

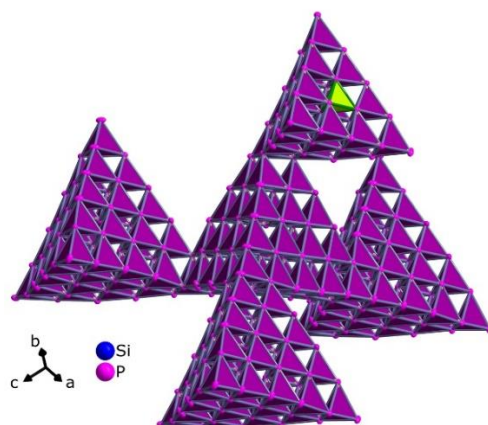


Figure 3. Three-dimensional fused T5 supertetrahedra composed of SiP_4 tetrahedra as in $\text{KSi}_2\text{P}_3\text{-}t/960$. Every T5 cluster lacks a central silicon atom indicated by the green P_4 tetrahedron in the upper T5 cluster (one tetrahedral basis layer of a T5 supertetrahedron was removed for clarity).

We detected a mixture of two phases at 1020 °C before $\text{KSi}_2\text{P}_3\text{-}mC96$ is completely transformed to a tetragonal modification at 1040°C, denoted as $\text{KSi}_2\text{P}_3\text{-}t/960$. Figure 2 shows the high temperature diffraction patterns. The additional reflection at about 9.8° indicates crystallization of the silica capillary. We were able to solve and refine the structure of this metastable high temperature polymorph quenched to room temperature with single-crystals. For details we refer to the experimental section in the Supporting Information). Table 1 summarizes the single-crystal data of $\text{KSi}_2\text{P}_3\text{-}t/960$ in space group $I4_1/acd$ (No. 142). Atom positions and displacement factors are given in Tables S1 and S2 of the Supporting Information. $\text{KSi}_2\text{P}_3\text{-}t/960$ is also built from SiP_4 tetrahedra, but now forming three dimensional networks of T5 supertetrahedra as shown in Figure 3. Every T5 cluster features a missing silicon site in its center, affecting the adjacent four phosphorus atoms by shifting them slightly towards the vacancy. This leads to shorter average P–P distances of 3.2 Å compared to 3.7 Å of the phosphorus atoms not neighboring the missing site. This appears counter-intuitive but has been already observed in several T5 supertetrahedral compounds, such as B_2S_3 ,^[39] LiSi_2P_3 ,^[16] *HT*- and *LT*- NaSi_2P_3 ^[31] or UCR-15.^[40] A likely explanation could be the preservation of charge neutrality in the interior of the T5 entity, since the T5 cluster is a section of the sphalerite-type structure with silicon defects resulting in the sum formula of Si_3P_4 . However, this binary compound has not been confirmed experimentally, but predicted by DFT calculations.^[41-42]

The T5 clusters share one common SiP_4 tetrahedron resulting in a three-dimensional anionic network with giant voids interpenetrated by a second crystallographically equivalent network.

These can be ascribed hierarchically to a diamond type network, resembling the structure of homeotypic $\text{HT-NaSi}_2\text{P}_3$.^[31]

Table 1. Single crystal data of the high temperature polymorph KSi_2P_3 -t/960. The dataset was collected at 25 °C on a Bruker D8 Quest diffractometer.

Formula	KSi_2P_3 -t/960
space group	$I4_1/acd$ (No. 142)
$a / \text{Å}$	21.9221(15)
$c / \text{Å}$	39.868(3)
$V_{\text{cell}} / \text{Å}^3$	19160(3)
Z	128
$\rho_{\text{X-ray}} / \text{g}\cdot\text{cm}^{-3}$	2.088
$\lambda / \text{Å}$	0.71073 (Mo-K α)
μ / mm^{-1}	1.937
θ -range / °	2.120 – 30.586
reflections measured	459701
independent reflections	7358
parameters	283
R_{σ}	0.0095
R_{int}	0.0452
$R_1 (F^2 > 2\sigma(F^2)) / \text{all}$	0.0391 / 0.0438
$wR_2 (F^2 > 2\sigma(F^2)) / \text{all}$	0.0919 / 0.0951
Goof	1.102
restraints	1
$\Delta\rho_{\text{max/min}} / \text{e}\cdot\text{Å}^{-3}$	+1.610 / -1.374

The potassium ions reside in big cavities of the supertetrahedral networks with large displacement factors and an average occupancy factor of 0.4. All eleven potassium positions are partially occupied and thus disordered (see Figure 4), similar to $\text{HT-NaSi}_2\text{P}_3$, which indicates a high mobility of potassium ions already at room temperature.

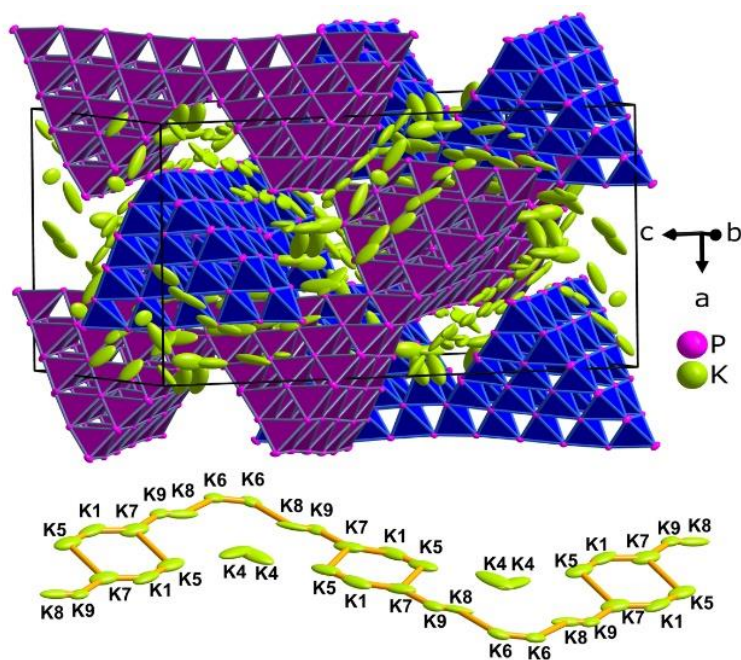


Figure 4. Unit cell of KSi_2P_3 -*t*/960 with large displacement factors of the K ions (top, ellipsoids with 90 % probability) and K positions in the voids along [111] indicating a possible ion migration pathway (bottom, ellipsoids with 50 % probability).

KSi_2P_3 -*t*/960 goes through displacive phase transitions upon cooling. As shown in Figure 5, KSi_2P_3 -*t*/960 exhibits a splitting of the most intense reflections at a diffraction angle range of 13.1 to 13.7° ($\text{Mo-K}\alpha_1$) at 155°C . Two of these split reflections approach each other while the third moves towards a higher angle of about 14° beginning at 80°C , indicating a third phase transition. These phase transitions occur upon heating and cooling of a KSi_2P_3 sample making this T5 compound enantiotropic (see Figure 5). We were not able to synthesize suitable single-crystals of the two low temperature modifications mainly due to twinning. Therefore, we stabilized the different modifications for powder diffraction analysis at ambient conditions. While the room temperature modification is easily producible with conventional solid-state methods, small amounts of the other modification could only be obtained by a modified synthesis as described in the Supporting Information. The $\text{Cu-K}\alpha_1$ diffraction patterns and Rietveld fits of the respective modifications are shown in Figure 6 (enlarged in the SI Figures S1-3) highlighting their most prominent differences consisting in the splitting, the intensity distribution, and the shifting towards higher diffraction angles of the indicated reflections. Acceptable refinements were obtained by *translationsgleiche* (*t*2) symmetry reductions from tetragonal KSi_2P_3 -*t*/960 (spacegroup $I4_1/acd$) to the orthorhombic and monoclinic subgroups of KSi_2P_3 -*o*F1952 ($Fddd$) and KSi_2P_3 -*m*C928 ($C2/c$).

Note that the potassium positions were calculated from the symmetry reduced single-crystal structure data of KSi_2P_3 -*t*/960. Therefore, these positions do not strictly follow the *Bärnighausen tree* while silicon and phosphorus do. The displacive phase transitions are mainly contractions of the crystal structure as visible in Table 2, thus increasing the crystallographic density along with the symmetry reduction (note that the cell parameters given in Table 2 appear dissimilar due to different space groups).

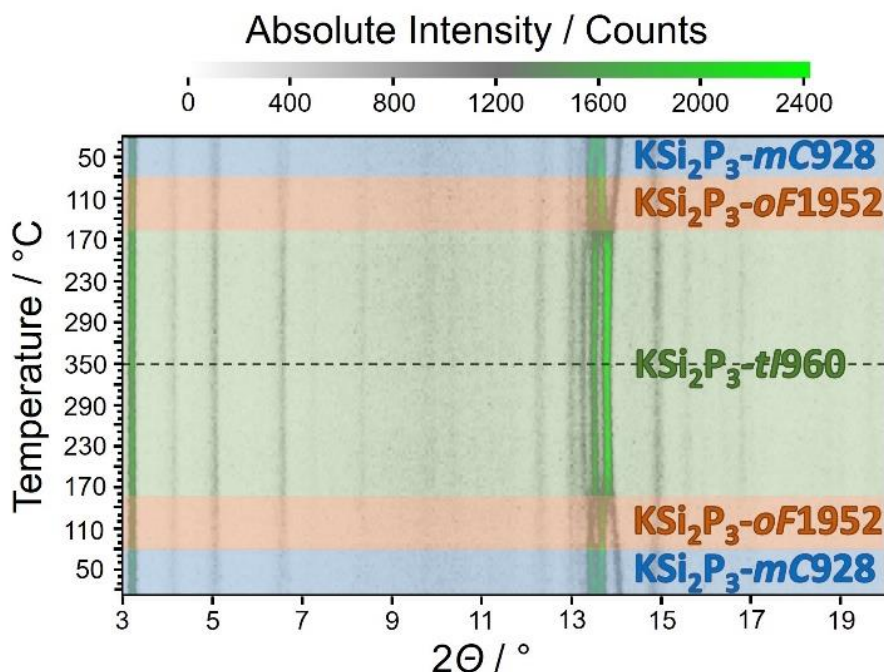


Figure 5. High temperature X-ray powder diffraction (Mo- $\text{K}\alpha_1$) of a KSi_2P_3 -mC928 sample upon heating to 350 °C and subsequent cooling. KSi_2P_3 -mC928 (highlighted in blue) transforms at 80 °C into KSi_2P_3 -oF1952 (orange) before another phase transition at 155 °C yields in KSi_2P_3 -t/960 (green). The same phase transitions are observable upon cooling making the T5 compound enantiotropic.

Table 2. Rietveld refinement results of the T5 KSi_2P_3 modifications.

Modification	KSi_2P_3 -t/960	KSi_2P_3 -oF1952	KSi_2P_3 -mC928
space group	$I4_1/acd$ (No. 142)	$Fddd$ (No. 70)	$C2/c$ (No. 15)
stability range / °C	> 155	155 – 80	< 80
a / Å	21.8826(3)	31.5291(10)	31.8337(4)
b / Å	21.8826(3)	30.5475(5)	30.4796(3)
c / Å	40.2923(8)	39.9611(13)	25.2909(2)
β / °	90	90	128.7029(8)
V_{cell} / Å ³	19293.8(6)	38487(2)	19150.3(4)
$\rho_{\text{X-ray}}$ / g·cm ⁻³	2.07651(6)	2.08417(12)	2.11092(5)

Structural characterization by EDX and NMR

We have confirmed the composition and structure model of KSi_2P_3 -mC928 with EDX (Figure S4, Table S7) and NMR measurements under MAS conditions. The ^{29}Si spectrum (Figure S5) has broad signals between δ (^{29}Si) = -12 to -26 ppm originating from 32 crystallographically inequivalent silicon atoms on general Wyckoff sites. Since the structure of KSi_2P_3 -mC928 is homeotypic to HT - NaSi_2P_3 , the ^{31}P spectra are comparable as visible in Figure 7. KSi_2P_3 -mC928 exhibits four broad signals within almost the same chemical shift range compared to the tetragonal sodium phase. Integration of these signals in the KSi_2P_3 -mC928 spectrum yields the same intensity distribution of 4:4:3:1 confirming the structural similarity to HT - NaSi_2P_3 .^[31]

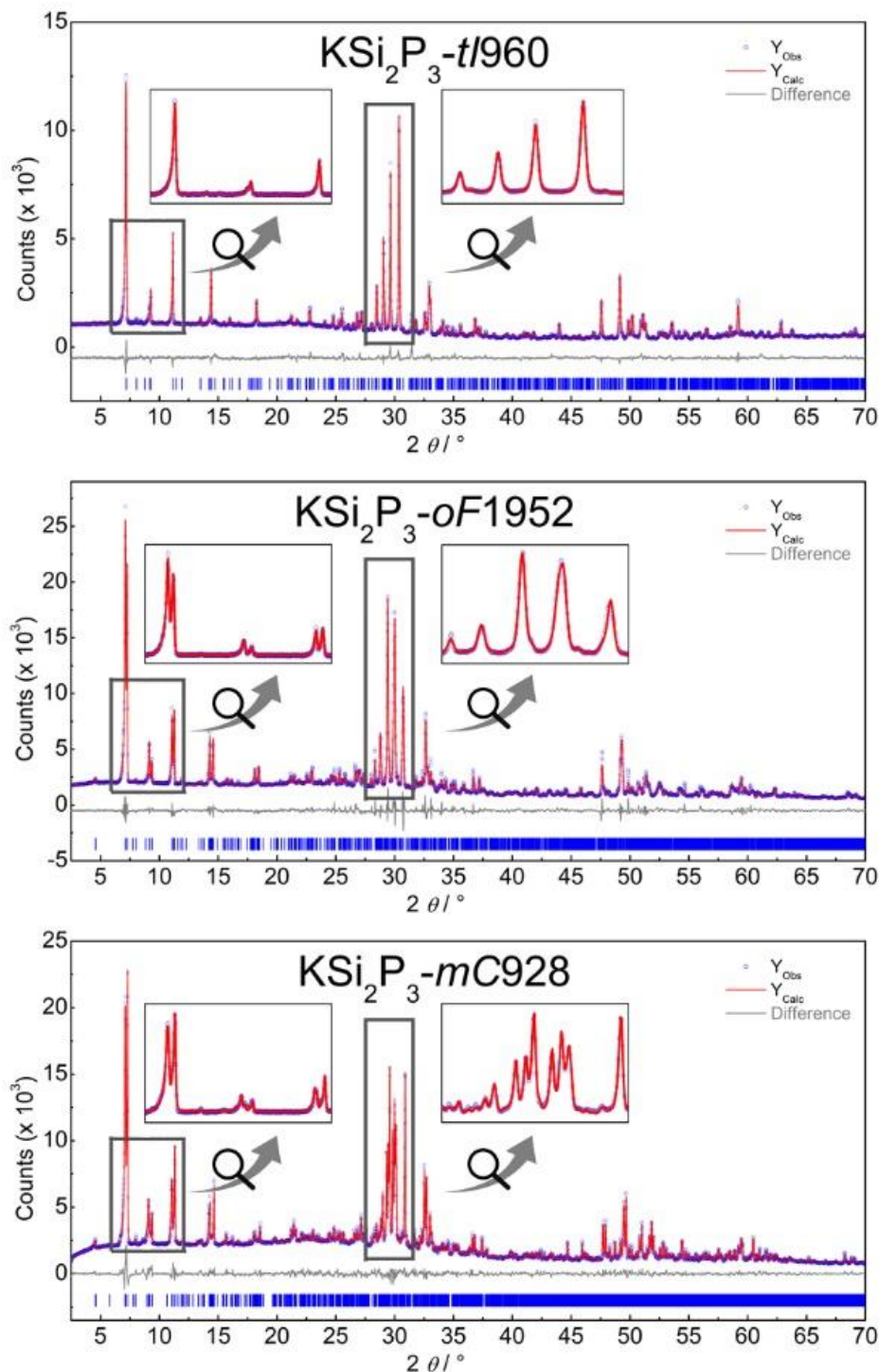


Figure 6. Powder X-ray diffraction patterns ($\text{Cu-K}\alpha_1$) of tetragonal (top), orthorhombic (middle) and monoclinic (bottom) KSi_2P_3 .

However, the resonance frequencies of $\text{KSi}_2\text{P}_3\text{-mC928}$ are more complicated than in $\text{HT-NaSi}_2\text{P}_3$ due to the symmetry reduction from tetragonal to monoclinic, leading to a splitting of all resonances and impeding a simple intensity assignment to the respective phosphorus atoms. Assuming that the upfield signal at $\delta(^{31}\text{P}) = -298.7$ ppm is the result of only one phosphorus atom, a sectional intensity integration of the whole spectrum can be conducted. It results in 49 distinct

atoms being very close to the number of 48 atoms as predicted by X-ray diffraction. Hence, the NMR measurements are in line with the structure discussion above.

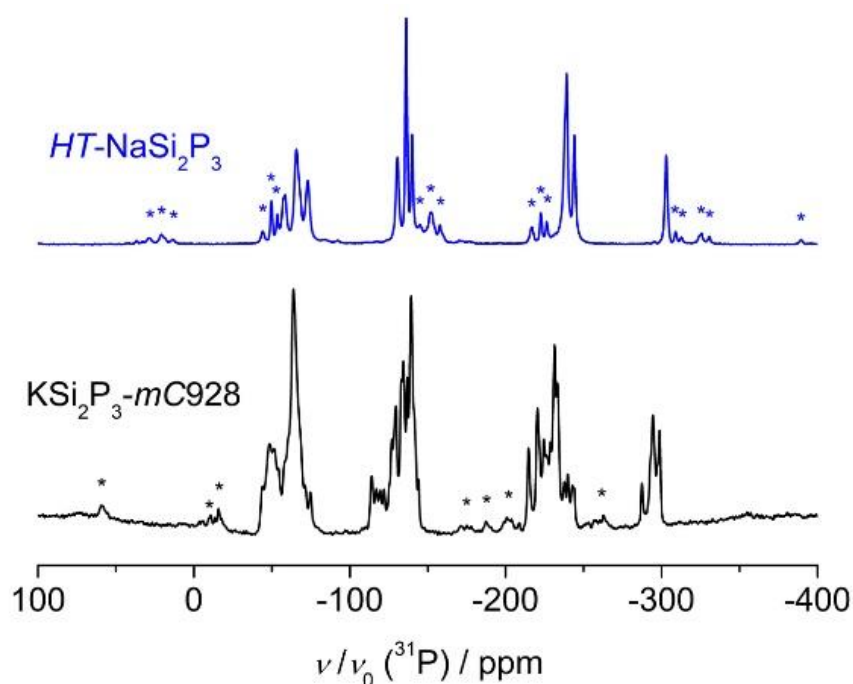


Figure 7. Normalized ^{31}P MAS NMR spectra of $\text{HT-NaSi}_2\text{P}_3$ (top, blue) and $\text{KSi}_2\text{P}_3\text{-mC928}$ (bottom, black) at 25 kHz and a magnetic field of $B_0 = 11.7$ T. Rotational side bands are indicated by asterisks.

Potassium ion conduction in KSi_2P_3

We identified possible migration pathways of all polymorphs of KSi_2P_3 from geometrical calculations yielding four large channels through the structure, which are interconnected by short passages along every supertetrahedral face. This indicates a 3D ion conduction similar to NaSi_2P_3 . The calculated migration paths are visualized in Figure S6-S8 in the Supporting Information.

We have shown recently,^[31] that the ionic conductivity in supertetrahedral phosphidosilicates increases with increasing cluster size. In view of the T5 structure of KSi_2P_3 , high K-ion mobility is also to be expected in contrast to the T3 structure. We applied electrochemical impedance spectroscopy (EIS) and potentiostatic polarization measurements as described in the SI on several samples from different batches to assess the ionic and electronic conductivity. All results are listed in Table S9 and S10 and a representative impedance spectrum at -20 °C (sample 2b in Table S9) is shown in Figure 8. The measurements were performed at low temperatures to deconvolute the bulk properties of the material and to avoid phase changes that already occur at 80 °C influencing the performance. The spectrum contains high and low frequency contributions followed by a spike resulting from the polarization of K ions at the blocking electrodes at low frequencies. The spectrum is fitted by the equivalent circuit model depicted in the inset in Figure 8. For the high frequency semicircle modelled by R1-CPE1, an effective capacitance $C_{\text{eff}} = (Q/(R^{\alpha-1}))^{1/\alpha}$ of 8 pF is calculated that corresponds to a relative permittivity of 24. This is a typical value for the bulk contributions of a solid inorganic material.^[43] The low frequency semicircle (R2-CPE2) possesses a much larger C_{eff} of $9 \cdot 10^{-7}$ F, thus it presumably stems from grain boundaries or a surface layer.^[43]

The low frequency semicircle CPE3 models the polarization of ions at the electrode. The ionic conductivity σ_{bulk} (K^+) of nine measured samples stemming from three different batches (cf. Table S9) is between $0.13\text{--}2.6 \cdot 10^{-4} \text{ S/cm}$ with an average activation energy of $0.20 \pm 0.04 \text{ eV}$. The observed spread in conductivities is typical for a solid ion conductor as previously revealed in a round robin study of sulfide electrolytes^[44] and can be rationalized here by batch to batch variations as well as differences in pellet preparation, annealing and sputtering of each sample. The highest bulk conductivity we found is $2.6 \cdot 10^{-4} \text{ S/cm}$ at room temperature with an activation energy of 0.21 eV (plotted in Figure S9), which is consistent with the averaged activation energy of the high frequency semicircle of all samples ($0.20 \pm 0.04 \text{ eV}$). This result is directly compared to literature data in Figure 1, highlighting its uniqueness as first non-oxide K ion conductor with high ionic conductivity at room temperature and below (down to $-20 \text{ }^\circ\text{C}$) and a low activation energy, indicating facile ion migration within the large channels of the structure. KSi_2P_3 exhibits an even higher ionic conductivity than K- β -Alumina single-crystals. Compared to other potassium ion conductors, KSi_2P_3 does not contain redox active transition metals nor expensive or environmentally hazardous elements.

The total ionic conductivity of all samples is between $0.045\text{--}2.0 \cdot 10^{-4} \text{ S/cm}$ and can be calculated from R_{tot} as sum of R_1+R_2 with $\sigma_{\text{tot}} = d/(A \cdot R_{\text{tot}})$ with d being the thickness and A the area of the sample. This shows that even the total ionic conductivity is reasonably fast for an ionic conductor at room temperature. The activation energy of the low frequency semicircle ($R_2\text{-CPE2}$) of $0.19 \pm 0.03 \text{ eV}$ resembles the activation energy of the bulk process (also cf. Figure S9). Thus, there is no indication of the presence of highly resistive grain boundaries. The similar activation energy rather points to a current constriction phenomenon that could result from a limited contact area between the grains, which is consistent with the low geometrical density of $77 \pm 3 \%$ of the sample pellets.^[45] Therefore, by optimizing the sample preparation and microstructure, the total conductivity may be enhanced further.

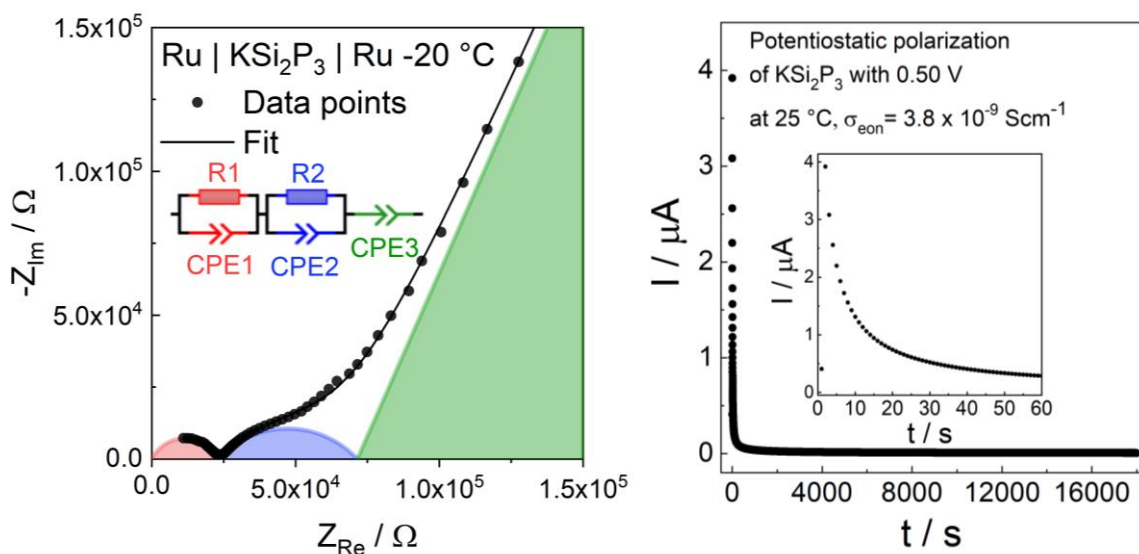


Figure 8. Left: Impedance spectra of KSi_2P_3 at $-20 \text{ }^\circ\text{C}$ (sample 6 in Table S9), fitted with the equivalent circuit model shown in the inset. The spectrum can be deconvoluted into bulk (high frequency semicircle $R_1\text{CPE1}$) and surface/interlayer contributions (low frequency semicircle). Right: Potentiostatic polarization curve over 5 h showing a low electronic conductivity of $3.8 \cdot 10^{-9} \text{ S/cm}$. Inset shows data at short times.

The partial electronic conductivity was measured by a potentiostatic polarization experiment over several hours at 0.25 and 0.5 V for several samples (cf. Table S10). A representative plot is shown in Figure 8 (right). The electronic conductivity is $0.09\text{-}1.1\cdot 10^{-8}$ S/cm, resulting in a transference number $\tau_i = \sigma_{\text{ion}}/(\sigma_{\text{ion}}+\sigma_{\text{eon}})$ of 0.9998. This suggests that this material can be classified as a predominantly ionic conductor.

Conclusion

In summary, we have identified three new polymorphs of KSi_2P_3 with T5 supertetrahedra and K-ion conductivities up to $2.6\cdot 10^{-4}$ S/cm at 25 °C. The hitherto known modification consists of T3 supertetrahedra without partially occupied K sites, which hampers ion conduction. We demonstrate fast potassium ion conduction through three-dimensional connected voids between the large T5 supertetrahedra. KSi_2P_3 contains low cost, non-redox active, and environmentally abundant elements. As the first non-oxide solid material, KSi_2P_3 extends the compositional space of solid potassium ion conductors, which is key for the rational design of further potassium solid electrolytes. Nevertheless, beside the exploration on other unknown potassium phosphidosilicates continuative work on this title compound is to be conducted to prove the suitability for application in solid-state batterie.

Acknowledgements

We thank Peter Mayer for supporting crystallographic discussions, Wolfgang Schnick for access to analytical devices, the Deutsche Forschungsgemeinschaft (DFG) and the German Federal Ministry of Research and Education (BMBF), project 03XP0177B (FestBatt), for financial support.

Author Contributions

AH, AKH conceived and designed this study; AH conducted the synthesis and was responsible for measuring SCXRD, PXRD, EDX; AKH measured EIS and potentiostatic polarization; AH performed structure determination; O. measured NMR; AH performed the calculation of TOPOS data and analysed MAS NMR; AKH analysed EIS and potentiostatic polarization; AH and AKH interpreted the interplay of structure and conductivity; AH and AKH wrote sections of the manuscript; All authors wrote and commented on the manuscript.

References

- [1] M. Armand, J. M. Tarascon, *Nature* **2008**, *451*, 652-657.
- [2] J. C. Bachman, S. Muy, A. Grimaud, H. H. Chang, N. Pour, S. F. Lux, O. Paschos, F. Maglia, S. Lupart, P. Lamp, L. Giordano, Y. Shao-Horn, *Chem. Rev.* **2016**, *116*, 140-162.
- [3] Y. Wang, S. Song, C. Xu, N. Hu, J. Molenda, L. Lu, *Nano Materials Science* **2019**, *1*, 91-100.
- [4] Z. Zhang, Y. Shao, B. Lotsch, Y.-S. Hu, H. Li, J. Janek, L. F. Nazar, C.-W. Nan, J. Maier, M. Armand, L. Chen, *Energy Environ. Sci.* **2018**, *11*, 1945-1976.
- [5] R. Chen, W. Qu, X. Guo, L. Li, F. Wu, *Mater. Horizons* **2016**, *3*, 487-516.
- [6] Y.-G. Lee, S. Fujiki, C. Jung, N. Suzuki, N. Yashiro, R. Omoda, D.-S. Ko, T. Shiratsuchi, T. Sugimoto, S. Ryu, J. H. Ku, T. Watanabe, Y. Park, Y. Aihara, D. Im, I. T. Han, *Nat. Energy* **2020**, *5*, 299-308.
- [7] Z. Liu, W. Fu, E. A. Payzant, X. Yu, Z. Wu, N. J. Dudney, J. Kiggans, K. Hong, A. J. Rondinone, C. Liang, *J. Am. Chem. Soc.* **2013**, *135*, 975-978.

- [8] M. A. Kraft, S. P. Culver, M. Calderon, F. Böcher, T. Krauskopf, A. Senyshyn, C. Dietrich, A. Zevalkink, J. Janek, W. G. Zeier, *J. Am. Chem. Soc.* **2017**, *139*, 10909-10918.
- [9] M. A. Kraft, S. Ohno, T. Zinkevich, R. Koerver, S. P. Culver, T. Fuchs, A. Senyshyn, S. Indris, B. J. Morgan, W. G. Zeier, *J. Am. Chem. Soc.* **2018**, *140*, 16330-16339.
- [10] N. Kamaya, K. Homma, Y. Yamakawa, M. Hirayama, R. Kanno, M. Yonemura, T. Kamiyama, Y. Kato, S. Hama, K. Kawamoto, A. Mitsui, *Nat. Mater.* **2011**, *10*, 682-686.
- [11] X. Li, J. Liang, J. Luo, M. Norouzi Banis, C. Wang, W. Li, S. Deng, C. Yu, F. Zhao, Y. Hu, T.-K. Sham, L. Zhang, S. Zhao, S. Lu, H. Huang, R. Li, K. R. Adair, X. Sun, *Energy Environ. Sci.* **2019**, *12*, 2665-2671.
- [12] H.-J. Steiner, H. D. Lutz, *Z. Anorg. Allg. Chem.* **1992**, *613*, 26-30.
- [13] T. Asano, A. Sakai, S. Ouchi, M. Sakaida, A. Miyazaki, S. Hasegawa, *Adv. Mater.* **2018**, *30*, 1803075.
- [14] L. Toffoletti, H. Kirchhain, J. Landesfeind, W. Klein, L. van Wüllen, H. A. Gasteiger, T. F. Fässler, *Chem. - Eur. J.* **2016**, *22*, 17635-17645.
- [15] H. Eickhoff, L. Toffoletti, W. Klein, G. Raudaschl-Sieber, T. F. Fässler, *Inorg. Chem.* **2017**, *56*, 6688-6694.
- [16] A. Haffner, T. Bräuniger, D. Johrendt, *Angew. Chem. Int. Ed.* **2016**, *55*, 13585-13588.
- [17] S. Strangmüller, H. Eickhoff, D. Müller, W. Klein, G. Raudaschl-Sieber, H. Kirchhain, C. Sedlmeier, V. Baran, A. Senyshyn, V. L. Deringer, L. van Wüllen, H. A. Gasteiger, T. F. Fässler, *J. Am. Chem. Soc.* **2019**, *141*, 14200-14209.
- [18] K. Vignaroban, R. Kushagra, A. Elango, P. Badami, B. E. Mellander, X. Xu, T. G. Tucker, C. Nam, A. M. Kannan, *Int. J. Hydrogen Energy* **2016**, *41*, 2829-2846.
- [19] M. Sawicki, L. L. Shaw, *RSC Adv.* **2015**, *5*, 53129-53154.
- [20] N. Yabuuchi, K. Kubota, M. Dahbi, S. Komaba, *Chem. Rev.* **2014**, *114*, 11636-11682.
- [21] H. Pan, Y.-S. Hu, L. Chen, *Energy Environ. Sci.* **2013**, *6*, 2338-2360.
- [22] H. Vikström, S. Davidsson, M. Höök, *Appl. Energy* **2013**, *110*, 252-266.
- [23] A. Hayashi, K. Noi, A. Sakuda, M. Tatsumisago, *Nat. Commun.* **2012**, *3*, 856.
- [24] M. Kaus, M. Guin, M. Yavuz, M. Knapp, F. Tietz, O. Guillon, H. Ehrenberg, S. Indris, *J. Phys. Chem. C* **2017**, *121*, 1449-1454.
- [25] M. Guin, F. Tietz, O. Guillon, *Solid State Ionics* **2016**, *293*, 18-26.
- [26] A. Hooper, *J. Phys. D: Appl. Phys.* **1977**, *10*, 1487-1496.
- [27] L. Zhang, D. Zhang, K. Yang, X. Yan, L. Wang, J. Mi, B. Xu, Y. Li, *Adv. Sci.* **2016**, *3*, 1600089.
- [28] A. Hayashi, N. Masuzawa, S. Yubuchi, F. Tsuji, C. Hotehama, A. Sakuda, M. Tatsumisago, *Nat. Commun.* **2019**, *10*, 5266.
- [29] Z. Zhang, E. Ramos, F. Lalère, A. Assoud, K. Kaup, P. Hartman, L. F. Nazar, *Energy Environ. Sci.* **2018**, *11*, 87-93.
- [30] M. Duchardt, U. Ruschewitz, S. Adams, S. Dehnen, B. Roling, *Angew. Chem. Int. Ed.* **2018**, *57*, 1351-1355.
- [31] A. Haffner, A.-K. Hatz, I. Moudrakovski, B. V. Lotsch, D. Johrendt, *Angew. Chem. Int. Ed.* **2018**, *57*, 6155-6160.
- [32] S. Komaba, T. Hasegawa, M. Dahbi, K. Kubota, *Electrochem. Commun.* **2015**, *60*, 172-175.
- [33] J. C. Pramudita, D. Sehwat, D. Goonetilleke, N. Sharma, *Adv. Energy Mater.* **2017**, *7*, 1602911.
- [34] H. Yuan, H. Li, T. Zhang, G. Li, T. He, F. Du, S. Feng, *J. Mater. Chem. A* **2018**, *6*, 8413-8418.
- [35] A. Eftekhari, *J. Power Sources* **2004**, *126*, 221-228.
- [36] B. Eisenmann, M. Somer, *Z. Naturforsch. B* **1984**, *39*, 736-738.
- [37] K. Feng, L. Kang, W. Yin, W. Hao, Z. Lin, J. Yao, Y. Wu, *J. Solid State Chem.* **2013**, *205*, 129-133.
- [38] H. Li, J. Kim, T. L. Groy, M. O'Keeffe, O. M. Yaghi, *J. Am. Chem. Soc.* **2001**, *123*, 4867-4868.
- [39] T. Sasaki, H. Takizawa, K. Uheda, T. Yamashita, T. Endo, *J. Solid State Chem.* **2002**, *166*, 164-170.
- [40] C. Wang, X. Bu, N. Zheng, P. Feng, *J. Am. Chem. Soc.* **2002**, *124*, 10268-10269.
- [41] M. Huang, Y. P. Feng, A. T. L. Lim, J. C. Zheng, *Phys. Rev. B* **2004**, *69*, 054112.
- [42] G. Gopal Khan, S. J. Clark, N. R. Bandyopadhyay, *Int. J. Mod. Phys. B* **2010**, *24*, 5487-5494.
- [43] J. T. S. Irvine, D. C. Sinclair, A. R. West, *Adv. Mater.* **1990**, *2*, 132-138.
- [44] S. Ohno, T. Bernges, J. Buchheim, M. Duchardt, A.-K. Hatz, M. A. Kraft, H. Kwak, A. L. Santhosha, Z. Liu, N. Minafra, F. Tsuji, A. Sakuda, R. Schlem, S. Xiong, Z. Zhang, P. Adelhelm, H. Chen, A. Hayashi, Y. S. Jung, B. V. Lotsch, B. Roling, N. M. Vargas-Barbosa, W. G. Zeier, *ACS Energy Lett.* **2020**, 910-915.
- [45] J. Fleig, J. Maier, *J. Am. Ceram. Soc.* **1999**, *82*, 3485-3493.

3.4.1 Supporting Information for “Polymorphism and fast Potassium-Ion Conduction in the T5 Supertetrahedral Phosphidosilicate KSi_2P_3 ”

Table of Contents

- **Experimental Section** containing the synthesis, single-crystal and powder X-ray diffraction, temperature-dependent powder X-ray diffraction and EDX, NMR and electrical spectroscopy measurements as well as the geometrical pathway calculation.
- **Additional crystallographic data** on KSi_2P_3 -*t*/960 (Table S1, S2), KSi_2P_3 -*o*F1952 (Table S3, S4) and KSi_2P_3 -*m*C928 (Table S5, S6) derived from the symmetry reduced KSi_2P_3 -*t*/960 modification
- **Powder X-ray diffraction** patterns and Rietveld refinements of KSi_2P_3 -*t*/960 (Figures S1), KSi_2P_3 -*o*F1952 (Figure S2) and KSi_2P_3 -*m*C928 (Figure S3)
- **Elemental analysis** by EDX and scanning electron microscopy of KSi_2P_3 -*m*C928 (Figure S4, Table S7)
- **^{29}Si solid-state MAS NMR** of KSi_2P_3 -*m*C928 (Figure S5)
- **Geometrical analysis** of possible K ion migration pathways of KSi_2P_3 -*t*/960 (Figure S6), KSi_2P_3 -*o*F1952 (Figure S7) and KSi_2P_3 -*m*C928 (Figure S8)
- **Ionic conductivities** and activation energies of a selection of potassium ion conductors from literature (Table S8), results of electrochemical characterization of KSi_2P_3 -*m*C928 (Table S9), Arrhenius plot of sample 3a (Figure S9) and results of polarization measurements of KSi_2P_3 -*m*C928 (Table S10).
- **References**

Experimental Procedures

Synthesis

Like most of alkaline and alkaline-earth phosphidosilicates the title compound is highly moisture sensitive leading to hydrolysis within a few minutes by contact with air. Therefore, all manipulations were conducted under inert conditions.

KSi_2P_3 -*m*C928 can be obtained as an air sensitive and dark red polycrystalline powder by reacting directly a stoichiometric elemental mixture. To this end, metallic potassium (1 eq., 0.0208 g, 99.95 %), silicon powder (2 eq., 0.0299 g, 99.999 %) and red phosphorus (3 eq., 0.0494 g, 99.999+ %) were mixed in an argon filled glovebox and loaded into an alumina crucible and sealed in silica ampoules under argon atmosphere. To prevent bursting of the ampoule the temperature of the tube furnace was raised slowly to 200 °C with a 20 °C/h rate before the mixture was reacted for 60 h at 1060 °C. To produce larger amounts of KSi_2P_3 -*m*C928 we synthesized the known T3 compound as precursor.

Therefore, we mixed potassium (1 eq., 0.1039 g), silicon (2 eq., 0.1495 g) and phosphorus (3 eq., 0.2471 g), and heated the mixture to 700 °C with a 10 °C/h rate for 30 h. The intermediate was ground and reheated again to 700 °C for 30 h yielding in a phase-pure precursor. This precursor was inserted in a preheated furnace at 1060 °C and reacted for 2 h before the temperature settled to 25 °C with 40 °C/h. Since we failed to produce the polymorphs $\text{KSi}_2\text{P}_3\text{-}oF1952$ and $\text{KSi}_2\text{P}_3\text{-}t/960$ by different temperature programs, we were able to intercept small amounts of these by applying three equivalents of an in situ formed crystallization agent of K_3P . To this end, a mixture of potassium (5 eq., 0.0618 g), silicon (1 eq., 0.0085 g) and phosphorus (3 eq., 0.0294 g) was prepared likewise and heated to 100 °C within 5 h before the temperature was raised to 800 °C or 950 °C with 100 °C/h for 60 h, respectively.

Single-Crystal X-ray Diffraction.

The crystal structure of the T5 compound was successfully solved and refined only for the $\text{KSi}_2\text{P}_3\text{-}t/960$ polymorph. Due to the sensitivity to air and moisture, single-crystals were prepared under dried paraffin oil and transferred into oil filled and sealed glass capillaries (Hilgenberg GmbH) with an inner diameter of 0.2 mm. Diffraction data of the whole Ewald's sphere were collected with a Bruker D8 Quest device with Mo- $\text{K}\alpha$ radiation, Photon II detector and Göbel mirror optics. With the software package APEX3 the data reduction and absorption correction were processed before the structure was solved by direct methods and refined with the SHELX package.

Powder X-ray Diffraction.

Phase-pure polycrystalline samples of each polymorph were ground, filled and sealed in Hilgenberg glass capillaries with an inner diameter of 0.2 mm under argon atmosphere. Diffraction data were obtained from a StadiP powder diffractometer (STOE & Cie GmbH) with Cu- $\text{K}\alpha_1$ radiation and Mythen 1K detector (Dectris) and a Ge (111) monochromator in Debye-Scherrer geometry. Based on the single-crystal structure of $\text{KSi}_2\text{P}_3\text{-}t/960$ the according diffractogram was refined with the Rietveld method implemented in the TOPAS software. For the Rietveld refinement of the $\text{KSi}_2\text{P}_3\text{-}oF1952$ polymorph the single-crystal structure of $\text{KSi}_2\text{P}_3\text{-}t/960$ was solved assuming an orthorhombic unit cell. Based on these data, the powder pattern was indexed and refined with manually adjusted cell parameters. The powder refinement of the $\text{KSi}_2\text{P}_3\text{-}mC928$ polymorph was processed likewise.

Temperature-Dependent Powder X-ray Diffraction.

For the investigation of phase transitions the respective polycrystalline samples were ground and loaded in Hilgenberg silica glass capillaries with an inner diameter of 0.4 mm and sealed with grease for pressure compensation. Diffraction data collection under argon atmosphere was also performed on a STOE StadiP diffractometer with Mo- $\text{K}\alpha_1$ radiation, Ge monochromator, a resistance graphite furnace and IP-PSD detector. For the transition of the T3 compound described by Feng *et al.* to $\text{KSi}_2\text{P}_3\text{-}t/960$ (Figure 1) a sample was heated beginning at room temperature to 1045 °C in steps of 20 °C with a 5 °C/min heating rate. At each step the temperature was kept constant and a diffractogram was collected. For the phase transitions solely involving the T5 compounds in Figure 5 the sample was

heated to 350 °C and cooled to room temperature with the same heating rate but every 5 °C a diffraction pattern was recorded.

EDX Analysis.

The elemental composition of KSi_2P_3 -*mC928* was verified by energy dispersive X-ray spectroscopy with an EVO-MA10 Zeiss scanning electron microscope with a field emission gun and X-Flash 410-M X-ray detector. Polycrystalline samples were prepared under inert conditions in a glovebox on electronic conducting and adhesive carbon pads. These were inserted in the SEM quickly due to hydrolysis. The collected data were processed with QUANTAX200 software in which signals of oxygen and carbon were not taken to account.

Solid-State NMR.

A X-ray pure sample of KSi_2P_3 -*mC928* was loaded into a zirconia rotor of 4 mm in diameter for the silicon and into a 2.5 mm rotor for the phosphorus spectra and placed into a Bruker Avance III 500 spectrometer with a magnetic field strength of 11.74 T. The sample was rotated with 10 kHz and 25 kHz for the respective silicon and phosphorus spectra under MAS conditions with Larmor frequencies of ν_0 (^{31}P) = 202.5 MHz and ν_0 (^{29}Si) = 99.38 MHz. All spectra were indirectly referenced to ^1H at 0 ppm in 0.1 % TMS (4 mm rotor) and -0.1240 ppm in 100 % TMS (2.5 mm rotor).

Conductivity Measurements.

The KSi_2P_3 -*mC928* samples were ground thoroughly and compacted to a pellet of about 0.5-1.0 mm thickness and 5 mm in diameter by uniaxial cold pressing (10 kN) and then annealed under argon at 800 °C for 10 h. The large thickness of the pellets was required for sputtering and annealing. The pellets had densities of about 78 ± 3 % (Table S8). The pellets were sputtered with ruthenium as ion-blocking electrodes on both sides. Electrochemical impedance spectroscopy (EIS) for every sample was measured for several temperature cycles between 25 and -20 °C with 5 °C steps inside a glovebox under argon atmosphere. Higher temperatures were avoided to avoid phase changes influencing the performance. The samples were subsequently used for the polarization measurements to extract the electronic partial conductivity at 25 °C. For these a voltage of 0.25 and 0.5 V was applied for 5-10 h each and the drop in resulting current measured. The resistance was calculated from the current measured at a steady state after several hours. EIS and polarization measurements were performed with an IVIUM compactstat.h (24 bit instrument) in a two-electrode setup using a RHD INSTRUMENTS Microcell HC cell stand loaded with RHD INSTRUMENTS TSC Battery cells. The spectra were recorded in a frequency range of 1 MHz–0.01 Hz and rms AC voltage of 50 mV was applied. The analysis of the impedance spectra was carried out with the RelaxIS3 software from RHD INSTRUMENTS. The linearity, stability and causality were checked by the Kramers-Kronig-relation before fitting the data.

Geometrical Pathway Analysis.

The identification of possible potassium migration pathways was conducted with the ToposPro software package. Therefore, based on the crystal structures the voids accessible for potassium ions were calculated using the ionic radius for potassium and covalent radius for phosphorus atoms since calculations on Ba_2SiP_4 showed predominantly covalent behavior of the anionic Si-P network.

Afterwards the channels were calculated connecting the possible potassium voids with at least 3.1 Å in diameter. The results are shown in Figure S6-S8.

Table S1. Fractional atomic coordinates, equivalent displacement parameters (\AA^2) and occupancy factors of KSi_2P_3 -t1960.

atom	Wyckoff	x	y	z	U_{eq}	Occ. (<1)
Si1	32g	0.01336 (3)	0.13475 (3)	0.31216 (2)	0.01251 (11)	
Si2	32g	0.11118 (3)	0.26473 (3)	0.31162 (2)	0.01299 (11)	
Si3	32g	0.12699 (3)	0.34243 (3)	0.00244 (2)	0.01433 (12)	
Si4	32g	0.12716 (3)	0.15085 (3)	0.37593 (2)	0.01241 (11)	
Si5	32g	0.25467 (3)	0.33227 (3)	0.06290 (2)	0.01332 (11)	
Si6	32g	0.26842 (3)	0.22218 (3)	0.12512 (2)	0.01347 (11)	
Si7	32g	0.28474 (3)	0.11150 (3)	0.18786 (2)	0.01398 (12)	
Si8	16e	0.29477 (4)	0	$\frac{1}{4}$	0.01299 (15)	
Si9	16d	0	$\frac{1}{4}$	0.00359 (2)	0.01502 (16)	
P1	32g	0.05818 (3)	0.20620 (3)	0.40372 (2)	0.01319 (10)	
P2	32g	0.06423 (3)	0.29646 (3)	0.03746 (2)	0.02339 (14)	
P3	32g	0.06794 (3)	0.19514 (3)	0.27753 (2)	0.01429 (11)	
P4	32g	0.08297 (3)	0.08147 (3)	0.34163 (2)	0.01326 (11)	
P5	32g	0.09091 (3)	0.03417 (3)	0.09325 (2)	0.01942 (12)	
P6	32g	0.18135 (3)	0.21133 (3)	0.34107 (2)	0.01352 (11)	
P7	32g	0.19082 (3)	0.39756 (3)	0.03518 (2)	0.01286 (10)	
P8	32g	0.19672 (3)	0.02117 (3)	0.02977 (2)	0.01887 (12)	
P9	32g	0.19967 (3)	0.27053 (3)	0.09466 (2)	0.01848 (12)	
P10	32g	0.31478 (3)	0.27727 (3)	0.02760 (2)	0.01449 (11)	
P11	32g	0.33477 (3)	0.17519 (3)	0.22294 (2)	0.01504 (11)	
P12	32g	0.34720 (3)	0.05309 (3)	0.15492 (2)	0.01351 (11)	
K1	32g	0.0305 (2)	0.06606 (13)	0.02603 (11)	0.108 (3)	0.409 (5)
K2	32g	0.07481 (19)	0.18388 (14)	0.10302 (14)	0.142 (3)	0.436 (4)
K3	32g	0.07998 (6)	0.08214 (14)	0.21173 (5)	0.1581 (16)	0.820 (5)
K4	32g	0.1508 (2)	0.3851 (3)	0.13536 (14)	0.170 (5)	0.427 (4)
K5	32g	0.18701 (11)	0.2800 (2)	0.19937 (10)	0.105 (2)	0.468 (5)

K6	32g	0.20248 (8)	0.01439 (9)	0.14389 (6)	0.0651 (6)	0.5
K7	32g	0.2161 (3)	0.1692 (5)	0.2668 (3)	0.111 (5)	0.163 (4)
K8	32g	0.3209 (6)	0.0292 (4)	0.0672 (5)	0.113 (9)	0.189 (8)
K9	32g	0.34676 (15)	0.04711 (12)	0.04386 (10)	0.0569 (10)	0.459 (8)
K10	16e	0.0999 (3)	0	¼	0.058 (4)	0.125 (5)
K11	16d	0	¼	0.1075 (3)	0.186 (13)	0.193 (7)

Table S2. Atomic displacement parameters (\AA^2) of KSi_2P_3 -t1960.

atom	U^{11}	U^{22}	U^{33}	U^{12}	U^{13}	U^{23}
Si1	0.0125 (3)	0.0124 (2)	0.0126 (2)	-0.00107 (19)	-0.00011 (19)	-0.0002 (2)
Si2	0.0137 (3)	0.0120 (3)	0.0133 (3)	-0.00081 (19)	-0.0003 (2)	0.0002 (2)
Si3	0.0140 (3)	0.0155 (3)	0.0135 (3)	-0.0032 (2)	-0.0015 (2)	-0.0005 (2)
Si4	0.0123 (2)	0.0124 (2)	0.0125 (2)	-0.00036 (19)	-0.0007 (2)	0.0001 (2)
Si5	0.0128 (3)	0.0127 (3)	0.0144 (3)	0.0010 (2)	-0.0015 (2)	0.0005 (2)
Si6	0.0124 (2)	0.0131 (3)	0.0149 (3)	0.0005 (2)	-0.0003 (2)	0.0014 (2)
Si7	0.0138 (3)	0.0135 (3)	0.0147 (3)	0.0001 (2)	0.0008 (2)	0.0016 (2)
Si8	0.0119 (3)	0.0136 (4)	0.0135 (3)	0	0	0.0024 (3)
Si9	0.0142 (4)	0.0176 (4)	0.0132 (4)	-0.0041 (3)	0	0
P1	0.0128 (2)	0.0132 (2)	0.0135 (2)	0.00034 (18)	-0.00005 (18)	-0.00033 (18)
P2	0.0226 (3)	0.0339 (4)	0.0136 (3)	-0.0140 (3)	-0.0016 (2)	0.0008 (2)
P3	0.0162 (2)	0.0135 (2)	0.0132 (2)	-0.00242 (19)	0.00104 (19)	-0.00036 (19)
P4	0.0123 (2)	0.0127 (2)	0.0148 (2)	-0.00039 (18)	-0.00019 (18)	-0.00054 (19)
P5	0.0209 (3)	0.0134 (2)	0.0240 (3)	-0.0002 (2)	0.0086 (2)	0.0006 (2)
P6	0.0130 (2)	0.0130 (2)	0.0146 (2)	-0.00006 (18)	0.00024 (18)	0.00081 (19)

P7	0.0130 (2)	0.0122 (2)	0.0134 (2)	-0.00055 (18)	-0.00209 (18)	-0.00035 (18)
P8	0.0216 (3)	0.0118 (2)	0.0233 (3)	0.0014 (2)	0.0099 (2)	0.0009 (2)
P9	0.0136 (2)	0.0190 (3)	0.0229 (3)	0.0002 (2)	-0.0022 (2)	0.0064 (2)
P10	0.0142 (2)	0.0144 (2)	0.0148 (2)	0.00248 (19)	-0.00186 (19)	-0.00053 (19)
P11	0.0168 (3)	0.0137 (2)	0.0146 (2)	-0.00091 (19)	0.0011 (2)	0.00096 (19)
P12	0.0129 (2)	0.0135 (2)	0.0141 (2)	-0.00012 (18)	-0.00010 (18)	0.00136 (19)
K1	0.160 (5)	0.0456 (14)	0.119 (3)	-0.0022 (18)	-0.113 (4)	0.0196 (16)
K2	0.088 (3)	0.0397 (15)	0.298 (7)	-0.0017 (14)	-0.026 (3)	-0.017 (3)
K3	0.0359 (7)	0.303 (4)	0.1350 (17)	0.0462 (12)	-0.0338 (8)	-0.149 (2)
K4	0.0581 (19)	0.220 (8)	0.231 (8)	0.004 (3)	0.022 (3)	-0.200 (7)
K5	0.0507 (13)	0.143 (4)	0.122 (3)	-0.0142 (15)	0.0403 (15)	-0.097 (3)
K6	0.0391 (8)	0.0557 (10)	0.1003 (15)	0.0023 (7)	-0.0236 (9)	-0.0492 (10)
K7	0.061 (5)	0.134 (8)	0.136 (8)	-0.027 (5)	0.058 (5)	-0.097 (7)
K8	0.100 (8)	0.041 (4)	0.199 (18)	0.037 (5)	-0.118 (11)	-0.069 (7)
K9	0.0648 (15)	0.0371 (10)	0.069 (2)	0.0009 (10)	-0.0448 (14)	-0.0176 (11)
K10	0.012 (3)	0.073 (7)	0.090 (9)	0	0	0.014 (6)
K11	0.24 (2)	0.26 (3)	0.058 (6)	-0.15 (2)	0	0

Table S3. Fractional atomic coordinates, equivalent displacement parameters (\AA^2) and occupancy factors of KSi_2P_3 - oF1952.

atom	Wyckoff	x	y	z	U_{eq}	Occ. (<1)
Si1	32h	0.00479 (2)	0.27318 (2)	0.12527 (2)	0.01361 (11)	
Si2	32h	0.01178 (2)	0.11103 (2)	0.37389 (2)	0.01247 (11)	
Si3	32h	0.01526 (2)	0.14230 (2)	0.00260 (2)	0.01448 (12)	
Si4	32h	0.05198 (2)	0.33666 (2)	0.18803 (2)	0.01406 (12)	
Si5	32h	0.06065 (2)	0.17594 (2)	0.43765 (2)	0.01250 (11)	
Si6	32h	0.06200 (2)	0.17319 (2)	0.31147 (2)	0.01304 (11)	
Si7	32h	0.07404 (2)	0.06072 (2)	0.31200 (2)	0.01261 (11)	
Si8	32h	0.07675 (2)	0.06208 (2)	0.43818 (2)	0.01300 (11)	
Si9	32h	0.13900 (2)	0.01191 (2)	0.37575 (2)	0.01251 (11)	
Si10	32h	0.28886 (2)	0.20650 (2)	0.31273 (2)	0.01341 (11)	
Si11	32h	0.29344 (2)	0.03874 (2)	0.06307 (2)	0.01337 (11)	
Si12	32h	0.35270 (2)	0.10252 (2)	0.00017 (2)	0.01303 (11)	
Si13	32h	0.35775 (2)	0.26533 (2)	0.25226 (2)	0.01437 (12)	
Si14	32h	0.41345 (2)	0.05176 (2)	0.06233 (2)	0.01397 (11)	
Si15	32h	0.47694 (2)	0.00462 (2)	0.12505 (2)	0.01355 (11)	
Si16	32h	$\frac{1}{8}$	$\frac{1}{8}$	0.00375 (2)	0.01510 (16)	
Si17	32h	$\frac{1}{8}$	$\frac{1}{8}$	0.50341 (2)	0.01498 (16)	
P1	32h	0.00084 (2)	0.33225 (2)	0.09179 (2)	0.01325 (10)	
P2	32h	0.00490 (2)	0.17015 (2)	0.27689 (2)	0.01504 (11)	
P3	32h	0.01494 (2)	0.03536 (2)	0.15519 (2)	0.01840 (12)	
P4	32h	0.01490 (2)	0.05368 (2)	0.40875 (2)	0.01353 (10)	
P5	32h	0.01870 (2)	0.04604 (2)	0.27746 (2)	0.01453 (11)	
P6	32h	0.04995 (2)	0.39708 (2)	0.15509 (2)	0.01344 (10)	
P7	32h	0.06266 (2)	0.27846 (2)	0.15691 (2)	0.01947 (12)	
P8	32h	0.06356 (2)	0.11848 (2)	0.47231 (2)	0.01426 (11)	
P9	32h	0.06966 (2)	0.13391 (3)	0.03762 (2)	0.02356 (14)	

P10	32h	0.07398 (2)	0.11781 (2)	0.34612 (2)	0.01319 (10)	
P11	32h	0.07974 (2)	0.00505 (2)	0.47276 (2)	0.01508 (11)	
P12	32h	0.13154 (2)	0.06365 (2)	0.27737 (2)	0.01437 (11)	
P13	32h	0.13220 (2)	0.07403 (2)	0.40355 (2)	0.01314 (10)	
P14	32h	0.13389 (3)	0.06969 (2)	0.53729 (2)	0.02334 (14)	
P15	32h	0.14092 (2)	0.33790 (2)	0.02959 (2)	0.01892 (12)	
P16	16g	0.14654 (2)	0.45586 (2)	0.03499 (2)	0.01285 (10)	
P17	16g	0.19640 (2)	0.01505 (2)	0.34091 (2)	0.01353 (10)	
P18	32h	0.28553 (2)	0.26483 (2)	0.34449 (2)	0.01857 (12)	
P19	32h	0.29425 (2)	0.10329 (2)	0.03535 (2)	0.01282 (10)	
P20	32h	0.29600 (2)	0.26879 (2)	0.22222 (2)	0.01444 (11)	
P21	32h	0.35297 (2)	0.04977 (2)	0.09525 (2)	0.01352 (10)	
P22	32h	0.41233 (2)	0.10883 (2)	0.02994 (2)	0.01882 (12)	
P23	32h	0.41780 (2)	0.00069 (2)	0.15852 (2)	0.01320 (10)	
P24	32h	0.47171 (2)	0.06245 (2)	0.09341 (2)	0.01939 (12)	
K1	32h	0.01614 (10)	0.04712 (12)	0.05120 (9)	0.0984 (13)	0.4524 (13)
K2	32h	0.0241 (3)	0.4426 (3)	0.0171 (3)	0.119 (4)	0.180 (2)
K3	32h	0.04659 (12)	0.51614 (11)	0.05070 (9)	0.0979 (13)	0.4524 (13)
K4	32h	0.04759 (13)	0.01829 (13)	0.02654 (11)	0.1260 (19)	0.4524 (13)
K5	32h	0.0498 (2)	0.3002 (2)	0.0001 (2)	0.085 (3)	0.180 (2)
K6	32h	0.05293 (8)	0.39980 (8)	0.04371 (7)	0.0536 (7)	0.433 (3)
K7	32h	0.07121 (12)	0.25495 (16)	0.03342 (10)	0.0793 (15)	0.433 (3)
K8	32h	0.0748 (3)	0.39580 (18)	0.0670 (3)	0.114 (5)	0.180 (2)
K9	32h	0.10838 (6)	0.34408 (6)	0.10600 (6)	0.0574 (6)	0.4524 (13)
K10	32h	0.1170 (2)	0.48199 (13)	0.11428 (15)	0.181 (4)	0.4524 (13)

K11	32h	0.12912 (12)	0.05465 (11)	0.10258 (15)	0.144 (2)	0.4524 (13)
K12	32h	0.15791 (14)	0.00681 (13)	0.04421 (12)	0.0903 (14)	0.4524 (13)
K13	32h	0.24512 (16)	0.32121 (12)	0.28301 (9)	0.0837 (15)	0.4524 (13)
K14	32h	0.25704 (14)	0.34247 (14)	0.29456 (12)	0.0953 (16)	0.4524 (13)
K15	32h	0.26800 (13)	0.1326 (2)	0.11486 (16)	0.178 (4)	0.4524 (13)
K16	32h	0.3079 (3)	0.2264 (4)	0.0167 (3)	0.145 (6)	0.180 (2)
K17	32h	0.35030 (8)	0.19656 (8)	0.04419 (7)	0.0596 (9)	0.475 (5)
K18	32h	0.35428 (19)	0.1742 (3)	0.0681 (4)	0.107 (5)	0.180 (2)
K19	32h	0.40601 (6)	0.14139 (6)	0.10622 (6)	0.0586 (6)	0.4524 (13)
K20	32h	0.51814 (13)	0.04806 (13)	0.02635 (11)	0.115 (2)	0.433 (3)
K21	32h	0.55468 (11)	0.12945 (12)	0.10261 (15)	0.143 (2)	0.4524 (13)

Table S4. Atomic displacement parameters (\AA^2) of KSi_2P_3 -oF1952.

atom	U^{11}	U^{22}	U^{33}	U^{12}	U^{13}	U^{23}
Si1	0.0134 (3)	0.0121 (3)	0.0154 (3)	0.0004 (2)	-0.0009 (2)	-0.0012 (2)
Si2	0.0129 (3)	0.0120 (2)	0.0125 (3)	-0.0001 (2)	-0.0006 (2)	-0.0005 (2)
Si3	0.0119 (3)	0.0181 (3)	0.0134 (3)	0.0008 (2)	0.0016 (2)	-0.0006 (2)
Si4	0.0137 (3)	0.0135 (3)	0.0149 (3)	-0.0002 (2)	-0.0019 (2)	-0.0005 (2)
Si5	0.0135 (3)	0.0114 (3)	0.0126 (3)	0.0002 (2)	0.0001 (2)	-0.0002 (2)
Si6	0.0122 (3)	0.0136 (3)	0.0133 (3)	-0.0007 (2)	0.0001 (2)	-0.0002 (2)
Si7	0.0116 (3)	0.0137 (3)	0.0125 (3)	-0.0001 (2)	-0.0003 (2)	0.0000 (2)
Si8	0.0137 (3)	0.0120 (3)	0.0134 (3)	0.0008 (2)	-0.0005 (2)	0.0000 (2)
Si9	0.0120 (2)	0.0127 (3)	0.0128 (3)	0.0000 (2)	-0.0004 (2)	0.0006 (2)
Si10	0.0119 (3)	0.0139 (3)	0.0144 (3)	-0.0002 (2)	0.0015 (2)	0.0009 (2)

Si11	0.0140 (3)	0.0118 (3)	0.0144 (3)	0.0001 (2)	-0.0005 (2)	0.0013 (2)
Si12	0.0126 (3)	0.0128 (3)	0.0137 (3)	-0.0009 (2)	-0.0018 (2)	0.0017 (2)
Si13	0.0178 (3)	0.0115 (3)	0.0137 (3)	-0.0009 (2)	0.0006 (2)	0.0015 (2)
Si14	0.0136 (3)	0.0138 (3)	0.0145 (3)	0.0001 (2)	-0.0007 (2)	0.0017 (2)
Si15	0.0123 (3)	0.0132 (3)	0.0152 (3)	-0.0002 (2)	-0.0013 (2)	0.0006 (2)
Si16	0.0119 (4)	0.0201 (4)	0.0133 (4)	0.0016 (3)	0	0
Si17	0.0196 (4)	0.0119 (4)	0.0134 (4)	0.0018 (3)	0	0
P1	0.0130 (2)	0.0123 (2)	0.0145 (2)	-0.00027 (19)	0.00018 (19)	-0.00056 (19)
P2	0.0145 (2)	0.0163 (3)	0.0144 (3)	-0.0016 (2)	-0.0016 (2)	0.0002 (2)
P3	0.0165 (3)	0.0162 (3)	0.0225 (3)	-0.0027 (2)	0.0032 (2)	-0.0060 (2)
P4	0.0130 (2)	0.0130 (2)	0.0146 (2)	-0.00002 (19)	-0.00054 (19)	0.00062 (19)
P5	0.0121 (2)	0.0169 (3)	0.0146 (3)	0.0000 (2)	-0.00100 (19)	-0.0016 (2)
P6	0.0130 (2)	0.0133 (2)	0.0139 (2)	0.00030 (19)	-0.00125 (19)	-0.00099 (19)
P7	0.0170 (3)	0.0175 (3)	0.0239 (3)	0.0038 (2)	-0.0066 (2)	-0.0057 (2)
P8	0.0172 (3)	0.0123 (2)	0.0132 (2)	0.0011 (2)	0.0010 (2)	0.00041 (19)
P9	0.0145 (3)	0.0425 (4)	0.0137 (3)	0.0058 (3)	0.0007 (2)	-0.0018 (3)
P10	0.0128 (2)	0.0134 (2)	0.0134 (2)	-0.00020 (19)	0.00014 (19)	-0.00022 (19)
P11	0.0161 (3)	0.0142 (2)	0.0149 (3)	0.0016 (2)	0.0002 (2)	0.0014 (2)
P12	0.0125 (2)	0.0175 (3)	0.0131 (2)	-0.0013 (2)	0.00052 (19)	-0.0010 (2)
P13	0.0134 (2)	0.0128 (2)	0.0132 (2)	0.00020 (19)	-0.00040 (19)	-0.00018 (19)
P14	0.0418 (4)	0.0143 (3)	0.0140 (3)	0.0054 (3)	-0.0017 (3)	0.0007 (2)
P15	0.0183 (3)	0.0153 (3)	0.0232 (3)	-0.0050 (2)	-0.0079 (2)	0.0063 (2)

P16	0.0130 (2)	0.0121 (2)	0.0135 (2)	-0.00039 (19)	-0.00125 (19)	0.00153 (19)
P17	0.0130 (2)	0.0133 (2)	0.0142 (2)	0.00003 (19)	0.00083 (19)	0.00052 (19)
P18	0.0163 (3)	0.0165 (3)	0.0229 (3)	-0.0028 (2)	0.0062 (2)	-0.0030 (2)
P19	0.0121 (2)	0.0132 (2)	0.0132 (2)	-0.00044 (19)	-0.00187 (19)	0.00136 (19)
P20	0.0166 (3)	0.0120 (2)	0.0147 (3)	-0.0002 (2)	0.0015 (2)	0.00097 (19)
P21	0.0134 (2)	0.0131 (2)	0.0140 (2)	-0.00039 (19)	-0.00103 (19)	0.00084 (19)
P22	0.0154 (3)	0.0181 (3)	0.0230 (3)	-0.0049 (2)	-0.0066 (2)	0.0076 (2)
P23	0.0122 (2)	0.0130 (2)	0.0145 (2)	0.00020 (19)	-0.00060 (19)	-0.00031 (19)
P24	0.0173 (3)	0.0171 (3)	0.0238 (3)	-0.0036 (2)	-0.0057 (2)	0.0063 (2)
K1	0.0762 (18)	0.103 (2)	0.116 (3)	-0.0385 (17)	-0.0327 (17)	0.090 (2)
K2	0.137 (8)	0.079 (5)	0.141 (8)	-0.044 (5)	0.115 (7)	-0.032 (5)
K3	0.102 (2)	0.0782 (18)	0.113 (2)	-0.0404 (17)	0.089 (2)	-0.0344 (18)
K4	0.117 (3)	0.123 (3)	0.138 (3)	-0.072 (2)	-0.082 (3)	0.110 (3)
K5	0.064 (4)	0.067 (4)	0.125 (7)	-0.038 (3)	-0.005 (4)	0.004 (4)
K6	0.0485 (13)	0.0471 (12)	0.0653 (15)	-0.0129 (9)	0.0423 (11)	-0.0179 (11)
K7	0.072 (2)	0.103 (3)	0.063 (2)	-0.062 (2)	0.0267 (16)	-0.0345 (19)
K8	0.109 (6)	0.029 (2)	0.206 (11)	-0.028 (3)	0.139 (8)	-0.033 (4)
K9	0.0437 (10)	0.0392 (9)	0.0894 (15)	-0.0076 (7)	0.0477 (10)	-0.0163 (9)
K10	0.149 (6)	0.152 (3)	0.243 (8)	-0.088 (4)	0.168 (6)	-0.132 (5)
K11	0.0635 (19)	0.0707 (19)	0.298 (7)	-0.0248 (16)	-0.031 (3)	0.007 (3)
K12	0.100 (3)	0.070 (2)	0.101 (3)	-0.053 (2)	-0.053 (2)	0.024 (2)

K13	0.109 (3)	0.078 (2)	0.0634 (19)	0.067 (2)	0.0371 (19)	0.0278 (16)
K14	0.073 (2)	0.107 (3)	0.105 (3)	0.059 (2)	0.027 (2)	0.056 (2)
K15	0.148 (3)	0.140 (6)	0.245 (8)	-0.082 (4)	0.131 (5)	-0.162 (6)
K16	0.086 (6)	0.162 (9)	0.186 (11)	-0.051 (6)	0.046 (6)	-0.147 (9)
K17	0.0502 (12)	0.0544 (14)	0.0741 (17)	-0.0147 (10)	0.0201 (11)	-0.0476 (13)
K18	0.036 (3)	0.100 (6)	0.185 (10)	-0.031 (3)	0.035 (4)	-0.120 (7)
K19	0.0392 (9)	0.0448 (10)	0.0918 (16)	-0.0081 (7)	0.0168 (9)	-0.0497 (10)
K20	0.110 (3)	0.110 (3)	0.124 (3)	-0.063 (2)	0.097 (3)	-0.072 (2)
K21	0.0715 (19)	0.0630 (19)	0.294 (7)	-0.0253 (16)	0.004 (3)	-0.027 (3)

Table S5. Fractional atomic coordinates, equivalent displacement parameters (\AA^2) and occupancy factors of KSi_2P_3 - mC928.

atom	Wyckoff	x	y	z	U_{eq}	Occ. (<1)
Si1	8f	0.01059 (3)	0.08657 (3)	0.12466 (4)	0.01386 (14)	
Si2	8f	0.02438 (3)	0.20656 (3)	0.12618 (4)	0.01322 (14)	
Si3	8f	0.10233 (3)	0.14729 (3)	0.49963 (4)	0.01295 (14)	
Si4	8f	0.10506 (3)	0.26526 (3)	0.49476 (4)	0.01428 (15)	
Si5	8f	0.12044 (3)	0.02307 (3)	0.25011 (4)	0.01345 (14)	
Si6	8f	0.12122 (3)	0.37501 (3)	0.49248 (4)	0.01509 (15)	
Si7	8f	0.12393 (3)	0.07676 (3)	0.12365 (4)	0.01288 (14)	
Si8	8f	0.13614 (3)	0.13901 (3)	0.24847 (4)	0.01235 (14)	
Si9	8f	0.13643 (3)	0.18935 (3)	0.12471 (4)	0.01237 (14)	
Si10	8f	0.14792 (3)	0.49521 (3)	0.24947 (4)	0.01353 (14)	
Si11	8f	0.14847 (3)	0.25478 (3)	0.25055 (4)	0.01348 (14)	
Si12	8f	0.14864 (3)	0.44801 (3)	0.12396 (4)	0.01392 (14)	
Si13	8f	0.23715 (3)	0.01178 (3)	0.25221 (4)	0.01226 (14)	
Si14	8f	0.23828 (3)	0.06065 (3)	0.12467 (4)	0.01238 (14)	
Si15	8f	0.24875 (3)	0.07406 (3)	0.37603 (4)	0.01247 (14)	

Si16	8f	0.24976 (3)	0.17326 (3)	0.12365 (4)	0.01280 (14)
Si17	8f	0.26510 (3)	0.23824 (3)	0.25222 (4)	0.01245 (14)
Si18	8f	0.26536 (3)	0.18800 (3)	0.37708 (4)	0.01292 (14)
Si19	8f	0.26760 (3)	0.39226 (3)	0.00456 (4)	0.01411 (14)
Si20	8f	0.26922 (3)	0.46115 (3)	0.12545 (4)	0.01330 (14)
Si21	8f	0.27472 (3)	0.30198 (3)	0.37606 (4)	0.01400 (14)
Si22	8f	0.35179 (3)	0.04344 (3)	0.12612 (4)	0.01324 (14)
Si23	8f	0.35270 (3)	0.10271 (3)	0.00033 (4)	0.01294 (14)
Si24	8f	0.36027 (3)	0.01527 (3)	0.50518 (4)	0.01438 (15)
Si25	8f	0.36173 (3)	0.06201 (3)	0.37704 (4)	0.01282 (14)
Si26	8f	0.36236 (3)	0.11099 (3)	0.24850 (4)	0.01243 (14)
Si27	8f	0.36412 (3)	0.16344 (3)	0.12466 (4)	0.01384 (14)
Si28	8f	0.37728 (3)	0.17595 (3)	0.37597 (4)	0.01244 (14)
Si29	8f	0.37842 (3)	0.37498 (3)	0.00686 (4)	0.01496 (15)
Si30	8f	0.37971 (3)	0.22693 (3)	0.25012 (4)	0.01336 (14)
Si31	8f	0.39381 (3)	0.28885 (3)	0.37456 (4)	0.01329 (14)
Si32	8f	0.48691 (3)	0.35773 (3)	0.00452 (4)	0.01427 (15)
P1	8f	0.03099 (3)	0.02827 (3)	0.18682 (4)	0.01930 (15)
P2	8f	0.03229 (3)	0.07973 (3)	0.05445 (4)	0.01497 (14)
P3	8f	0.04549 (3)	0.14704 (2)	0.19048 (4)	0.01341 (13)
P4	8f	0.04657 (3)	0.20399 (3)	0.05552 (4)	0.01434 (13)
P5	8f	0.05946 (3)	0.26497 (3)	0.18963 (4)	0.01828 (15)
P6	8f	0.06791 (3)	0.20577 (2)	0.42927 (4)	0.01281 (13)
P7	8f	0.07346 (3)	0.26873 (2)	0.55486 (4)	0.01437 (13)
P8	8f	0.07845 (4)	0.31966 (3)	0.42477 (4)	0.02338 (18)
P9	8f	0.07888 (3)	0.08767 (3)	0.44013 (4)	0.01865 (15)
P10	8f	0.07908 (3)	0.14653 (2)	0.56998 (4)	0.01280 (13)
P11	8f	0.09628 (4)	0.43033 (3)	0.42477 (4)	0.02333 (18)

P12	8f	0.10673 (3)	0.50489 (2)	0.05379 (4)	0.01495 (14)
P13	8f	0.11747 (4)	0.39092 (3)	0.05920 (4)	0.01889 (15)
P14	8f	0.11985 (4)	0.48503 (3)	0.31045 (4)	0.01827 (15)
P15	8f	0.12153 (4)	0.43733 (3)	0.18618 (4)	0.01935 (15)
P16	8f	0.14496 (3)	0.01491 (2)	0.18250 (4)	0.01334 (13)
P17	8f	0.14615 (3)	0.06357 (3)	0.05536 (4)	0.01407 (13)
P18	8f	0.15788 (3)	0.08221 (2)	0.31708 (4)	0.01310 (13)
P19	8f	0.15922 (3)	0.18644 (3)	0.05537 (4)	0.01408 (13)
P20	8f	0.17049 (3)	0.13220 (2)	0.19288 (4)	0.01299 (13)
P21	8f	0.17405 (3)	0.25082 (2)	0.18358 (4)	0.01318 (13)
P22	8f	0.17417 (3)	0.19640 (2)	0.31820 (4)	0.01342 (13)
P23	8f	0.18538 (3)	0.31265 (3)	0.31383 (4)	0.01931 (15)
P24	8f	0.19167 (3)	0.14093 (3)	0.55918 (4)	0.01873 (15)
P25	8f	0.24046 (3)	0.49917 (2)	0.31644 (4)	0.01304 (13)
P26	8f	0.24088 (3)	0.39653 (2)	0.07003 (4)	0.01281 (13)
P27	8f	0.24198 (3)	0.45005 (2)	0.18982 (4)	0.01328 (13)
P28	8f	0.25895 (3)	0.04599 (3)	0.05550 (4)	0.01437 (13)
P29	8f	0.26860 (3)	0.01870 (2)	0.44511 (4)	0.01446 (13)
P30	8f	0.27172 (3)	0.07398 (2)	0.30776 (4)	0.01310 (13)
P31	8f	0.27221 (3)	0.17027 (3)	0.05450 (4)	0.01497 (14)
P32	8f	0.27243 (3)	0.11780 (2)	0.19289 (4)	0.01303 (13)
P33	8f	0.28609 (3)	0.17602 (2)	0.30777 (4)	0.01310 (13)
P34	8f	0.28633 (3)	0.13155 (2)	0.44530 (4)	0.01427 (13)
P35	8f	0.28759 (3)	0.23508 (2)	0.18251 (4)	0.01349 (13)
P36	8f	0.30217 (3)	0.29995 (2)	0.31017 (4)	0.01332 (13)
P37	8f	0.30297 (3)	0.24510 (2)	0.44625 (4)	0.01493 (14)
P38	8f	0.35696 (3)	0.38389 (3)	0.07458 (4)	0.02317 (18)
P39	8f	0.35932 (3)	0.46447 (3)	0.18895 (4)	0.01838 (15)

P40	8f	0.38865 (3)	0.04425 (2)	0.07067 (4)	0.01267 (13)	
P41	8f	0.38875 (4)	0.16234 (3)	0.05984 (4)	0.01876 (15)	
P42	8f	0.39406 (3)	0.05361 (2)	0.31818 (4)	0.01334 (13)	
P43	8f	0.39503 (3)	0.10297 (2)	0.19049 (4)	0.01341 (13)	
P44	8f	0.40587 (4)	0.22172 (3)	0.18682 (4)	0.01915 (15)	
P45	8f	0.40924 (3)	0.16779 (2)	0.31705 (4)	0.01304 (13)	
P46	8f	0.42037 (3)	0.28552 (3)	0.31104 (4)	0.01847 (15)	
P47	8f	0.46757 (3)	0.36610 (3)	0.07458 (4)	0.02309 (18)	
P48	8f	0.59099 (3)	0.11846 (2)	0.05470 (4)	0.01410 (13)	
K1	8f	0.00400 (11)	0.48393 (13)	0.1022 (2)	0.1009 (17)	0.4651 (13)
K2	8f	0.00821 (12)	0.45226 (17)	0.0528 (3)	0.132 (3)	0.4651 (13)
K3	8f	0.0348 (2)	0.04687 (15)	0.6016 (2)	0.0987 (16)	0.4651 (13)
K4	8f	0.03536 (14)	0.09404 (8)	0.28768 (16)	0.0602 (8)	0.4651 (13)
K5	8f	0.03740 (8)	0.33105 (12)	0.07673 (15)	0.1671 (19)	0.889 (3)
K6	8f	0.0477 (3)	0.37071 (16)	0.2044 (5)	0.154 (3)	0.4651 (13)
K7	8f	0.0504 (4)	0.2998 (3)	-0.0002 (6)	0.088 (3)	0.180 (2)
K8	8f	0.0798 (15)	0.0219 (12)	0.534 (2)	1.25 (4)	0.778 (5)
K9	8f	0.0935 (3)	0.37923 (16)	0.2960 (5)	0.155 (3)	0.4651 (13)
K10	8f	0.1088 (7)	0.1461 (2)	0.3666 (8)	0.111 (5)	0.180 (2)
K11	8f	0.14408 (14)	0.05317 (10)	0.58778 (18)	0.0575 (8)	0.4651 (13)
K12	8f	0.1517 (2)	0.26613 (13)	0.3977 (2)	0.1011 (16)	0.4651 (13)
K13	8f	0.15285 (16)	0.14977 (11)	0.41214 (18)	0.0589 (9)	0.4651 (13)

K14	8f	0.19353 (11)	0.30305 (10)	0.08763 (17)	0.0574 (8)	0.4651 (13)
K15	8f	0.1998 (4)	0.0499 (3)	0.4998 (6)	0.089 (3)	0.180 (2)
K16	8f	0.20003 (10)	0.35828 (8)	0.21193 (16)	0.0594 (8)	0.4651 (13)
K17	8f	0.2056 (3)	0.29772 (17)	0.4472 (3)	0.129 (2)	0.4651 (13)
K18	8f	0.2101 (7)	0.1921 (4)	0.4667 (7)	0.127 (6)	0.180 (2)
K19	8f	0.2095 (4)	0.2738 (4)	0.0338 (6)	0.108 (5)	0.180 (2)
K20	8f	0.21050 (14)	0.41881 (12)	0.42323 (15)	0.1666 (18)	0.889 (3)
K21	8f	0.2136 (4)	0.3258 (4)	0.1362 (8)	0.108 (5)	0.180 (2)
K22	8f	0.23815 (12)	0.39179 (8)	0.28818 (16)	0.0584 (8)	0.4651 (13)
K23	8f	0.31688 (14)	0.29675 (15)	0.1016 (2)	0.0995 (16)	0.4651 (13)
K24	8f	0.32425 (14)	0.26794 (16)	0.0523 (3)	0.122 (2)	0.4651 (13)
K25	8f	0.3278 (5)	0.4242 (4)	0.3638 (8)	0.105 (5)	0.180 (2)
K26	8f	0.35392 (18)	0.37509 (13)	0.2502 (3)	0.214 (3)	0.778 (5)
K27	8f	0.36922 (18)	0.49889 (9)	0.07631 (15)	0.1726 (19)	0.889 (3)
K28	8f	0.45716 (9)	0.25098 (9)	0.07616 (15)	0.1722 (19)	0.889 (3)
K29	8f	0.4730 (3)	0.44538 (15)	0.2048 (4)	0.148 (3)	0.4651 (13)
K30	8f	0.4791 (3)	0.48160 (17)	0.0533 (3)	0.126 (2)	0.4651 (13)
K31	8f	0.4819 (2)	0.30457 (15)	0.2049 (4)	0.145 (3)	0.4651 (13)
K32	8f	0.49076 (10)	0.10036 (10)	0.08816 (17)	0.0579 (8)	0.4651 (13)
K33	8f	0.4921 (3)	0.1041 (2)	0.1348 (8)	0.107 (5)	0.180 (2)
K34	8f	0.4930 (3)	0.0582 (4)	0.0339 (8)	0.135 (7)	0.180 (2)

K35	8f	0.49767 (8)	0.15602 (8)	0.21243 (16)	0.0602 (8)	0.4651 (13)
K36	4e	0	0.22907 (15)	¼	0.199 (3)	0.778 (5)
K37	4e	0	0.52111 (15)	¼	0.199 (4)	0.778 (5)

Table S6. Atomic displacement parameters (\AA^2) of KSi_2P_3 - mC928.

atom	U^{11}	U^{22}	U^{33}	U^{12}	U^{13}	U^{23}
Si1	0.0122 (3)	0.0135 (3)	0.0144 (3)	0.0005 (3)	0.0074 (3)	0.0008 (3)
Si2	0.0111 (3)	0.0139 (3)	0.0142 (3)	0.0003 (3)	0.0076 (3)	0.0006 (3)
Si3	0.0114 (3)	0.0126 (3)	0.0133 (3)	-0.0005 (3)	0.0068 (3)	-0.0018 (3)
Si4	0.0155 (3)	0.0119 (3)	0.0132 (3)	-0.0014 (3)	0.0077 (3)	-0.0016 (3)
Si5	0.0131 (3)	0.0123 (3)	0.0153 (4)	0.0006 (3)	0.0089 (3)	0.0012 (3)
Si6	0.0175 (4)	0.0118 (3)	0.0132 (3)	-0.0013 (3)	0.0080 (3)	0.0000 (3)
Si7	0.0127 (3)	0.0134 (3)	0.0133 (3)	0.0011 (3)	0.0084 (3)	0.0005 (3)
Si8	0.0118 (3)	0.0120 (3)	0.0128 (3)	0.0002 (3)	0.0073 (3)	0.0003 (3)
Si9	0.0115 (3)	0.0134 (3)	0.0126 (3)	0.0002 (3)	0.0076 (3)	0.0000 (3)
Si10	0.0145 (3)	0.0132 (3)	0.0154 (4)	-0.0009 (3)	0.0104 (3)	-0.0010 (3)
Si11	0.0123 (3)	0.0131 (3)	0.0153 (4)	-0.0002 (3)	0.0086 (3)	-0.0008 (3)
Si12	0.0145 (3)	0.0135 (3)	0.0149 (4)	-0.0010 (3)	0.0096 (3)	-0.0018 (3)
Si13	0.0124 (3)	0.0126 (3)	0.0123 (3)	0.0003 (3)	0.0079 (3)	0.0006 (3)
Si14	0.0121 (3)	0.0132 (3)	0.0127 (3)	-0.0001 (3)	0.0081 (3)	-0.0001 (3)
Si15	0.0131 (3)	0.0113 (3)	0.0126 (3)	0.0001 (3)	0.0077 (3)	0.0003 (3)
Si16	0.0123 (3)	0.0136 (3)	0.0129 (3)	0.0005 (3)	0.0080 (3)	-0.0004 (3)
Si17	0.0117 (3)	0.0129 (3)	0.0124 (3)	-0.0004 (3)	0.0072 (3)	-0.0007 (3)
Si18	0.0129 (3)	0.0121 (3)	0.0131 (3)	-0.0006 (3)	0.0076 (3)	0.0001 (3)
Si19	0.0135 (3)	0.0178 (4)	0.0134 (3)	0.0003 (3)	0.0095 (3)	-0.0006 (3)
Si20	0.0149 (3)	0.0117 (3)	0.0144 (3)	-0.0007 (3)	0.0095 (3)	-0.0013 (3)
Si21	0.0136 (3)	0.0136 (3)	0.0147 (4)	-0.0013 (3)	0.0087 (3)	-0.0020 (3)
Si22	0.0139 (3)	0.0136 (3)	0.0144 (3)	-0.0002 (3)	0.0099 (3)	-0.0006 (3)

Si23	0.0145 (3)	0.0126 (3)	0.0135 (3)	-0.0018 (3)	0.0095 (3)	-0.0019 (3)
Si24	0.0171 (4)	0.0115 (3)	0.0134 (3)	0.0004 (3)	0.0088 (3)	0.0017 (3)
Si25	0.0134 (3)	0.0120 (3)	0.0131 (3)	-0.0007 (3)	0.0082 (3)	-0.0001 (3)
Si26	0.0135 (3)	0.0118 (3)	0.0128 (3)	-0.0002 (3)	0.0084 (3)	-0.0004 (3)
Si27	0.0155 (3)	0.0135 (3)	0.0142 (3)	-0.0004 (3)	0.0099 (3)	-0.0008 (3)
Si28	0.0131 (3)	0.0115 (3)	0.0124 (3)	-0.0003 (3)	0.0077 (3)	-0.0004 (3)
Si29	0.0124 (3)	0.0196 (4)	0.0134 (3)	0.0015 (3)	0.0082 (3)	0.0001 (3)
Si30	0.0144 (3)	0.0121 (3)	0.0150 (4)	-0.0009 (3)	0.0097 (3)	-0.0012 (3)
Si31	0.0129 (3)	0.0120 (3)	0.0144 (3)	-0.0011 (3)	0.0081 (3)	-0.0016 (3)
Si32	0.0108 (3)	0.0176 (4)	0.0136 (3)	0.0012 (3)	0.0071 (3)	0.0007 (3)
P1	0.0133 (3)	0.0173 (4)	0.0236 (4)	0.0006 (3)	0.0094 (3)	0.0055 (3)
P2	0.0131 (3)	0.0160 (3)	0.0146 (3)	0.0011 (3)	0.0079 (3)	-0.0001 (3)
P3	0.0126 (3)	0.0133 (3)	0.0140 (3)	0.0002 (2)	0.0080 (3)	0.0009 (2)
P4	0.0119 (3)	0.0166 (3)	0.0146 (3)	0.0011 (2)	0.0082 (3)	0.0016 (3)
P5	0.0123 (3)	0.0164 (3)	0.0225 (4)	0.0003 (3)	0.0088 (3)	-0.0031 (3)
P6	0.0119 (3)	0.0121 (3)	0.0131 (3)	-0.0009 (2)	0.0070 (3)	-0.0018 (2)
P7	0.0141 (3)	0.0119 (3)	0.0143 (3)	-0.0006 (2)	0.0073 (3)	-0.0009 (2)
P8	0.0297 (4)	0.0144 (4)	0.0135 (4)	-0.0050 (3)	0.0069 (3)	-0.0006 (3)
P9	0.0121 (3)	0.0153 (3)	0.0228 (4)	-0.0003 (3)	0.0079 (3)	-0.0066 (3)
P10	0.0110 (3)	0.0131 (3)	0.0134 (3)	-0.0003 (2)	0.0070 (3)	-0.0010 (2)
P11	0.0331 (5)	0.0144 (4)	0.0135 (3)	-0.0044 (3)	0.0097 (3)	0.0006 (3)
P12	0.0154 (3)	0.0144 (3)	0.0142 (3)	0.0003 (3)	0.0086 (3)	-0.0015 (3)
P13	0.0245 (4)	0.0181 (4)	0.0232 (4)	-0.0088 (3)	0.0193 (3)	-0.0079 (3)
P14	0.0241 (4)	0.0164 (3)	0.0224 (4)	-0.0037 (3)	0.0184 (3)	-0.0029 (3)
P15	0.0254 (4)	0.0169 (3)	0.0237 (4)	-0.0070 (3)	0.0191 (3)	-0.0066 (3)
P16	0.0129 (3)	0.0128 (3)	0.0141 (3)	0.0003 (2)	0.0082 (3)	0.0005 (2)
P17	0.0122 (3)	0.0170 (3)	0.0130 (3)	0.0001 (3)	0.0078 (3)	-0.0011 (3)
P18	0.0138 (3)	0.0120 (3)	0.0145 (3)	0.0005 (2)	0.0092 (3)	0.0006 (2)

P19	0.0130 (3)	0.0170 (3)	0.0130 (3)	0.0015 (3)	0.0083 (3)	0.0009 (3)
P20	0.0129 (3)	0.0133 (3)	0.0131 (3)	0.0006 (2)	0.0081 (3)	0.0005 (2)
P21	0.0125 (3)	0.0129 (3)	0.0144 (3)	-0.0002 (2)	0.0085 (3)	0.0001 (2)
P22	0.0131 (3)	0.0130 (3)	0.0142 (3)	-0.0005 (2)	0.0084 (3)	-0.0009 (2)
P23	0.0144 (3)	0.0170 (3)	0.0237 (4)	-0.0010 (3)	0.0102 (3)	-0.0066 (3)
P24	0.0122 (3)	0.0179 (4)	0.0231 (4)	-0.0010 (3)	0.0094 (3)	-0.0079 (3)
P25	0.0133 (3)	0.0129 (3)	0.0143 (3)	0.0002 (2)	0.0092 (3)	0.0001 (2)
P26	0.0140 (3)	0.0129 (3)	0.0136 (3)	-0.0012 (2)	0.0095 (3)	-0.0014 (2)
P27	0.0142 (3)	0.0130 (3)	0.0137 (3)	-0.0009 (2)	0.0090 (3)	-0.0012 (2)
P28	0.0139 (3)	0.0165 (3)	0.0148 (3)	-0.0006 (3)	0.0098 (3)	-0.0015 (3)
P29	0.0177 (3)	0.0117 (3)	0.0147 (3)	0.0006 (3)	0.0103 (3)	0.0010 (2)
P30	0.0135 (3)	0.0128 (3)	0.0134 (3)	-0.0004 (2)	0.0084 (3)	-0.0002 (2)
P31	0.0159 (3)	0.0158 (3)	0.0148 (3)	0.0013 (3)	0.0102 (3)	0.0001 (3)
P32	0.0127 (3)	0.0131 (3)	0.0132 (3)	-0.0001 (2)	0.0079 (3)	-0.0004 (2)
P33	0.0131 (3)	0.0125 (3)	0.0135 (3)	-0.0002 (2)	0.0081 (3)	0.0001 (2)
P34	0.0167 (3)	0.0126 (3)	0.0128 (3)	-0.0013 (3)	0.0088 (3)	-0.0006 (2)
P35	0.0140 (3)	0.0131 (3)	0.0144 (3)	-0.0004 (2)	0.0093 (3)	-0.0005 (2)
P36	0.0126 (3)	0.0127 (3)	0.0138 (3)	-0.0005 (2)	0.0077 (3)	-0.0012 (2)
P37	0.0157 (3)	0.0145 (3)	0.0144 (3)	-0.0024 (3)	0.0091 (3)	-0.0017 (3)
P38	0.0145 (3)	0.0417 (5)	0.0138 (3)	0.0033 (3)	0.0090 (3)	-0.0017 (3)
P39	0.0160 (3)	0.0162 (3)	0.0227 (4)	-0.0017 (3)	0.0117 (3)	-0.0062 (3)
P40	0.0144 (3)	0.0118 (3)	0.0133 (3)	-0.0016 (2)	0.0093 (3)	-0.0019 (2)
P41	0.0270 (4)	0.0154 (3)	0.0230 (4)	-0.0079 (3)	0.0200 (3)	-0.0065 (3)
P42	0.0139 (3)	0.0128 (3)	0.0140 (3)	0.0005 (2)	0.0089 (3)	0.0008 (2)
P43	0.0142 (3)	0.0133 (3)	0.0139 (3)	-0.0009 (2)	0.0092 (3)	-0.0010 (2)
P44	0.0254 (4)	0.0170 (4)	0.0233 (4)	-0.0065 (3)	0.0192 (3)	-0.0055 (3)
P45	0.0131 (3)	0.0119 (3)	0.0143 (3)	-0.0001 (2)	0.0085 (3)	-0.0006 (2)
P46	0.0218 (4)	0.0159 (3)	0.0230 (4)	-0.0060 (3)	0.0165 (3)	-0.0062 (3)

P47	0.0134 (3)	0.0414 (5)	0.0137 (3)	0.0053 (3)	0.0080 (3)	0.0017 (3)
P48	0.0147 (3)	0.0122 (3)	0.0129 (3)	0.0009 (2)	0.0072 (3)	-0.0004 (2)
K1	0.0221 (11)	0.078 (2)	0.119 (3)	-0.0107 (13)	0.0011 (15)	0.032 (2)
K2	0.0230 (12)	0.122 (4)	0.147 (4)	-0.0064 (17)	-0.0007 (18)	0.087 (3)
K3	0.122 (3)	0.104 (3)	0.114 (3)	0.084 (3)	0.095 (3)	0.087 (3)
K4	0.113 (2)	0.0407 (12)	0.093 (2)	0.0177 (13)	0.097 (2)	0.0178 (12)
K5	0.0533 (11)	0.227 (3)	0.141 (2)	-0.0290 (15)	0.0193 (12)	0.133 (2)
K6	0.155 (5)	0.067 (3)	0.323 (10)	0.001 (3)	0.189 (7)	0.035 (4)
K7	0.100 (7)	0.066 (5)	0.128 (9)	-0.040 (5)	0.086 (7)	-0.011 (5)
K8	1.02 (7)	1.16 (8)	1.74 (11)	-0.16 (6)	0.93 (8)	-0.36 (8)
K9	0.177 (6)	0.068 (3)	0.327 (10)	0.043 (3)	0.209 (7)	0.036 (4)
K10	0.268 (15)	0.030 (3)	0.198 (11)	0.042 (6)	0.226 (12)	0.033 (6)
K11	0.0756 (19)	0.0529 (16)	0.0699 (18)	0.0382 (14)	0.0577 (17)	0.0451 (14)
K12	0.200 (5)	0.078 (2)	0.119 (3)	0.051 (3)	0.145 (4)	0.033 (2)
K13	0.104 (2)	0.0518 (15)	0.0717 (19)	0.0235 (17)	0.080 (2)	0.0204 (14)
K14	0.0390 (13)	0.0525 (16)	0.0711 (18)	0.0169 (11)	0.0290 (13)	0.0452 (14)
K15	0.086 (6)	0.066 (5)	0.135 (9)	0.030 (5)	0.077 (7)	-0.004 (5)
K16	0.0437 (12)	0.0450 (13)	0.092 (2)	0.0236 (10)	0.0433 (14)	0.0487 (14)
K17	0.237 (6)	0.122 (4)	0.140 (4)	0.108 (4)	0.173 (5)	0.082 (3)
K18	0.263 (17)	0.084 (7)	0.156 (11)	0.059 (9)	0.191 (13)	0.040 (7)
K19	0.071 (6)	0.121 (9)	0.125 (9)	0.029 (6)	0.056 (6)	0.098 (8)
K20	0.216 (3)	0.228 (3)	0.142 (2)	0.192 (3)	0.154 (2)	0.134 (2)
K21	0.060 (5)	0.102 (7)	0.191 (12)	0.056 (5)	0.091 (7)	0.127 (9)
K22	0.0751 (17)	0.0441 (12)	0.091 (2)	0.0344 (12)	0.0686 (17)	0.0471 (13)
K23	0.0601 (19)	0.104 (3)	0.117 (3)	0.0241 (19)	0.046 (2)	0.090 (3)
K24	0.0500 (18)	0.116 (3)	0.132 (4)	0.010 (2)	0.022 (2)	0.100 (3)

K25	0.112 (8)	0.102 (7)	0.182 (12)	0.092 (7)	0.131 (9)	0.122 (8)
K26	0.199 (4)	0.178 (3)	0.363 (6)	0.143 (3)	0.223 (5)	0.232 (4)
K27	0.340 (5)	0.133 (2)	0.149 (2)	-0.168 (3)	0.204 (3)	-0.0889 (18)
K28	0.0656 (12)	0.135 (2)	0.148 (2)	-0.0593 (14)	-0.0194 (13)	0.0890 (19)
K29	0.188 (6)	0.074 (3)	0.304 (9)	-0.024 (3)	0.212 (7)	-0.006 (3)
K30	0.202 (6)	0.119 (3)	0.139 (4)	-0.119 (4)	0.147 (4)	-0.106 (3)
K31	0.124 (5)	0.071 (3)	0.299 (9)	-0.018 (2)	0.159 (6)	0.004 (3)
K32	0.0154 (9)	0.0486 (15)	0.0725 (19)	0.0004 (8)	0.0082 (11)	0.0192 (14)
K33	0.016 (3)	0.032 (3)	0.190 (13)	-0.003 (2)	0.021 (5)	0.029 (6)
K34	0.030 (4)	0.091 (8)	0.164 (12)	-0.016 (4)	-0.002 (5)	0.047 (8)
K35	0.0155 (8)	0.0404 (12)	0.094 (2)	0.0040 (8)	0.0178 (11)	0.0172 (12)
K36	0.435 (9)	0.098 (3)	0.337 (7)	0	0.375 (8)	0
K37	0.0228 (12)	0.100 (3)	0.337 (8)	0	0.041 (3)	0

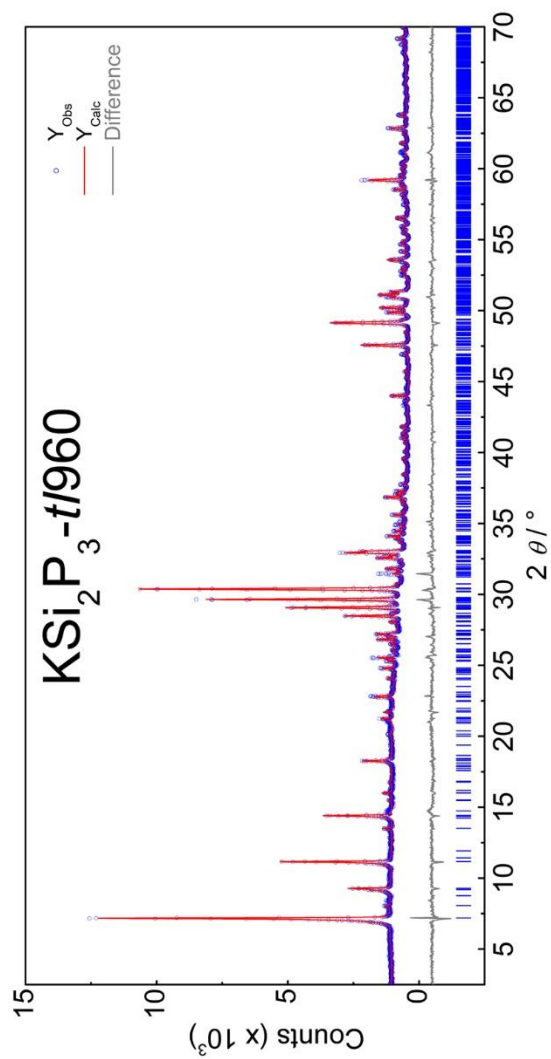


Figure S1. Cu- $\text{K}\alpha_1$ X-ray powder diffraction pattern of KSi_2P_3 -t/960 (blue) with Rietveld fit (red line) and difference plot (grey).

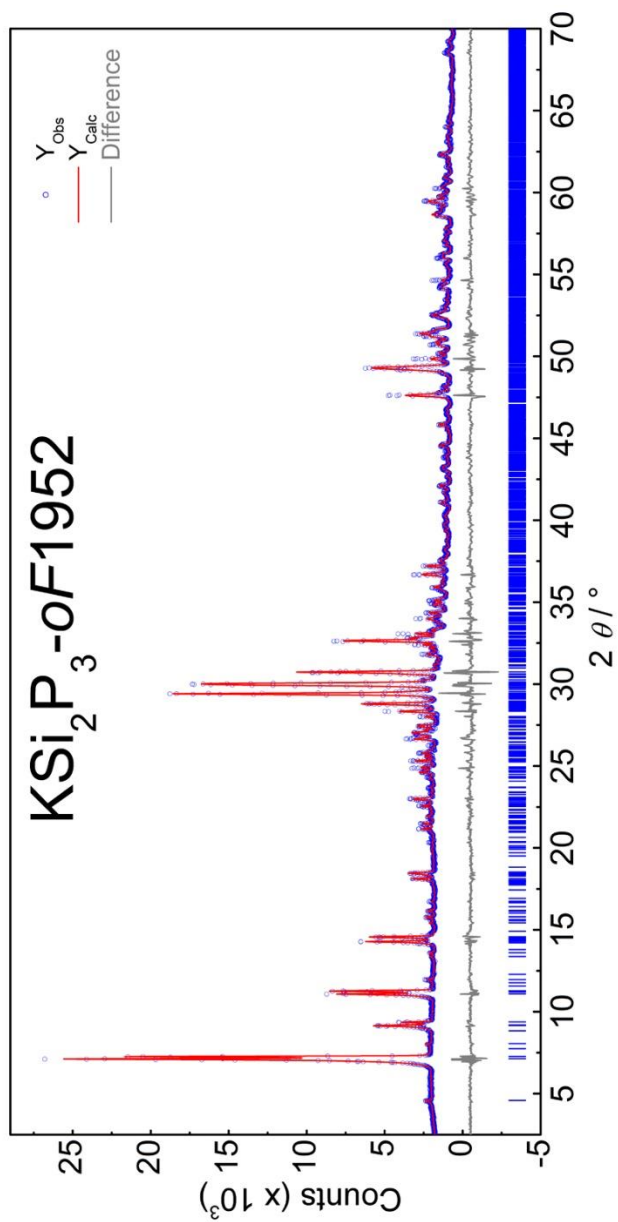


Figure S2. $\text{Cu-K}\alpha_1$ X-ray powder diffraction pattern of KSi_2P_3 -oF1952 (blue) with Rietveld fit (red line) and difference plot (grey).

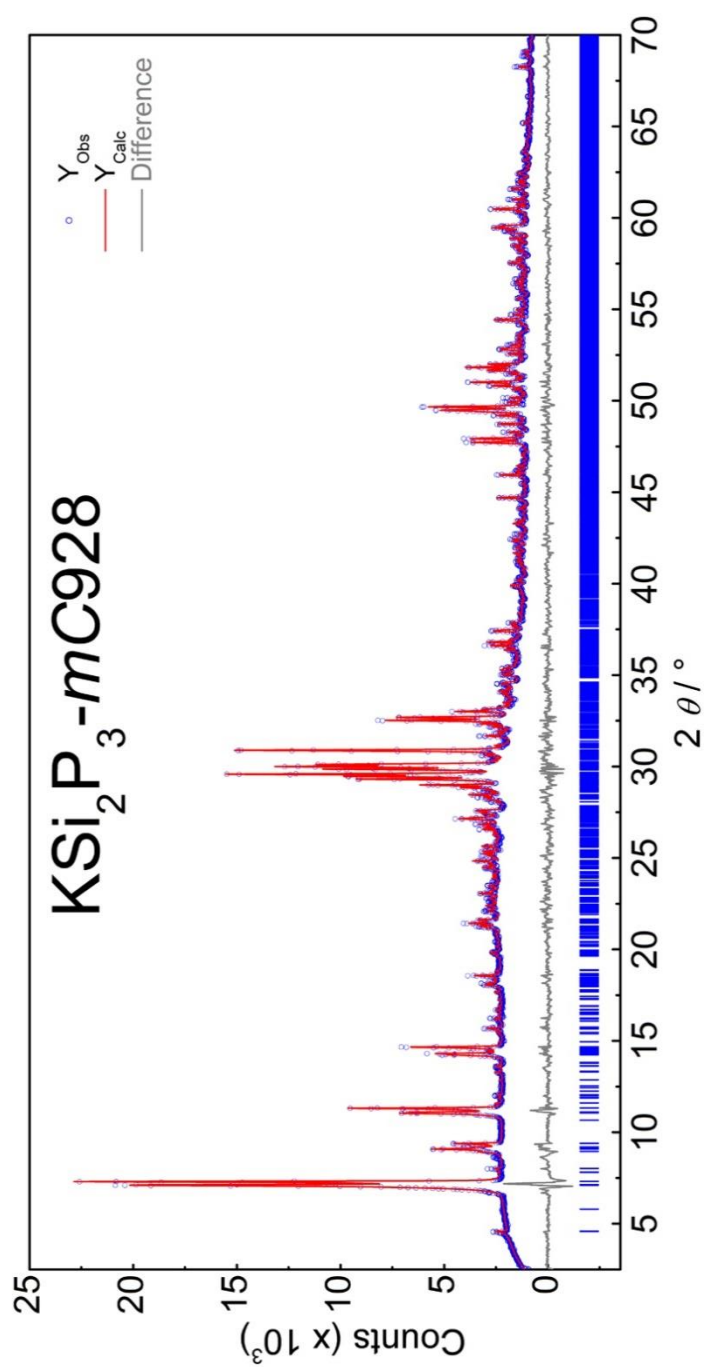


Figure S3. $\text{Cu-K}\alpha_1$ X-ray powder diffraction pattern of KSi_2P_3 -mC928 (blue) with Rietveld fit (red line) and difference plot (grey).

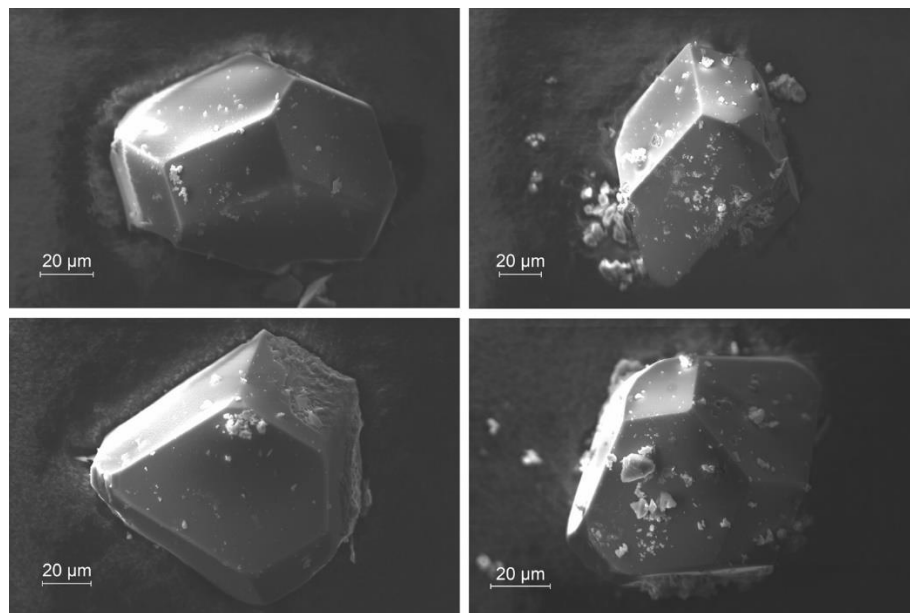


Figure S4. Representative scanning electron microscopic photographs of KSi_2P_3 -mC928.

Table S7. Elemental analysis by EDX of KSi_2P_3 -mC928, signals of oxygen were not taken into account due to hydrolysis.

	K	Si	P
EDX point 1 / atom-%	18.65	31.51	49.84
EDX point 2 / atom-%	17.23	31.86	50.91
EDX point 3 / atom-%	18.21	31.09	50.71
EDX point 4 / atom-%	15.82	33.82	50.36
EDX point 5 / atom-%	16.23	32.17	51.59
EDX point 6 / atom-%	18.83	31.19	49.98
EDX point 7 / atom-%	17.30	30.54	52.16
EDX point 8 / atom-%	16.98	30.98	52.04
EDX point 9 / atom-%	18.61	30.54	50.85
EDX point 10 / atom-%	19.08	30.06	50.87
EDX point 11 / atom-%	16.41	32.46	51.12
EDX point 12 / atom-%	17.38	32.08	50.54
EDX point 13 / atom-%	18.00	30.22	51.78
EDX point 14 / atom-%	17.96	32.50	49.54
Average / atom-%	17.62	31.50	50.88
Calculated / atom-%	16.66	33.33	50.00

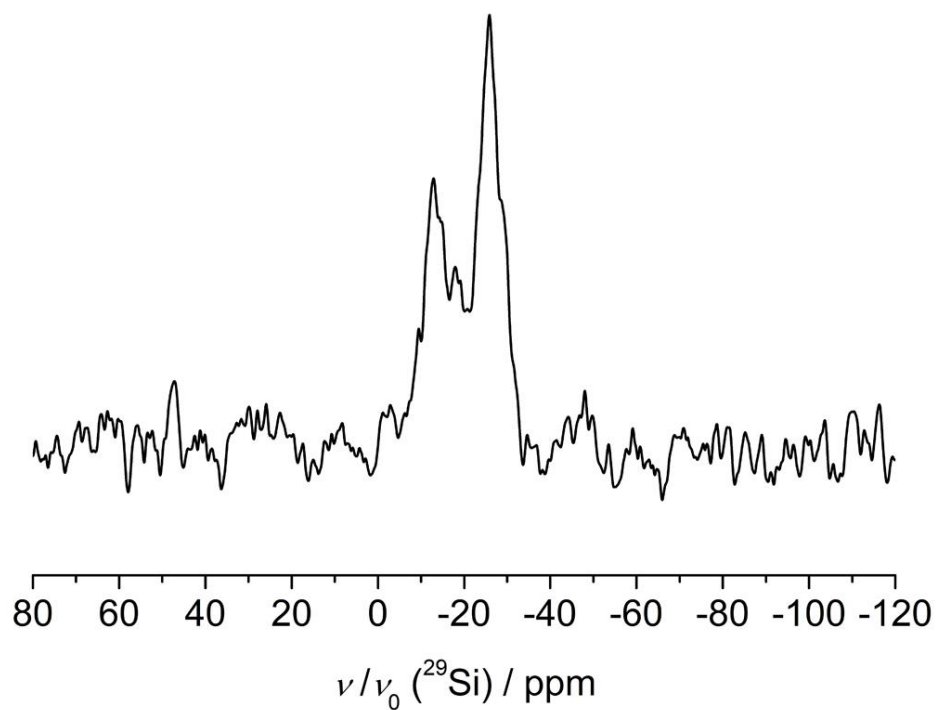


Figure S5. ^{29}Si -MAS-NMR spectrum of a KSi_2P_3 -mC928 sample with a rotation frequency of 10 kHz acquired at a magnetic field of 11.7 T. Three very broad signals are visible at $\delta(^{29}\text{Si}) = -12.9$, -17.9 and -25.9 ppm resulting from 32 crystallographically independent Si atoms on general Wyckoff sites. The chemical shift is comparable to known phosphidosilicates.

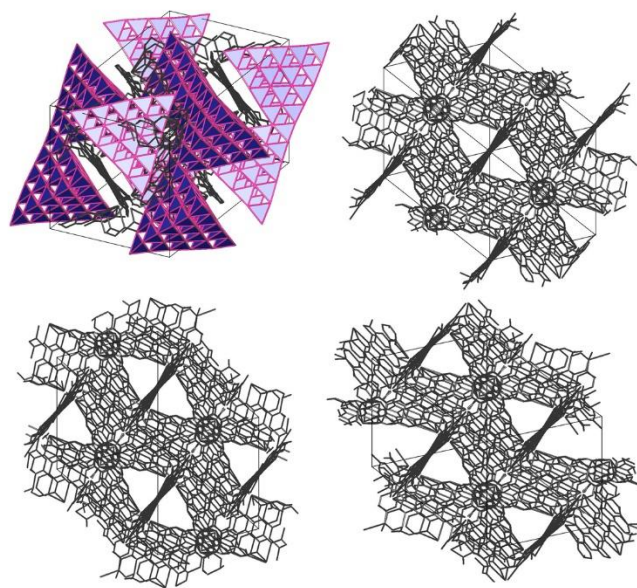


Figure S6. Geometrically calculated pathways for potassium ion migration in KSi_2P_3 -tI960. Four main channels are formed along $[111]$ (top, left), $[-111]$ (top, right), $[1-1]$ (bottom left) and $[11-1]$ (bottom, right), which are connected by shorter passages along every supertetrahedral face resulting in an isotropic 3D ion conduction.

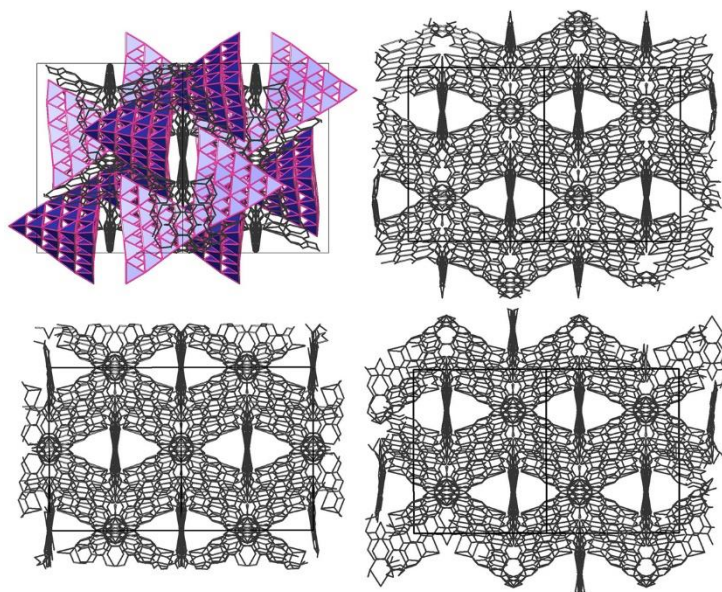


Figure S7. Geometrically calculated pathways for potassium ion migration in KSi_2P_3 -oF1952. Four main channels are formed along $[101]$ (top, left), $[-101]$ (top, right), $[011]$ (bottom left) and $[0-11]$ (bottom, right), which are connected by shorter passages along every supertetrahedral face resulting in an isotropic 3D ion conduction.

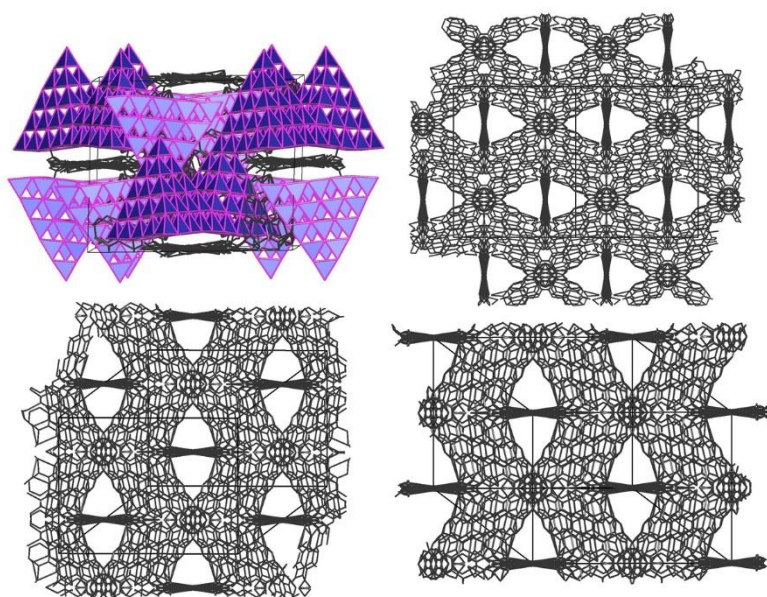


Figure S8. Geometrically calculated pathways for potassium ion migration in KSi_2P_3 -mC928. Four main channels are formed along $[001]$ (top, left), $[101]$ (top, right), $[112]$ (bottom left) and $[1-12]$ (bottom, right), which are connected by shorter passages along every supertetrahedral face resulting in an isotropic 3D ion conduction.

Table S8. Ionic conductivity and activation energy of selected solid potassium ion conductors; a visualization is shown in Figure 1 main text.

Compound	$T / ^\circ\text{C}$	$\sigma(\text{K}^+) / \text{Scm}^{-1}$	E_a / eV	Reference
KSi ₂ P ₃	25	1×10^{-4}	0.20	<i>This work</i>
K ₂ Fe ₄ O ₇	25	5×10^{-2}	0.08 ^[*]	[1]
K-β-Alumina*	25	6.5×10^{-5}	0.29	[1-2]
KFeO ₂	300	3×10^{-4}	-	[3]
K _{0.7} Cd _{0.15} FeO ₂	300	2×10^{-3}	0.24	[3]
K _{0.4} Cd _{0.3} FeO ₂	300	2.5×10^{-2}	0.24	[3]
KGaO ₂	400	1×10^{-4}	0.47	[3-4]
K _{0.89} Pb _{0.1} GaO ₂	400	1×10^{-3}	0.47	[4-5]
K _{0.7} Sr _{0.15} GaO ₂	400	1×10^{-2}	0.23	[4-5]
KAlO ₂	400	1×10^{-3}	-	[4, 6]
K _{1.90} Pb _{0.05} AlO ₂	400	2.5×10^{-3}	0.29	[6]
K _{1.90} Ba _{0.05} AlO ₂	400	5.8×10^{-2}	0.23	[6]
γ -K _{1.8} Al _{1.9} M _{0.1} O ₄ (M = Ta, Nb)	300	$5\text{-}8 \times 10^{-3}$	0.23-0.26	[6-7]
K _{1.8} Ga _{1.9} V _{0.1} O ₄	400	1×10^{-3}	0.47	[7-8]
K _{1.8} Fe _{1.9} P _{0.1} O ₄	300	76×10^{-3}	0.35	[8-9]
K _{1.8} Al _{1.9} P _{0.1} O ₄	200	5×10^{-3}	0.21	[9-10]
K _{0.9} Al _{0.9} Ti _{0.1} O ₂	400	4×10^{-3}	-	[10-11]
K _x M _{x/2} Ti _{8-x/2} O ₁₆ (M = Zn, Ni) $x=1.6$	300	1×10^{-4}	0.23	[11-12]
K _{1.6} Mg _{0.8} Ti _{7.2} O ₁₆	300	1×10^{-4}	0.29	[12-13]
0.8 La ₂ O ₂ SO ₄ -0.2 (0.8 K ₂ SO ₄ -0.2 CaSO ₄)	>800	1×10^{-2}	-	[13-14]
0.35 Gd ₂ O ₃ -0.3KNO ₂	600	2×10^{-1}	-	[14-15]
K ₃ Sb ₄ BO ₁₃	300	3×10^{-5}	0.33	[15-17]
K ₂ SbPO ₆	400	4×10^{-6}	0.82	[16, 18]
K ₃ Sb ₃ P ₂ O ₁₄	400	6×10^{-6}	0.59	[16, 18]
K ₅ Sb ₅ P ₂ O ₂₀	300	2×10^{-5}	0.52	[16, 18]

[#] Data extrapolated. [*] Data of single crystals.

Table S9. Results of electrochemical impedance spectroscopy and polarization measurements of KSi_2P_3 -mC928 of three batches (1-3) of KSi_2P_3 .

Sample	Relative pellet density / %	$\sigma_{\text{bulk}} / \text{Scm}^{-1}$	$\sigma_{\text{Tot}} / \text{Scm}^{-1}$	$E_a (\sigma_{\text{bulk}}) / \text{eV}$	$E_a (\sigma_2) / \text{eV}$	$C_{\text{eff1}} / \text{F}$	$C_{\text{eff2}} / \text{F}$	$\epsilon = \frac{Cd}{\epsilon_0 A}$
1a	79	1.3E-05	4.8E-06	0.23	0.34*	1.4E-10	3.3E-05	442
1b	81	2.7E-05	7.2E-06	0.21	0.19	9.9E-11	1.8E-05	381
1c	73	1.9E-05	4.5E-06	0.12	0.39*	2.4E-11	2.4E-05	92
2a	77	5.4E-05	1.1E-05	0.18	0.16	1.6E-11	2.0E-06	64
2b	72	4.5E-05	7.7E-06	0.22	0.19	7.8E-12	9.0E-07	24
2c	80	1.1E-04	1.8E-05	0.20	0.23	4.5E-11	1.0E-06	178
2d	80	2.5E-04	4.1E-05	0.22	0.16	5.8E-11	1.30E-06	211.52
3a	79	2.6E-04	1.4E-05	0.21	0.22	3.4E-11	4.20E-06	90.94
3b [#]	80	2.0E-04	2.0E-04	0.28	n.a.	3.0E-11	n.a.	92.15
Average	78	1.1E-04	3.4E-05	0.20	0.19			
St. dev.	3	9.6E-05	6.0E-05	0.04	0.03			

*Outlier not used for averaging [#]data fitted with R(1)CPE(1)-CPE(2) Model.

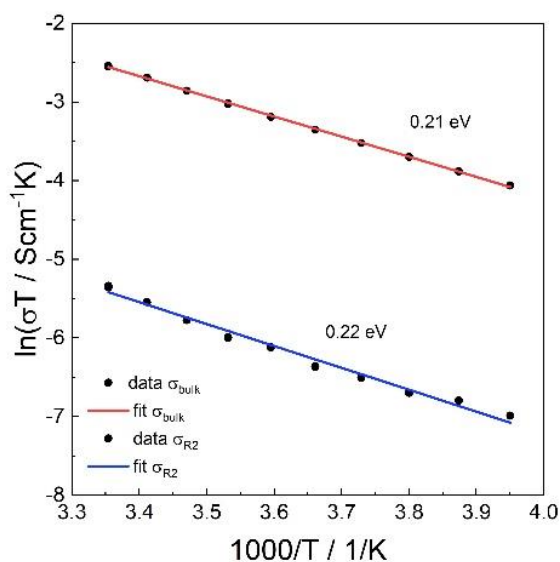


Figure S9. Plot of Arrhenius plot of sample 3a in Table S8 showing very similar activation energies of the high frequency process (bulk) and the low frequency process (R2).

Table S10. Results of polarization measurements of KSi_2P_3 -mC928.

Sample	Voltage / V	Current / A	R / Ω	$\sigma_{\text{eon}} / \text{Scm}^{-1}$
1b	0.25	1.90E-09	1.3E+08	2.6E-09
	0.50	1.00E-08	5.0E+07	6.8E-09
1c	0.25	6.70E-10	3.7E+08	8.9E-10
	0.50	3.40E-09	1.5E+08	2.3E-09
1d	0.25	2.60E-09	9.6E+07	3.6E-09
	0.50	5.50E-09	9.1E+07	3.8E-09
2b	0.25	9.70E-09	2.6E+07	1.1E-08
	0.50	1.18E-08	4.2E+07	6.6E-09
2d	0.25	8.83E-09	2.83E+07	1.14E-08
	0.50	1.67E-08	2.99E+07	1.08E-08
Average				6.0E-09
St. dev.				3.7E-9

References

- [1] H. Yuan, H. Li, T. Zhang, G. Li, T. He, F. Du, S. Feng, *J. Mater. Chem. A* **2018**, *6*, 8413-8418.
- [2] M. S. Whittingham, R. A. Huggins in *Proceedings of the 5th Material Research Symposium, Vol. 364*, Nat. Bur. Standard Pub., Solid State Chemistry, **1972**, pp. 139-154.
- [3] E. I. Burmakin, B. D. Antonov, G. S. Shekhtman, *Inorg. Mater.* **2010**, *46*, 540-544.
- [4] G. V. Nechaev, E. I. Burmakin, *Russ. J. Electrochem.* **2011**, *47*, 1411-1414.
- [5] G. V. Nechaev, E. I. Burmakin, *Russ. J. Electrochem.* **2011**, *47*, 457-460.
- [6] E. I. Burmakin, G. V. Nechaev, G. S. Shekhtman, *Russ. J. Electrochem.* **2008**, *44*, 1386-1392.
- [7] E. I. Burmakin, G. V. Nechaev, G. S. Shekhtman, S. V. Plaksin, *Russ. J. Electrochem.* **2009**, *45*, 934-937.
- [8] E. I. Burmakin, G. V. Nechaev, *Russ. J. Electrochem.* **2013**, *49*, 1001-1003.
- [9] E. I. Burmakin, G. S. Shekhtman, *Inorg. Mater.* **2008**, *44*, 882-885.
- [10] E. I. Burmakin, G. S. Shekhtman, *Russ. J. Electrochem.* **2005**, *41*, 1341-1344.
- [11] E. I. Burmakin, V. I. Voronin, L. Z. Akhtyamova, I. F. Berger, G. S. Shekhtman, *Russ. J. Electrochem.* **2005**, *41*, 783-788.
- [12] T. Takahashi, K. Kuwabara, *Electrochim. Acta* **1978**, *23*, 375-379.
- [13] T. Takahashi, K. Kuwabara, *Nippon Kagaku Kaishi* **1974**, *1974*, 1883-1887.
- [14] S. Yamamoto, S. Tamura, N. Imanaka, *J. Alloys Compd.* **2006**, *418*, 226-229.
- [15] Y.-W. Kim, A. Oda, N. Imanaka, *Electrochem. Commun.* **2003**, *5*, 94-97.
- [16] J.-M. Doux, N. Stephant, A. L. G. La Salle, O. Joubert, D. Guyomard, E. Quarez, *CrystEngComm* **2019**, *21*, 594-601.
- [17] J.-M. Doux, L. Leguay, A. Le Gal La Salle, O. Joubert, E. Quarez, *Solid State Ionics* **2018**, *324*, 260-266.
- [18] E. Wang, M. Greenblatt, *Chem. Mater.* **1991**, *3*, 542-546.

4.5 Finding the right blend: Interplay between structure and sodium ion conductivity in the system $\text{Na}_5\text{AlSi}_4 - \text{Na}_4\text{SiS}_4$

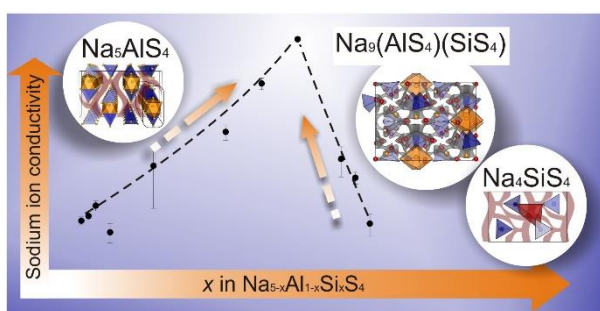
S. Harm*, A.-K. Hatz*, C. Schneider, C. Hofer, C. Hoch, B. V. Lotsch

*These authors contributed equally to this work

Published in *Frontiers in Chemistry* 2020, 8 (90).
DOI: 10.3389/fchem.2020.00090

Abstract

The rational design of high performance sodium solid electrolytes is one of the key challenges in modern battery research. In this work, we identify new sodium ion conductors in the substitution series $\text{Na}_{5-x}\text{Al}_{1-x}\text{Si}_x\text{S}_4$ ($0 \leq x \leq 1$), which are entirely based on earth abundant elements. These compounds exhibit conductivities ranging from $1.64 \cdot 10^{-7} \text{ Scm}^{-1}$ for Na_4SiS_4 to $2.04 \cdot 10^{-5} \text{ Scm}^{-1}$ for $\text{Na}_{8.5}(\text{AlSi}_4)_{0.5}(\text{SiS}_4)_{1.5}$ ($x = 0.75$). We determined the crystal structures of the Na^+ -ion conductors Na_4SiS_4 as well as hitherto unknown Na_5AlSi_4 and $\text{Na}_9(\text{AlSi}_4)(\text{SiS}_4)$. Na^+ -ion conduction pathways were calculated by bond valence energy landscape (BVEL) calculations for all new structures highlighting the influence of the local coordination symmetry of sodium ions on the energy landscape within this family. Our findings show that the interplay of charge carrier concentration and low site symmetry of sodium ions can enhance the conductivity by several orders of magnitude.



Introduction

In recent years, all-solid-state batteries (ASSB) have garnered attention as promising candidates for future battery applications in large scale mobility systems such as electric vehicles.¹⁻³ This is due to safety issues arising from liquid electrolytes applied in conventional lithium-ion batteries. Implementing solid electrolytes is thought to provide a more stable battery system, both thermally and mechanically. ASSBs can even pair this advantage with improved energy density through the use of Li or Na metal anodes and bipolar stacking. In prospect, the application of sodium containing materials produced from cheap and abundant sources could effectively cut down costs of ASSBs, thus enabling large-scale energy storage system solutions independent of limited lithium resources.⁴ One central component of an ASSB is the solid electrolyte. To be applicable for battery systems, the implemented solid electrolytes are required to show high ionic and low electronic conductivity, along with high electrochemical and structural stability, as well as low production costs.⁵ Regarding conductivity, the group of sulfides includes some of the best solid electrolytes to date. Especially thiophosphates, e.g. $\text{Li}_{10}\text{GeP}_2\text{S}_{12}$ (LGPS), $\text{Li}_6\text{PS}_5\text{X}$ ($\text{X} = \text{Cl}, \text{Br}, \text{I}$) and Na_3PS_4 , are promising materials due to their high ionic conductivities and soft mechanical nature enabling cold

pressing of the electrolyte instead of high temperature sintering.⁶⁻¹² These high ionic conductivities compared to most oxide solid electrolytes are supposed to stem from the high polarizability of the sulfide or thiophosphate anion lattice, facilitating Li or Na ion hopping in the bulk.^{13, 14} However, Zeier *et al.* showed that a softer lattice cannot only lower the migration barrier for charge carriers, but also affects the entropy of migration, which can negatively influence the overall ionic conductivity.^{15, 16} This 'softness' of the lattice is commonly tuned by isovalent or aliovalent substitution to obtain materials with even higher ionic conductivities. Isovalent substitution is typically employed to introduce softer, more polarizable anions, and to widen diffusion pathways as was studied recently for the solid electrolyte Na_3PS_4 . In its 'cubic' phase, Na_3PS_4 exhibits a room temperature ionic conductivity of up to $4.6 \cdot 10^{-4} \text{ Scm}^{-1}$.^{17, 18} By substitution of S with Se, values up to $1.16 \cdot 10^{-3} \text{ Scm}^{-1}$ can be achieved for Na_3PSe_4 .^{15, 19, 20} In addition to isovalent substitution, aliovalent substitution can be used to not only alter the polarizability of the lattice and influence the size of diffusion pathways, but also to tune the charge carrier concentration. Similar to the LGPS system,^{3, 6, 11, 12, 21-27} tetrel elements were employed in the $\text{Na}_{3+x}\text{T}_x\text{P}_{1-x}\text{S}_4$ ($T = \text{Si}, \text{Sn}$) system to increase the charge carrier density and increase the overall ionic conductivity. The Sn-containing compounds are structurally very similar to the LGPS-like $\text{Li}_{10}\text{SnP}_2\text{S}_{12}$ and show conductivities of $4 \cdot 10^{-5} \text{ Scm}^{-1}$ for $\text{Na}_{10}\text{SnP}_2\text{S}_{12}$ and the highest measured sodium ionic conductivity at room temperature for sulfides of $4 \cdot 10^{-3} \text{ Scm}^{-1}$ for $\text{Na}_{11}\text{Sn}_2\text{PS}_{12}$.^{22, 28, 29} Aliovalent silicon substitution studies were also conducted for the Na_3PS_4 phase achieving a maximum conductivity of $7.4 \cdot 10^{-4} \text{ Scm}^{-1}$ for a glass ceramic of composition $94(\text{Na}_3\text{PS}_4) \cdot 6(\text{Na}_4\text{SiS}_4)$.³⁰ The authors showed the presence of two ion conducting, hitherto unknown crystalline phases in this $\text{Na}_{3+x}\text{Si}_x\text{P}_{1-x}\text{S}_4$ system with formal compositions ' $\text{Na}_{11}\text{Si}_2\text{PS}_{12}$ ' and ' Na_4SiS_4 '. However, no structural information was given nor the reason for the large increase in conductivity of the amorphous ball-milled product ($\sigma = 10^{-5} \text{ Scm}^{-1}$) compared to the crystalline products ($\sigma = 10^{-7} \text{ Scm}^{-1}$). In this work we expand the materials space of sodium thio-ortho-tetrelates and -trielates by aliovalent substitution of Si in the aforementioned Na_4SiS_4 by Al, therefore increasing the number of charge carriers and expanding the lattice by a larger cation with reduced charge ($r(\text{Si}_{\text{Tetr.}}^{4+}) = 0.26 \text{ \AA}$, $r(\text{Al}_{\text{Tetr.}}^{3+}) = 0.39 \text{ \AA}$)³¹ to enhance sodium ion conductivity. We present the crystal structures of Na_5AlS_4 , Na_4SiS_4 and $\text{Na}_9(\text{AlS}_4)(\text{SiS}_4)$ and investigate their Na^+ ion migration pathways by bond valence energy landscape (BVLE) calculations. While Na_5AlS_4 was mentioned by Brown *et al.* and Na_4SiS_4 was reported recently by Tanibata *et al.*, no crystallographic data have been reported as yet.^{30, 32} In this work we map out the ionic conductivity of the aliovalent substitution series $\text{Na}_{5-x}\text{Al}_{1-x}\text{Si}_x\text{S}_4$ ($0 \leq x \leq 1$) and show that the conductivities can be significantly enhanced by tuning the charge carrier or defect concentration. Hereby, the more complex structure of $\text{Na}_{8.5}(\text{AlS}_4)_{0.25}(\text{SiS}_4)_{0.75}$ shows a flatter energy landscape and a jump to a higher conductivity by two orders of magnitude ($2.04 \cdot 10^{-5} \text{ Scm}^{-1}$) compared to the border phases Na_4SiS_4 and Na_5AlS_4 .

Experimental Section

Synthesis

Stoichiometric amounts of Na_2S (ALFA AESAR, 99%), Al_2S_3 (ALFA AESAR, 99%), Si (ball milled, ALFA AESAR, 99.999%), and S (GRUSSING, sublimed *in vacuo*) were used as starting materials. An excess

of 5 wt% sulfur was added to the mixture to ensure an oxidizing atmosphere during the reaction. Samples were prepared by thoroughly mixing and grinding the starting materials in an agate mortar. The resulting fine powders were transferred into glassy carbon crucibles, compacted and sealed under vacuum into quartz glass ampoules. The ampoules were subsequently transferred into a tube furnace and heated at $50\text{ }^\circ\text{C h}^{-1}$ to $600\text{ }^\circ\text{C}$ and annealed for 3d. Subsequently, the furnace was turned off. The ampoules were removed from the furnace when the temperature was below $100\text{ }^\circ\text{C}$ and transferred to a glovebox. Na_5AlSi_4 and Na_4Si_4 samples are off-white to yellow powders, probably from excess sulfur. $\text{Na}_{8.5}(\text{AlSi}_4)_{0.25}(\text{SiSi}_4)_{0.75}$ crystals were colorless cuboids of about $200\text{ }\mu\text{m}$ diameter embedded in an orange amorphous material, presumably solidified sodium polysulfide melt.

Powder X-ray Diffraction

From all samples powder X-ray diffractograms (PXRDs) were measured on a STOE STADI P diffractometer (Ge-(111) monochromator, DECTRIS Mythen 1 K detector) utilizing $\text{MoK}_{\alpha 1}$ or $\text{Cu-K}_{\alpha 1}$ radiation in Debye-Scherrer geometry. All samples were sealed in glass capillaries with diameters of 0.3 to 0.5mm under argon atmosphere in a glovebox. Indexing of PXRD data, structure solution by charge flipping and subsequent Rietveld refinements were carried out with the program TOPAS Academic v. 5.^{33, 34}

Single Crystal X-ray Diffraction

Single crystals of $\text{Na}_{8.5}(\text{AlSi}_4)_{0.25}(\text{SiSi}_4)_{0.75}$ were isolated under paraffin oil outside the glovebox and sealed in glass capillaries under oil. Single crystal X-ray diffraction (SCXRD) experiments were carried out with a BRUKER D8 Quest diffractometer using Mo-K_{α} radiation. Data handling, including a multi-scan absorption correction with the program SADABS, was done utilizing the BRUKER Apex 3 software package.³⁵ The structure solution and refinement were performed with the programs SHELXS97 and SHELXL97, respectively.³⁶

Solid-state Nuclear Magnetic Resonance Spectroscopy

Solid-state NMR spectra were measured on a BRUKER Avance III 500 instrument at a magnetic field of $B_0 = 11.74\text{ T}$. Magic-angle spinning (MAS) experiments were performed in zirconia spinners at a spinning speed of 10 kHz using a BRUKER 4 mm triple-channel probe. ^{27}Al and ^{29}Si spectra were referenced indirectly to ^1H in 0.1% TMS at 0.00 ppm.

Differential Scanning Calorimetry

For differential scanning calorimetry (DSC) measurement samples were sealed in small quartz ampoules (5 mm outer diameter, 10 – 15 mm length) under argon. To improve heat-flow the quartz ampoules were put in Pt-crucibles (6 mm diameter, 10 mm height). Measurements were then carried out using a NETZSCH STA 449 F5 Jupiter with an Argon flow of 40 mL min^{-1} in a temperature range between room temperature and $900\text{ }^\circ\text{C}$ and heating/cooling rates between 1 and 10 K min^{-1} . Data handling was performed with the NETZSCH Proteus software package.

Energy Dispersive X-Ray Analysis

Elemental composition was determined by energy-dispersive X-ray spectroscopy (EDX; detector: OXFORD INSTRUMENTS Inca Energy) and an image of the morphology was obtained using a JEOL JSM 6500 F scanning electron microscope (SEM; field emission gun, acceleration voltage 20 kV).

Bond Valence Energy Landscape Calculations

Bond valence energy landscape (BVEL) calculations were performed with the program 3Dbvsmapper.³⁷ The BV method calculates the bond valence sum (BVS) for a tested ion at each voxel grid point of a three-dimensional mesh in a unit cell. For a sodium ion at its equilibrium site relative to the other ions in the structure (often equal to the crystallographic site of the sodium ion) the bond valence sum should be equal to its oxidation state (+1). Deviations of the BVS display possible migration pathways for the tested ion.³⁸ For a detailed description of the method see the SI. Here, the BVEL method uses soft-bond-valence parameters and additional (penalty) terms to account for Coulombic attraction/repulsion terms.³⁹ The cutoff distance was fixed to a maximum value of 8 Å. The images were created with VESTA.⁴⁰

Electrochemical Impedance Spectroscopy

Electrochemical impedance spectroscopy and galvanostatic polarization measurements were performed with an Ivium compactstat.h (24 bit instrument) in a two-electrode setup using a RHD INSTRUMENTS Microcell HC cell stand loaded with RHD INSTRUMENTS TSC Battery cells performing measurements between 25 °C and 75 °C inside the glovebox under argon atmosphere. The spectra were recorded in a frequency range of 1 MHz - 0.1 Hz and an applied rms AC voltage between 30 mV and 100 mV. The analysis of the impedance spectra was carried out with the RelaxIS3 software from RHD INSTRUMENTS. The linearity, stability and causality was checked by applying the Kramers-Kronig-relation before fitting the data. Before measuring, the samples were ground thoroughly and compacted to a pellet of about 0.5 mm thickness and 5 mm diameter by uniaxial cold pressing (500 MPa). The obtained densities of the pellets were between 76-91 % with an error of 6 % (cf. Table S13). For impedance spectroscopy, the pellets were sandwiched between indium foil (ALFA AESAR, 0.127 mm thick, 99.99 %) to enhance the contact with the stainless steel electrodes of the cells. No reaction between In and the samples was observed. Every sample was measured twice, and for each sample several temperature cycles were conducted. The measurement uncertainties arise from the error propagation of the uncertainties in pellet thickness, area and in obtained resistance. For the galvanostatic polarization measurements stainless steel electrodes were used.

Results and Discussion

X-Ray Diffraction

From all samples in the $\text{Na}_{5-x}\text{Al}_{1-x}\text{Si}_x\text{S}_4$ ($0 \leq x \leq 1$) aliovalent substitution series PXRDs were measured to study the crystallinity and phase composition (additional crystallographic data for all structures are given in the supplementary information). Figure 1.1B shows that no complete solid solution is formed. Instead, three separate phases crystallize as a function of the degree of substitution x . This is consistent with the fact that the pseudo-binary border phases Na_5AlSi_4 and Na_4Si_5 do not crystallize isotypically as shown below. Regarding the volume of the respective crystalline phases depicted in Figure 1.1a, a Vegard-like dependence on the substitution value x for all phases can be observed and therefore partial miscibility within the respective phases can be assumed.⁴¹

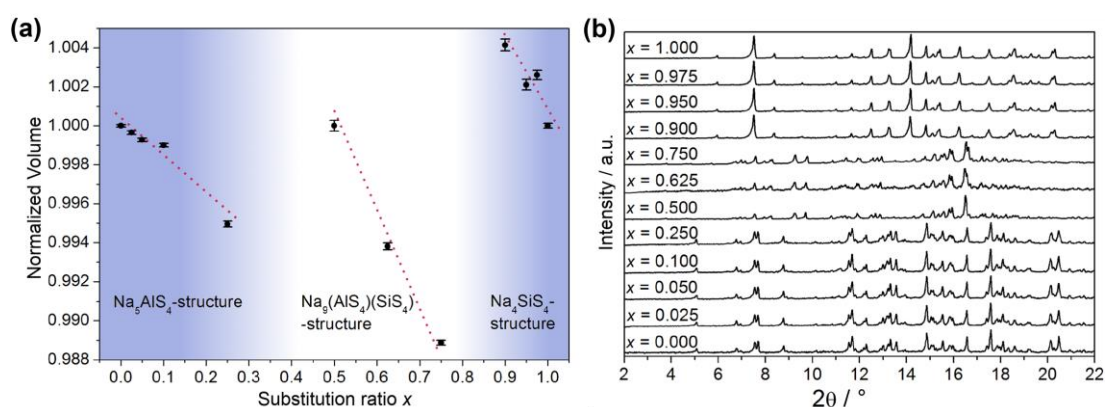


Figure 1.1 a) Normalized volume of the observed crystalline phases obtained by Rietveld refinement displayed against substitution value x ; error bars represent 3σ and the red lines are a guide to the eye to illustrate the Vegard-like dependence on x . b) PXRDs (Mo- $K_{\alpha 1}$ radiation) of all samples in the $\text{Na}_{5-x}\text{Al}_{1-x}\text{Si}_x\text{S}_4$ ($0 \leq x \leq 1$) substitution series.

Crystal Structure of Na_5AlSi_4 .

Since no suitable single crystals were obtained, the crystal structure of Na_5AlSi_4 was determined using powder X-ray data. The PXRD of Na_5AlSi_4 was indexed in the orthorhombic space group $Pbca$ (No.61) with $a = 12.0130(12)$ Å, $b = 7.05263(7)$ Å and $c = 21.5605(2)$ Å. The structure was solved by charge-flipping implemented in TOPAS Academic v.5 and refined with the Rietveld algorithm (Figure 1.2a). The structure is depicted in Figure 1.2. The compound crystallizes in the Na_5FeO_4 structure type and is composed of isolated $[\text{AlSi}_4]$ -tetrahedra and distorted $[\text{NaSi}_4]$ -tetrahedra and $[\text{NaSi}_6]$ -octahedra.⁴² The packing of the Al^{3+} atoms and therefore the packing of the $(\text{AlSi}_4)^{5-}$ -anions can be regarded as a slightly distorted α -uranium packing as was stated for isotypic Rb_5GaO_4 .⁴³ The BVEL calculations (cf. below) show that most likely the Na2 atom does not take part in the sodium ion conduction and can therefore be considered as being part of the lattice. Hence, the lattice can be regarded as hexagonally packed infinite chains of face-sharing $[\text{Na}_2\text{Si}_6]$ -octahedra connected via a common face to $[\text{AlSi}_4]$ -tetrahedra which alternate back and forth along a (Figure 1.2c).

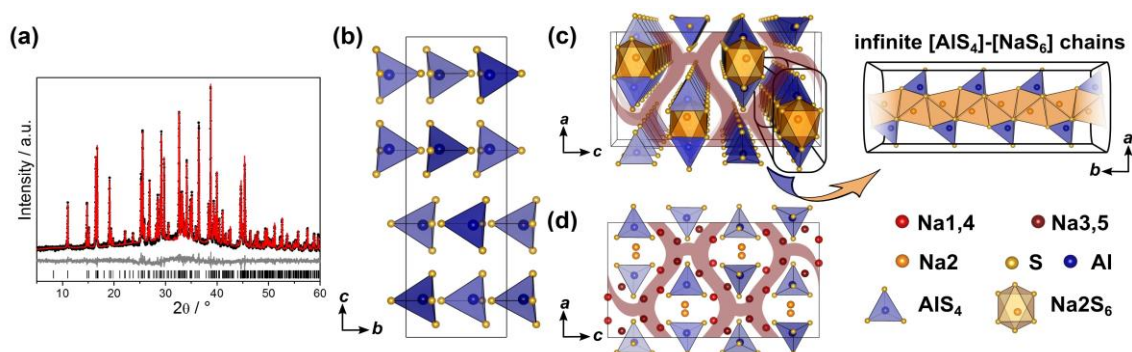


Figure 1.2: a) Rietveld refinement of Na_5AlSi_4 ($x = 0$) measured using $\text{Cu-K}\alpha_1$ radiation; black dots depict the measured data, red lines the Rietveld fit, gray lines the difference plot and black lines the respective reflection positions. b) $[\text{AlSi}_4]$ -tetrahedral sublattice in Na_5AlSi_4 viewed along a . c) Perspective view of the $[\text{AlSi}_4]$ -tetrahedral and $[\text{Na}_2\text{S}_6]$ octahedral arrangement parallel to b . d) Complete Na_5AlSi_4 structure with $[\text{AlSi}_4]$ tetrahedral arrangement viewed along b ; maroon curved lines represent sodium ion diffusion pathways determined by BVLE calculations.

Crystal Structure of Na_4SiS_4

The structure of Na_4SiS_4 was also determined from PXRD data. The diffractogram was indexed in the orthorhombic space group $P2_12_12_1$ (No.19) with $a = 13.6765(3)$ Å, $b = 8.7839(2)$ Å and $c = 6.88940(15)$ Å, solved using charge-flipping and refined by Rietveld refinement (Figure 1.3a). The structure is comprised of isolated $[\text{SiS}_4]$ -tetrahedra which are edge- and corner-sharing to distorted $[\text{NaS}_5]$ -octahedra (5+1 coordination, cf. below). The sulfur atom arrangement constitutes a distorted hexagonal close packing (hcp). Therefore, the structure can be regarded as a hcp of S^{2-} -anions with Si^{4+} and Na^+ filling tetrahedral and all octahedral voids, respectively. This highlights the similarity of this compound's structure with the thio-LiSICON family.⁵ However, this structure model does not account for the weak reflection at $2\theta \approx 5^\circ$, marked in Figure 1.3a. It stems from an elongation of the a -axis by a factor of three ($i3$ transition) to $a = 41.0301(7)$ Å and an ordering of sodium atoms Na10, Na11 and Na12 to form $[\text{NaS}_5]$ -pyramids in a one-up-twodown-pattern, leading to the superstructure shown in Figure 1.3.

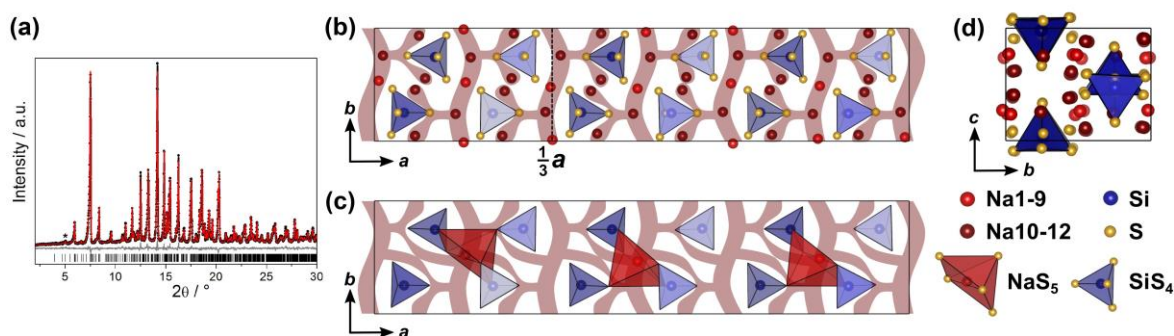


Figure 1.3: a) Rietveld refinement of Na_4SiS_4 ($x = 1$) measured using $\text{Mo-K}\alpha_1$ radiation, the super-structure reflection is marked by an asterisk; black dots depict the measured data, red lines the Rietveld fit, gray lines the difference plot and black lines the respective reflection positions. b) Na_4SiS_4 crystal structure parallel to c ; c) Na_4SiS_4 structure viewed along a ; d) $[\text{SiS}_4]$ -tetrahedra (blue) and $[\text{NaS}_5]$ -pyramidal (red) arrangement viewed parallel to c , showing the $[\text{NaS}_5]$ -pyramids in a one-up-two-down-pattern; maroon curved lines represent sodium ion diffusion pathways determined by BVLE calculations.

Crystal structure of $\text{Na}_9(\text{AlS}_4)(\text{SiS}_4)$

The double salt $\text{Na}_{10-2x}(\text{AlS}_4)_{2-2x}(\text{SiS}_4)_{2x}$ could be obtained in a compositional range of $0.5 \leq x \leq 0.75$. Samples with $x = 0.75$ yielded suitable crystals for SCXRD measurements, presumably because a poly-sulfide melt serves as a solvent for the compound at temperatures exceeding 300°C as shown by thermal analysis (cf. Figure S3). $\text{Na}_{8.5}(\text{AlS}_4)_{0.5}(\text{SiS}_4)_{1.5}$ ($x = 0.75$) crystallizes in the monoclinic space group Cc (No.9), with $a = 17.5673(6) \text{ \AA}$, $b = 13.5408(5) \text{ \AA}$, $c = 14.2543(5) \text{ \AA}$, and $\beta = 93.3683(13)$. Its crystal structure is comprised of isolated $[\text{Al}/\text{SiS}_4]$ -tetrahedra, and distorted tetrahedrally, trigonal-bipyramidally, square-pyramidally or octahedrally coordinated $[\text{NaS}_4]$ -, $[\text{NaS}_5]$ -, or $[\text{NaS}_6]$ -units (Figure 1.4, Figure S1). Additionally, the anion sublattice shows pseudo-inversion symmetry, which is broken by the sodium cations. Since BVEL calculations show that Na13 requires the highest energy to take part in ion migration (cf. below), it can be considered as part of the lattice. Therefore, the topology of the structure can be described as a distorted hexagonal packing of rods comprised of $[\text{Na}_{13}\text{S}_6]$ corner-sharing to four $[\text{Al}/\text{SiS}_4]$ -tetrahedra and interconnected by two corner-sharing $[\text{Al}/\text{SiS}_4]$ -tetrahedra parallel to c (Figure 1.4a). In contrast, for Na cations Na4, Na12, Na15 and Na18 (cf. Table S8) not taking part in the lattice, large anisotropic displacement parameters are found (see Table S9 and Figure S1). They occupy positions best described as two half-filled face-sharing $[\text{NaS}_4]$ -tetrahedra constituting an unresolved split position, which therefore explains the elongated shapes. The occupancy of Si vs. Al was not refined because of the similar atomic form factors of both elements, yet the Si/Al ratio was confirmed to be 3/1 by EDX measurements (cf. Table S11).

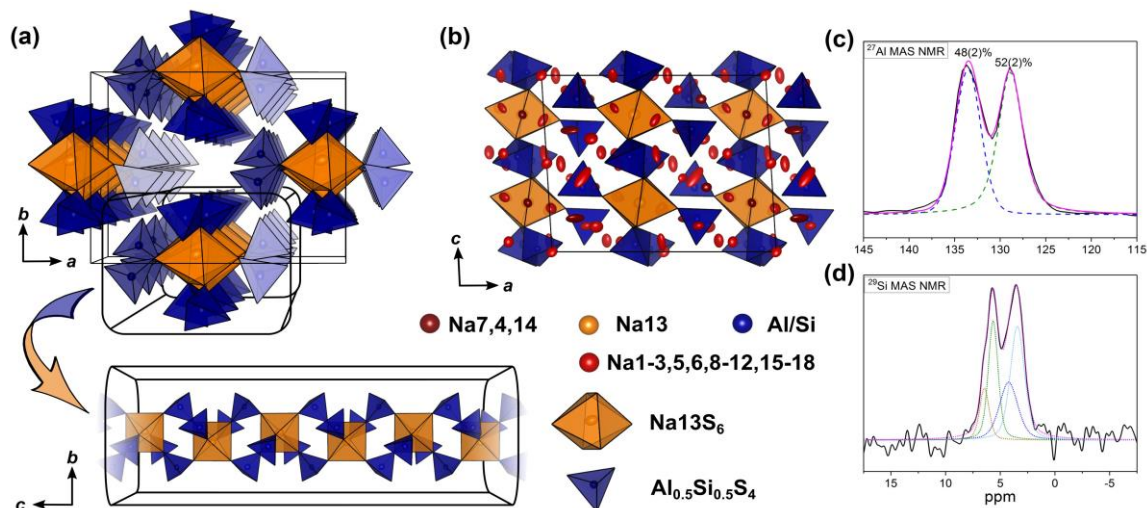


Figure 1.4: a) $[\text{Si}/\text{AlS}_4]$ -tetrahedral and $[\text{Na}_{13}\text{S}_6]$ -octahedral arrangement viewed along c and infinite $[\text{Si}/\text{AlS}_4]$ - $[\text{Na}_{13}\text{S}_6]$ -rods viewed parallel to a . b) $\text{Na}_9(\text{AlS}_4)(\text{SiS}_4)$ crystal structure viewed along b ; blue polyhedra depict $[\text{Si}/\text{AlS}_4]$ -tetrahedra, orange polyhedra depict $[\text{Na}_{13}\text{S}_6]$ -octahedra, red, dark red and yellow atoms depict Na, and blue atoms depict Si/Al; ellipsoids were drawn at 80% probability. c) Deconvoluted ^{27}Al MAS NMR spectrum of $\text{Na}_9(\text{AlS}_4)(\text{SiS}_4)$ ($x = 0.5$); purple line shows the overall fit, colored dashed lines represent the contributing pseudo-Voigt peaks, relative intensities are given with their respective standard deviation in parentheses. d) ^{29}Si MAS NMR spectrum of $\text{Na}_9(\text{AlS}_4)(\text{SiS}_4)$; colored dotted lines show a tentative signal distribution.

The mean Al/Si–S-distances (cf. Table S10) of all four atomic sites of $2.147(3) \text{ \AA}$ (SiS_4), $2.165(3) \text{ \AA}$ (Si_2S_4), $2.166(3) \text{ \AA}$ (Si_3S_4), and $2.160(3) \text{ \AA}$ (Si_4S_4) are in between the distance expected for tetrahedrally coordinated Si^{4+} –S of 2.10 \AA and Al^{3+} –S of 2.23 \AA .³¹ This suggests that all Al/Si sites

are occupied by silicon and aluminum with Si1 having a slightly higher Si/Al ratio than the other three sites. Since the single crystal was obtained from a sample with $x = 0.75$, the occupancy of sodium atoms was expected to be less than one to maintain charge neutrality. Therefore, the occupancy of all sodium atoms was freely refined (cf. Table S8) insofar as their occupancy factor was significantly ($\geq 3\sigma$) lower than one, yielding a total number of sodium atoms per unit cell of 66.9(2), which is in good agreement with the nominal value of 68.

NMR spectroscopy

To verify the assumption of a mixed occupancy of all four atomic Al/Si sites in the compound $\text{Na}_9(\text{AlS}_4)(\text{SiS}_4)$, ^{27}Al and ^{29}Si magic-angle spinning (MAS) NMR spectra were collected (Figure 1.4c, d). Both spectra show two clearly separated peaks with noticeable shoulders, especially in the ^{29}Si spectrum. Although four signals in each spectrum are expected due to the four crystallographically independent Al/Si sites, the occurrence of only two peaks in each spectrum is in good agreement with the crystal structure by taking into account that the $[\text{Al}/\text{SiS}_4]$ sub-lattice shows pseudo-inversion symmetry and therefore the chemical shifts of the respective nuclei should be very similar (or accidentally equal), resulting in two sets of two overlapping signals, which is apparent in the ^{29}Si spectrum and, to a lesser extent, also in the ^{27}Al spectrum. Additionally, the appearance of shoulders in the spectra suggests slightly different Si/Al occupancies for the atomic sites with pseudo-inversion symmetry, which is also corroborated by the mean Al/Si – S distances from SCXRD data.

Bond Valence Energy Landscape Calculations

BVEL calculations were performed in order to elucidate the minimum energy trajectories of the sodium ions and their dimensionalities in the three structures Na_5AlS_4 , $\text{Na}_9(\text{AlS}_4)(\text{SiS}_4)$, and Na_4SiS_4 . The bond valence approach was proven to be a valid starting point for discussing ion migration pathways in crystalline (ionic) solid electrolytes and electrode materials. The method provides reasonable pathways, comparable to those obtained by density functional theory (DFT) or molecular dynamics (MD) simulations.^{44,45} During ion migration (here Na^+) from one equilibrium site Na_i (often a crystallographic site) to an adjacent site Na_j , sodium surpasses one (or multiple) transition state(s). Meta-stable sites along the path are considered to be interstitial sites for sodium ions. In this work, we denote the calculated global minimum energy E_{\min}^{global} , the minimum energy within the infinitely connected pathway E_{\min}^{path} and the energy at which a infinitely connected pathway is formed $E_{\text{mig}}^{\text{path}}$. The energy required for overcoming the ion migration barrier height Δ is calculated by $\Delta E = |E_{\min}^{\text{path}} - E_{\text{mig}}^{\text{path}}|$. Subscript abbreviations denote the dimensionality of the pathway. Keeping in mind, that these calculated barrier heights for ion migration are overestimated, due to not taking lattice relaxations and coulombic repulsion of $\text{Na}^+ - \text{Na}^+$ into account, the BV method provides elucidating insights into probable ion migration pathways in a new structure.

BVEL calculations for Na_5AlS_4

In Figure 1.5 the result of the BVEL calculation of Na_5AlS_4 is depicted. To better decipher the individual, spatially distinct components of the overall Na ion trajectory, we introduce sections **A** and **B** in Figure 1.5a, and separately discuss each section. In section **A** tetrahedrally coordinated Na1 form a 2D-like conduction pathway in the ac plane. Two adjacent $[\text{Na1S}_4]$ tetrahedra are connected *via* shared faces of an $[\text{S}_6]$ -octahedron, creating a dumbbell-like conduction network between two Na1 sites as shown in Figure 1.5c. Unoccupied tetrahedral sites (see Figure 1.5c) loosely connect the Na1–Na1 dumbbells. Each of these dumbbells is connected to two Na3, which are residing in peninsular-like side pockets.

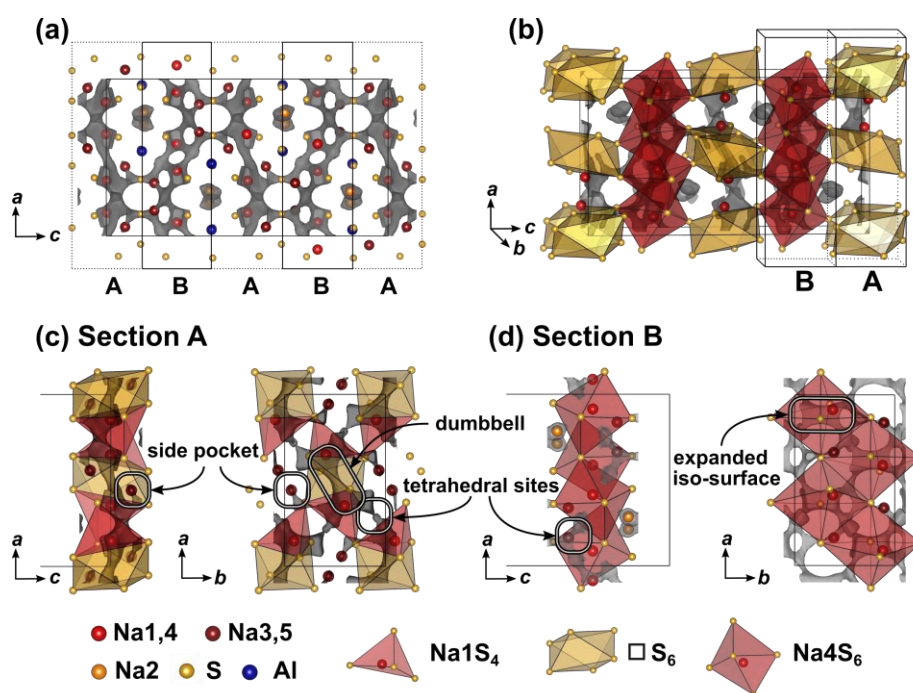


Figure 1.5: a) Na_5AlS_4 crystal structure viewed along b direction. Bond valence energy landscape at isoenergy value of -2.40eV ($E_{\text{min}}^{\text{global}} = -3.71\text{eV}$, $E_{\text{min}}^{\text{path}} = -3.43\text{eV}$, $E_{\text{mig}}^{\text{path}} = -2.58\text{eV}$, $\Delta E_{3D} = 0.83\text{eV}$). The unit cell is divided along the crystallographic c direction into alternating sections **A** and **B**. b) Na_5AlS_4 unit cell with sections **A** and **B**. c) Section **A** ($c = 0.9 - 1.1$) viewed along b and c . d) Section **B** ($c = 0.6 - 0.9$) viewed along b and c .

Section **B** comprises a two-dimensional network composed of larger areas of low sodium ion bond valence energy (expanded isosurface) connected *via* unoccupied tetrahedral sites. These rectangular shaped areas, residing inside an octahedral cavity created by six sulfide ions (red octahedron, Figure 1.5d), display regions in which sodium can migrate freely without passing through high energy bottlenecks. This region is visible at low bond valence isoenergy of -3.0eV in Figure S4 in the SI. Na4 resides in one of the corners of the expanded isosurface, thus creating a $[\text{Na4S}_6]$ coordination polyhedron. The $[\text{Na4S}_6]$ octahedra are connected *via* unoccupied tetrahedral sites forming a percolating network. The infinite $[\text{AlS}_4]$ - $[\text{NaS}_6]$ chains obstruct ion conduction along the crystallographic c direction, but allow connection of both sections **A** and **B** at the gap between two chains as depicted with the maroon colored curved lines in Figure 1.2c, d forming a zig-zag pattern along c and a two-dimensional pattern in the ab plane. Consequently,

despite its more dominant 2D conduction pathways in ab plane, Na_5AlSi_4 is expected to be a three-dimensional ion conductor.

BVEL calculations for Na_4Si_4

For simplification, the orthorhombic structure with a shorter a axis in Figure S5 instead of the superstructure of Na_4Si_4 in Figure 1.3 was used to calculate the bond valence energy landscape for Na_4Si_4 . This does not lead to an appreciably different BVEL outcome, since the superstructure is a result of sodium atom ordering. The anionic lattice remains the same in both structure models. Figure 1.6 depicts the structure of Na_4Si_4 together with bond valence energy surfaces of different isoenergy values.

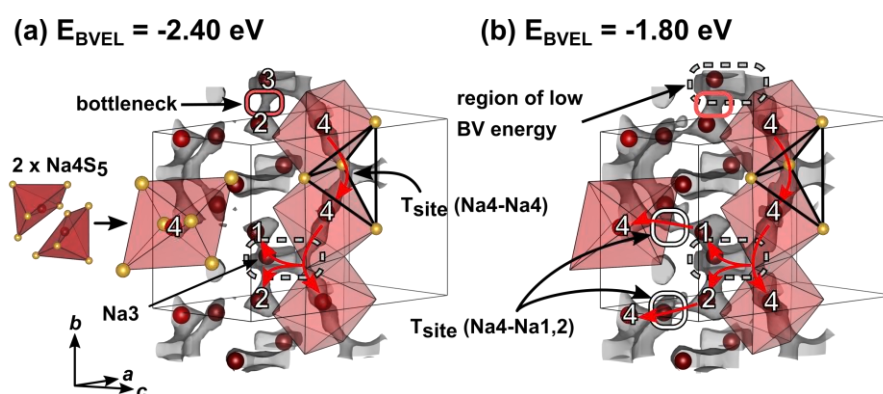


Figure 1.6: Crystal structure of Na_4Si_4 (simplified model without superstructure) with sodium atoms drawn in red and sulfur atoms drawn in yellow. Bond valence energy landscape at isoenergy values of a) -2.40eV and b) -1.80eV are drawn in gray ($E_{\text{min}^{\text{global}}} = -3.73\text{eV}$, $E_{\text{min}^{\text{path}}} = -3.73\text{eV}$, $E_{\text{mig}^{\text{path}}} = -2.68\text{eV}$, $\Delta E_{2\text{D}} = 1.05\text{eV}$). Red arrows depict sodium ion diffusion pathways. Numbers denote crystallographic sodium sites.

A more detailed illustration of the evolution of BVE isosurfaces can be found in Figure S5. As depicted in Figure 1.6, Na_4 occupies a distorted square pyramid. Two base-sharing pyramids form a larger octahedron with Na_4 preferentially occupying one half of the octahedron. In a short range, hopping through the common base of two adjacent square pyramids is energetically facile for Na_4 . For long-range diffusion, Na_4 can hop *via* a tetrahedral site spanned by two $[\text{Na}_4\text{S}_6]$ units into an expanded region of low bond valence energy (up or down along b). Na_3 resides close to one of the $[\text{Na}_4\text{S}_6]$ unit's corners. Despite being connected to this low energy site as well, Na_1 and Na_2 have to pass a bottleneck when diffusing to this site. Therefore, mainly Na_4 and Na_3 form a quasi-one-dimensional, channel-like structure in b direction. At slightly higher bond valence energies tetrahedral sites between $\text{Na}_4\text{-Na}_1$ and $\text{Na}_4\text{-Na}_2$ are accessible through small bottlenecks (see Figure 1.6b, gray isosurface marked with red ellipses). The resulting network percolates the unit cell in all crystallographic directions, resulting in 3D ion migration at higher energies ($\Delta_{3\text{D}} \approx 1.6 \text{ eV}$).

BVEL calculations for $\text{Na}_9(\text{AlSi}_4)(\text{Si}_4)$.

Compared to Na_5AlSi_5 and Na_4Si_4 , the double salt $\text{Na}_9(\text{AlSi}_4)(\text{Si}_4)$ is structurally more complex, since it features 18 sodium sites hosted in mostly distorted coordination polyhedra. Only Na_{13}

resides in a rather ordered $[\text{Na}_{13}\text{S}_6]$ -octahedron, which is bridged in c direction by corner-sharing $[\text{AlS}_4]^{5-}/[\text{SiS}_4]^{4-}$ -tetrahedra (cf. Figure 1.7 and Figure 1.4). In terms of conduction pathways, the sodium ions in $\text{Na}_9(\text{AlS}_4)(\text{SiS}_4)$ can be divided into isolated and migrating sodium ions. Migrating sodium ions, depicted as red spheres in Figure 1.7, reside inside the calculated BVEL network at isoenergy $E_{\text{mig}}^{\text{path}}$. Most of the sodium ions contributing to the three-dimensional conduction are mainly square-pyramidally coordinated, but also trigonal bipyramidal, tetrahedral or octahedral coordinated. Presumably, the low local coordination symmetry of those sodium ions and the therefore asymmetric charge distribution leads to less coulombic attraction facilitating ion hopping.

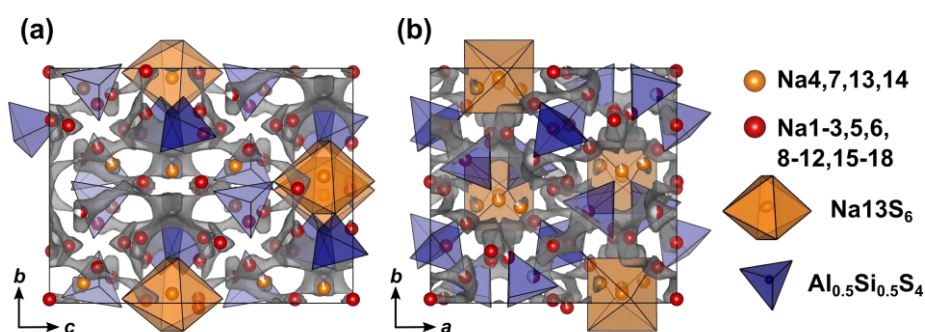


Figure 1.7: Crystal structure of $\text{Na}_9(\text{AlS}_4)(\text{SiS}_4)$ along a) a and b) c direction. The bond valence energy landscape at isoenergy value of -2.60 eV is drawn in gray ($E_{\text{min}}^{\text{global}} = -4.02\text{ eV}$, $E_{\text{min}}^{\text{path}} = -3.86\text{ eV}$, $E_{\text{mig}}^{\text{path}} = -2.64\text{ eV}$, $\Delta E_{3D} = 1.22\text{ eV}$).

However, the either trigonal bipyramidally ($\text{Na}_{4,7}$), tetrahedrally (Na_{14}) or octahedrally (Na_{13}) coordinated sodium ions are not connected to the conduction network at $E_{\text{mig}}^{\text{path}}$ and thus are considered to be members of the rigid framework (cf. Figure S6). At noticeably higher energy all sodium ions but Na_{13} connect to a large, expanded network. Summarizing, at $E_{\text{mig}}^{\text{path}}$ a very flat three-dimensional isoenergy surface with only a few bottle necks occupies a large volume fraction of the unit cell. Compared to Na_5AlS_4 and Na_4SiS_4 , in terms of conduction pathways, the sodium ions in $\text{Na}_9(\text{AlS}_4)(\text{SiS}_4)$ are expected to show higher mobility due to higher versatility in the sodium ion coordination and the resulting flatter potential energy surface for sodium ion migration.

Electrochemical Impedance Spectroscopy

Electrochemical impedance spectroscopy in the temperature range $25-75\text{ }^\circ\text{C}$ was conducted on cold pressed samples of all members in the series $\text{Na}_{5-x}\text{Al}_{1-x}\text{Si}_x\text{S}_4$ with ($0 \leq x \leq 1$). As depicted in Figure 1.8, they show averaged sodium ion conductivities ranging from $1.64 \cdot 10^{-7}\text{ Scm}^{-1}$ for Na_4SiS_4 up to $2.04 \cdot 10^{-5}\text{ Scm}^{-1}$ for $\text{Na}_{8.5}(\text{AlS}_4)_{0.5}(\text{SiS}_4)_{1.5}$. Galvanostatic polarization measurements (cf. Figure S7) confirm the mainly ion conducting nature of the materials with transference numbers of about 0.9998, thus being suitable as solid electrolyte in a battery. The conductivities in Figure 1.8 represent the total conductivities of the samples, modelled by a capacitor or constant phase element (CPE) and a resistance (R) in parallel. Where necessary, a second R-CPE-element was added, and in each spectrum, the polarization of ions at the interface of the blocking electrode was modelled by a CPE.

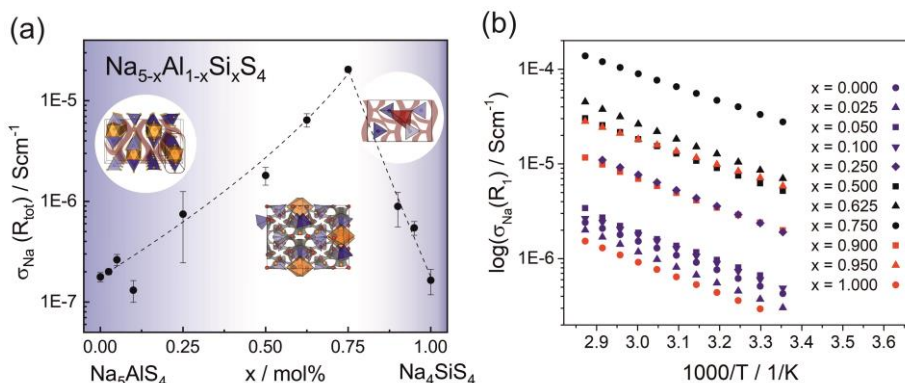


Figure 1.8: a) Sodium ion conductivity in the phase system $\text{Na}_{5-x}\text{Al}_{1-x}\text{Si}_x\text{S}_4$ with ($0 \leq x \leq 1$) as a function of the substitution factor x (visualized by dashed line). In the range of $x = 0.50 - 0.75$, where the material crystallizes in the $\text{Na}_9(\text{AlS}_4)(\text{SiS}_4)$ -structure, the highest average conductivity of $2.04 \cdot 10^{-5} \text{ Scm}^{-1}$ was observed. The unsubstituted phases Na_5AlS_4 and Na_4SiS_4 show a significantly lower ionic conductivity of $1.64 \cdot 10^{-7} \text{ Scm}^{-1}$ - $1.77 \cdot 10^{-7} \text{ Scm}^{-1}$, respectively. The error bars include the standard deviation of the sample and the error of the measurement of about 8%. b) Temperature dependent sodium ion conductivities calculated from R1 of all phases for a selection of measurements (all parameters for these particular measurements are given in Table S12 and Table S13). The different colors indicate the different crystal structures: Na_5AlS_4 -structure (blue), $\text{Na}_9(\text{AlS}_4)(\text{SiS}_4)$ -structure (black) and Na_4SiS_4 -structure (red)

Exemplary impedance spectra and equivalent circuits of each sample as well as the respective capacitances and ideality factors (α) are given in the SI in Figure S8 and Table S12. The effective capacitances (C_{eff}) were calculated by the Brug formula⁴⁶ $C_{\text{eff}} = (R(\text{CPE}))^{1/\alpha}/R$. The best conducting sample $\text{Na}_{8.5}(\text{AlS}_4)_{0.5}(\text{SiS}_4)_{1.5}$ shows only one semicircle with a capacitance of about $2 \cdot 10^{-10} \text{ F}$. The capacitances of the high frequency semicircle of all other samples are of the same order of magnitude, suggesting the same underlying processes. According to literature, the capacitance of $1 \cdot 10^{-10} \text{ F}$ corresponds to grain boundary contributions.⁴⁷ Thus, the high frequency arc contains the information about the bulk and grain boundaries, but the exact bulk contributions can not be deconvoluted. In some spectra a second semicircle at lower frequencies with capacitances of about $8 \cdot 10^{-8} \text{ F} - 6 \cdot 10^{-7} \text{ F}$ is present. The activation energies of this process, calculated according to $\sigma = \sigma_0/T \cdot e^{-E_a/k_B T}$ (with σ_0 being the prefactor, E_a the activation energy, k_B the Boltzmann constant and T the temperature), are higher than the activation energies obtained from the high frequency semicircles (cf. Table S14 and Table S15). Consequently, this semicircle may stem from an inhomogeneity in composition or an additional resistive layer on the surface.^{47, 48} Interestingly, the low frequency semicircle is absent for the best conducting sample $\text{Na}_{8.5}(\text{AlS}_4)_{0.5}(\text{SiS}_4)_{1.5}$ pointing to an easier handling of this material. To avoid a mingling of processes, only the data from the high frequency semicircle is applied for discussing the trends in activation energy and prefactor in the following. A plot only including conductivities calculated from the high frequency semicircles is given in Figure S9. It exhibits the same trend as in Figure 1.8 with $\text{Na}_{8.5}(\text{AlS}_4)_{0.5}(\text{SiS}_4)_{1.5}$ being the best conducting member of the series.

Discussion

Taking a closer look at Figure 1.8 and S9 reveals the strong influence of the number of charge carriers on the conductivity of each material. Going from the poor ionic conductor Na_5AlS_4 along the isotypic phases up to $x = 0.25$, the substitution of Al^{3+} with Si^{4+} introduces sodium vacancies,

which increases the conductivity. On the other end of the series, Na_4Si_4 shows a σ_{Na} in line with findings from.³⁰ Here, the amount of sodium ions is increased in the form of interstitials by substitution with Al^{3+} . The BVEL analysis suggests an occupation of tetrahedral sites between Na4-Na1 and Na4-Na2 as interstitial positions for the sodium ions (cf. Figure 1.6). This would be consistent with more efficient 3D ion migration in the structure and overall facilitation of the ion transport.

In the range of $x = 0.50 - 0.75$, where the $\text{Na}_9(\text{AlSi}_4)(\text{Si}_4)$ -structure is stable, the highest conductivities are found. The topology of $\text{Na}_9(\text{AlSi}_4)(\text{Si}_4)$ does not resemble the one of Na_4Si_4 but shows similarities to Na_5AlSi_4 with a distorted hexagonal packing of $[\text{Al}/\text{Si}_4][\text{Na}_2\text{S}_6]$ -chains. The structure features (migrating) Na ions whose highly distorted coordination polyhedra are connected to other sodium sites mostly *via* faces and edges, which facilitates ion hopping and approximates 3D diffusion.⁴⁹ In this sense, the double salt $\text{Na}_9(\text{AlSi}_4)(\text{Si}_4)$ thus shows similarities to the well known tetragonal LGPS-phase which shows exceptionally high ionic conductivity that is in part attributable to the low energy barrier for lithium diffusion between face-sharing $[\text{LiS}_4]$ -tetrahedra.^{25,50} Additionally, the BVEL analysis of $\text{Na}_9(\text{AlSi}_4)(\text{Si}_4)$ indicates a similar situation to the frustrated energy landscape leading to superionic diffusion in $\text{LiTi}_2(\text{PS}_4)_3$.⁵¹ The sodium coordination environments are more diverse and the coordination polyhedra more distorted in the double salt $\text{Na}_9(\text{AlSi}_4)(\text{Si}_4)$ compared to the border phases of the substitution series $\text{Na}_{5-x}\text{Al}_{1-x}\text{Si}_4$. This low local coordination symmetry of sodium and connection of its coordination polyhedra lead to a flat energy landscape for sodium cations in $\text{Na}_9(\text{AlSi}_4)(\text{Si}_4)$, which is beneficial for ion transport. By further exchanging $[\text{AlSi}_4]^{5-}$ anions by $[\text{Si}_4]^{4-}$ anions in $\text{Na}_9(\text{AlSi}_4)(\text{Si}_4)$, sodium vacancies are introduced. Within the series $\text{Na}_{5-x}(\text{AlSi}_4)_{1-x}(\text{Si}_4)_x$ the value $x = 0.75$ ($\text{Na}_{8.5}(\text{AlSi}_4)_{0.5}(\text{Si}_4)_{1.5}$) constitutes the optimum for the observed ionic conductivity of $2.04 \cdot 10^{-5} \text{ Scm}^{-1}$ and the lowest activation energy in the series of 0.30 eV as shown in Table S15, reflecting the flattening of the energy landscape proposed by the BVEL calculations. For all other members of the series the activation energies are rather similar within their standard deviation, at around 0.35–0.40 eV (cf. Figure S10). Besides, the prefactors σ_0 of the best conducting members of the series exceed the prefactors of the end members by one to two orders of magnitude (cf. Table S13), although the activation energy is lowered (cf. Figure S10). The prefactor takes into account the charge carrier density of mobile ions, the entropy of migration, the jump distance and the attempt frequency, among others. Recently, Kraft *et al.* systematically increased the lattice softness in a series of ionic conductors and noted that a decrease in activation energy is accompanied by a decrease in prefactor, which is in line with the Meyer-Nedel-rule.¹⁶ Accordingly, in cases where this rule applies, possible conductivity improvements via lattice softness engineering are inherently limited. However,⁵¹ showed for $\text{LiTi}_2(\text{PS}_4)_3$ that the highly distorted coordination polyhedra of lithium lead to a frustrated energy landscape, lowering the energy barrier, but increasing the prefactor due to longer jump distances and a higher entropy for the transition state. In $\text{Na}_{8.5}(\text{AlSi}_4)_{0.5}(\text{Si}_4)_{1.5}$ a similar influence on the prefactor as in $\text{LiTi}_2(\text{PS}_4)_3$ can be inferred due to the flattening of the energy landscape by the highly distorted sodium coordination polyhedra. However, the high prefactor for the sample $x = 0.95$ compared to the composition with the highest conductivity at $x = 0.75$ could hint to an even more complicated situation in this series of compounds, necessitating further studies on the complex interplay between structural factors and the energetics of ion transport in these systems.

Performance-wise, $\text{Na}_{8.5}(\text{AlS}_4)_{0.5}(\text{SiS}_4)_{1.5}$ with an ionic conductivity of $2.04 \cdot 10^{-5} \text{ Scm}^{-1}$ and an activation energy of 0.30 eV is comparable to compounds such as $\text{Na}_{10}\text{SnP}_2\text{S}_{12}$,²⁸ silicon substituted Na_3PS_4 ,³⁰ and $\text{HT-NaSi}_2\text{P}_3$.⁵² As can be concluded from the absence of additional resistances at lower frequencies, this material presumably shows an advantageous microstructure or pressing behavior. Furthermore, the smaller electron affinities of Al^{3+} and Si^{4+} may result in increased electrochemical stability at low potentials compared to thiophosphates such as Na_3PS_4 , which will be the subject of future studies.

Conclusion

We have presented the crystal structures and Na ion conductivities in the novel substitution series $\text{Na}_{5-x}\text{Al}_{1-x}\text{Si}_x\text{S}_4$ with ($0 \leq x \leq 1$), containing exclusively low-cost, earth-abundant and lightweight elements. For the best conducting compound $\text{Na}_{8.5}(\text{AlS}_4)_{0.5}(\text{SiS}_4)_{1.5}$ ($x = 0.75$), a relatively high sodium ion conductivity of $2.04 \cdot 10^{-5} \text{ Scm}^{-1}$ at room temperature with an activation energy of 0.30 eV was found, putting this material on par with typical sodium solid electrolytes such as silicon substituted Na_3PS_4 ³⁰ and $\text{Na}_{10}\text{SnP}_2\text{S}_{12}$.²⁸ Our analysis of impedance and BVEL data for the substitution series $\text{Na}_{5-x}\text{Al}_{1-x}\text{Si}_x\text{S}_4$ ($0 \leq x \leq 1$) unveils probable sodium ion migration paths and highlights the enhancement of the conductivity by the low local coordination symmetry of the sodium ions flattening out the potential energy landscape and the increase of sodium ion vacancies in $\text{Na}_{8.5}(\text{AlS}_4)_{0.5}(\text{SiS}_4)_{1.5}$. Concluding, the right blend of the cations Al^{3+} and Si^{4+} entails an optimized structure as well as optimal amount of charge carriers for fast sodium ion conduction.

Acknowledgments

We would like to thank Christian Minke for his assistance in measuring solid state NMR spectra, Juliane Stahl for her assistance in measuring SEM/EDX data and Arthur Haffner for his assistance in measuring SCXRD data.

Author Contributions

SH, AKH and BVL conceived and designed this study; SH and CaH conducted the synthesis; SH, AKH and CaH were responsible for measuring SCXRD, PXR, NMR and EIS; SH performed structure determination; CoH helped in interpretation of crystal structure data; CS performed the calculation and interpretation of BVEL data; AKH analysed measured EIS data; SH, AKH and CS wrote sections of the manuscript; All authors wrote and commented on the manuscript.

References

- [1] Goodenough, J. B. Rechargeable batteries: challenges old and new. *J. Solid State Electrochem.* **2012**, *16*, 2019–2029.
- [2] Janek, J.; Zeier, W. G. A solid future for battery development. *Nat. Energy* **2016**, *1*, 16141.
- [3] Kato, Y.; Hori, S.; Saito, T.; Suzuki, K.; Hirayama, M.; Mitsui, A.; Yonemura, M.; Iba, H.; Kanno, R. High-power all-solid-state batteries using sulfide superionic conductors. *Nat. Energy* **2016**, *1*, 16030.
- [4] Yabuuchi, N.; Kubota, K.; Dahbi, M.; Komaba, S. Research Development on Sodium Ion Batteries. *Chem. Rev.* **2014**, *114*, 11636–11682.
- [5] Lotsch, B. V.; Maier, J. Relevance of solid electrolytes for lithium-based batteries: A realistic view. *J. Electroceram.* **2017**, *38*, 128–141.

- [6] Kamaya, N.; Homma, K.; Yamakawa, Y.; Hirayama, M.; Kanno, R.; Yonemura, M.; Kamiyama, T.; Kato, Y.; Hama, S.; Kawamoto, K.; Mitsui, A. A lithium superionic conductor. *Nat. Mater.* **2011**, *10*, 682–686.
- [7] Rao, R. P.; Adams, S. Studies of lithium argyrodite solid electrolytes for all-solidstate batteries. *Phys. status solidi* **2011**, *208*, 1804–1807.
- [8] Jansen, M.; Henseler, U. Synthesis, structure determination, and ionic conductivity of sodium tetrathiophosphate. *J. Solid State Chem.* **1992**, *99*, 110–119.
- [9] Hayashi, A.; Noi, K.; Sakuda, A.; Tatsumisago, M. Superionic glass-ceramic electrolytes for room-temperature rechargeable sodium batteries. *Nat. Commun.* **2012**, *3*, 855–856.
- [10] Holzmann, T.; Schoop, L. M.; Ali, M. N.; Moudrakovski, I.; Gregori, G.; Maier, J.; Cava, R. J.; Lotsch, B. V. $\text{Li}_{0.6}[\text{Li}_{0.2}\text{Sn}_{0.8}\text{S}_2]$ - a layered lithium superionic conductor. *Energy Environ. Sci.* **2016**, *9*, 2578–2585.
- [11] Kuhn, A.; Gerbig, O.; Zhu, C.; Falkenberg, F.; Maier, J.; Lotsch, B. V. A new ultrafast superionic Li-conductor: ion dynamics in $\text{Li}_{11}\text{Si}_2\text{PS}_{12}$ and comparison with other tetragonal LGPS-type electrolytes. *Phys. Chem. Chem. Phys.* **2014**, *16*, 14669–14674.
- [12] Kuhn, A.; Köhler, J.; Lotsch, B. V. Single-crystal X-ray structure analysis of the superionic conductor $\text{Li}_{10}\text{GeP}_2\text{S}_{12}$. *Phys. Chem. Chem. Phys.* **2013**, *15*, 11620.
- [13] Wakamura, K. Roles of phonon amplitude and low-energy optical phonons on superionic conduction. *Phys. Rev. B* **1997**, *56*, 11593–11599.
- [14] Bachman, J. C.; Muy, S.; Grimaud, A.; Chang, H.-H.; Pour, N.; Lux, S. F.; Paschos, O.; Maglia, F.; Lupart, S.; Lamp, P.; Giordano, L.; Shao-Horn, Y. Inorganic SolidState Electrolytes for Lithium Batteries: Mechanisms and Properties Governing Ion Conduction. *Chem. Rev.* **2016**, *116*, 140–162.
- [15] Krauskopf, T.; Pompe, C.; Kraft, M. A.; Zeier, W. G. Influence of Lattice Dynamics on Na^+ Transport in the Solid Electrolyte $\text{Na}_3\text{PS}_{4-x}\text{Se}_x$. *Chem. Mater.* **2017**, *29*, 8859–8869.
- [16] Kraft, M. A.; Culver, S. P.; Calderon, M.; Bo, F.; Krauskopf, T.; Senyshyn, A.; Dietrich, C.; Zevalkink, A.; Janek, J.; Zeier, W. G. Influence of Lattice Polarizability on the Ionic Conductivity in the Lithium Superionic Argyrodites $\text{Li}_6\text{PS}_5\text{X}$ (X = Cl, Br, I). *J. Am. Chem. Soc.* **2017**, *139*, 10909–10918.
- [17] Hayashi, A.; Noi, K.; Tanibata, N.; Nagao, M.; Tatsumisago, M. High sodium ion conductivity of glass–ceramic electrolytes with cubic Na_3PS_4 . *J. Power Sources* **2014**, *258*, 420–423.
- [18] Krauskopf, T.; Culver, S. P.; Zeier, W. G. Local Tetragonal Structure of the Cubic Superionic Conductor Na_3PS_4 . *Inorg. Chem.* **2018**, *57*, 4739–4744.
- [19] Zhang, L.; Yang, K.; Mi, J.; Lu, L.; Zhao, L.; Wang, L.; Li, Y.; Zeng, H. Na_3PSe_4 : A Novel Chalcogenide Solid Electrolyte with High Ionic Conductivity. *Adv. Energy Mater.* **2015**, *5*, 1501294.
- [20] Krauskopf, T.; Muy, S.; Culver, S. P.; Ohno, S.; Delaire, O.; Shao-Horn, Y.; Zeier, W. G. Comparing the Descriptors for Investigating the Influence of Lattice Dynamics on Ionic Transport Using the Superionic Conductor $\text{Na}_3\text{PS}_{4-x}\text{Se}_x$. *J. Am. Chem. Soc.* **2018**, *140*, 14464–14473.
- [21] Kuhn, A.; Duppel, V.; Lotsch, B. V. Tetragonal $\text{Li}_{10}\text{GeP}_2\text{S}_{12}$ and Li_7GePS_8 – exploring the Li ion dynamics in LGPS Li electrolytes. *Energy Environ. Sci.* **2013**, *6*, 3548.
- [22] Bron, P.; Johansson, S.; Zick, K.; Schmedt auf der Günne, J.; Dehnen, S.; Roling, B. $\text{Li}_{10}\text{SnP}_2\text{S}_{12}$: An Affordable Lithium Superionic Conductor. *J. Am. Chem. Soc.* **2013**, *135*, 15694–15697.
- [23] Kato, Y.; Saito, R.; Sakano, M.; Mitsui, A.; Hirayama, M.; Kanno, R. Synthesis, structure and lithium ionic conductivity of solid solutions of $\text{Li}_{10}(\text{Ge}_{1-x}\text{M}_x)\text{P}_2\text{S}_{12}$ (M = Si, Sn). *J. Power Sources* **2014**, *271*, 60–64.
- [24] Hori, S.; Taminato, S.; Suzuki, K.; Hirayama, M.; Kato, Y.; Kanno, R. Structure-property relationships in lithium superionic conductors having a $\text{Li}_{10}\text{GeP}_2\text{S}_{12}$ -type structure. *Acta Crystallogr. Sect. B Struct. Sci. Cryst. Eng. Mater.* **2015**, *71*, 727–736.
- [25] Hori, S.; Kato, M.; Suzuki, K.; Hirayama, M.; Kato, Y.; Kanno, R. Phase Diagram of the $\text{Li}_4\text{GeS}_4 - \text{Li}_3\text{PS}_4$ Quasi-Binary System Containing the Superionic Conductor $\text{Li}_{10}\text{GeP}_2\text{S}_{12}$. *J. Am. Ceram. Soc.* **2015**, *98*, ed. by Sprenkle, V., 3352–3360.
- [26] Bron, P.; Dehnen, S.; Roling, B. $\text{Li}_{10}\text{Si}_{0.3}\text{Sn}_{0.7}\text{P}_2\text{S}_{12}$ – A low-cost and low-grainboundary-resistance lithium superionic conductor. *J. Power Sources* **2016**, *329*, 530–535.
- [27] Harm, S.; Hatz, A.-K.; Moudrakovski, I.; Eger, R.; Kuhn, A.; Hoch, C.; Lotsch, B. V. Lesson Learned from NMR: Characterization and Ionic Conductivity of LGPS-like Li_7SiPS_8 . *Chem. Mater.* **2019**, *31*, 1280–1288.
- [28] Richards, W. D.; Tsujimura, T.; Miara, L. J.; Wang, Y.; Kim, J. C.; Ong, S. P.; Uechi, I.; Suzuki, N.; Ceder, G. Design and synthesis of the superionic conductor $\text{Na}_{10}\text{SnP}_2\text{S}_{12}$. *Nat. Commun.* **2016**, *7*, 11009.

- [29] Duchardt, M.; Ruschewitz, U.; Adams, S.; Dehnen, S.; Roling, B. Vacancy-Controlled Na^+ Superionic Conduction in $\text{Na}_{11}\text{Sn}_2\text{PS}_{12}$. *Angew. Chemie Int. Ed.* **2018**, *57*, 1351–1355.
- [30] Tanibata, N.; Noi, K.; Hayashi, A.; Tatsumisago, M. Preparation and characterization of highly sodium ion conducting $\text{Na}_3\text{PS}_4 - \text{Na}_4\text{SiS}_4$ solid electrolytes. *RSC Adv.* **2014**, *4*, 17120–17123.
- [31] Shannon, R. D. Revised effective ionic radii and systematic studies of interatomic distances in halides and chalcogenides. *Acta Crystallogr.* **1976**, *A32*, 751–767.
- [32] Brown, A. P.; Tani, B. S. Powder X-ray diffraction identification of some new phases in the $\text{Na}_2\text{S} - \text{Al}_2\text{S}_3$ system. *Mater. Res. Bull.* **1987**, *22*, 1029–1037.
- [33] Coelho, A. A. TOPAS and TOPAS-Academic : an optimization program integrating computer algebra and crystallographic objects written in C++. *J. Appl. Crystallogr.* **2018**, *51*, 210–218.
- [34] Oszla'nyi, G.; Su't'o, A. The charge flipping algorithm. *Acta Crystallogr.* **2008**, *A64*, 123–134.
- [35] Krause, L.; Herbst-Irmer, R.; Sheldrick, G. M.; Stalke, D. Comparison of silver and molybdenum microfocus X-ray sources for single-crystal structure determination. *J. Appl. Crystallogr.* **2015**, *48*, 3–10.
- [36] Sheldrick, G. M. A short history of SHELX. *Acta Crystallogr. Sect. A Found. Crystallogr.* **2008**, *64*, 112–122.
- [37] Sale, M.; Avdeev, M. 3DBVSMAPPER: a program for automatically generating bond-valence sum landscapes. *J. Appl. Cryst.* **2012**, *45*, 1054–1056.
- [38] Nishitani, Y.; Adams, S.; Ichikawa, K.; Tsujita, T. Evaluation of magnesium ion migration in inorganic oxides by the bond valence site energy method. *Solid State Ionics* **2018**, *315*, 111–115.
- [39] Adams, S.; Rao, R. P. High power lithium ion battery materials by computational design. *Phys. Status Solidi A* **2011**, *208*, 1746–1753.
- [40] Momma, K.; Izumi, F. VESTA3 for three-dimensional visualization of crystal, volumetric and morphology data. *J. Appl. Cryst.* **2011**, *44*, 1272–1276.
- [41] Vegard, L. Die Konstitution der Mischkristalle und die Raumfu'llung der Atome. *Z. Phys.* **1921**, *5*, 17–26.
- [42] Brachtel, G.; Hoppe, R. Neue Oxoferrate(III). Zur Kenntnis von Na_5FeO_4 . *Z. anorg. allg. Chem.* **1978**, *446*, 77–86.
- [43] Bender, J.; Wohlfarth, A.; Hoch, C. Crystal Structures of New Alkali Metal-rich Oxometallates: Rubidium Aluminate Tetrahydroxide, $\text{Rb}_9(\text{AlO}_4)(\text{OH})_4$, Rubidium Orthogallate, Rb_5GaO_4 , Caesium bis-Chromate(IV) Oxide, $\text{Cs}_{10}(\text{CrO}_4)_2\text{O}$, and Caesium Diindate, $\text{Cs}_8\text{In}_2\text{O}_7$. *Z. Naturforsch. B* **2010**, *65*, 1416–1426.
- [44] Xiao, R.; Li, H.; Chen, L. High-throughput design and optimization of fast lithium ion conductors by the combination of bond-valence method and density functional theory. *Sci. Rep.* **2015**, *5*, 14227.
- [45] Avdeev, M.; Sale, M.; Adams, S.; Rao, R. P. Screening of the alkali-metal ion containing materials from the Inorganic Crystal Structure Database (ICSD) for high ionic conductivity pathways using the bond valence method. *Solid State Ionics* **2012**, *225*, 43–46.
- [46] Brug, G.; van den Eeden, A.; Sluyters-Rehbach, M.; Sluyters, J. The analysis of electrode impedances complicated by the presence of a constant phase element. *J. Electroanal. Chem. Interfacial Electrochem.* **1984**, *176*, 275–295.
- [47] Irvine, J. T. S.; Sinclair, D. C.; West, A. R. Electroceramics: Characterization by Impedance Spectroscopy. *Adv. Mat.* **1990**, *2*, 132–138.
- [48] Bruce, P. G.; West, A. R. The A-C Conductivity of Polycrystalline LISICON, $\text{Li}_{2+2x}\text{Zn}_{1-x}\text{GeO}_4$, and a Model for Intergranular Constriction Resistances. *J. Electrochem. Soc.* **1983**, *130*, 662–669.
- [49] West, A. R.; Bruce, P. G. Tetragonal-Packed Crystal Structures. *Acta Crystallogr.* **1982**, *38*, 1891–1896.
- [50] Wang, Y.; Richards, W. D.; Ong, S. P.; Miara, L. J.; Kim, J. C.; Mo, Y.; Ceder, G. Design principles for solid-state lithium superionic conductors. *Nat. Mater.* **2015**, *14*, 1026–1031.
- [51] Di Stefano, D.; Miglio, A.; Robeyns, K.; Filinchuk, Y.; Lechartier, M.; Senyshyn, A.; Ishida, H.; Spannenberger, S.; Prutsch, D.; Lunghammer, S.; Rettenwander, D.; Wilkening, M.; Roling, B.; Kato, Y.; Hautier, G. Superionic Diffusion through Frustrated Energy Landscape. *Chem.* **2019**, *5*, 2450–2460.
- [52] Haffner, A.; Hatz, A.-K.; Moudrakovski, I.; Lotsch, B. V.; Johrendt, D. Fast Sodium Ion Conductivity in Supertetrahedral Phosphidosilicates. *Angew. Chem. Int. Ed.* **2018**, *57*, 6155–6160.

4.5.1 Supporting Information for "Finding the right blend: Interplay between structure and sodium ion conductivity in the system Na₅AlS₄ – Na₄SiS₄"

Crystallographic data for Na₅AlS₄

Table S1: Crystallographic data and information for the structure solution and refinement from powder X-ray diffraction data for Na₅AlS₄. Standard deviations are given in parentheses. These data were deposited in the Cambridge Crystallographic Data Centre and were given the deposition number CCDC 1980422.

<i>Na₅AlS₄</i>	
crystal system	orthorhombic
space group	<i>Pbca</i> , (Nr. 61)
lattice params.	<i>a</i> 12.01930(12) Å
	<i>b</i> 7.05236(7) Å
	<i>c</i> 21.5605(2) Å
<i>V</i> [Å ³]	1827.56(3)
<i>Z</i>	8
calc. density [gcm ⁻³]	1.96398(3)
diffractometer	STOE STADI P, CuK _{α1} -radiation Debye-Scherrer geometry
temperature [K]	295
absorption coefficient [mm ⁻¹]	12.1231(2)
refined 2θ region [°]	3 – 90
<i>R_{exp}</i>	6.054
<i>R_p</i>	5.187
<i>R_{wp}</i>	6.604
Goof	1.091
<i>RBragg</i>	1.949
number of refined params.	60
number of background params.	12

Crystallographic data for Na₅AlS₄

Table S2: Standardized fractional atomic coordinates¹ and isotropic displacement parameters [\AA^2] for Na₅AlS₄. Standard

Atom	occupation-factor	Wyckoff-position	x	y	z	Biso
S1	1	8c	0.3713(4)	0.2046(6)	0.9571(3)	2.58(15)
S2	1	8c	0.4477(3)	0.8520(5)	0.3783(3)	2.50(12)
S3	1	8c	0.1402(3)	0.2426(6)	0.6222(4)	3.29(12)
S4	1	8c	0.6317(4)	0.7610(6)	0.2113(3)	3.4(2)
Al1	1	8c	0.0399(3)	0.8312(5)	0.8737(3)	2.70(14)
Na1	1	8c	0.3521(5)	0.9080(9)	0.5013(3)	3.8(2)
Na2	1	8c	0.2869(4)	0.5531(8)	0.3658(3)	3.6(2)
Na3	1	8c	0.5579(6)	0.5658(9)	0.4332(3)	4.6(2)
Na4	1	8c	0.5863(5)	0.3809(10)	0.2501(3)	4.3(2)
Na5	1	8c	0.8373(5)	0.1078(9)	0.8294(3)	2.9(2)

deviations are given in parentheses.

Table S3: Interatomic distances in Na₅AlS₄. Standard deviations are given in parentheses.

i: $-\frac{1}{2}x+\frac{1}{2}y-\frac{1}{2}z$; ii: $-x+1, y-\frac{1}{2}, -z+\frac{1}{2}$; iii: $x, -y+\frac{1}{2}, z+\frac{1}{2}$; iv: $x, -y+\frac{1}{2}, z+\frac{1}{2}$; v: $-\frac{1}{2}x+\frac{1}{2}y+\frac{1}{2}z$; vi: $-\frac{1}{2}x+\frac{1}{2}y+\frac{1}{2}z$; vii: $-x+1, y+\frac{1}{2}, -z+\frac{1}{2}$; viii: $-\frac{1}{2}x+\frac{1}{2}y-\frac{1}{2}z$; ix: $-\frac{1}{2}x+\frac{1}{2}y+\frac{1}{2}z$; x: $-x, y-\frac{1}{2}, -z+\frac{1}{2}$; xi: $x-\frac{1}{2}, -y+\frac{1}{2}, -z+\frac{1}{2}$; xii: $x-\frac{1}{2}, y, -z+\frac{1}{2}$; xiii: $-x+1, y+\frac{1}{2}, -z+\frac{1}{2}$; xiv: $x+\frac{1}{2}, -y+\frac{1}{2}, -z+\frac{1}{2}$; xv: $x+\frac{1}{2}, y, -z+\frac{1}{2}$; xvi: $x-\frac{1}{2}, -y+\frac{1}{2}, -z+\frac{1}{2}$; xvii: $-x+\frac{1}{2}, -y+\frac{1}{2}, z+\frac{1}{2}$; xviii: $-x, y+\frac{1}{2}, -z+\frac{1}{2}$; xix: $x, -y+\frac{1}{2}, z-\frac{1}{2}$; xx: $-x+\frac{1}{2}, -y+1, z-\frac{1}{2}$; xxi: $-x+1, y-\frac{1}{2}, -z+\frac{1}{2}$; xxii: $x, -y+\frac{1}{2}, z-\frac{1}{2}$; xxiii: $x-\frac{1}{2}, y, -z+\frac{1}{2}$; xxiv: $x+\frac{1}{2}, -y+\frac{1}{2}, -z+\frac{1}{2}$; xxv: $-x+\frac{1}{2}, -y+1, z+\frac{1}{2}$; xxvi: $x+\frac{1}{2}, y, -z+\frac{1}{2}$

Atom1	Atom2	distance [\AA]	Atom1	Atom2	distance [\AA]	
S1	Al1	2.274(8) ⁱ	S2	S2	2.241(5) ^{xvii}	
	Na3	2.696(8) ⁱⁱ		S3	2.255(6) ^{xviii}	
	Na2	2.864(8) ⁱⁱⁱ		S1	2.274(8) ^{ix}	
	Na1	2.902(8) ^{iv}		Na2	3.084(7) ^{iv}	
	Na1	2.958(8) ^v		Na1	S3	2.857(10) ^{ix}
	Na3	2.989(8) ⁱⁱⁱ		S1	2.902(8) ^{xix}	
S2	Al1	2.241(5) ^{vi}	S2	S2	2.918(8)	
	Na3	2.689(8)		S1	2.958(8) ^{xx}	
	Na4	2.804(9) ^{vii}		Na2	S4	2.822(8) ^{xxi}
	Na5	2.805(7) ^{viii}		S1	2.864(8) ^{xxii}	
	Na2	2.873(7)		S2	2.873(7)	
	Na1	2.918(8)		S4	2.898(8) ^{xxiii}	

S3	Na2	3.168(6) ^{ix}	Na3	Al1	3.084(7) ^{xix}
	Al1	2.255(6) ^x		S2	3.168(6) ⁱ
	Na3	2.672(8) ^{xi}		S3	2.672(8) ^{xxiv}
	Na5	2.757(7) ^{xii}		S2	2.689(8)
	Na5	2.792(8) ^{xiii}		S1	2.696(8) ^{xiii}
S4	Na1	2.857(10) ^j	Na4	S1	2.989(8) ^{xxii}
	Na4	2.961(10) ^{xi}		S2	2.804(9) ^{xxi}
	Al1	2.236(9) ^{xiv}		S4	2.861(8)
	Na5	2.736(8) ^{viii}		S4	2.876(8) ^{xxi}
	Na2	2.822(8) ^{vii}		S3	2.961(10) ^{xxiv}
Al1	Na4	2.861(8)	Na5	S4	2.736(8) ^{xxv}
	Na4	2.876(8) ^{vii}		S3	2.757(7) ^{xxvi}
	Na2	2.898(8) ^{xv}		S3	2.792(8) ⁱⁱ
	S4	2.236(9) ^{xvi}		S2	2.805(7) ^{xxv}

Crystallographic data for Na₄Si₄

Table S4: Crystallographic data and information for the structure solution and refinement from powder X-ray diffraction data for Na₄Si₄. Standard deviations are given in parentheses. These data were deposited in the Cambridge Crystallographic Data Centre and were given the deposition number CCDC 1980423.

Na ₄ Si ₄	
crystal system	orthorhombic
space group	<i>P</i> 2 ₁ 2 ₁ 2 ₁ , (Nr. 19)
lattice params.	<i>a</i> 41.0301(7) Å
	<i>b</i> 8.78409(14) Å
	<i>c</i> 6.88962(12) Å
<i>V</i> [Å ³]	2483.10(7)
<i>Z</i>	12
calc. density [gcm ⁻³]	1.99260(6)
diffractometer	STOE STADI P, MoK _{α1} -radiation Debye-Scherrer geometry
temperature [K]	295
absorption coefficient [mm ⁻¹]	1.42581(4)

refined 2 θ region [°]	2 – 50
R_{exp}	5.390
R_p	4.127
R_{wp}	5.377
Goof	0.998
R_{Bragg}	1.825
number of refined params.	109
number of background params.	10

Table S5: Standardized fractional atomic coordinates¹ and isotropic displacement parameters [Å^2] for Na₄Si₄. Standard deviations are given in parentheses.

Atom	occupation-factor	Wyckoff-position	x	y	z	B_{iso}
S1	1	4a	0.0315(5)	0.056(3)	0.908(3)	0.8(2)
S2	1	4a	0.3654(5)	0.065(3)	0.904(3)	0.8(2)
S3	1	4a	0.6993(5)	0.051(3)	0.907(3)	0.8(2)
S4	1	4a	0.0621(5)	0.758(3)	0.436(3)	1.54(10)
S5	1	4a	0.3963(5)	0.748(3)	0.447(3)	1.54(10)
S6	1	4a	0.7289(5)	0.752(3)	0.430(3)	1.54(10)
S7	1	4a	0.1346(5)	0.548(3)	0.422(4)	1.5(2)
S8	1	4a	0.4662(5)	0.537(3)	0.434(3)	1.5(2)
S9	1	4a	0.8019(5)	0.548(3)	0.408(3)	1.5(2)
S10	1	4a	0.2185(4)	0.249(3)	0.669(3)	1.37(10)
S11	1	4a	0.5436(4)	0.247(3)	0.662(3)	1.37(10)
S12	1	4a	0.8813(5)	0.246(3)	0.667(4)	1.37(10)
Si1	1	4a	0.2216(6)	0.246(4)	0.962(3)	1.58(10)
Si2	1	4a	0.5555(6)	0.248(4)	0.973(4)	1.58(10)
Si3	1	4a	0.8868(5)	0.245(4)	0.980(3)	1.58(10)
Na1	1	4a	0.2394(6)	0.048(4)	0.386(5)	2.0(3)
Na2	1	4a	0.5763(7)	0.045(4)	0.406(5)	2.0(3)
Na3	1	4a	0.9051(6)	0.056(4)	0.408(4)	2.0(3)
Na4	1	4a	0.2435(6)	0.443(4)	0.381(5)	0.9(3)

Na5	1	4a	0.5760(6)	0.452(4)	0.384(5)	0.9(3)
Na6	1	4a	0.9166(5)	0.433(3)	0.379(3)	0.9(3)
Na7	1	4a	0.1518(7)	0.241(5)	0.256(5)	3.2(2)
Na8	1	4a	0.4840(7)	0.242(5)	0.244(5)	3.2(2)
Na9	1	4a	0.8199(7)	0.241(5)	0.255(5)	3.2(2)
Na10	1	4a	-0.0079(6)	1.036(4)	0.235(4)	3.4(2)
Na11	1	4a	0.3330(9)	1.011(5)	0.238(7)	3.4(2)
Na12	1	4a	0.6706(8)	0.979(4)	0.270(6)	3.4(2)

Table S6: Interatomic distances in Na₄Si₄. Standard deviations are given in parentheses. i: $x-\frac{1}{2}, -y+\frac{1}{2}, -z+2$; ii: $x-\frac{1}{2}, -y+\frac{1}{2}, -z+1$; iii: $x, y-1, z+1$; iv: $-x+1, y-\frac{1}{2}, -z+2$; v: $-x+\frac{1}{2}, -y, z+\frac{1}{2}$; vi: $x+\frac{1}{2}, -y+\frac{1}{2}, -z+2$; vii: $x+\frac{1}{2}, -y+\frac{1}{2}, -z+1$; viii: $-x+\frac{1}{2}, -y, z+\frac{1}{2}$; ix: $x+1, y+\frac{1}{2}, -z+2$; x: $-x+1, y+\frac{1}{2}, -z+2$; xi: $-x+\frac{1}{2}, -y+1, z+2$; xii: $x-\frac{1}{2}, -y+\frac{1}{2}, -z+1$; xiii: $-x, y-\frac{1}{2}, -z+2$; xiv: $-x+\frac{1}{2}, -y+1, z+2$; xv: $x+\frac{1}{2}, -y+\frac{1}{2}, -z+1$; xvi: $-x+1, y-\frac{1}{2}, -z+2$; xvii: $-x+\frac{1}{2}, -y, z-\frac{1}{2}$; xviii: $-x+\frac{1}{2}, -y, z-\frac{1}{2}$; xix: $-x+\frac{1}{2}, -y+1, z-\frac{1}{2}$; xx: $-x+\frac{1}{2}, -y+1, z-\frac{1}{2}$; xxi: $x, y+1, z-1$; xxii: $-x, y+\frac{1}{2}, z+\frac{1}{2}$.

Atom1	Atom2	distance [Å]	Atom1	Atom2	distance [Å]
S1	Si2	2.15(4) ⁱ	Si2	S5	2.05(3) ^{iv}
	Na5	2.72(4) ⁱⁱ		S1	2.15(4) ^{vi}
	Na10	2.78(4) ⁱⁱⁱ		S8	2.15(4) ^{iv}
	Na6	2.80(3) ^{iv}		S11	2.20(3)
	Na8	2.83(4) ⁱⁱ		Na6	3.10(4) ^{xiv}
	Na8	2.92(5) ^v		Na3	3.15(5) ^{viii}
S2	Si3	2.05(4) ⁱ	Si3	S2	2.05(4) ^{vi}
	Na11	2.70(5) ⁱⁱⁱ		S7	2.06(4) ^{iv}
	Na9	2.76(4) ⁱⁱ		S12	2.17(3)
	Na6	2.87(3) ⁱⁱ		S4	2.18(3) ^{iv}
	Na7	2.96(5) ^v		Na2	3.01(4) ^{viii}
	Na5	2.98(4) ^{iv}		Na5	3.14(5) ^{xiv}
S3	Si1	2.19(4) ^{vi}	Na1	S9	2.64(4) ^{xvi}
	Na4	2.69(4) ^{vii}		S10	2.77(4)
	Na12	2.84(4) ⁱⁱⁱ		S6	2.95(5) ⁱⁱ
	Na9	2.88(5) ^{viii}		S9	3.05(4) ⁱⁱ
	Na7	2.89(4) ^{vii}		Si1	3.08(5) ^{xvii}
	Na4	2.92(3) ^{iv}		S6	3.11(4) ^{xvi}
S4	Si3	2.18(3) ^{ix}	Na2	S7	2.80(4) ^{vii}
	Na6	2.80(3) ^x		S11	2.84(4)
	Na8	2.84(4) ^{xi}		S8	2.92(4) ^{xvi}
	Na5	2.89(4) ^{xii}		S4	2.93(4) ^{vii}
	Na2	2.93(4) ⁱⁱ		Si3	3.01(4) ^{xviii}

S5	Na10	3.18(4) ⁱⁱⁱ	Na3	S12	2.63(4)
	Si2	2.05(3) ^{ix}		S7	2.80(4) ^{xvi}
	Na3	2.88(4) ⁱⁱ		S8	2.85(3) ^{vii}
	Na7	2.90(4) ^{xi}		S5	2.88(4) ^{vii}
	Na5	3.11(4) ^x		Si2	3.15(5) ^{xviii}
S6	Na6	3.16(4) ^{xii}	Na4	S3	2.69(4) ⁱⁱ
	Si1	2.16(3) ^{ix}	S10	2.81(4)	
	Na1	2.95(5) ^{vii}	S3	2.92(3) ^{ix}	
	Na4	2.95(4) ^x	S6	2.95(4) ^{xvi}	
	Na9	3.01(4) ^{xi}	S6	3.04(4) ^{xii}	
S7	Na4	3.04(4) ^{xv}	Si1	3.13(5) ^{xix}	
	Na1	3.11(4) ^x	Na5	S1	2.72(4) ^{vii}
	Si3	2.06(4) ^{ix}	S4	2.89(4) ^{xv}	
	Na12	2.60(4) ^{xii}	S11	2.95(4)	
	Na2	2.80(4) ⁱⁱ	S2	2.98(4) ^{ix}	
S8	Na3	2.80(4) ^x	S5	3.11(4) ^{xvi}	
	Na9	2.80(4) ^x	Si3	3.14(5) ^{xx}	
	Na7	3.01(5)	Na6	S4	2.80(3) ^{xvi}
	Si2	2.15(4) ^{ix}	S1	2.80(3) ^{ix}	
	Na10	2.60(4) ^{xv}	S2	2.87(3) ^{vii}	
S9	Na3	2.85(3) ⁱⁱ	S12	2.95(3)	
	Na2	2.92(4) ^x	Si2	3.10(4) ^{xx}	
	Na8	2.99(4)	S5	3.16(4) ^{xv}	
	Na8	2.99(4) ^x	Na7	S9	2.79(4) ^{xvi}
	Si1	2.18(4) ^{ix}	S3	2.89(4) ⁱⁱ	
S10	Na1	2.64(4)	S5	2.90(4) ^{xix}	
	Na7	2.79(4)	S2	2.96(5) ^{xvi}	
	Na11	2.80(5)	S7	3.01(5)	
	Na9	2.98(5)	Na8	S1	2.83(4) ^{vii}
	Na1	3.05(4) ^{vii}	S4	2.84(4) ^{xix}	
S11	Si1	2.02(3)	S1	2.92(5) ^{xcii}	
	Na1	2.77(4)	S8	2.99(4)	
	Na4	2.81(4)	S8	2.99(4) ^{xvi}	
	Na12	3.13(4) ^{xii}	Na9	S2	2.76(4) ^{vii}
	Na11	3.14(5) ^{xi}	S7	2.80(4) ^{xvi}	
S11	Si2	2.20(3)	S3	2.88(5) ^{xviii}	
	Na2	2.84(4)	S9	2.98(5)	
	Na10	2.92(4) ^{xi}	S6	3.01(4) ^{xx}	
	Na10	2.94(4) ^{xv}	Na10	S8	2.60(4) ^{xii}
	Na5	2.95(4)	S1	2.78(4) ^{xxi}	

S12	Si3	2.17(3)	Na11	S11	2.92(4) ^{xi}
	Na3	2.63(4)		S11	2.94(4) ^{xii}
	Na6	2.95(3)		S4	3.18(4) ^{xxii}
	Na11	2.98(5) ^{xv}		S2	2.70(5) ^{xxi}
	Na12	2.99(4) ^{xiv}		S9	2.80(5) ^{xii}
Si1	S10	2.02(3)	Na12	S12	2.98(5) ^{xii}
	S6	2.16(3) ^{iv}		S10	3.14(5) ^{xix}
	S9	2.18(4) ^{iv}		S7	2.60(4) ^{xv}
	S3	2.19(4) ⁱ		S3	2.84(4) ^{xxi}
	Na1	3.08(5) ^v		S12	2.99(4) ^{xx}
	Na4	3.13(5) ^{xi}		S10	3.13(4) ^{xv}

Crystallographic data for $\text{Na}_{8.5}(\text{AlSi}_4)_{0.5}(\text{SiS}_4)_{1.5}$

Table S7: Crystallographic data and information for the structure solution and refinement from powder X-ray diffraction data for $\text{Na}_{8.5}(\text{AlSi}_4)_{0.5}(\text{SiS}_4)_{1.5}$. Standard deviations are given in parentheses. These data were deposited in the Cambridge Crystallographic Data Centre and were given the deposition number CCDC 1980426.

$\text{Na}_{16.76(6)}(\text{AlSi}_4)(\text{SiS}_4)_3$	
crystal system	monoclinic
space group	Cc , (Nr. 9)
lattice params.	a 17.5673(6) Å
	b 13.5408(5) Å
	c 14.2543(5) Å
	β 93.3683(13)°
V [Å ³]	3384.9(2)
Z	8
calculated density [gcm ⁻³]	1.982
diffractometer	Bruker D8 Quest (microfocus), Mo K_{α} -radiation, Göbel mirror optics
temperature [K]	295
absorption coefficient [mm ⁻¹]	1.382

ϑ -range [°]	2.32 – 27.50
indexing range	$-22 \leq h \leq 22$, $-17 \leq k \leq 17$, $-18 \leq l \leq 18$
number of measured reflexions	66764
number of independent reflexions	7778
number of independent reflexions ($I \geq 2\sigma(I)$)	6660
R_{int}	0.0532
R_{σ}	0.0302
$F(000)$	1984
corrections	Lorentz-, polarization-, absorption-effects
absorption correction	multi-scan (SADABS) ²
structure solution	direct methods, SHELXS97 ³
structure refinement	least-squares on F^2 , SHELXL97 ³
number of free params.	350
Goof	1.040
R values (reflexions satisfying $I \geq 2\sigma(I)$)	$R1 = 0.0348$, $wR2 = 0.0814$
R values (all data)	$R1 = 0.0448$, $wR2 = 0.0863$
residual electron density [$e^-/\text{\AA}^{-3}$]	0.625/-0.499
twin law	(-1 0 0, 0 -1 0, 0 0 -1)
batch scale factor	0.46

Table S8: Standardized fractional atomic coordinates¹ and equivalent isotropic displacement parameters [\AA^2] for Na_{8.5}(AlS₄)_{0.5}(SiS₄)_{1.5}. Standard deviations are given in parentheses.

Atom	occupation-factor	Wyckoff-position	x	y	z	$U_{equiv.}$
Na1	1	4a	0.0000(2)	0.0160(3)	0.0160(3)	0.0403(8)
Na2	1	4a	0.0079(2)	0.2210(4)	0.2467(3)	0.0558(11)

S1	1	4a	0.04013(12)	0.0236(2)	0.31978(15)	0.0379(5)
S2	1	4a	0.04982(12)	0.2071(2)	0.05134(14)	0.0389(5)
Na3	1	4a	0.0627(2)	0.2428(3)	0.4983(4)	0.0610(12)
S3	1	4a	0.07158(13)	0.4809(2)	0.24654(15)	0.0352(5)
Na4	1	4a	0.1121(3)	0.0854(3)	0.6894(2)	0.0776(14)
S4	1	4a	0.14462(12)	0.5680(2)	0.03750(13)	0.0360(5)
Si1	1	4a	0.15165(12)	0.07480(14)	0.36658(15)	0.0250(4)
Si2	1	4a	0.15633(12)	0.57514(15)	0.19140(14)	0.0255(4)
Na5	0.895(8)	4a	0.1588(2)	0.3388(3)	0.1468(2)	0.0488(10)
S5	1	4a	0.16361(13)	0.0715(2)	0.51778(14)	0.0450(6)
S6	1	4a	0.16354(13)	0.2241(2)	0.3200(2)	0.0492(6)
Na6	0.805(14)	4a	0.2040(3)	0.1103(4)	0.1413(3)	0.067(2)
Na7	0.823(7)	4a	0.2062(2)	0.4083(2)	0.3655(2)	0.0318(8)
S7	1	4a	0.23822(13)	0.0183(2)	0.8137(2)	0.0394(5)
Na8	1	4a	0.2465(2)	0.2575(3)	0.5632(3)	0.0551(10)
S8	1	4a	0.25849(12)	0.2932(2)	0.00555(15)	0.0384(5)
S9	1	4a	0.26822(12)	0.5230(2)	0.23772(15)	0.0409(5)
Na9	1	4a	0.3017(2)	0.7230(4)	0.3090(3)	0.0563(11)
Na10	1	4a	0.3087(2)	0.4838(3)	0.0561(2)	0.0400(8)
Na11	0.848(7)	4a	0.3162(2)	0.1925(3)	0.3152(2)	0.0421(10)
Na12	1	4a	0.3179(2)	0.0119(4)	0.4977(3)	0.0756(15)
S10	1	4a	0.36523(10)	0.35601(14)	0.44868(12)	0.0274(4)
S11	1	4a	0.36644(13)	0.11952(15)	0.13820(14)	0.0355(5)
Si3	1	4a	0.37248(11)	0.24120(15)	0.04104(14)	0.0251(4)
S12	1	4a	0.38285(11)	0.19002(15)	0.63956(13)	0.0315(4)
Na13	1	4a	0.4038(3)	0.03996(10)	0.7780(4)	0.0429(3)
Na14	0.931(5)	4a	0.4046(3)	0.43673(10)	0.2774(3)	0.0344(5)
S13	1	4a	0.42616(11)	0.8087(2)	0.41727(14)	0.0355(5)
Si4	1	4a	0.43545(11)	0.24254(14)	0.51666(13)	0.0200(4)
S14	1	4a	0.44125(12)	0.11958(15)	0.41900(13)	0.0336(4)
S15	1	4a	0.44322(10)	0.35692(15)	0.10912(12)	0.0280(4)
Na15	0.934(8)	4a	0.4911(2)	0.0193(4)	0.0547(4)	0.070(2)
Na16	1	4a	0.4949(2)	0.1838(3)	0.2455(2)	0.0511(9)
Na17	0.498(12)	4a	0.6027(3)	0.1125(4)	0.4185(4)	0.029(2)
S16	1	4a	0.64521(14)	0.2255(2)	0.2408(2)	0.0464(6)
Na18	1	4a	0.6571(3)	0.3469(3)	0.4219(3)	0.101(2)

Table S9: Anisotropic displacement coefficients [\AA^2] for Na_{8.5}(AlS₄)_{0.5}(SiS₄)_{1.5}. U_{ij} is defined by: $U_{ij} = \exp[-2\pi^2(U_{11}(ha^*)^2 + \dots + 2U_{21}hka^*b^*)]$. Standard deviations are given in parentheses.

Atom	U_{11}	U_{22}	U_{33}	U_{23}	U_{13}	U_{12}
Na1	0.041(2)	0.038(2)	0.043(2)	0.0120(15)	0.009(2)	0.000(2)
Na2	0.039(2)	0.086(3)	0.041(2)	0.011(2)	-0.003(2)	0.012(2)
S1	0.0258(12)	0.0487(12)	0.0387(11)	-0.0098(9)	-0.0018(9)	-0.0132(9)
S2	0.0284(11)	0.0524(13)	0.0350(10)	-0.0109(10)	-0.0057(9)	0.0035(10)
Na3	0.030(2)	0.053(2)	0.100(3)	0.011(2)	-0.001(2)	0.001(2)
S3	0.0316(12)	0.0352(10)	0.0392(11)	-0.0022(8)	0.0046(8)	-0.0031(9)
Na4	0.119(3)	0.087(3)	0.0269(15)	0.0142(15)	0.008(2)	-0.040(2)
S4	0.0289(10)	0.0538(12)	0.0249(9)	0.0074(8)	-0.0008(7)	0.0046(9)
Si1	0.0206(10)	0.0213(9)	0.0330(10)	-0.0008(8)	0.0009(8)	-0.0006(8)
Si2	0.0203(10)	0.0303(11)	0.0260(9)	0.0073(8)	0.0013(8)	0.0007(8)
Na5	0.047(2)	0.074(2)	0.0256(12)	-0.0047(12)	0.0054(11)	-0.0092(15)
S5	0.0284(11)	0.076(2)	0.0312(10)	-0.0177(10)	0.0022(8)	-0.0026(11)
S6	0.0266(11)	0.0288(10)	0.091(2)	0.0030(11)	-0.0079(11)	0.0033(8)
Na6	0.065(4)	0.086(4)	0.050(3)	-0.018(2)	0.006(2)	0.010(3)
Na7	0.0388(14)	0.0251(13)	0.032(2)	-0.0004(11)	0.0026(11)	0.0020(11)
S7	0.0337(12)	0.0322(10)	0.0539(13)	-0.0034(9)	0.0157(10)	-0.0032(9)
Na8	0.033(2)	0.062(3)	0.070(2)	0.018(2)	0.00(2)	0.012(2)
S8	0.0236(11)	0.0520(13)	0.0390(11)	-0.0186(10)	-0.0022(8)	0.0085(9)
S9	0.0276(12)	0.0585(14)	0.0365(11)	0.0045(10)	0.0017(9)	0.0085(10)
Na9	0.039(2)	0.093(3)	0.036(2)	0.003(2)	-0.0061(15)	-0.026(2)
Na10	0.035(2)	0.040(2)	0.045(2)	0.0006(15)	0.003(2)	0.005(2)
Na11	0.027(2)	0.058(2)	0.040(2)	-0.0115(15)	-0.0123(13)	0.0148(15)
Na12	0.033(2)	0.125(4)	0.069(2)	0.063(2)	-0.002(2)	0.001(2)
S10	0.0272(10)	0.0257(9)	0.0289(9)	-0.0001(7)	-0.0013(7)	0.0009(7)
S11	0.0433(13)	0.0315(10)	0.0313(10)	0.0022(8)	-0.0002(9)	-0.0068(9)
Si3	0.0210(10)	0.0280(10)	0.0261(9)	-0.0030(8)	0.0008(8)	-0.0011(9)
S12	0.0267(10)	0.0409(10)	0.0273(8)	0.0101(8)	0.0049(7)	-0.0030(8)
Na13	0.0519(8)	0.0342(7)	0.0429(7)	0.001(2)	0.0052(6)	0.008(2)
Na14	0.0247(7)	0.0494(9)	0.0287(7)	0.000(2)	-0.0015(5)	-0.002(2)
S13	0.0248(10)	0.0508(12)	0.0307(9)	0.0101(9)	-0.0009(7)	0.0016(9)
Si4	0.0194(10)	0.0236(9)	0.0168(8)	0.0016(7)	0.0001(7)	0.0010(8)
S14	0.0388(12)	0.0319(10)	0.0302(10)	-0.0038(8)	0.0037(8)	0.0041(8)
S15	0.0256(10)	0.0310(9)	0.0272(9)	-0.0072(7)	-0.0016(7)	-0.0052(8)
Na15	0.026(2)	0.074(3)	0.108(4)	-0.053(2)	-0.007(2)	-0.001(2)

Na16	0.042(2)	0.049(2)	0.065(2)	-0.0140(15)	0.0269(15)	-0.0106(13)
Na17	0.031(3)	0.027(3)	0.029(3)	0.002(2)	0.004(2)	0.014(2)
S16	0.0368(13)	0.0221(9)	0.079(2)	-0.0110(10)	-0.0073(11)	0.0018(8)
Na18	0.105(3)	0.056(2)	0.151(4)	0.057(2)	0.085(3)	0.032(2)

Table S10: Interatomic distances in Na_{8.5}(AlS₄)_{0.5}(SiS₄)_{1.5}. Standard deviations are given in parentheses.

i: $x, -y, z-\frac{1}{2}$; ii: $x-\frac{1}{2}, y-\frac{1}{2}, z$; iii: $x-\frac{1}{2}, -y+\frac{1}{2}, z-\frac{1}{2}$; iv: $x, -y, z+\frac{1}{2}$; v: $x, -y+1, z+\frac{1}{2}$; vi: $x-\frac{1}{2}, -y+\frac{1}{2}, z+\frac{1}{2}$; vii: $x-\frac{1}{2}, y+\frac{1}{2}, z$; viii: $x, -y+1, z-\frac{1}{2}$; ix: $x+\frac{1}{2}, y+\frac{1}{2}, z$; x: $x+\frac{1}{2}, -y+\frac{1}{2}, z+\frac{1}{2}$; xi: $x+\frac{1}{2}, -y+\frac{1}{2}, z-\frac{1}{2}$; xii: $x+\frac{1}{2}, y-\frac{1}{2}, z$;

Atom1	Atom2	distance [Å]	Atom1	Atom2	distance [Å]	
Na1	S1	2.756(4) ⁱ	S9	Na10	2.808(4)	
	S2	2.815(4)		Na18	2.818(5) ⁱⁱⁱ	
	S15	2.870(4) ⁱⁱ		Na9	2.954(4) ^{viii}	
	S10	2.990(4) ⁱⁱⁱ		Na17	3.203(6) ⁱⁱⁱ	
	S5	3.105(4) ⁱ		Na14	2.696(5)	
	Si4	3.474(4) ⁱⁱⁱ		Na10	2.775(4)	
	Na4	3.526(5) ⁱ		Na9	2.939(5)	
	Na10	3.528(2) ⁱⁱ		Na9	S13	2.848(4)
	Na14	3.557(5) ⁱⁱⁱ		S16	2.862(5) ^{vii}	
	Na18	3.559(5) ⁱⁱⁱ		S8	2.954(4) ^v	
	Na3	3.674(5) ⁱ		S12	3.108(4) ^{viii}	
	Na6	4.205(6)		Si3	3.498(4) ^v	
Na2	S12	2.866(4) ⁱⁱⁱ	Na18	3.513(6) ^{vii}		
	S6	2.869(4)	Na8	3.590(5) ^{viii}		
	S1	2.912(5)	Na13	3.716(5) ^{viii}		
	S2	2.929(4)	Na2	3.779(2) ^{ix}		
	S13	3.129(5) ⁱⁱ	Na17	4.188(7) ^{vii}		
	Na5	3.470(6)	Na10	S10	2.866(4) ^{viii}	
	Si4	3.483(4) ⁱⁱⁱ	S15	2.984(4)		
	Na3	3.670(6)	Si3	3.482(4)		
	Na13	3.756(6) ⁱⁱⁱ	Na7	3.490(5) ^{viii}		
	Na9	3.779(2) ⁱⁱ	Na1	3.528(2) ^{ix}		
Na6	4.121(7)	Na14	3.546(5)			
S1	Si1	2.147(3)	Na8	3.672(5) ^{viii}		
	Na14	2.692(5) ⁱⁱ	Na17	4.220(6) ⁱⁱⁱ		
	Na4	2.739(4) ⁱ	Na11	S14	2.758(4)	
S2	Na1	2.756(4) ^{iv}	S11	2.895(4)		
	Si4	2.151(3) ⁱⁱⁱ	S10	3.012(4)		
	Na18	2.811(4) ⁱⁱⁱ	S7	3.165(5) ⁱ		
	Na5	2.896(4)	Na16	3.350(2)		

	Na6	3.208(6)		Si4	3.520(4)
	Na17	3.259(6) ⁱⁱⁱ		Na13	3.557(5) ⁱ
Na3	S13	2.750(4) ⁱⁱ		Na12	3.570(5)
	S5	2.922(5)	Na12	S11	2.775(4) ^{iv}
	S4	2.975(5) ^v		S14	2.892(5)
	S15	3.020(5) ^{vi}		S7	2.928(5) ⁱ
	S6	3.192(5)		Na15	3.130(2) ^{iv}
	Na8	3.311(2)		S12	3.307(6)
	Si1	3.389(5)		Na6	3.378(6) ^{iv}
	Si3	3.439(4) ^{vi}		Na13	3.624(7) ⁱ
	Na4	3.527(6)		Na18	3.712(7) ⁱⁱ
	Na15	3.567(7) ^{vi}	S10	Si4	2.164(3)
	Na1	3.674(5) ^{iv}		Na14	2.799(5)
S3	Si2	2.145(3)		Na10	2.866(4) ^v
	Na5	2.886(4)		Na1	2.990(4) ^x
	Na7	2.994(4)	S11	Si3	2.159(3)
	Na13	3.020(6) ⁱⁱⁱ		Na12	2.775(4) ⁱ
	Na15	3.049(6) ^{vii}		Na16	2.790(4)
	Na17	3.053(6) ^{vii}		Na15	2.890(5)
	Na16	3.060(4) ^{vii}		Na13	2.985(4) ⁱ
Na4	S5	2.665(4)	Si3	S13	2.158(3) ^{viii}
	S16	2.717(5) ^{vi}		S15	2.191(3)
	S1	2.739(4) ^{iv}		Na3	3.439(4) ^{xi}
	S7	2.901(5)		Na9	3.498(4) ^{viii}
	Na6	3.199(7) ^{iv}	S12	Si4	2.149(3)
	S15	3.212(5) ^{vi}		Na13	2.841(4)
	Si1	3.370(4) ^{iv}		Na2	2.866(4) ^x
	Na18	3.485(6) ^{vi}		Na9	3.108(4) ^v
	Na1	3.526(5) ^{iv}	Na13	S13	2.864(4) ^v
	Na8	3.840(6)		S11	2.985(4) ^{iv}
	Na16	3.851(6) ^{vi}		S14	2.998(4) ^{iv}
S4	Si2	2.193(3)		S3	3.020(6) ^x
	Na7	2.756(4) ^{viii}		Na16	3.471(4) ^{iv}
	Na15	2.802(5) ^{vii}		Na11	3.557(5) ^{iv}
	Na8	2.974(5) ^{viii}		Na12	3.624(7) ^{iv}
	Na3	2.975(5) ^{viii}		Na15	3.700(8) ^{iv}
	Na17	3.040(6) ⁱⁱⁱ		Na9	3.716(5) ^v
	Na10	3.095(4)		Na2	3.756(6) ^x
Si1	S6	2.143(3)	Na14	S1	2.692(5) ^{ix}
	S7	2.146(3) ⁱ		S15	2.752(5)
	S5	2.154(3)		Na1	3.557(5) ^x
	Na18	3.185(4) ⁱⁱ		Na16	3.813(4)
	Na4	3.370(4) ⁱ		Na4	3.934(7) ^{xi}

	Na11	3.418(5)	S13	Si3	2.158(3)
	Na6	3.426(5)		Na3	2.750(4)
	Na12	3.480(4)		Na13	2.864(4)
Si2	S9	2.155(3)		Na2	3.129(5)
	S16	2.167(3) ^{vii}		Na15	3.209(6) ^v
	Na5	3.264(5)	Si4	S2	2.151(3) ^x
	Na16	3.325(4) ^{vii}		S14	2.176(3)
	Na8	3.365(5) ^{viii}		Na1	3.474(4) ^x
	Na7	3.431(4)		Na2	3.483(4) ^x
	Na17	3.461(5) ^{vii}	S14	Na15	2.801(4) ^{iv}
	Na15	3.483(5) ^{vii}		Na16	2.835(4)
Na5	S8	2.814(4)		Na17	2.838(6)
	S6	2.913(4)		Na13	2.998(4) ⁱ
	Na6	3.196(7)	S15	Na1	2.870(4) ^{ix}
	Na7	3.316(4)		Na3	3.020(5) ^{xi}
	S9	3.363(5)		Na16	3.145(4)
	Na17	3.408(6) ⁱⁱⁱ		Na4	3.212(5) ^{xi}
	Na10	3.586(5)	Na15	S14	2.801(4) ⁱ
	Na15	3.991(6) ^{vii}		S4	2.802(5) ^{xii}
S5	Na12	2.859(5)		S3	3.049(6) ^{xii}
	Na8	2.961(5)		Na12	3.130(2) ⁱ
	Na6	3.085(6) ^{iv}		S13	3.209(6) ^{viii}
	Na1	3.105(4) ^{iv}		Na17	3.354(7) ⁱ
	Na18	3.333(5) ⁱⁱ		Si2	3.483(5) ^{xii}
S6	Na7	2.673(4)		Na16	3.513(5)
	Na11	2.721(4)		Na3	3.567(7) ^{xi}
	Na6	3.095(6)		Na13	3.700(8) ⁱ
Na6	S11	2.859(6)		Na5	3.991(6) ^{xii}
	S7	3.044(6) ⁱ	Na16	S16	2.705(4)
	S5	3.085(6) ⁱ		S3	3.060(4) ^{xii}
	Na4	3.199(7) ⁱ		Na17	3.171(6)
	Na18	3.238(7) ⁱⁱⁱ		Si2	3.325(4) ^{xii}
	Na11	3.270(6)		Na13	3.471(4) ⁱ
	S8	3.318(6)		Na4	3.851(6) ^{xi}
	Na12	3.378(6) ⁱ	Na17	S4	3.040(6) ^x
Na7	S9	2.674(4)		S3	3.053(6) ^{xii}
	S4	2.756(4) ^v		S16	3.088(6)
	S10	3.053(4)		S8	3.203(6) ^x
	Na17	3.418(5) ^{vii}		S2	3.259(6) ^x
	Na10	3.490(5) ^v		Na18	3.315(7)
	Na8	3.518(5)		Na15	3.354(7) ^{iv}
	Na11	3.599(5)		Na5	3.408(6) ^x
	Na14	3.793(6)		Na7	3.418(5) ^{xii}

S7	Si1	2.146(3) ^{iv}		Si2	3.461(5) ^{xii}
	Na18	2.828(4) ^{vi}	S16	Si2	2.167(3) ^{xii}
	Na12	2.928(5) ^{iv}		Na4	2.717(5) ^{xi}
	Na13	2.997(6)		Na9	2.862(5) ^{xii}
	Na6	3.044(6) ^{iv}		Na18	3.058(6)
	Na11	3.165(5)		Na8	3.187(5) ^{xi}
Na8	S12	2.730(4)	Na18	S2	2.811(4) ^x
	S4	2.974(5) ^v		S8	2.818(5) ^x
	S10	3.032(4)		S7	2.828(4) ^{xi}
	S16	3.187(5) ^{vi}		Si1	3.185(4) ^{ix}
	Si2	3.365(5) ^v		Na6	3.238(7) ^x
	Si4	3.429(4)		S5	3.333(5) ^{ix}
	Na9	3.590(5) ^v		Na4	3.485(6) ^{xi}
	Na10	3.672(5) ^v		Na9	3.513(6) ^{xii}
	Na12	3.694(7)		Na1	3.559(5) ^x
S8	Si3	2.155(3)		Na12	3.712(7) ^{ix}

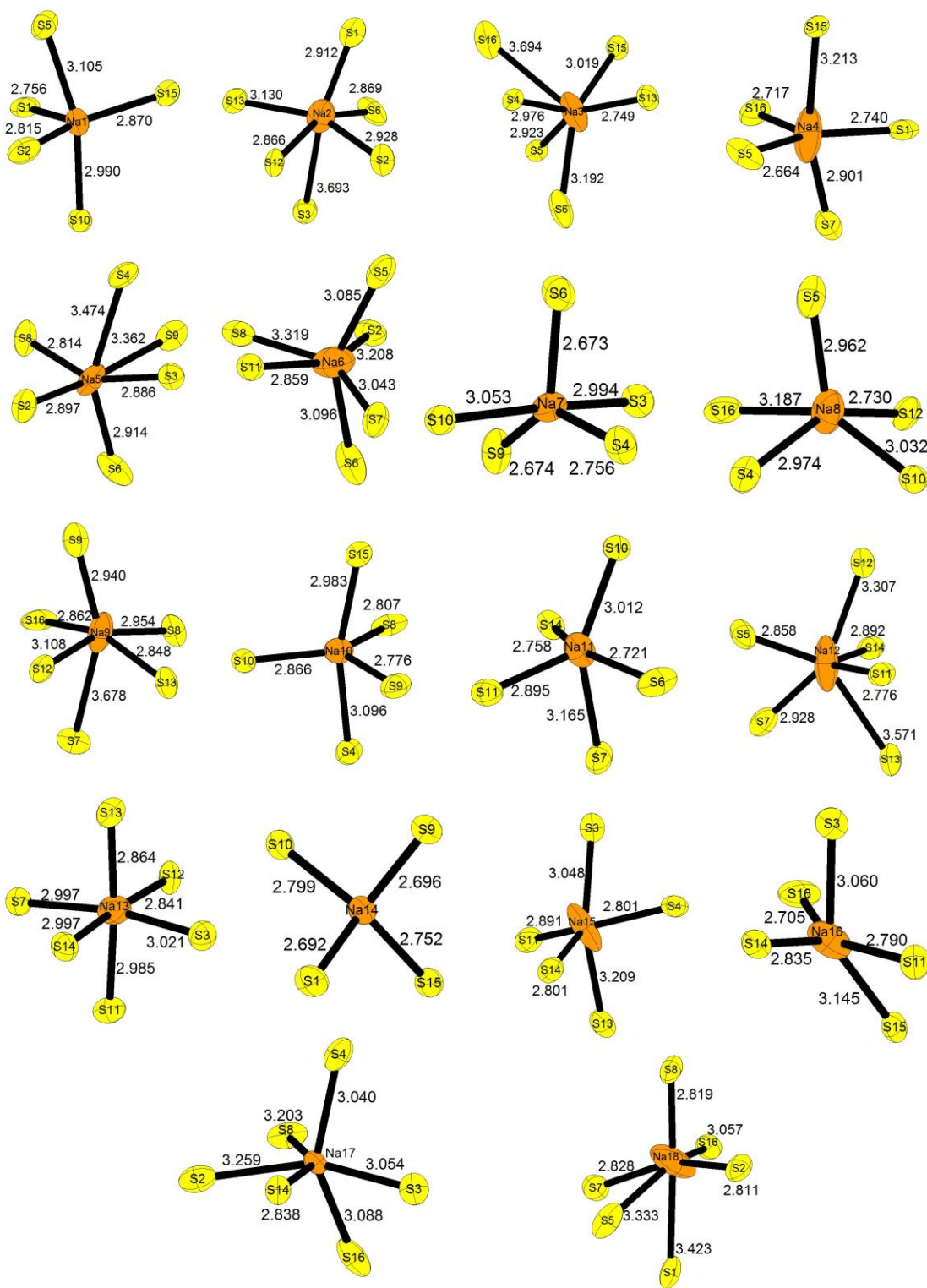


Figure S1: Sodium ion coordination in $\text{Na}_{8.5}(\text{AlSi}_4)_{0.5}(\text{SiSi}_4)_{1.5}$. Na–S distances are given in Å. Sodium atoms are depicted in orange, sulfur atoms in yellow. Ellipsoids are drawn at 80% probability.

Thermal analysis

Due to the occurrence of crystalline side phases in Na_5AlS_4 samples, the synthesis conditions had to be optimized. Therefore, DSC measurements were done for the pseudo-binary border phases Na_4SiS_4 and Na_5AlS_4 . Both compounds were synthesized in small (6 mm diameter) sealed carbon coated quartz ampoules at 600 °C suited for DSC measurements and annealed for 3 h. The subsequent DSC measurements are depicted in figure S2. Both compounds show broad endothermic signals during heating at 608 °C (Na_4SiS_4) and 722 °C (Na_5AlS_4), respectively, which are attributed to a complicated multi-step melting process of the materials. In the case of Na_5AlS_4 , this is presumed to be a decomposition reaction which also takes place at lower temperatures, albeit at a slower rate, since samples synthesized at 650 °C and above showing increasing amounts of an unknown crystalline side phase. This decomposition behaviour, at least to crystalline side phases, was not observed for Na_4SiS_4 . However, the maximum synthesis temperatures were chosen to be below the onset of melting of Na_4SiS_4 at 600 C, which was suitable for all products.

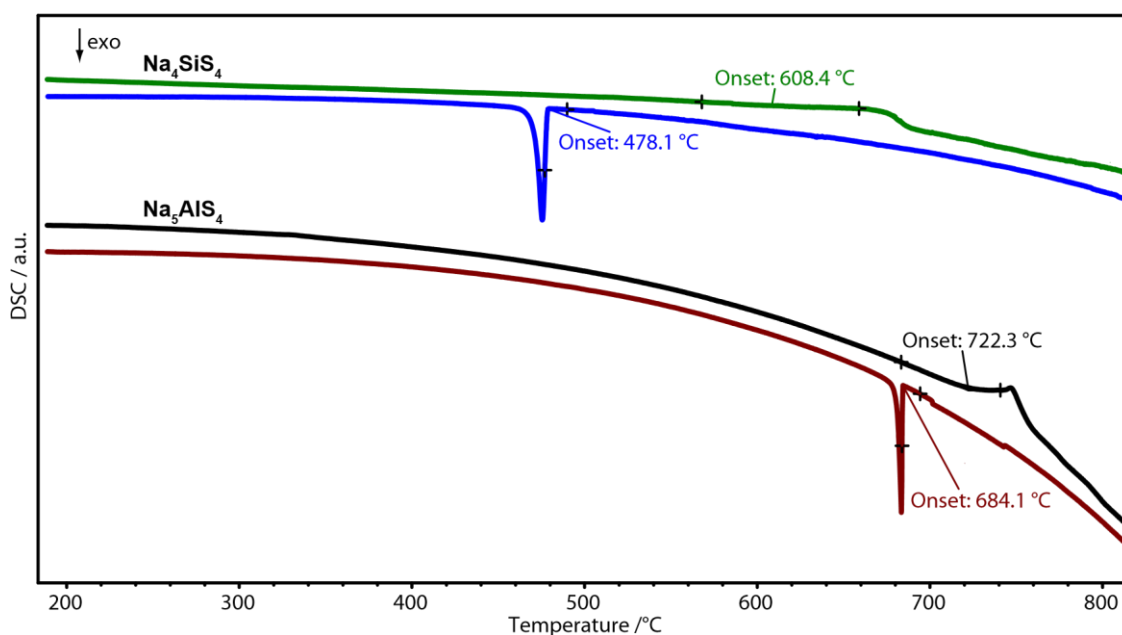


Figure S2: DSC measurement of Na_4SiS_4 and Na_5AlS_4 ; green and blue lines represent the heating and cooling ramps of Na_4SiS_4 , respectively, measured at 5 Kmin^{-1} , black and red lines represent the heating and cooling ramps of Na_5AlS_4 , respectively, measured at 2 Kmin^{-1} .

In addition, we were interested why the only sample showing big single crystals ($d \approx 200 \mu\text{m}$) was with $x = 75\%$ for $\text{Na}_{5-x}\text{Al}_{1-x}\text{Si}_x\text{S}_4$. Therefore, the synthesis conditions were mimicked by heating the precursors to 600 °C for 3 h directly in the DSC machine and measuring the thermal signals during subsequent cooling. The DSC curve (cf. Fig. S3) shows two distinct exothermic signals at 542 °C and 299 C. The first signal probably corresponds to the crystallization of $\text{Na}_{8.5}(\text{AlS}_4)_{0.5}(\text{SiS}_4)_{1.5}$ from the melt and the latter is in good accordance with the melting point of sodium tetrasulfide (Na_2S_4 , m.p.=300

C).⁴ The signal's broad nature also suggests the presence of sodium polysulfides with higher chain lengths. This polysulfide melt could be beneficial for crystal growth by acting as a solvent for the targeted phase $\text{Na}_{8.5}(\text{AlS}_4)_{0.5}(\text{SiS}_4)_{1.5}$. Since there are no indications of crystalline polysulfides in the PXRD or isolated sodium and sulfur rich areas in SEM/EDX measurements, we suppose that the polysulfide melt forms from unreacted Na_2S and excess S during the reaction and gets gradually consumed with progressing reaction time.

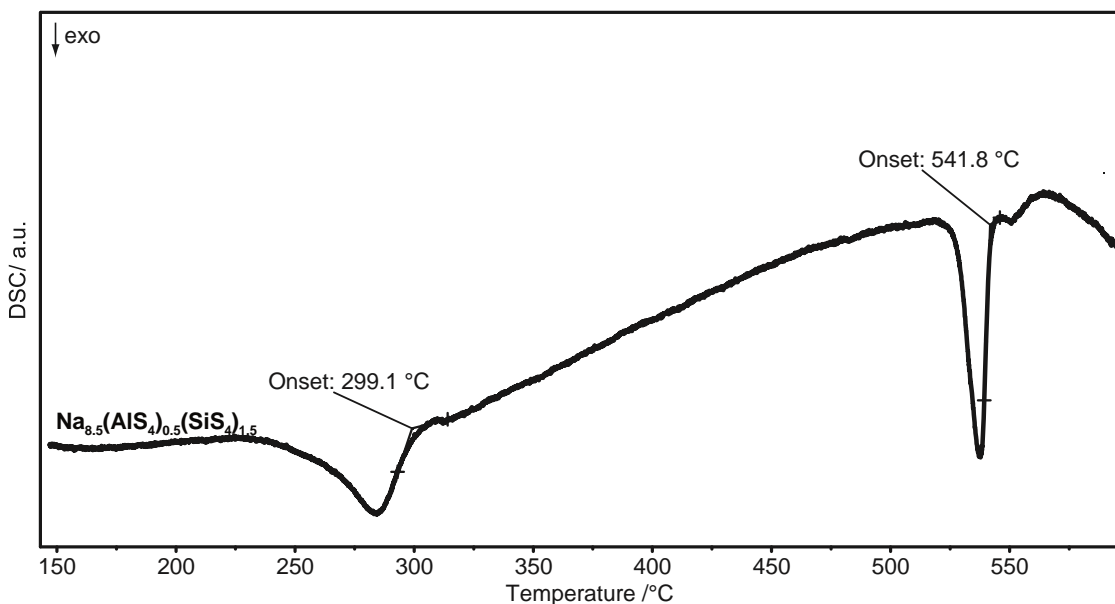


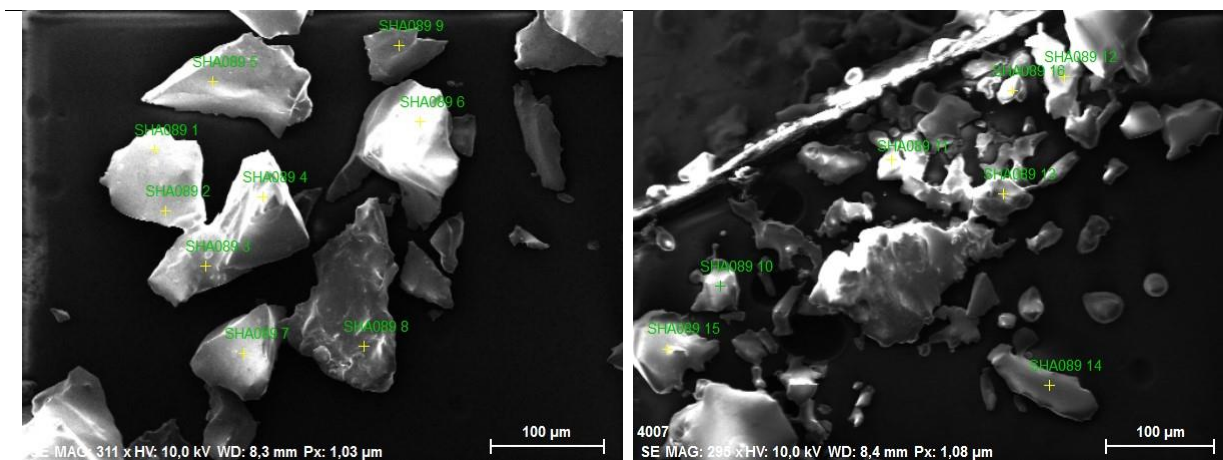
Figure S3: DSC measurement of $\text{Na}_{5-x}\text{Al}_{1-x}\text{Si}_x\text{S}_4$, $x = 75\%$; the measurement corresponds to the cooling of the sample at a rate of 5 Kmin^{-1} after annealing it at 600 °C for 3 h.

Electron microscopy

Since the Al/Si occupancy for the single crystal data of $\text{Na}_{8.5}\text{Al}_{0.5}\text{Si}_{1.5}\text{S}_8$ ($x = 0.75$) could not be refined because of the similar atomic form factors of the two elements, EDX spectroscopy was used to determine the composition. Table S11 shows the normalized results, averages, the respective standard deviations for O, Na, Al, Si and S, as well as SEM micrographs depicting the positions on the sample. From the SEM micrographs and the values for oxygen it is evident that the sample was partially hydrolyzed on the surface by being in contact with air although exposure time was less than 30 s. While the values for Na and S are systematically too low and show a large spread supposedly due to hydrolysis and the strongly hygroscopic behavior of the sample, Al/Si ratios are within a small error margin and show a slightly lower Al/Si ratio as expected from the weighted precursors, which is in good accordance with the data obtained from SCXRD.

Table S11: Results of EDX measurements for $\text{Na}_{8.5}\text{Al}_{0.5}\text{Si}_{1.5}\text{S}_8$ ($x = 0.75$) in atom% normalized to the sum of Al and Si being 4. SEM micrographs depict the positions on the sample.

Position	O	Na	Al	Si	S
SHA089 1	4.693	15.884	0.998	3.002	11.717
SHA089 2	8.492	12.860	1.076	2.924	11.379
SHA089 3	10.782	12.075	0.722	3.278	17.440
SHA089 4	8.844	15.756	0.928	3.072	15.796
SHA089 5	7.596	13.464	1.022	2.978	12.397
SHA089 6	12.085	14.975	0.730	3.270	18.945
SHA089 7	7.760	12.525	1.070	2.930	10.467
SHA089 8	6.326	14.372	0.915	3.085	10.921
SHA089 9	18.805	14.123	0.832	3.168	11.439
SHA089 10	8.225	13.775	0.857	3.143	12.760
SHA089 11	5.089	14.522	0.881	3.119	11.512
SHA089 12	7.019	13.404	0.985	3.015	11.388
SHA089 13	6.663	10.975	1.025	2.975	10.186
SHA089 14	6.982	11.258	0.974	3.026	9.481
SHA089 15	8.892	12.715	1.012	2.988	12.023
SHA089 16	2.589	15.593	0.902	3.098	11.485
average	8	14	0.9	3.1	12
std. deviation	4	2	0.1	0.1	3



BVEL calculations

Description of BVEL calculations

In this section, we describe the general procedure of calculating bond valence sums and bond valence energy landscapes using the program 3Dbvsmapper. We also discuss the limitations of this method.

In practice, the program 3DBVSMAPPER executes the following procedure:

- [1] Removal of all atoms of low occupancy ($\text{SOF} < 0.05$).
- [2] Removal of the tested ion (here Na^+).
- [3] Creation of equal size voxel points across the unit cell (here: 0.2 \AA).
- [4] Calculation of the BVEL at each point in real space.
- [5] Analysis of the volumetric data: calculation of the global minimum energy $E_{\text{min}}^{\text{global}}$, the minimum energy within the infinitely connected pathway $E_{\text{min}}^{\text{path}}$ and the energy $E_{\text{mig}}^{\text{path}}$, at which an infinitely connected pathway is formed. (vi) Generation of a periodic grid file (*.grd).

The output file of *.grd extension can be used as a volumetric data input for VESTA.⁵ Although the BV approach used in this work provides quite accurate insights into ion migration pathways in possible crystalline solid ion conductors, some factors are not considered in this method. In DFT and molecular dynamics calculations the relaxation of the anionic lattice during ion migration through a bottleneck is usually considered. This relaxation, however, is lowering the potential energy of the transition state and therefore lowering E_{mig} , compared to the energy of the transition state calculated by the BV approach. Additionally, coulombic repulsion of $\text{Na}^+\text{--Na}^+$ is not included in this model, since all tested ions are removed from the structure before calculation. This can lead to underestimating the energy at real space points of higher test ion probability (e.g. along the conduction pathway), since the BV calculated energy landscape mimics a migration network for one test ion per unit cell. This is less important for materials with low concentrations of the migrating ion but plays a more crucial role in materials with high mobile ion concentrations. Pathways might be clogged by repulsion of ions with the same charge, may they be of the same or different kind, thus increasing E_{mig} . Additionally, the BV method is restricted to mostly ionic compounds, excluding compounds with a more covalent bonding character and metals. Despite these methodological drawbacks, calculated bond valence energy landscapes provide fast and computationally cheap access for investigating ion migration pathways in crystalline (ionic) solids.

BVEL calculations of Na_5AlSi_4

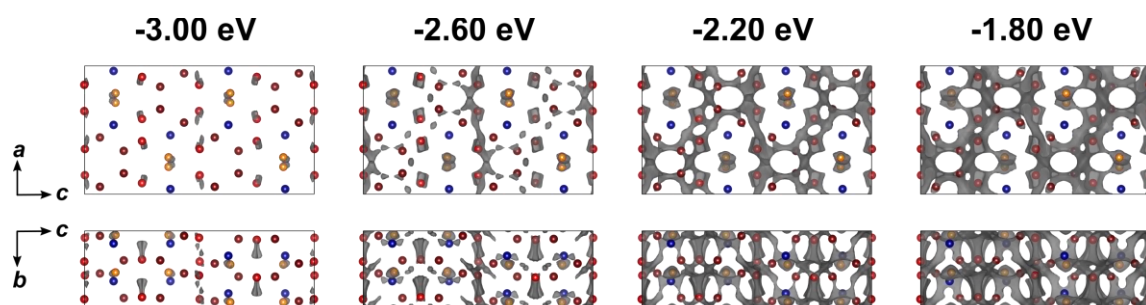


Figure S4: Crystal structure of Na_5AlS_4 with Na atoms drawn in red (migrating ions) and orange (isolated ions), Al atoms drawn in blue and sulfur atoms depicted in yellow. Bond valence energy landscape at different isoenergy values are drawn in grey.

BVEL calculations of Na_4SiS_4

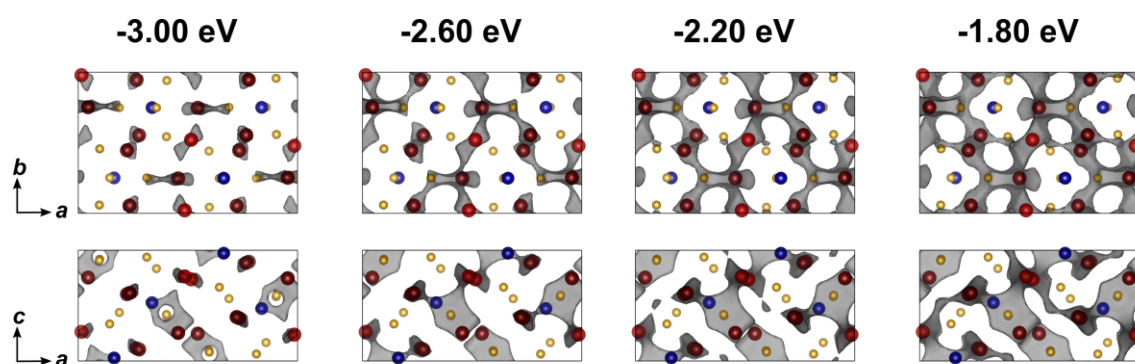


Figure S5: Crystal structure of Na_4SiS_4 with Na atoms drawn in red, Si atoms drawn in blue and sulfur depicted in yellow. Bond valence energy landscape at different isoenergy values are drawn in grey.

BVEL calculations of $\text{Na}_9(\text{AlS}_4)(\text{SiS}_4)$

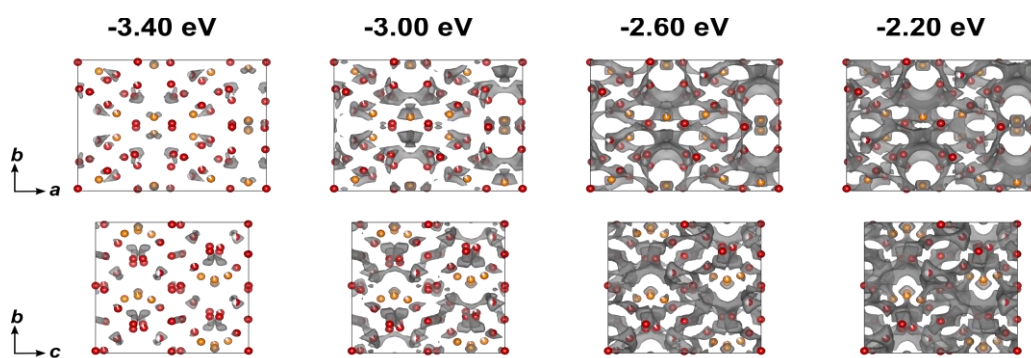


Figure S6: Crystal structure of $\text{Na}_9(\text{AlS}_4)(\text{SiS}_4)$ with Na atoms drawn in red (migrating ions) and orange (isolated ions). Bond valence energy landscape at different isoenergy values are drawn in grey.

Electrochemical characterization

Galvanostatic polarization measurements

A transference number t_{ion} of 0.9998 of a representative sample ($\text{Na}_{5-x}\text{Al}_{1-x}\text{Si}_x\text{S}_4$ with $x = 0.05$) was determined by direct current galvanostatic polarization measurements using blocking-electrodes (stain less steel). The material is thus a mainly ionic conductor.^{6,7}

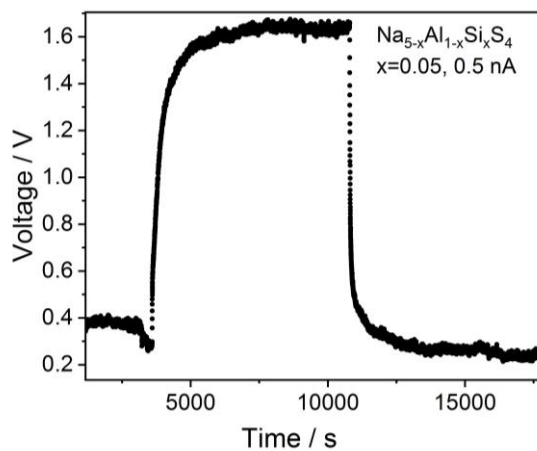


Figure S7: Galvanostatic polarization measurement of $\text{Na}_{5-x}\text{Al}_{1-x}\text{Si}_x\text{S}_4$ with $x = 0.05$ with a current of 0.5 nA shows an electronic conductivity of $6 \times 10^{-11} \text{ S cm}^{-1}$ and a transference number of 0.9998. The material is clearly a mainly ionic conducting material.

Electrochemical impedance spectroscopy

Table S12: Ionic conductivities calculated from R_1 and R_{Tot} ($=R_1+R_2$) and the respective capacitances of representative measurements shown in Figure S8 at 25 °C of $\text{Na}_{5-x}\text{Al}_{1-x}\text{Si}_x\text{S}_4$ with ($0 \leq x \leq 1$). The electrode area was 0.20 cm^2 and the thickness of the pellets in the range of 0.35-0.75 mm.

x	σ_{R1} / Scm^{-1}	σ_{RTot} / Scm^{-1}	C_{eff1} / F	CPE_1	α_1	C_{eff2} / F	CPE_2	α_2
0.00	4.27E-7	1.52E-7	2.26E-10	3.11E-10	0.96	1.75E-8	8.46E-8	0.59
0.025	3.72E-7	2.18E-7	1.86E-10	3.15E-10	0.94	2.35E-8	1.54E-7	0.59
0.05	6.41E-7	2.86E-7	1.96E-10	2.77E-10	0.96	2.02E-8	1.63E-7	0.50
0.10	4.81E-7	1.27E-7	2.19E-10	5.55E-10	0.90	3.44E-7	6.29E-7	0.42
0.25	1.82E-6	5.47E-7	2.22E-10	-	-	2.48E-8	8.48E-8	0.76
0.50	5.19E-6	2.76E-6	2.06E-10	-	-	5.11E-8	4.53E-7	0.63
0.625	7.14E-6	-	2.41E-10	3.63E-10	0.97	-	-	-
0.75	2.78E-5	-	1.86E-10	-	-	-	-	-
0.90	2.31E-6	1.46E-6	2.00E-10	-	-	4.56E-8	1.53E-7	0.78
0.95	5.83E-6	7.64E-7	2.75E-10	-	-	2.81E-8	1.59E-7	0.67
1.00	2.85E-7	-	1.58E-10	-	-	-	-	-

Table S13: Pellet density of $\text{Na}_{5-x}\text{Al}_{1-x}\text{Si}_x\text{S}_4$ with ($0 \leq x \leq 1$) samples shown in Figure S8 and their activation energies with prefactor σ_0 averaged over several temperature cycles.

x	pellet density	$E_a(R1)$ / eV	standard deviation (E_a)	σ_0 / KScm^{-1}	standard deviation (σ_0)
0.00	0.87	0.35	0.01	118	39
0.025	0.81	0.36	0.02	154	99
0.05	0.91	0.37	0.01	288	74
0.10	0.86	0.35	0.01	116	26
0.25	0.80	0.37	0.003	1059	154
0.50	0.87	0.35	0.01	1106	278
0.625	0.87	0.36	0.01	2954	681
0.75	0.88	0.31	0.001	1684	59
0.90	0.88	0.34	0.01	394	86
0.95	0.80	0.40	0.01	4389	1603
1.00	0.76	0.36	0.01	78	24

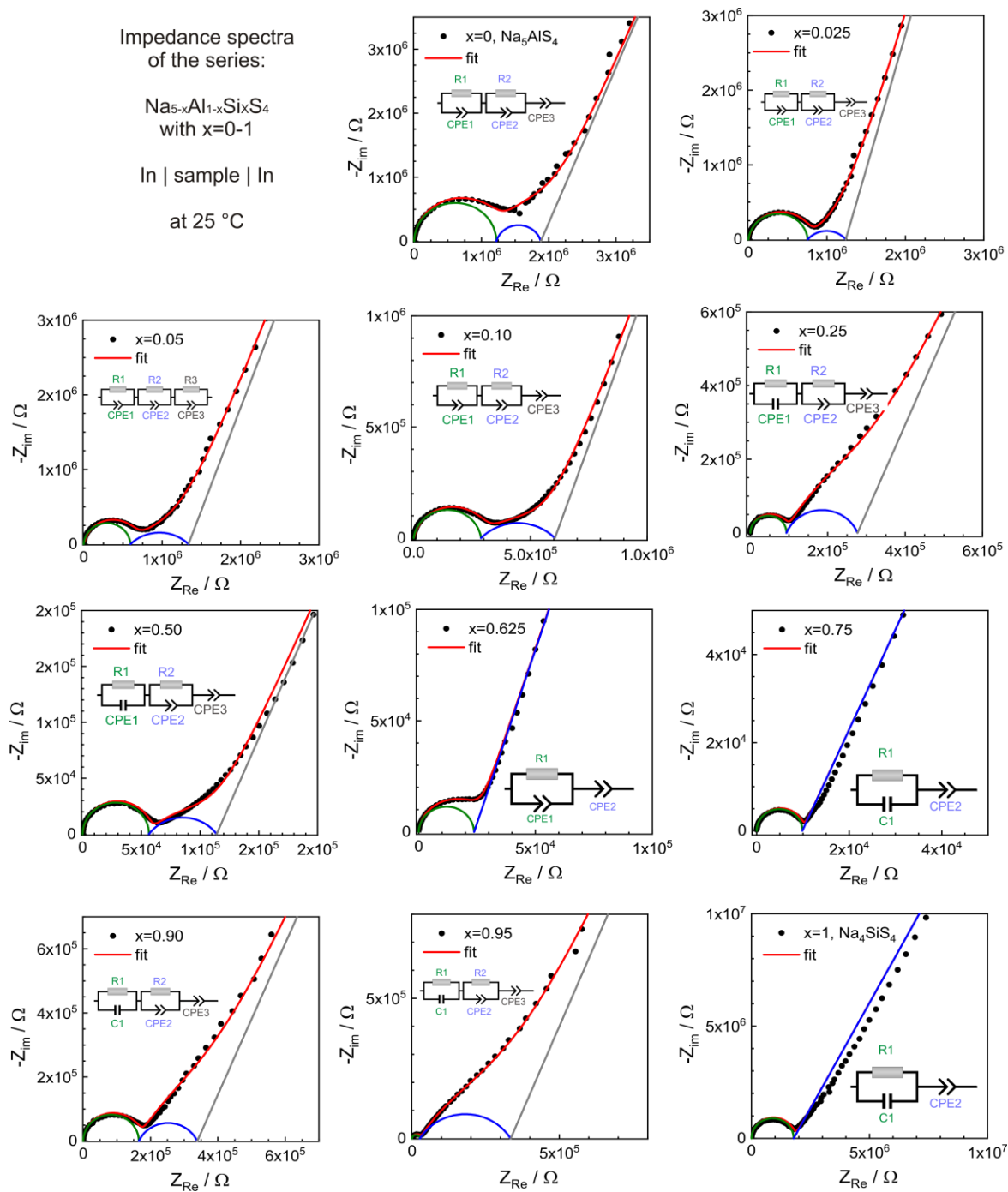


Figure S8: For each member of the series $\text{Na}_{5-x}\text{Al}_{1-x}\text{Si}_x\text{S}_4$ with $(0 \leq x \leq 1)$ a representative impedance spectrum with fit and equivalent circuit model at 25 °C is given. The according values for conductivity, capacitance, activation energy and the prefactor are given in Tables 12 and 13. For $x=0.625, 0.75$ and 1.00 the inclusion of a low frequency semicircle into the model leads to overfitting. Thus, the best fitting model consists only of one RC- or RCPE-element in series to a CPE.

Table S14: Ionic conductivity data calculated from R_{Tot} and averaged over all samples measured for each member of the series $\text{Na}_{5-x}\text{Al}_{1-x}\text{Si}_x\text{S}_4$ with $(0 \leq x \leq 1)$ at 25 °C. The activation energies $\sigma(R_{Tot})$ were averaged over all samples and several temperature cycles for each sample. The electrode area was 0.20 cm² and the thickness of the pellet in the range of 0.35-0.75 mm.

x	$\sigma_{R_{Tot}} / \text{Scm}^{-1}$	Standard deviation and error	$E_a(R_2) / \text{eV}$	Standard deviation
0.00	1.68E-07	1.91E-08	0.38	0.09
0.025	2.01E-07	1.35E-08	0.50	0.04
0.05	2.63E-07	3.35E-08	0.42	0.04
0.10	1.31E-07	3.22E-08	0.46	0.04
0.25	7.49E-07	5.04E-07	0.39	0.04
0.50	1.81E-06	3.63E-07	0.37	0.08
0.625	-	-	-	-
0.75	-	-	-	-
0.90	8.93E-07	3.34E-07	0.36	0.04
0.95	5.46E-07	8.57E-08	0.63	0.03
1.00	-	-	-	-

Table S15: Ionic conductivity data calculated from R_1 and averaged over all samples measured for each member of the series $\text{Na}_{5-x}\text{Al}_{1-x}\text{Si}_x\text{S}_4$ with $(0 \leq x \leq 1)$ at 25 °C. The activation energies $\sigma(R_1)$ were averaged over all samples and several temperature cycles for each sample. The electrode area was 0.20 cm² and the thickness of the pellet in the range of 0.35-0.75 mm.

x	$\sigma_{R_1} / \text{Scm}^{-1}$	Standard deviation and error	E_a / eV	Standard deviation
0.00	3.20E-07	3.12E-08	0.35	0.01
0.025	3.07E-07	3.65E-08	0.39	0.02
0.05	6.42E-07	8.99E-08	0.37	0.02
0.10	1.29E-06	8.20E-08	0.37	0.01
0.25	2.06E-06	1.38E-07	0.38	0.01
0.50	7.04E-06	4.23E-07	0.36	0.01
0.625	6.44E-06	2.69E-07	0.33	0.02
0.75	2.04E-05	1.32E-06	0.31	0.01
0.90	1.89E-06	2.04E-07	0.33	0.01
0.95	4.49E-06	1.16E-06	0.37	0.01
1.00	1.64E-07	4.64E-08	0.38	0.01

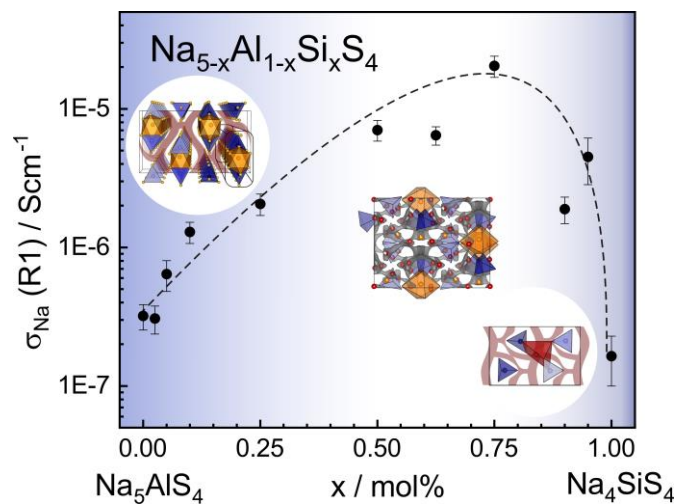


Figure S9: Ionic conductivities calculated exclusively from the resistance of the high frequency semicircle (R1) excluding resistive processes occurring for some member of in $\text{Na}_{5-x}\text{Al}_{1-x}\text{Si}_x\text{S}_4$ with ($0 \leq x \leq 1$). The error bars denote the error and the standard deviation of the values.

Activation Energies

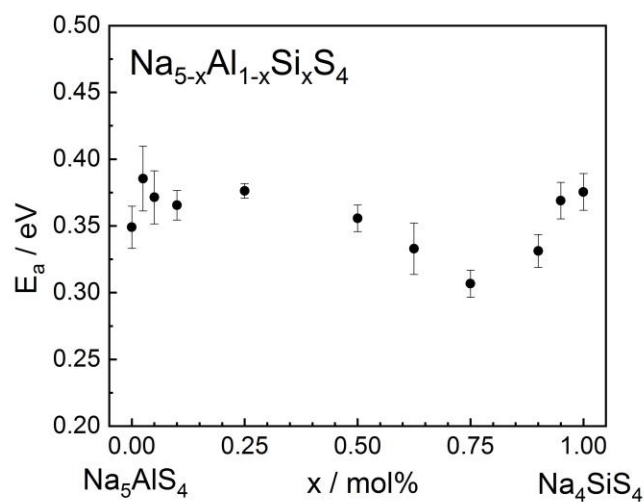


Figure S10: The measured activation energies range from 0.30–0.38 eV for the whole substitution range of $\text{Na}_{5-x}\text{Al}_{1-x}\text{Si}_x\text{S}_4$ with ($0 \leq x \leq 1$). The lowest activation energy can be found in the double salt at $x=0.75$. The error bars denote the error and the standard deviation of the values.

References

- [1] Parthé, E.; Gelato, L. M. The standardization of inorganic crystal-structure data. *Acta Crystallogr. Sect. A Found. Crystallogr.* 1984, *40*, 169–183.
- [2] Krause, L.; Herbst-Irmer, R.; Sheldrick, G. M.; Stalke, D. Comparison of silver and molybdenum microfocus X-ray sources for single-crystal structure determination. *J. Appl. Crystallogr.* 2015, *48*, 3–10.
- [3] Sheldrick, G. M. A short history of SHELX. *Acta Crystallogr. Sect. A Found. Crystallogr.* 2008, *64*, 112–122.

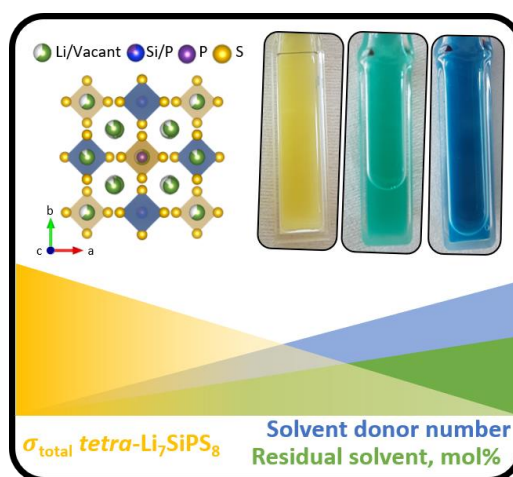
- [4] D'Ans; Lax, *D'Ans-Lax Taschenbuch für Chemiker und Physiker*, 3rd ed.; Blachnik, R., Ed.; Springer: Berlin, Heidelberg, 1998.
- [5] Momma, K.; Izumi, F. VESTA3 for three-dimensional visualization of crystal, volumetric and morphology data. *J. Appl. Cryst.* 2011, *44*, 1272–1276.
- [6] Maier, J., *Physical Chemistry of Ionic Materials: Ions and Electrons in Solids*; John Wiley & Sons, Inc.: Chichester England, 2004, pp 419–462.
- [7] Harm, S.; Hatz, A.-K.; Moudrakovski, I.; Eger, R.; Kuhn, A.; Hoch, C.; Lotsch, B. V. Lesson Learned from NMR: Characterization and Ionic Conductivity of LGPS-like Li_7SiPS_8 . *Chem. Mater.* 2019, *31*, 1280–1288.

4.6 Chemical stability and ionic conductivity of LGPS-type solid electrolyte tetra-Li₇SiPS₈ after solvent treatment

A.-K. Hatz, R. Calaminus, J. Feijoo, F. Treber, J. Blahusch, T. Lenz, M. Reichel, K. Karaghiosoff, N. M. Vargas-Barbosa, B. V. Lotsch

Abstract

To scale up production of solid-state batteries, new routes for processing air sensitive thiophosphate based solid electrolytes need to be developed. To set a basis for this, we investigate the chemical stability and ionic conductivity of the LGPS-type lithium-ion conductor tetra-Li₇SiPS₈ (LiSiPS) processed with various organic solvents. We elucidate the nature of colorful polysulfides that arise during solvent treatment and trace back their origin to the dissolution of the Li₃PS₄-type amorphous side phase typically present in LiSiPS. We find that water and alcohols decompose LiSiPS by nucleophilic attack into oxygen-substituted thiophosphates and thioethers and propose a reaction mechanism for the latter. Moreover, we confirm that quaternary thiophosphates can be recrystallized from MeOH solutions upon subsequent high temperature treatment. Aprotic solvents with donor numbers smaller than 15 kcalmol⁻¹ are suitable for wet processing quaternary thiophosphates because both the crystal structure of the electrolyte and a high ionic conductivity > 1 mScm⁻¹ are retained. Using anisole as a case study, we clarify that residual water content up to 800 ppm does not lead to a significant deterioration in the ionic conductivity when compared to dry solvents (≤ 5 ppm). Additionally, we observe a decrease in ionic conductivity with increasing amount of solvent residue, which depends not only on the donor number of the solvent, but also on the vapor pressure and interactions between the solvent molecules and thiophosphate groups in the solid electrolyte. Thus, optimization of solvent processing methods of thiophosphate electrolytes is a multifaceted challenge. This work provides transferable insights regarding the stability of LiSiPS against organic solvents that may enable competitive and large-scale thiophosphate-based solid electrolyte processing.



Introduction

Over the last decade, thiophosphate-based lithium solid electrolytes have garnered significant attention due to their high room temperature ionic conductivities (>1 mScm⁻¹), which often surpass those of commercial liquid, polymer and oxide-based solid electrolytes.¹⁻⁵ For the large-scale preparation of solid-state batteries (SSBs) using thiophosphate-based solid electrolytes (SEs), wet chemical processes like tape casting (slurry coating) and electrode infiltration are very promising as they could enable cheap and effective roll-to-roll production of SSBs.⁶⁻⁸ Thus, easy processability of the SEs, as well as scalability of each production step are necessary prerequisites for commercial applications.⁹ Since thiophosphate SEs are often unstable against polar solvents,^{10, 11} it is necessary to study the behavior of a specific SE in a variety of solvents to find the most

suitable processing solvent. Such systematic studies help us better understand SE-solvent interactions as well as identify compatible polymer binders. With regards to binder selection, it is also important to determine the range of applicable solvents.¹⁰

Only a handful of reports on the compatibility of thiophosphate-based SEs with organic solvents are available: mainly amorphous $x\text{Li}_2\text{S}-(100-x)\text{P}_2\text{S}_5$, Li_3PS_4 , $\text{Li}_7\text{P}_3\text{S}_{11}$ and $\text{Li}_6\text{PS}_5\text{Cl}$ have been studied. Lee *et al.* proposed that the polarity of the solvent is the most critical parameter.¹⁰ They found that *N*-methyl-2-pyrrolidone (NMP), the most polar solvent studied in that report, turned blue upon contact with the $75\text{Li}_2\text{S}-25\text{P}_2\text{S}_5$ glassy ceramic, concluding that the SE degraded. Conversely, samples treated with the significantly less polar solvents heptane, toluene and *p*-xylene retained their structure as indicated by their unchanged powder X-ray diffraction (PXRD) patterns. Exposure to the slightly polar tetrahydrofuran (THF), however, lead to a yellow coloring of the solution and an altered diffractogram, presumably due to the formation of a THF complex.⁹ Yamamoto *et al.*, on the other hand, ordered the effect of solvents on glassy $75\text{Li}_2\text{S}-25\text{P}_2\text{S}_5$ according to the donor number (DN).¹² The DN reflects the risk of the SE being decomposed by nucleophilic attack from the solvent. In that study, samples exposed to solvents with a DN below 14 kcal mol^{-1} , such as decane, anisole and toluene, maintained roughly the same ionic conductivity compared to the untreated material. Conversely, the conductivity of samples subjected to solvents with higher DNs drastically decreased. In the case of $\text{Li}_7\text{P}_3\text{S}_{11}$, Tan *et al.* identified a qualitative trend between the solvent polarity and even more clearly between the solvent dielectric constant and its degradative effect on $\text{Li}_7\text{P}_3\text{S}_{11}$, which was only stable in toluene and *p*-xylene.¹³ As the polarity or the dielectric constant of the solvent increases, the degradation of the SE increased and the ionic conductivity decreased. Supported by DFT calculations, the authors attribute this behavior to the solvation free energies of $\text{P}_2\text{S}_7^{4-}$ becoming more favorable as the dielectric constant of solvent increases. This means that $\text{P}_2\text{S}_7^{4-}$ more likely dissolves in polar solvents with high dielectric constants. In addition, reaction energies for the formation of $\text{P}_2\text{S}_6^{4-}$ and S^{2-} from $\text{Li}_7\text{P}_3\text{S}_{11}$ become more favorable with increasing dielectric constant of the solvent. For $\text{Li}_6\text{PS}_5\text{Cl}$, Ruhl *et al.* showed a minor influence on the performance of solid-state battery half-cells upon treatment with acetonitrile (ACN), but a large increase in cell resistance after treatment with toluene and THF.¹⁴ Jung *et al.* demonstrated that an oxysulfide coating on SE particles results on an increased stability and retention of high ionic conductivity in SEs processed in solvents such as toluene, acetonitrile, toluene and ethyl acetate.¹⁵

As representative of quaternary thiophosphate-based SEs, the thio-LiSiCON $\text{Li}_{3.25}\text{Ge}_{0.25}\text{P}_{0.75}\text{S}_4$ and the prominent superionic conductor $\text{Li}_{10}\text{GeP}_2\text{S}_{12}$ (LGPS) were subject to treatment with solvents such as hydrazine, heptane, toluene, triglyme, THF, 1,2-dimethoxyethane (DME) and methanol (MeOH).¹⁶⁻²¹ $\text{Li}_{3.25}\text{Ge}_{0.25}\text{P}_{0.75}\text{S}_4$ can be synthesized from hydrazine and is stable in heptane.²¹⁻²³ LGPS turned out to be stable in toluene, THF, and DME with only a small decrease in conductivity. It reacts with triglyme forming a colorful solution, but this can be prevented by adding lithium salts forming a solvate ionic liquid.²⁰ In MeOH, LGPS decomposes and forms an amorphous product. However, after a high temperature heat treatment, LGPS recrystallized with only minor impurities and acceptable ionic conductivity.¹⁹

Understanding the behavior of thiophosphate based SEs in solvents also supports the search for solvent-based synthesis routes.^{9, 24} Several materials such as $50\text{Li}_2\text{S}\cdot 50\text{P}_2\text{S}_5$,²⁵ Li_3PS_4 ,²⁶⁻³² $\text{Li}_7\text{P}_3\text{S}_{11}$,³³⁻³⁵ $\text{Li}_7\text{P}_2\text{S}_8$,³⁶ Li_4PS_4 ³⁷ and argyrodites^{32, 38-40} were synthesized in solvents such as ethanol (EtOH),

THF, DME and ACN, among others. However, suitable solvent-based synthesis routes for quaternary LGPS-type materials have yet to be developed. The above-mentioned hydrazine-based route is not suitable for upscaling due to its high toxicity and being on the candidate list of substances of very high concern for authorization in the European Union.⁴¹ Notably, the dissolution of several thiophosphate species (LGPS, Li₆PS₅Cl) in alcohols was observed and exploited for synthesis, but the underlying mechanism is not understood and the mainly amorphous reaction products have not been characterized so far.^{14, 19, 39, 40}

Here, we report a systematic study regarding the compatibility of tetra-L₇SiPS₈ (LiSiPS) with a broad variety of solvents. LiSiPS is part of the widely known LGPS-type family, more specifically of the silicon-substituted compounds.^{1-3, 42-44} The substitution of Ge with Si significantly reduces the costs, thus silicon-substituted LGPS materials are promising candidates for large-scale production. A prominent member of this class is Li_{9.54}Si_{1.74}P_{1.44}S_{11.7}C_{0.3}, which is one of the fastest LGPS-type ionic conductors known to date with 25 mS cm⁻¹ at room-temperature.³ The room temperature ionic conductivity of LiSiPS is above 2 mS cm⁻¹, thus sufficiently high for applications in a SSB. Moreover, the material is very ductile, facilitating mechanical contact between battery components. LiSiPS crystallizes at 500 °C, but the product usually contains an amorphous side phase with a proposed stoichiometry of “Li_{3.2}Si_{0.2}P_{0.8}S₄” making LiSiPS a glassy ceramic. This amorphous phase limits the overall conductivity of LiSiPS.¹

To test the chemical stability of LGPS-type LiSiPS, we subjected it to 16 solvents with properties ranging from protic polar to aprotic nonpolar. LiSiPS (10 wt%) was dispersed for 48 h in the respective solvent (90 wt%) under Schlenk line conditions. Subsequently, the solvent was evaporated under vacuum (1x10⁻³ mbar). First, we show the decomposition products of LiSiPS in water and propose a decomposition mechanism for LiSiPS in alcohols. Moreover, we confirm that quaternary thiophosphates can be recrystallized from MeOH solutions following heat treatment at temperatures greater than 500 °C. Second, after comparing structural integrity of the products *via* PXRD and solid-state nuclear magnetic resonance spectroscopy (ssNMR) and determining the ionic conductivity *via* electrochemical impedance spectroscopy (EIS), we find that LiSiPS is mostly stable in aprotic solvents. Only the amorphous side phase, rather than LiSiPS, reacts with solvents forming colorful polysulfide species as characterized by UV/Vis-spectroscopy and electron paramagnetic resonance spectroscopy (EPR). Using the example of anisole, we clarify that residual water in the solvents up to 800 ppm does not significantly deteriorate the ionic conductivity and find that the ionic conductivity of the processed SE decreases with increasing donor number of the solvent as well as residual solvent accumulated in the product as validated by thermogravimetric analysis (TGA). Physical properties such as polarity, viscosity and dielectric constant do not seem to play a significant role. Our findings should be transferable to similar SE systems, contributing to the development of large-scale processing methods for solid-state battery components in the future.

Experimental

Synthesis of tetra-Li₇SiPS₈ and solvent treatment

tetra-Li₇SiPS₈ (LiSiPS) was synthesized from stoichiometric amounts of Li₂S (SIGMA ALDRICH, 99.9 %), Si (ALFA AESAR, 99.999 %), red phosphorus (P, MERCK, 99 %) and Sulphur (S, GRÜSSING, 99 %, sublimed in *vacuo*) with an excess of 5 wt% of S to ensure complete oxidation. The starting materials were mixed and heated at 525 °C for 100 h (ramp 50°C/h) in glassy carbon crucibles,

which were sealed in quartz ampoules under vacuum (1×10^{-3} mbar). The as-obtained LiSiPS (PXRD in SI Figure 9, ³¹P MAS NMR in Figure 5b), was treated with organic solvents by mixing 10 wt% of LiSiPS with 90 wt% of the respective solvent under Schlenk conditions. The quality, origin and residual water content (determined by coulometric Karl Fischer titration) of the organic solvents are listed in SI Table 1. Unless otherwise noted, the solvents were used as purchased without drying or further purification to ensure close proximity to industrial applications. The mixture was stirred for 48 h. Subsequently, the solvent was evaporated under vacuum (1×10^{-3} mbar). Samples treated with alcohols, water and NMP were further treated by heating up to 100 °C under vacuum for complete removal of the solvents. Post solvent treatment, dry fine powders were obtained. In the case of cyclohexane, toluene, anisole, ACN, dimethyl carbonate (DMC), THF, and the alcohols the powders were colorless. In the case of propionitrile (PCN), propylene carbonate (PC) and pyridine the powders turned yellow. Finally, upon treatment with trimethylamine (TEA) and NMP the powders turned orange and dark green, respectively.

Electrochemical Impedance Spectroscopy

The ionic conductivity of LiSiPS before and after solvent treatment was determined by EIS. By uniaxial cold pressing (10 kN), the samples were compacted to pellets of about 0.5-1.0 mm thickness with a diameter of 5 mm. The relative densities of the pellets corrected by the weight fraction and density of the respective solvent are given in SI Table 1 and were in the range of 86 ± 5 %. The pellets were sputtered with ruthenium as ion-blocking electrodes on both sides. Impedance spectra (1 MHz–1 Hz, rms AC voltage of 50 mV) of triplicates of every sample were measured during heating and cooling between 25 and -20 °C with 5 °C steps and 1 h of equilibration time inside a glovebox under argon atmosphere. The samples treated with alcohols were measured between 25 and 75 °C. For EIS an IVIUM compactstat.h (24 bit instrument) in a two-electrode setup using a RHD INSTRUMENTS Microcell HC cell stand loaded with RHD INSTRUMENTS TSC Battery cells was used. The analysis of the spectra was carried out with RelaxIS3 from RHD INSTRUMENTS.

UV/Vis Spectroscopy

The absorption properties of suspensions with the same concentration as for the solvent treatment study (10 wt% LiSiPS) with a total amount of solvent of 0.2-0.3 mL were measured in a quartz cell within an integrating sphere with an AGILENT CARY 5000 UV-Vis spectrophotometer. LiSiPS was filled into the sealed quartz cell inside the glovebox and the solvent added under inert gas atmosphere.

Thermogravimetric Analysis

For TGA, the samples were filled into corundum crucibles under argon inside a glovebox. Measurements were carried out using a NETZSCH, STA 449 F5 Jupiter with an Argon flow of 20 mL/min in a temperature range between 20 °C and 200 °C and a heating rate of 10 K/min with a subsequent holding period of 60 min at 200 °C. Data handling was performed with the NETZSCH Proteus software package.

Karl-Fischer-Titration of water in solvent

The amount of water in the solvents was measured by coulometric Karl Fischer titration with a 899 Coulometer from METROHM. Prior to the measurements, a standard with 1000 ppm water was

tested. Prior to titration of triethylamine (TEA) and pyridine, an excess of dry benzoic acid was added to neutralize the bases and keep the pH value in the appropriate range.

MAS Solid State NMR and solution NMR

Solid-state NMR spectra were measured on a BRUKER Avance III 500 instrument at a magnetic field of $B_0 = 11.74$ T. Magic-angle spinning (MAS) experiments were performed in zirconia spinners at a spinning speed of 10 kHz using a BRUKER 4 mm triple-channel probe. The ^1H spectra were referenced directly and the ^{31}P , ^6Li spectra indirectly to ^1H in 0.1% trimethylsilane (TMS) at 0.00 ppm. Solution NMR spectra ($^{31}\text{P}\{^1\text{H}\}$ and ^1H NMR referenced to 85% H_3PO_4 and TMS respectively) were recorded at 298 K in the respective solvent on a JEOL 400 MHz device.

Powder X-ray Diffraction

PXRD measurements were carried out on a STOE Stadi P diffractometer with $\text{Mo-K}_{\alpha 1}$ irradiation, a Ge(111) monochromator in Debye-Scherrer geometry. Samples were mixed with a silicon standard and sealed in glass capillaries with a diameter of 0.5 mm under argon.

Electron Paramagnetic Resonance

The EPR measurement was conducted on a BRUKER EMX Nano. For that, a small amount of the dispersion was sealed in a glass capillary under argon.

Scanning Electron Microscopy

The morphology of the samples was imaged using a JEOL JSM 6500 F scanning electron microscope (SEM; field emission gun, acceleration voltage 2 kV).

Results

Behavior of LiSiPS against protic solvents

The interaction of thiophosphates with protic solvents such as alcohols plays a key role for the synthesis of thiophosphate-based SEs. So far, most reports focus on the lithium argyrodites and only one report discusses the dissolution of LGPS in MeOH and recrystallization by high temperature treatment (550 °C for 8 h).^{8, 9, 19, 38, 39} A thorough understanding of the decomposition and/or dissolution process of thiophosphate SEs is critical to elucidate their solvent stability and help to develop electrode infiltration methods for LGPS-type materials. Here, we report, for the first time, the decomposition mechanism of the ortho-thiophosphate LiSiPS in alcohols as monitored by NMR spectroscopy. LiSiPS readily dissolves in the protic solvents MeOH and EtOH, whereas in *i*PrOH, it rather forms a suspension as visible in Figure 1c. After removal of the alcohols, the PXRDs in SI Figure 1 suggest the decomposition and complete loss of crystallinity for LiSiPS. The product is amorphous and only weak and broad reflections stemming from Li₂S and other unknown phases are present, both of which are not observed in the pristine LiSiPS sample (cf. SI Figure 9). The ionic conductivity of the decomposed LiSiPS products is very low (10⁻¹⁰-10⁻⁶ Scm⁻¹) and the activation energies are high (0.35-0.55 eV) as shown in Figure 1c.

We propose a decomposition/dissolution mechanism that proceeds *via* a nucleophilic attack of methanol on the PS₄³⁻ anion in LiSiPS, as illustrated in Figure 1b. After an initial protonation step, the methoxy group attacks the phosphorus and HS⁻ is released.⁴⁵ Subsequently, it is likely that a thiono-thiolo rearrangement occurs and the methyl group is transferred to a sulfide.^{46, 47} The ³¹P{¹H} liquid NMR spectrum of LiSiPS in MeOH-D₄ in Figure 1a shows the splitting of the phosphorus signal into a septet at *ca.* 129.0 ppm caused by the coupling of phosphorus with three chemically equivalent deuterium nuclei of the methyl group. The small coupling constant of 2.4 Hz indicates a coupling over a bridging sulfur atom.^{48, 49} The reaction proceeds with a second solvent molecule that attacks another P–S bond and leads to further substitution of sulfur with oxygen as is supported by the observed signal at 92 ppm in Figure 1a. The necessary release of a thio-organyl group could explain the strong foul smell of the solutions. A higher degree of substitution of sulfur with oxygen atoms would shift the ³¹P{¹H} signal towards even lower frequencies. After solvent removal, the chemical shift of the signals in the solid-state ³¹P MAS NMR spectrum in SI Figure 2 is very similar to the signals found in the liquid NMR spectrum discussed above, showing that no further reactions take place upon drying. The ¹³C and ¹H MAS NMR in SI Figure 2 confirm the retention of organic components, the chemical shifts of which are very similar to those of the initial alcohols in the sample. The high intensity of the signal at 92 ppm in the ³¹P MAS NMR spectrum of the MeOH treated samples suggests that the di-substituted species is the main product after drying. In the sample treated with *i*PrOH, the weak signal at 92 ppm suggests that only one substitution of sulfur by oxygen takes place, which is reasonable because *i*PrOH is more sterically hindered than the other linear alcohols studied here.

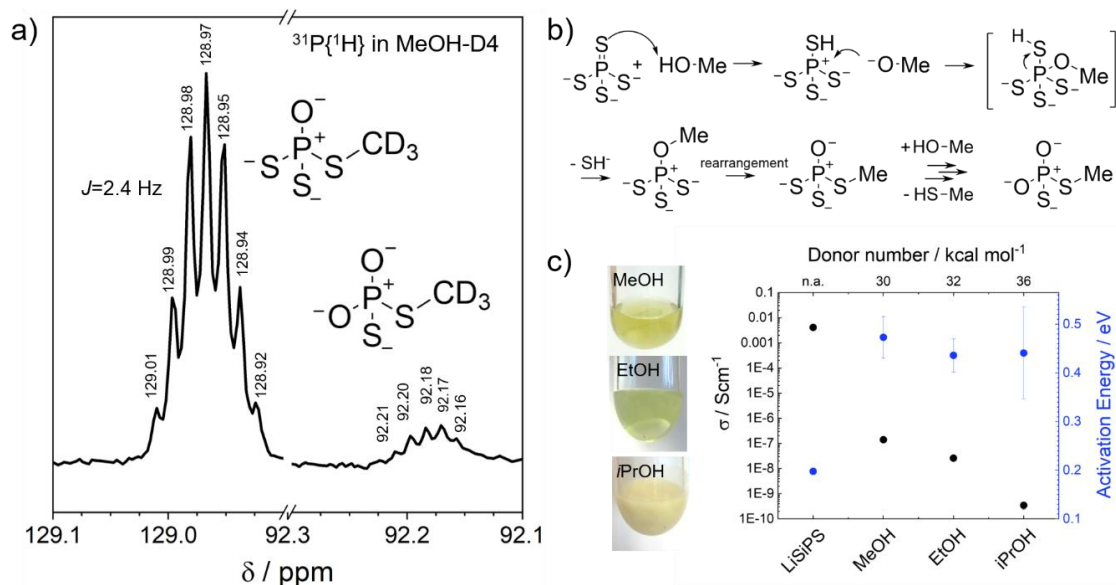


Figure 1 a) $^{31}\text{P}\{^1\text{H}\}$ liquid NMR spectrum of LiSiPS dissolved in MeOH-D₄ showing the coupling of D with P, thus indicating a nucleophilic attack of the solvent on the PS_4^{3-} anion and subsequent rearrangement of the organic moiety. b) Proposed reaction mechanism of decomposition of LiSiPS in MeOH leading to the formation of an oxygen substituted thioether. c) Ionic conductivity and activation energy of LiSiPS treated with alcohols in the order of DN.

We also considered a nucleophilic attack by water molecules, a common contaminant in alcohol solvents. However, substitution of sulfur by oxygen (without methyl-group bonded either to oxygen or sulfur) would neither lead to the observed coupling of deuterium with phosphorus in the liquid NMR nor to the large shift to higher frequencies observed in the MAS NMR. Moreover, the typical decomposition products of LiSiPS after exposure to water (*vide infra*) - PS_3O^{3-} , $\text{PS}_2\text{O}_2^{3-}$, PSO_3^{3-} and PO_4^{3-} species with chemical shifts of 82–87, 68, 37 and 3 ppm in the ^{31}P MAS NMR, respectively - are absent. The substitution of sulfur with oxygen following the proposed mechanism in Figure 1b is consistent with previous reports on the synthesis of thiophosphate argyrodites in EtOH where the presence of anionic PO_xS_y species decrease the ionic conductivity.³⁹

A previous report shows that it is possible to recrystallize LGPS after MeOH treatment (2 wt% of LGPS in MeOH) *via* heat treatment at 550 °C for 8 h under vacuum. The obtained LGPS exhibited only a small amount of impurities ($\gamma\text{-Li}_3\text{PO}_4$ and Li_4GeS_4) and an ionic conductivity above 1 mScm^{-1} .¹⁹ We applied a similar approach to test whether such a recrystallization was possible for the MeOH-treated LiSiPS material. To this end, the MeOH-exposed sample was treated at the original synthesis conditions at 525 °C for 100 h in a quartz ampule *in vacuo*. Under these conditions, only the orthorhombic phase of LiSiPS (*ortho*-LiSiPS, 57 %) was recovered (albeit with a slight enrichment in Si content), with large amounts of $\gamma\text{-Li}_3\text{PO}_4$ (36 %) and Li_2S (7 %) impurities (cf. SI Figure 1b, values obtained by Rietveld refinement).

To better understand the degradation of LiSiPS in protic solvents, we also monitored the degradation products of the title compound upon treatment with degassed deionized water. LiSiPS dissolves in water and the solution shows a weak green color as visible in the inset in Figure 2a. After drying, the white solid product is mostly amorphous, with a small fraction of unknown crystalline phases, some of which can be reasonably matched to LiOH from the PXRD in Figure 2a. The solid state ^{31}P MAS NMR in Figure 2b reveals that the main species of the phosphorus-containing decomposition products are di- and tri-oxo-substituted thiophosphates, i.e. $\text{PO}_2\text{S}_2^{3-}$ and

PO₃S³⁻, at 68 and 37 ppm, respectively. These results agree with previous reports by Hayashi *et al.*⁵⁰ for a series of conductive oxysulfide glasses (Li₂S-SiS₂-Li₃PO₄) and with crystalline Na₃PO₂S₂ ($\delta_{\text{iso}} = 59$ ppm)⁵¹, Na₃PO₃S ($\delta_{\text{iso}} = 33$ ppm)⁵¹ and NaBa(PO₃S)·9H₂O (34 ppm)⁵². The thiophosphate PS₄³⁻ and phosphate PO₄³⁻ anions give signals at around 86 and 9 ppm, respectively.^{53, 54} For the decomposition of a thiophosphate a step-wise mechanism is expected leading initially to POS₃³⁻ (82-87 ppm)⁵⁰, followed by the formation of PO₂S₂³⁻, PO₃S³⁻ and eventually PO₄³⁻.⁵⁵ We partially monitor such a step-wise decomposition mechanism via liquid ³¹P NMR in SI Figure 3, where after 30 min mainly the di- and tri-oxo-substituted thiophosphates are present, which subsequently convert into the tri-oxo-substituted thiophosphate and the phosphate anion (3.46 ppm) after 48 h. The ²⁹Si MAS NMR in SI Figure 4 shows that a SiO₃S⁴⁻ (thio)silicate anion (-68 ppm) is also present after decomposition.^{50, 56} The ¹H and ⁶Li MAS NMR spectra in SI Figure 4 indicate various chemically distinct lithium positions presumably stemming from the various amorphous phases and the presence of Si-OH bonds.⁵⁷ Taken together, these results provide insights into the decomposition processes of LiSiPS in protic solvents including water.

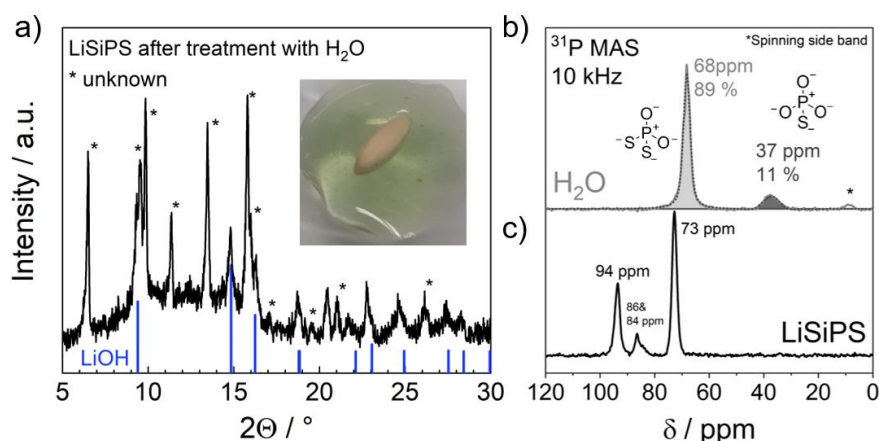


Figure 2 a) PXRD of LiSiPS after treatment with degassed deionized water showing no resemblance with pristine LiSiPS (cf. SI Figure 9). A large background indicates the presence of amorphous species and some reflections from crystalline phases are present that either stem from LiOH or cannot be assigned. The inset shows a photograph of the greenish solution. b) Solid state ³¹P MAS spectra show the signals of the formed oxygen substituted thiophosphates in the dried product and c) of pristine LiSiPS.

Behavior of LiSiPS against aprotic solvents

For processing battery materials on industrial scale, the used solvent should be low-cost, low-toxic and environmentally friendly. However, since the dispersion of thiophosphate-based SEs with water or other protic solvents is not appropriate as shown above, we turned to aprotic solvents. Ideally, after processing, the high ionic conductivity of the thiophosphate-based SE is preserved, but costly procedures such as drying of solvents prior to use can be avoided to minimize the overall cost. Therefore, we set out to determine the influence of residual water in aprotic solvents first using the example of LiSiPS in anisole. Although, at present, anisole is not a common solvent in battery production, recent solvent selection guides^{58, 59} recommend anisole as green solvent due to its low toxicity and other benign properties. It is a solvent with moderate polarity making it moderately miscible with water allowing us to study the impact of trace water quite-well in comparison to solvents with a lower polarity. In comparison to more polar solvents, anisole is not

known to act as a strong nucleophile, despite the presence of an oxygen containing group. Thus, it is an appropriate candidate to test the influence of residual water during solvent treatment.

We prepared a series of anisole/water mixtures and quantified the water content by Karl Fischer titration. The as-purchased anisole contained 203 ppm of water. When dried over molecular sieve for 48 h at room temperature, a low amount of 5 ppm residual water remained. We next prepared anisole/water solutions with 192 ppm and 795 ppm by adding a well-defined amount of water to the dry anisole under Schlenk conditions to mimic the as-purchased anisole and to have a sample with an even higher water content. Subsequently, the solutions were transferred to the glovebox for exposure of LiSiPS to these anisole/water solutions under argon atmosphere. Photographs of the samples in SI Figure 5 show that LiSiPS in anisole-5 ppm and anisole-192 ppm forms a colorless suspension. However, the suspension turns dark green in anisole-795 ppm, similar to that observed with LiSiPS exposed to pure water, becoming lighter over time. Nevertheless, after solvent removal the color disappears. Since the PXRD did not reveal any structural changes for all water contents, we turned to ³¹P solid-state MAS NMR to probe the possible presence of signals pertaining to the amorphous PS_xO_y phases occurring at 82-87, 68, 37 or 3 ppm (see above).

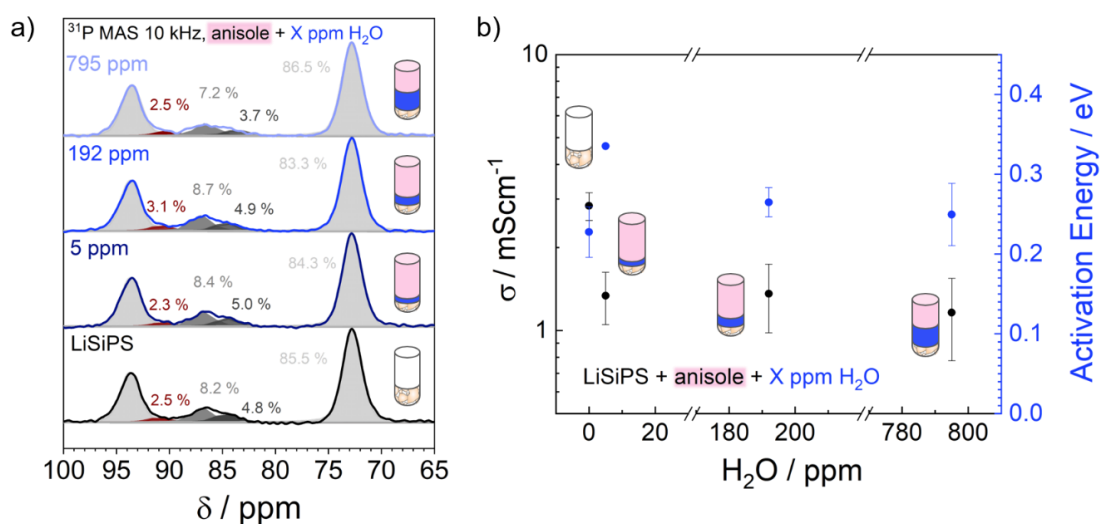


Figure 3 a) ³¹P solid state MAS NMR and b) impedance measurement of the LiSiPS samples treated with anisole containing an increasing amount of water from 5 to 795 ppm. The material composition and ionic conductivity is very similar for all samples regardless of the added amount of water. The conductivity drops in comparison to the initial sample (from 2.8 mScm⁻¹ to approximately 1.3 mScm⁻¹) even for the thoroughly dried anisole.

For the pristine sample, ³¹P solid-state MAS NMR clearly shows the two signals of LiSiPS at 94 and 73 ppm, which correspond to isolated [PS₄]³⁻ units on the 4d site (occupied by Si and P) and 2b (occupied exclusively by P) phosphorus site, respectively (Figure 3a).¹ Based on previous reports,^{1, 25, 54} we assign the additional peak at 90 ppm to *ortho*-LiSiPS and the peaks at 86 and 84 ppm to an amorphous *ortho*-thiophosphate-related “Li₃PS₄”-type side phase, and a polymeric PS₃⁻ species, respectively. The corresponding ⁶Li MAS NMR spectra show one major species at 0.58 ppm and one minor species at 1.05 ppm, which are assigned to LiSiPS and amorphous Li₃PS₄-like phases, respectively (SI Figure 4). On the basis of these assignments, the ³¹P MAS NMR spectra were fitted to obtain the phase fractions of the pristine and solvent-treated LiSiPS samples (Figure 3a). In this context, we emphasize the value of complementing diffraction data with solid-state NMR

methods as a local probe to ascertain and quantify the presence of amorphous side-phases in polycrystalline thiophosphate-based powder samples. Comparing the series of spectra of LiSiPS treated with the anisole-water mixtures in Figure 3a, no significant changes occur (no additional signals, no large change in relative phase fractions in the ³¹P and ⁶Li NMR). Only the ¹H MAS spectra in SI Figure 4 show the presence of silanol groups (two signals around 1 ppm) and a broader background at higher ppm for the anisole-795 ppm treated sample, probably stemming from protonation and adsorbed molecular water, respectively. Additionally, the anisole-5 ppm spectrum contains one sharp signal at ~0 ppm (that was also found for p-xylene and toluene, see SI Figure 10), possibly stemming from a proton in proximity to a silicon atom explaining the high field shift. However, the exact origin of that signal and its absence in anisole-192 ppm are unclear.

Next, the influence of the residual water content on the ionic conductivity of the solid electrolyte, the key performance indicator, was probed. During pellet preparation, the anisole-5ppm treated LiSiPS was very sticky compared to the fine granular powders of the pristine LiSiPS and LiSiPS treated with anisole-192 ppm and anisole-795 ppm, which is reflected by the SEM images in SI Figure 7. On average, the anisole-5 ppm sample contains much larger secondary particles than the other samples. Nevertheless, as presented in Figure 3b, the ionic conductivity of the anisole treated samples drops to about half of the initial conductivity value (from 2.8 mScm⁻¹ to approximately 1.3 mScm⁻¹ of three pellets each), while the shapes of the impedance spectra are very similar (SI Figure 5b). Surprisingly, the activation energy of the sample with the lowest amount of residual water is the highest among all samples. The pellet density, the chosen model for fitting the impedance spectra, effective capacitances at low temperatures and the mass loss corresponding to the amount of residual solvent measured by TGA are listed in SI Table 3, but do not show a specific trend. We conclude from these findings that the residual amount of water in the solvent does not determine the properties of the solvent-treated LiSiPS. The latter is also supported by the fact that we do not observe a clear trend of ionic conductivity with increasing water content in all aprotic solvents tested, as will be discussed in the following (SI Figure 8).

Next, we exposed LiSiPS to common aprotic solvents with varying physical and chemical properties such as polarity, dielectric constant, viscosity, and donor number. LiSiPS forms chemically stable dispersions in all of these aprotic solvents, showing none or only minor signs of deterioration (*vide infra*). The suspensions show a variety of different colors (from colorless, yellow, over green to blue) depending on the solvent as shown in the photographs in Figure 4a, similar to previous observations on thiophosphate suspensions.^{10, 12, 14, 20, 25, 26, 60} UV-Vis measurements suggest the formation of various polysulfide species in the solvent phase of the LiSiPS suspensions. These species are tentatively assigned according to previous literature in Figure 4b.⁶¹⁻⁶³ The deep blue color of the NMP suspension stems from a radical species confirmed *via* EPR spectroscopy (cf. SI Figure 11), which is assigned to the [S₃]⁻ radical anion (617 nm). The yellow color in THF could be due to the presence of [S₂]⁻ and [S₄]²⁻ species (400 nm and 420 nm, respectively). In ACN and PC, the turquoise and dark green colors possibly originate from a mixture of [S₃]⁻ and [S₆]²⁻ anions, the presence of the latter is assigned to the bands at 475 and 350 nm. In the case of the green suspensions treated with PCN and pyridine, they could contain a mixture of [S₃]⁻ and [S₄]²⁻ anions. However, a solvatochromic effect on the polysulfides or the stabilization of more exotic sulfur species cannot be ruled out entirely because the absorbance of the samples is quite broad below 500 nm. Due to the low concentration of the polysulfide species in the suspensions, Raman

spectroscopy measurements did not yield reliable spectra for further analysis. In order to deconvolute all polysulfide species involved, an in-depth study at higher concentrations supported by mass spectrometry measurements would be necessary.

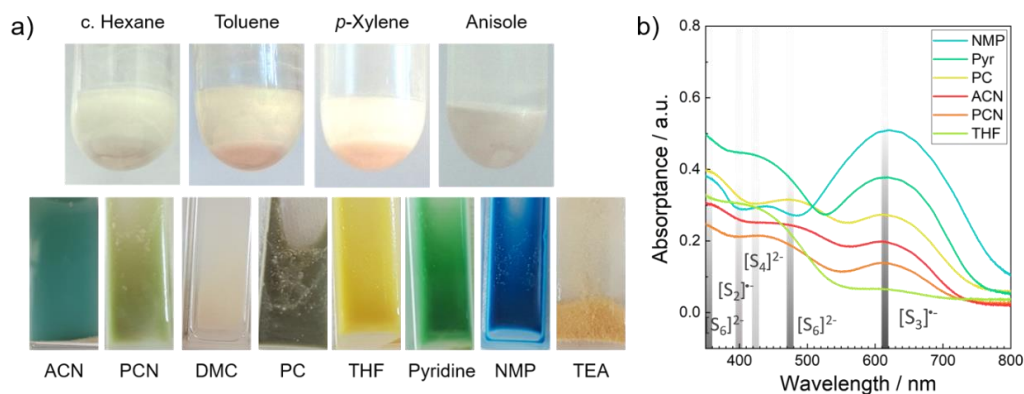


Figure 4: a) Photographs of LiSiPS dispersed in various solvents. b) UV-Vis spectra of colorful suspensions of LiSiPS in various solvents with a tentative assignment to polysulfide species according to [61-63].

Despite the formation of polysulfides, the PXRD pattern of the pristine LiSiPS is largely unchanged for all samples treated with aprotic solvents, suggesting retention of the tetragonal LiSiPS structure (SI Figure 9). Although the latter result suggests that the samples remain intact upon solvent treatment, solid-state ³¹P MAS NMR spectra provide evidence of chemical changes after solvent processing. For the pristine sample, we observe the characteristic signals of LiSiPS at 94 and 73 ppm,¹ and additional signals between 84 – 86 ppm pertaining to an amorphous “Li₃PS₄”-type side phases and polymeric PS₃⁻ species, already present in pristine LiSiPS (Figure 3a). The ³¹P NMR spectra were fitted to obtain the phase fractions of the pristine and solvent-treated LiSiPS samples (Figure 5b). The corresponding ⁶Li MAS NMR spectra are given in SI Figure 10a.

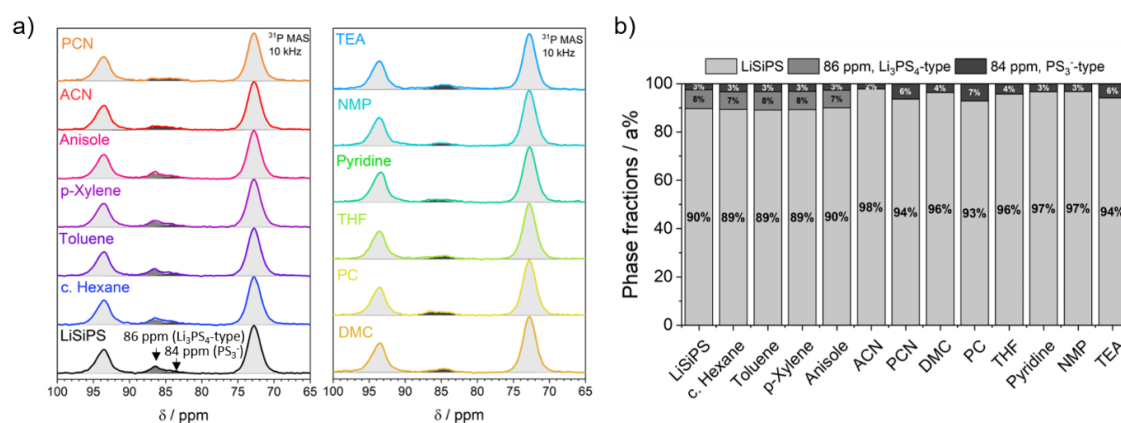


Figure 5: a) Fitted ³¹P solid-state MAS NMR spectra of LiSiPS before and after treatment with aprotic solvents showing a reduction in Li₃PS₄-type amorphous side phase (86 ppm) upon treatment with solvents with high DN numbers (DN > 15). b) Plot of atom percent of fractions from fitted NMR spectra in a).

The ³¹P solid-state MAS-NMR spectra for solvent-treated LiSiPS samples show that the signals for the amorphous and polymeric PS₃⁻ species are the most affected after the treatment. For samples treated with solvents with DN < 15 kcalmol⁻¹ (from cyclohexane up to ACN), the phase fraction distribution remains similar to that of the pristine LiSiPS. However, for solvents with a DN ≥ 15 kcalmol⁻¹, we observe that the amount of “Li₃PS₄”-type side phase with the signal at

86 ppm is reduced. In addition, the corresponding ⁶Li MAS NMR spectra show a reduction of side phase (1.00 ppm) in those solvent-treated samples (SI Figure 10a). Previous studies on LGPS powders treated with THF (DN = 20 kcalmol⁻¹) report on both presence and absence of colorful species in the suspensions.^{18, 19, 21, 64} However, according to Yuan *et al.*²¹ a LGPS/THF suspension only turns yellow upon adding elemental sulfur, indicating the formation of polysulfides. The authors conclude that phase pure LGPS is stable in THF (DN = 20 kcalmol⁻¹). Since the PXRDs and NMRs of solvent-treated LiSiPS suggest no changes in the bulk crystalline structure either, we infer that LiSiPS shows the same solvent stability as LGPS. As the MAS NMR results suggest, we hypothesize that upon solvent treatment, primarily the amorphous side phases of LiSiPS dissolve and produce the various colorful polysulfide species identified *via* UV-Vis.²¹

Moreover, the broadening of the NMR signal at 84 ppm and the disappearance of the NMR signal of the initial side phase after drying hints to a change in the composition of the amorphous side phase. We hypothesize that the polysulfide species in the suspensions incorporate *via* P-S-P bonds upon drying, forming P-[S]_n-P precipitates either on the surface of the SE particles or as segregated particles. The observed formation of S-S bonds is generally undesired, because these species lead to a reduction of conductivity in thiophosphate compounds and an increased cell resistance.^{60, 65}

At room temperature, the pristine LiSiPS sample shows a total ionic conductivity of 4 mScm⁻¹. Upon solvent treatment, the ionic conductivity is reduced for all samples and shows a general decreasing trend that scales with the DN of the solvents (Figure 6a). The corresponding impedance spectra are in SI Figure 13 and SI Table 3. Other physical solvent and sample properties, such as polarity (Et(30)), viscosity, dielectric constant, vapor pressure/boiling point of the solvent, residual amount of water and pellet density do not show a strong correlation with the ionic conductivity (cf. SI Figure 12, SI Figure 8, values in SI Table 2 and SI Table 3). The activation energy of the samples slightly increases with increasing DN with a few exceptions (Figure 6a). The variation is minor, but hints to an altered particle surface that hinders ion transport.

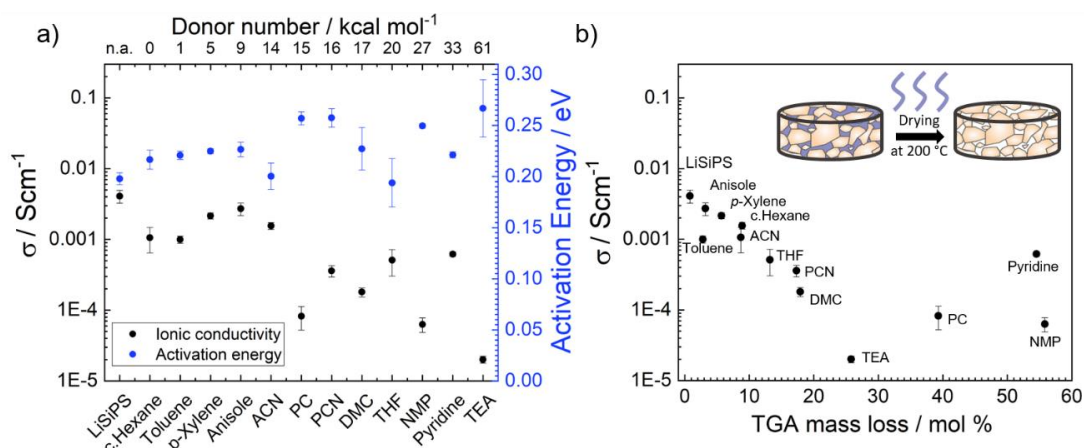


Figure 6. a) Ionic conductivity of LiSiPS after solvent treatment showing a decline after a maximum at 9 kcalmol⁻¹ with increasing donor number (DN). The desired high ionic conductivity above 1 mScm⁻¹ is only persevered after treatment with a solvent with a DN below 15. The activation energy of LiSiPS shows only minor changes after treatment with various solvents. b) The ionic conductivity vs. TGA mass loss in mol % showing a decrease with increasing amount of residual solvent.

In SI Figure 13, the data are grouped according to the properties and functional groups of the solvents: cyclohexane and those with phenyl moieties, those with nitrogen-containing moieties and those with oxygen-containing moieties. Although the DN is not the only parameter that

influences the ionic conductivity, within these classifications, the trend of decreasing ionic conductivity with DN becomes more evident.

Despite the general decrease in conductivity, samples treated with cyclohexane and those with phenyl moieties (toluene, *p*-xylene) retain a high ionic conductivity above 1 mScm⁻¹. The sample treated with *p*-xylene shows the best performance in this group. We observe that the processed SE powder became “sticky” after treatment with cyclohexane and toluene. The SEM images in SI Figure 14 show that after solvent treatment the morphology of the sample is different from that of the pristine LiSiPS. In general, the samples tend to agglomerate and form larger particles. In the cyclohexane-treated sample, new fibre-like structures are present (cf. magnification image). The origin of these fibres remains unclear but seems to be a sticky phase that hinders ion transport (due to the observed increase in activation barrier and reduced ionic conductivity). Our observations are similar to a recent report for solvent-treated Li₆PS₅Cl: when treated with toluene, the particles are reported to be embedded in a sticky matrix. The toluene treated sample shows a reduced ionic conductivity and increased cell resistance when tested in a solid-state battery configuration.¹⁴

Among the samples treated with solvents that have N-containing moieties, only the sample treated with acetonitrile retains a good ionic conductivity (> 1 mScm⁻¹) and lowers the activation energy. The improved conductivity might result from beneficial ion-dipole interaction of the nitrile group as reported before for acrylonitrile butadiene rubber (NBR) with 75Li₂S-25P₂S₅.¹⁰ As the DN of the solvents in this group increases, the ionic conductivity is significantly reduced. The microstructural changes as visible in the SEM images in SI Figure 15 are small. Only the sample treated with TEA shows severe agglomeration, whereas the well performing sample treated with acetonitrile is a finely dispersed powder.

In the group of oxygen containing solvents (O-terminated moieties), the sample treated with anisole shows the highest conductivity among all samples, and a fine powdery microstructure (cf. SEM images in SI Figure 16). The other samples show more agglomeration (in particular NMP-treated LiSiPS) and some such as propylene carbonate and NMP-treated LiSiPS appear puffy. The samples treated with alcohols (MeOH, *i*PrOH and EtOH) decompose, in line with our results described above and included into the comparison for the sake of completeness.

Thermogravimetric analysis (TGA) of all samples shows that evaporation of the solvents at 10⁻³ mbar is not enough to remove the solvent phase of all samples. We observe that substantial amounts of solvent residue of up to 56 mol% (13.2 wt% for NMP) remain in the samples (SI Figure 17). The presence of residual solvent is also evidenced in ¹H solid-state MAS NMR spectra (SI Figure 10). Since the calculated density of the pellets does not decrease significantly despite the residual solvent weight fraction (in comparison to the pristine LiSiPS, cf. SI Table 3), we presume that the solvent wets the surface of the SE particles and infiltrates interparticle voids. As such, we explored the role of residual solvent content on the ionic conductivity. Overall, the ionic conductivity decreases with increasing molar amount of solvent in the sample (cf. Figure 6a and SI Figure 18a). In the case of PC and NMP, with the lowest vapor pressures from all the solvents in this study, we determine solvent fractions greater than 35 mol%. However, the amount of residual solvent does not solely depend on the vapor pressure, but also on solvent-particle interactions. The latter is most evident for the pyridine-treated LiSiPS in which, despite a vapor pressure similar to toluene (20 hPa at 20 °C) a large fraction of it remains in the sample. It was recently reported that strong

interactions of pyridine (py) and thiophosphate groups leads to the breakage of P₄S₁₀ adamantane cages into the stabilized py₂P₂S₅ complex.⁶⁶ Interestingly, the conductivity after treatment with pyridine is still relatively high (6x10⁻⁴ S cm⁻¹) indicating that strong solvent-thiophosphate interactions are not necessarily detrimental for the performance. Taken together, the results indicate that the residual solvent acts as a low conductivity phase that significantly hinders, and possibly dominates, the measured ionic conductivity of the processed samples. To verify the influence of a subsequent drying step on the ionic conductivity, the samples with the highest fractions of residual solvent (NMP and pyridine) were subjected to a heat treatment resembling the TGA measurement (2 h at 200 °C in Ar flow). Quite unexpectedly, the temperature treatment does not affect the samples equally: the total ionic conductivity of the NMP sample increases, whereas for the pyridine-treated sample it decreases (SI Figure 18b,c). These results suggest a complex interplay between the physical properties of a solvent, the solvent-particle interactions and the ensuing (chemical) changes at the interparticle grain boundaries, the latter being difficult to probe directly. In practice, thermal treatment of slurries above 100 °C should be avoided because this exceeds the stability range of common cathode active materials. Therefore, even if we could process the material further to improve its ionic conductivity, this additional thermal treatment would not make it into present battery assembly line methods.

Discussion

Our results show that the influence of solvent processing of LiSiPS samples on the resulting ionic conductivity is multifaceted. The conductivity of all samples is reduced after solvent processing and we identified a $\Delta N = 14$ kcal mol⁻¹ (ACN) as the threshold below which tetra-LiSiPS samples with application-relevant ionic conductivities⁶⁷ of at least 1 mS cm⁻¹ at room temperature are obtained. However, the latter threshold does not apply for pyridine-treated samples nor for solvents with low vapor pressures (PC and NMP). In the case of the latter two solvents, we determined large solvent fractions remaining in the samples. The residual solvent acts as a low conductivity phase that hinders interparticle lithium transport as schematically shown in Figure 5b. In other words, the ionic conductivity of lithium in the solvent phase controls the overall transport properties of the treated sample.

Over the timescale of our experiments, solvent molecules interact primarily with the amorphous side phase of LiSiPS. Such interactions lead to the formation of soluble polysulfides that might precipitate as segregated particles upon drying (cf. Figure 7d), and microstructural changes of the samples. The microstructural changes may also be accompanied by chemical changes at the surface of the solid electrolyte particles (cf. Figure 7c). Such compositional changes at the solid electrolyte-solvent interface have been reported and systematically studied by Busche *et al.* for LAGP-based solid electrolytes exposed to liquid electrolytes.⁶⁸ In the latter, the authors describe the formation of a new resistive “solid-liquid electrolyte interphase” (SLEI) as a result of decomposition products of the solid electrolyte, the solvent and the lithium salt in the solvent. The formation mechanism of such a SLEI on LiPON thin films has also been reported.⁶⁹ Since we observe that the activation energy of all samples increases upon solvent processing, either the formation of such SLEIs or new resistive side-phases may occur (see Figure 7c and d, respectively). The formation of a SLEI is not necessarily detrimental as it might serve the purpose of improving the electrochemical stability of thiophosphates against cathode active materials or even Li metal. Since the *p*-xylene, anisole and ACN treated samples retain reasonable ionic conductivities, they

serve as good candidates to determine their oxidative stability *via* step-wise cyclic voltammetry measurements.⁷⁰ Such experiments are currently underway in our lab.

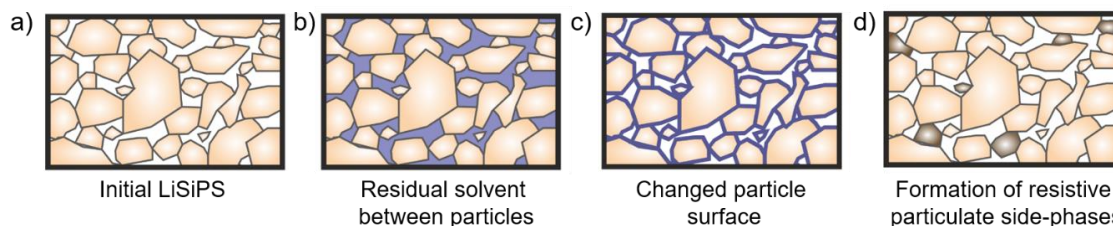


Figure 7 Schematic representation of a) initial LiSiPS microstructure b) LiSiPS with residual solvent inside pores, c) LiSiPS after formation of a solid-electrolyte liquid interface (SLEI) and d) LiSiPS with precipitations of low conducting phases.

Furthermore, the proposed reaction mechanism for the decomposition of thiophosphate electrolytes in alcohols explains why LGPS-type material can be partially recrystallized upon a high temperature heat treatment. The thiophosphate anion is decomposed but only a partial substitution of sulfur with oxygen takes place. Consequently, upon high temperature heat treatment, the alcohols are removed, and *ortho*-LiSiPS can be recovered as SiS₄³⁻ enriched phase, probably containing un- or not fully oxygen-substituted thiophosphates among a γ -Li₃PO₄ side phase.

Finally, we expect our findings to be transferable to other thiophosphates, including thio-LiSiCONs such as Li_{3.25}[Si_{0.25}P_{0.75}]S₄.⁷¹ Their chemical reactivity should be very similar, with some differences as the metal ion changes from Si⁴⁺ to Ge⁴⁺ to Sn⁴⁺. According to the HSAB concept, we predict an increased stability of the softer acid Sn⁴⁺ against hard bases such as water and most solvents, as already described for the Li₄SnS₄ compound.⁷² Moreover, to prevent the nucleophilic attack on the lithium thiophosphates during processing, the approach of adding lithium salt such as LiTFSI to the solvent or applying an oxysulfide-coating prior to solvent processing are complimentary promising approaches.^{15, 20}

Conclusions

In summary, we evaluated the stability of LGPS-type LiSiPS against a large variety of solvents with properties ranging from protic polar to aprotic nonpolar. We find that LiSiPS is structurally stable in aprotic solvents but decomposes into oxygen-substituted thiophosphates in water, and into oxygen-substituted thioethers in alcohols. The latter finding may serve as a blueprint to develop a solvent-based synthesis route or electrode infiltration method. We clarify that the observed colors of several LiSiPS suspensions stem from the formation of polysulfide species upon the dissolution of the Li₃PS₄-type amorphous side phase, rather than the crystalline high-conducting phase.

We further find that the relatively high ionic conductivities are largely preserved in *p*-xylene, anisole and ACN, and demonstrate that LiSiPS can tolerate up to 800 ppm of residual water in solvents using anisole as an example. Overall, the conductivity of the material decreases and the activation energy increases with increasing donor number of the solvent, hinting to a formation of resistive solid electrolyte-liquid interphases. Our findings should be transferable to similar quaternary systems, contributing to the development of large-scale processing methods for solid-state battery components in the future.

Acknowledgments

We would like to thank Christian Minke for his assistance in measuring solid-state NMR spectra, and SEM and Takayoshi Oshima and Alberto Jimenez-Solano for support to measure and interpret UV/Vis-Spectra. Financial support was provided by the German Federal Ministry of Research and Education (BMBF), project 03XP0177B (FestBatt), the Deutsche Forschungsgemeinschaft (DFG) via the Cluster of Excellence “e-conversion” (project number EXC2089/1–390776260), and the Center for NanoScience (CeNS).

References

- [1] S. Harm, A.-K. Hatz, I. Moudrakovski, R. Eger, A. Kuhn, C. Hoch and B. V. Lotsch, *Chem. Mater.*, 2019, **31**, 1280-1288.
- [2] Y. Kato, S. Hori and R. Kanno, *Adv. Energy Mater.*, 2020, **10**, 2002153.
- [3] Y. Kato, S. Hori, T. Saito, K. Suzuki, M. Hirayama, A. Mitsui, M. Yonemura, H. Iba and R. Kanno, *Nat. Energy*, 2016, **1**, 16030.
- [4] M. A. Kraft, S. Ohno, T. Zinkevich, R. Koerver, S. P. Culver, T. Fuchs, A. Senyshyn, S. Indris, B. J. Morgan and W. G. Zeier, *J. Am. Chem. Soc.*, 2018, **140**, 16330-16339.
- [5] X. Bai, Y. Duan, W. Zhuang, R. Yang and J. Wang, *J. Mater. Chem. A*, 2020, **8**, 25663-25686.
- [6] T. Ates, M. Keller, J. Kulisch, T. Adermann and S. Passerini, *Energy Storage Mater.*, 2019, **17**, 204-210.
- [7] Y. J. Nam, D. Y. Oh, S. H. Jung and Y. S. Jung, *J. Power Sources*, 2018, **375**, 93-101.
- [8] D. H. Kim, D. Y. Oh, K. H. Park, Y. E. Choi, Y. J. Nam, H. A. Lee, S.-M. Lee and Y. S. Jung, *Nano Lett.*, 2017, **17**, 3013-3020.
- [9] M. Ghidui, J. Ruhl, S. P. Culver and W. G. Zeier, *J. Mater. Chem. A*, 2019, **7**, 17735-17753.
- [10] K. Lee, S. Kim, J. Park, S. H. Park, A. Coskun, D. S. Jung, W. Cho and J. W. Choi, *J. Electrochem. Soc.*, 2017, **164**, A2075-A2081.
- [11] S. Ito, S. Fujiki, T. Yamada, Y. Aihara, Y. Park, T. Y. Kim, S.-W. Baek, J.-M. Lee, S. Doo and N. Machida, *J. Power Sources*, 2014, **248**, 943-950.
- [12] M. Yamamoto, Y. Terauchi, A. Sakuda and M. Takahashi, *Sci. Rep.*, 2018, **8**, 1212.
- [13] D. H. S. Tan, A. Banerjee, Z. Deng, E. A. Wu, H. Nguyen, J.-M. Doux, X. Wang, J.-h. Cheng, S. P. Ong, Y. S. Meng and Z. Chen, *ACS Appl. Energy Mater.*, 2019, **2**, 6542-6550.
- [14] J. Ruhl, L. M. Riegger, M. Ghidui and W. G. Zeier, *Adv. Energy Sustainability Res.*, 2021, **2**, 2000077.
- [15] W. D. Jung, M. Jeon, S. S. Shin, J.-S. Kim, H.-G. Jung, B.-K. Kim, J.-H. Lee, Y.-C. Chung and H. Kim, *ACS Omega*, 2020, **5**, 26015-26022.
- [16] Y. Wang, Z. Liu, X. Zhu, Y. Tang and F. Huang, *J. Power Sources*, 2013, **224**, 225-229.
- [17] Y. J. Nam, S.-J. Cho, D. Y. Oh, J.-M. Lim, S. Y. Kim, J. H. Song, Y.-G. Lee, S.-Y. Lee and Y. S. Jung, *Nano Lett.*, 2015, **15**, 3317-3323.
- [18] K. Suzuki, N. Mashimo, Y. Ikeda, T. Yokoi, M. Hirayama and R. Kanno, *ACS Appl. Energy Mater.*, 2018, **1**, 2373-2377.
- [19] K. Suzuki, A. Yageta, Y. Ikeda, N. Mashimo, S. Hori, M. Hirayama and R. Kanno, *Chem. Lett.*, 2020, **49**, 1379-1381.
- [20] D. Y. Oh, Y. J. Nam, K. H. Park, S. H. Jung, S.-J. Cho, Y. K. Kim, Y.-G. Lee, S.-Y. Lee and Y. S. Jung, *Adv. Energy Mater.*, 2015, **5**, 1500865.
- [21] H. Yuan, H.-X. Nan, C.-Z. Zhao, G.-L. Zhu, Y. Lu, X.-B. Cheng, Q.-B. Liu, C.-X. He, J.-Q. Huang and Q. Zhang, *Batter. Supercaps*, 2020, **3**, 596-603.
- [22] T. Inada, K. Takada, A. Kajiyama, M. Kouguchi, H. Sasaki, S. Kondo, M. Watanabe, M. Murayama and R. Kanno, *Solid State Ion.*, 2003, **158**, 275-280.
- [23] I. Inada, T. Kobayashi, N. Sonoyama, A. Yamada, S. Kondo, M. Nagao and R. Kanno, *J. Power Sources*, 2009, **194**, 1085-1088.
- [24] A. Miura, N. C. Rosero-Navarro, A. Sakuda, K. Tadanaga, N. H. H. Phuc, A. Matsuda, N. Machida, A. Hayashi and M. Tatsumisago, *Nat. Rev. Chem.*, 2019, **3**, 189-198.
- [25] M. Calpa, N. C. Rosero-Navarro, A. Miura, K. Terai, F. Utsuno and K. Tadanaga, *Chem. Mater.*, 2020, **32**, 9627-9632.
- [26] S. Teragawa, K. Aso, K. Tadanaga, A. Hayashi and M. Tatsumisago, *J. Mater. Chem. A*, 2014, **2**, 5095-5099.
- [27] N. H. H. Phuc, M. Totani, K. Morikawa, H. Muto and A. Matsuda, *Solid State Ion.*, 2016, **288**, 240-243.
- [28] H. Wang, Z. D. Hood, Y. Xia and C. Liang, *J. Mater. Chem. A*, 2016, **4**, 8091-8096.
- [29] Z. Liu, W. Fu, E. A. Payzant, X. Yu, Z. Wu, N. J. Dudney, J. Kiggans, K. Hong, A. J. Rondinone and C. Liang, *J. Am. Chem. Soc.*, 2013, **135**, 975-978.
- [30] N. H. H. Phuc, K. Morikawa, T. Mitsuhiro, H. Muto and A. Matsuda, *Ionics*, 2017, **23**, 2061-2067.
- [31] D. Y. Oh, D. H. Kim, S. H. Jung, J.-G. Han, N.-S. Choi and Y. S. Jung, *J. Mater. Chem. A*, 2017, **5**, 20771-20779.

- [32] M. Duchardt, M. Diels, B. Roling and S. Dehnen, *ACS Appl. Energy Mater.*, 2020, 3, 6937-6945.
- [33] Y. Wang, D. Lu, M. Bowden, P. Z. El Khoury, K. S. Han, Z. D. Deng, J. Xiao, J.-G. Zhang and J. Liu, *Chem. Mater.*, 2018, 30, 990-997.
- [34] S. Ito, M. Nakakita, Y. Aihara, T. Uehara and N. Machida, *J. Power Sources*, 2014, 271, 342-345.
- [35] X. Yao, D. Liu, C. Wang, P. Long, G. Peng, Y.-S. Hu, H. Li, L. Chen and X. Xu, *Nano Lett.*, 2016, 16, 7148-7154.
- [36] E. Rangasamy, Z. Liu, M. Gobet, K. Pilar, G. Sahu, W. Zhou, H. Wu, S. Greenbaum and C. Liang, *J. Am. Chem. Soc.*, 2015, 137, 1384-1387.
- [37] S. J. Sedlmaier, S. Indris, C. Dietrich, M. Yavuz, C. Dräger, F. von Seggern, H. Sommer and J. Janek, *Chem. Mater.*, 2017, 29, 1830-1835.
- [38] Y. B. Song, D. H. Kim, H. Kwak, D. Han, S. Kang, J. H. Lee, S.-M. Bak, K.-W. Nam, H.-W. Lee and Y. S. Jung, *Nano Lett.*, 2020, 20, 4337-4345.
- [39] S. Yubuchi, M. Uematsu, M. Deguchi, A. Hayashi and M. Tatsumisago, *ACS Appl. Energy Mater.*, 2018, 1, 3622-3629.
- [40] L. Zhou, K.-H. Park, X. Sun, F. Lalère, T. Adermann, P. Hartmann and L. F. Nazar, *ACS Energy Lett.*, 2019, 4, 265-270.
- [41] ECHA, Candidate list of Substances of Very High Concern for Authorisation <https://echa.europa.eu/de/candidate-list-table/-/dislist/details/0b0236e1807da31d>, (accessed 15.12.2020, 2020).
- [42] S. Hori, K. Suzuki, M. Hirayama, Y. Kato, T. Saito, M. Yonemura and R. Kanno, *Faraday Discuss.*, 2014, 176, 83-94.
- [43] P. Bron, S. Johansson, K. Zick, J. Schmedt auf der Günne, S. Dehnen and B. Roling, *J. Am. Chem. Soc.*, 2013, 135, 15694-15697.
- [44] A. Kuhn, O. Gerbig, C. Zhu, F. Falkenberg, J. Maier and B. V. Lotsch, *Phys. Chem. Chem. Phys.*, 2014, 16, 14669-14674.
- [45] F. Robertson and J. Wu, *Org. Lett.*, 2010, 12, 2668-2671.
- [46] C. D. Poulter and D. S. Mautz, *J. Am. Chem. Soc.*, 1991, 113, 4895-4903.
- [47] K. Bruzik and W. J. Stec, *J. Org. Chem.*, 1981, 46, 1618-1624.
- [48] G. A. Gray, *J. Am. Chem. Soc.*, 1973, 95, 7736-7742.
- [49] M. M. Basti and L. A. LaPlanche, *Chem. Phys. Lipids*, 1990, 54, 99-113.
- [50] A. Hayashi, K. Tadanaga, M. Tatsumisago, T. Minami and Y. Miura, *J. Ceram. Soc. Japan*, 1999, 107, 510-516.
- [51] M. Pompetzki, L. van Wüllen and M. Jansen, *Z. Anorg. Allg. Chemie*, 2004, 630, 384-388.
- [52] K. Kazmierczak, Joachim G. Heck and Henning A. Höpfe, *Z. Anorg. Allg. Chemie*, 2010, 636, 409-413.
- [53] C. Dietrich, M. Sadowski, S. Siculo, D. A. Weber, S. J. Sedlmaier, K. S. Weldert, S. Indris, K. Albe, J. Janek and W. G. Zeier, *Chem. Mater.*, 2016, 28, 8764-8773.
- [54] H. Eckert, Z. Zhang and J. H. Kennedy, *Chem. Mater.*, 1990, 2, 273-279.
- [55] H. Maki, Y. Ueda and H. Nariai, *J. Phys. Chem. B*, 2011, 115, 3571-3577.
- [56] A. Hayashi, R. Komiya, M. Tatsumisago and T. Minami, in *Solid State Ion.*, WORLD SCIENTIFIC, 2000, pp. 177-186.
- [57] H. N. Kim and S. K. Lee, *Geochim. Cosmochim. Acta*, 2013, 120, 39-64.
- [58] C. M. Alder, J. D. Hayler, R. K. Henderson, A. M. Redman, L. Shukla, L. E. Shuster and H. F. Sneddon, *Green Chem.*, 2016, 18, 3879-3890.
- [59] D. Prat, A. Wells, J. Hayler, H. Sneddon, C. R. McElroy, S. Abou-Shehada and P. J. Dunn, *Green Chem.*, 2016, 18, 288-296.
- [60] N. Riphaut, B. Stiaszny, H. Beyer, S. Indris, H. A. Gasteiger and S. J. Sedlmaier, *J. Electrochem. Soc.*, 2019, 166, A975-A983.
- [61] R. Steudel and T. Chivers, *Chem. Soc. Rev.*, 2019, 48, 3279-3319.
- [62] T. Chivers and I. Drummond, *Inorg. Chem.*, 1972, 11, 2525-2527.
- [63] K. H. Wujcik, D. R. Wang, A. Raghunathan, M. Drake, T. A. Pascal, D. Prendergast and N. P. Balsara, *J. Phys. Chem. C*, 2016, 120, 18403-18410.
- [64] L. Cong, Y. Li, W. Lu, J. Jie, Y. Liu, L. Sun and H. Xie, *J. Power Sources*, 2020, 446, 227365.
- [65] Z. Lin, Z. Liu, W. Fu, N. J. Dudney and C. Liang, *Angew. Chem. Int. Ed.*, 2013, 52, 7460-7463.
- [66] M. Ghidui, R. Schlem and W. Zeier, *Batter. Supercaps*, 2020, DOI: 10.1002/batt.202000317.
- [67] A. Bielefeld, D. A. Weber and J. Janek, *ACS Appl. Mater. Interfaces*, 2020, 12, 12821-12833.
- [68] M. R. Busche, T. Drossel, T. Leichtweiss, D. A. Weber, M. Falk, M. Schneider, M.-L. Reich, H. Sommer, P. Adelhelm and J. Janek, *Nat. Chem.*, 2016, 8, 426-434.
- [69] M. Weiss, B.-K. Seidlhofer, M. Geiß, C. Geis, M. R. Busche, M. Becker, N. M. Vargas-Barbosa, L. Silvi, W. G. Zeier, D. Schröder and J. Janek, *ACS Appl. Mater. Interfaces*, 2019, 11, 9539-9547.
- [70] G. F. Dewald, S. Ohno, M. A. Kraft, R. Koerver, P. Till, N. M. Vargas-Barbosa, J. Janek and W. G. Zeier, *Chem. Mater.*, 2019, 31, 8328-8337.
- [71] L. Zhou, A. Assoud, A. Shyamsunder, A. Huq, Q. Zhang, P. Hartmann, J. Kulisch and L. F. Nazar, *Chem. Mater.*, 2019, 31, 7801-7811.

- [72] K. H. Park, D. Y. Oh, Y. E. Choi, Y. J. Nam, L. Han, J.-Y. Kim, H. Xin, F. Lin, S. M. Oh and Y. S. Jung, *Adv. Mater.*, 2016, 28, 1874-1883.

4.6.1 Supporting Information for “Chemical stability and ionic conductivity of LGPS-type solid electrolyte tetra-Li₇SiPS₈ after solvent treatment”

SI Table 1 List of solvents, their abbreviation used in the text, supplier, purity and water content measured by Karl Fischer titration.

Solvent	Abbreviation	Supplier	purity	Septum seal	H ₂ O / ppm
Cyclohexane	c. Hexane	Brenntag	>99 %	No	18
Toluene		Acros Organics	Anhydrous, 99.85 %	Yes	161
<i>p</i> -Xylene		Acros Organics	99 %	No	176
Anisole		Merck	≥ 99 %	No	203
Acetonitrile	ACN	Merck	Anhydrous, 99.8 %	Yes	70
Propylene carbonate	PC	Sigma Aldrich	Anhydrous, 99.7 %	Yes	118
Propionitrile	PCN	Sigma Aldrich	99 %	No	705
Dimethyl carbonate	DMC	Sigma Aldrich	Anhydrous, 99 %	Yes	118
Tetrahydrofuran	THF	Fischer	99 %	No	65.9
<i>N</i> -methyl-2-pyrrolidone	NMP	Sigma Aldrich	Anhydrous, 99.5 %	Yes	10.7
Methanol	MeOH	VWR	> 99 %	No	503
Ethanol	EtOH	Roth	≥ 99.9 %	No	1134
Pyridine		Sigma Aldrich	> 99 %	No	164
Isopropanol	<i>i</i> PrOH	Fischer	HPLC	No	45
Triethylamine	TEA	Sigma Aldrich	≥ 99 %	No	488
Water	H ₂ O	d.i.	degassed	Yes	-

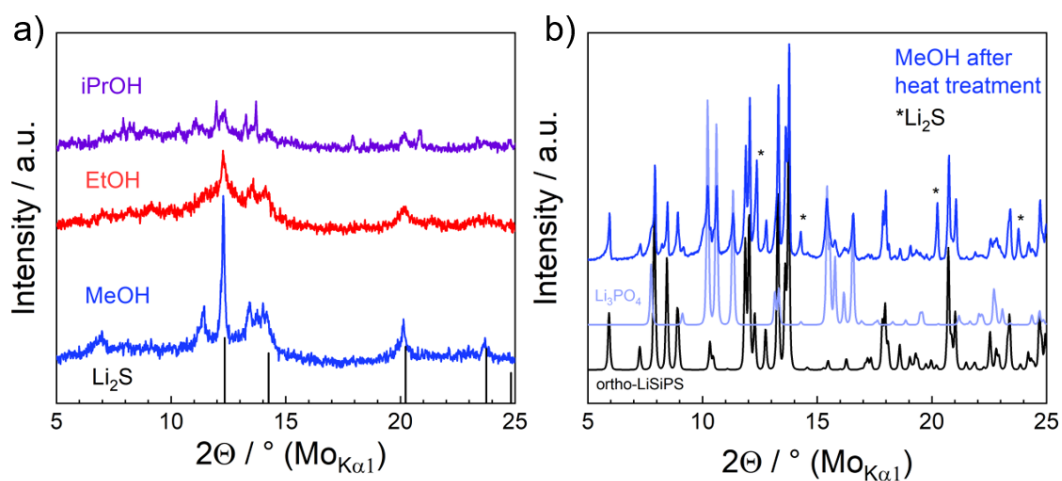
SI Table 2 Table of physical properties of LiSiPS and solvents used in this study. Donor number = DN^[1] empirical polarity parameter = $E_t(30)$ ⁶⁵ Boiling point = BP; Vapor pressure at 20 °C= VP; dielectric constant = ϵ .^[2]

Solvent	classification	DN / kcalmol ⁻¹	$E_t(30)$ / kcalmol ⁻¹	BP / °C	VP / hPa	ϵ	Viscosity / mPa*s	Density / gcm ⁻³
LiSiPS		-	-	-	-	-	-	1.91
c. Hexane	aprotic nonpolar	0	30.9	81	104	2	0.89	0.78
Toluene	aprotic nonpolar	1	33.9	110	29	2.4	0.55	0.87
<i>p</i> -Xylene	aprotic nonpolar	5	33.1	138	8.7	2.3	0.65	0.86
Anisole	aprotic weakly polar	9	37.1	154	3.2	4.3	0.98	0.99
ACN	aprotic polar	14	45.6	82	97	37.5	0.34	0.79
PC	aprotic polar	15	46.0	242	0.04	2.5	2.8	1.21

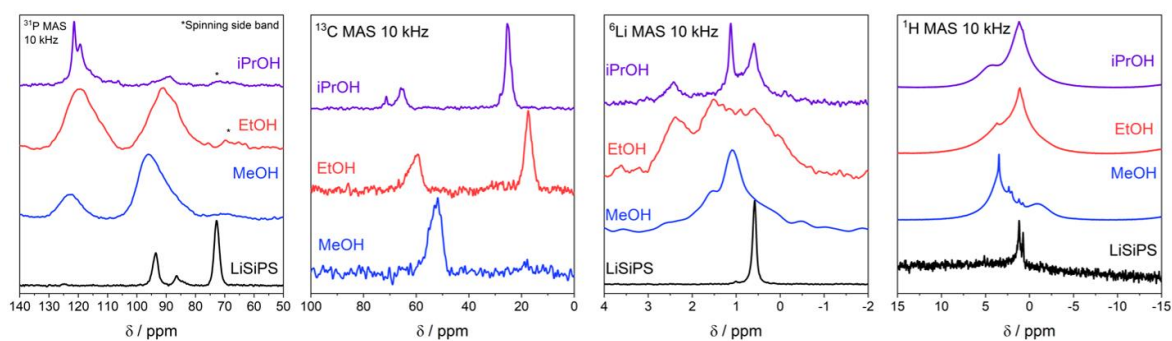
PCN	aprotic polar	16	43.6	97	52	27.7	0.44	0.79
DMC	aprotic polar	17	38.2	90	53	3.1	0.63	1.07
THF	aprotic weakly polar	20	37.4	66	200	7.5	0.46	0.89
NMP	aprotic polar	27	42.2	202	0.32	33	1.66	1.03
MeOH	protic polar	30	55.4	65	128	33	0.54	0.79
EtOH	protic polar	32	51.9	78	59	24	1.08	0.79
Pyridine	aprotic weakly polar	33	40.5	115	20	13	0.88	0.98
<i>i</i> PrOH	protic polar	36	48.4	82	44	19	2.07	0.78
TEA	aprotic weakly polar	61	32.1	89	72	32	0.36	0.73

SI Table 3 List of relative pellet density, TGA mass loss in wt%, fitting model for equivalent circuit analysis of EIS data with R being a resistance, C a capacitor, P a constant phase element (CPE) and effective capacitances calculated by $C_{eff} = Q^{1/\alpha} R^{(1/\alpha)-1}$ with α and Q being defined for a CPE as $Z_{CPE} = 1/(Q(j\omega)^\alpha)$. *spectrum at -20 °C fitted with RP-P

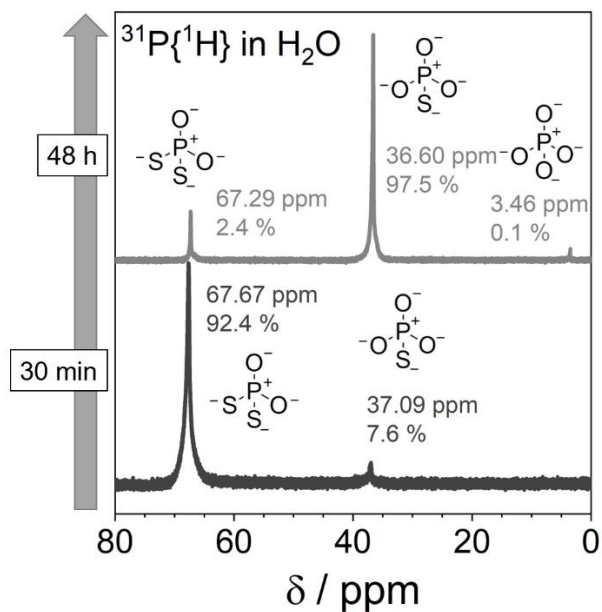
Sample	$\rho_{\text{pellet}} / \rho(\text{m}_{\text{LiSiPS}}^* + \text{m}_{\text{solvent}}^* / \rho_{\text{solvent}}) / \%$	TGA mass loss / wt %	Equivalent circuit model	C or C _{eff} at -20 °C / F
LiSiPS	87	1.3	RP	5E-11*
Anisole-5 ppm	84	1.3	RP-P	2E-10
Anisole-192 ppm	84	1.7	RP	1E-10*
Anisole-795 ppm	84	2.2	RP	1E-10*
LiSiPS	91	0.8	R-P	3E-11*
c. Hexane	88	1.98	RP	1E-10*
Toluene	83	0.7	RP-P	1E-10
<i>p</i> -Xylene	90	1.64	RP	2E-10*
Anisole	84	0.94	RP	1E-10*
ACN	86	1.01	RP-P	2E-10
PC	87	10.01	RP-P	1E-10
PCN	93	2.57	RP-P	2E-10
DMC	88	4.28	RP-P	1E-10
THF	81	2.57	RP-P	8E-11
NMP	92	13.29	RP-P	7E-11
MeOH			RP-P	1E-11
EtOH			RP-P	2E-11
Pyridine	91	10.66	RP-P	7E-11
<i>i</i> PrOH			RP-RP-P	1E-11
TEA	88	6.74	RP-P	1E-10



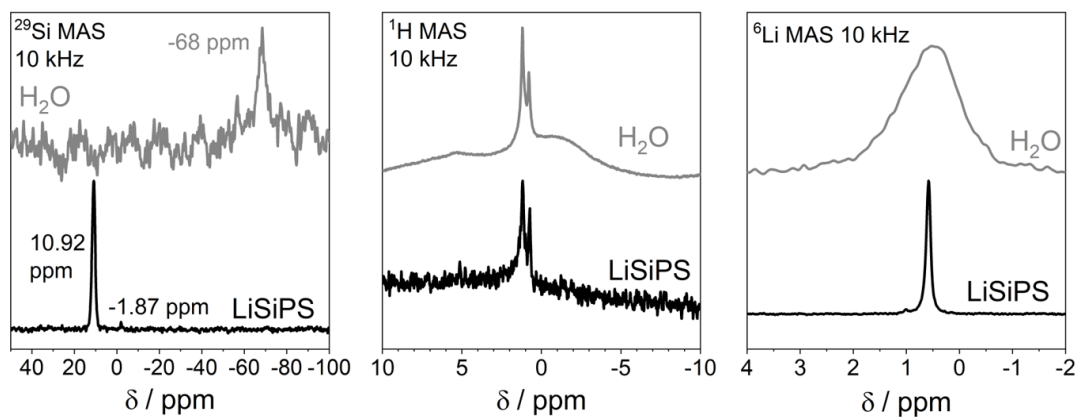
SI Figure 1: a) XRD of decomposition product of LiSiPS after treatment with alcohols. b) Product of LiSiPS decomposed in Methanol after subsequent heat treatment at 525 °C for 100 h in a sealed quartz ampule. A mixture of ortho-LiSiPS (with adjusted lattice parameters), Li₃PO₄ and Li₂S is obtained.



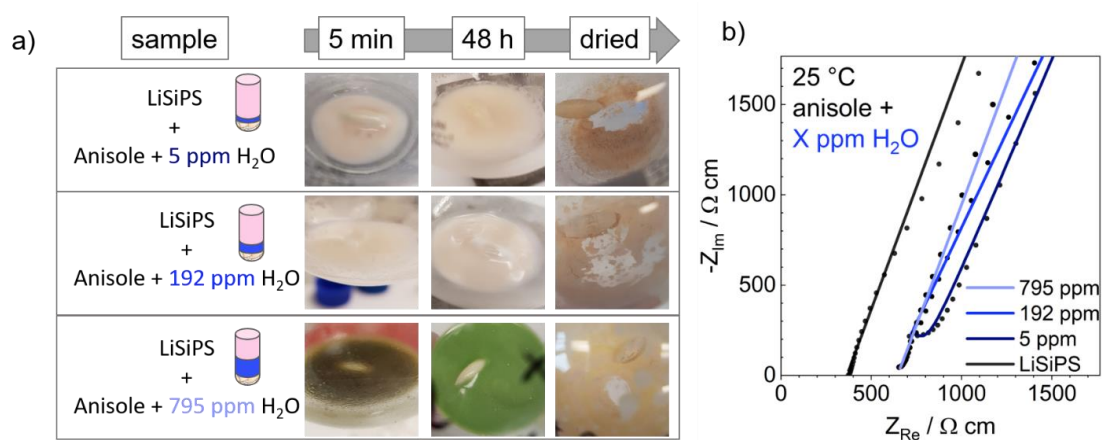
SI Figure 2: Solid state NMR spectra of decomposition product of LiSiPS after treatment with alcohols.



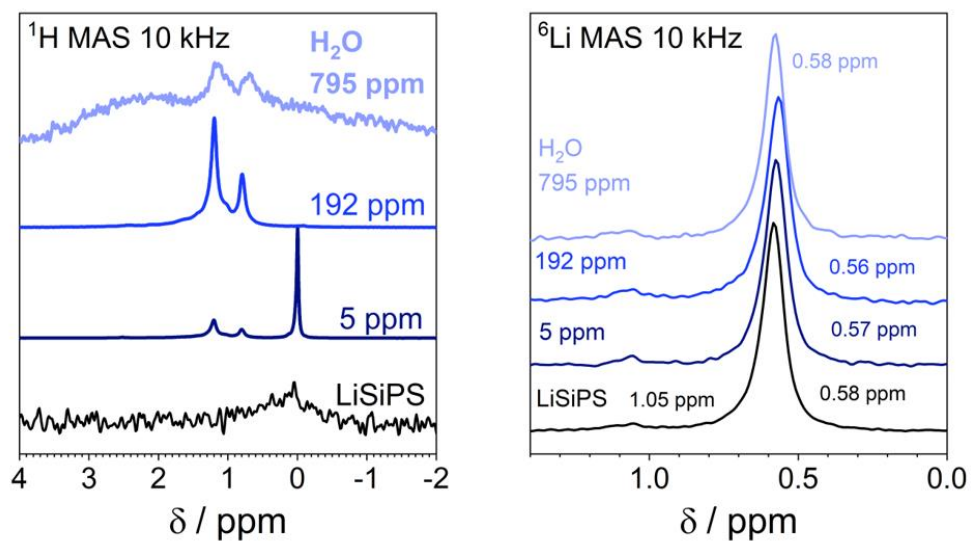
SI Figure 3 Liquid NMR of a highly concentrated solution of LiSiPS in degassed deionized water following the decomposition reaction into oxygen-substituted thiophosphates after 30 min and 48 h.



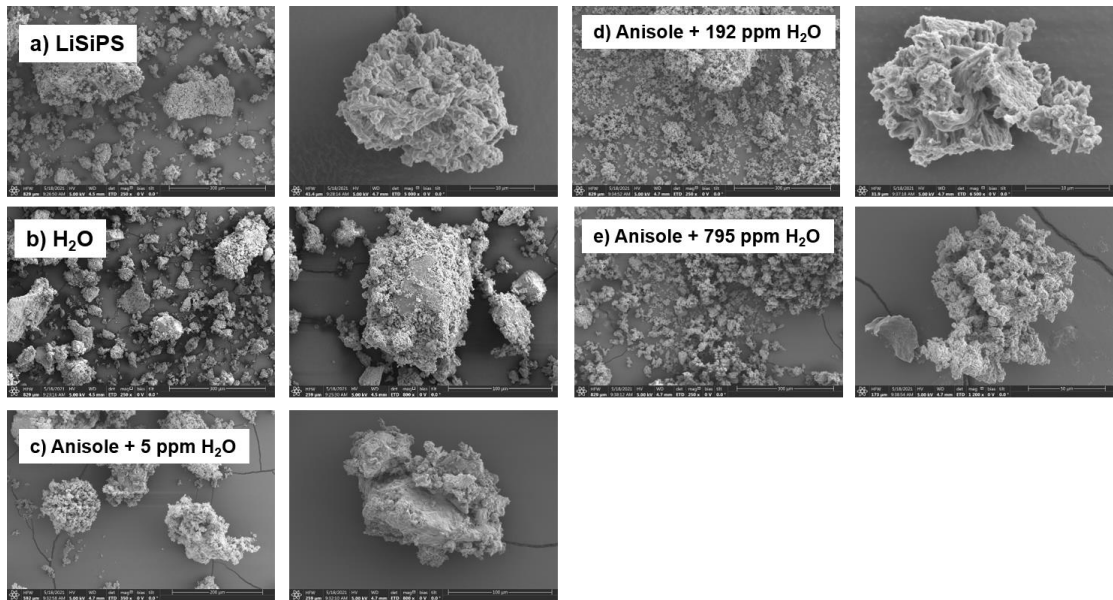
SI Figure 4 ²⁹Si, ¹H and ⁶Li MAS solid state NMR from pristine LiSiPS (black) treated degassed deionized water for 48 h and dried under vacuum (grey, denoted as H₂O).



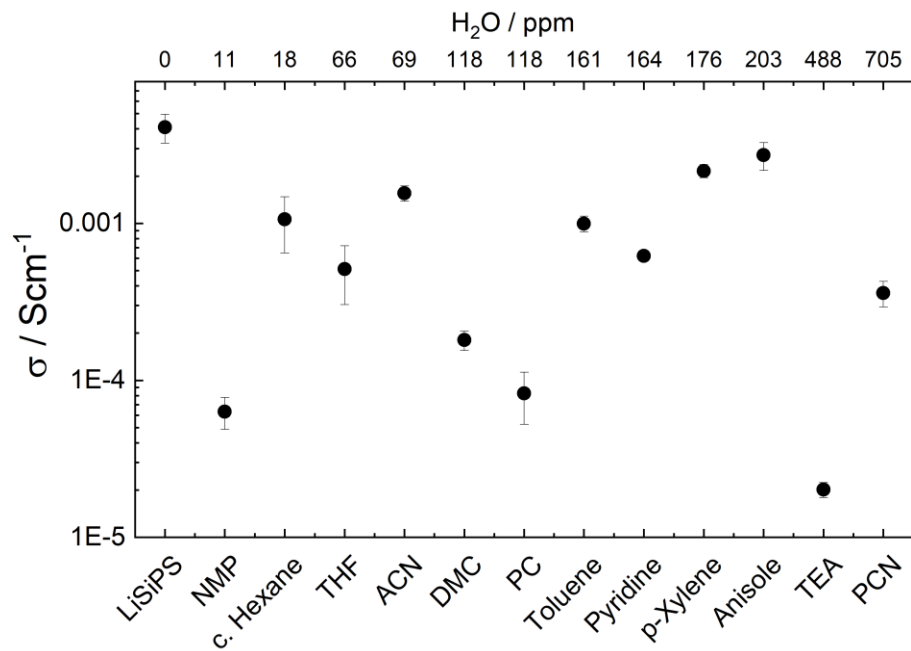
SI Figure 5 a) Photographs of the LiSiPS samples treated with anisole containing an increasing amount of water from 5 to 795 ppm and b) impedance spectra of all samples.



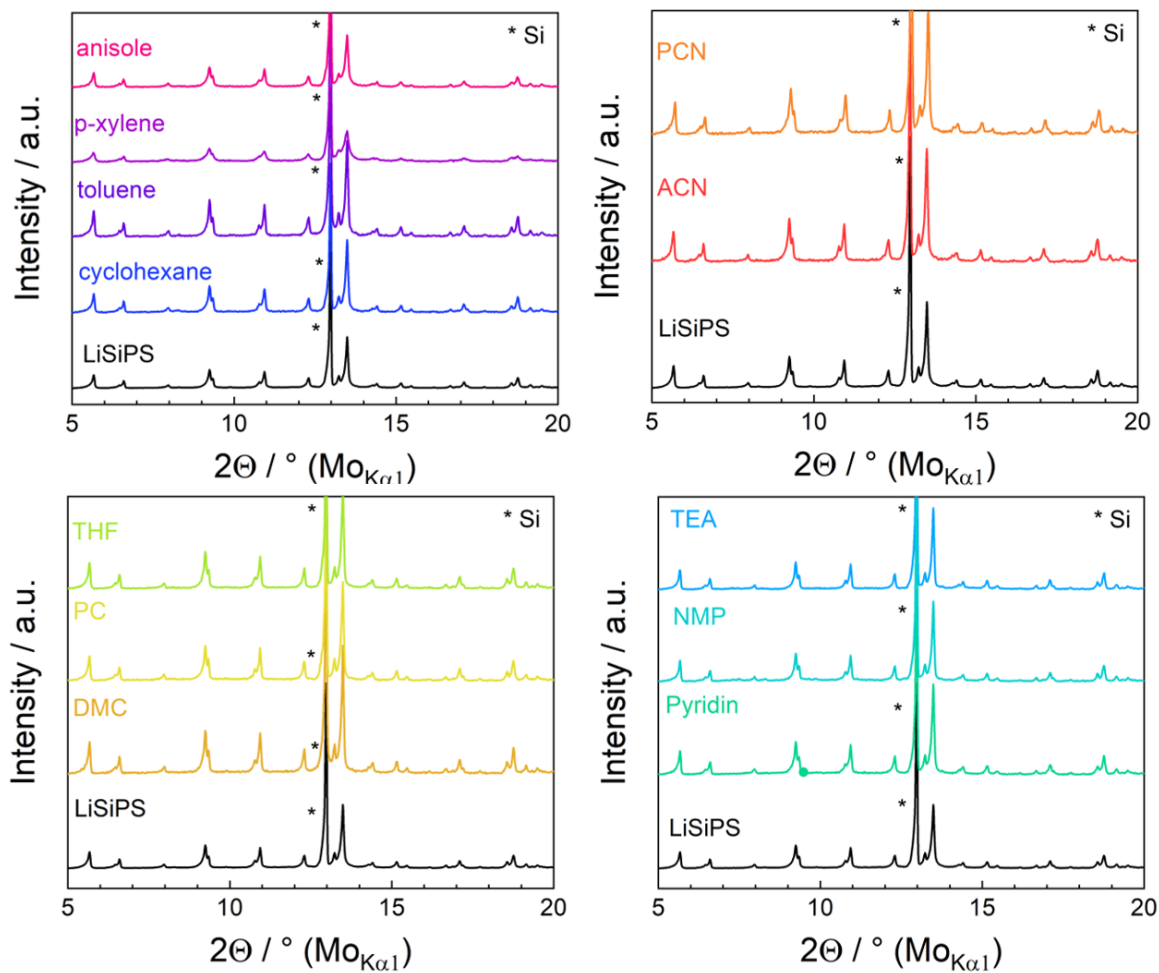
SI Figure 6 ¹H and ⁶Li MAS solid state NMR from LiSiPS treated with anisole containing an increasing amount of water ranging from 5 to 795 ppm.



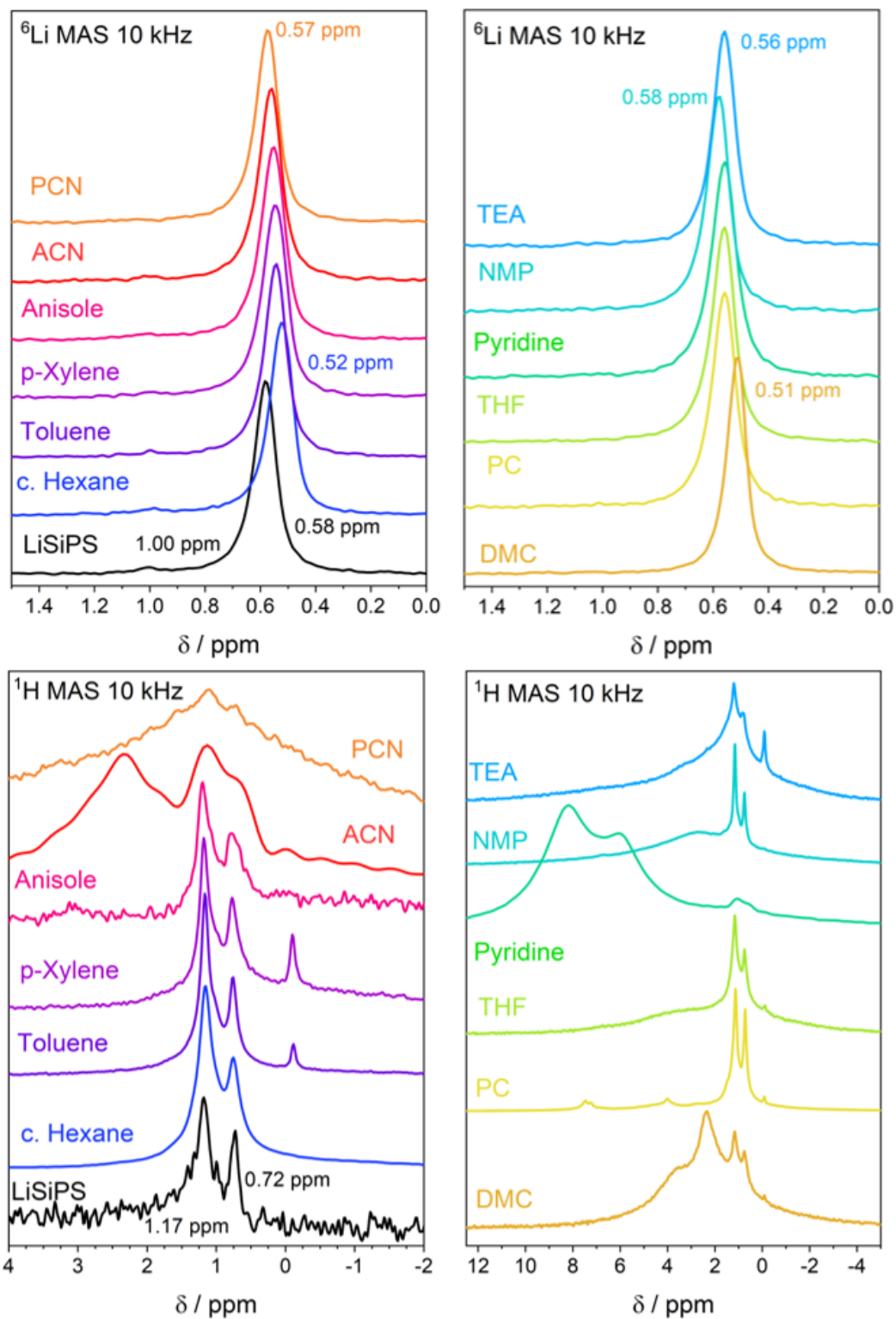
SI Figure 7 SEM images from LiSiPS treated with d.i. water and anisole containing an increasing amount of water ranging from 5 to 795 ppm. The material treated with anisole containing larger amount of water show smaller secondary particles.



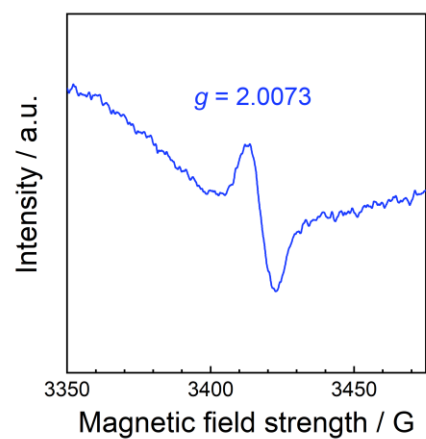
SI Figure 8 Ionic conductivity of solvent-processed LiSiPS samples arranged in order of increasing residual water content.



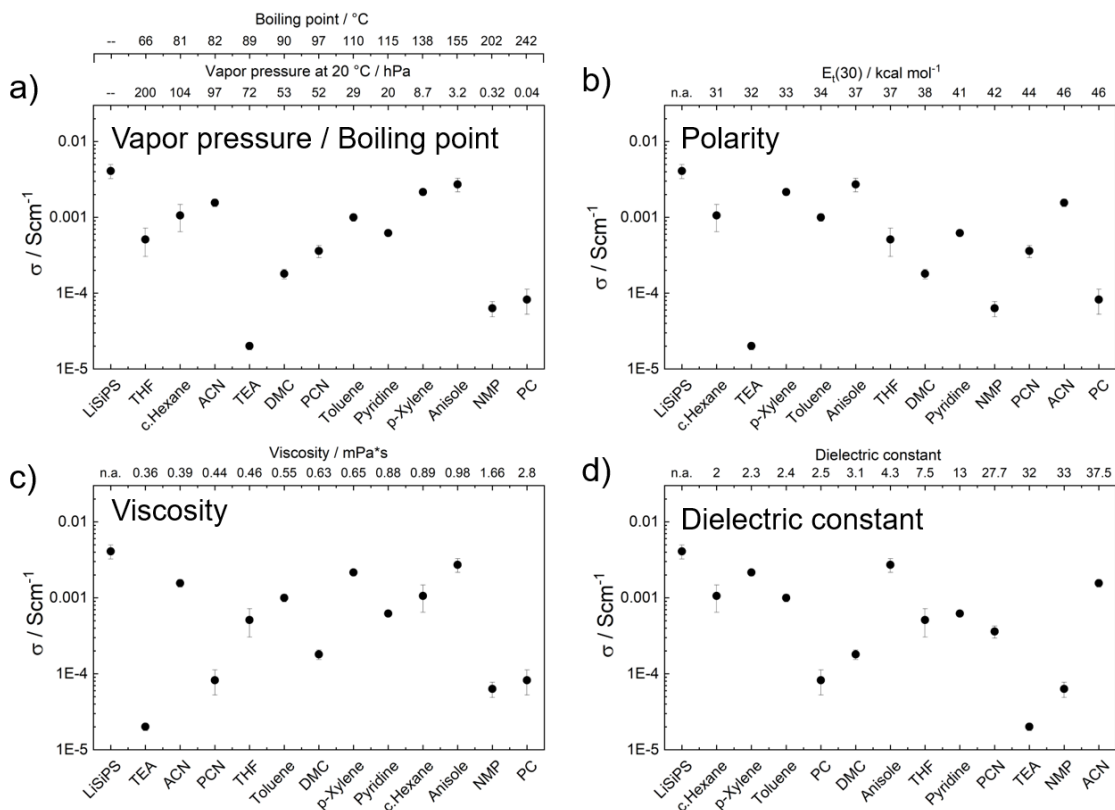
SI Figure 9 XRD patterns of LiSiPS after treatment in aprotic solvents showing a retention of the initial crystal structure being phase pure tetra-LiSiPS. As reference for the XRD measurements, a silicon standard was added to the sample. In the diffractograms the Si reflection is marked with an asterisk.



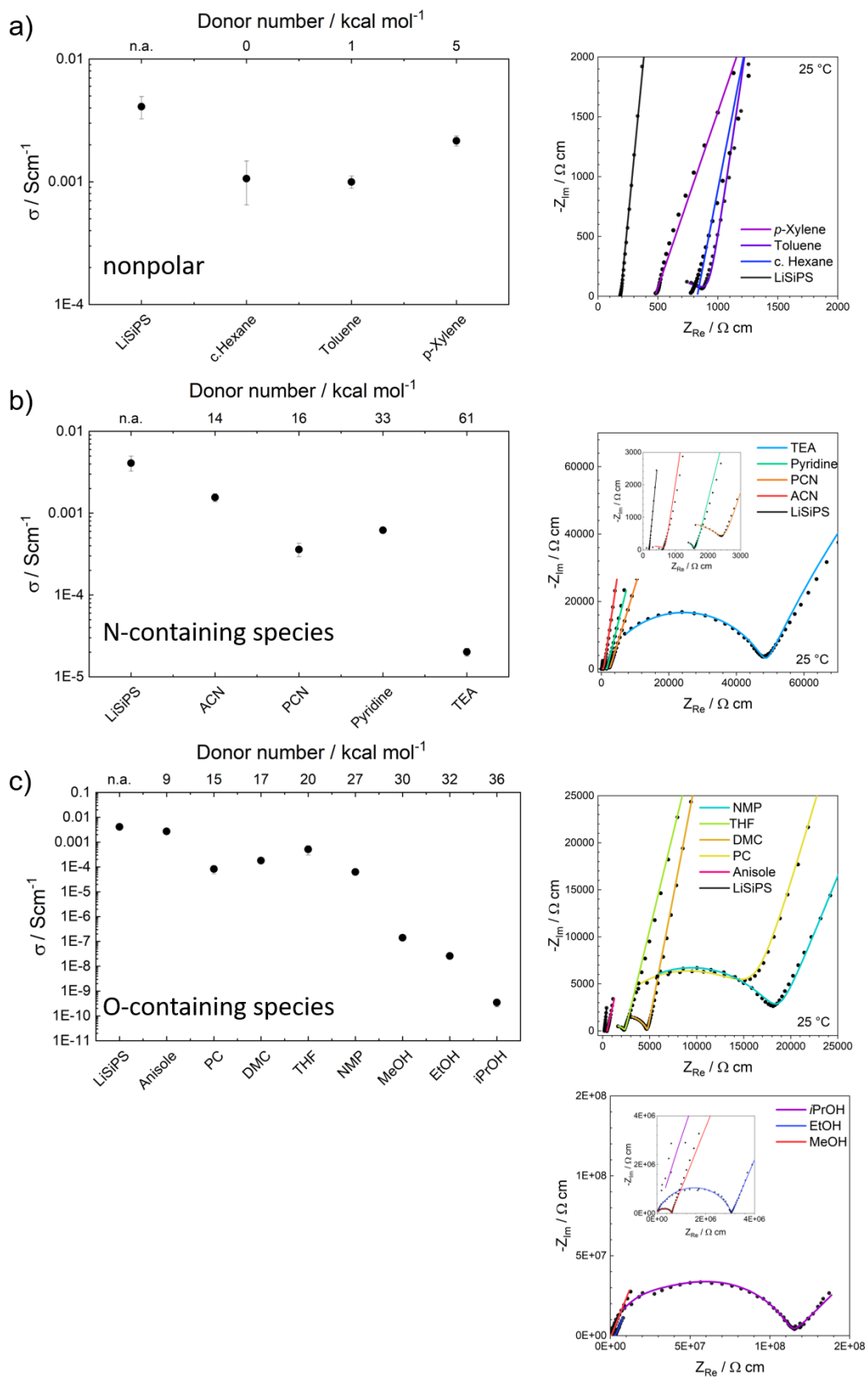
SI Figure 10: ⁶Li and ¹H MAS NMR spectra of solvent treated LiSiPS. Interestingly, the strong signal in the ⁶Li-spectra shifts slightly with varying solvent. This shift does not follow the nature of the solvent (e.g. donor number, dielectric constant, residual amount of solvent etc.) Thus, the chemical environment of lithium seems to be influenced by a complex interplay of solvent and LiSiPS.



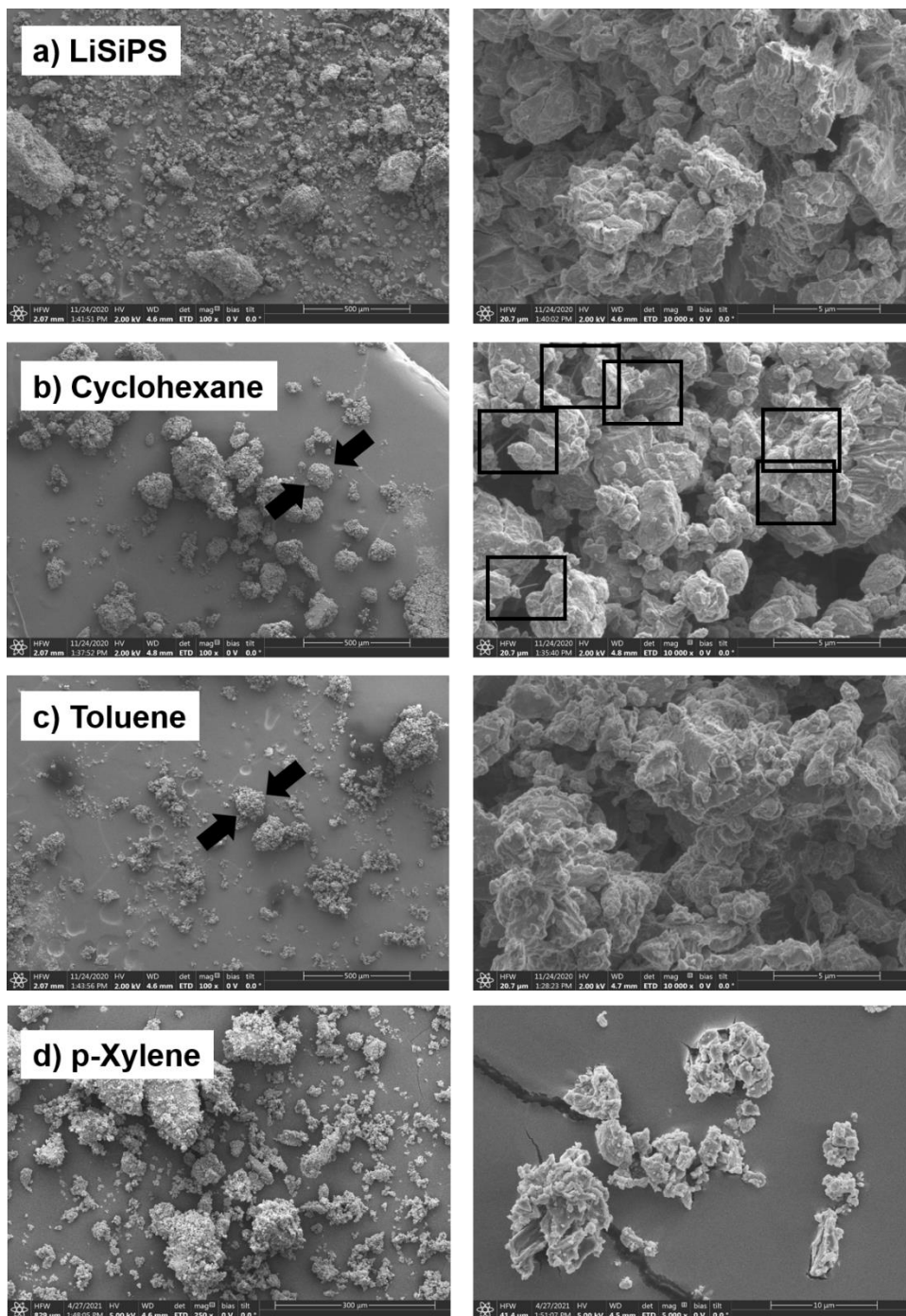
SI Figure 11: EPR spectrum of LiSiPS in NMP corroborates the presence of the radical anions. Since $[S_3]^-$ is the dominant species in the UV/Vis spectrum, the EPR signal originates presumably from $[S_3]^-$. The g value of 2.007 of the weak signal differs from literature values of e.g. ultramarine (2.029)^[3] and $[S_3]^-$ in 2.029 in TEGDME^[4] and DMF^[5], and 2.015 in NMP^[6]. However, we find the signal shifting when the concentration or time after dispersion changes indicating a change in chemical environment and concentration.



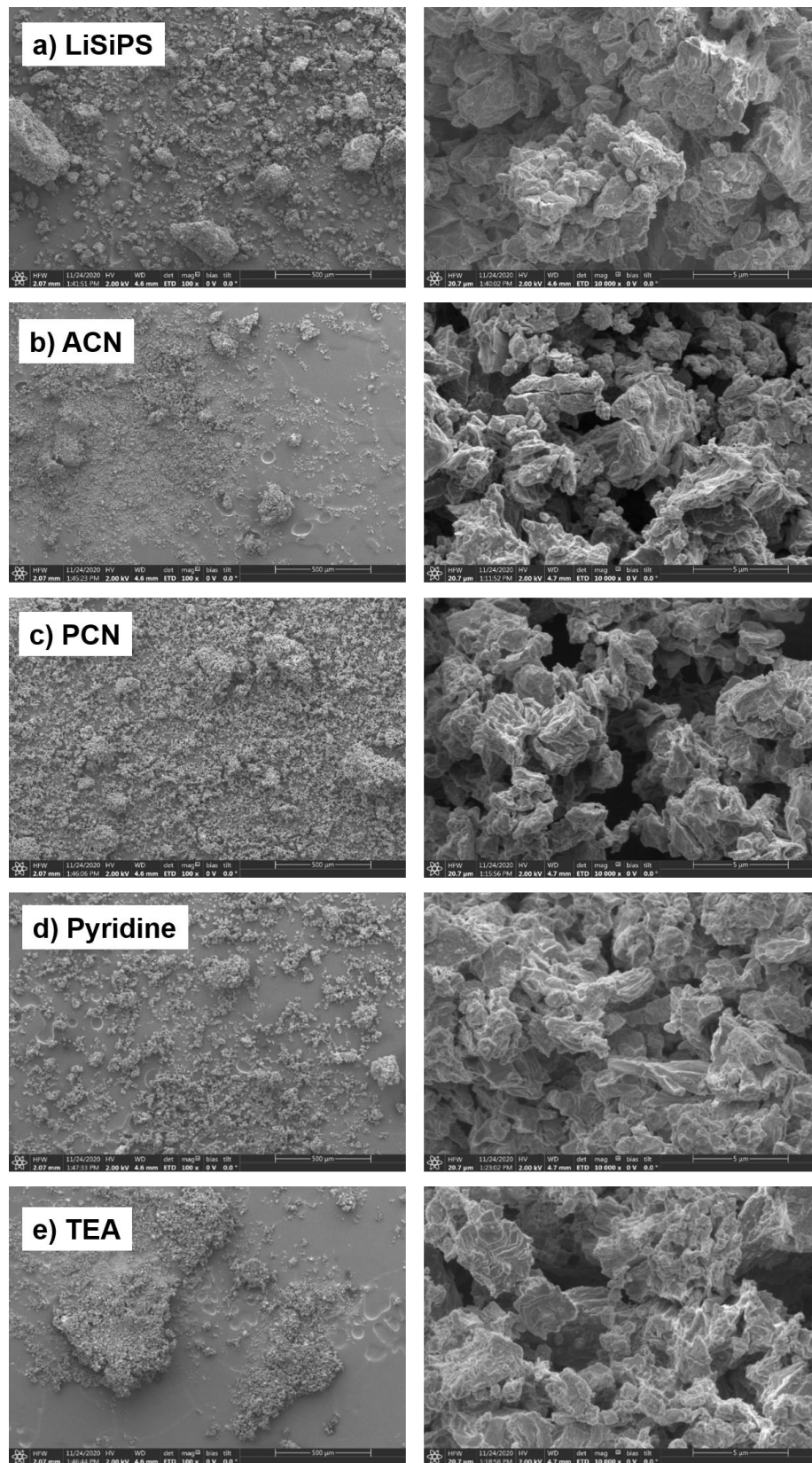
SI Figure 12 Physical properties of the solvent such as a) vapor pressure/boiling point b) polarity ($E_t(30)$) c) viscosity and d) dielectric constant do not show a strong correlation with the ionic conductivity of LiSiPS after solvent treatment.



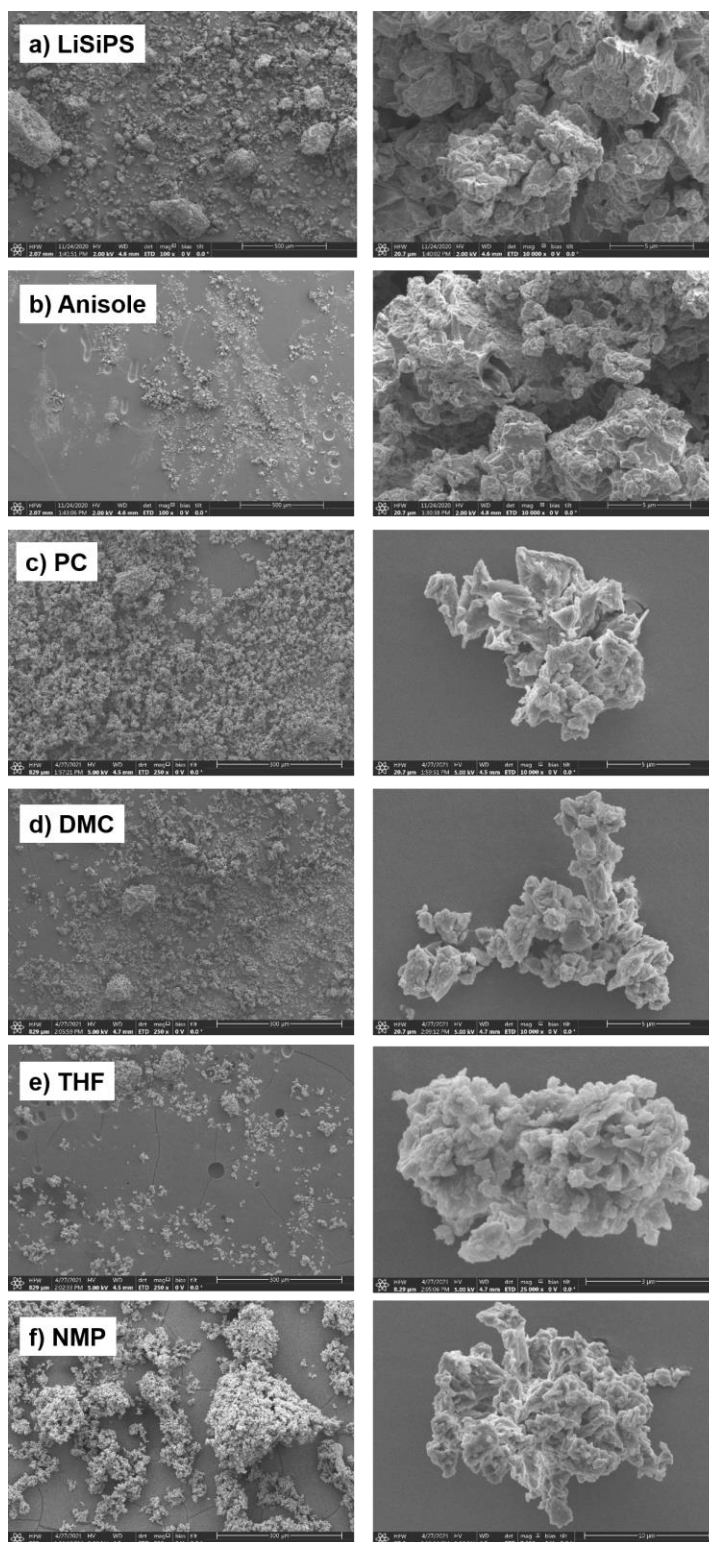
SI Figure 13: Ionic conductivity as function of donor number group according to the properties and functional groups of solvent. The respective impedance spectra are given next to the plot. a) non-polar solvents b) solvents containing a N-terminated moiety and c) solvents containing a O-terminated moiety being able to interact with the solid electrolyte.



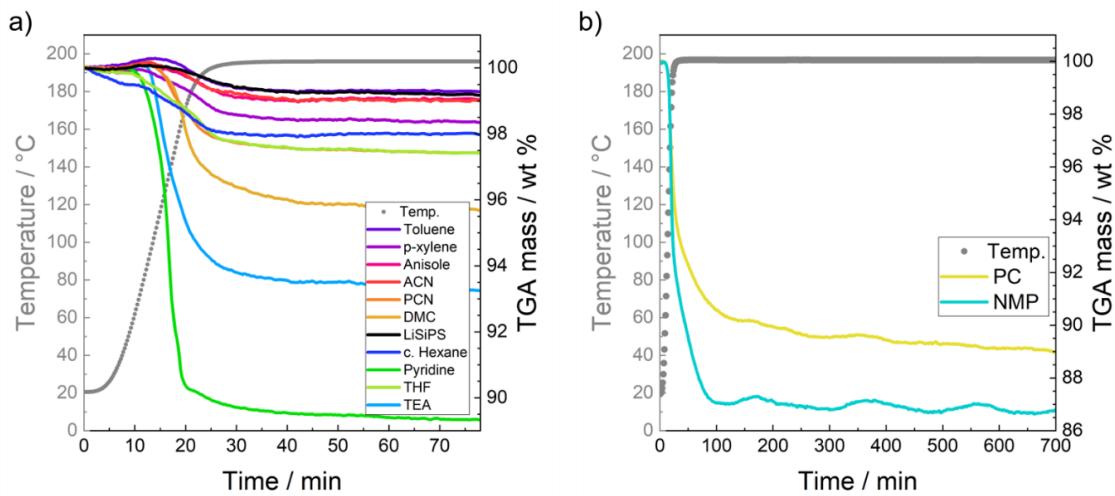
SI Figure 14: SEM images of LiSiPS before and after solvent treatment with nonpolar solvents.



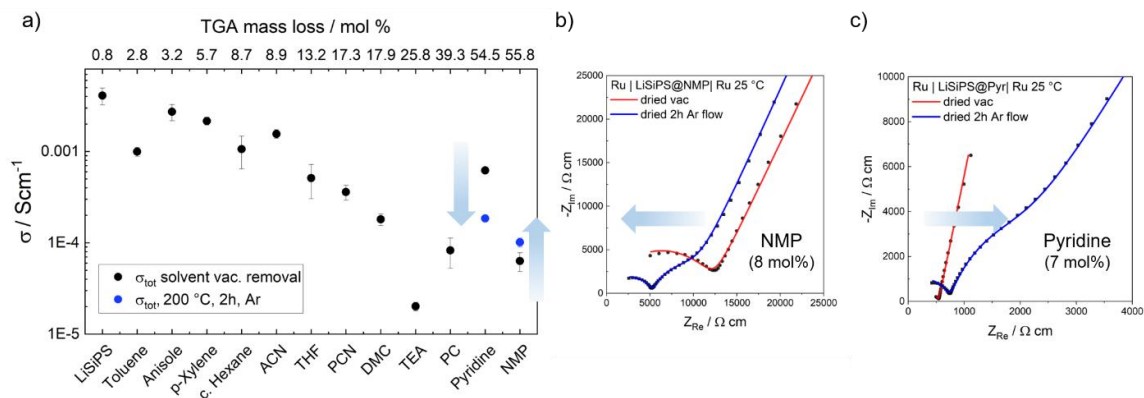
SI Figure 15 SEM images of LiSiPS after solvent treatment with N-containing solvents.



SI Figure 16 SEM images of LiSiPS after solvent treatment with O-containing solvents.



SI Figure 17: TGA mass data of solvent treated LiSiPS after a) heating period of 58 min at 200 °C and b) after 680 min at 200 °C for the solvents NMP and PC that possess the highest boiling point and lowest vapor pressure in the series.



SI Figure 18: a) The ionic conductivity decreases as function of molar weight loss, i.e. residual solvent fraction (measured by TGA). The samples with the highest amount of residual solvent (NMP, Pyridine) were subjected to an additional heat treatment step in accordance with the TGA measurement (2 h at 200 °C in Ar flow) resulting in a solvent residue of 8 mol% for NMP and 7 mol% for pyridine, respectively) and the ionic conductivity was remeasured (b and c). The resistivity of the NMP-treated sample decreases (b), but the resistivity of the pyridine-treated sample increases (c). These results hints to a complicated behaviour upon drying with possible interfacial reactions that are impeding ionic transport.

References

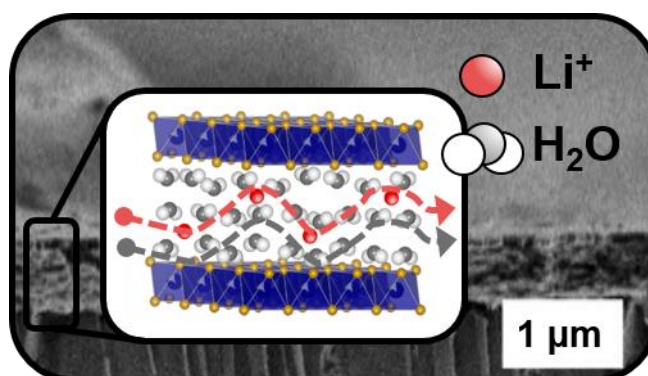
- [1] aC. Reichardt, *Chem. Rev.* **1994**, *94*, 2319-2358; bY. Marcus, *Chem. Soc. Rev.* **1993**, *22*, 409-416.
- [2] Properties of Solvents Used in Organic Chemistry. <http://murov.info/orgsolvents.htm> (accessed 01.07.2020).
- [3] R. Steudel, T. Chivers, *Chem. Soc. Rev.* **2019**, *48*, 3279-3319.
- [4] K. H. Wujcik, D. R. Wang, A. Raghunathan, M. Drake, T. A. Pascal, D. Prendergast, N. P. Balsara, *J. Phys. Chem. C* **2016**, *120*, 18403-18410.
- [5] G. Zhang, H. Yi, H. Chen, C. Bian, C. Liu, A. Lei, *Org. Lett.* **2014**, *16*, 6156-6159.
- [6] W. Tan, C. Wang, X. Jiang, *Org. Chem. Front.* **2018**, *5*, 2390-2394.

4.7 Fast Water-Assisted Lithium-Ion Conduction in Restacked Lithium Tin Sulfide Nanosheets

A.-K. Hatz, I. Moudrakovski, S. Bette, M. Terban, M. Etter, M. Joos, N. M. Vargas-Barbosa, R. E. Dinnebier, B. V. Lotsch

Abstract

While two-dimensional (2D) materials may preserve some intrinsic properties of the corresponding layered bulk material, new characteristics arise from their pronounced anisotropy or confinement effects. Recently, exceptionally high ionic conductivities were discovered in 2D materials such as graphene oxide and vermiculite. Here, we report on the water-assisted fast conduction of lithium-



ions in restacked lithium tin sulfide nanosheets. $\text{Li}_{0.8}\text{Sn}_{0.8}\text{S}_2$ exfoliates spontaneously in water and can be restacked into homogenous films in which the lithium content is decreased, and a partial substitution of sulfur with hydroxyl groups takes place. Using a recursive supercell refinement approach in reciprocal space along with real-space pair distribution function analysis, we describe restacked lithium tin sulfide as partially turbostratically disordered material composed of lithium-containing and lithium-depleted layers. In humid air, the material takes up multiple layers of water that coordinates lithium-ions in the space between the layers, increasing the stacking distance and screening the interaction between lithium-ions and the anionic layers. This results in a 1000-fold increase in ionic conductivity up to 47 mS cm^{-1} at high humidities. Orientation-dependent impedance spectroscopy suggests a facile in-plane conduction and a hindered out-of-plane conduction. Pulsed field gradient nuclear magnetic resonance spectroscopy reveals a fast, simultaneous diffusion of a majority and a minority species for both ^7Li and ^1H , suggesting water-assisted lithium diffusion to be at play. This study enlarges the family of nanosheet-based ionic conductors and helps to rationalize the transport mechanism of lithium-ions enabled by hydration in a nanoconfined 2D space.

Introduction

Several technological applications require improved development and understanding of materials with fast ion transport that can be easily fabricated on a large scale. In this regard, 2D materials have garnered significant attention as their anisotropic properties and miniature dimensions are attractive for various fields including nano(opto)electronics, energy conversion and storage, catalysis, membranes, or nanofluidics.^{1,2} When such materials contain nanoconfined fluids, they can exhibit rapid ion diffusion and transport kinetics.² Deeper insight into the mechanisms underlying this behavior is desired.

Compared to their bulk counterparts, 2D single layers and restacked materials generally show different physical properties,³⁻⁷ often developing new and useful characteristics due to their

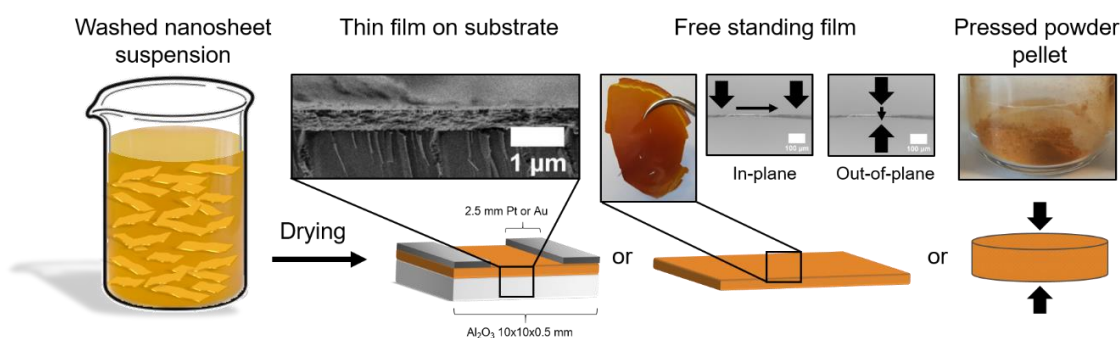


Figure 1. Fabrication method for three types of sample: First, by immersion of $\text{Li}_{0.8}\text{Sn}_{0.8}\text{S}_2$ in water exfoliated Li-TS nanosheets are obtained. Second, after washing the suspension by centrifuging, homogeneous thin films either on an alumina substrate (thickness about $1\ \mu\text{m}$, magnification in Figure S5e) or free standing (thickness about $10\ \mu\text{m}$) can be fabricated by drop-casting and drying at RT. By grinding the free standing films and compacting the powder, a pellet with a random orientation of nanosheets is created. The black arrows indicate the orientation of electrodes during conductivity measurement.

pronounced anisotropy and/or confinement effects.^{6, 8, 9} The most prominent example of this behavior is graphene.^{3, 10-13} For instance, lithium shows fast chemical diffusion in bilayer graphene and water flows exceptionally fast in artificial nanochannels built from graphene. The fast flow of water is associated with increased structural order in nanoconfined water, and ionic motion which depends on the interaction of the hydration shells with the channel walls.^{13, 14} Besides, graphene oxide (GO), a derivative of graphene, also shows unusual diffusion properties.¹⁵⁻¹⁹ GO films that are formed by restacking GO nanosheets take up water from the environment, which is embedded in the nanoconfined space between the layers. These hydrated systems show exceptionally fast conduction of different ions such as H^+ , K^+ , Mg^{2+} , and Ca^{2+} . The ionic conductivities at low electrolyte concentrations ($< 50\ \text{mM}$) in GO films even exceed the conductivity of the cations in aqueous salt solutions.¹⁶ In this case, conductivity is rather independent of electrolyte concentration, which is characteristic of surface-charge governed ionic transport. Similar results were observed for GO samples exposed to a high relative humidity (RH). These show fast proton conduction up to $\sigma = 4 \times 10^{-4}\ \text{S cm}^{-1}$ for thick multi-layer films at 60 % RH and $\sigma = 7 \times 10^{-3}\ \text{S cm}^{-1}$ for single GO layers at 95 %.^{17, 20} It is assumed that the hydrophilic surface groups such as -O-, -OH, and -COOH attract protons from adsorbed water, which propagate through hydrogen-bonding networks along the adsorbed water film.²⁰

Ion conduction properties have been examined in only a few other restacked nanosheet materials. Vermiculite layers were assembled into a nanofluidic device showing high proton conductivity using a near neutral solutions ($\sigma = 6 \times 10^{-3}\ \text{S cm}^{-1}$) with the advantage of higher thermal stability than GO. In that system, the conductance of lithium-ions stemming from a LiCl solution and being transported through the vermiculite layers was also demonstrated.²¹ Besides, a remarkably high in-plane hydroxyl conductivity of $10^{-1}\ \text{S cm}^{-1}$ was observed in single-layer, layered double hydroxides (LDH).²² Moreover, thin films fabricated from the exfoliated and restacked phosphoantimonates HSbP_2O_8 ²³ and $\text{H}_3\text{Sb}_3\text{P}_2\text{O}_{14}$ ²⁴ that show a large swelling upon water exposure, exhibit an increase in proton conductance of several orders of magnitude upon exposure to relative humidities from 0 to 100 %. This increase is larger than the change observed for the non-exfoliated, bulk layered material, pointing to higher ionic mobilities in the restacked

materials compared to their bulk counterpart, which makes them interesting candidates for photonic humidity sensing applications.²⁵

In this study, the fast, water-assisted conduction of lithium-ions in restacked lithium tin sulfide (Li-TS) is reported. Its parental bulk material $\text{Li}_{0.8}\text{Sn}_{0.8}\text{S}_2$ is a solid lithium-ion conductor.^{26, 27} Under exposure to humidity, $\text{Li}_{0.8}\text{Sn}_{0.8}\text{S}_2$ forms defined hydrates that exhibit order of magnitudes higher ionic conductivity than in the dry state. The impact of hydration on the structure and transport properties on $\text{Li}_{0.8}\text{Sn}_{0.8}\text{S}_2$ was first preliminarily shown by Holzmann *et al.*²⁸ and then fully disclosed by Joos *et al.*²⁷. Moreover, $\text{Li}_{0.8}\text{Sn}_{0.8}\text{S}_2$ can be easily exfoliated into individual layers in liquid water and restacked into homogenous films either on a substrate or even free-standing (cf. with Figure 1).^{24, 29} Due to the ultra-high refractive index of $n = 2.5$, thin Li-TS films have been utilized as stimuli-responsive 1D photonic crystals and upon hydration by water vapor a strong swelling of the films was reported by Szendrei *et al.*³⁰ In line with previous reports correlating swelling upon humidity exposure and ion conduction, we find that the total conductivity of restacked Li-TS is indeed highly dependent on the relative humidity of the environment and reaches up to 47 mS cm^{-1} . Orientation-dependent measurements indicate a preferred in-plane conduction (in between the layers). Moreover, we develop a structural model for the dry and hydrated restacked Li-TS and demonstrate by pulsed field gradient nuclear magnetic resonance spectroscopy (PFG NMR) that the diffusion of the lithium-ions and water takes place simultaneously.

Experimental

Preparation of restacked nanosheets

The precursor material $\text{Li}_{0.8}\text{Sn}_{0.8}\text{S}_2$ was prepared and exfoliated according to Kuhn and Holzmann *et al.*^{26, 29}. The nanosheet suspension was washed once by centrifuging at 20000 rpm for 10 min and then redispersing in purified water. Since during exfoliation H_2S evolves, exfoliation should be conducted in a fume hood. The pH of the suspensions was measured with a pH indicator paper. For thin films of restacked nanosheets on a substrate, 4 mL of the suspension (1 mg mL^{-1}) was drop-cast onto alumina substrates (CRYSTEC, $10 \times 10 \times 0.5 \text{ mm}$, single crystal cleaved along (0001), polished on one side) placed in a plastic reservoir with a volume of 12.6 cm^3 and slowly dried at room temperature. By this procedure, thin films with a thickness of about 1-3 μm were obtained. The thickness of the films on a substrate was measured by scanning electron microscopy with a Merlin SEM (ZEISS). To fabricate free-standing films and powder samples, the suspension was poured in a vessel made of polypropylene and dried between 25–60 °C in an oven for several days. Subsequently, the films could be simply peeled-off the vessel. The thickness of the free-standing films was measured by evaluation of images made by an optical microscope (LEICA DM 2500 M).

X-ray measurements

X-ray powder diffraction (XRPD) experiments were conducted using a STOE STADI P diffractometer (Mo- $\text{K}\alpha_1$ radiation, Ge(111) monochromator, MYTHEN 1 K Detector) in Debye-Scherrer geometry. For humidity-dependent measurements, capillaries were stored under water-saturated atmosphere before sealing. Rietveld refinements were carried out with the program TOPAS v. 6.0.³¹

Total scattering measurements were carried out using the high energy Powder Diffraction and Total Scattering Beamline P02.1 of PETRA III at the Deutsches Elektronen-Synchrotron (DESY, more

details are in the SI). X-ray total scattering data were collected in rapid acquisition mode (RAPDF).³² A large-area 2D PERKIN ELMER XRD1621 detector (2048x2048 pixels, 200x200 μm^2 each) was used at a sample-to-detector distance of approximately 304 mm. Samples were loaded into 1.8 mm ID and 1.9 mm OD polyimide capillaries (COLE-PARMER) and measured at room temperature. The incident energy of the X-rays was 59.858 keV ($\lambda=0.20713$ Å). Data integration and reduction to the pair distributions functions (PDFs) were performed using fit2D³³ and xPDFsuite^{34,35} respectively. Structure refinements were performed using both PDFgui³⁶ and Diffpy-CMI³⁷.

Impedance spectroscopy

Electrochemical impedance spectroscopy (EIS) was performed with an IVIUM compactstat.h (24-bit instrument) in an enclosed two-electrode setup. The relative humidity of the stagnant gas was controlled using saturated salt solutions.^{38,39} Each sample was equilibrated at the respective RH for 24 h. After this time, no further change in conductivity was measurable. For in-plane measurements, the films on alumina substrates were sputter-coated with 80–100 nm gold or platinum electrodes, while the free-standing films contacted with carbon foils in a home-built measurement cell. The relative density of the films of about $91\pm 8\%$ was calculated from the measured weight and thickness of the films and normalized on the crystallographic density of LiSnS_2 . The measurement cell for the in-plane measurement was a gas-tight SCHOTT glass with a total volume of 250 mL equipped with humidity and temperature sensors from SENSIRION installed inside the chamber. The chamber was submerged in water and kept at a defined temperature with a JULABO FP50ME thermostat. For out-of-plane measurements, the samples were pressed between two pieces of carbon foil in a TSC Battery cell from RHD INSTRUMENTS, humidified for 24 h in a desiccator at the respective humidity and then sealed gas-tight. The same films as for in-plane measurements were also sample out-of-plane as well as pressed pellets (8 mm diameter, pressed with 40 kN, relative density normalized on crystallographic density of LiSnS_2 is about $85\pm 3\%$). The applied rms AC voltage was 100 mV for films and 10 mV for the pellets. The setup applied for measuring the dry pellet (with sputtered ruthenium metal electrodes) and under varying partial water pressure is described in the SI section 7.1. Impedance spectra were analyzed using the RELAXIS3 software (RHD INSTRUMENTS).

Nuclear magnetic resonance spectroscopy

^1H , ^7Li , ^6Li , and ^{119}Sn solid state NMR spectra were obtained on a BRUKER AVANCE III 400 MHz instrument at Larmor frequencies of 400.1, 58.8, 155.6, and 149.2 MHz, respectively ($B_0 = 9.4$ T). ^1H spectra are externally referenced to tetramethylsilane (TMS, $\delta_{iso} = 0.0$ ppm) and ^7Li spectra to a 9.7 M aqueous solution of LiCl ($\delta_{iso} = 0.0$ ppm). ^{119}Sn spectra are referenced to tetramethyltin ($\text{Sn}(\text{CH}_3)_4$, $\delta_{iso} = 0.0$ ppm) with solid SnO_2 used as a secondary chemical shift standard ($\delta_{iso} = -603.0$ ppm relative to $\text{Sn}(\text{CH}_3)_4$).⁴⁰ Magic-angle spinning (MAS) experiments were performed in ZrO_2 spinners at a spinning frequency of 5–14 kHz using a BRUKER 4 mm double channel probe. The temperature of the samples was controlled using a BRUKER BVT3000 temperature controller and was calibrated using the ^{207}Pb signal in $\text{Pb}(\text{NO}_3)_2$.⁴¹

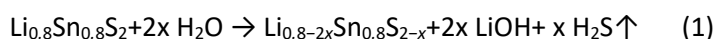
For pulsed field gradient (PFG) NMR measurements, the samples were sealed in a glass tube with an additional fitted glass rod inside to reduce the dead volume and to avoid desorption and evaporation of water during the experiments. ^7Li and ^1H NMR measurements were performed on

a BRUKER AVANCE III 400 MHz instrument ($B_0 = 9.4$ T; ^1H Larmor frequency of 400.1 MHz, ^7Li Larmor frequency of 155.56 MHz), equipped with a diff60 single gradient diffusion probe. The probe allows for pulse field gradients g of up to 30 Tm^{-1} and variable temperature measurements up to $+150$ °C. The diffusion measurements were accomplished using a stimulated echo pulse sequence.⁴² The echo attenuation curves $S(g, \delta, \Delta)$ were processed using a bi-exponential form of the Stejskal–Tanner equation,⁴³ $S(g, \delta, \Delta) = S_{0A} \exp(-\gamma^2 \delta^2 g^2 D_A (\Delta - \delta/3)) + S_{0B} \exp(-\gamma^2 \delta^2 g^2 D_B (\Delta - \delta/3))$, accounting for the at-least two independently moving nuclei (species A and B) with distinct effective diffusion coefficients D_A and D_B . Here, γ is the ^1H or ^7Li gyromagnetic ratio, respectively, g is the strength and δ the duration of the pulse field gradient, and Δ is the time interval between the field gradients that defines the diffusion time scale. The signal intensity of each ^1H and ^7Li spectrum was obtained by applying peak area integrals. The PFG data were analyzed with TOPSPIN3.6 (BRUKER).

Results and Discussion

Exfoliation and Chemical Composition

Exfoliation of $\text{Li}_{0.8}\text{Sn}_{0.8}\text{S}_2$ in water can be described by the formal removal of Li_2S , which is realized by evaporation of H_2S and the formation of LiOH in aqueous solution according to (1).



This exfoliation process is distinct from the exfoliation of Li intercalated Li_xSnS_2 , featuring partly reduced Sn(II), in aqueous solution into exfoliated SnS_2 , LiOH , and H_2 .⁴⁴⁻⁴⁶ As previously shown by Kuhn *et al.*²⁹, the in-plane structure of the exfoliated material is reminiscent of a “defective” variant of SnS_2 , with a lower electron density at the S positions indicating the presence of sulfur vacancies. This suggests a (partial) filling of the sulfur vacancies by hydroxide ions according to (2).



Following the pH during exfoliation gives more information about this process: instead of obtaining a basic pH as expected from (1), the stable nanosheet suspension is neutral at pH 7 and after long periods of time, the pH shifts into the acidic regime (pH = 4-5 after months in a sealed bottle), indicating an acid-base process to be at play. These pH changes can be rationalized by the gradual incorporation of hydroxyl groups (or oxygen) into the sulfur vacancies in $[\text{Sn}_{0.8}\text{S}_{2-x}]^{-(0.8-2x)}$ over time. During this process, protons are released into the suspension according to (2). The insertion of hydroxyl groups is consistent with the appearance of signals at -740, -660, and -585 ppm in the ^{119}Sn NMR spectra that are clearly distinct from SnS_2 and SnO_2 (Figure S1-2). Raman spectra also support the insertion of hydroxyl groups (Figure S4). The shift of the most intense signal of Li-TS to higher wavenumbers with respect to SnS_2 is consistent with bonding interactions between tin and oxygen. Moreover, 2D ^1H - ^{119}Sn NMR correlation spectra of the dry sample indicate that residual protons are present near to oxygen-tin bonds species, again suggesting that hydroxyl ions replace sulfur ions (Figure S3a).

After the initial hydroxide insertion step, slow hydrolysis of the nanosheets proceeds. After several months of long storage in aqueous solution or as dry material in air, thermodynamically stable SnO_2 particles start to form on the surface of Li-TS films as shown in Figures S5c and S5d. To prevent further hydrolysis and to remove excess LiOH (cf. Figure S5a-b), the suspension was

centrifuged and washed with purified water once before further investigations. The restacked Li-TS was used as freshly prepared as possible and investigated in two different states: the "dry" state and the "hydrated" state (see schematics in Figure 2). Upon exposure to humid air, the layers reversibly adsorb water likely driven by the large hydration energy of lithium-ions as already demonstrated by ellipsometric porosimetry.³⁰

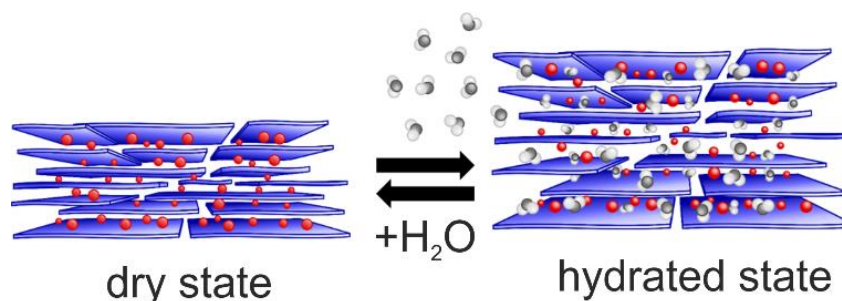


Figure 2. Upon exposure to water vapor, water molecules adsorb between the restacked nanosheets and lead to swelling of the material.

The dry state is obtained by heating the sample overnight at 120 °C under vacuum and subsequent handling under Ar. In this state, most of the adsorbed water is removed, and only 1.5 wt% residual water is present (Figure S6b, data point at 0 % RH). The restacked Li-TS retains about 44±8 % of the initial lithium content (Table S1) and shows one broad signal in the ⁶Li MAS NMR spectrum in the dry state and two distinct sharper signals in the hydrated state (cf. Figure 4c). Moreover, as already suggested by solid state ¹¹⁹Sn NMR, the elemental analysis (SI section 3 Table S1-3) also indicates a partial substitution of sulfide with hydroxide (OH:S = 0.19) in the anionic network lowering the S:Sn ratio towards ≤ 2 while preserving the initially present tin vacancies. The exact composition varies slightly for each batch.

At high RHs (100 % for 24 h) Li-TS adsorbs up to 32 wt% water (TGA data in Figure S6b, c, and d). This corresponds roughly to 9 water molecules per lithium-ion and 2.6 water molecules per sum formula. In summary, the exfoliation process changes the tin-sulfur-oxygen content significantly while substantial amounts of lithium-ions are washed out, making the exfoliated, restacked material chemically distinct from both pristine Li_{0.8}Sn_{0.8}S₂ and SnS₂.

Structural Characterization

Restacked Li-TS films prepared by drop casting show a homogeneous thickness between 20 nm and several μm (see Figure 1 and Figure S5b, d). To better understand the 3D structure, the powdered materials were further investigated using XRPD and PDF analysis. The diffraction patterns for the dry and hydrated material on a lab diffractometer (Mo-K_{α1} radiation) are shown in Figure S6 and the synchrotron measurement with Rietveld refinement⁴⁷ in Figure 3a.

First, we will discuss the structure of the dry Li-TS sample (details see SI 5.1-5.2 and Figure S7-14). The patterns show broad, triangular-shaped "Warren-type" peaks characteristic of orientational (i.e., turbostratic) disordered layers as visualized in Figure 3a.⁴⁸ Such peaks are often observed when layered materials such as tetravalent sulfides are restacked from suspension.⁴⁹ Additionally, the 003 basal reflection is split into two overlapping Bragg peaks suggesting a modulation of the

interlayer distance, likely by interstratification effects. Thus, by applying a supercell approach^{50,51} the microstructure of the stacking-faulted dry Li-TS was approximated by a combination of stacking faults and turbostratic disorder as summarized in the following.

The structure of dry Li-TS contains basic stacking motifs related to Li-containing $\text{Li}_{4x}\text{Sn}_{1-x}\text{S}_2$ ($x > 0$) (with an interlayer distance of 6.137(50) Å) and “defective”, Li-depleted SnS_2 optimized to for the C19-type stacking (with an interlayer distance of 5.90(10) Å). The former motif can be approximated and modelled by the structure of anhydrous LiSnS_2 ⁵² with a reduced lithium and tin occupancy similar to the parental material. This $\text{Li}_{0.8}\text{Sn}_{0.8}\text{S}_2$ model has a typical CdCl_2 -like C19 stacking with lithium residing between the layers. Exfoliation in water presumably removes lithium-ions that were originally located on Sn sites (inside the Sn-S layers) and lithium-ions in the interlayer galleries between the Sn-S layers in the parental material. This removal of lithium-ions leaves behind lithium vacancies within the Sn-S layers. However, no information on the distribution of voids within the layers and on the presence of intra-layer lithium could be extracted

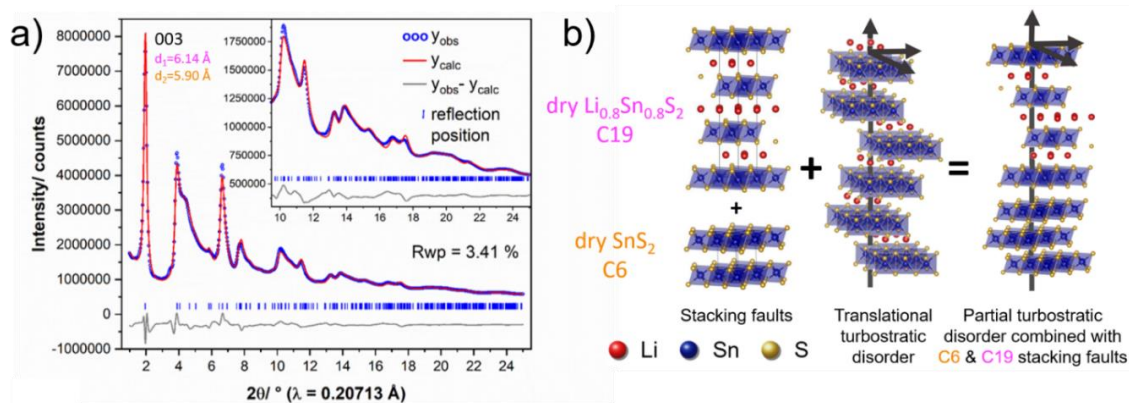


Figure 2. a) Rietveld refinement of XRPD of dry restacked Li-TS showing the presence of faults between a regular CdCl_2 -type (C19) for the $\text{Li}_{0.8}\text{Sn}_{0.8}\text{S}_2$ -type and CdI_2 -type (C6) stacking for the lithium depleted SnS_2 -type regions in the material, as well as random variations of the stacking vectors within the ab -plane as deduced for the structural model discussed in the text and in the SI. b) The structure of restacked Li-TS nanosheets can be understood as partial translational turbostratic disorder of layers combined with stacking faults between SnS_2 -type (C6) and $\text{Li}_{0.8}\text{Sn}_{0.8}\text{S}_2$ -type (C19) regions.

from the refinements. In ^6Li MAS NMR of restacked dry Li-TS inter- and intralayer lithium positions are no longer distinguishable (cf. Figure 4c) hinting to broad dispersion of lithium positions caused by the structural disorder. Consequently, the question whether intralayer lithium is removed entirely cannot be unambiguously resolved from the MAS NMR and PXRD data. The other motif is more similar to pure SnS_2 . The model exhibits a CdI_2 -like C6 stacking with vacant octahedral, interlayer cation positions in the hexagonal close packed anion lattice (see Figure S12). This presence of SnS_2 -like regions is likely caused by exfoliation and restacking which generates lithium vacancies in the interlayer space, leading to the large overall lithium deficiency in Li-TS.

However, the sole combination of faultless $\text{Li}_{0.8}\text{Sn}_{0.8}\text{S}_2$ and SnS_2 structure models is not sufficient to describe the structure of dried Li-TS (cf. Figure S14, $R_{\text{wp}}=12.21\%$). To obtain a satisfactory description of the experimental data, both faulting between these two motifs as well as turbostratic disordering of each layer is required ($R_{\text{wp}}=3.41\%$). Dry, restacked Li-TS thus contains a high faulting concentration ($\sim 40\%$) of CdI_2 -type (C6) (SnS_2 -like) within CdCl_2 -type (C19) ($\text{Li}_{0.8}\text{Sn}_{0.8}\text{S}_2$ -like) interlayer associations, depending on the local presence or absence of lithium, as visualized in Figure 3b. This is in agreement with the loss of 40 % of initial lithium content in the

refined Li-TS sample (Table S2 sample 11). The layer orientations are significantly (though not completely) modulated by turbostratic disorder, with the refinement converging to random in-plane translations of $\pm 42.5\%$ of the ab -dimensions.

Turning to the pattern from the hydrated Li-TS sample (Figure 4a, and further explanation in SI 5.3 and Figures S15-19), the basal reflection is shifted to a lower angle than that seen for the dry sample. This shift indicates a significant increase in interlayer distance due to the intercalation of water. Depending on the sample and its history, interlayer distances ranging from 9.3 to 11.9 and 12.8 Å were observed (vs. 6.1 Å in dry Li-TS), which could be associated with the intercalation of roughly two or three layers of water, respectively (SI Figure 10). The difference between 11.9 vs.

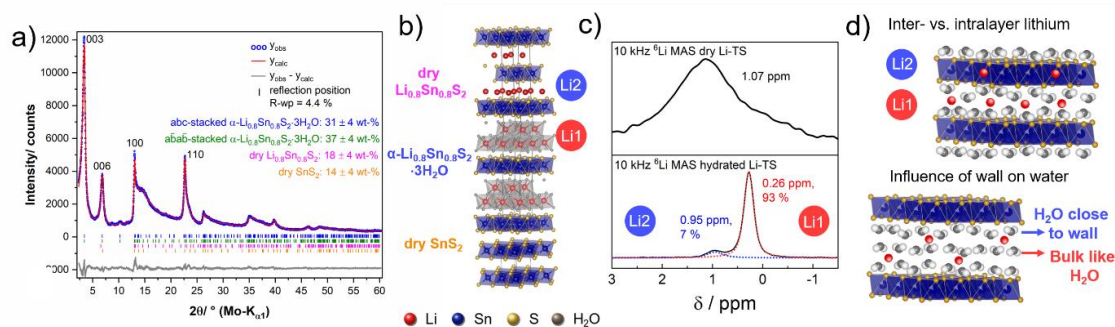


Figure 3. a) Rietveld refinement of hydrated restacked Li-TS. The structural model includes 2 phases of hypothetical $\text{Li}_{0.8}\text{Sn}_{0.8}\text{S}_2 \cdot 3\text{H}_2\text{O}$ representing different local stacking orders as well as $\text{Li}_{0.8}\text{Sn}_{0.8}\text{S}_2$ - and SnS_2 -structured regions. b) Schematic of the structural model used in the Rietveld refinement in a). c) ^6Li MAS NMR shows two distinct species in the hydrated state resembling the presence of a majority and a minority species also found in PFG NMR, and only one very broad downfield shifted signal in the dry state. d) Alternative models: Inter- and intralayer positions of lithium and water molecules (top) and those close to the pore wall or in the centre of a nanoconfined 2D channel (bottom) exhibiting a low and a high diffusion coefficient, respectively, as proposed by Osti et al.

12.8 Å possibly stems from the change of octahedral to tetrahedral coordination of the lithium-ions between the layers (cf. Figure S16).

The diffraction patterns in Figure S15 indicate further structural characteristics in the hydrated state and can only be sufficiently well described by the inclusion of two phases of hypothetical $\text{Li}_{0.8}\text{Sn}_{0.8}\text{S}_2 \cdot 3\text{H}_2\text{O}$ representing different local stacking orders (abc-stacked $\alpha\text{-Li}_{0.8}\text{Sn}_{0.8}\text{S}_2 \cdot 3\text{H}_2\text{O}$ + abāb-stacked $\alpha\text{-Li}_{0.8}\text{Sn}_{0.8}\text{S}_2 \cdot 3\text{H}_2\text{O}$, Fig. S19), as well as regions containing dry $\text{Li}_{0.8}\text{Sn}_{0.8}\text{S}_2$ and dry SnS_2 (cf. Figure 4a, and SI 5.3).

First, the interlayer distances are modulated by random variations in both the number of intercalated water layers and the relative orientations of the Sn-S layers. This is supported by the fact that the basal reflections 003 are more broadened than the 100 reflection, which would not be expected for simple turbostratic disorder with identical layer distances.⁵³ Second, the characteristic triangular Warren-type peak shape indicates that the hydrated samples contain a high density of stacking faults as with the dry sample. Third, there are domains without any water intercalation, as indicated by the larger-than-expected intensity of the second order basal reflection (006) of the hydrated state, due to the overlap of the dry-state basal reflection. From these considerations, a model for the highly hydrated material was derived. Due to the high number of possible structural defects, we could not use the approach for fitting the XRPD pattern that was applied for the dry samples. Instead, we used a multiphase approach, similar to the one applied for SnTiO_3 ⁵⁴, in which each phase represents certain microstructural features of the sample. Three layers of water ($\text{Li}_{0.8}\text{Sn}_{0.8}\text{S}_2 \cdot 3\text{H}_2\text{O}$) were used to describe the average hydrated

domains. Since tin and sulfur are by far the strongest scatterers in the structure, shifts between staggered and eclipsed stacking of the $\text{SnS}_{6/3}$ -octahedra layers have the strongest impact on the diffraction pattern. The intercalation of three layers of water can lead to a C19-type (Figure S18, a) or C6-type-like stacking (Figure S18, b) of the $\text{SnS}_{6/3}$ -octahedra layers, so phases for both types were included. Phases of non-hydrated $\text{Li}_{0.8}\text{Sn}_{0.8}\text{S}_2$ and SnS_2 were also both included to describe the non-hydrated faulting domains. The final fit and a visualized representation of the different domains in the material is shown in Figure 4a and b.

The resulting two environments for lithium are in line with the two lithium signals found in the ^6Li MAS NMR spectrum of hydrated Li-TS in Figure 4c. The signal at 0.26 ppm is shifted towards higher fields with respect to that of the dry sample, presumably due to the presence of a high amount of surrounding water screening the electrostatic interaction between lithium and sulfur as visualized in Figure 4b. The peak at 0.95 ppm corresponds to a low water content, being similar to the dry material. Thus, these findings help to interpret the PFG NMR data in Figure 7 that suggest the presence of two lithium species in the hydrated samples: a mobile and a fairly immobile species. In the hydrated layers, where three layers of intercalated water are present, the lithium cations are fairly mobile. In contrast, in the non-hydrated layers the lithium-ions show a lower local mobility and therefore give a NMR signal similar to the dry sample. Notably, we associate the main influence on the chemical shifts of the two types of lithium-ions with the difference in surrounding water content, but we cannot disregard the possibility that under hydration lithium-ions fill vacancies inside the S-Sn layers as visualized in Figure 4d on the top. This might also explain the existence of two lithium species with distinct diffusion coefficients.

PDF data were measured and analyzed to support the reciprocal-space analysis and further investigate details of the atomic structure (see SI for more details). Most notably, the PDFs for both dry and hydrated samples were very similar and could be suitably described by a single SnS_2 -layer model refinement.⁵⁵ This confirms the strongly turbostratic nature of the layers in both states, resulting in weak correlation between interlayer atom-pairs, and further rules out any likelihood for ordered bi- or multi-layer stacks. For the dry sample, a similar goodness-of-fit could be achieved for a turbostratic, 3D model with only three layers in the unit cell compared to the 2D, single-layer model. This further suggests that preferred, relative orientations likely exist depending on the amount and distribution of intercalated lithium. The preference of the data toward models with in-plane distortions is indicative of local distortions of the Sn-Sn distances due to the presence of discrete vacancies and/or Li substitutions, and a misfit of the second nearest neighbor shell suggests that the atoms in the turbostratically disordered layers also distort slightly out-of-plane. This was tested using supercells of both single layer (2×2) and 3D ($2 \times 1 \times 1$) models by allowing each Sn and S atom to distort slightly off its symmetrically allowed position in only the z-direction. While distinctive features of the data could not be identified to determine whether Sn site vacancies (or possibly Li substitutions) are locally ordered or random, refinements suggest that the density of vacancies/substitutions is relatively low.

The hydrated material measured at the synchrotron had a lower water content compared to the samples of the Rietveld refinement, due to drying during transport to the synchrotron. The layer distance of 9 Å associated with a bilayer of water was observed, but with lower relative intensity compared to the non-hydrated basal reflection in the same dataset. However, a significant SAXS signal increasing toward the Q_{min} ($= 0.4 \text{ \AA}^{-1}$) of the measurement was observed, which did not

appear in the dried sample. This may suggest smaller domain sizes in the hydrated samples or possibly scattering effects due to other microstructural effects such as delamination.

Transport properties

Conductivity measurements

The electrical properties of Li-TS are distinct from the parental $\text{Li}_{0.8}\text{Sn}_{0.8}\text{S}_2$ ²⁶ and SnS_2 ⁵⁶, but similar to the properties of $\text{Li}_{0.8}\text{Sn}_{0.8}\text{S}_2$ hydrates.²⁷ To assess the ion conduction properties of dry Li-TS first, a pellet pressed from fine ground powder was measured under argon flow (cf. SI section 7.1 and Figure S26). The obtained EIS semicircles are severely depressed and are not well-described with a single Par(R, CPE) equivalent circuit (R: resistance, CPE: constant phase element).

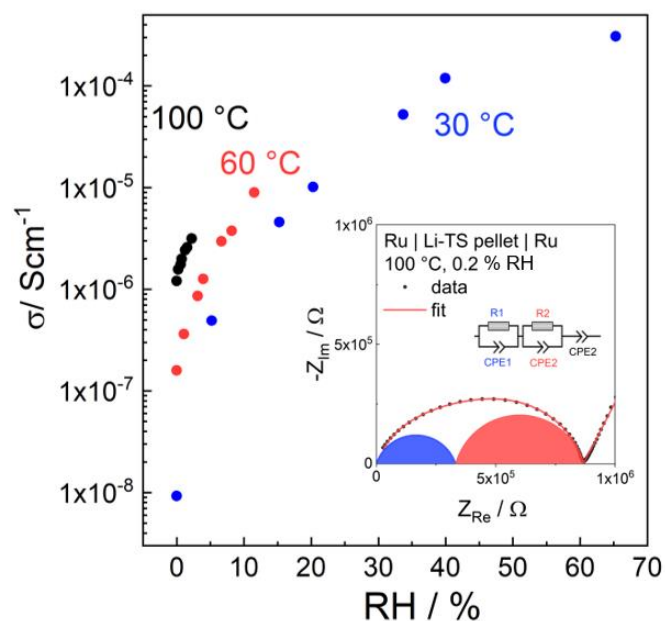


Figure 4. Total ionic conductivity of a Li-TS pellet as a function of relative humidity at varying temperatures (30, 60 and 100 °C) clearly shows a large impact of hydration. The inset shows the impedance spectrum at 100 °C and low RH. For these measurements, sputtered ruthenium was used to contact the pelletized samples.

Regarding the structural analysis of Li-TS and comparing it with the parental compound $\text{Li}_{0.8}\text{Sn}_{0.8}\text{S}_2$, one might still expect the dominant mobile charge carrier to be Li defects after exfoliation. However, the increased complexity of the granular microstructure and structural disorder suggest prominent changes in diffusion paths, which directly affect the relaxation times. Therefore, rather than one defined process, we should consider a distribution of relaxation times for this system, which explains the severe depression of the observed EIS arc and requires a fitting with two Par(R, CPE) elements in series (cf. Figure S26). Hence, we will only consider the total (DC) resistance of the sample (i.e. the intercept of the semicircle with the Z_{re} axis at low frequencies), $R_1+R_2=R_{tot}$, corresponding to the total conductivity $\sigma = d/(AR_{tot})$ with d being the thickness and A the area of the sample. The conductivity of dry Li-TS has an activation energy of (0.55 ± 0.2) eV and a room temperature magnitude of $(3.4 \pm 0.5) \times 10^{-8}$ S cm^{-1} . This conductivity is lower than in the parent $\text{Li}_{0.8}\text{Sn}_{0.8}\text{S}_2$ compound ($<10^{-5}$ S cm^{-1}), probably caused by the depletion of lithium-ions in restacked Li-TS as well as structural changes.

Furthermore, the restacked Li-TS shows ion conducting properties which are intriguingly sensitive to the humidity of the environment. Li-TS was measured as a function of water vapor pressure ($p_{\text{H}_2\text{O}}$) at temperatures ranging from 30-100 °C in Figure S27. At high temperatures and low humidities ($\leq 2\%$ RH at 100 °C, $\leq 25\%$ RH at 60 and 30 °C) the same (R)(CPE)-(R)(CPE)-CPE model as for the dry Li-TS can be applied (inset in Figure 5). However, upon a certain degree of hydration of the pellet (Figure 6b, starting from a RH of 15 % at 60 °C) the semicircle is fit only by one R-CPE element with a dielectric constant of 50 (being similar to the species with the low dielectric constant in dry Li-TS). Figure 5 shows the large impact of the hydration on the ionic conductivity at varying temperatures. At 30 °C, the conductivity increases by several orders of magnitude from 10^{-8} to 10^{-4} S cm $^{-1}$, which is much more drastically than at 100 °C. Since the structural characterization showed that water incorporates in the bulk of the material, the strong increase in conductivity is enabled by incorporated H $_2$ O. Since the interaction of lithium-ions with the anionic Sn-S layers is screened by the coordination with water, we assume an increase in mobility of the lithium-ions leading to the high ionic conductivities. At 100 °C the humidity is low, consequently, only a small amount of water incorporates into the structure, leading only to a small increase in conductivity. Even though the formation of a surface layer which becomes conducting under very humid conditions, especially at low temperatures, is possible, the dominance of bulk conduction is supported from the structural analysis and surface effects were therefore neglected. Nevertheless, we cannot entirely rule out the formation of new mobile carriers, such as protons and hydroxide ions, that could contribute to the ionic conductivity (besides Li $^+$), and/or a more complex underlying transport mechanism (SI 7.1). Hydroxyl substituted Sn-S is in principle capable of acid/base chemistry, but a change in pH of the nanosheets suspension during exfoliation and restacking lead only to a decrease in observed conductivity. As stated below, probing these non-structural charge carriers is challenging and NMR (*vide infra*) shows no additional signal for protons or hydroxides in the hydrated state making a detection of the influence of additional charge carriers not feasible.

To probe the dimensionality of ion transport, which is often preferred in the lateral plane of the nanosheets, as observed in other restacked and single layer materials^{21,22}, a foil-like free-standing film of Li-TS was measured using in-plane and out-of-plane geometries and compared to a pellet with a random orientation of layers (cf. Figure S28). To ensure full hydration, the samples were exposed to 100% RH and equilibrated for 24 h at RT. The in-plane conductivity exceeds the out-of-plane conductivity by more than two orders of magnitude, indicating facile transport along the layers. This suggests that the lithium cations move easily through the water-filled space between the Sn-S layers, but have limited opportunity to move perpendicular to the layers from one interlayer gallery to the one below or above. Remarkably, Li-TS films show ionic conductivity in the temperature range down to -25 °C as shown in Figure S29, i.e., below the freezing point of water, without any sharp change in value. This points to a melting point depression for water as observed in other nanoporous and nanoconfined 2D systems.⁵⁷⁻⁵⁹ The pellet sample measured under these conditions has a conductivity of 0.1 mS cm $^{-1}$, which is lower than the conductivity in the in-plane but higher than in the out-of-plane orientation of the free-standing film. This is consistent with a mixed orientation of layers decreasing the conductivity.

To probe even thinner Li-TS films and to enhance the mechanical stability, Li-TS was coated onto an alumina substrate. The ionic conductivity as a function of relative humidity of the film on the substrate is presented in Figure 6 in comparison to the pellet measurement at 30 °C. With

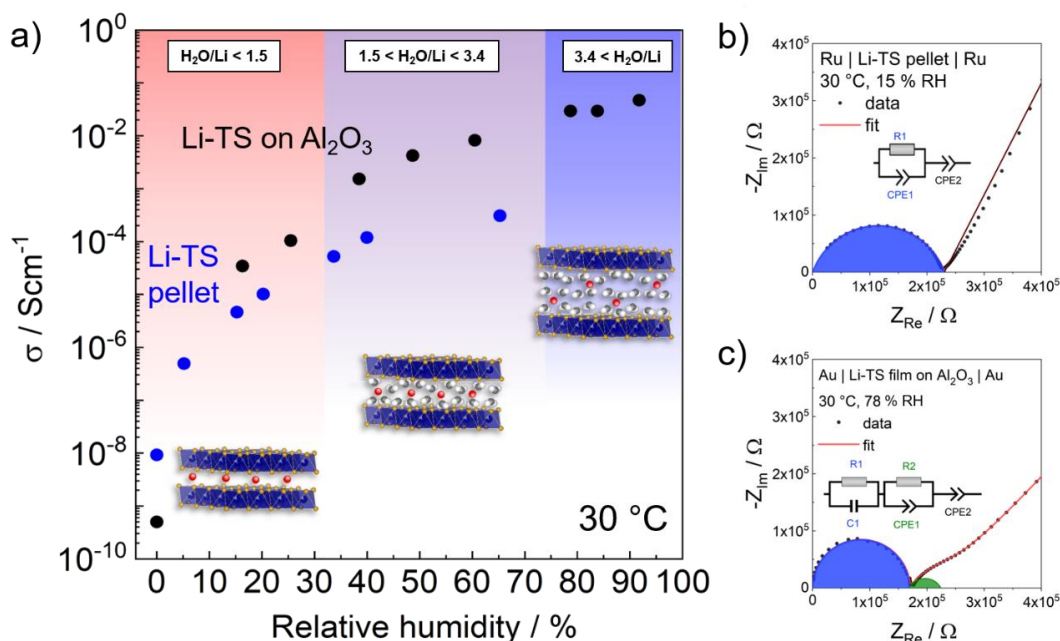


Figure 5. a) Ionic conductivity as a function of relative humidity at 30 °C of the restacked nanosheet thin film on Al₂O₃ in comparison to the pellet. With increasing water content the ionic conductivity increases by orders of magnitude. b) Impedance spectrum of the Li-TS pellet at 30 °C at medium RH showing only one semicircle. c) Impedance spectrum of a Li-TS thin film on a Al₂O₃ substrate at 30 °C and high RH. The pelletized samples were measured using sputtered ruthenium, whereas the films were measured using sputtered gold or platinum as contacts.

increasing relative humidity (16 to 92 % RH), the resistance of the thin film on alumina drops and the in-plane ionic conductivity increases drastically over three orders of magnitude from $\sigma_{EIS} = 0.03\text{--}47 \text{ mS cm}^{-1}$. Figure 6c shows a representative impedance spectrum fitted with the given model to extract the resistance of the spectrum. The model includes one Par(R, C) in series to another Par(R, CPE) to account for the high (R1 and C1) and low (R2 and CPE1) frequency semicircles that are attributed to the bulk properties and contributions from processes at the electrode, respectively. The polarization of ions at the interface of the blocking electrode was modelled by CPE2. The ionic conductivity (σ_{EIS}) is calculated from impedance spectra by applying $\sigma_{EIS} = l/(AR_1)$ with l being the distance between the electrodes, A the surface area of the sample calculated from the length of the electrode and the thickness of the film (cf. Figure 1 and values in SI Table 5), and R_1 .⁶⁰

On thin films some transport of charge carriers on the surface could influence the EIS measurement, but as water clearly incorporates into the structure as shown above and the measurements of the pellet suggests, we attribute the measured conductivity to the bulk process within the film. The conductivity (cf. Figure 6) can be roughly assigned to three regimes associated with an increased H₂O/Li ratio deduced from TGA measurements (Figure S6b and c): with increasing H₂O/Li ratio the conductivity increases. In the regime with $3.4 < \text{H}_2\text{O/Li}$ a maximum conductivity of 47 mS cm^{-1} can be found at 92 % RH. It is on par with state-of-the-art solid lithium-

ion conductors.⁶¹ The activation energy of the thin film on alumina in the regime with $3.4 < \text{H}_2\text{O}/\text{Li}$ of 0.29 eV as measured at 76 % RH in the temperature range of 45-70 °C (cf. Figure S30) is very similar to the activation energy of the $\text{Li}_{0.8}\text{Sn}_{0.8}\text{S}_2$ -hydrates and lithium montmorillonite, and only slightly smaller than in sodium vermiculite (0.50 eV).^{27, 62, 63} Notably, the out-of-plane activation energy of 0.27 eV, determined from the measurement (Figure S29) at 76 % RH, is very similar to the activation energy of the in-plane measurement. The in-plane conductivity of 9 mS cm^{-1} of the free-standing film is a factor of three smaller than the film on a substrate. This might be an effect of the more heterogeneous microstructure or increased thickness (factor 10-30) of the free-standing films in comparison to the very uniform thin-films on a substrate.

Diffusion study by PFG NMR

Having established a high ionic conductivity of hydrated Li-TS nanosheet films, the nature of ionic charge carriers cannot be unambiguously resolved by EIS. Measurements with ion blocking electrodes cannot distinguish between different ionic charge carriers (e.g., Li^+ or H^+), while the use of Li metal as a Li-selective electrode proved impossible due to decomposition of Li in the presence of water. Likewise, proton conducting materials such as Nafion are known to also conduct lithium-ions.⁶⁴ The use of an aqueous lithium salt solution as done by Raidongia *et al.*¹⁶ was not feasible since the restacked Li-TS nanosheets redisperse in solution. Thus, to further elucidate the type of charge carriers and the corresponding diffusivities, ^7Li and ^1H pulsed field gradient NMR was applied on powder samples. Similar to EIS, PFG NMR probes the long range ion dynamics of a sample. PFG NMR measures diffusion processes in the 10-100 ms regime on a μm length scale (*vide infra*) and EIS measures the conduction of ions in a time domain of 1×10^{-6} -100 s over the whole sample thickness (mm length scale). PFG NMR has already been used for investigating the mobility of lithium-ions and water in a variety of materials such as carbon nanotubes,⁶⁵ organo-functionalized GO,⁶⁶ hydrated zeolites,^{67, 68} liquid and solid lithium-ion conductors,⁶⁹⁻⁷³ among others.

All of the following ^7Li and ^1H PFG NMR measurements were conducted on the same sample to elucidate the interplay of lithium-ions with the adsorbed water. In the dry state, where the conductivity is very low $< 10^{-7} \text{ S cm}^{-1}$, no measurable diffusion of ^7Li or ^1H was found by PFG NMR. In the hydrated state, the typical signal of adsorbed mobile water is visible at 4.57 ppm in the ^1H MAS NMR in Figure S3b. Due to a lack of detectable protonic charge carriers (6.5-7 ppm),⁷⁴⁻⁷⁶ a contribution of protons to the conductivity is neglected for the interpretation of the data and we assume molecular water to be the dominant mobile species. The PFG NMR data, after exposure to 100 % RH for a week (42 wt% H_2O), show a similar behavior for water and lithium-ions following a biexponential decay (cf. Figure 7). In general, PFG NMR probes the self-diffusion of a nucleus by measuring the attenuation of the static NMR signal as a function of the field gradient strength g . While a mono-exponential decay is expected for a single diffusing species with a 3D trajectory, our data cannot be explained based on this simple model (long dashed lines in Figure 7). Assuming 2D diffusion as observed by PFG NMR for layered zirconium beryllium hydrides^{77, 78} and the parent lattice hydrates of $\text{Li}_{0.6}[\text{Li}_{0.2}\text{Sn}_{0.8}\text{S}_2]$ ²⁸ also does not reproduce our data satisfactorily (dashed curved lines in Figure 7). A reasonably good fit for both the ^7Li and ^1H data was obtained only by using a bi-exponential model including two distinct diffusion coefficients. The population distribution of the diffusion coefficients is roughly 20 to 80 % (SI Figure 31) for both nuclei. Due to differences in

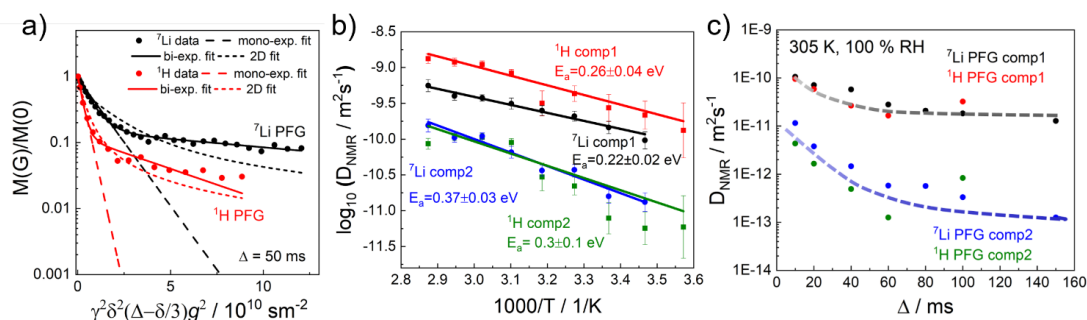


Figure 6. a) The bi-exponential fit of the ^1H and ^7Li attenuation curves of the normalized peak area as a function of $(\gamma^2\delta^2(\Delta-\delta/3)g^2)$ in 10^{10}sm^{-2} compared to a mono-exponential decay and to the 2D diffusion model according to Stoll *et al.*^{77,78}. b) Diffusion coefficients of all components extracted from ^1H and ^7Li PFG NMR data. The diffusivity of ^1H is of the same order of magnitude as that of ^7Li . c) The diffusion coefficients of components 1 only slightly depend on the diffusion time Δ , but components 2 show a stronger dependence, indicating some sort of inhibition on a larger distance.

the relaxation behavior of the different nuclei, quantification of PFG NMR data is inherently difficult. Nevertheless, the existence of two diffusing species is supported by the ratio of 7 % for the peak at 0.95 ppm (minority species, 20 % in PFG NMR) and 93 % for the peak 0.26 ppm (majority species, 80 % in PFG NMR) in the ^6Li MAS spectrum Figure 4. From here on we refer to the diffusion coefficients originating from the majority species as component 1 and the ones of the minority species as component 2 for both ^7Li and ^1H diffusivity measurements. The higher diffusion coefficient (component 1) always stems from the majority species. Variable temperature ^7Li MAS measurements show a slow exchange of the two species. Therefore, the origin of the bi-exponential decay in the PFG data can be attributed to the presence of two independent, mobile lithium species in the sample, which is in agreement with the presence of both hydrated and non-hydrated Li species from structural analysis (Figure 4b). An alternative interpretation of the observed bi-exponential decay follows the model of Osti *et al.*⁷⁹ (visualized in Figure 4d), which was developed for different diffusion coefficients of water in nanoconfined spaces, e.g., in vermiculite clays. The water interacting with the wall is significantly slowed down in comparison to fast water in the middle of the confined space. However, observing a similar bi-exponential decay for ^1H and ^7Li suggests a coupled movement of lithium-ions and water similar to the movement of sodium ions with their hydration sphere in vermiculite.⁶³ In the latter case, water coordinates the sodium ions between the $\text{SiO}_2 - \text{Al}_2\text{O}_3$ layers and sodium ions move by dragging their hydration shells along (i.e., their motion is accompanied by water motion). In restacked Li-TS, the high diffusion coefficients of the majority species (component 1) at 305 K are of the same order of magnitude for both nuclei: $D_{\text{H}_2\text{O}} = 4.3 \times 10^{-10} \text{m}^2\text{s}^{-1}$ is two times higher than D_{Li^+} , which is $2.1 \times 10^{-10} \text{m}^2\text{s}^{-1}$.

The value for $D_{\text{H}_2\text{O}}$ is very close to diffusivities observed for water in Li-vermiculite⁸⁰ ($D_{\text{H}_2\text{O}} = 3.4 \times 10^{-10} \text{m}^2\text{s}^{-1}$) and Li-montmorillonite⁸¹ ($D_{\text{H}_2\text{O}} = 4 \times 10^{-10} \text{m}^2\text{s}^{-1}$), which also show 2D confinement of water and have alkali cations between anionic layers. Unfortunately, the diffusion coefficients of the alkali cations were not measured in that study. The diffusion coefficients of a sample exposed to 100 % RH for a shorter period of time (1 d (identical to EIS samples) vs 1 week) are slightly lower and almost identical for both nuclei (see Figure S32). Apparently, interlayer water gradually becomes more bulk like, and the diffusion coefficient of water approaches the value of water in 1 M LiCl (of $D_{\text{H}_2\text{O}} = 1.73 \times 10^{-9} \text{m}^2\text{s}^{-1}$).

However, D_{Li^+} exceeds the diffusivity of lithium-ions in the hydrated zeolite LiLSX and in Li- β -alumina single crystals as determined by PFG NMR by one order of magnitude.^{67, 68, 82} Of note, the D_{Li^+} value is also two times higher than the diffusion coefficient of the fully hydrated $Li_{0.8}Sn_{0.8}S_2$ ²⁷, very similar to the diffusion coefficient of lithium observed for a LiCl solution in Nafion⁶⁴, and only slightly lower than free lithium-ions in 1M LiCl solution ($8.0 \times 10^{-10} \text{ m}^2 \text{ s}^{-1}$).

The low diffusion coefficients of ^7Li and ^1H component 2 at 305 K in Figure 7b are of similar magnitude with $D_{H_2O} = 2.1 \times 10^{-11} \text{ m}^2 \text{ s}^{-1}$ and $D_{Li^+} = 3.7 \times 10^{-11} \text{ m}^2 \text{ s}^{-1}$, and ca. one order of magnitude lower than component 1. The diffusion coefficients of ^7Li and ^1H as a function of temperature show an activation energy of 0.24 eV for the fast species and 0.4 eV for the slow species. The lower activation energy is close to the activation energy determined by EIS. A variation of gradient spacings and, hence, diffusion times Δ (Figure 7c), results in very similar diffusion coefficients. This is particularly the case for the fast-diffusing species, indicating essentially free lithium diffusion unimpeded by grain boundaries. This suggests a continuous diffusion path for hydrated Li throughout the sample. The slow species is impeded much more, possibly due to confinement within dry regions of the sample. The behavior of the ^1H diffusion coefficients with Δ is extremely similar to that of the ^7Li coefficients, further strengthening the assumption of a water-assisted transport of lithium. The isotropic displacement calculated by $r_{rms} = \sqrt{2D_{NMR}\Delta}$ results in 4-6 μm for ^7Li and ^1H (component 1) and 1.5-2 μm for component 2. This distance spans several layers and is thus consistent with lithium-ion transport through the bulk of the material.

To evaluate whether the diffusion data probe the same process as the EIS measurements, the NMR conductivity (σ_{NMR}) was calculated based on the Nernst-Einstein equation $\sigma_{NMR} = D_{NMR}^{tr} n z^2 e^2 / k_B T$ with n being the charge carrier concentration, e the elementary charge, k_B the Boltzmann constant, and T the temperature using the diffusion coefficient D_{NMR}^{tr} obtained by PFG NMR (details see in SI section). Assuming a lithium content of roughly 40 % relative to the initial lithium content in the parental $Li_{0.8}Sn_{0.8}S_2$ based on ICP analysis, $n = 4.6 \times 10^{27} \text{ m}^{-3}$ is obtained. To account for the increase in interlayer spacing (d) upon hydration (dilution of charge carrier concentration), n is multiplied with $d_{dry-Li-TS} / d_{hydrated-Li-TS}$. From this, the conductivity is calculated as a weighted sum of the fast species with D_{comp1} (93 %) and the slow species with D_{comp2} (7 %) by $\sigma_{NMR} = (D_{comp1} n_{comp1} z^2 + D_{comp2} n_{comp2} z^2) e^2 / k_B T$. In this way, a σ_{NMR} of roughly 20 mS cm^{-1} is obtained, which is in good agreement with the in-plane conductivity obtained from EIS. We therefore conclude that (i) most of the lithium-ions contribute to the in-plane conduction, and (ii) PFG NMR probes the same long-range transport phenomenon as EIS. Our findings are consistent with lithium-ions being the dominant charge carriers and possible proton or hydroxide conduction is judged to be minor.

Conclusions

In summary, we elucidated the exfoliation of $Li_{0.8}Sn_{0.8}S_2$ in water and determined the chemical composition of the restacked Li-TS material, which is clearly distinct from the parental $Li_{0.8}Sn_{0.8}S_2$ and SnS_2 . The number of lithium-ions is severely decreased and spectroscopic analysis suggests the incorporation of hydroxyl groups into sulfur vacancies during exfoliation. We established a 3D structural model based on XRPD and PDF analyses for the highly disordered restacked Li-TS. The structure forms through turbostratic stacking of layers, where the relative orientation of neighboring layers can be classified as akin to either $Li_{0.8}Sn_{0.8}S_2$ (C19, CdCl_2 -type) or SnS_2 (C6, CdI_2 -

type), depending on the local presence or absence of lithium-ions. Upon hydration, the increase in the stacking distance can be explained by the incorporation of water coordinating the lithium-ions. However, a fraction of material remains in the dry state or contains lithium depleted SnS_2 -type regions. The presence of these different phases gives rise to different lithium-ion hydration states between the layers. By impedance spectroscopy, we show an increase of lithium-ion conductivity over several orders of magnitude upon hydration and a preferred conduction in the in-plane direction of the layers. That increase is presumably caused by the screening of the interaction of the lithium-ions with the anionic Sn-S layers by the incorporated water molecules enhancing the lithium-ion mobility. Furthermore, by PFG NMR, we show that the high conductivity upon hydration results from mainly co-diffusion of water and lithium-ions. PFG NMR was applied to follow the lithium-ion diffusion in nanosheets for the first time and the similar, fast diffusion coefficients $D_{\text{Li}^+} = 2.1 \times 10^{-10} \text{ m}^2 \text{ s}^{-1}$ and $D_{\text{H}_2\text{O}} = 4.3 \times 10^{-10} \text{ m}^2 \text{ s}^{-1}$ at 305 K indicate a coupled movement of lithium-ions and water. This points to water-assisted lithium-ion conduction possibly similar to sodium ion conduction in vermiculite.^{63, 83} Besides, the presence of both highly mobile and fairly immobile lithium-ion species observed by PFG is rationalized by the distribution of lithium-ions between hydrated and non-hydrated states in restacked Li-TS.

In conclusion, despite the differences in composition and a high degree of disorder, the fast water-assisted lithium-ion conduction observed in the parental $\text{Li}_{0.8}\text{Sn}_{0.8}\text{S}_2$ is persevered in Li-TS after restacking. Moreover, the exfoliation process allows the fabrication of large oriented thin films exhibiting an even faster lithium-ion conduction of up to 47 mS cm^{-1} in the in-plane direction of the layers. Thus, our study shows that alkali cations in restacked 2D Li-TS nanosheets are highly mobile depending on their hydration state, and sheds light on the role of water-assisted lithium-ion transport in this 2D system.

Supporting Information

Includes additional powder X-ray diffraction data, PDF data as well as explanations and details on the refinement models, thermal analysis, elemental analysis, ICP and EDX measurements and SEM micrographs, and additional impedance measurements and PFG NMR data

Author Contributions

A-KH, NMV-B and BL conceived and designed this study. A-KH conducted the synthesis and was responsible for measuring IR/Raman spectroscopy, PXRD and EIS. IM measured MAS and PFG NMR. ME and MT performed the synchrotron PXRD and PDF measurements. BS and MT performed the modelling of the PXRD and PDF data. MJ performed additional EIS measurements. A-KH analyzed all EIS and NMR data. The manuscript was written through contributions of A-KH, SB, MT and MJ. NMV-B, RED and BVL revised the manuscript. All authors have given approval to the final version of the manuscript.

Funding Sources

Financial support was granted by the German Federal Ministry of Research and Education (BMBF), project 03XP0177B (FestBatt) and the Center for NanoScience (CeNS). MWT gratefully acknowledges support from BASF. We acknowledge DESY (Hamburg, Germany), a member of the Helmholtz Association HGF, for the provision of experimental facilities. Parts of this research were carried out at beamline P02.1.

Acknowledgement

J. Blahusch for TGA measurements and V. Duppel and C. Minke for SEM/EDX analysis. J. Obel and M.-L. Schreiber for ICP-OES and EA measurements and A. Muenchinger for supporting the PFG measurements. K. Mechlem for support during python coding. G. Majer, H.-D. Kreuer, R. Usiskin, and S. Harm for fruitful discussions.

References

- [1] Nicolosi, V.; Chhowalla, M.; Kanatzidis, M. G.; Strano, M. S.; Coleman, J. N., Liquid Exfoliation of Layered Materials. *Science* **2013**, *340* (6139), 1226-1229.
- [2] Augustyn, V.; Gogotsi, Y., 2D Materials with Nanoconfined Fluids for Electrochemical Energy Storage. *Joule* **2017**, *1* (3), 443-452.
- [3] Zhu, Y.; Murali, S.; Cai, W.; Li, X.; Suk, J. W.; Potts, J. R.; Ruoff, R. S., Graphene and Graphene Oxide: Synthesis, Properties, and Applications. *Adv. Mater.* **2010**, *22* (35), 3906-3924.
- [4] Bhimanapati, G. R.; Lin, Z.; Meunier, V.; Jung, Y.; Cha, J.; Das, S.; Xiao, D.; Son, Y.; Strano, M. S.; Cooper, V. R.; Liang, L.; Louie, S. G.; Ringe, E.; Zhou, W.; Kim, S. S.; Naik, R. R.; Sumpter, B. G.; Terrones, H.; Xia, F.; Wang, Y.; et al., e., Recent Advances in Two-Dimensional Materials beyond Graphene. *ACS Nano* **2015**, *9* (12), 11509-11539.
- [5] Butler, S. Z.; Hollen, S. M.; Cao, L.; Cui, Y.; Gupta, J. A.; Gutiérrez, H. R.; Heinz, T. F.; Hong, S. S.; Huang, J.; Ismach, A. F.; Johnston-Halperin, E.; Kuno, M.; Plashnitsa, V. V.; Robinson, R. D.; Ruoff, R. S.; Salahuddin, S.; Shan, J.; Shi, L.; et al., e., Progress, Challenges, and Opportunities in Two-Dimensional Materials Beyond Graphene. *ACS Nano* **2013**, *7* (4), 2898-2926.
- [6] Chhowalla, M.; Shin, H. S.; Eda, G.; Li, L.-J.; Loh, K. P.; Zhang, H., The chemistry of two-dimensional layered transition metal dichalcogenide nanosheets. *Nat. Chem.* **2013**, *5*, 263.
- [7] Sun, P.; Ma, R.; Sasaki, T., Recent progress on exploring exceptionally high and anisotropic H⁺/OH⁻ ion conduction in two-dimensional materials. *Chem. Sci.* **2018**, *9* (1), 33-43.
- [8] Weber, D.; Schoop, L. M.; Duppel, V.; Lippmann, J. M.; Nuss, J.; Lotsch, B. V., Magnetic Properties of Restacked 2D Spin 1/2 honeycomb RuCl₃ Nanosheets. *Nano Lett.* **2016**, *16* (6), 3578-3584.
- [9] Huo, C.; Yan, Z.; Song, X.; Zeng, H., 2D materials via liquid exfoliation: a review on fabrication and applications. *Sci. Bull.* **2015**, *60* (23), 1994-2008.
- [10] Kühne, M.; Paolucci, F.; Popovic, J.; Ostrovsky, P. M.; Maier, J.; Smet, J. H., Ultrafast lithium diffusion in bilayer graphene. *Nat. Nanotechnol.* **2017**, *12*, 895.
- [11] Esfandiari, A.; Radha, B.; Wang, F. C.; Yang, Q.; Hu, S.; Garaj, S.; Nair, R. R.; Geim, A. K.; Gopinadhan, K., Size effect in ion transport through angstrom-scale slits. *Science* **2017**, *358* (6362), 511-513.
- [12] Gopinadhan, K.; Hu, S.; Esfandiari, A.; Lozada-Hidalgo, M.; Wang, F. C.; Yang, Q.; Tyurnina, A. V.; Keerthi, A.; Radha, B.; Geim, A. K., Complete steric exclusion of ions and proton transport through confined monolayer water. *Science* **2019**, *363* (6423), 145-148.
- [13] Radha, B.; Esfandiari, A.; Wang, F. C.; Rooney, A. P.; Gopinadhan, K.; Keerthi, A.; Mishchenko, A.; Janardanan, A.; Blake, P.; Fumagalli, L.; Lozada-Hidalgo, M.; Garaj, S.; Haigh, S. J.; Grigorieva, I. V.; Wu, H. A.; Geim, A. K., Molecular transport through capillaries made with atomic-scale precision. *Nature* **2016**, *538* (7624), 222-225.
- [14] Mouterde, T.; Keerthi, A.; Poggioli, A. R.; Dar, S. A.; Siria, A.; Geim, A. K.; Bocquet, L.; Radha, B., Molecular streaming and its voltage control in ångström-scale channels. *Nature* **2019**, *567* (7746), 87-90.
- [15] Joshi, R. K.; Carbone, P.; Wang, F. C.; Kravets, V. G.; Su, Y.; Grigorieva, I. V.; Wu, H. A.; Geim, A. K.; Nair, R. R., Precise and Ultrafast Molecular Sieving Through Graphene Oxide Membranes. *Science* **2014**, *343* (6172), 752-754.
- [16] Raidongia, K.; Huang, J., Nanofluidic Ion Transport through Reconstructed Layered Materials. *J. Am. Chem. Soc.* **2012**, *134* (40), 16528-16531.
- [17] Karim, M. R.; Hatakeyama, K.; Matsui, T.; Takehira, H.; Taniguchi, T.; Koinuma, M.; Matsumoto, Y.; Akutagawa, T.; Nakamura, T.; Noro, S.-i.; Yamada, T.; Kitagawa, H.; Hayami, S., Graphene Oxide Nanosheet with High Proton Conductivity. *J. Am. Chem. Soc.* **2013**, *135* (22), 8097-8100.

- [18] Jiang, G.; Goledzinowski, M.; Comeau, F. J. E.; Zarrin, H.; Lui, G.; Lenos, J.; Veileux, A.; Liu, G.; Zhang, J.; Hemmati, S.; Qiao, J.; Chen, Z., Free-Standing Functionalized Graphene Oxide Solid Electrolytes in Electrochemical Gas Sensors. *Adv. Funct. Mater.* **2016**, *26* (11), 1729-1736.
- [19] Borini, S.; White, R.; Wei, D.; Astley, M.; Haque, S.; Spigone, E.; Harris, N.; Kivioja, J.; Ryhänen, T., Ultrafast Graphene Oxide Humidity Sensors. *ACS Nano* **2013**, *7* (12), 11166-11173.
- [20] Hatakeyama, K.; Karim, M. R.; Ogata, C.; Tateishi, H.; Funatsu, A.; Taniguchi, T.; Koinuma, M.; Hayami, S.; Matsumoto, Y., Proton Conductivities of Graphene Oxide Nanosheets: Single, Multilayer, and Modified Nanosheets. *Angew. Chem. Int. Ed. Engl.* **2014**, *126* (27), 7117-7120.
- [21] Shao, J.-J.; Raidongia, K.; Koltonow, A. R.; Huang, J., Self-assembled two-dimensional nanofluidic proton channels with high thermal stability. *Nat. Commun.* **2015**, *6*, 7602.
- [22] Sun, P.; Ma, R.; Bai, X.; Wang, K.; Zhu, H.; Sasaki, T., Single-layer nanosheets with exceptionally high and anisotropic hydroxyl ion conductivity. *Sci. Adv.* **2017**, *3* (4), 1602629.
- [23] Ganter, P.; Szendrei, K.; Lotsch, B. V., Towards the Nanosheet-Based Photonic Nose: Vapor Recognition and Trace Water Sensing with Antimony Phosphate Thin Film Devices. *Adv. Mater.* **2016**, *28* (34), 7436-7442.
- [24] Szendrei, K.; Ganter, P.; Sánchez-Sobrado, O.; Eger, R.; Kuhn, A.; Lotsch, B. V., Touchless Optical Finger Motion Tracking Based on 2D Nanosheets with Giant Moisture Responsiveness. *Adv. Mater.* **2015**, *27* (41), 6341-6348.
- [25] Deniard-Courant, S.; Piffard, Y.; Barboux, P.; Livage, J., Relative humidity influence on the water content and on the protonic conductivity of the phosphatoantimonic acids $HnSbnP2O3n+5, xH2O$ ($n = 1, 3, 5$). *Solid State Ion.* **1988**, *27* (3), 189-194.
- [26] Holzmann, T.; Schoop, L. M.; Ali, M. N.; Moudrakovski, I.; Gregori, G.; Maier, J.; Cava, R. J.; Lotsch, B. V., $Li0.6[Li0.2Sn0.8S2]$ - a layered lithium superionic conductor. *Energy Environ. Sci.* **2016**, *9* (8), 2578-2585.
- [27] Joos, M.; Schneider, C.; Münchinger, A.; Moudrakovski, I.; Usiskin, R.; Maier, J.; Lotsch, B. V., Impact of hydration on ion transport in $Li2Sn2S5-xH2O$. *Journal of Materials Chemistry A* **2021**, DOI: 10.1039/D1TA04736A.
- [28] Holzmann, T. Investigations on the Structure, Exfoliation Behavior and Electronic Properties of Layered Tin Sulfides. Ph.D. Thesis, LMU, Munich, Germany, 2016.
- [29] Kuhn, A.; Holzmann, T.; Nuss, J.; Lotsch, B. V., A facile wet chemistry approach towards unilamellar tin sulfide nanosheets from $Li4xSn1-xS2$ solid solutions. *J. Mater. Chem. A* **2014**, *2* (17), 6100-6106.
- [30] Szendrei-Temesi, K.; Sanchez-Sobrado, O.; Betzler, S. B.; Durner, K. M.; Holzmann, T.; Lotsch, B. V., Lithium Tin Sulfide—a High-Refractive-Index 2D Material for Humidity-Responsive Photonic Crystals. *Adv. Funct. Mater.* **2018**, *28* (14), 1705740.
- [31] Coelho, A. A., TOPAS and TOPAS-Academic: an optimization program integrating computer algebra and crystallographic objects written in C++. *J. Appl. Crystallogr.* **2018**, *51* (1), 210-218.
- [32] Chupas, P. J.; Qiu, X.; Hanson, J. C.; Lee, P. L.; Grey, C. P.; Billinge, S. J. L., Rapid-acquisition pair distribution function (RA-PDF) analysis. *J. Appl. Crystallogr.* **2003**, *36* (6), 1342-1347.
- [33] Hammersley, A. P.; Svensson, S. O.; Hanfland, M.; Fitch, A. N.; Hausermann, D., Two-dimensional detector software: From real detector to idealised image or two-theta scan. *High Press. Res.* **1996**, *14* (4-6), 235-248.
- [34] Juhás, P.; Davis, T.; Farrow, C. L.; Billinge, S. J. L., PDFgetX3: a rapid and highly automatable program for processing powder diffraction data into total scattering pair distribution functions. *J. Appl. Crystallogr.* **2013**, *46* (2), 560-566.
- [35] Yang, X.; Juhas, P.; Farrow, C. L.; Billinge, S. J. L., xPDFsuite: an end-to-end software solution for high throughput pair distribution function transformation, visualization and analysis. *arXiv* **2014**, 1402.3163.
- [36] Farrow, C. L.; Juhas, P.; Liu, J. W.; Bryndin, D.; Bozin, E. S.; Bloch, J.; Proffen, T.; Billinge, S. J., PDFfit2 and PDFgui: computer programs for studying nanostructure in crystals. *J. Phys. Condens. Matter* **2007**, *19* (33), 335219.
- [37] Juhás, P.; Farrow, C. L.; Yang, X.; Knox, K. R.; Billinge, S. J., Complex modeling: a strategy and software program for combining multiple information sources to solve ill posed structure and nanostructure inverse problems. *Acta Crystallogr. A Found. Adv.* **2015**, *71* (Pt 6), 562-8.
- [38] P. W. Winston, D. H. B., Saturated Solutions for the Control of Humidity in Biological Research. *Ecology* **1960**, *41*, 232-237.
- [39] L. Greenspan, J. R., Humidity Fixed Points of Binary Saturated Aqueous Solutions. *J. Res. Natl. Bur. Stand* **1977**, *81A*, 89-96.

- [40] Harris, R. K.; Becker, E. D.; Cabral De Menezes, S. M.; Granger, P.; Hoffman, R. E.; Zilm, K. W., Further conventions for NMR shielding and chemical shifts IUPAC recommendations 2008. *Solid State Nucl. Magn. Reson.* **2008**, *33* (3), 41-56.
- [41] Massiot, D.; Fayon, F.; Capron, M.; King, I.; Le Calvé, S.; Alonso, B.; Durand, J.-O.; Bujoli, B.; Gan, Z.; Hoatson, G., Modelling one- and two-dimensional solid-state NMR spectra. *Magn. Reson. Chem.* **2002**, *40* (1), 70-76.
- [42] Tanner, J. E., Use of the Stimulated Echo in NMR Diffusion Studies. *J. Chem. Phys.* **1970**, *52* (5), 2523-2526.
- [43] Stejskal, E. O.; Tanner, J. E., Spin Diffusion Measurements: Spin Echoes in the Presence of a Time-Dependent Field Gradient. *J. Chem. Phys.* **1965**, *42* (1), 288-292.
- [44] Liu, Y.; Kang, H.; Jiao, L.; Chen, C.; Cao, K.; Wang, Y.; Yuan, H., Exfoliated-SnS₂ restacked on graphene as a high-capacity, high-rate, and long-cycle life anode for sodium ion batteries. *Nanoscale* **2015**, *7* (4), 1325-1332.
- [45] Schöllhorn, R.; Roer, W.; Wagner, K., Topotactic formation and exchange reactions of hydrated layered tin sulfides A_x(H₂O)_ySnS₂. *Monatsh. Chem.* **1979**, *110* (5), 1147-1152.
- [46] Lefebvre-Devos, I.; Olivier-Fourcade, J.; Jumas, J. C.; Lavela, P., Lithium insertion mechanism in SnS₂. *Phys. Rev. B* **2000**, *61* (4), 3110-3116.
- [47] Rietveld, H. M., A profile refinement method for nuclear and magnetic structures. *J. Appl. Crystallogr.* **1969**, *2* (2), 65-71.
- [48] Warren, B. E., X-Ray Diffraction in Random Layer Lattices. *Phys. Rev.* **1941**, *59* (9), 693-698.
- [49] Mangelsen, S.; Srinivasan, B. R.; Schürmann, U.; Kienle, L.; Näther, C.; Bensch, W., Nanostructured tungsten sulfides: insights into precursor decomposition and the microstructure using X-ray scattering methods. *Dalton Trans.* **2019**, *48* (4), 1184-1201.
- [50] Ainsworth, C. M.; Lewis, J. W.; Wang, C.-H.; Coelho, A. A.; Johnston, H. E.; Brand, H. E. A.; Evans, J. S. O., 3D Transition Metal Ordering and Rietveld Stacking Fault Quantification in the New Oxychalcogenides La₂O₂Cu₂-4xCd₂xSe₂. *Chem. Mater.* **2016**, *28* (9), 3184-3195.
- [51] Coelho, A. A.; Evans, J. S. O.; Lewis, J. W., Averaging the intensity of many-layered structures for accurate stacking-fault analysis using Rietveld refinement. *J. Appl. Crystallogr.* **2016**, *49* (5), 1740-1749.
- [52] Le Blanc, A.; Rouxel, J., Sur les types structuraux des composés intercalaires MSnS₂ (M= Li, Na, K, Rb). *C. R. Acad. Sci. C* **1972**, *274*, 786-788.
- [53] Bette, S.; Hinrichsen, B.; Pfister, D.; Dinnebier, R. E., A routine for the determination of the microstructure of stacking-faulted nickel cobalt aluminium hydroxide precursors for lithium nickel cobalt aluminium oxide battery materials. *J. Appl. Crystallogr.* **2020**, *53* (1), 76-87.
- [54] Diehl, L.; Bette, S.; Pielhofer, F.; Betzler, S.; Moudrakovski, I.; Ozin, G. A.; Dinnebier, R.; Lotsch, B. V., Structure-Directing Lone Pairs: Synthesis and Structural Characterization of SnTiO₃. *Chem. Mater.* **2018**, *30* (24), 8932-8938.
- [55] Terban, M. W.; Shi, C.; Silbernagel, R.; Clearfield, A.; Billinge, S. J. L., Local Environment of Terbium(III) Ions in Layered Nanocrystalline Zirconium(IV) Phosphonate-Phosphate Ion Exchange Materials. *Inorg. Chem.* **2017**, *56* (15), 8837-8846.
- [56] Voznyi, A.; Kosyak, V.; Opanasyuk, A.; Tirkusova, N.; Grase, L.; Medvids, A.; Mezinskis, G., Structural and electrical properties of SnS₂ thin films. *Mater. Chem. Phys.* **2016**, *173*, 52-61.
- [57] Fukatsu, Y.; Morikawa, K.; Ikeda, Y.; Tsukahara, T., Temperature and Size Effects on Structural and Dynamical Properties of Water Confined in 1-10 nm scale Pores Using Proton NMR Spectroscopy. *Anal. Sci.* **2017**, *33* (8), 903-909.
- [58] Swenson, J.; Bergman, R.; Howells, W. S., Quasielastic neutron scattering of two-dimensional water in a vermiculite clay. *J. Chem. Phys.* **2000**, *113* (7), 2873-2879.
- [59] Bergman, R.; Swenson, J.; Börjesson, L.; Jacobsson, P., Dielectric study of supercooled 2D water in a vermiculite clay. *J. Chem. Phys.* **2000**, *113* (1), 357-363.
- [60] Dong, B. X.; Bennington, P.; Kambe, Y.; Sharon, D.; Dolejsi, M.; Strzalka, J.; Burnett, V. F.; Nealey, P. F.; Patel, S. N., Nanoscale film conductivity measurements reveal interfacial influence on ion transport in polymer electrolytes. *Mol. Syst. Des. Eng.* **2019**, *4* (3), 597-608.
- [61] Zhang, Z.; Shao, Y.; Lotsch, B.; Hu, Y.-S.; Li, H.; Janek, J.; Nazar, L. F.; Nan, C.-W.; Maier, J.; Armand, M.; Chen, L., New horizons for inorganic solid state ion conductors. *Energy Environ. Sci.* **2018**, *11* (8), 1945-1976.
- [62] García, N. J.; Bazán, J. C., Conductivity in Na⁺- and Li⁺-montmorillonite as a function of equilibration humidity. *Solid State Ion.* **1996**, *92* (1), 139-143.
- [63] Whittingham, M. S., Sodium ion conduction in single crystal vermiculite. *Solid State Ion.* **1987**, *25* (4), 295-300.

- [64] Stenina, I. A.; Sistas, P.; Rebrov, A. I.; Pourcelly, G.; Yaroslavtsev, A. B., Ion mobility in Nafion-117 membranes. *Desalination* **2004**, *170* (1), 49-57.
- [65] Liu, X.; Pan, X.; Zhang, S.; Han, X.; Bao, X., Diffusion of Water Inside Carbon Nanotubes Studied by Pulsed Field Gradient NMR Spectroscopy. *Langmuir : the ACS journal of surfaces and colloids* **2014**, *30* (27), 8036-8045.
- [66] Enotiadis, A.; Angjeli, K.; Baldino, N.; Nicotera, I.; Gournis, D., Graphene-Based Nafion Nanocomposite Membranes: Enhanced Proton Transport and Water Retention by Novel Organo-functionalized Graphene Oxide Nanosheets. *Small* **2012**, *8* (21), 3338-3349.
- [67] Beckert, S.; Stallmach, F.; Toufar, H.; Freude, D.; Kärger, J.; Haase, J., Tracing Water and Cation Diffusion in Hydrated Zeolites of Type Li-LSX by Pulsed Field Gradient NMR. *J. Phys. Chem. C* **2013**, *117* (47), 24866-24872.
- [68] Freude, D.; Beckert, S.; Stallmach, F.; Kurzhals, R.; Täschner, D.; Toufar, H.; Kärger, J.; Haase, J., Ion and water mobility in hydrated Li-LSX zeolite studied by ^1H , ^6Li and ^7Li NMR spectroscopy and diffusometry. *Micropor. Mesopor. Mat.* **2013**, *172*, 174-181.
- [69] Harm, S.; Hatz, A.-K.; Moudrakovski, I.; Eger, R.; Kuhn, A.; Hoch, C.; Lotsch, B. V., Lesson Learned from NMR: Characterization and Ionic Conductivity of LGPS-like Li_7SiPS_8 . *Chem. Mater.* **2019**, *31* (4), 1280-1288.
- [70] Kuhn, A.; Gerbig, O.; Zhu, C.; Falkenberg, F.; Maier, J.; Lotsch, B. V., A new ultrafast superionic Li-conductor: ion dynamics in $\text{Li}_{11}\text{Si}_2\text{PS}_{12}$ and comparison with other tetragonal LGPS-type electrolytes. *Phys. Chem. Chem. Phys.* **2014**, *16* (28), 14669-14674.
- [71] DiStefano, D.; Miglio, A.; Robeyns, K.; Filinchuk, Y.; Lechartier, M.; Senyshyn, A.; Ishida, H.; Spannenberger, S.; Prutsch, D.; Lunghammer, S.; Rettenwander, D.; Wilkening, M.; Røling, B.; Kato, Y.; Hautier, G., Superionic Diffusion through Frustrated Energy Landscape. *Chem* **2019**, *5* (9), 2450-2460.
- [72] Xiang, Y.-X.; Zheng, G.; Zhong, G.; Wang, D.; Fu, R.; Yang, Y., Toward understanding of ion dynamics in highly conductive lithium-ion conductors: Some perspectives by solid state NMR techniques. *Solid State Ion.* **2018**, *318*, 19-26.
- [73] Saito, Y.; Yamamoto, H.; Nakamura, O.; Kageyama, H.; Ishikawa, H.; Miyoshi, T.; Matsuoka, M., Determination of ionic self-diffusion coefficients of lithium electrolytes using the pulsed field gradient NMR. *J. Power Sources* **1999**, *81-82*, 772-776.
- [74] Ratcliffe, C. I.; Ripmeester, J. A.; Tse, J. S., NMR chemical shifts of dilute ^1H in inorganic solids. *Chem. Phys. Lett.* **1985**, *120* (4), 427-432.
- [75] Xue, X.; Kanzaki, M., Proton Distributions and Hydrogen Bonding in Crystalline and Glassy Hydrated Silicates and Related Inorganic Materials: Insights from High-Resolution Solid-State Nuclear Magnetic Resonance Spectroscopy. *J. Am. Ceram. Soc.* **2009**, *92* (12), 2803-2830.
- [76] Mastikhin, V. M.; Mudrakovsky, I. L.; Nosov, A. V., ^1H NMR magic angle spinning (MAS) studies of heterogeneous catalysis. *Prog. Nuc. Magn. Reson. Spectrosc.* **1991**, *23* (3), 259-299.
- [77] Stoll, M.; Kaess, U.; Majer, G.; Barnes, R. G., Nuclear magnetic resonance studies of hydrogen diffusion in the layer-structured system ZrClHx . *J. Alloys Compd.* **1997**, *253-254*, 435-440.
- [78] Kimmerle, F.; Majer, G.; Kaess, U.; Maeland, A. J.; Conradi, M. S.; McDowell, A. F., NMR Studies of hydrogen diffusion in $\text{ZrBe}_2\text{H}_{1.4}$. *J. Alloys Compd.* **1998**, *264* (1), 63-70.
- [79] Osti, N. C.; Coté, A.; Mamontov, E.; Ramirez-Cuesta, A.; Wesolowski, D. J.; Diallo, S. O., Characteristic features of water dynamics in restricted geometries investigated with quasi-elastic neutron scattering. *Chem. Phys.* **2016**, *465-466*, 1-8.
- [80] Poinsignon, C.; Estrade-Szwarczopf, H.; Conard, J.; Dianoux, A. J., Structure and dynamics of intercalated water in clay minerals. *Physica B: Condens. Matter* **1989**, *156-157*, 140-144.
- [81] Cebula, D. J.; Thomas, R. K.; White, J. W., Diffusion of Water in Li-Montmorillonite Studied by Quasielastic Neutron Scattering. *Clays Clay Miner.* **1981**, *29* (4), 241-248.
- [82] Chowdhury, M. T.; Takekawa, R.; Iwai, Y.; Kuwata, N.; Kawamura, J., Lithium ion diffusion in Li β -alumina single crystals measured by pulsed field gradient NMR spectroscopy. *J. Chem. Phys.* **2014**, *140* (12), 124509.
- [83] Stanley Whittingham, M., Transport properties of the mineral vermiculite. *Solid State Ion.* **1989**, *32-33*, 344-349.

4.7.1 Supporting Information for “Fast Water-Assisted Lithium Ion Conduction in Restacked Lithium Tin Sulfide Nanosheets”

Table of contents

1. Nuclear magnetic resonance	304
2. Raman/Infrared spectroscopy	306
3. Determination of element composition by EDX, ICP and combustion analysis	306
4. BSE and SEM analysis of restacked nanosheets	308
5. X-ray diffraction and thermogravimetric analysis	309
5.1 Considerations on the layer constitution	309
5.2 Refinement of the crystal- and the microstructure of dry restacked lithium tin sulfide nanosheets from XRPD data	313
5.3 Refinement of the Microstructure of hydrated Li-TS from XRPD data	317
6. PDF Analysis of the Local Structures in Dry and Hydrated LiSnS ₂	324
7. Analysis of electronic properties	335
7.1 Pellet EIS measurements as function of temperature and humidity	335
8. PFG NMR population analysis	339
Calculation of charger carrier concentration in hydrated Li-TS	339
References	340

1. Nuclear magnetic resonance

The appearance of a broad signal at -660 ppm in the ¹¹⁹Sn spectrum of the dry material (Figure S1, a) that is shifted to higher field compared to SnS₂ (cf. Figure S1 and Figure S2) hints to tin coordinated with oxygen instead of sulfur. During the ¹H-¹¹⁹Sn cross polarization experiment (¹H-¹¹⁹Sn-CP), the relative intensity of the signal at -660 ppm increases, indicating a close proximity of hydrogen and tin. In the hydrated state (Figure SS1), water in close proximity to tin leads to an even larger shift of the signal towards -582 ppm (similar to SnO₂ at -603 ppm¹). This signal is especially pronounced in the CP experiment of the hydrated material. The ¹H spectrum in the dry state (Figure SS2) features signals at 5.29 ppm and 3.08 ppm which are similar to the hydroxyl signals in hydrated SnO₂.² In the hydrated state, these signals are overlapped with a broad signal at 4.57 ppm that is typical for the chemical shift of mobile water adsorbed in the structure. The ¹¹⁹Sn-¹H-LG-HETCOR experiment of the dry samples allows to determine which ¹H signal is closest to which Sn atom (cf. Figure SS3). It shows the vicinity of the hydrogen atoms at 3.08 ppm to the SnO₂-type tin atoms at -600 ppm and of the atoms at 5.29 ppm to the tin atoms at -660 and -750 ppm.

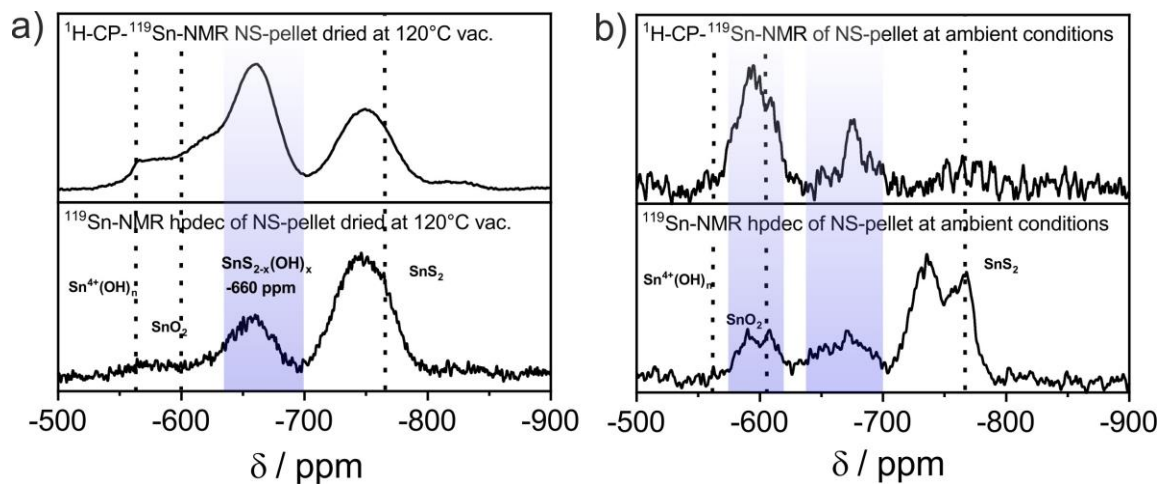


Figure S51 HPDEC ^{119}Sn NMR and ^1H - ^{119}Sn cross polarization experiments of a) a dry NS sample (120°C under vacuum) and b) and hydrated NS sample at ambient conditions. The chemical shifts of SnS_2 and $\text{Na}_2\text{Sn}(\text{OH})_6$ were taken from Figure S2. $\text{Na}_2\text{Sn}(\text{OH})_6$ shows a sharp peak at -564 ppm representing $\text{Sn}^{4+}(\text{OH})_n$ entities. SnO_2 was used as chemical shift standard in this work ($\delta_{\text{iso}} = -603.0$ ppm relative to $\text{Sn}(\text{CH}_3)_4$).

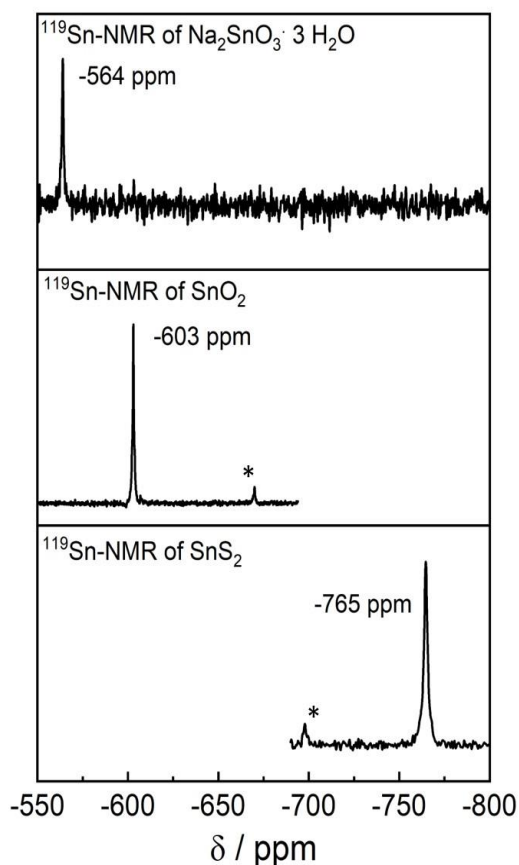


Figure S2 MAS ^{119}Sn NMR spectra of SnS_2 , SnO_2 and $\text{Na}_2\text{SnO}_3 \cdot 3\text{H}_2\text{O}$ for comparison. Spinning side bands are marked by an asterisks.

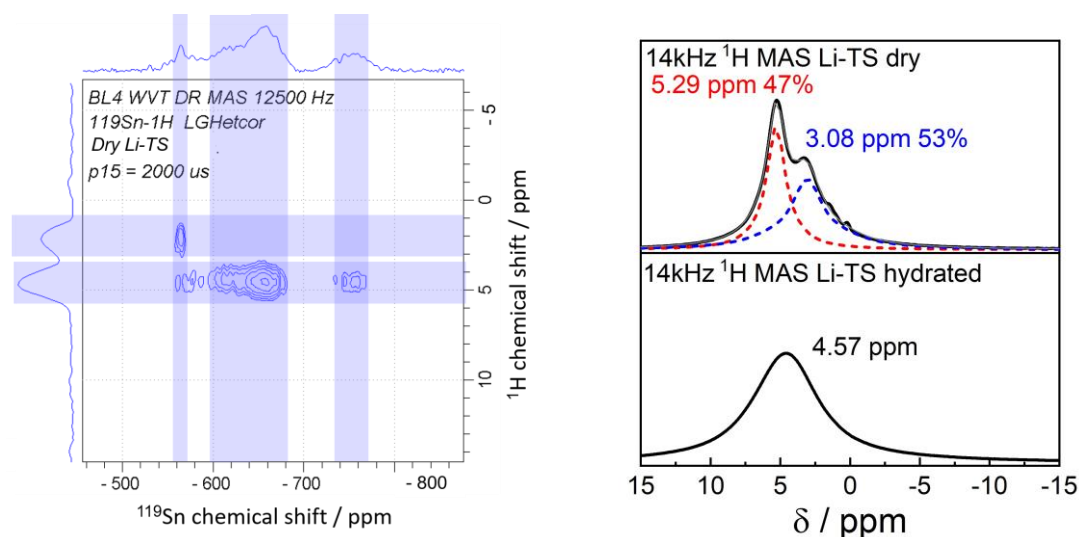


Figure S3 a) ^{119}Sn - ^1H LG HETCOR experiment shows the attachment of residual water and hydroxyl groups to tin. b) ^1H MAS NMR at 14 kHz of dry (120°C under vacuum) and hydrated Li-TS in comparison. Positions of peaks in dry sample resemble hydroxyl groups in tin dioxide and chemical shift in the hydrated sample fits mobile water.

2. Raman/Infrared spectroscopy

Raman spectra were registered on a JOBIN YVON Typ V O10 labram single grating spectrometer, equipped with a double super razor edge filter and a Peltier-cooled CCD camera (JOBIN YVON). The incident Laser wavelength was 632 nm. All samples were measured in sealed glass capillaries. For infrared spectroscopy a Spectrum BX FT-IR-Spektrometer from PERKIN ELMER equipped with a diamond ATR unit from SMITHS DETECTION was used.

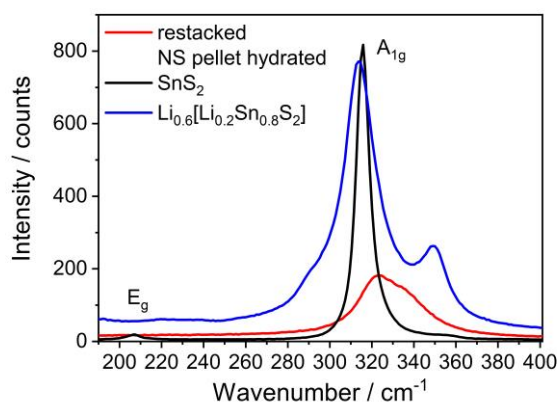


Figure S4 Raman spectroscopy of restacked hydrated NS in comparison to SnS_2 . The spectrum of Li-TS is clearly different from SnS_2 where only Sn-S vibrations are present: the most intense signal of Li-TS is shifted to higher wavenumbers indicating a bond from tin to atoms with a lower weight such as oxygen instead of sulfur. In addition, a second broad signal is present similar to the signal of $\text{Li}_{0.6}[\text{Li}_{0.2}\text{Sn}_{0.8}\text{S}_2]$ at 350 cm^{-1} . Overall, the signals are broadened probably due to the ultra-thin thickness of the nanosheet (phonon confinement in nanomaterials).³

3. Determination of element composition by EDX, ICP and combustion analysis

To determine the amount of sulfur the sulfur analyzer CS-800 from ELTRA was used and for hydrogen and oxygen the Elemental analyzer Vario El. For quantitative determination of Li and Sn in the samples, ICP-OES was performed with a VISTA-PRO ICP-OES spectrometer.

To determine the composition of the nanosheet films, various methods were applied and a sum formula for compound was deduced. After washing, 40 wt % of the initial lithium content remains in the material according to ICP-OES SI Table S1. The IR spectrum in SI Figure S1 shows the absence of typical lithium containing side phases such as $\text{LiOH}\cdot\text{H}_2\text{O}$ and Li_2CO_3 . The Sn to S ratio determined by EDX ranges between 1.6 to 2.0 with about 20 wt% of oxygen being present (including residuals of absorbed water on the sheets) (cf. SI Table S2). Freshly exfoliated samples have a Sn:S ratio of 2 whereas older samples have a slightly lower ratio due to aging (within several months). A sulfur content of about 31 wt % of a sample dried under vacuum and handled under inert gas atmosphere (to remove adsorbed water) was independently measured *via* combustion analysis, which also shows the presence of oxygen and hydrogen (cf. SI Table S3). For pure SnS_2 35 wt % of sulfur would be expected. From these experimental results the averaged sum formula $\text{Li}_{0.3}[\text{Sn}_{0.8}\text{S}_{1.6}(\text{OH})_{0.3}]\cdot 0.1\text{H}_2\text{O}$ is deduced. The exact composition varies slightly for each batch.

Table S1 Determination of Li:Sn ratio by ICP-OES after washing for one time, the average of two measurements of each sample is presented.

Sample	Li:Sn ratio; Sn = 0.8
Sample 1	0.41
Sample 2	0.26
Sample 3	0.42
Sample 4	0.36
Sample 5	0.38
Sample 6	0.35
Sample 7	0.30
Sample 8	0.28
Sample 9	0.32
Sample 10	0.32
Sample 11	0.47
Average	0.35 ± 0.06

Table S2 Determination of Sn:S ratio and oxygen content by EDX.

Sample	Sn / w%	S / w%	O / w%	Sn:S
Sample 12 (8 months suspension)	29.91	49.15	19.81	1.64
Sample 12	29.88	48.88	19.47	1.64
Sample 8 (stored 8 months)	28.12	47.78	22.78	1.70
Sample 8	29.26	48.95	20.00	1.67
Sample 13 (4 months suspension)	28.29	50.78	19.63	1.80
Sample 13	29.18	51.65	18.08	1.77
Sample 13	29.46	52.86	16.9	1.80
Sample 14 (1 month suspension)	33.82	66.18	no data	1.96
Sample 14	32.52	67.48	no data	2.07
Sample 14	33.12	66.88	no data	2.02

Table S3 Determination of S, O and H content of the dry sample 8 via combustion analysis.

Element	content w%
Sulfur	31.3
Oxygen	4.5
Hydrogen	0.4

4. BSE and SEM analysis of restacked nanosheets

Elemental composition was determined by energy-dispersive X-ray spectroscopy (EDX) with an OXFORD INSTRUMENTS INCA Energy detector. Images of the morphology were obtained using a JEOL JSM 6500 F scanning electron microscope. The thickness of the thin films on alumina were determined with a Merlin SEM (ZEISS).

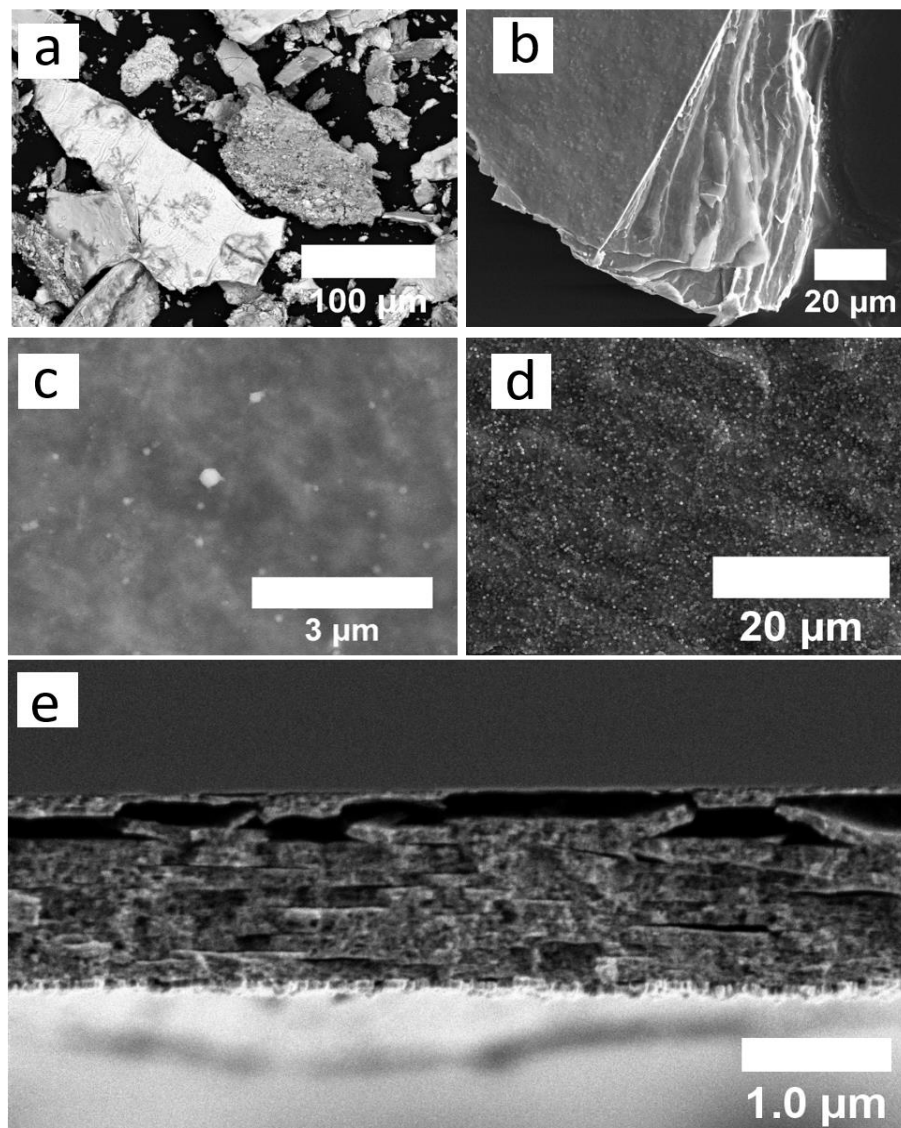


Figure S5 Electron microscopy of restacked LTS NSs a) BSE image of nanosheets without washing step showing the non-uniformity of the sample; b) zoom in on restacked NSs after one washing step; c) close-up on oxygen rich particles (determined by EDX) on the surface of the nanosheets after storing them for several months in air d) many oxygen rich particles are visible after a heat treatment at 450 °C under Ar. e) higher magnification SEM image of Li-TS nanosheets on an Al_2O_3 substrate that shows the ordered layering of the nanosheets in the xy-plane.

5. X-ray diffraction and thermogravimetric analysis

For thermogravimetric analysis (TGA) measurements, powder samples were equilibrated at the respective relative humidities for 24 h (or the given time in the text) and then quickly transferred in an alumina crucible. The measurements were carried out using a NETZSCH STA 449 F5 Jupiter with an Argon flow of 40 mLmin^{-1} in a temperature range between 20 and $140 \text{ }^\circ\text{C}$ and a heating rate of 1 Kmin^{-1} . Data handling was performed with the NETZSCH Proteus software package.

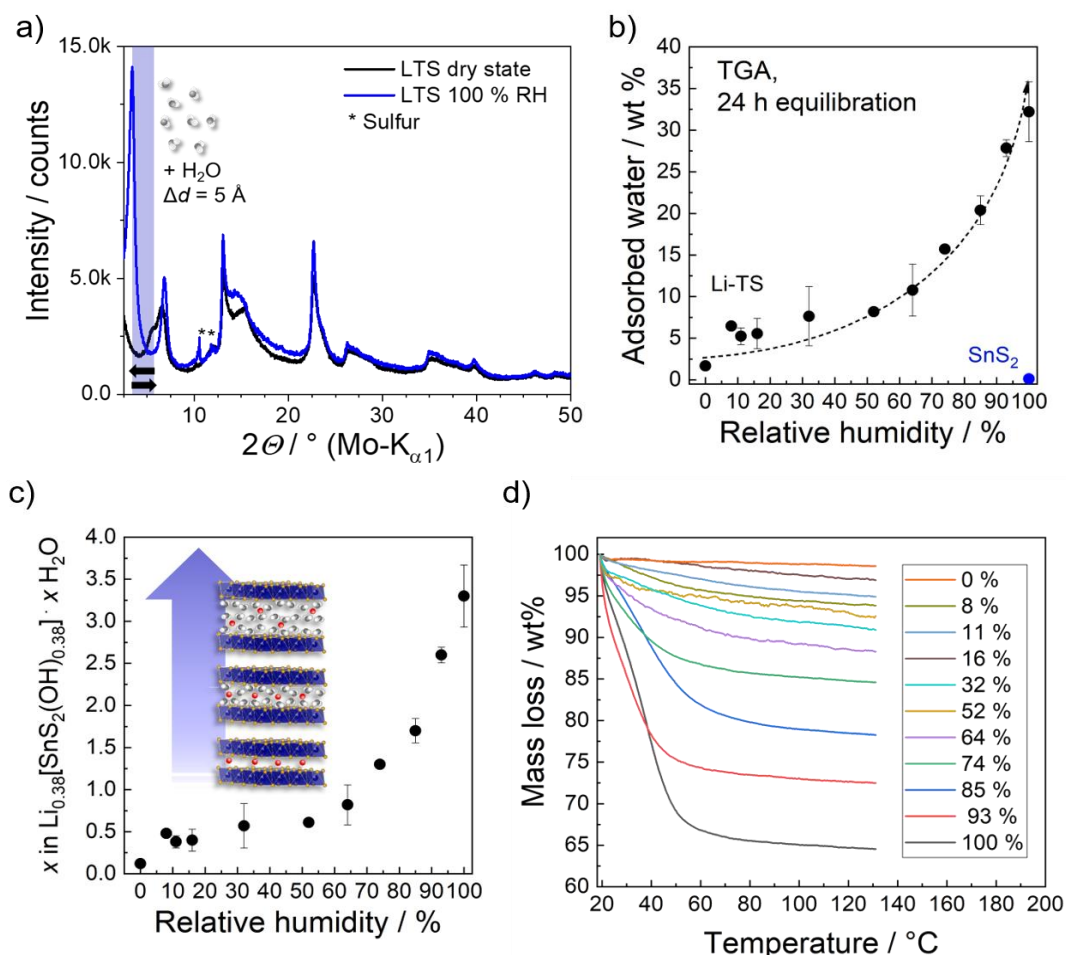


Figure S7 a) The XRPD measurements show the hydration of the Li-TS NSs upon exposure to 100 % RH for one day in comparison to a dry sample ($120 \text{ }^\circ\text{C}$, vac. over night) showing an increase in d-spacing of about 5 \AA (from 6 to 12 \AA) indicating the incorporation of three water layers into the structure. b) Li-TS loses about 32 wt% of water after hydration at 100 % RH in the TGA. SnS₂ that shows no significant weight loss is given as reference. c) This corresponds to 2.6 water per sum formula: $\text{Li}_{0.3}[\text{Sn}_{0.8}\text{S}_{1.6}(\text{OH})_{0.3}] \cdot 2.6\text{H}_2\text{O}$. d) The TGA data as mass loss vs. temperature. To calculate the mass loss (adsorbed water) in b) two such measurements were averaged.

5.1 Considerations on the layer constitution

For any refinements concerning the stacking order and stacking faults of a layered material, the layer constitution can be a very crucial point. In this study a lithium tin sulfide, analogous to the material described by Holzman *et al.*⁴ was used as starting material. They describe the structure of lithium tin sulfide $\text{Li}_{0.8}\text{Sn}_{0.8}\text{S}_2$ (from the series $\text{Li}_{4x}\text{Sn}_{1-x}\text{S}_2$ with $x = 0.2$) using a monoclinic unit cell with two symmetrically independent tin positions. Both tin sites are occupied by tin, lithium, or a vacancy to a different degree. Hence, the distribution of voids within the tin sublattice can be

denoted as *partially ordered* (Figure S7, b). The voids that might be partially filled by lithium cations can also be distributed *randomly*. This leads to a smaller unit cell and to a trigonal lattice symmetry (Figure S7, a). On the other hand, the voids can be distributed *fully ordered*, i.e. the distance between voids is maximized. A prominent example for fully ordered voids are classical layered honeycomb compounds, like Li_2SnS_3 , where $1/3$ of the octahedral voids are vacant. This also leads to a condensed honeycomb motif (Figure S7, c-e) in the tin sublattice and to a trigonal lattice or monoclinic (in case of an abc-like [the small Latin letter indicates the layer position] stacking order, see below) symmetry but to a larger unit cell volume. It should be noted that for any trigonal supercell with an ordered void distribution, a monoclinic cell with $a' = a$, $b' = a \cdot \cos(\pi/6)$ and $\gamma' = 90^\circ$ can be found, with the same amount of voids in the tin sublattice but with a different void distribution (Figure S8). An important consequence of these considerations is that in the random void distribution in- or out-of-plane distortions of the tin sublattice are forbidden by lattice symmetry (local non-crystallographic distortions may still occur), while partially or fully ordered voids lead to unit cell metrics that allows these distortions.

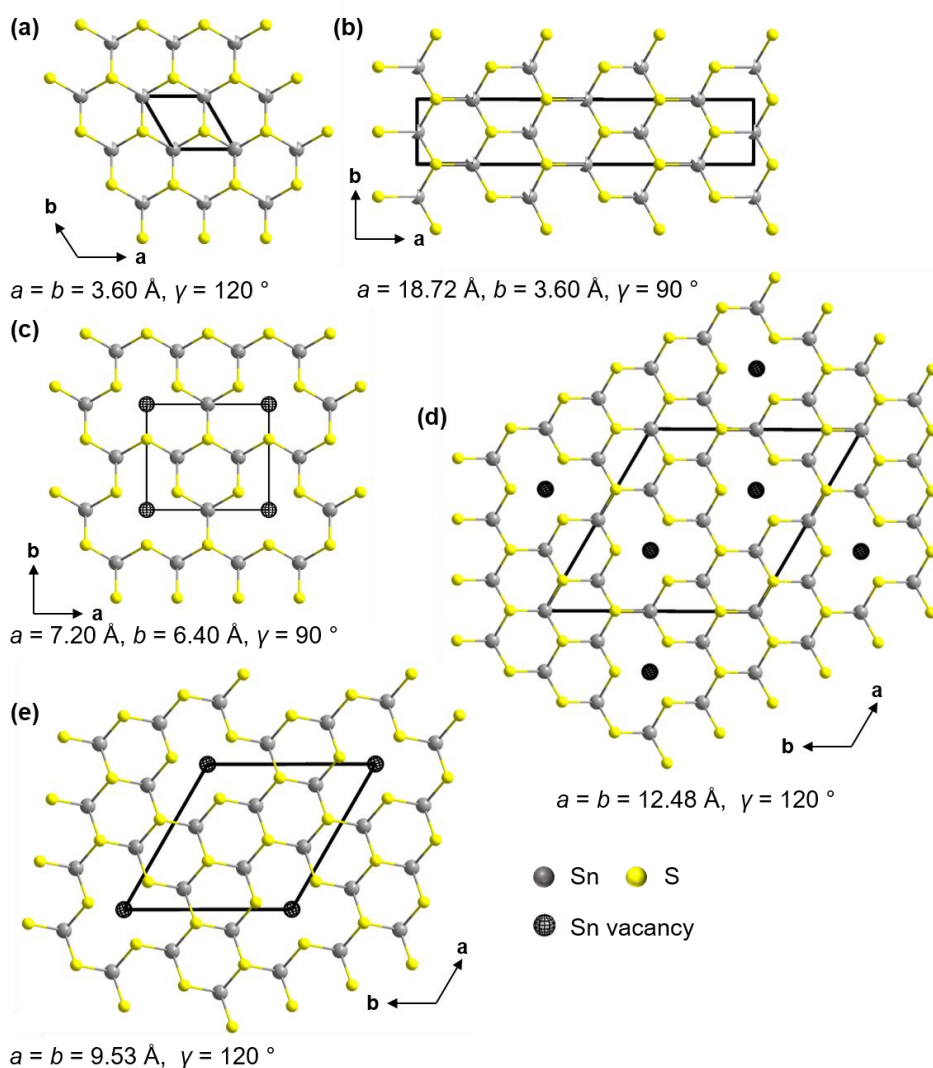


Figure S7 Possible distribution of voids in the Sn-sublattice of $\text{Li}_4x\text{Sn}_{1-x}\text{S}_2$ ($x > 0$): (a) fully random distribution, (b) partial ordered distribution, fully ordered distribution with (c) $1/4$, (d) $1/6$ and (e) $1/7$ of the tin position being vacant. Partially filled atom symbols indicate partially occupied sites, the lattice parameters were derived from the smallest ideal, trigonal cell of $\text{Li}_4x\text{Sn}_{1-x}\text{S}_2$ ($x > 0$) with fully random void distribution (a).

As shown, the distribution of voids has a major impact on the diffraction pattern. The difference in the XRPD pattern between partially ordered and fully disordered voids (Figure S9, a, b) seems to be negligible and to affect only the reflection intensities, but possible distortions of the monoclinic lattice and the $\text{SnS}_{6/3}$ octahedra can lead to peak splitting or to the appearance of new reflections. The presence of ordered voids leads to the appearance of additional reflections with low intensity. The lower the amount of voids, the lower the intensity of these reflections. In some cases, an ordered void (Figure S9, d, e) distribution leads to the appearance of additional small reflections in the low 2θ angle region, which can be easily misinterpreted as “superstructure” reflections. The measured diffraction pattern of the $\text{Li}_{0.8}\text{Sn}_{0.8}\text{S}_2$ (Figure S9, grey pattern, $x=0.20$) starting material exhibits additional small reflections in the low and medium 2θ angle region clearly pointing to an ordered distribution of voids within the tin sublattice. In addition, some of the high intensity reflections are shifted, which indicates a considerable distortion of the lattice. The intensity of the additional peaks suggests that 1/5 or more of the tin positions are vacant, which is in accordance to the reported phase composition.⁴ A detailed analysis of the structure, however is beyond the scope of this manuscript and will be done separately.

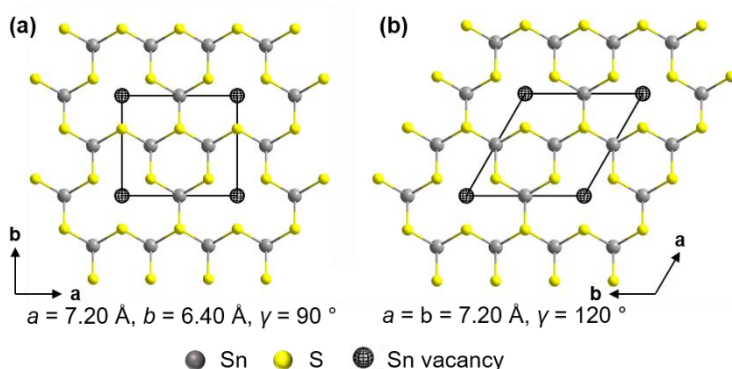


Figure S8 Possible ordered void distribution within a tin sublattice with 1/4 of the tin positions being vacant leading either to (a) a monoclinic or orthorhombic (which depends on the stacking order, see below) or to (b) a trigonal cell setting.

Although a strong movement of Sn^{4+} cations through the sulfide sublattice appears to be unlikely to occur during exfoliation and restacking, a careful comparison of the diffraction patterns before and after restacking reveals some differences (Figure S10). Most striking is that lithium tin sulfide (Li-TS) after exfoliation, restacking, and drying exhibits fewer and broader peaks than the starting material ($\text{Li}_{0.8}\text{Sn}_{0.8}\text{S}_2$), which means that both the lateral and the vertical domain sizes decrease during this procedure. The triangular peak shape also indicates strong stacking fault disorder that evolves during restacking. Strong anisotropic line broadening is most likely also the reason why there are less peaks in the diffraction pattern. A comparison of the positions of strong reflection reveals some structural details: reflections with $h00$ and $h0l$ indices (Figure S10, green background) are shifted towards higher diffraction angles, after exfoliation, restacking and drying whereas the $00l$ basal reflection remains (yellow background) at the same position. This means the lateral extension of the unit cell shrinks, which indicates some out-of-plane distortion of tin atoms whereas the interlayer distance remains almost constant. Another interesting feature is the position of the low intensity reflection at around $4.4^\circ 2\theta$ (Figure S10, grey background), which indicates either an ordered distribution of the voids (Figure S8) or an interstratification of water (see below). As this peak is shifted towards lower diffraction angles after exfoliation, drying and

restacking, which is in contrast to the $h00$ and $h0l$ that are shifted to higher diffraction angles, it can be most likely assigned to domains with intercalated water layers. Nevertheless, the distribution of voids within the tin sublattice can be still ordered, as the small intensity reflection that are associated with this ordering are vastly broadened due to stacking fault disorder (Figure S11, c, magenta pattern) and low domain size.

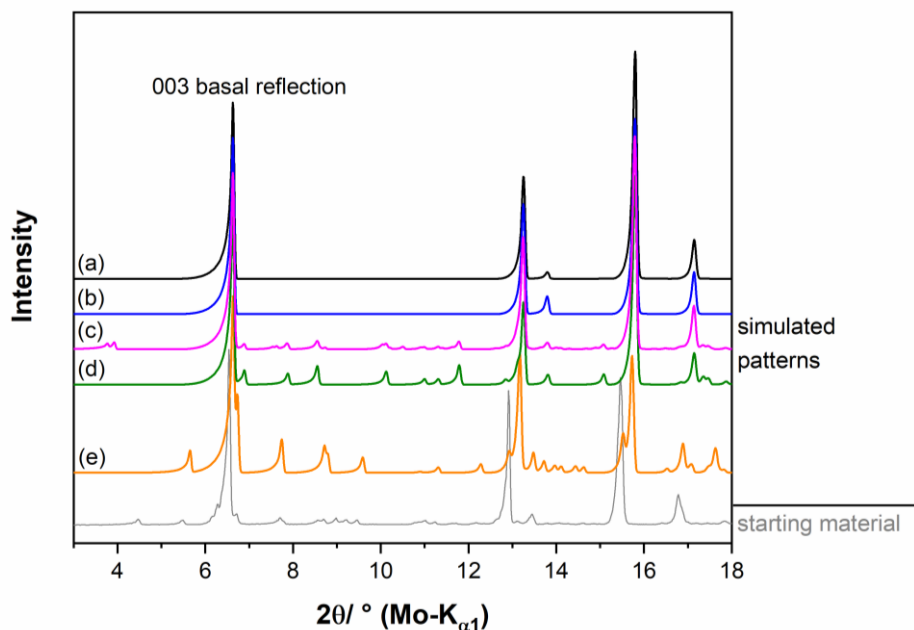


Figure S9 Comparison of simulated XRPD patterns of $\text{Li}_{0.8}\text{Sn}_{0.8}\text{S}_2$ using different layer constitutions in terms of void distribution within the tin sublattice: (a) fully disordered distribution (Figure S7, a), partially ordered distribution (Figure S7, b), ordered distribution in a trigonal lattice with $1/6$ of the tin positions being vacant (Figure S7, e), (d) ordered distribution in a trigonal lattice with $1/4$ of the tin positions being vacant (Figure S8, b), (e) ordered distribution in a monoclinic lattice with $1/4$ of the tin positions being vacant (Figure S7, a). The XRPD patterns were normalized to the peak maximum of the 003 basal reflection.

Due to the pronounced tendency of layered honeycomb compounds for randomly oriented stacking vectors (Figure S11, a), especially after restacking, the hypothetical diffraction pattern of abc-stacked $\text{Li}_{0.8}\text{Sn}_{0.8}\text{S}_2$ with a disordered void distribution and of randomly oriented abc-stacked $\text{Li}_{0.8}\text{Sn}_{0.8}\text{S}_2$ with an ordered void distribution are almost identical. Due to the smaller lateral extent of the unit cell, using a structural model with a disordered void distribution speeds up the numerical calculations by more than two orders of magnitude. Therefore, we decided to use this model as an approximation for the layer setup for the following semi-quantitative analyses on the microstructures of hydrated and dry restacked Li-TS.

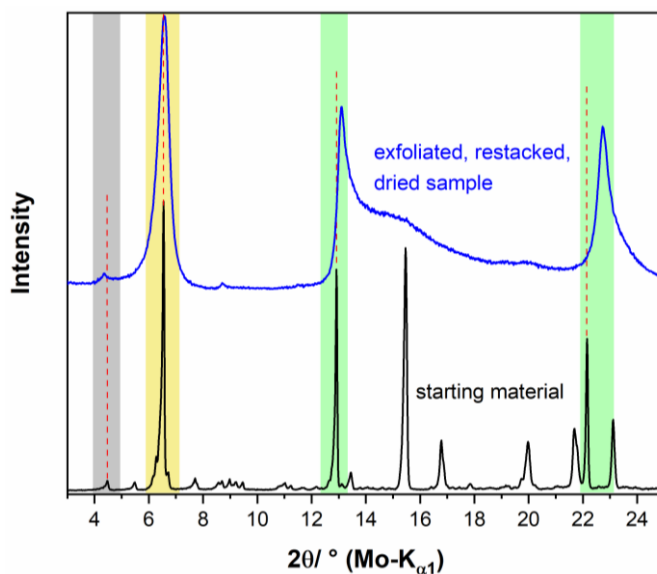


Figure S10 Comparison of the XRPD patterns of $\text{Li}_{0.8}\text{Sn}_{0.8}\text{S}_2$ before and after exfoliation, restacking and drying. Reflections indicating the lateral dimension of the unit cell are indicated by green background, reflection corresponding to the vertical extension of the unit cell, i.e. the inter layer spacing by yellow background and reflections that cannot be unambiguously assigned by grey background. Selected reflection positions in the XRPD pattern of the starting material are indicated by red dashed lines.

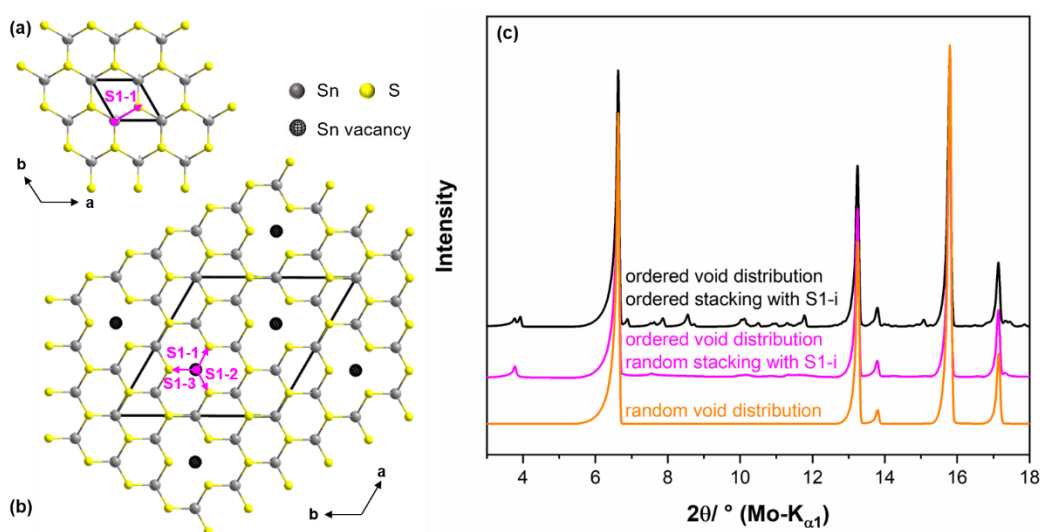


Figure S11 Possible distribution of voids in the Sn-sublattice of $\text{Li}_{0.8}\text{Sn}_{0.8}\text{S}_2$: (a) fully random distribution, (b) fully ordered distribution with 1/6 of the tin position being vacant. Projections of possible stacking vectors, $S1-i$, leading to equivalent staggered abc -like layer stacking, onto the ab plane are shown as magenta arrows. (c) Comparison of simulated XRPD patterns using different layer setups and stacking orders.

5.2 Refinement of the crystal- and the microstructure of dry restacked lithium tin sulfide nanosheets from XRPD data

A close inspection of the diffraction pattern of the dried Li-TS material in Figure 2a (main text) and SI Figure S6 and Figure S14 reveals clear indicators for different kinds of disorder in the material. First, the non 00l reflections exhibit strong anisotropic broadening and triangular peak shapes, which is indicative for stacking fault disorder.^{5, 6} Second, the splitting of the 003 basal reflection

into two overlapping Bragg peaks suggests that the interlayer distance is modulated by the disorder.

Different structure models are published for the ideal, faultless structure of anhydrous Li_xSnS_y .^{7,8} In most models an overall CdCl_2 -type stacking order is suggested. The lithium ions are situated in the octahedral voids in-between the SnS_2 -layer, which leads to an overall $(\text{B}\alpha\text{C})\beta(\text{A}\gamma\text{B})\alpha(\text{C}\delta\text{A})$ stacking order, where capital Latin letters indicate anion positions and small Greek letters refer to cation positions, the SnS_2 layers are indicated by round brackets (c.f. Figure S4). Pure SnS_2 exhibits a CdI_2 -like stacking with vacant, octahedral, interlayer cation positions, leading to an $(\text{B}\alpha\text{C})(\text{B}\alpha\text{C})$ stacking order and to a considerably smaller interlayer distance of 5.88 Å⁹ vs. 6.1319 Å for LiSnS_2 ¹⁰ as illustrated in Figure S12.

The lithium deficiency in the restacked Li-TS nanosheets (loss of 40 % of initial lithium content) and splitting of the basal reflections suggest the presence of stacking faults between CdCl_2 - and CdI_2 -type stacking. These transitions are associated with lithium vacancies in the latter stacking type, leading to a shorter z-component of the relating stacking vector S_2 in Figure S12. Turbostratic-like disorder can be additionally expected as this is often observed in layered,

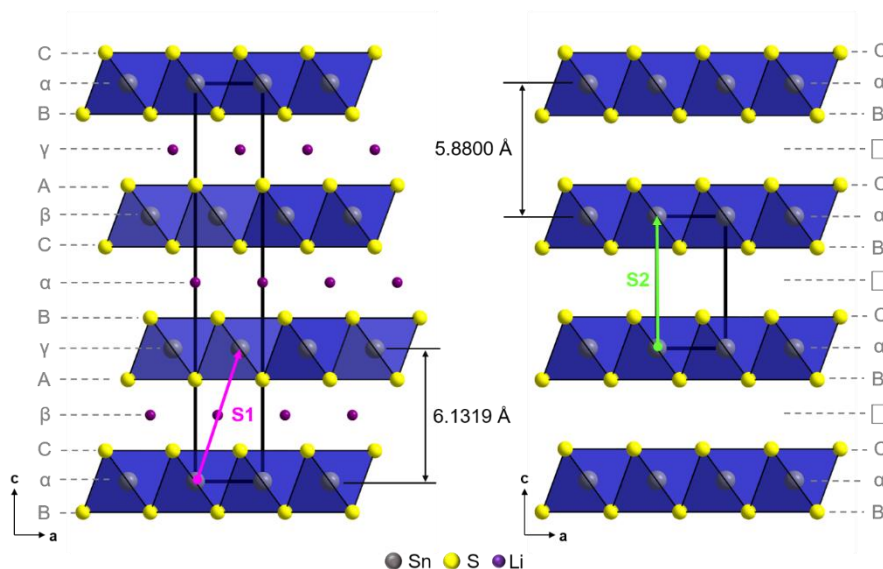


Figure S8 Illustration of the most common stacking orders and interlayer distances in LiSnS_2 (refined as lithium and tin deficient $\text{Li}_{0.8}\text{Sn}_{0.8}\text{S}_2$ and SnS_2). The positions of cation layers are indicated by small Greek letters and the positions of anion sublayers by capital Latin letters. The stacking vectors, describing the transition from one layer to the next is represented by magenta and green arrows.

tetravalent sulfides.¹¹ Thus, C6-type faults associated with interlayer lithium vacancies within the C19-type basic stacking of LiSnS_2 , were also included in the model. The amount of faulting is defined by a fault probability P_x (Table S4). This accounts for the lithium deficiency in the material, leading to an idealized composition of $\text{Li}_{0.8-x}\text{Sn}_{0.8}\text{S}_2$. The turbostratic components of the stacking vectors is modelled by adding random shifts within in ab -plane (eq. 1, rc). This has already been successfully applied to the microstructural refinement of $\text{NiCl}(\text{OH})$ ¹² and $\text{CoO}(\text{OH})$ ¹³. Different extents of turbostratic disorder can be simulated by varying the limits of these random shifts (eq. 1, $\text{lim}rc$). A limit of 0.5 in fractional coordinates corresponds to a random shift of ± 0.5 in the a - and b -directions and therefore to complete turbostratic disorder.

Table S4 Transition probability matrix applied for the refinement of the microstructure of LiSnS_2 . The parameter P_x describes the amount of C6-type faults in the overall C19-type stacking order of the material (Figure S1), the stacking vectors are given in (eq. 1).

from↓/to→	C19-type interlayer lithium	C6-type interlayer void
C19-type interlayer lithium	$1-P_x, S1$	$P_x, S1$
C19-type interlayer lithium	$1-P_x, S2$	$P_x, S2$
$= \begin{pmatrix} \frac{2}{3} + rc \\ \frac{1}{3} + rc \\ \frac{1}{3} \end{pmatrix}$ $S1$ with $-\text{limrc} \leq rc \leq \text{limcr}$	$= \begin{pmatrix} 0 + rc \\ 0 + rc \\ 0.3205 \end{pmatrix}$ $S2$	(eq. 1)

The program TOPAS 6.0¹⁴ was used to refine the XRPD patterns of the Li-TS material. A supercell approach^{15, 16} was used to approximate the stacking faulted microstructure. Stacks of 500 layers were generated, and 100 of these supercells were averaged. An automated series of refinements were conducted in which the parameters P_x , limrc and the z-components of the stacking vectors were varied incrementally in a grid search approach.^{17, 18} The optimization process was carried out many time iteratively as it was done for $\text{Ag}_3\text{LiIr}_2\text{O}_6$ and $\text{Ag}_3\text{LiRu}_2\text{O}_6$ optimization sequentially: the random component (minrc) of the stacking vectors, the stacking fault probability (P_x), the z-component of stacking vector S1, 4. the z-component of stacking vector S2 and the z-coordinate of the sulphur atoms.

A selection of the final grids is presented in Figure S13. The introduction of turbostratic components to the microstructure leads to a steep decrease of the R_{wp} value and finally to a broad minimum at $\text{limrc} = 0.425(25)$ (Figure S13, a). This indicates that the layers are highly

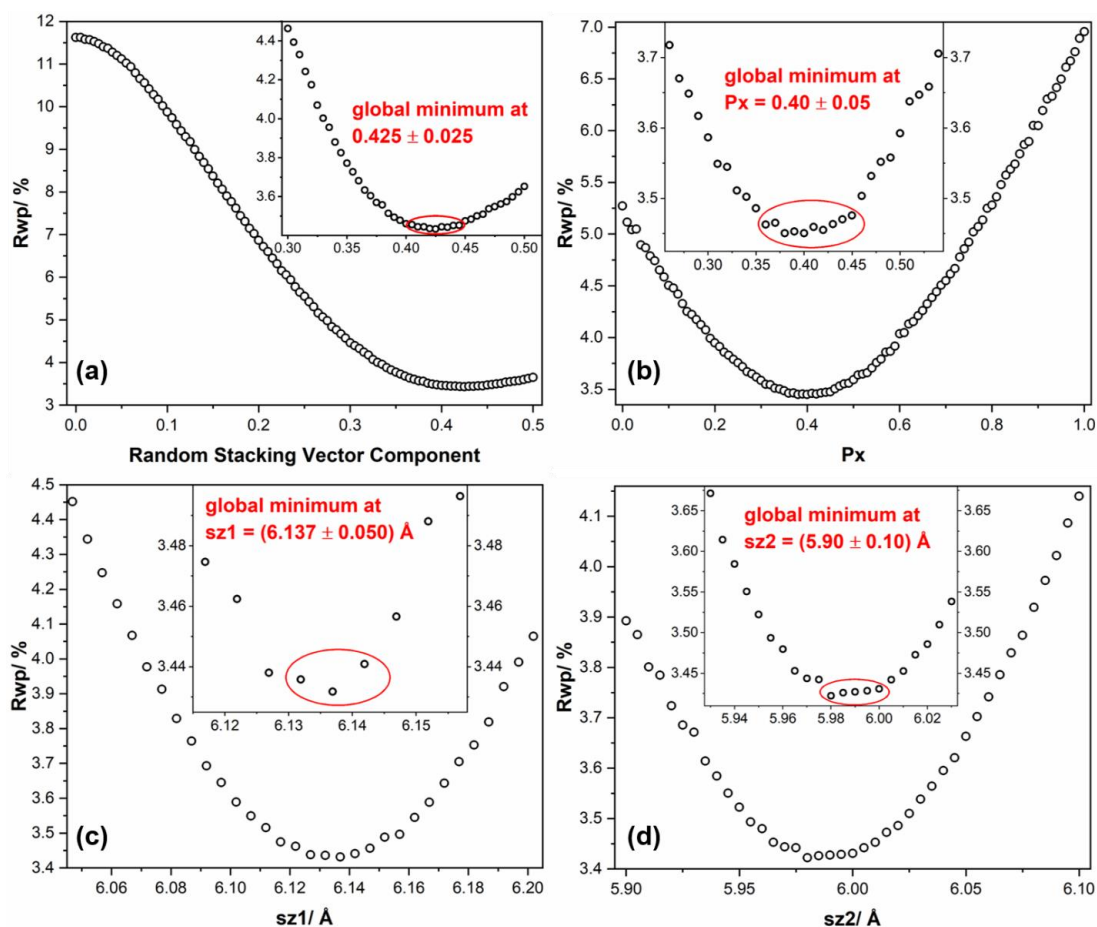


Figure S13 Final, one dimensional grids of the optimization of (a) the random component of the stacking vectors, (b) the stacking fault probability for transitions from the $CdCl_2$ -type stacking order to the CdI_2 -type stacking order that is associated with Li-vacancies, (c) the z-component of the stacking vector of the $CdCl_2$ -type stacking order, and (d) the z-component of the stacking vector of the CdI_2 -type stacking order.

turbostratically disordered but not completely random. Introducing stacking faults leads to further improvement of the R_{wp} value from 5.3 % (at $P_x = 0.0$) to 3.4 % at the global minimum of $P_x = 0.40(5)$. This corresponds to a lithium deficiency of 40 % and therefore to a phase composition of $Li_{0.5}Sn_{0.8}S_2$, which is in agreement with the chemical analyses of sample 11 in Table S1 that was used for the measurements. The interlayer distances, i.e. the z-components of the stacking vectors were optimized to $6.137(50) \text{ Å}$ for the C19-type stacking and to $5.90(10) \text{ Å}$ for the C6-type stacking respectively, which is close to the interlayer distances of $LiSnS_2$ (6.1319 Å) and SnS_2 (5.88 Å) given in the literature.⁶

Examples of the graphical results of the final Rietveld¹⁹ refinements are presented in Figure S14. Any attempt to refine the pattern without turbostratic disorder leads a severe misfit of the diffraction pattern and an unacceptable R_{wp} -value of 12.21 % (Figure S14, a). Using only turbostratic disorder and no stacking faults ($P_x = 0$) for describing the microstructure of Li-TS leads to a better fit (Figure S14, b) and a considerably lower R_{wp} value of 5.11 %. As the splitting of the basal reflection cannot be modelled this way, the fit in the low 2θ part of the diffraction pattern is not acceptable. When both stacking faults and the turbostratic disorder is used (Figure S14, c) both the shape of the basal reflection and the vastly broadened non 00l reflection can be

described sufficiently with a R_{wp} value of 3.41 %. This proves that both kinds of disorder are present in the microstructure of the Li-TS material.

In summary, it can be concluded that the C19-type stacking of $\text{Li}_{0.8}\text{Sn}_{0.8}\text{S}_2$ is heavily faulted by C6-type stacked layers. The stacking faults are associated with lithium-vacancies in the interlayer space. The layer orientations are also significantly modulated by turbostratic-like disorder. However, the compound is not fully turbostratically disorder, such that the C19- and C6-type stacking ordering still act as centres of gravity in the microstructure of this compound.

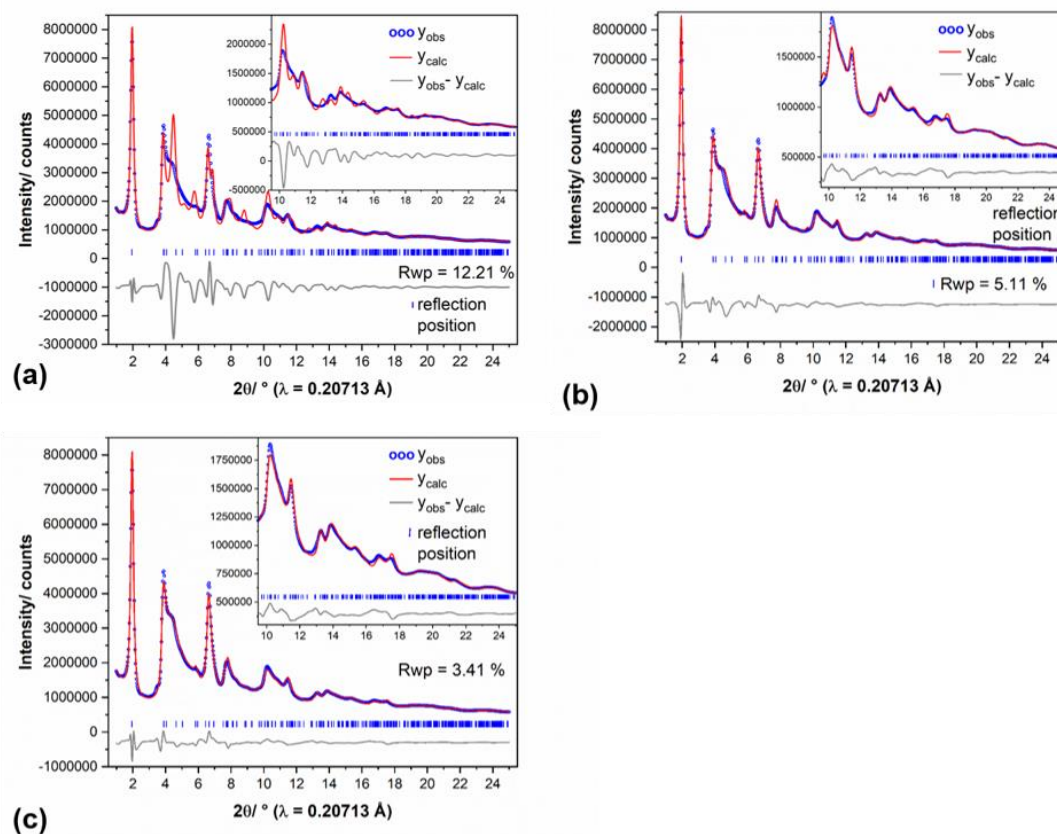


Figure S14 Graphical result of the final Rietveld refinement of dry Li-TS using an averaged model of 100 supercells each containing 500 layers including (a) only faults between a regular CdCl_2 -type and CdI_2 -type stacking with a fault probability of 40 %, (b) only random variations of the stacking vector of the CdCl_2 -type stacking of ± 0.425 (fractional coordinates) (c) both effects.

5.3 Refinement of the Microstructure of hydrated Li-TS from XRPD data

Dry Li-TS is produced by dehydration of the hydrated phase. The XRPD pattern of the dried sample (Figure S15, a), however, indicates that the drying procedure is sometime not fully completed. In the XRPD pattern, the main reflections (003, 100, and 110) can be indexed by the trigonal cell of $\text{Li}_{0.8}\text{Sn}_{0.8}\text{S}_2$. A few additional reflections cannot be indexed. A sharp reflection corresponding to a lattice plane distance of 9.3 Å (Figure S15, a, inset) indicates that the by-product has a similar unit cell structure but a larger interlayer distance, which is caused by the presence of intercalated water. The diffraction patterns of the hydrated samples (Figure S15, b, c) exhibit similarities to the pattern of the dried sample: strong peaks are located at the positions of the 100 and 110 reflections (Figure S15, red dashed lines). However, the position of the basal reflection is severely

shifted towards lower diffraction angles for the hydrated samples. Interestingly the shifting of the basal reflection depends of the sample history and always corresponds to considerably larger lattice plane distances (11.9 Å and 12.8 Å) than the basal reflection of the hydrated by-product of the dried (9.3 Å) sample. Moreover for Li-TS (100 % RH, 2 weeks), the positions of the intense reflection in the range of (6-7)° 2θ does not fully correspond to the second order reflection of the basal peak, which should refer to a lattice plane distance of 6.4 Å. These observations lead to the following conclusions:

- the setup and the dimensions of the SnS₆/3 octahedra layers is identical for the dry and the hydrated samples as the 100 and 110 reflections are located at identical positions
- due to the characteristic trigonal Warren-type peak shape, the dry and the hydrated samples both contain a high density of stacking faults
- the number of intercalated water layers can vary as seen from the positions of the basal reflections of the by-product of the dried sample and the hydrated samples
- the setup of the water intercalation layers can vary as the position of the basal reflection of the hydrated samples exhibits slight shifting
- the interlayer distance of the hydrated sample is modulated by random variation of the setup of the water intercalation layers and by variation of the number of water intercalation layers, as the basal reflections (003) are more broadened than the 100 reflection¹⁸
- within the structure of the hydrated samples, there are domains which do not show any water intercalation as this leads to a seeming shift of the second order basal reflection (006) towards a higher diffraction angle

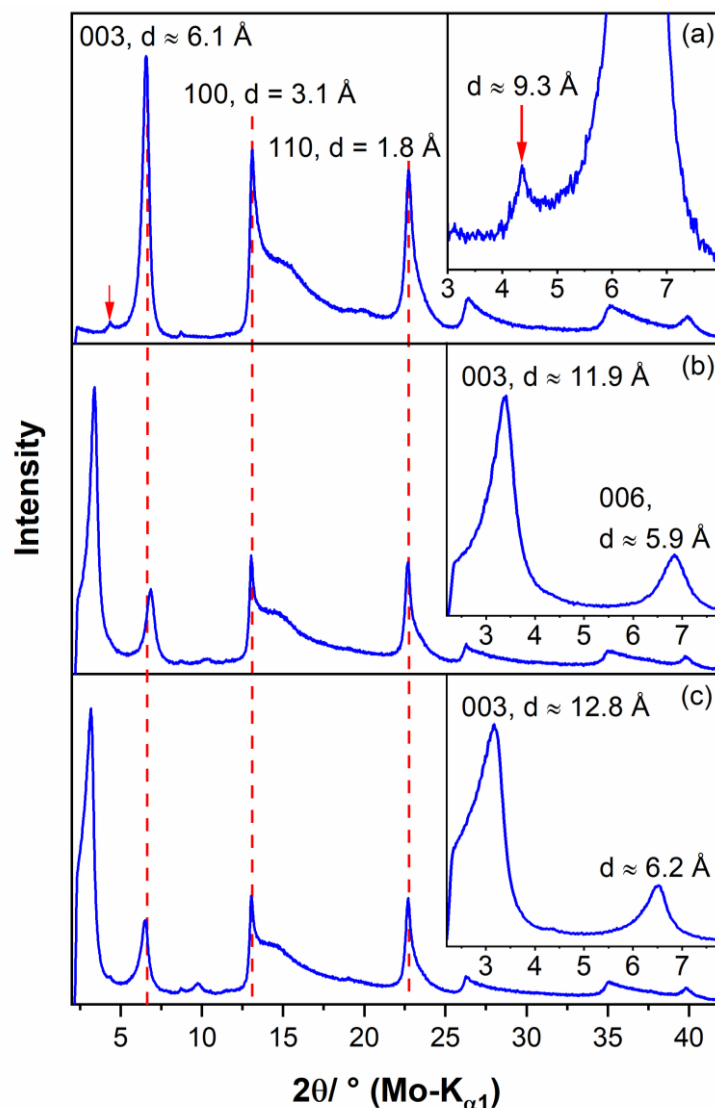


Figure S15. Measured XRPD patterns of (a) dry Li-TS nanosheets, (b) dry Li-TS after rehydrated at 100 % RH in capillary for two weeks (c) Li-TS hydrated at 100 % RH in capillary for two weeks.

Due to the disordered character of the hydrated samples, the constitution of the water layers cannot be determined *ab initio*. The position of the basal reflection (Figure S15, a, inset) of the by-product of the dried sample corresponds to a lattice plane distance of approx. 9.3 Å. With respect to the packing of the atoms in the $\text{Li}_{0.8}\text{Sn}_{0.8}\text{S}_2$ model and to the broadening of the interlayer distance of ≈ 3 Å (Figure S16, a, b), it can be assumed that two layers of water are intercalated in a way that a close-packing of the atoms is still maintained. They can only be located in the proximity of the lithium cations, leading to layers of edge sharing $\text{Li}(\text{H}_2\text{O})_{6/3}$ octahedra (Figure S16, b yellow octahedra) and to a phase composition of $\text{Li}_{0.8}\text{Sn}_{0.8}\text{S}_2 \cdot 2\text{H}_2\text{O}$. An octahedral coordination of lithium by water is not unusual as this has already been observed in highly hydrated lithium salts like $\text{LiClO}_4 \cdot 3\text{H}_2\text{O}$ ²⁰ or $\text{LiNO}_3 \cdot 3\text{H}_2\text{O}$ ²¹. Further intercalation of water leads to an increase of the interlayer distance. By intercalating three layers of water an interlayer distance of approx. 11.9 Å can be achieved (Figure S16, c), as observed for dry Li-TS after rehydrated at 100 % RH in a capillary for two weeks (Figure S15, b). This leads to a phase composition of $\text{Li}_{0.8}\text{Sn}_{0.8}\text{S}_2 \cdot 3\text{H}_2\text{O}$ with lithium occupying half of the octahedral voids of the inter layer water

framework, which is possible considering the amount of water found by TGA (Figure S6b, c). As lithium also tends to a tetrahedral coordination, the formation of tetrahedral voids by interlayer water could be possible. Due to minimal Li-O distances of approx. 2 Å, this second hypothetical polymorph of $\text{Li}_{0.8}\text{Sn}_{0.8}\text{S}_2 \cdot 3\text{H}_2\text{O}$ would exhibit a larger interlayer distance of approx. 12.8 Å (Figure S16, d), as observed for Li-TS (hydrated at 100 % RH in a capillary for two weeks in Figure S15, c).

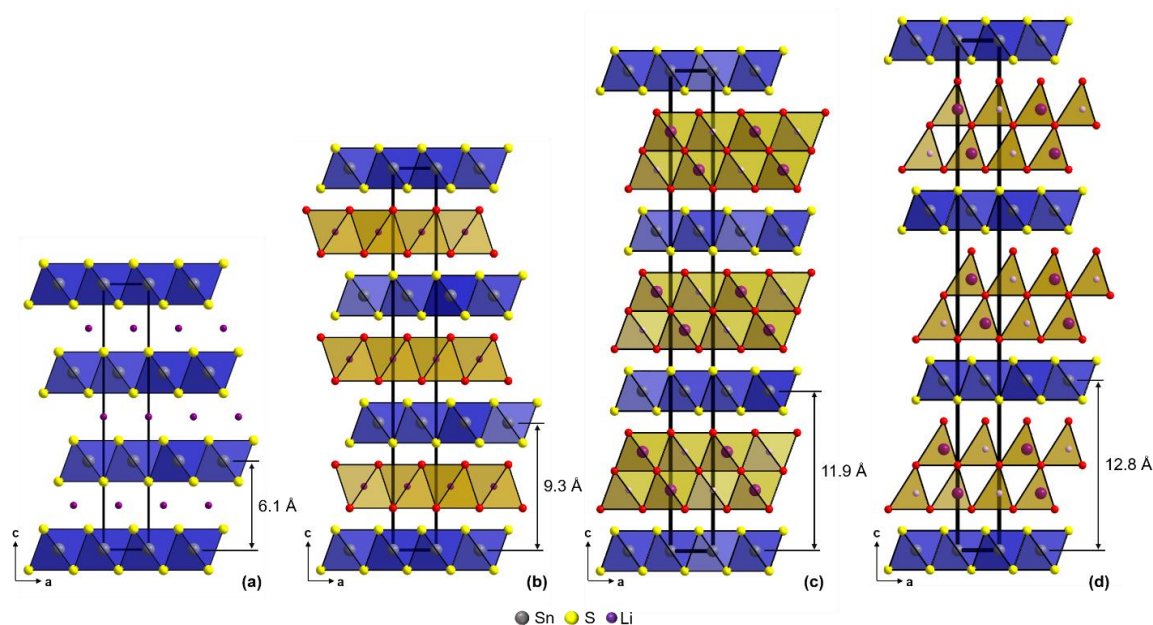


Figure S16. Packing diagrams of (a) $\text{Li}_{0.8}\text{Sn}_{0.8}\text{S}_2$ modelled as LiSnS_2 , (b) hypothetical $\text{Li}_{0.8}\text{Sn}_{0.8}\text{S}_2 \cdot 2\text{H}_2\text{O}$, (c) hypothetical $\alpha\text{-Li}_{0.8}\text{Sn}_{0.8}\text{S}_2 \cdot 3\text{H}_2\text{O}$ with octahedrally coordinated, half-occupied lithium positions, and (d) $\beta\text{-Li}_{0.8}\text{Sn}_{0.8}\text{S}_2 \cdot 3\text{H}_2\text{O}$ with tetrahedrally coordinated, half-occupied lithium positions. $\text{SnS}_{6/3}$ octahedra are presented in blue, and $\text{LiO}_{6/3}$ octahedra and $\text{LiO}_{1/10}\text{S}_{3/3}$ tetrahedra are presented in yellow. The interlayer distances, corresponding to the lattice plane distances of the most intense 003 basal reflections are also given.

Many different kinds of stacking fault could appear in the hypothetical lithium tin sulfide phases. We present this in detail for the $\text{Li}_{0.5}\text{Sn}_{0.8}\text{S}_2 \cdot 2\text{H}_2\text{O}$ and $\text{Li}_{0.5}\text{Sn}_{0.8}\text{S}_2 \cdot 3\text{H}_2\text{O}$ structure models. Two stacking orders in the $\text{SnS}_{6/3}$ - and $\text{Li}(\text{H}_2\text{O})_{6/3}$ -octahedra layers arranged in an alternating fashion can be derived from the layer constitution: 1. a staggered C19-type stacking with a $(\text{B}\alpha\text{C})[\text{A}\beta\text{C}](\text{A}\gamma\text{B})[\text{C}\alpha\text{B}](\text{C}\beta\text{A})[\text{B}\gamma\text{A}]$ stacking order in which tin layers are indicated by round and lithium layers by square brackets; 2. An eclipsed C6-type stacking with a $(\text{B}\alpha\text{C})\text{B}\alpha\text{C}[\text{B}\alpha\text{C}]$ stacking order (Figure S17). As tin and sulfur are by far the strongest scatters in the crystal structure, shift between staggered and eclipsed stacking of the $\text{SnS}_{6/3}$ octahedra layers have the strongest impact on the diffraction pattern. The intercalation of three layers of water can also lead to a C19-type (Figure S18, a) or C6-type-like stacking (Figure S18, b) of the $\text{SnS}_{6/3}$ octahedra layers. In Figure S18 small Latin letters indicate the position of entire $\text{SnS}_{6/3}$ octahedra layers. As the orientation of the $\text{SnS}_{6/3}$ octahedra is inverted for neighboring layers, the stacking sequence can be denoted as $\text{a}\bar{\text{a}}\bar{\text{a}}$ -type stacking. For the structural models containing more water layers, a larger number of stacking faults needs to be considered. In addition to the pure shifting of layers, water could also occupy empty lithium positions, which causes further distortion of the interlayer water frame.

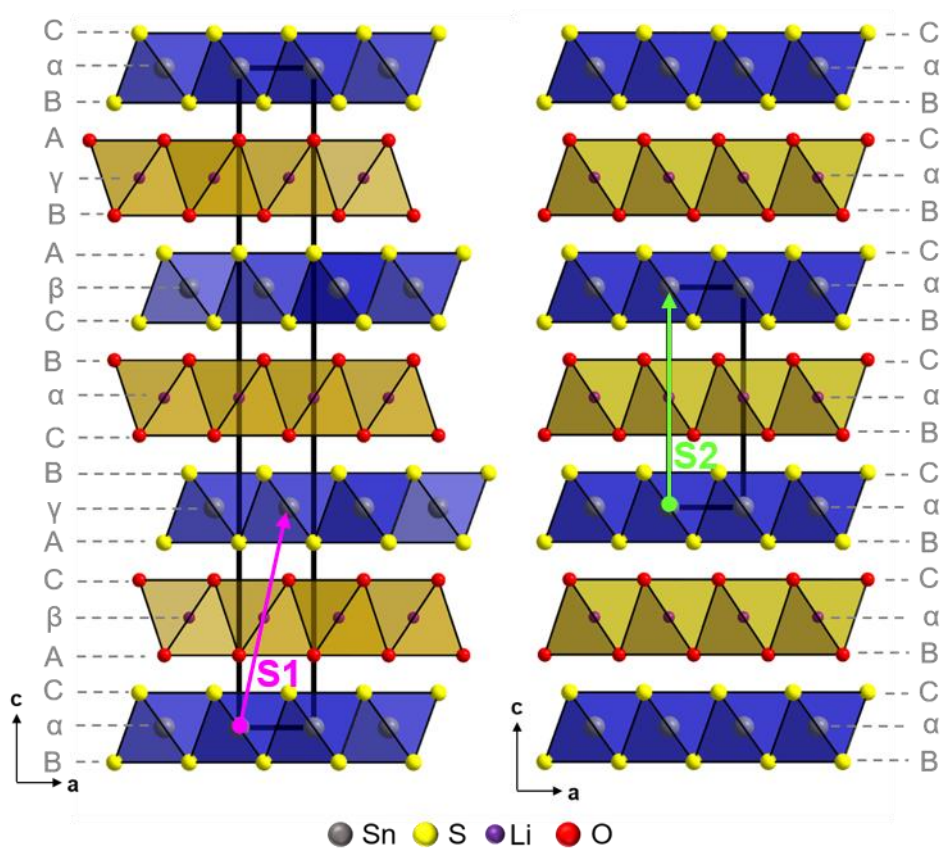


Figure S17. Illustration of the most likely stacking orders in hydrated $\text{Li}_{0.8}\text{Sn}_{0.8}\text{S}_2 \cdot 2\text{H}_2\text{O}$. The positions of cation layers are indicated by small Greek letters and the positions of anion sublayers by capital Latin letters. The stacking vectors, describing the transition from one layer to the next is represented by magenta and green arrows. $\text{SnS}_{6/3}$ octahedra are presented in blue and $\text{LiO}_{6/3}$ octahedra in yellow.

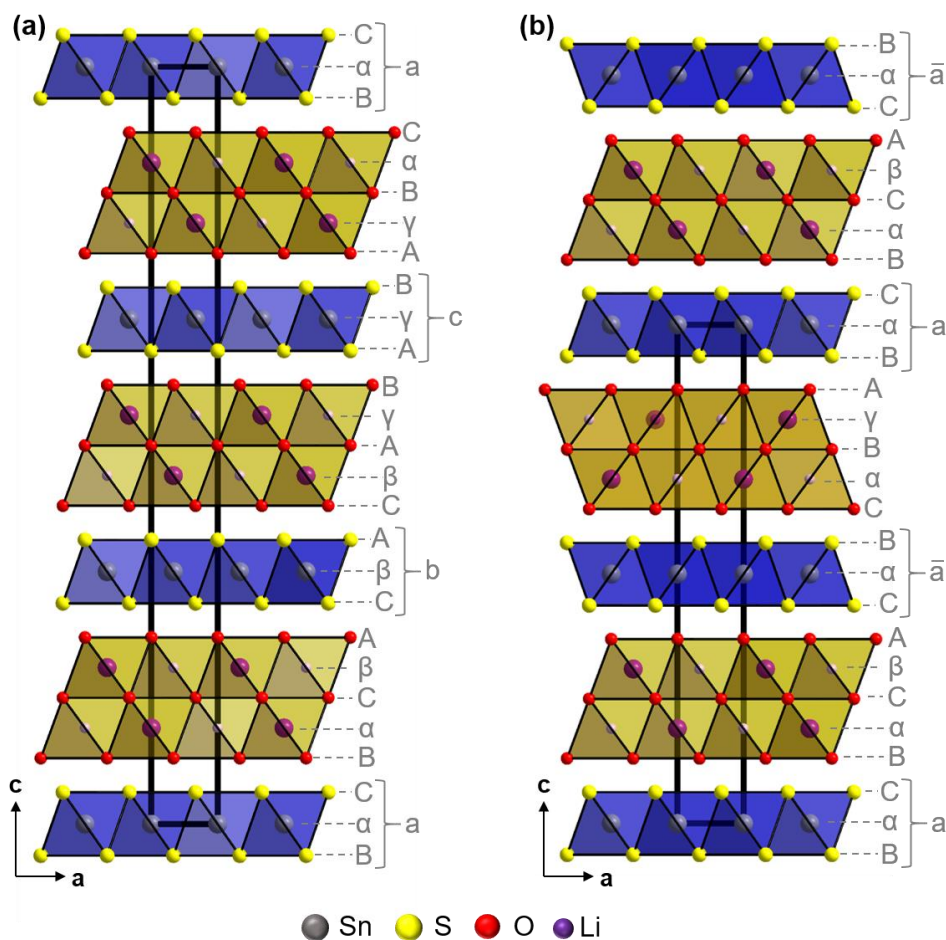


Figure S18 Illustration of two possible stacking orders in hydrated $\text{Li}_{0.8}\text{Sn}_{0.8}\text{S}_2 \cdot 3\text{H}_2\text{O}$. The positions of cation layers are indicated by small Greek letters and the positions of anion sublayers by capital Latin letters. The position of entire $\text{SnS}_{6/3}$ octahedra layers are indicated by small Latin letters, a bar on top of the letter indicates that the layer position is identical but the setup of the sulphide layers is inverted. $\text{SnS}_{6/3}$ octahedra are presented in blue and $\text{LiO}_{6/3}$ octahedra in yellow.

In order to support our structural considerations on the water intercalation, we refined the powder pattern of dry Li-TS after rehydration at 100 % RH in capillary for two weeks (Figure S15, b). Due to the high number of possible structural defects, we cannot use the approach for fitting the XRPD pattern that was applied for the dry samples. Instead, we used a multiphase approach, similar to one applied for SnTiO_3 ²², in which every phase used represents certain features of the microstructure of the sample. In order to account for the anisotropic peak broadening caused by structural disorder, symmetry adapted spherical harmonics of 4th order were applied to the peak profiles. In a first attempt, two phases of $\alpha\text{-Li}_{0.8}\text{Sn}_{0.8}\text{S}_2 \cdot 3\text{H}_2\text{O}$ with octahedrally coordinated lithium ions as described in Figure S18 were used. Identical setups of the $\text{SnS}_{6/3}$ octahedra layers were used and the lattice parameters constrained. By applying this approach, the most intense 003 reflection and the high 2θ -range of the diffraction pattern could be suitably fitted (Figure S19, a). The 006 reflection, however, exhibits a considerable misfit in the peak intensity. This is not an effect of the stacking faults within the structure of $\text{Li}_{0.8}\text{Sn}_{0.8}\text{S}_2 \cdot 3\text{H}_2\text{O}$, as these defects only lead to peak broadening. Therefore, reflections that are affected by stacking faults are usually overestimated in intensity. The comparatively high intensity of the 006 reflection in conjunction with the peak position referring to a lattice plane distance of approx. 6 Å suggests that there are non-hydrated domains of $\text{Li}_{0.8}\text{Sn}_{0.8}\text{S}_2$ or SnS_2 within the crystals. Hence, the inclusion of these

phases into the refinement led to a good fit of the diffraction pattern (Figure S19, b). The resulting phase content (Figure S19) should not be over interpreted due to parameter correlations. When we carried out the refinements multiple times, while applying different sequences of parameter refinements, we obtained equivalent fits but varying phase contents. In all attempts the phases representing hydrated $\text{Li}_{0.8}\text{Sn}_{0.8}\text{S}_2 \cdot 3\text{H}_2\text{O}$ (abc-stacked $\alpha\text{-Li}_{0.8}\text{Sn}_{0.8}\text{S}_2 \cdot 3\text{H}_2\text{O}$ + a \bar{b} a \bar{b} -stacked $\alpha\text{-Li}_{0.8}\text{Sn}_{0.8}\text{S}_2 \cdot 3\text{H}_2\text{O}$) were estimated with a summed content of more than 66 wt %. Thus, the majority of the layers in the hydrated samples exhibits an intercalation of multiple layers of water.

These findings could explain the NMR data (Figure S4, a and Figure S7) that suggested the presence of two lithium species in the hydrated samples: a mobile and a fairly immobile species. When there are three or more layers of intercalated water present, the lithium cations are distributed over a large number of voids that are only half or less occupied. Consequently, the lithium ions can easily move from one void to the adjacent place. When there are also non-hydrated layers present in the sample, the lithium ions will show a lower mobility and therefore give an NMR signal similar to the dry sample. The movement of the lithium ions within the water layers creates distortions in the framework of intercalated water that results in shifts of adjacent SnS_2 layers. Accordingly, these layers are more or less *floating* on the intercalated water and are therefore severely disordered. This explains the severe stacking fault disorder that we found in dry Li-TS as it is produced by dehydration of the hydrated samples.

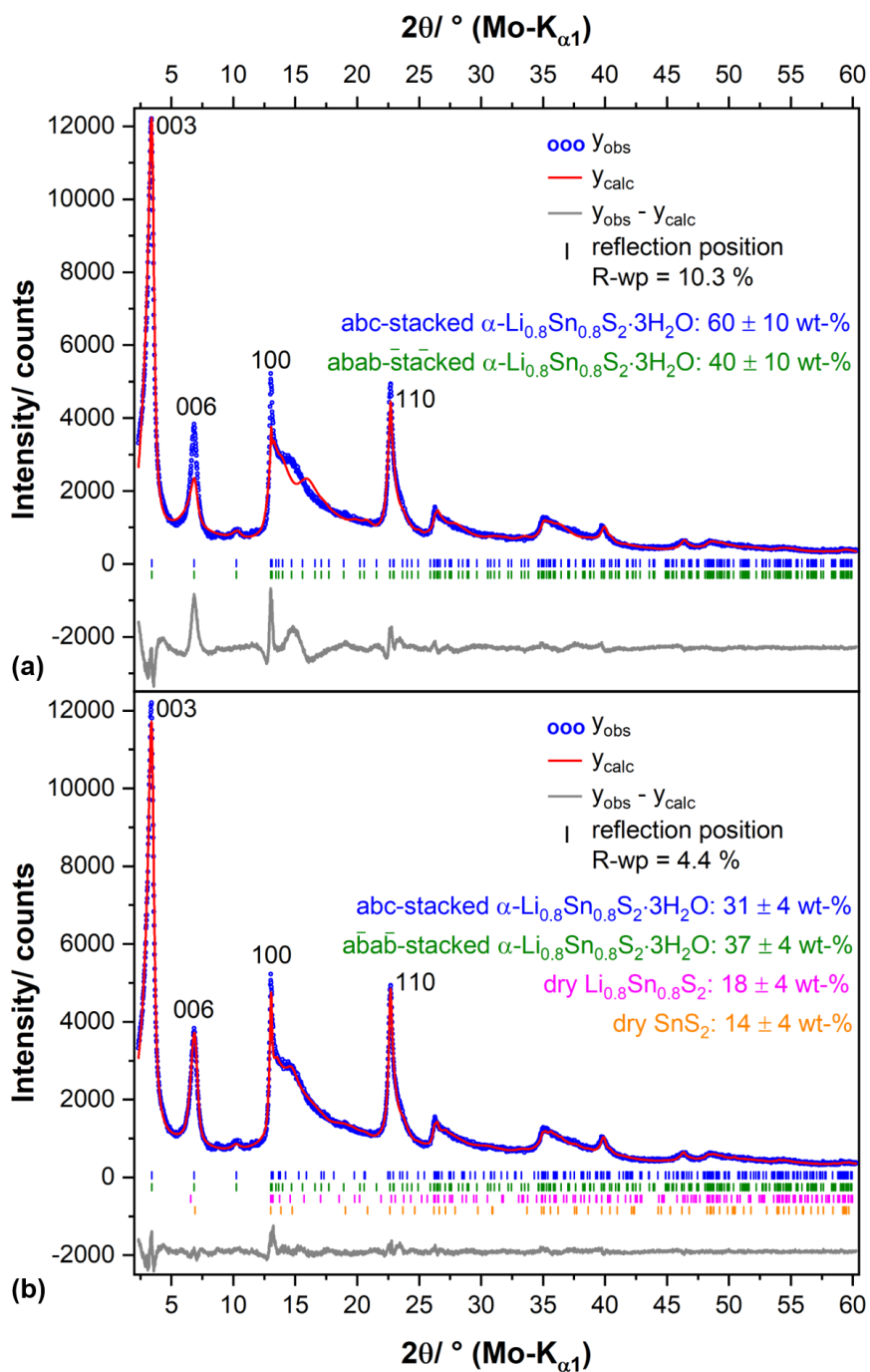


Figure S19. Graphical results of the final Rietveld refinements of b) dry Li-TS after rehydrated at 100 % RH in capillary for two weeks (a) using 2 phases of hypothetical $\alpha\text{-Li}_{0.8}\text{Sn}_{0.8}\text{S}_2\cdot 3\text{H}_2\text{O}$ representing different local stacking order and (b) also including dry $\text{Li}_{0.8}\text{Sn}_{0.8}\text{S}_2$ and dry SnS_2 into the refinement.

6. PDF Analysis of the Local Structures in Dry and Hydrated LiSnS₂

Total scattering measurements were carried out using the high energy Powder Diffraction and Total Scattering Beamline P02.1 of PETRA III at the Deutsches Elektronen-Synchrotron (DESY). X-ray total scattering data were collected in rapid acquisition mode (RAPDF).³¹ A large-area 2D PERKIN ELMER XRD1621 detector (2048x2048 pixels, 200x200 μm² each) was used at a sample-to-detector distance of approximately 304 mm. Samples were loaded into 1.8 mm ID/1.9 mm OD polyimide capillaries (Cole-Parmer) and measured at room temperature. For relative humidity dependent measurements capillaries were stored under the respective humidity for one day before sealing. The incident energy of the X-rays was 59.858 keV (λ=0.20713 Å). A measurement of Si was collected at room temperature as a standard for calibration of the setup. Calibration was performed, and the raw 2D intensity was corrected for polarization and azimuthally integrated and converted to 1D intensity versus Q (Q = 4π sin θ/λ is the magnitude of the scattering momentum transfer, with 2θ scattering angle) using the software Fit2D.²³

Further correction and normalization of the integrated 1D diffraction intensities were carried out to obtain the total scattering structure function, F(Q), which was Fourier transformed to obtain the pair distribution function (PDF), G(r) using PDFgetX3²⁴ within xPDFsuite²⁵. The maximum value used in the Fourier transform of the total scattering data (Q_{max}) was 24.0 Å⁻¹. Real-space structure model refinements to the PDF data were carried out using PDFgui²⁶. The resolution parameter due to Q-space resolution, Q_{damp} = 0.0346 Å⁻¹ was determined from Si and used for further fitting.

Real-space structure refinement:

Analysis of the PDF provides a useful method for interpreting structure information from total scattering data. It provides a sensitive probe of the local structure in amorphous and nanostructured materials, because it does not require symmetry, and treats both Bragg and diffuse scattering equally.²⁷ A diffraction measurement over a wide range of momentum transfer and with good statistics is required to obtain suitable PDFs for structure analysis. Starting with a 2D data collection of diffracted intensities, azimuthal integration results in the 1D, isotropic powder pattern, which contains the coherent scattering intensities I(Q) from the atoms in the sample, defined by the Debye equation²⁷, as

$$I(Q) = \sum_i \sum_{j \neq i} f_i(Q) f_j(Q) \frac{\sin(Qr_{ij})}{Qr_{ij}}. \quad (1)$$

In order to obtain the pair distribution function, by the formalism of Egami and Billinge²⁶, the measured powder diffraction intensities are first normalized by the average form factor squared to obtain the total scattering structure function S(Q), defined as

$$S(Q) = \frac{I(Q) - \langle f(Q)^2 \rangle + \langle f(Q) \rangle^2}{\langle f(Q) \rangle^2} \quad (2)$$

The experimental PDF, denoted G(r), is the truncated Fourier transform of the reduced, total scattering structure function, F(Q) = Q[S(Q) - 1], as

$$G(r) = \frac{2}{\pi} \int_{Q_{min}}^{Q_{max}} F(Q) \sin(Qr) dQ, \quad (3)$$

where $G(r)$ is the magnitude of the scattering momentum transfer. For elastic scattering,

$$Q = 4\pi \sin\theta / \lambda, \quad (4)$$

where λ is the probe wavelength and 2θ is the scattering angle. In practice, values of Q_{min} and Q_{max} are determined by the experimental setup, and Q_{max} is often reduced below the experimental maximum to reduce the effects of low signal-to-noise in the high- Q region on the Fourier transformation.

The PDF gives the scaled probability of finding two atoms in a material a distance r apart and is relative to the density of atom pairs in the material. For a macroscopic scatterer, $G(r)$ is calculated from a known structure model according to

$$G(r) = 4\pi r [\rho(r) - \rho_0], \quad (5)$$

$$\rho(r) = \frac{1}{4\pi r^2 N} \sum_i \sum_{j \neq i} \frac{f_i f_j}{\langle f \rangle^2} \delta(r - r_{ij}). \quad (6)$$

Here, ρ_0 is the average number density of the material and $\rho(r)$ is the local atomic pair density, which is the mean weighted density of neighbor atoms at distance r from an atom at the origin. The sums in $\rho(r)$ run over all atoms in the sample, f_i is the scattering factor of atom i , $\langle f \rangle$ is the average scattering factor and r_{ij} is the distance between atoms i and j . In this study, Eqs. 5 and 6 were used to fit the PDF generated from a structure model to the experimental PDFs in using the programs PDFgui²⁵ and by Eqs. 1, 2, and 3 in DIFFPY-CMI²⁸. The delta functions in Eq. 5 were Gaussian-broadened and the equation was modified to account for signal damping and broadening due to experimental effects. PDF modeling was performed by adjusting the lattice parameters, atomic displacement parameters (ADPs), correlated motion of neighboring atoms $\delta 2$, domain size (*spdiameter*), and the scale factor. The refinements were run by minimizing R_w , calculated as

$$R_w = \sqrt{\frac{\sum_{i=1}^n [G_{obs}(r_i) - G_{calc}(r_i, P)]^2}{\sum_{i=1}^n G_{obs}(r_i)^2}}, \quad (7)$$

which was used to quantify the goodness-of-fit for the model.

To develop further insights into the local atomic structuring of the layers, pair distribution function (PDF) analysis was performed on synchrotron x-ray total scattering measurements of the dry (same sample as in Figure S15, a) and hydrated samples (at 100 % RH for 24 h).²⁹ The data are shown at various stages of data reduction in Figure S20 using xPDFsuite.³⁰⁻³² Other than additional scattering intensities present at very low momentum transfer Q , the diffraction patterns and resulting structure functions and PDFs are highly similar, indicative of the similar layer structures and predominantly turbostratically disordered stacking relationships.

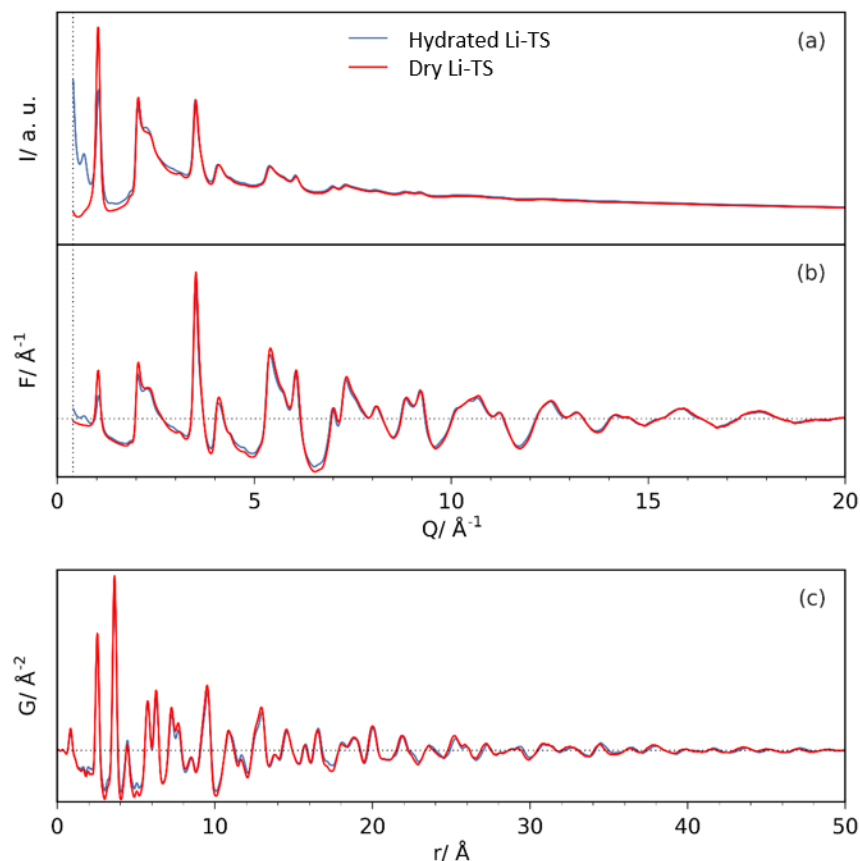


Figure S9 Different stages of total scattering data reduction: (a) background subtracted diffraction patterns, (b) reduced total scattering structure functions, and (c) the resulting PDFs (truncated with $Q_{max} = 24 \text{ \AA}^{-1}$).

In order to confirm the local validity of the models developed to describe the x-ray diffraction patterns, we investigated the short-range structure of the dried sample via real-space model refinements using either PDFgui³³ and Diffpy-CMI.³⁴ Due to the small effect of Li atoms on the simulated PDFs (due to low-Z) and apparent disagreement with the ordered model Li sites, we neglected the interlayer content. The results of different model refinements are shown in Figure S21

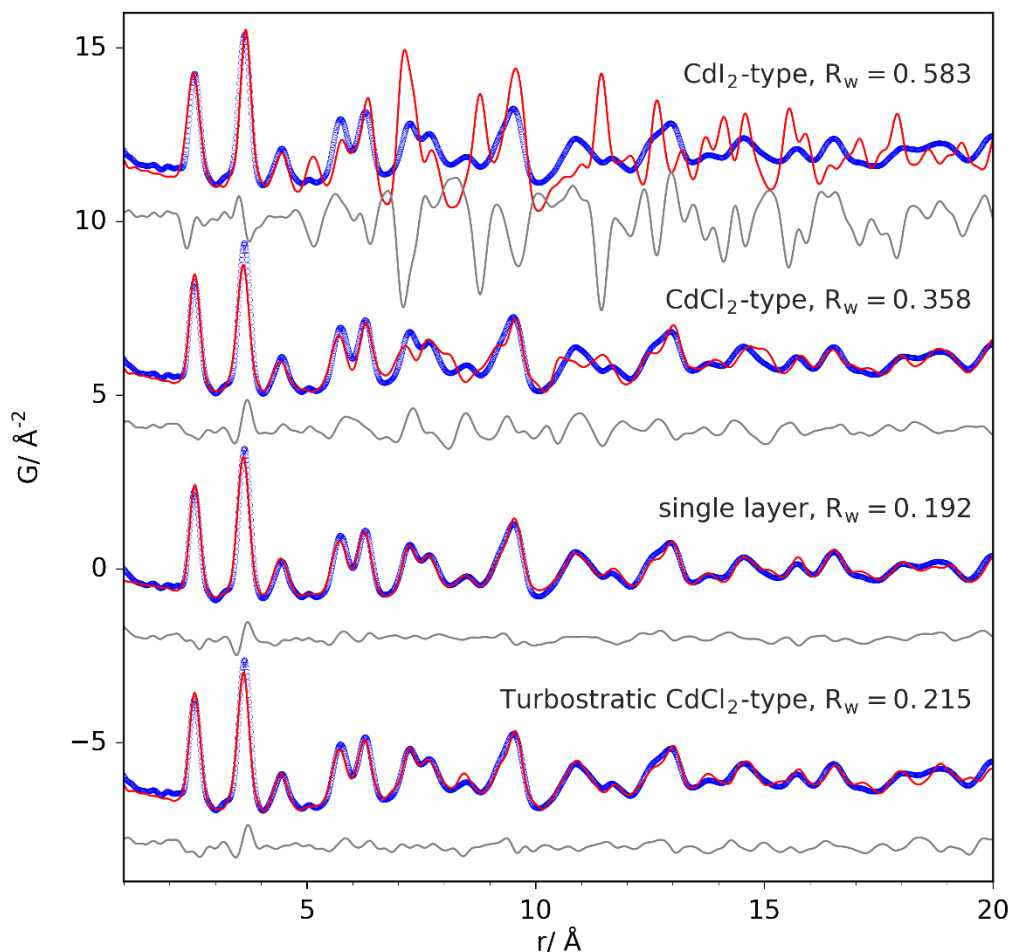


Figure S10 Results of real-space structure refinement to the dry Li-TS sample PDF: from top to bottom are the resulting simulated PDFs from refinement of a CdI_2 -type structure, CdCl_2 -type structure, single layer, and a turbostratic CdCl_2 -type structure allowing rigid body translations of the three layers.

We first compared the ideal CdI_2 - and CdCl_2 -type stacking orders to the PDF data. The vertical stacking vector (z -component only) of the CdI_2 -type stacking leads to a high multiplicity of specific interlayer Sn distances that are not strongly observed in the experimental data, e.g. ~ 7.1 Å between Sn and the nearest Sn neighbour of the same atom in the adjacent layer. Therefore, reasonable refinement of this structure was not possible, suggesting that the presence of perfectly eclipsed layers is unlikely. However, the ideal CdCl_2 -type stacking order gave reasonable agreement to the observed data, allowing refinement of lattice parameters a and c , an antisymmetric z -component shift of opposing S atoms, atomic displacement parameters (ADPs) for Sn and S, and a real-space damping factor for limited domain coherence. This suggests that neighboring layers prefer relatively shifted orientations. Despite the significant improvement in agreement to experimental data, the agreement is still poor with large discrepancies remaining in the residual. Two-phase refinement of both structures did not substantially improve the residual features, suggesting that the remaining misfit does not simply come from CdI_2 -type faults.

To investigate the limits of turbostratic ordering, we performed a refinement of a single layer (with periodic boundary conditions in the a and b directions, i.e. a 2D model, using the same structure parameters as for the CdCl_2 -type structure refinement) as previously performed for turbostratically disordered, layered Zr-phenyl-phosphonate-phosphate ion exchange materials³⁵. Here, the single layer is placed in a unit cell with a very large c unit cell parameter such that there

are no neighboring layers within the distances analysed in real space. The scattering is then simulated using the Debye equation, and the small-angle scattering (SAXS) intensities are truncated prior to Fourier transformation. For comparison, the experimental data was also reprocessed with a minimum scattering momentum transfer $Q_{min} = 1.1 \text{ \AA}^{-1}$, which removes low frequency, interlayer density modulations in the real-space PDF from the stacking peak (003 for CdCl₂-type stacking). The resulting fit is very good, indicating that a single layer structure can describe nearly all the fine features of the PDF. This indicates that the atomic-level ordering of the material comes predominantly from the structure of the intralayer motifs, and that turbostratic disorder from layer to layer leads to very weak, or absent, positional correlations between the Sn and S atoms in opposing layers averaged over all interlayer pairs, in good agreement with the high degree of turbostratic disorder found in the Rietveld refinements.

We further tested turbostratic disordering of the CdCl₂-type cell, with three layers, to develop a potential 3D model for the local structure. The resulting refinement is also compared in Figure S21. Here, the 3 layers of the unit cell were each allowed to freely translate as rigid bodies in the *a*, *b*, and *c* directions. This led to a very similar goodness-of-fit to the single layer model. The refined model suggests on-average interlayer distances of 6.2(2) Å, and in-plane interlayer offsets of 1.4(8) Å (for comparison the CdI₂-type and CdCl₂-type offsets are 0 and 1.205 Å respectively), which is in good agreement with Rietveld refinement (i.e. random shifts of ±0.425 in fractional coordinates = 1.537 Å for the refined cell). That a similar goodness-of-fit to the single layer model could be achieved with only three layers further supports the Rietveld result: the structure is not completely turbostratically disordered and preferred, relative orientations may exist depending on the amount and distribution of intercalated Li.

We also tested the data for signals corresponding to distortions of the in-plane distances, as may be suggested by the presence of Sn vacancies, as well as for ordered and disordered vacancy models, shown in Figure S21. Single-layer models representing distorted layer structures with in-plane modulations of the Sn sublattice due to Sn vacancies or Li substitutions were taken from the structures published for Li₂SnS₃ (Li_{4x}Sn_{1-x}S₂ (x=0.33))⁸ and Li_{0.8}Sn_{0.8}S₂(Li_{4x}Sn_{1-x}S₂ (x=0.2))⁴ with monoclinic symmetries. An additional distorted layer was generated by allowing $a \neq b$ for the CdCl₂-type single layer. All three distorted layer models perform slightly better than the non-distorted layer model suggesting differing in-plane Sn-Sn distances. However, the Sn-Sn distance is still underestimated by the model with a homogeneous shift to higher distances, suggesting that there must also be out-of-plane distortions of the Sn positions.

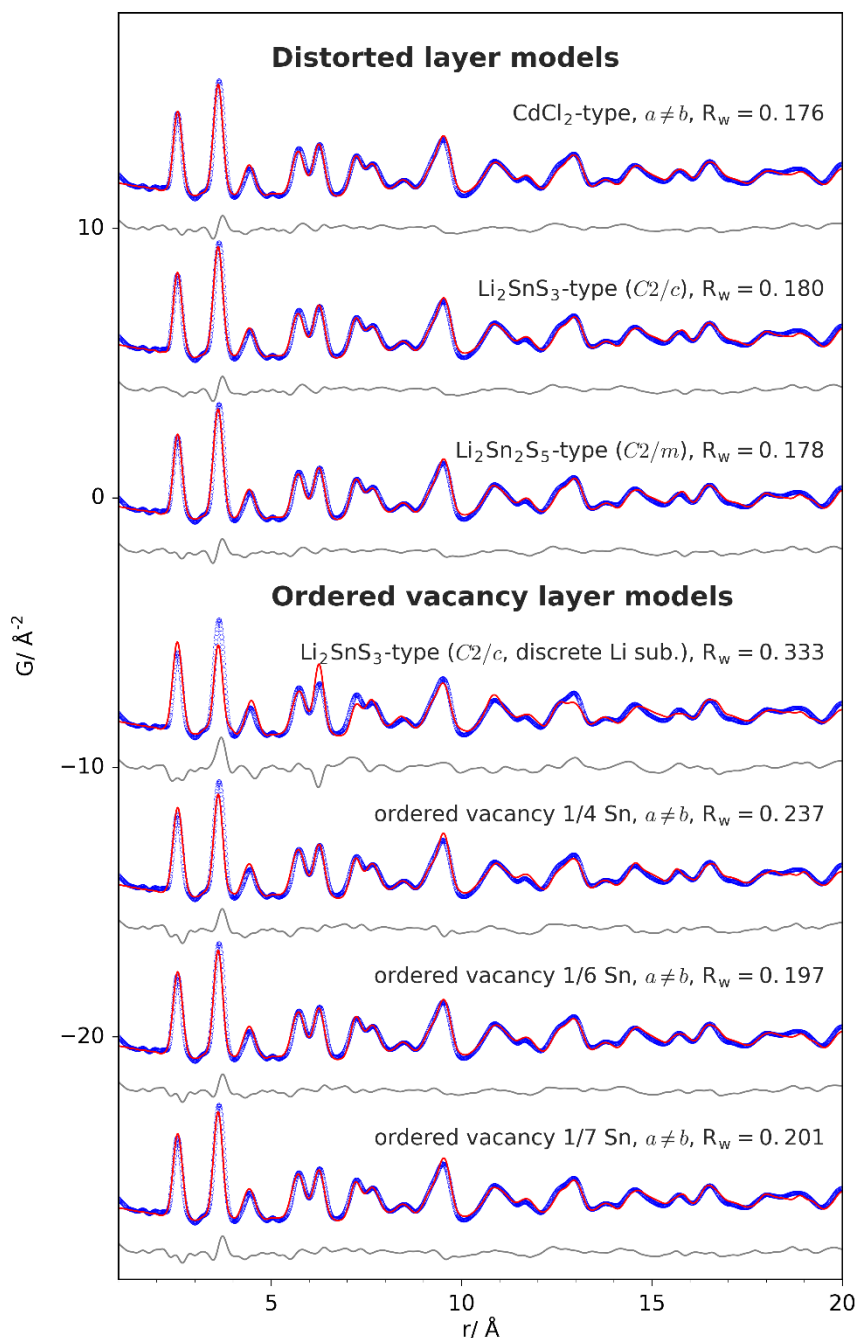


Figure S11 Results of real-space structure refinement to the dry LiSnS_2 sample PDF allowing for refinement of the z -component of the atoms off of their symmetry allowed positions. This improved the fit of the second nearest neighbour peak at 3.6 \AA , corresponding to both S-S and primarily Sn-Sn pairs, in both single layer and turbostratic CdCl_2 -type structure models.

Single-layer models with ordered Sn vacancies/substitutions included the Li_2SnS_3 model with $1/3$ Li substitutions obtained from the Materials Project database (code 1190364).³⁶ The other ordered vacancy models were built from the CdCl_2 -type single layer after refinement to the dry sample PDF and included the $1/4$, $1/6$, and $1/7$ ordered vacancy models presented in Figure S21. The $1/3$ and $1/4$ models performed particularly worse, while slightly better fits to the $1/6$ and $1/7$ models suggest that localized vacancy ordering cannot yet be ruled out. The effects of random, discrete Sn vacancies were tested using 10×10 expanded cell layers with Sn vacancies randomly generated and averaged over three separate iterations, Figure S23. Random Sn vacancies show

systematic reductions in relative peak intensities, which we do not observe. This is strong evidence in the measured data; however, correlating effects of the Li sites required may have an effect on the relative intensities in particular of the first two peaks.

As mentioned, all refinements of both the single layer and turbostratic 3D models led to a misfit

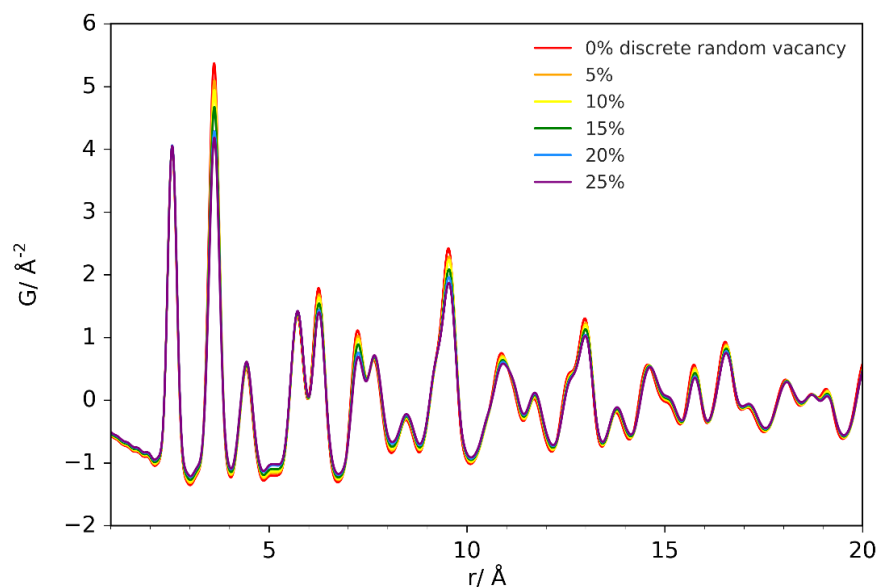


Figure S12 Results of real-space structure refinement to the dry LiSnS_2 sample PDF allowing for refinement of the z -component of the atoms off of their symmetry allowed positions. This improved the fit of the second nearest neighbour peak at 3.6 Å, corresponding to both S-S and primarily Sn-Sn pairs, in both single layer and turbostratic CdCl_2 -type structure models.

of the second peak at 3.6 Å. These models slightly under-predict the distance of this peak, which has contributions from both S-S and Sn-Sn pair distances, but predominantly from Sn-Sn pairs due to its significantly larger scattering power. The misfit could not be described by intralayer expansion in the ab -plane, or even by allowing distortion through separately refined a and b parameters. Thus, it is suggested that a slightly higher observed Sn-Sn (or S-S) pair distance could be accounted for by out-of-plane distortions. This was tested using supercells of both single layer (2×2) and 3D ($2 \times 1 \times 1$) models by allowing each Sn and S atom to distort slightly off of its symmetrically allowed position in only the z -direction. The resulting refinements, shown in Figure S24, show improved goodness-of-fit and suitably describe the second neighbor peak. This suggests that locally, the Sn sites can distort slightly out-of-plane, likely correlated with the presence or absence of vacancies or Li substitutions, as well as intercalating content. Therefore, localized distortions at various sites along a given layer pair may impact the distribution of interlayer distances apparent by stacking-peak shape as discussed in the Rietveld section.

We have shown that the peaks in the PDF of the dry sample are predominantly accounted for by the SnS_2 intralayer structuring. This is primarily due to the turbostratic randomization of relative interlayer orientations, which reduces the on-average positional correlations between interlayer atom-pairs. As shown in Figure S20 (c), the hydrated sample shows a highly similar PDF signal, bolstering the maintenance of the intralayer structure in the hydrated state, despite significant changes in interlayer spacing and water content. Thus, the primary changes in structure between

the dry and hydrated sample appear to be only in the distribution of interlayer density (including the hydration state of some intercalated Li ions), as evidenced by the changes in low angle diffraction intensities.

The hydrated sample measured by total scattering showed a slightly different diffraction pattern from the hydrated samples measured with the lab diffractometer. While the dry sample shows only a stacking peak associated with the ~ 6 Å interlayer distance, this hydrated sample showed peaks at ~ 6 and 9 Å, but no peak associated with the ~ 12 Å stacking distance. There is however a significant amount of SAXS signal. This may suggest smaller domains sizes in the hydrated samples or possibly effects due to diffraction from separate, delaminated domains.

To extract and demonstrate the interlayer density signals in the two samples, we have processed the PDFs with high ($= 0.4 \text{ \AA}^{-1}$) and low ($= 1.1 \text{ \AA}^{-1}$) Q_{min} values, which include and exclude the low angle Bragg components respectively.³⁵ Then the high Q_{min} PDF is subtracted from the low Q_{min} signal. Thus, only termination ripples associated with the Q_{min} value are present. This process is

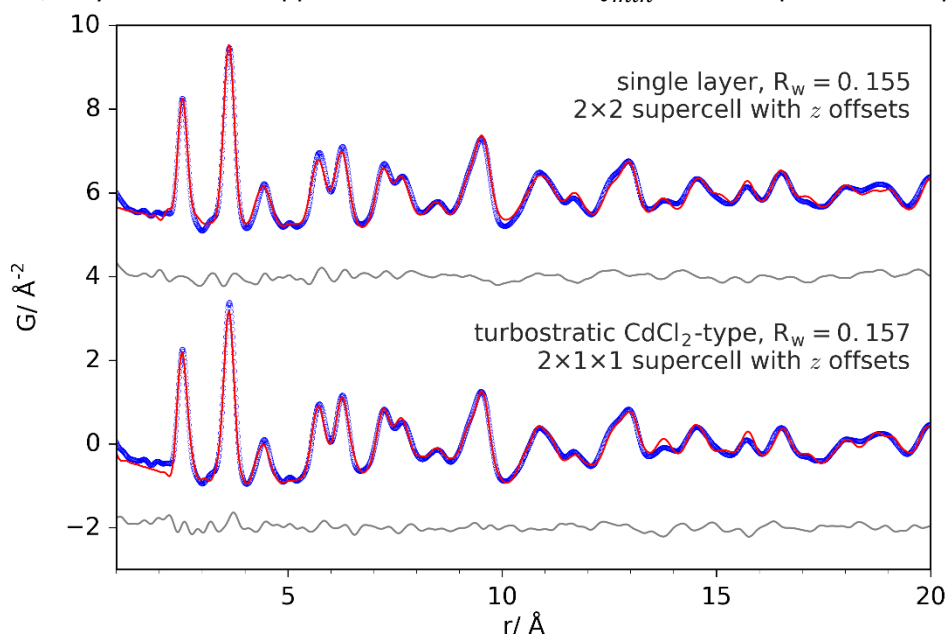


Figure S13 Results of real-space structure refinement to the dry LiSnS_2 sample PDF allowing for refinement of the z -component of the atoms off of their symmetry allowed positions. This improved the fit of the second nearest neighbour peak at 3.6 Å, corresponding to both S - S and primarily Sn - Sn pairs, in both single layer and turbostratic CdCl_2 -type structure models.

demonstrated in Figure S25 for both dried and hydrated samples. Figure S25 (c,d) show that the signal from the interlayer density modulations is very small in the atomic PDFs, primarily due to the weighting of high- Q information during the data reduction. Turbostratic density modulations were generated from the structure models developed during the Rietveld analysis for comparison. This was performed by giving the atoms in the structure very large ADPs in the ab -plane and a separate but also very large ADP in the c direction. Thus, all atomic-pair correlations are damped out (without termination effects), leaving only signal coming from the contrast in modulation between layer and interlayer content densities. Figure S25 (e) shows that the interlayer modulation for the dried sample agrees very well with a single stacking frequency. Figure S25 (f) show that the modulation for the hydrated sample is much more complicated. It also contains the non-hydrated stacking frequency as indicated by the 6 Å Bragg peak in the diffraction patterns, and should contain the 9 Å frequency component as well, which would correspond roughly to two

layers of water in the void. The other frequencies, we cannot determine exactly, due to the cutoff of the low angle feature and associated truncation effects.

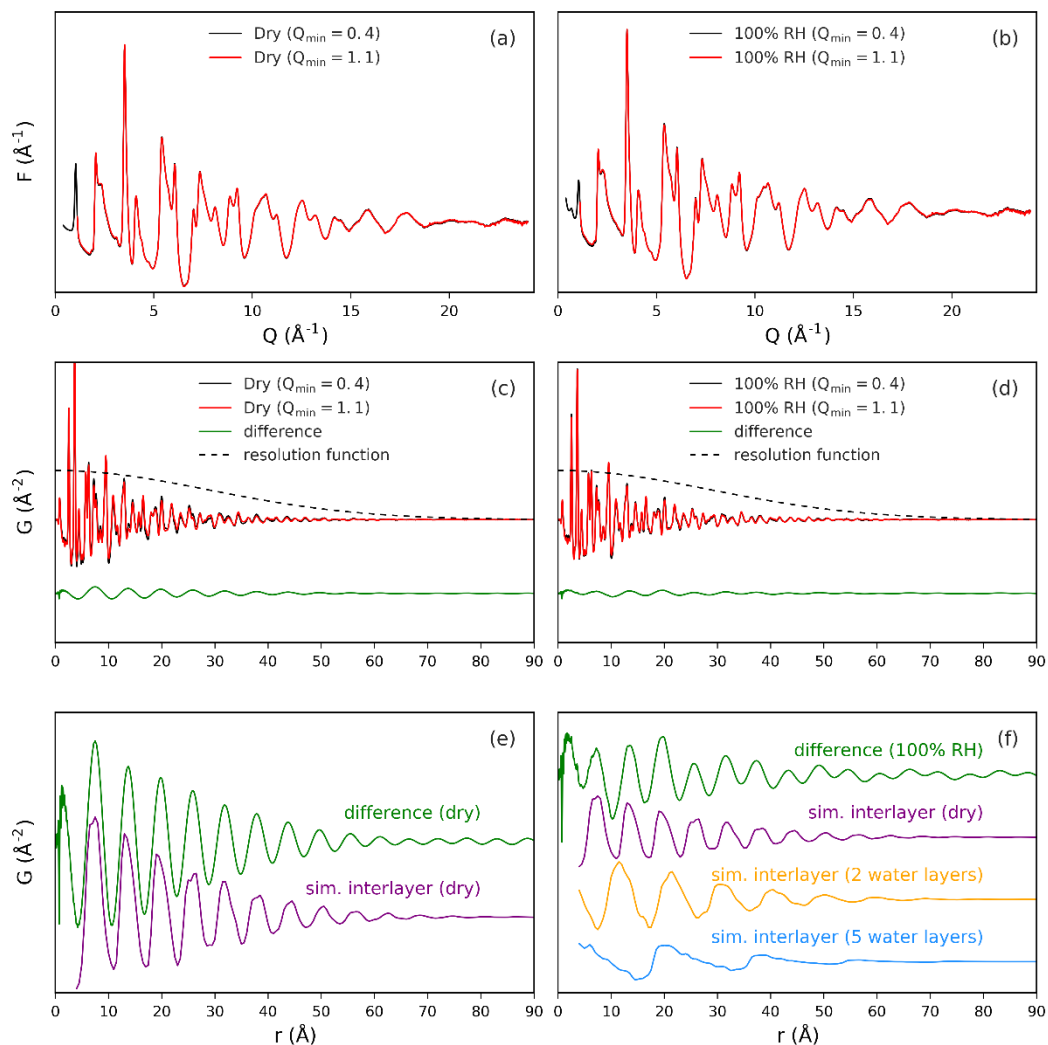


Figure S14 Demonstration of steps for extracting and comparing the turbostratic interlayer density modulations for dried and hydrated samples: (a,b) application of different Q_{\min} values, (c,d) transformation and subtraction of PDFs with and without low- Q information, and (e,f) comparison of simulated turbostratic density modulations for dry layers, or different levels of hydration.

7. Analysis of electronic properties

7.1 Pellet EIS measurements as function of temperature and humidity

To assess the ion conduction properties of dry Li-TS, EIS measurements were conducted on a pellet pressed (~15 kN) from fine ground powder that was dried at 120 °C under vacuum for ~16 h. The pellet was sputtered with Ru (99.95 %, LESKER, DC sputtering with EMITECH K575X, 100 mA current, 4 min sputter time under Ar) on both sides and contacted with Pt electrodes in a quartz sample holder. EIS was measured under constant argon flow (100 sccm) with a NOVOCONTROL Alpha-A analyzer (2-wire measurement, 10^6 to 10^{-1} Hz, 0.1 V amplitude). The temperature was ramped between 25-100 °C (EUROTHERM temperature controller) in 10 K steps with 3600 s equilibration time. After another 3600 s a measurement at the same temperature was conducted. The sample temperature at each step was measured with a dedicated thermocouple next to the pellet.

The same sample was used for EIS measurements at 30, 60 and 100 °C while varying the humidity in the measurement cell. The humidity or partial pressure of water was set with a single-walled glass container (humidifier) which was immersed in a thermostat (F 25, JULABO) to regulate its temperature. The humidifier contained water through which dry argon was flushed connected with the measurement cell. The humidified argon was mixed with dry argon close to the measurement cell to reach lower partial pressures of water. Both dry and wet Ar gas were set in the range 0-50 sccm and the thermostat temperature was varied between 5 and 20 °C (0-23.3 mbar). The exhaust gas humidity after the sample was checked with a humidity (ROTOTRONIC MESSGERÄTE GMBH) and dew point (EE355-PA1, E+E ELEKTRONIK GMBH) sensor. Gas flows were adjusted with flow controllers (FC-7700C, Aera) and the complete set-up as well as measurement cell were leaked checked (helium leak detector, UL 200 dry, OERLIKON LEYBOLD VACUUM).

EIS measurement of pellet of dry Li-TS

The severely depressed arc in the impedance spectrum in Figure S26a is fitted by two elements of a resistance (R) in parallel to a constant phase element (CPE) in series. The CPE element in series accounts for the polarization of lithium ions at the blocking electrode. The resulting conductivities and dielectric constants are shown in Figure S26b and c. The dielectric constant calculated via $\epsilon_r = Cd/A\epsilon_0$ of the high frequency signal (ϵ_1) is about 50-70 and of the low frequency signal (ϵ_2) between 150-200. Both of these ranges are too high for conventional bulk responses, but are in line with the dielectric behaviour in the parental compound $\text{Li}_{0.8}\text{Sn}_{0.8}\text{S}_2$.³⁷

The total ionic conductivity $\sigma(R_{\text{Tot}})$, calculated from the sum of $R_1+R_2=R_{\text{Tot}}$, is $3.4\pm 0.5\times 10^{-8} \text{ Scm}^{-1}$ with an activation energy of $0.55\pm 0.2 \text{ eV}$.

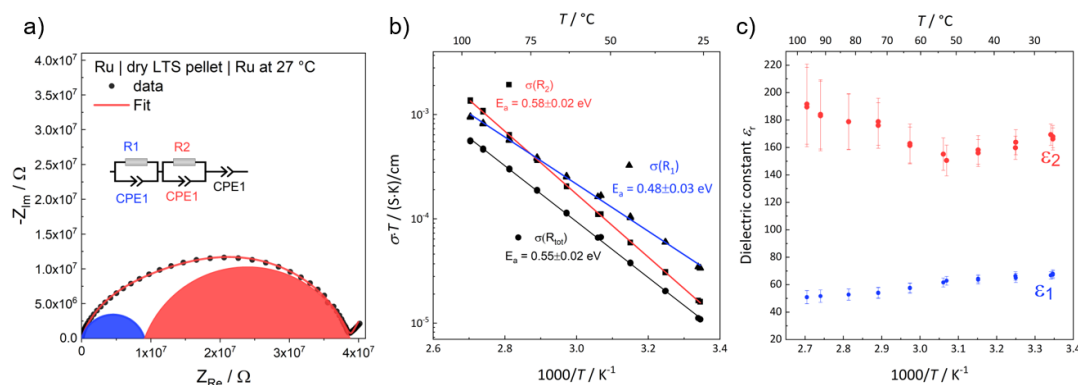


Figure S26 Results of EIS measurement of dry Li-TS pellet under argon flow. a) representative impedance spectrum with the equivalent model used for fitting given as inset b) σT as function of $1000/T$ with the determined activation energies for the total and the deconvoluted ionic conductivity of both processes. c) dielectric constant of the both processes fitted in a.

Ionic conductivity of Li-TS pellet samples as a function of water vapor pressure

The dependence of the ionic conductivity as a function of water vapor pressure at varying temperatures ranging from 30–100 °C was probed as shown in Figure S27. Representative impedance spectra are given as inset.

At high temperatures and low humidities the same (R)(CPE)-(R)(CPE)-CPE model as for the dry Li-TS can be applied. However, upon a certain degree of hydration of the pellet (cf. Figure S27b, starting from a $p(\text{H}_2\text{O})$ of 13 mbar at 60 °C) the semicircle is fitted only by one R-CPE element with a dielectric constant of 50. The change in fitting could simply be due to the shift in relaxation time with decreasing resistance, or a change in charge carrier.

In principle, we can think of two basic mechanisms how the incorporation of H_2O could influence the ion transport: (1) the dominant charge carrier is directly affected and its mobility is enhanced with the uptake of H_2O (change in kinetic properties), (2) a new mobile carrier with superior mobility is created, which takes over as the new dominant carrier species (change in concentration/thermodynamic property). In either case – (1) or (2) – the conductivity is directly affected by the amount of H_2O incorporated. Since the interaction of lithium ions with the anionic layers is screened by the coordination with water, we assume an increase in mobility of the lithium ions. However, the entire mechanism is probably a mixture of the two above and could be even more complicated.

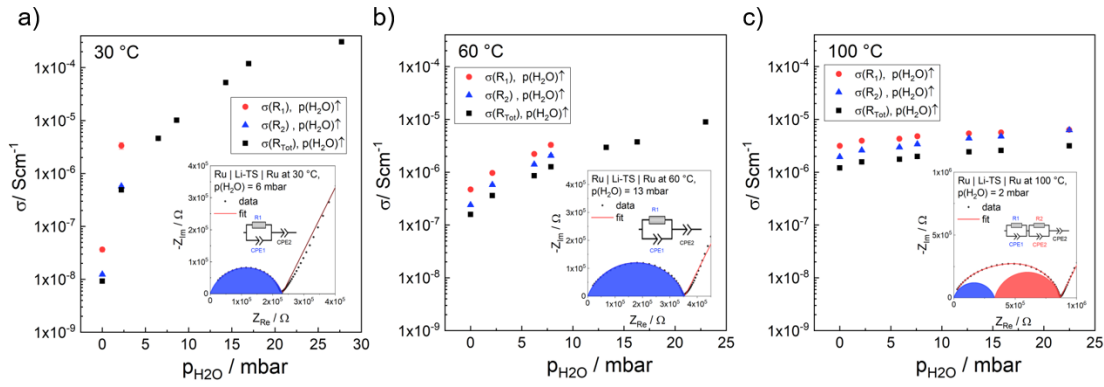


Figure S27 Plots of ionic conductivity as a function of water vapor pressure with representative impedance spectra and equivalent circuit models at a) 30 °C b) 60 °C and c) 100 °C.

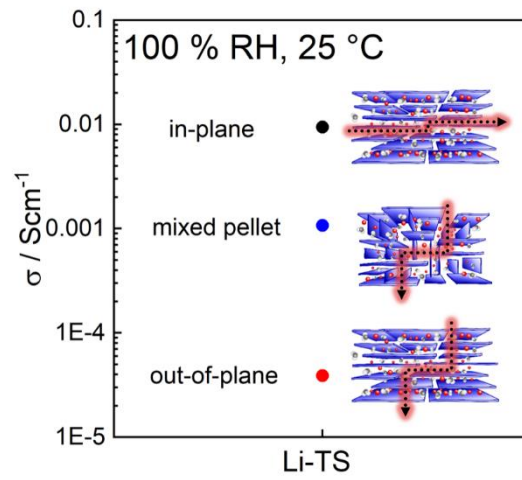


Figure S28 Ionic conductivity as a function of the orientation of electrodes on free standing films and powder pellets probing the in-plane and out-of-plane conductivity, respectively. The in-plane conductivity is magnitudes higher for Li-TS, indicating facile movement of cations between restacked nanosheets at high humidity.

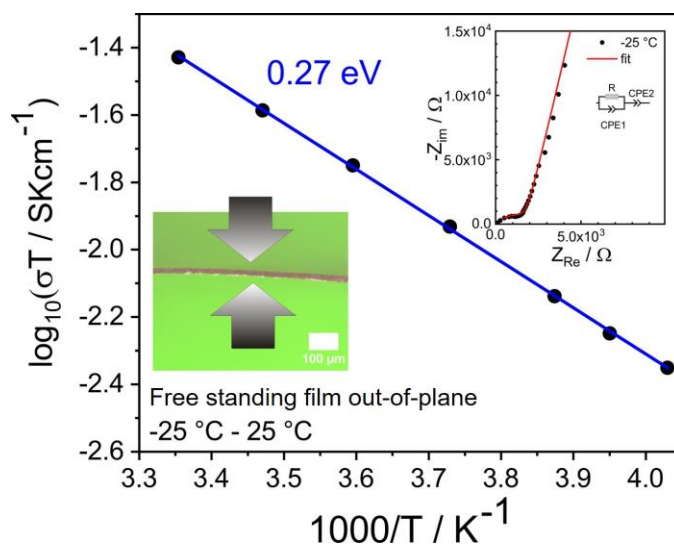


Figure S29 Ionic conductivity as a function of temperature between -25 and $25 \text{ }^\circ\text{C}$ at 76 \%RH of a free-standing film of restacked Li-TS NSs measured in the out-of-plane direction shows a lower conductivity compared to in plane measurements. The spectra are modelled by an equivalent circuit with a resistance (R) and a constant phase element (CPE1) in parallel and a CPE2 in series to take the polarization of ions at the blocking electrode into account. The image of the free-standing thin film was taken with a $10\times$ magnification with an optical microscope and show the thickness of about $20 \mu\text{m}$.

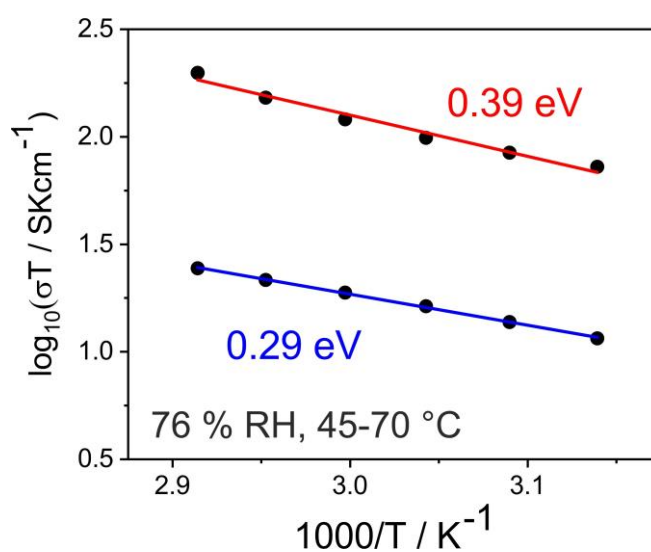


Figure S30 From measurements of the Li-TS thin film on a Al_2O_3 substrate at constant relative humidity of 76 \% between $40 \text{ }^\circ\text{C}$ and $70 \text{ }^\circ\text{C}$, the activation energies of the high-frequency semicircle (bulk properties, blue) and low-frequency semicircle (electrode contributions, red) in Figure S6c were extracted to be 0.29 and 0.39 eV , respectively.

8. PFG NMR population analysis

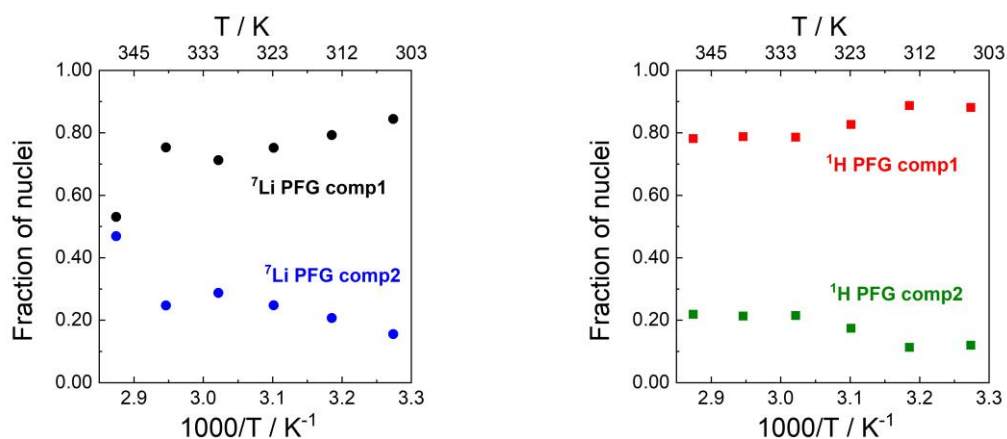


Figure S31 Population analysis of hydrated (100 % RH; 1 week) L-TS PFG NMR measurements showing a fraction of 20 % immobile and 80 % fast species resembling the presence of a majority and minority species in the ^6Li MAS spectrum in Figure S4 main text. The difference in absolute values of the fractions of species, are probably due to broadening of the ^7Li spectra that are the basis for diffusion analysis with respect to the ^6Li MAS spectra.

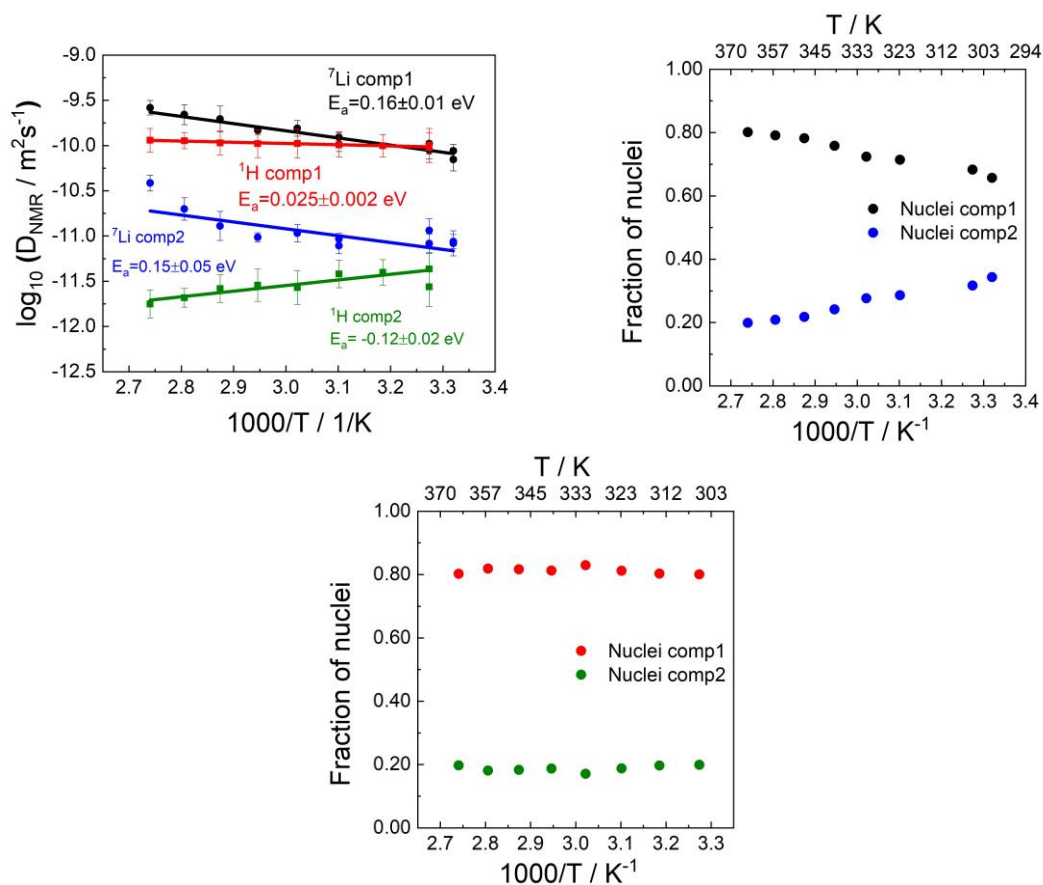


Figure S32 PFG NMR and population analysis of hydrated sample at 100 % RH for 24 h. In this slightly drier sample, the diffusion coefficient of ^7Li and ^1H match very well with $9.5 \times 10^{-11} \text{ m}^2 \text{ s}^{-1}$. The fractions analysis shows a fraction of 20 % immobile and 80 % mobile lithium ions. The diffusion behaviour of ^1H close to room temperature matches the behaviour of lithium very well, but deviates at higher temperatures, probably due to water leaving the sample. This is possible because the dead volume of the NMR spinner despite all efforts is not zero.

Calculation of charger carrier concentration in hydrated Li-TS

To convert the measured diffusivities from PFG NMR into conductivity, the Nernst-Einstein equation (see main text) was applied. The charge carrier concentration (lithium ions) n_{Li} was estimated with:

$$n_{Li} = \frac{Z_{Li}}{V_{cryst}} \cdot 0.4 \cdot \frac{d_{dry-Li-TS}}{d_{hydrated-Li-TS}}$$

where Z_{Li} and V_{cryst} are the number of Li atoms (5.01) and volume (438.8 \AA^3) per unit cell of the parental $\text{Li}_{0.8}\text{Sn}_{0.8}\text{S}_2$ ⁴ and $d_{dry-Li-TS}$ and $d_{hydrated-Li-TS}$ are the interlayer spacing of dry Li-TS (6.1 Å) and hydrated Li-TS (11.9 Å).

References

- [1] Cossement, C.; Darville, J.; Gilles, J.-M.; Nagy, J. B.; Fernandez, C.; Amoureux, J.-P., Chemical shift anisotropy and indirect coupling in SnO_2 and SnO . *Magn. Reson. Chem.* **1992**, *30* (3), 263-270.
- [2] Narsimha, K.; Reddy, B. M.; Rao, P. K.; Mastikhin, V. M., Characterization of vanadium oxide catalysts supported on tin dioxide by vanadium-51 and proton solid-state NMR spectroscopy. *J. Phys. Chem.* **1990**, *94* (19), 7336-7337.
- [3] Frey, G. L.; Tenne, R.; Matthews, M. J.; Dresselhaus, M. S.; Dresselhaus, G., Raman and resonance Raman investigation of MoS_2 nanoparticles. *Phys. Rev. B* **1999**, *60* (4), 2883-2892.
- [4] Holzmann, T.; Schoop, L. M.; Ali, M. N.; Moudrakovski, I.; Gregori, G.; Maier, J.; Cava, R. J.; Lotsch, B. V., $\text{Li}_{0.6}[\text{Li}_{0.2}\text{Sn}_{0.8}\text{S}_2]$ - A layered lithium superionic conductor. *Energy & Environmental Science* **2016**.
- [5] Warren, B. E., X-Ray Diffraction in Random Layer Lattices. *Phys. Rev.* **1941**, *59* (9), 693-698.
- [6] Welberry, T. R.; Butler, B. D., Interpretation of diffuse X-ray scattering via models of disorder. *J. Appl. Crystallogr.* **1994**, *27* (3), 205-231.
- [7] Le Blanc, A.; Rouxel, J., Sur les types structuraux des composés intercalaires MSnS_2 (M= Li, Na, K, Rb). *C. R. Acad. Sci. C* **1972**, *274*, 786-788.
- [8] Kuhn, A.; Holzmann, T.; Nuss, J.; Lotsch, B. V., A facile wet chemistry approach towards unilamellar tin sulfide nanosheets from $\text{Li}_x\text{Sn}_{1-x}\text{S}_2$ solid solutions. *J. Mater. Chem. A* **2014**, *2* (17), 6100-6106.
- [9] Hazen, R. M.; Finger, L. W., The crystal structures and compressibilities of layer minerals at high pressure. I. SnS_2 , berndtite. *Am. Mineral.* **1978**, *63*, 289-292.
- [10] Persson, K., Materials Data on LiSnS_2 (SG:164) by Materials Project. **2014**.
- [11] Mangelsen, S.; Srinivasan, B. R.; Schürmann, U.; Kienle, L.; Näther, C.; Bensch, W., Nanostructured tungsten sulfides: insights into precursor decomposition and the microstructure using X-ray scattering methods. *Dalton Trans.* **2019**, *48* (4), 1184-1201.
- [12] Bette, S.; Dinnebier, R. E.; Freyer, D., Structure solution and refinement of stacking-faulted $\text{NiCl}(\text{OH})$. *J. Appl. Crystallogr.* **2015**, *48* (6), 1706-1718.
- [13] Kudielka, A.; Bette, S.; Dinnebier, R. E.; Abeykoon, M.; Pietzonka, C.; Harbrecht, B., Variability of composition and structural disorder of nanocrystalline CoOOH materials. *J. Mater. Chem. C* **2017**, *5* (11), 2899-2909.
- [14] Coelho, A. A., TOPAS and TOPAS-Academic: an optimization program integrating computer algebra and crystallographic objects written in C++. *J. Appl. Crystallogr.* **2018**, *51* (1), 210-218.
- [15] Ainsworth, C. M.; Lewis, J. W.; Wang, C.-H.; Coelho, A. A.; Johnston, H. E.; Brand, H. E. A.; Evans, J. S. O., 3D Transition Metal Ordering and Rietveld Stacking Fault Quantification in the New Oxychalcogenides $\text{La}_2\text{O}_2\text{Cu}_{2-4x}\text{Cd}_{2x}\text{Se}_2$. *Chem. Mater.* **2016**, *28* (9), 3184-3195.
- [16] Coelho, A. A.; Evans, J. S. O.; Lewis, J. W., Averaging the intensity of many-layered structures for accurate stacking-fault analysis using Rietveld refinement. *J. Appl. Crystallogr.* **2016**, *49* (5), 1740-1749.
- [17] Bette, S.; Takayama, T.; Duppel, V.; Poulain, A.; Takagi, H.; Dinnebier, R.; Ernst, Crystal structure and stacking faults in the layered honeycomb, delafossite-type materials $\text{Ag}_3\text{LiIr}_2\text{O}_6$ and $\text{Ag}_3\text{LiRu}_2\text{O}_6$. *Dalton Trans.* **2019**, *48*, 9250-9259.

- [18] Bette, S.; Hinrichsen, B.; Pfister, D.; Dinnebier, R. E., A routine for the determination of the microstructure of stacking-faulted nickel cobalt aluminium hydroxide precursors for lithium nickel cobalt aluminium oxide battery materials. *J. Appl. Crystallogr.* **2020**, *53* (1).
- [19] Rietveld, H. M., A profile refinement method for nuclear and magnetic structures. *J. Appl. Crystallogr.* **1969**, *2* (2), 65-71.
- [20] Chomnilpan, S.; Liminga, R.; Tellgren, R., Refinement of pyroelectric lithium perchlorate trihydrate. *Acta Crystallogr., Sect. B: Struct. Sci., Cryst. Eng. Mater.* **1977**, *33*, 3954-3957.
- [21] Hermansson, K.; Thomas, J. O.; Olovsson, I., Hydrogen Bond Studies. CXXXVIII. Neutron Diffraction Studies of $\text{LiNO}_3(\text{H}_2\text{O})_3$ at 120 and 295 K. *Acta Crystallogr., Sect. B: Struct. Sci., Cryst. Eng. Mater.* **1980**, *36*, 1032-1040.
- [22] Diehl, L.; Bette, S.; Pielhofer, F.; Betzler, S.; Moudrakovski, I.; Ozin, G. A.; Dinnebier, R.; Lotsch, B. V., Structure-Directing Lone Pairs: Synthesis and Structural Characterization of SnTiO_3 . *Chem. Mater.* **2018**, *30* (24), 8932-8938.
- [23] Hammersley, A. P.; Svensson, S. O.; Hanfland, M.; Fitch, A. N.; Hausermann, D., Two-dimensional detector software: From real detector to idealised image or two-theta scan. *High Press. Res.* **1996**, *14* (4-6), 235-248.
- [24] Juhás, P.; Davis, T.; Farrow, C. L.; Billinge, S. J. L., PDFgetX3: a rapid and highly automatable program for processing powder diffraction data into total scattering pair distribution functions. *J. Appl. Crystallogr.* **2013**, *46* (2), 560-566.
- [25] Farrow, C. L.; Juhas, P.; Liu, J. W.; Bryndin, D.; Božin, E. S.; Bloch, J.; Proffen, T.; Billinge, S. J., PDFfit2 and PDFgui: computer programs for studying nanostructure in crystals. *J. Phys. Condens. Matter* **2007**, *19* (33), 335219.
- [26] T. Egami, S. J. L. B., *Underneath the Bragg peaks: structural analysis of complex materials*. 2 ed.; Elsevier: Amsterdam, 2012.
- [27] Debye, P., Zerstreung von Röntgenstrahlen. **1915**, *351* (6), 809-823.
- [28] Juhás, P.; Farrow, C. L.; Yang, X.; Knox, K. R.; Billinge, S. J., Complex modeling: a strategy and software program for combining multiple information sources to solve ill posed structure and nanostructure inverse problems. *Acta Crystallogr. A Found. Adv.* **2015**, *71* (Pt 6), 562-8.
- [29] Billinge, S., Nanometre-scale structure from powder diffraction: total scattering and atomic pair distribution function analysis. *International Tables for Crystallography* **2019**, *H*, 649-672.
- [30] Billinge, S. J. L.; Farrow, C. L., Towards a robust ad hoc data correction approach that yields reliable atomic pair distribution functions from powder diffraction data. *Journal of Physics: Condensed Matter* **2013**, *25* (45), 454202.
- [31] Juhás, P.; Davis, T.; Farrow, C. L.; Billinge, S. J. L., PDFgetX3: a rapid and highly automatable program for processing powder diffraction data into total scattering pair distribution functions. *Journal of Applied Crystallography* **2013**, *46* (2), 560-566.
- [32] Peterson, P. F.; Božin, E. S.; Proffen, T.; Billinge, S. J. L., Improved measures of quality for the atomic pair distribution function. *Journal of Applied Crystallography* **2003**, *36* (1), 53-64.
- [33] Farrow, C. L.; Juhas, P.; Liu, J. W.; Bryndin, D.; Božin, E. S.; Bloch, J.; Proffen, T.; Billinge, S. J. L., PDFfit2 and PDFgui: computer programs for studying nanostructure in crystals. *Journal of Physics: Condensed Matter* **2007**, *19* (33), 335219.
- [34] Juhás, P.; Farrow, Christopher L.; Yang, X.; Knox, Kevin R.; Billinge, Simon J. L., Complex modeling: a strategy and software program for combining multiple information sources to solve ill posed structure and nanostructure inverse problems. *Acta Crystallographica Section A Foundations and Advances* **2015**, *71* (6), 562-568.
- [35] Terban, M. W.; Shi, C.; Silbernagel, R.; Clearfield, A.; Billinge, S. J. L., Local Environment of Terbium(III) Ions in Layered Nanocrystalline Zirconium(IV) Phosphonate-Phosphate Ion Exchange Materials. *Inorg. Chem.* **2017**, *56* (15), 8837-8846.
- [36] Jain, A.; Ong, S. P.; Hautier, G.; Chen, W.; Richards, W. D.; Dacek, S.; Cholia, S.; Gunter, D.; Skinner, D.; Ceder, G.; Persson, K. A., Commentary: The Materials Project: A materials genome approach to accelerating materials innovation. **2013**, *1* (1), 011002.
- [37] Joos, M.; Schneider, C.; Münchinger, A.; Moudrakovski, I.; Usiskin, R.; Maier, J.; Lotsch, B. V., Impact of hydration on ion transport in $\text{Li}_2\text{Sn}_2\text{S}_5 \cdot x\text{H}_2\text{O}$. *Journal of Materials Chemistry A* **2021**, DOI: 10.1039/D1TA04736A.

5 Summary, Conclusion and Outlook

This work gave an overview of the contemporary battery research tackling the question of raising performance, but also becoming safer, cheaper and more sustainable. It introduced the basic concepts of ionic diffusion and conduction in ionic crystals and identified strategies to tune the performance. Then, electrochemical impedance spectroscopy was presented as method of choice to measure the ionic conductivity, which is the key performance indicator of solid electrolytes.

The development of solid electrolytes for lithium, but also sodium and potassium ion based technologies is key to progress, since SSBs are one of the most promising concepts currently under investigation. Therefore, we developed several solid electrolytes in a variety of projects in this thesis (cf. Figure 23).

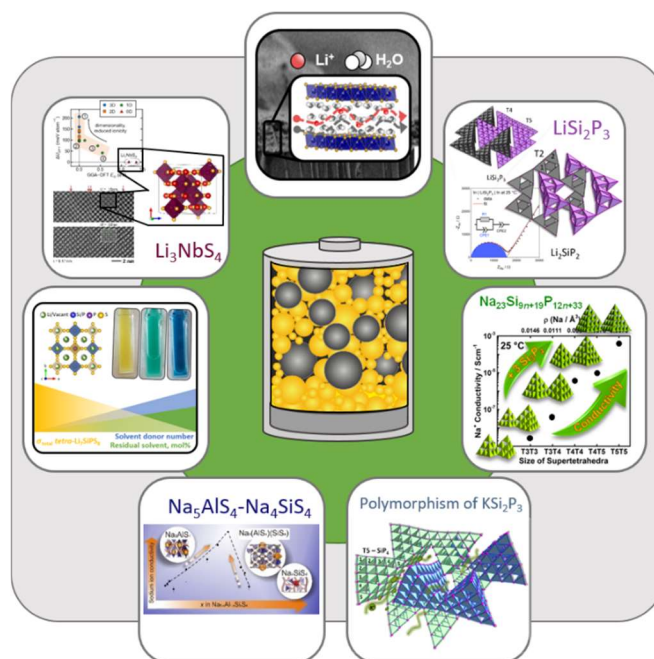


Figure 23 Graphical summary of all projects presented in this work. Starting from the top middle going clockwise: chapter 4.7, chapter 4.2, chapter 4.3, chapter 4.4, chapter 4.5, chapter 4.6, chapter 4.1.

In the emerging field of phosphidosilicate based solid electrolytes, we introduced several new systems and/or report on their ionic conductivity and elucidate their structure–property–relationship. The ionic conductivity and diffusivity of lithium ions in known Li_2SiP_2 and LiSi_2P_3 (chapter 4.2) is reported. The bulk conductivity of polycrystalline LiSi_2P_3 of $2.5 \times 10^{-4} \text{ S cm}^{-1}$ is estimated from PFG NMR measurements and is comparable to the conductivity of its sodium and potassium containing cousins presented later in this work. However, our comparison of conductivity from EIS and PFG NMR diffusivities exposes grain boundaries as limiting factor of performance (to $3.1 \times 10^{-5} \text{ S cm}^{-1}$). These findings complement the available data on ionic motion in lithium phosphidosilicates.

For a series of supertetrahedral sodium phosphidosilicates (chapter 4.3) an increase in ionic conductivity with increasing supertetrahedra size is found.¹⁴ In total, the structures and sodium ion conductivities of six new compounds ($\text{Na}_{19}\text{Si}_{13}\text{P}_{25}$, $\text{Na}_{23}\text{Si}_{19}\text{P}_{33}$, $\text{Na}_{23}\text{Si}_{28}\text{P}_{45}$, $\text{Na}_{23}\text{Si}_{37}\text{P}_{57}$, $LT\text{-NaSi}_2\text{P}_3$ and $HT\text{-NaSi}_2\text{P}_3$) were presented. The new compounds consist of SiP_4 tetrahedra assembled into interpenetrating networks of T3 to T5 supertetrahedral clusters. The ionic conductivity in the series increases dramatically by going from $\text{Na}_{23}\text{Si}_{19}\text{P}_{33}$ (T3T3), only possessing fully occupied sodium positions and relatively small channels between the rigid phosphidosilicate anionic supertetrahedra, to $HT\text{-NaSi}_2\text{P}_3$ ($\text{Na}_{23}\text{Si}_{46}\text{P}_{69}$, T5T5) by formally adding charge neutral “ Si_3P_4 ”. This leads to a dilution of sodium ions as the charge density of the anionic supertetrahedral networks decreases. This change boosted the ionic conductivity from initially 2×10^{-9} to $4 \times 10^{-4} \text{ S cm}^{-1}$ at $25 \text{ }^\circ\text{C}$ and lowered the activation energy from 0.47 eV to 0.25 eV in $HT\text{-NaSi}_2\text{P}_3$. That trend is in accordance with the general prerequisites for fast ion conduction in crystalline solids such as a highly ordered, immobile sublattice providing continuous open channels for ion transport and minimizing the activation (migration) energy while providing high charge carrier concentrations.

We applied the obtained insights to develop the first non-oxide based fast potassium ion conductor KSi_2P_3 (chapter 4.4) exhibiting a low E_a of 0.20 eV and an ionic conductivity of $3 \times 10^{-4} \text{ S cm}^{-1}$ at 25 °C.¹⁵ We showed that the known T3 KSi_2P_3 polymorph passes through a reconstructive phase transition to the tetragonal T5 polymorph at 1020 °C that is isostructural to its sodium cousin. It is also composed of SiP_4 tetrahedra forming interpenetrating networks of large T5 supertetrahedra. Additionally, upon cooling down to about 155 °C and 80 °C T5 KSi_2P_3 shows enantiotropic displacive phase transitions. T5 KSi_2P_3 is the fastest potassium ion conductor not containing any redox active transition metals (vs. $\text{K}_2\text{Fe}_4\text{O}_7$) known to-date and allows the exploration of new K-SSB systems.

Moreover, in this work light was shed on the trend in ionic conductivity in the Na_5AlSi_4 – Na_4Si_4 series (chapter 4.5).¹⁶ Here, the interplay of charge carrier concentration and low site symmetry of sodium ions lead to orders of magnitude increased conductivity. In this series containing three new structures, we rationalized the superior properties of $\text{Na}_{8.5}(\text{AlSi}_4)_{0.5}(\text{SiSi}_4)_{1.5}$ by a flattening of the energy landscape by the presence of highly distorted sodium coordination polyhedra. The origin of the increase in conductivity in this structure in respect to the border phases Na_5AlSi_4 and Na_4Si_4 , is a lowering of the energy barrier while the pre-exponential factor increases. This contradicts the Meyer–Neldel–rule, as introduced earlier by Di Stefano *et al.*¹³⁶ and this concept of flattening of the energy landscape by the presence of highly distorted coordination polyhedra is highly promising to find new fast ion conductors. The complex interplay between structural factors and the energetics of ion transport in these systems needs to be studied further.

Despite showing promising high ionic conductivities, the introduced new solids electrolytes are still far away from an application in real SSBs. The next step is the investigation of their thermodynamic and kinetic stability in contact to the electrodes and the formation of possible SEIs. By the introduction of more ionic defects by systematic substitution studies, the conductivity should be pushed to the desired $> 10 \text{ mS cm}^{-1}$ for an application of a solid electrolyte as catholyte. Besides, the development of new ways of processing to optimize the microstructure and limit the negative influence of grain boundaries is key. On the long run, the development of an upscaling route is inevitable enabling the synthesis of these new materials in large quantities. Since the introduction of new elements and material classes produces new safety problems, possible health hazards arising from the potential development of phosphane from the family of phosphidosilicates and hydrogen sulfide from the thio-tetrelates and –triates during processing and application have to be considered early on.²³

More in general, the development of solely inorganic ceramic solid electrolytes can be put into question. The concept of hybrid-electrolytes⁷⁴ combining for example traditional polymer or liquid and inorganic solid electrolytes or ionic conductive and/or structural components could enable a better contact between electrolyte and electrodes by retaining high ionic conductivity and mechanical stability. However, at the moment the search for hybrid systems just started and a lot of tasks have to be tackled until superiority or failure is demonstrated. Probably, the race for the best electrolyte will be won system by system, depending on the exact cell chemistry. Therefore, the aforementioned introduction of ways to enhance the interface stability towards the electrodes, to improve mechanical properties, microstructure and percolation paths, and to find low cost processing routes for upscaling, will be crucial research questions for the future.

To look beyond the discovery of entirely new materials already in this work, the solution based processing and the influence of nano-sizing and humidity on already known solid electrolytes was investigated. The fast solid electrolyte Li_7SiPS_8 (chapter 4.6) was treated with a variety of solvents and we found that LiSiPS is stable in aprotic solvents, but decomposes in protic solvents. For industrial slurry fabrication, we demonstrated the suitability of aprotic solvents with a donor number smaller $< 15 \text{ kcal mol}^{-1}$ and using anisole as a case study, we showed that a residual water content up to 800 ppm does not lead to a significant deterioration in the ionic conductivity when

compared to dry solvents. Additionally, a decomposition mechanism for ortho–thiophosphates in alcohols into oxygen–substituted thioethers was proposed. These insights open up the path to develop slurry based cathode fabrication and potentially a solvent based synthesis route not based on trial and error but on fundamental understanding of the underlying processes.

In chapter 4.7, restacked Li–TS after being exfoliated in water and shaped into thin films, possessing a structure dominated by severe disorder and locally varying lithium content, was demonstrated to be capable of fast water–assisted lithium ion conduction exceeding that of parental $\text{Li}_{0.8}\text{Sn}_{0.8}\text{S}_2$. This highlights the possibility of nano–structuring solid electrolytes without losing the good conduction properties and gives an example of a lithium ion conducting material for which the presence of environmental humidity is not destructive but beneficial. The development of a detailed structural model, as well as the proof of lithium ions being the main charge carriers in Li–TS rather than protons by the combination of PFG NMR and impedance spectroscopy hopefully contributes to a deeper understanding of other restacked nanosheet materials by making their structure–property relationship better accessible. Nevertheless, at this stage the influence of the effects of water in the electrolyte on the behavior of an entire battery is unclear. Possibly, the high voltage of a regular LIB leads to electrolysis of water into hydrogen and oxygen gas, possibly destructing the cell pack. Therefore, alternative low potential or water based battery systems should be considered to be combined with materials such as restacked Li–TS.

Since for a low cost and sustainable battery, the elimination of Co and potentially also Ni is advantageous, a closer look was taken on two new lithium metal sulfide based cathode materials (chapter 4.1). In that project, the poor battery performance of the ordered, rock–salt–type cathode materials Li_3NbS_4 and Li_3TaS_4 was rationalized by their inherently poor electronic properties demonstrated by electronic measurements and theoretical calculations. The evaluation of the local microstructure and short–range order by HRTEM highlighted the importance of short–range order inhibiting lithium diffusion, worsening the overall battery performance, and the need to look out for amorphous side phases severely altering the electronic and ionic properties of a material. This work thus highlights the importance of microstructural and local structure analysis of emerging classes of highly reversible, high capacity lithium metal sulphide cathodes and beyond.

6 References

- [1] European Green Deal, https://ec.europa.eu/info/strategy/priorities-2019-2024/european-green-deal_en, (accessed 29.05.2021, 2021).
- [2] Circular Economy Action Plan, https://ec.europa.eu/environment/strategy/circular-economy-action-plan_en#:~:text=%20The%20new%20Circular%20Economy%20Action%20presents%20measures,Lead%20gl%20obal%20efforts%20on%20circular%20economy.%20More%20, (accessed 29.05.2021).
- [3] European Industrial Strategy, https://ec.europa.eu/info/strategy/priorities-2019-2024/europe-fit-digital-age/european-industrial-strategy_en#:~:text=%20The%20single%20market%20%201%20make%20companies,innovation%204%20give%20consumers%20more%20choice%20More%20, (accessed 29.05.2021).
- [4] European Battery Alliance, https://ec.europa.eu/growth/industry/policy/european-battery-alliance_en, (accessed 29.05.2021).
- [5] S. Ohno, A. Banik, G. F. Dewald, M. A. Kraft, T. Krauskopf, N. Minafra, P. Till, M. Weiss and W. G. Zeier, *Progress in Energy*, 2020, **2**.
- [6] T. Famprakis, P. Canepa, J. A. Dawson, M. S. Islam and C. Masquelier, *Nature Materials*, 2019, DOI: 10.1038/s41563-019-0431-3.
- [7] Q. Ma and F. Tietz, *ChemElectroChem*, 2020, **7**, 2693-2713.
- [8] A. Mauger, C. M. Julien, A. Paoletta, M. Armand and K. Zaghib, *Materials*, 2019, **12**, 3892.
- [9] O. Sheng, C. Jin, X. Ding, T. Liu, Y. Wan, Y. Liu, J. Nai, Y. Wang, C. Liu and X. Tao, *Advanced Functional Materials*, 2021, DOI: <https://doi.org/10.1002/adfm.202100891>, 2100891.
- [10] Z. Wang, J. Liu, M. Wang, X. Shen, T. Qian and C. Yan, *Nanoscale Advances*, 2020, **2**, 1828-1836.
- [11] J. Janek and W. G. Zeier, *Nat. Energy*, 2016, **1**, 16141.
- [12] D. Andre, S.-J. Kim, P. Lamp, S. F. Lux, F. Maglia, O. Paschos and B. Stiaszny, *J. Mater. Chem. A*, 2015, **3**, 6709-6732.
- [13] H. S. Hirsh, Y. Li, D. H. S. Tan, M. Zhang, E. Zhao and Y. S. Meng, *Advanced Energy Materials*, 2020, **10**, 2001274.
- [14] A. Haffner, A.-K. Hatz, I. Moudrakovski, B. V. Lotsch and D. Johrendt, *Angew. Chem. Int. Ed. Engl.*, 2018, **57**, 6155-6160.
- [15] A. Haffner, A.-K. Hatz, O. E. O. Zeman, C. Hoch, B. V. Lotsch and D. Johrendt, *Angew. Chem. Int. Ed. Engl.*, 2021, **60**, 13641-13646.
- [16] S. Harm, A.-K. Hatz, C. Schneider, C. Hofer, C. Hoch and B. V. Lotsch, *Frontiers in Chemistry*, 2020, **8**.
- [17] S. Harm, A.-K. Hatz, I. Moudrakovski, R. Eger, A. Kuhn, C. Hoch and B. V. Lotsch, *Chem. Mater.*, 2019, **31**, 1280-1288.
- [18] *Rechargeable Batteries - Materials, Technologies and New Trends*, Springer, Cham, 1 edn., 2015.
- [19] *Automotive Battery Technology*, Springer, Cham, 1 edn., 2014.
- [20] C. Julien, A. Mauger, A. Vijn and K. Zaghib, *Lithium Batteries - Science and Technology*, Springer, Cham, 1 edn.
- [21] S. Petrovic, *Battery Technology Crash Course*, Springer, Cham, 1 edn.
- [22] S. Randau, D. A. Weber, O. Kötz, R. Koerver, P. Braun, A. Weber, E. Ivers-Tiffée, T. Adermann, J. Kulisch, W. G. Zeier, F. H. Richter and J. Janek, *Nature Energy*, 2020, **5**, 259-270.
- [23] W. Huang, X. Feng, X. Han, W. Zhang and F. Jiang, *Cell Reports Physical Science*, 2021, **2**.
- [24] T. Placke, R. Kloepsch, S. Dühnen and M. Winter, *Journal of Solid State Electrochemistry*, 2017, **21**, 1939-1964.
- [25] P. Minnmann, L. Quillmann, S. Burkhardt, F. H. Richter and J. Janek, *Journal of The Electrochemical Society*, 2021, DOI: 10.1149/1945-7111/abf8d7.
- [26] S. M. Bak, E. Hu, Y. Zhou, X. Yu, S. D. Senanayake, S. J. Cho, K. B. Kim, K. Y. Chung, X. Q. Yang and K. W. Nam, *ACS Appl Mater Interfaces*, 2014, **6**, 22594-22601.
- [27] J. Asenbauer, T. Eisenmann, M. Kuenzel, A. Kazzazi, Z. Chen and D. Bresser, *Sustainable Energy & Fuels*, 2020, **4**, 5387-5416.
- [28] J. W. Choi and D. Aurbach, *Nature Reviews Materials*, 2016, **1**, 16013.
- [29] X. Zuo, J. Zhu, P. Müller-Buschbaum and Y.-J. Cheng, *Nano Energy*, 2017, **31**, 113-143.
- [30] B. Ding, Z. Cai, Z. Ahsan, Y. Ma, S. Zhang, G. Song, C. Yuan, W. Yang and C. Wen, *Acta Metallurgica Sinica (English Letters)*, 2020, **34**, 291-308.
- [31] <https://www.industr.com/de/neues-anodenmaterial-steigert-leistung-von-lithium-ionen-akkus-2571395>, (accessed 03.06.2021).
- [32] H. Wiggers and J. Lyubina, Online, 2021.
- [33] W.-J. Zhang, *Journal of Power Sources*, 2011, **196**, 13-24.
- [34] C. P. Sandhya, B. John and C. Gouri, *Ionics*, 2014, **20**, 601-620.
- [35] T. Krauskopf, F. H. Richter, W. G. Zeier and J. Janek, *Chem Rev*, 2020, **120**, 7745-7794.
- [36] P. G. Bruce, L. J. Hardwick and K. M. Abraham, *MRS Bulletin*, 2011, **36**, 506-512.
- [37] J.-G. Zhang, W. Xu, J. Xiao, X. Cao and J. Liu, *Chemical Reviews*, 2020, **120**, 13312-13348.
- [38] Y. Jie, X. Ren, R. Cao, W. Cai and S. Jiao, *Advanced Functional Materials*, 2020, **30**.
- [39] Y. Kato, S. Hori, T. Saito, K. Suzuki, M. Hirayama, A. Mitsui, M. Yonemura, H. Iba and R. Kanno, *Nat. Energy*, 2016, **1**, 16030.
- [40] Y.-G. Lee, S. Fujiki, C. Jung, N. Suzuki, N. Yashiro, R. Omoda, D.-S. Ko, T. Shiratsuchi, T. Sugimoto, S. Ryu, J. H. Ku, T. Watanabe, Y. Park, Y. Aihara, D. Im and I. T. Han, *Nat. Energy*, 2020, **5**, 299-308.

- [41] W. Li, S. Lee and A. Manthiram, *Advanced materials*, 2020, **32**, e2002718.
- [42] M. Li and J. Lu, *Science*, 2020, **367**, 979-980.
- [43] J. Yoon, Lex in depth: a solid case for the next generation of batteries, <https://www.ft.com/content/c4e075b8-7289-4756-9bfe-60bf50f0cf66> (accessed 29.05.2021, 2021).
- [44] F. Flamary-Mespoulie, A. Boulineau, H. Martinez, M. R. Suchomel, C. Delmas, B. Pecquenard and F. Le Cras, *Energy Storage Mater.*, 2020, **26**, 213-222.
- [45] A. Fotouhi, D. Auger, L. O'Neill, T. Cleaver and S. Walus, *Energies*, 2017, **10**.
- [46] S. Dörfler, H. Althues, P. Härtel, T. Abendroth, B. Schumm and S. Kaskel, *Joule*, 2020, **4**, 539-554.
- [47] J. H. Kang, J. Lee, J. W. Jung, J. Park, T. Jang, H. S. Kim, J. S. Nam, H. Lim, K. R. Yoon, W. H. Ryu, I. D. Kim and H. R. Byon, *ACS Nano*, 2020, **14**, 14549-14578.
- [48] D. Liu, W. Zhu, J. Trottier, C. Gagnon, F. Barry, A. Guerfi, A. Mauger, H. Groult, C. M. Julien, J. B. Goodenough and K. Zaghib, *RSC Adv.*, 2014, **4**, 154-167.
- [49] L. de Biasi, A. O. Kondrakov, H. Geßwein, T. Brezesinski, P. Hartmann and J. Janek, *The Journal of Physical Chemistry C*, 2017, **121**, 26163-26171.
- [50] S. Zhang, J. Ma, Z. Hu, G. Cui and L. Chen, *Chemistry of Materials*, 2019, **31**, 6033-6065.
- [51] S. Klein, P. Barmann, T. Beuse, K. Borzutzki, J. E. Frerichs, J. Kasnatscheew, M. Winter and T. Placke, *ChemSusChem*, 2021, **14**, 595-613.
- [52] S. Klein, P. Barmann, O. Fromm, K. Borzutzki, J. Reiter, Q. Fan, M. Winter, T. Placke and J. Kasnatscheew, *Journal of Materials Chemistry A*, 2021, **9**, 7546-7555.
- [53] Y. K. Sun, S. T. Myung, B. C. Park, J. Prakash, I. Belharouak and K. Amine, *Nat Mater*, 2009, **8**, 320-324.
- [54] R. J. Clément, Z. Lun and G. Ceder, *Energy Environ. Sci.*, 2020, **13**, 345-373.
- [55] A. Sakuda, K. Ohara, T. Kawaguchi, K. Fukuda, K. Nakanishi, H. Arai, Y. Uchimoto, T. Ohta, E. Matsubara, Z. Ogumi, K. Kuratani, H. Kobayashi, M. Shikano, T. Takeuchi and H. Sakaebe, *Sci. Rep.*, 2018, **8**, 15086.
- [56] A. Sakuda, T. Takeuchi, K. Okamura, H. Kobayashi, H. Sakaebe, K. Tatsumi and Z. Ogumi, *Sci. Rep.*, 2014, **4**, 4883.
- [57] C. J. Hansen, J. J. Zak, A. J. Martinolich, J. S. Ko, N. H. Bashian, F. Kaboudvand, A. Van der Ven, B. C. Melot, J. Nelson Weker and K. A. See, *J. Am. Chem. Soc.*, 2020, **142**, 6737-6749.
- [58] Y. Kawasaki, H. Tsukasaki, T. Ayama, S. Mori, M. Deguchi, M. Tatsumisago, A. Sakuda and A. Hayashi, *ACS Appl. Energy Mater.*, 2021, **4**, 20-24.
- [59] F. Marchini, S. Saha, D. Alves Dalla Corte and J. M. Tarascon, *ACS Appl. Mater. Interfaces*, 2020, **12**, 15145-15154.
- [60] A. J. Martinolich, J. J. Zak, D. N. Agyeman-Budu, S. S. Kim, N. H. Bashian, A. Irshad, S. R. Narayan, B. C. Melot, J. Nelson Weker and K. A. See, *Chem. Mater.*, 2021, **33**, 378-391.
- [61] S. Saha, G. Assat, M. T. Sougrati, D. Foix, H. Li, J. Vergnet, S. Turi, Y. Ha, W. Yang, J. Cabana, G. Rousse, A. M. Abakumov and J.-M. Tarascon, *Nat. Energy*, 2019, **4**, 977-987.
- [62] A. Sakuda, K. Kuratani, T. Takeuchi, H. Kiuchi, T. Kawaguchi, M. Shikano, H. Sakaebe and H. Kobayashi, *Electrochem.*, 2017, **85**, 580-584.
- [63] A. Sakuda, T. Takeuchi, H. Kobayashi, H. Sakaebe, K. Tatsumi and Z. Ogumi, *Electrochem.*, 2014, **82**, 880-883.
- [64] A. Sakuda, T. Takeuchi, M. Shikano, H. Sakaebe and H. Kobayashi, *Front. Energy*, 2016, **4**.
- [65] R. Koerver, F. Walther, I. Aygün, J. Sann, C. Dietrich, W. G. Zeier and J. Janek, *J. Mater. Chem. A*, 2017, **5**, 22750-22760.
- [66] W. D. Richards, L. J. Miara, Y. Wang, J. C. Kim and G. Ceder, *Chem. Mater.*, 2016, **28**, 266-273.
- [67] W. Zhang, T. Leichtweiß, S. P. Culver, R. Koerver, D. Das, D. A. Weber, W. G. Zeier and J. Janek, *ACS Appl. Mater. Interfaces*, 2017, **9**, 35888-35896.
- [68] K. Xu, *Chemical Reviews*, 2004, **104**, 4303-4418.
- [69] S. S. Zhang, *Journal of Power Sources*, 2006, **162**, 1379-1394.
- [70] C. Xu, G. Yang, D. Wu, M. Yao, C. Xing, J. Zhang, H. Zhang, F. Li, Y. Feng, S. Qi, M. Zhuo and J. Ma, *Chem Asian J*, 2021, **16**, 549-562.
- [71] B. B. Owens, *Solid State Ionics*, 1981, **3-4**, 273-275.
- [72] V. S. Mallela, V. Ilankumaran and N. S. Rao, *Indian Pacing Electrophysiol J*, 2004, **4**, 201-212.
- [73] <https://www.electrive.com/2021/03/03/actually-we-are-the-pioneer-of-solid-state-battery/>, (accessed 07.06.2021).
- [74] X. Liu, X. Li, H. Li and H. B. Wu, *Chemistry – A European Journal*, 2018, **24**, 18293-18306.
- [75] J. Y. Hwang, S. T. Myung and Y. K. Sun, *Chem Soc Rev*, 2017, **46**, 3529-3614.
- [76] A. Pehlken, S. Albach and T. Vogt, *The International Journal of Life Cycle Assessment*, 2015, **22**, 40-53.
- [77] Y. Tian, G. Zeng, A. Rutt, T. Shi, H. Kim, J. Wang, J. Koettgen, Y. Sun, B. Ouyang, T. Chen, Z. Lun, Z. Rong, K. Persson and G. Ceder, *Chemical Reviews*, 2020, DOI: 10.1021/acs.chemrev.0c00767.
- [78] E. A. Wu, S. Banerjee, H. Tang, P. M. Richardson, J. M. Doux, J. Qi, Z. Zhu, A. Grenier, Y. Li, E. Zhao, G. Deysher, E. Sebti, H. Nguyen, R. Stephens, G. Verbist, K. W. Chapman, R. J. Clement, A. Banerjee, Y. S. Meng and S. P. Ong, *Nat Commun*, 2021, **12**, 1256.
- [79] F. Duffner, N. Kronemeyer, J. Tübke, J. Leker, M. Winter and R. Schmuch, *Nature Energy*, 2021, DOI: 10.1038/s41560-020-00748-8.
- [80] J. Wang, H. Wang, X. Zang, D. Zhai and F. Kang, *Batteries & Supercaps*, 2020, **4**, 554.

- [81] V. Anoopkumar, J. Bibin and T. Mercy, *ACS Applied Energy Materials*, 2020, **3**, 9478-9492.
- [82] A. Eftekhari, Z. Jian and X. Ji, *ACS Appl Mater Interfaces*, 2017, **9**, 4404-4419.
- [83] W. Zhang, Y. Liu and Z. Guo, *Science Advances*, 2019, **5**, 7412.
- [84] Q. Yao and C. Zhu, *Advanced Functional Materials*, 2020, **30**, 2005209.
- [85] H. Yuan, H. Li, T. Zhang, G. Li, T. He, F. Du and S. Feng, *Journal of Materials Chemistry A*, 2018, **6**, 8413-8418.
- [86] B. V. Lotsch and J. Maier, *J. Electroceramics*, 2017, **38**, 128-141.
- [87] F. Zheng, M. Kotobuki, S. Song, M. O. Lai and L. Lu, *J. Power Sources*, 2018, **389**, 198-213.
- [88] C. S. Nimisha, K. Y. Rao, G. Venkatesh, G. M. Rao and N. Munichandraiah, *Thin Solid Films*, 2011, **519**, 3401-3406.
- [89] S. Hong, Y. Wang, N. Kim and S. B. Lee, *Journal of Materials Science*, 2021, DOI: 10.1007/s10853-021-05832-2.
- [90] S. P. Ong, Y. Mo, W. D. Richards, L. Miara, H. S. Lee and G. Ceder, *Energy Environ. Sci.*, 2013, **6**, 148-156.
- [91] A. Bielefeld, D. A. Weber and J. Janek, *ACS Appl. Mater. Interfaces*, 2020, **12**, 12821-12833.
- [92] F. Walther, S. Randau, Y. Schneider, J. Sann, M. Rohnke, F. H. Richter, W. G. Zeier and J. Janek, *Chemistry of Materials*, 2020, **32**, 6123-6136.
- [93] S. P. Culver, R. Koerver, W. G. Zeier and J. Janek, *Advanced Energy Materials*, 2019, **9**.
- [94] Y. Xiao, L. J. Miara, Y. Wang and G. Ceder, *Joule*, 2019, **3**, 1252-1275.
- [95] Z. Wu, Z. Xie, A. Yoshida, Z. Wang, X. Hao, A. Abudula and G. Guan, *Renewable and Sustainable Energy Reviews*, 2019, **109**, 367-385.
- [96] W. Hou, X. Guo, X. Shen, K. Amine, H. Yu and J. Lu, *Nano Energy*, 2018, **52**, 279-291.
- [97] J.-J. Kim, K. Yoon, I. Park and K. Kang, *Small Methods*, 2017, **1**.
- [98] N. Kamaya, K. Homma, Y. Yamakawa, M. Hirayama, R. Kanno, M. Yonemura, T. Kamiyama, Y. Kato, S. Hama, K. Kawamoto and A. Mitsui, *Nature Materials*, 2011, **10**, 682-686.
- [99] Y. Kato, S. Hori and R. Kanno, *Adv. Energy Mater.*, 2020, **10**, 2002153.
- [100] A. Kuhn, O. Gerbig, C. Zhu, F. Falkenberg, J. Maier and B. V. Lotsch, *Phys. Chem. Chem. Phys.*, 2014, **16**, 14669-14674.
- [101] A. Kuhn, V. Duppel and B. V. Lotsch, *Energy & Environmental Science*, 2013, **6**, 3548-3552.
- [102] M. A. Kraft, S. P. Culver, M. Calderon, F. Böcher, T. Krauskopf, A. Senyshyn, C. Dietrich, A. Zevalkink, J. Janek and W. G. Zeier, *Journal of the American Chemical Society*, 2017, **139**, 10909-10918.
- [103] A. Gautam, M. Sadowski, M. Ghidui, N. Minafra, A. Senyshyn, K. Albe and W. G. Zeier, *Advanced Energy Materials*, 2021, **11**, 2003369.
- [104] A. Gautam, M. Sadowski, N. Prinz, H. Eickhoff, N. Minafra, M. Ghidui, S. P. Culver, K. Albe, T. F. Fässler, M. Zobel and W. G. Zeier, *Chemistry of Materials*, 2019, **31**, 10178-10185.
- [105] L. Zhou, N. Minafra, W. G. Zeier and L. F. Nazar, *Acc Chem Res*, 2021, DOI: 10.1021/acs.accounts.0c00874.
- [106] S. Ohno, T. Bernges, J. Buchheim, M. Duchardt, A.-K. Hatz, M. A. Kraft, H. Kwak, A. L. Santhosha, Z. Liu, N. Minafra, F. Tsuji, A. Sakuda, R. Schlem, S. Xiong, Z. Zhang, P. Adelhelm, H. Chen, A. Hayashi, Y. S. Jung, B. V. Lotsch, B. Roling, N. M. Vargas-Barbosa and W. G. Zeier, *ACS Energy Letters*, 2020, **5**, 910-915.
- [107] N. Tanibata, K. Noi, A. Hayashi and M. Tatsumisago, *RSC Advances*, 2014, **4**, 17120-17123.
- [108] N. Tanibata, K. Noi, A. Hayashi, N. Kitamura, Y. Idemoto and M. Tatsumisago, *ChemElectroChem*, 2014, **1**, 1130-1132.
- [109] S. Xiong, Z. Liu, L. Yang, Y. Ma, W. Xu, J. Bai and H. Chen, *Materials Today Physics*, 2020, **15**, 100281.
- [110] A. Kuhn, T. Holzmann, J. Nuss and B. V. Lotsch, *J. Mater. Chem. A*, 2014, **2**, 6100-6106.
- [111] J. A. Brant, D. M. Massi, N. A. W. Holzwarth, J. H. MacNeil, A. P. Douvalis, T. Bakas, S. W. Martin, M. D. Gross and J. A. Aitken, *Chemistry of Materials*, 2015, **27**, 189-196.
- [112] T. Holzmann, L. M. Schoop, M. N. Ali, I. Moudrakovski, G. Gregori, J. Maier, R. J. Cava and B. V. Lotsch, *Energy & Environmental Science*, 2016, **9**, 2578-2585.
- [113] T. Kaib, S. Haddadpour, M. Kapitein, P. Bron, C. Schröder, H. Eckert, B. Roling and S. Dehnen, *Chemistry of Materials*, 2012, **24**, 2211-2219.
- [114] G. Sahu, Z. Lin, J. Li, Z. Liu, N. Dudney and C. Liang, *Energy Environ. Sci.*, 2014, **7**, 1053-1058.
- [115] K. H. Park, D. Y. Oh, Y. E. Choi, Y. J. Nam, L. Han, J.-Y. Kim, H. Xin, F. Lin, S. M. Oh and Y. S. Jung, *Advanced Materials*, 2016, **28**, 1874-1883.
- [116] M. Joos, C. Schneider, A. Münchinger, I. Moudrakovski, R. Usiskin, J. Maier and B. V. Lotsch, *Journal of Materials Chemistry A*, 2021, DOI: 10.1039/D1TA04736A.
- [117] T. Holzmann, *Investigations on the Structure, Exfoliation Behavior and Electronic Properties of Layered Tin Sulfides*, LMU, Munich, 2016.
- [118] A. Haffner, T. Bräuniger and D. Johrendt, *Angew. Chem. Int. Ed. Engl.*, 2016, **55**, 13585-13588.
- [119] L. Toffoletti, H. Kirchhain, J. Landesfeind, W. Klein, L. vanWüllen, H. A. Gasteiger and T. F. Fässler, *Chem. Eur. J.*, 2016, **22**, 17635-17645.
- [120] D. Y. Oh, D. H. Kim, S. H. Jung, J.-G. Han, N.-S. Choi and Y. S. Jung, *J. Mater. Chem. A*, 2017, **5**, 20771-20779.
- [121] T. Ates, M. Keller, J. Kulisch, T. Adermann and S. Passerini, *Energy Storage Mater.*, 2019, **17**, 204-210.
- [122] M. Yamamoto, Y. Terauchi, A. Sakuda and M. Takahashi, *Sci. Rep.*, 2018, **8**, 1212.
- [123] Y. J. Nam, S.-J. Cho, D. Y. Oh, J.-M. Lim, S. Y. Kim, J. H. Song, Y.-G. Lee, S.-Y. Lee and Y. S. Jung, *Nano Letters*, 2015, **15**, 3317-3323.

- [124] D. H. S. Tan, A. Banerjee, Z. Deng, E. A. Wu, H. Nguyen, J.-M. Doux, X. Wang, J.-h. Cheng, S. P. Ong, Y. S. Meng and Z. Chen, *ACS Appl. Energy Mater.*, 2019, **2**, 6542-6550.
- [125] D. H. Kim, D. Y. Oh, K. H. Park, Y. E. Choi, Y. J. Nam, H. A. Lee, S.-M. Lee and Y. S. Jung, *Nano Lett.*, 2017, **17**, 3013-3020.
- [126] H. Tuller, in *Springer Handbook of Electronic and Photonic Materials*, eds. S. Kasap and P. Capper, Springer International Publishing, Cham, 2017, DOI: 10.1007/978-3-319-48933-9_11.
- [127] N. Wiberg, *Lehrbuch der Anorganischen Chemie*, 2008.
- [128] J. Maier, *Physical Chemistry of Ionic Materials*, John Wiley & Sons, Chichester, 2004.
- [129] Y. Gao, A. M. Nolan, P. Du, Y. Wu, C. Yang, Q. Chen, Y. Mo and S.-H. Bo, *Chemical Reviews*, 2020, **120**, 5954-6008.
- [130] H. Mehrer, *Fundamentals, Methods, Materials, Diffusion-Controlled Processes*, Springer, Berlin, Heidelberg, 1 edn.
- [131] P. Heitjans and J. Kärger, *Diffusion in Condensed Matter* Springer, Berlin, Heidelberg, 2 edn.
- [132] T. Krauskopf, S. P. Culver and W. G. Zeier, *Chemistry of Materials*, 2018, **30**, 1791-1798.
- [133] S. Muy, J. C. Bachman, L. Giordano, H.-H. Chang, D. L. Abernathy, D. Bansal, O. Delaire, S. Hori, R. Kanno, F. Maglia, S. Lupart, P. Lamp and Y. Shao-Horn, *Energy & Environmental Science*, 2018, **11**, 850-859.
- [134] G. H. Vineyard, *Journal of Physics and Chemistry of Solids*, 1957, **3**, 121-127.
- [135] K. Toyoura, Y. Koyama, A. Kuwabara, F. Oba and I. Tanaka, *Physical Review B*, 2008, **78**, 214303.
- [136] D. Di Stefano, A. Miglio, K. Robeyns, Y. Filinchuk, M. Lechartier, A. Senyshyn, H. Ishida, S. Spinnenberger, D. Prutsch, S. Lunghammer, D. Rettenwander, M. Wilkening, B. Roling, Y. Kato and G. Hautier, *Chem*, 2019, **5**, 2450-2460.
- [137] T. Krauskopf, S. P. Culver and W. G. Zeier, *Inorganic Chemistry*, 2018, **57**, 4739-4744.
- [138] R. Schlem, S. Muy, N. Prinz, A. Banik, Y. Shao-Horn, M. Zobel and W. G. Zeier, *Advanced Energy Materials*, 2020, **10**, 1903719.
- [139] J. Lee, A. Urban, X. Li, D. Su, G. Hautier and G. Ceder, *Science*, 2014, **343**, 519-522.
- [140] H. Ji, A. Urban, D. A. Kitchaev, D.-H. Kwon, N. Artrith, C. Ophus, W. Huang, Z. Cai, T. Shi, J. C. Kim, H. Kim and G. Ceder, *Nat. Commun.*, 2019, **10**, 592.
- [141] M. Brinek, C. Hiebl, K. Hogrefe, I. Hanghofer and H. M. R. Wilkening, *J Phys Chem C Nanomater Interfaces*, 2020, **124**, 22934-22940.
- [142] A. Lundén, *Solid State Communications*, 1988, **65**, 1237-1240.
- [143] H. L. Tuller, D. P. Button and D. R. Uhlmann, *Journal of Non-Crystalline Solids*, 1980, **40**, 93-118.
- [144] H. Stöffler, T. Zinkevich, M. Yavuz, A.-L. Hansen, M. Knapp, J. Bednarčík, S. Randau, F. H. Richter, J. Janek, H. Ehrenberg and S. Indris, *The Journal of Physical Chemistry C*, 2019, **123**, 10280-10290.
- [145] A.-K. Hatz, I. Moudrakovski, S. Bette, M. Terban, M. Joos, N. M. Vargas-Barbosa, R. E. Dinnebier and B. V. Lotsch, *Chem. Mater.*, 2021, submitted.
- [146] M. E. Orazem and B. Tribollet, *Electrochemical Impedance Spectroscopy*, John Wiley & Sons, Inc., Hoboken, New Jersey, 1 edn., 2008.
- [147] A. Lasia, in *Modern Aspects of Electrochemistry*, eds. B. E. Conway, J. O. M. Bockris and R. E. White, Springer US, Boston, 2002, DOI: 10.1007/0-306-46916-2_2, pp. 143-248.
- [148] *Impedance Spectroscopy*, John Wiley & Sons, Inc., Hoboken, New Jersey, 2 edn., 2005.
- [149] R. A. Huggins, *Ionics*, 2002, **8**, 300-313.
- [150] J. Maier, in *Modern Aspects Of Electrochemistry*, eds. C. Vayenas, R. E. White and M. E. Gamboa-Aldeco, Springer New York, New York, NY, 2007, DOI: 10.1007/978-0-387-46108-3_1, pp. 1-138.
- [151] J. T. S. Irvine, D. C. Sinclair and A. R. West, *Adv. Mater.*, 1990, **2**, 132-138.
- [152] J. Fleig and J. Maier, *J. Am. Ceram. Soc.*, 1999, **82**, 3485-3493.
- [153] R. S. R. LLC., The Inductance of Your Electrode, (accessed 23.03.2021, 2021).
- [154] G. J. Brug, A. L. G. van den Eeden, M. Sluyters-Rehbach and J. H. Sluyters, *J. Electroanal. Chem. Interf. Electrochem.*, 1984, **176**, 275-295.
- [155] J. Fleig, S. Rodewald and J. Maier, *Journal of Applied Physics*, 2000, **87**, 2372-2381.
- [156] J. Fleig, S. Rodewald and J. Maier, *Solid State Ionics*, 2000, **136-137**, 905-911.
- [157] J. Fleig, *Solid State Ionics*, 2002, **150**, 181-193.
- [158] J. C. Maxwell, *A Treatise on Electricity and Magnetism*, Clarendon Press, 1873.
- [159] T. van Dijk and A. J. Burggraaf, *physica status solidi (a)*, 1981, **63**, 229-240.
- [160] M. J. Verkerk, B. J. Middelhuis and A. J. Burggraaf, *Solid State Ionics*, 1982, **6**, 159-170.
- [161] J. Maier, *Berichte der Bunsengesellschaft für physikalische Chemie*, 1986, **90**, 26-33.
- [162] J. Fleig, *Solid State Ionics*, 2000, **131**, 117-127.
- [163] J. E. Bauerle, *Journal of Physics and Chemistry of Solids*, 1969, **30**, 2657-2670.
- [164] J. Fleig and J. Maier, *Journal of The Electrochemical Society*, 1998, **145**, 2081-2089.
- [165] J. Fleig and J. Maier, *Journal of the European Ceramic Society*, 1999, **19**, 693-696.
- [166] P. Bron, S. Dehnen and B. Roling, *Journal of Power Sources*, 2016, **329**, 530-535.
- [167] J. Maier, *Physical Chemistry of Ionic Materials*, John Wiley & Sons, Chichester, 2004.
- [168] A. Senocrote, I. Moudrakovski, G. Y. Kim, T.-Y. Yang, G. Gregori, M. Grätzel and J. Maier, *Angew. Chem. Int. Ed.*, 2017, **56**, 7755-7759.

-
- [169] Wei Gao and N. M. Sammes, *An Introduction to Electronic and Ionic Materials*, World Scientific Publishing Co. Pte. Ltd, Singapore, 1999.
- [170] R. Turner, *Magnetic Resonance Imaging*, 1993, **11**, 903-920.
- [171] R. Hoffman, Diffusion NMR, <http://chem.ch.huji.ac.il/nmr/techniques/other/diff/diff.html>, (accessed 01.05.2020).
- [172] E. O. Stejskal and J. E. Tanner, *Int. J. Chem. Phys.*, 1965, **42**, 288-292.
- [173] A. Einstein, *Ann. Phys.*, 1905, 549.

7 Appendix

7.1 List of Publications

7.1.1 First-authored

- Hatz, A.-K.; Calaminus, R.; Feijoo, J.; Treber, F.; T. Lenz, Blahusch, J.; Reichel, M.; N. M. Vargas-Barbosa; K. Karaghiosoff; Lotsch, B. V., Chemical stability and ionic conductivity of LGPS-type solid electrolyte tetra-Li₇SiPS₈ after solvent treatment, *ACS Energy Mater.*, 2021 submitted.
- A.-K. Hatz; I. Moudrakovski; S. Bette; M. Terban; M. Etter; M. Joos; N. M. Vargas-Barbosa; R. E. Dinnebier; Lotsch, B. V, Fast Water-Assisted Lithium Ion Conduction in Restacked Lithium Tin Sulfide Nanosheets, *Chem. Mater.*, 2021 submitted.
- Haffner, A.; Hatz, A.-K.; Zeman, O. E. O.; Hoch, C.; Lotsch, B. V.; Johrendt, D., Polymorphism and fast Potassium-Ion Conduction in the T5 Supertetrahedral Phosphidosilicate KSi₂P₃, *Angew. Chem. Int. Ed. Engl.* **2021**, *60* (24), 13641-13646.
- S. Harm, A.-K. Hatz, C. Schneider, C. Hoefler, C. Hoch and B. V. Lotsch, Finding the Right Blend: Interplay Between Structure and Sodium Ion Conductivity in the System Na₅AlS₄-Na₄Si₄, *Frontiers in Chemistry*, 2020, **8**.
- Haffner, A.-K. Hatz, I. Moudrakovski, B. V. Lotsch and D. Johrendt, Fast Sodium-Ion Conductivity in Supertetrahedral Phosphidosilicates, *Angew. Chem. Int. Ed. Engl.*, 2018, **57**, 6155-6160.

7.1.2 Second-authored

- S. Ohno, T. Bernges, J. Buchheim, M. Duchardt, A.-K. Hatz, M. A. Kraft, H. Kwak, A. L. Santhosha, Z. Liu, N. Minafra, F. Tsuji, A. Sakuda, R. Schlem, S. Xiong, Z. Zhang, P. Adelhelm, H. Chen, A. Hayashi, Y. S. Jung, B. V. Lotsch, B. Roling, N. M. Vargas-Barbosa and W. G. Zeier, How Certain Are the Reported Ionic Conductivities of Thiophosphate-Based Solid Electrolytes? An Interlaboratory Study, *ACS Energy Lett.*, 2020, 910-915.
- Haffner, A.-K. Hatz, C. Hoch, B. V. Lotsch and D. Johrendt, Synthesis and Structure of the Sodium Phosphidosilicate Na₂SiP₂, *Eur. J. Inorg. Chem.*, 2020, **7**, 617-621.
- S. Harm, A.-K. Hatz, I. Moudrakovski, R. Eger, A. Kuhn, C. Hoch and B. V. Lotsch, Lesson Learned from NMR: Characterization and Ionic Conductivity of LGPS-like Li₇SiPS₈, *Chem. Mater.*, 2019, **31**, 1280-1288.
- C. Lermer, A. Senocrate, I. Moudrakovski, T. Seewald, A.-K. Hatz, P. Mayer, F. Pielnhofer, J. A. Jaser, L. Schmidt-Mende, J. Maier and B. V. Lotsch, Completing the Picture of 2-(Aminomethylpyridinium) Lead Hybrid Perovskites: Insights into Structure, Conductivity Behavior, and Optical Properties, *Chem. Mater.*, 2018, **30**, 6289-6297.

7.2 Contributions to Conferences

7.2.1 Oral presentations

- 17.10.2018**
Functional Oxide Seminar, MPI FKF, Stuttgart
A.-K. Hatz, I. Moudrakovski and B. V. Lotsch, Water assisted lithium ion conductivity in thin films of restacked tin sulfide nanosheets
- 29.-31.07.2019**
NIM Summer Retreat, Kloster Seon
A.-K. Hatz, I. Moudrakovski and B. V. Lotsch, A Detective's work: Taking a close look on ion conduction in restacked lithium tin sulfide nanosheets
Best Presentation Award
- 04.02.2020**
FestBatt Cluster Workshop, Maria Laach
A.-K. Hatz, R. Calaminus, R. Eger, S. Harm, M. A. Plaß, C. Schneider, N. M. Vargas-Barbosa and B. V. Lotsch, In search of further development, upscaling and understanding of sulfides based solid electrolytes

7.2.2 Poster presentations

- 23.–25.11.2016**
Bunsenkolloquium, Solid–state–Batteries II, Frankfurt
A.-K. Hatz, T. Holzmann, I. Moudrakovski, V. Duppel and B. V. Lotsch, A Novel Thin Film Li-ion Conductor by Solution Based Deposition of 2D Nanosheets in the System Li-Sn-S
- 18.–23.06.2017**
Solid State Ionics 21, Padua
A.-K. Hatz, T. Holzmann, I. Moudrakovski, K. Szendrei, V. Duppel and B. V. Lotsch Water–assisted Li-ion Conductivity in Thin Films of Restacked $\text{Li}_{0.4}\text{H}_{0.4}[\text{Sn}_{0.8}\text{S}_{1.6}\text{O}_{0.4}]$ -Nanosheets
- 22.–23.02.2018**
Dechema, 27th ATC, Frankfurt
A. Haffner, A.-K. Hatz, I. Moudrakovski, B. V. Lotsch and D. Johrendt, Supertetrahedral phosphidosilicates as fast sodium ion conductors
Best Poster Award
- 14.–16.11.2018**
Bunsenkolloquium, Solid–state–Batteries III, Frankfurt
A.-K. Hatz, L. German, C. Schneider, R. Dinnebier and B. V. Lotsch, Towards new Li solid electrolytes by substitution of Sn with the transition metals Zr/Hf in the superionic conductor $\text{Li}_2\text{Sn}_2\text{S}_5$
- 16.–21.06.2019**
Solid State Ionics 22, Pyeong Chang
S. Harm, A.-K. Hatz, I. Moudrakovski, R. Eger, A. Kuhn, C. Hoch and B. V. Lotsch A Lesson Learned from NMR: Characterization and Ionic Conductivity of LGPS-like Li_7SiPS_8
- 04.-06.09.2019**
The Future of NIM, Tutzing
A.-K. Hatz, L. German, C. Schneider, R. Dinnebier and B. V. Lotsch, Towards novel Li solid electrolytes by substitution of Sn in the superionic conductor $\text{Li}_2\text{Sn}_2\text{S}_5$ with the transition metals Zr/Hf

7.3 Curriculum Vitae

Aug. 2016 – data PhD candidate at the department of Nanochemistry at Max Planck Institute for Solid State Research and the Ludwig-Maximilians-Universität Munich

Oct. 2013 – May 2016 Master of Science in Chemistry at the LMU Munich

Oct. 2010 – Sept. 2013 Bachelor of Science in Chemistry and Biochemistry at the LMU Munich

2008 – 2010 Gymnasium Tutzing, higher education entrance qualification

2007 – 2008 Visiting student at Yanqing Highschool (第一职业学校, 庆县, 北京)

Prizes and awards

2018 Poster prize of the Journals of Solid State Chemistry at ATC2018

2016 Award of the Dr. Klaus Römer Foundation for Master thesis

2011–2016 Scholarship of the German National Academic Foundation